# Models for the analysis and simulation of glide-symmetric metasurface waveguides

Boris Fischer

Sorbonne Université
Laboratoire Génie Electrique et Electronique de Paris



Ecole doctorale SMAER (ED 391)
Sciences mécaniques, acoustique, électronique et robotique de Paris

# Models for the analysis and simulation of glide-symmetric metasurface waveguides

**Thèse de doctorat d'électronique**

*Doctorant:*
Boris Fischer

*Directeur:*
Prof. Guido Valerio

Présentée et soutenue publiquement le 28 octobre 2022

Devant un jury composé de :

| | |
|---|---|
| Mme. Agnès Maître<br>Professeure des universités, Sorbonne Université | Présidente du jury |
| M. Antonio Clemente<br>Research scientist (HDR), CEA-Leti Grenoble | Rapporteur |
| M. Simon Horsley<br>Associate professor, University of Exeter | Rapporteur |
| M. Renaud Loison<br>Professeur des universités, INSA Rennes | Examinateur |
| M. Guido Valerio<br>Professeur des universités, Sorbonne Université | Directeur de thèse |
| M. Julien Sarrazin<br>Maître de conférences (HDR), Sorbonne Université | Membre invité |

*This work is dedicated to Professor Hélène Dumontet,*
*who passed away just a few weeks before my thesis defense.*

*Beyond her outstanding research career, she dedicated herself to her teaching duties.*
*She is the mother of the Cursus Master Ingénierie in France,*
*an educational establishment of excellence.*

*She expected the best of her students,*
*because she had the deepest respect for them.*

**Abstract**

A periodic waveguide is glide-symmetric (G-S) when it is invariant after a translation of half a period and a mirroring operation with respect to the propagation plane. G-S metasurface waveguides meet some of the challenges of modern wireless communication systems. Among other features, they offer wide-band behavior for high data rates through reduced frequency dispersion. However, they are difficult to model due to strong multi-modal coupling between the metasurfaces. In this thesis, we develop new modeling tools to better understand the properties of G-S parallel-plate waveguides (PPWs) and to accelerate their design. We use these tools for the design of a reconfigurable phase-shifter in integrated glide symmetry (GS).

A mode-matching method derives the dispersion equation of corrugated and holey PPWs. Solving this equation yields the Brillouin diagram of the waveguides, in which the first dispersion curve is almost linear due to the low-dispersive behavior of GS. We show that this behavior is due to the impact of the Floquet harmonics in the dispersion equation. This allows us to prove the linearity of the G-S dispersion curve by simplifying all the frequency dependencies in the dispersion equation. This works as long as one or two modes are enough to describe the field variation at the surface of the corrugations, which is the case for small and medium corrugations. Additionally, it is shown that a G-S corrugated PPW with small gap has the same dispersive behavior as a non-glide-symmetric (nGS) waveguide with half the period and twice the gap.

In order to accelerate the parametric studies of G-S devices, a quasi-static homogenization method is developed for metasurface waveguides. The dispersion equation is simplified and solved in the quasi-static regime. A closed-form formula for the effective refractive index of corrugated and holey PPWs is found. Given the low dispersion of GS, this formula accurately describes the waveguide over a wide band. Additionally, we combine it to an in-house two-dimensional finite-element method in order to incorporate the modal information of arbitrary hole shapes. This formula extends the realm of study for holey metasurface waveguides, opening the door to unusual shapes and to fast structure optimization in terms of density or anisotropy.

The second opportunity offered by this quasi-static homogenization technique is analytical insight into the differences between G-S and nGS waveguides. The impact of the different structure parameters on the refractive index can be evaluated analytically. It is shown that the ratio between the G-S and nGS refractive index can be tuned with the dielectrics in the waveguide. Moreover, closed-form expressions of the quasi-static fields are derived. By integrating the transverse fields across the unit cell, an effective Bloch impedance is defined for PPWs with square and circular holes. Combined with the closed-form index formula, we prove analytically that this increases the effective Bloch impedance and the permeability of the effective medium in the G-S waveguide.

Finally, the quasi-static index formula is used to design a reconfigurable contactless phase-shifter. This phase-shifter is based on changing the effective hole depth of the holes in the metasurface waveguide. The quasi-static formula helps find the structure that is most sensitive to the hole depth. These findings are transposed to substrate-integrated holes, which allow full integration of the device in dielectric layers and improve its performance. In order to enable contactless reconfiguration, the holes are closed with high-impedance surfaces, that are moved to change the

effective hole depth while preventing any leakage. Simulations show that a low-loss 360° phase-shifter can be implemented in a ridge gap waveguide, making use of electromagnetic bandgap technology. The design comprises a special transition, developed to feed the phase-shifter with a rectangular waveguide, with an insertion loss of 0.4 dB.

**Résumé**

Quand un guide d'onde périodique est invariant après une translation d'une demi-période et une réflexion, il forme une symétrie glissée (SG). Les guides à métasurfaces avec SG répondent à certaines des exigences contemporaines de systèmes de communications sans fils, de part leur faible dispersion fréquentielle. Cependant, ils sont difficiles à modéliser en raison du fort couplage multi-modal qui naît entre les métasurfaces. Dans cette thèse, nous développons de nouveaux outils pour mieux comprendre les propriétés de la SG et pour accélérer la conception de guides plans avec SG. Nous appliquons ces outils pour concevoir un déphaseur reconfigurable intégré avec SG.

Une méthode de raccordement multi-modal permet d'obtenir l'équation de dispersion de guides plans avec SG, pour des métasurfaces à corrugations et pour des métasurfaces à trous. En résolvant cette équation, on trouve un premier mode dont la courbe de dispersion est presque linéaire, en raison de la faible dispersion avec SG lorsque les métasurfaces sont proches. Nous montrons que ce comportement est dû à l'impact des harmoniques dans l'équation de dispersion. Cela nous permet de prouver que la courbe de dispersion est linéaire uniquement avec SG. Ces simplifications sont valides lorsque un ou deux modes suffisent à décrire la variation des champs à la surface des corrugations, ce qui est le cas pour des corrugations fines et moyennes. De plus, il est démontré que lorsque l'intervalle entre les métasurfaces est petit, le guide à corrugations avec SG a le même comportement dispersif qu'un guide sans SG qui aurait un intervalle double et une demi périodicité.

Une méthode d'homogénéisation quasi-statique est développée pour des guides à métasurfaces. L'équation de dispersion est simplifiée et résolue dans le régime quasi-statique. On aboutit à une formule analytique de l'indice de réfraction équivalent pour des guides plans à SG, avec corrugations ou avec trous. Cette formule est valide sur une large bande de fréquences, grâce à la faible dispersion fréquentielle. Afin de l'étendre à des formes de trous arbitraires, nous développons une méthode des éléments finis en deux dimensions, afin de pouvoir incorporer les informations modales de ces trous dans la formule. Cette formule ouvre le champ des possibles pour ces guides à métasurfaces creuses, rendant concevable l'optimisation rapide de ces structures et l'exploration de nouvelles formes de trous.

Cette méthode d'homogénéisation quasi-statique rend également possible l'étude analytique des différences entre guides avec ou sans SG, notamment afin d'observer l'impact des différents paramètres de la structure sur l'indice de réfraction. Ainsi, on démontre que l'on peut contrôler le rapport entre les indices avec ou sans SG en changeant la densité des diélectriques dans le guide. De plus, nous dérivons des expressions analytiques pour les champs quasi-statiques à partir de la formule de l'indice. En intégrant ces champs entre les deux métasurfaces, on peut définir une impédance équivalente de Bloch pour des guides avec trous carrés ou circulaires. On arrive à montrer analytiquement que l'impédance de Bloch et la perméabilité relative du matériau de propagation équivalent sont augmentées par la SG.

Enfin, la formule d'indice quasi-statique est utilisée pour concevoir un déphaseur à reconfiguration sans contact, basée sur le changement de profondeur des trous. La formule permet de trouver rapidement les trous qui offrent la meilleure sensibilité à ce changement de profondeur. On peut transposer ces études à des métasurfaces diélectriques dans lesquelles les trous sont recréés avec des vias métalliques, ce qui facilite la fabrication du guide. Afin de permettre une reconfiguration sans contact,

les trous sont fermés par des métasurfaces à haute impédance. En éloignant ces métasurfaces, on change la profondeur des trous. Cette technologie permet de concevoir un déphaseur de 360° avec faibles pertes. Le prototype inclut une transition conçue pour connecter ce déphaseur à un guide rectangulaire, avec perte d'insertion de 0.4 dB.

# Acknowledgements

A PhD doesn't last three years. That is because it doesn't start on day 1, but much earlier. It is the extension of years of building up, of acquiring tools, but must importantly of gaining inspiration. Science has its own appeal, but inspiration is human. And as such, teachers are the primary source of inspiration. The best of them manage to combine their passion to the respect for their students. Such people inspired or even encouraged me to pursue my studies ever further: Michel Ivrlac at TUM, Hélène Dumontet at Sorbonne Université, my master thesis superviser Alexander Paulus, Stéphane Frigot during preparatory school, Mrs.Asin for her math classes in high-school,... The list could go on and on.

This PhD would not have happened without the trust and financial support of the doctoral school Smaer (Sciences Mécaniques, Acoustique, Electronique et Robotique de Paris), directed by Djimédo Kondo and Faiz BEN AMAR. Within the framework of Sorbonne Université, they maintain a fruitful framework for the training of young scientists. A special mention goes to setting up a very insightful PhD Day, where the interdisciplinary nature of the doctoral school was successfully highlighted.

Only five months into this PhD, the Covid pandemic broke out. It had a huge influence on the work pace, communication with colleagues, prospects of conferences... Yet, and despite home-office, it is once more human relationships that have made this journey worth it. Chloé Hamel-Dellenbach and Loris Baudet have worn the lab on their shoulders. Despite that, Chloé still found the energy to check in with me on a regular basis, making me feel that I belonged to a working organization. Loris encouraged me to come back to the campus to take badminton lessons with him, which triggered the reconnection with the lab in the aftermath of the lockdown.

My fellow PhD office colleagues (Sheno, Rudy, Alexandro,...) made it worth staying for more than just lessons. And not just them. The people that work at the former Laboratoire Electronique et Electromagnétisme (which merged into the GeePs when I arrived), lead by Aziz Benlarbi-Delai, have created something unique. A place where one must not fight in order to survive, a place where generosity is valued as much as expertise. The heart of such a place lives on with researchers like Muriel Darces, Aurélie Gensbittel, Cyril Dahon, Julien Sarrazin, ... and many others.

But this journey was made even richer by all the students that I had the honor of working with. Sylvain Feruglio trusted me with teaching assignments, in association with Bruce Denby, Dimitri Galayko and Jeanne Treuttel. This has been a life-

saver. In the first months of the PhD journey, one's sense of purpose can be put to the test. There is no better cure than being asked for help, and unfortunately the pandemic made students in need of unprecedented support. Their courageous struggling in these difficult times has been an inspiration.

Despite the lockdowns, the international research community found ways to preserve the collaboration channels that are vital for any kind of scientific progress. Parts of this work are the result of interesting discussions with Simon Horsley from Exeter University, Oscar Quevedo-Teruel from KTH, Francisco Mesa from Universidad de Sevilla, and many more talented scientists that push the limits of knowledge further with their every-day efforts. Nothing is achieved alone.

But there is one person without whom this thesis would simply not exist. Guido Valerio took me in for a research internship in my third Bachelor year. He introduced me to the field of electromagnetics before I even knew who Maxwell was. At the same time, I discovered the fascinating topic of metasurface waveguides. All my subsequent educational choices were motivated by this hopeful question: maybe one day Guido would accept to be my PhD supervisor? After my master's degree, once again, he gave me the unique opportunity of working with him on the topic of higher symmetries, for which he is one of the leading experts. I benefited from his dynamism at international conferences, from his wide network in universities all over the world, and from his experience of the research world. There is no other way of saying it: he is an *excellent* supervisor. During these three years, I was completely free, yet never lost. Guido is the reason why today, I dare to consider myself not only a student, but also a researcher. I rejoice at the thought of many more students having the chance of working with Guido Valerio.

In usual times, the impact of family on one's professional life is obvious, because they are the ones to whom we come each night after work. In Covid times, family is everything. The absence of a proper office environment can only be compensated by increased personal relationships. My parents and my family-in-law have been simply marvelous, offering me advice, literally cool working places, and many of these heart-warming moments that recharge the batteries.

At times, I was a mess. Pursuing a PhD is mostly demanding because it is requires surpassing yourself on a psychological level. These three years have been an emotional roller-coaster. I usually hate roller-coasters. And yet, I enjoyed this one immensely, because at every single step, my wife Alexandra has been at my side. *"Love lifts us up where we belong."*

# Introduction

**Modern wireless communications** Recent years have seen a large development of communicating devices in the framework of what is commonly called the internet of things (IoT) [1], [2]. Ongoing deployment of the 5G mobile network has given rise to multiple innovations, from autonomous vehicles [3], [4] and augmented reality [5] to enhanced medical monitoring [6], and at a larger scale to connected cities [7] and smart industry [8]. The ever-growing spatial industry is in need of communication tools as well, both for deep-space exploration as for improved airborne and satellite links [9], [10]. These networks deal with high data rates, at the scale of multigigabits per second [11]. Limited space-time-frequency ressources force subsequent communication systems to be upgraded to millimeter waves, where there are still available band candidates [12]. Consequently, these systems must meet following requirements:

- operation at high frequencies where large bandwidths enable high-speed communication;
- high energy return to compensate the attenuation of high-frequency wave propagation;
- low-cost manufacturing and conformability in order to meet the plurality of the IoT market demand.

This is just the start: the commercialization of the 5G network is well underway, already sparking research initiatives about 6G, with talk about terabits per second at millimeter waves and beyond [13]–[16]. Therefore, it is urgent to develop millimeter wave communication devices that easily conform to the ever-growing diversity of connected applications.

**Directive antenna systems** Considering a wireless communication link, the Friis radio link formula [17, p. 673] indicates that the power received by an antenna decreases with increasing operating frequency. In order to compensate this attenuation, the involved antennas need to concentrate the power in the direction of the communication link, by means of high gain and beamforming [18]. While beamforming arrays exist in integrated waveguide technology, e.g. Butler matrices made of microstrip or coplanar waveguides [19], they are expensive and bulky. An alternative to beamforming arrays are lens antennas [20]. A radiating structure is associated to a lens that focuses the beam

in the desired direction. Moving the radiating structure along the lens shifts the beam direction.

The wave propagation properties of the lenses are due to a controlled variation of the refractive index within the lens. In order to obtain the desired index variation, the lens is made of different dielectric layers, in an onion-like arrangement [21]–[23], or the effective density of single medium is controlled through its porosity [24], [25]. But this involves complex and expensive manufacturing. Moreover, propagation in dielectric media results in higher losses within the antenna. That is why the use of metamaterials instead of dielectric materials is of great interest for the design of lens antennas.

**Metamaterials** Metamaterials are made of a periodic arrangement of geometric structures, called cells. The size of one cell is much smaller than the wavelength of the harmonic fields propagating through the metamaterial. As such, a metamaterial can be represented by an homogeneous medium with equivalent propagation characteristics, that may not be achievable with available homogeneous media [26]. These equivalent propagation characteristics are dependent on the geometrical features of the cells. Therefore, by changing the geometry of the cells, the desired characteristics are obtained without changing the propagation medium. The latter shall be low-loss, in the best case vacuum. Consequently, metamaterials are a low-loss alternative for refractive index grading by changing the geometric features of the cells. If the cell geometry is simple, e.g. a hole drilled in a perfectly electrically conducting (PEC) plate, manufacturing can be low-cost. If the arrangement of cells is kept in one plane, one speaks of metasurfaces. Metasurfaces are more conformable than their three-dimensional (3-D) counterparts, they require simpler design methods, and they are easier to manufacture [27]. As such, planar lens antennas have been designed by grading the index, not by a change of dielectric, but by replacing one face of the waveguide by a metasurface with varying impedance impedance surface [28]–[31].

Although metasurfaces are a promising technology of modern wireless communication systems, they must satisfy one additional constraint: the propagation characteristics must be stable over a large bandwidth. Indeed, despite simple control of the propagation characteristics with the cell geometry, this is usually valid at one observation frequency. Like most homogeneous materials, metamaterials tend to be dispersive i.e., their propagation characteristics change with frequency. If this happens within the frequency bandwidth used for high-speed communication, the transmitted information becomes distorted, or even partially or fully lost. Therefore, one seeks for metamaterials with low dispersion.

**Higher symmetries** In recent years, low-dispersive behavior has been observed for metasurface waveguides displaying special symmetries, called higher symmetries. The idea is that the periodicity of the cells is broken from one cell to the next by introducing an additional geometrical operation e.g., rotation (twist symmetry) or mirroring (glide

symmetry). It is observed that periodic waveguides with such higher symmetries have less dispersion than their non-symmetric counterparts [32], [33]. This lower dispersion leads to an isotropic behavior over a wider frequency band for isotropic structures [34]. In contrast, anisotropic performances can be boosted by adding a higher symmetry [35]. Additionally, a higher effective refractive index is achievable [33], [36]. These features in the passbands of higher-symmetric waveguides are combined to a shifting of the stopbands that occur for periodic metasurfaces. The first stopbands disappear, while stopbands at higher frequencies become larger [37]. These features make higher-symmetric waveguides interesting candidates for low-loss microwave devices for energy-efficient, low-cost and small-sized communication systems.

Early papers describe the impact of higher symmetries in waveguiding structures [38]–[40], while recent works propose multi-modal models to characterize wave propagation in the presence of higher symmetries [41]–[43]. Although these models fully describe the higher-symmetric structures, they require an iterative solver in the last step of getting the effective propagation characteristics as a function of frequency. In other words, there are no analytical expressions for the effective propagation properties of higher-symmetric structures. This prevents from further understanding why a simple shift or rotation in the cell arrangement leads to such unusual features. Moreover, it complicates the design of electromagnetic devices, given that a parametric study is involved each time special propagation characteristics are needed [44].

New models are needed to give further insight about the particular features of higher symmetries, and to accelerate the design of higher-symmetric devices. This thesis focuses on such models for glide-symmetric (G-S) metasurface waveguides. The first goal is getting some understanding about the special propagation features enabled by glide symmetry (GS). The second goal is the development of fast and reliable techniques to characterize the effective properties of G-S waveguides, with as little numerical input as possible.

**Outline** In chapter 1 of this thesis, higher-symmetric metasurfaces are presented. The main uses of metasurfaces in microwave devices are overviewed. Higher symmetries are explained, and the generalized Floquet theorem for GS is presented. The applications of GS in recent years are listed. The limits of existing modeling methods for G-S waveguides are reviewed.

One of these modeling methods is developed in chapter 2: the mode-matching method (MMM), which has been generalized for G-S waveguides in [45]. Modal decompositions of the fields, combined with the enforcement of boundary conditions, yield the dispersion equation of the waveguide. The MMM is applied to a corrugated parallel-plate waveguide (PPW), which yields a one-dimensional (1-D) periodicity. The case of two-dimensional (2-D) periodicity is addressed too: a PPW pierced with an array of holes. Both G-S and mirror-symmetric structures are considered.

Chapter 3 is an attempt to prove that GS reduces the dispersion of metasurface waveguides. It relies on the accurate dispersion equation derived with the MMM, and

shows that the corresponding dispersion curve can be linearized under certain restrictions. This linearization highlights the impact of the different harmonic waves on the dispersive behavior of the waveguide, depending on their field symmetry. The resulting effect of GS on the form of the dispersion equation is studied for both corrugated and holey PPWs.

The second challenge, namely the development of a fast modeling technique, is covered in chapter 4. Given the low dispersion of G-S waveguides, it is sufficient to solve the dispersion equation at one particular frequency to characterize wave propagation over a wide band. In the quasi-static regime, a closed-form formula for the effective refractive index is found, both for corrugated and holey PPWs. It is fully analytic for canonical hole shapes, and can be combined to a 2-D finite element method for arbitrary hole shapes.

This quasi-static framework is further exploited in chapter 5. The closed-form formula of the effective refractive index gives further analytical insight about the higher refractive index achieved for some G-S waveguides. Moreover, a quasi-static characteristic waveguide impedance is defined, which allows for the full extraction of the effective constitutive parameters. As a consequence, G-S features such as their higher magnetic density are demonstrated.

Finally, chapter 6 puts the quasi-static refractive index formula to use for the design of a reconfigurable metasurface waveguide. High-impedance metasurfaces are used to change the effective depth of the holes in a contactless mechanical reconfiguration. The quasi-static formula is shown to be useful for the design of more complicated structures, such as substrate-integrated hole (SIH) metasurfaces, which are more easily manufacturable. Such a reconfigurable unit cell can then be used for the implementation of reconfigurable phase-shifter.

The conclusion of this thesis puts forward the advances made during the last three years of research. Possible uses of the developed methods are summarized, as well as their limitations. It also elaborates on potential research perspectives based on this work.

Appendices contain details about the techniques and mathematical derivations made throughout this report, with one appendix corresponding to each chapter. A list of figures follows the table of contents. A review of the mathematical conventions, acronym definitions and literature references used throughout this report are found in the last pages.

# Table of contents

**Abstract** i

**Résumé** iii

**Acknowledgements** v

**Introduction** vii

**Table of contents** xi

**List of figures** xv

**1 Glide-symmetric metasurface waveguides for modern communications 1**
1.1 Metasurfaces in microwave devices . . . . . 1
1.1.1 Reflection, transmission, and radiation . . . . . 2
1.1.2 Surface-wave metasurfaces . . . . . 6
1.1.3 Towards reconfigurability . . . . . 8
1.2 Fundamental concepts of higher symmetries . . . . . 8
1.2.1 Periodicity and Floquet condition . . . . . 9
1.2.2 Brillouin diagram . . . . . 10
1.2.3 Floquet harmonics and Floquet theorem . . . . . 11
1.2.4 Higher symmetries . . . . . 12
1.2.5 Generalized Floquet theorem for glide symmetry . . . . . 17
1.3 Properties and applications of glide-symmetric metasurfaces . . . . . 18
1.3.1 Electromagnetic bandgap applications . . . . . 18
1.3.2 Increased refractive index and low dispersion . . . . . 22
1.3.3 Isotropic and anisotropic behavior . . . . . 25
1.3.4 Effective magnetic response . . . . . 25
1.3.5 The challenge of modeling glide-symmetric metasurface waveguides 26

**2 Mode-matching and dispersion equation of glide-symmetric waveguides 27**
2.1 Corrugated parallel-plate waveguide . . . . . 28
2.1.1 Mirrored and glide-symmetric corrugated parallel-plate waveguide 28
2.1.2 Modal decomposition of the fields . . . . . 29

2.1.3 Mode-matching in the glide-symmetric parallel-plate waveguide . . 30
2.1.4 Mode-matching in the mirror-symmetric parallel-plate waveguide . 32
2.1.5 Dispersion equations . . . . . 33
2.1.6 Numerical solution: truncation of higher modes and harmonics . . 33
2.1.7 Validity of mode-matching for corrugated parallel-plate waveguides 35
2.2 Holey parallel-plate waveguide . . . . . 37
2.2.1 Holey glide-symmetric parallel-plate waveguide . . . . . 37
2.2.2 Modal decomposition of the fields . . . . . 37
2.2.3 Mode-matching in the glide-symmetric holey parallel-plate waveguide 40
2.2.4 Dispersion equation . . . . . 43
2.2.5 Example: rectangular holes . . . . . 45
2.2.6 Example: circular holes . . . . . 46
Chapter landmarks . . . . . 50

**3 Study of the low-dispersive behavior of glide symmetry 51**
3.1 Low-dispersive behavior enabled by glide symmetry . . . . . 52
3.2 Impact of the harmonics in the parallel-plate waveguide with small gap . . 55
3.2.1 Dismissal of odd-order harmonics . . . . . 55
3.2.2 Coupling of symmetric and antisymmetric harmonics . . . . . 56
3.3 Equivalence of glide-symmetric and non-glide structures . . . . . 59
3.4 Linearization of the reduced glide-symmetric dispersion equation . . . . . 61
3.4.1 Simplified glide-symmetric dispersion equation . . . . . 61
3.4.2 Linearization for 1 corrugation mode . . . . . 62
3.4.3 Linearization for 2 corrugation modes . . . . . 63
3.4.4 Validity of linearized dispersion models . . . . . 64
3.5 Holey parallel-plate waveguides . . . . . 69
Chapter landmarks . . . . . 71

**4 Quasi-static homogenization of glide-symmetric waveguides 73**
4.1 Quasi-static refractive index formula of a corrugated parallel-plate waveguide 74
4.1.1 Low-frequency reformulation of the dispersion equation . . . . . 75
4.1.2 Analytic low-frequency refractive index . . . . . 77
4.1.3 Numerical study of the low-frequency effective refractive index . . 78
4.1.4 Quasi-static homogenization of non-glide parallel-plate waveguides 81
4.2 Quasi-static refractive index formula of a holey parallel-plate waveguide . 82
4.2.1 Distinction between fundamental and higher harmonics . . . . . 82
4.2.2 Simplification of the matrix coefficients . . . . . 83
4.2.3 Total dispersion matrix . . . . . 86
4.2.4 Quasi-static homogenization . . . . . 87
4.3 Canonical hole shapes . . . . . 88
4.3.1 Dismissal of the modes without dispersive effect . . . . . 88
4.3.2 Modal functions for rectangular and circular holes . . . . . 88
4.3.3 Convergence and time gain . . . . . 89
4.3.4 Parametric studies . . . . . 92

4.3.5 Optimization of glide-symmetric holey parallel-plate waveguides . . 96
4.4 Arbitrary hole shapes . . . 100
4.4.1 Numerical extension with finite-element method . . . 100
4.4.2 Shape optimization . . . 106
4.4.3 Exploration of imaginative shapes . . . 108
4.5 Frequency validity . . . 112
4.5.1 Dependency on the frequency dispersion and the effective density . 112
4.5.2 Improving the frequency validity . . . 113
Chapter landmarks . . . 117

**5 Quasi-static analysis of the properties of glide symmetry 121**
5.1 Effective refractive index . . . 122
5.1.1 Dominant modes in the quasi-static regime . . . 122
5.1.2 Does glide symmetry systematically increase the refractive index? . 124
5.1.3 Giant refractive index for asymptotically small gap . . . 129
5.2 Effective constitutive material parameters . . . 133
5.2.1 Impedance matching by means of holey metasurfaces . . . 133
5.2.2 Quasi-static fields . . . 144
5.2.3 Bloch impedance and impedance matching . . . 150
5.2.4 Effects of glide symmetry on the constitutive parameters . . . 162
Chapter landmarks . . . 170

**6 Substrate-integrated reconfigurable glide-symmetric phase-shifter 173**
6.1 Preliminary quasi-static studies for reconfiguration . . . 175
6.1.1 Refractive index sensitivity to the hole depth . . . 175
6.1.2 Improved sensitivity with substrate-integrated holes . . . 177
6.1.3 Necessity of glide symmetry for hole depth impact . . . 182
6.1.4 Extension of the Bloch impedance to substrate-integrated holes . . 184
6.2 Design of the reconfigurable unit cell . . . 185
6.2.1 Reconfiguring the hole depth with high-impedance metasurfaces . . 185
6.2.2 High-impedance metasurfaces . . . 186
6.2.3 Reconfigurable unit cell in the Ku band . . . 193
6.3 Design of a reconfigurable phase-shifter . . . 198
6.3.1 Holey ridge gap waveguide . . . 199
6.3.2 Variable phase-shift . . . 203
6.3.3 Feed . . . 207
6.3.4 Prototyping . . . 209
Chapter landmarks . . . 218

**Conclusion 219**

**List of published and upcoming papers 225**

**A Details to the review of glide-symmetric metasurfaces 227**

A.1 Spectrum of multiple periodic cells . . . 227
A.2 Proof of the generalized Floquet theorem . . . 228
A.3 Modeling of glide-symmetric metasurface waveguides . . . 229
A.3.1 Full-wave solvers . . . 229
A.3.2 Existing analytic methods . . . 230
A.3.3 Multi-modal transfer matrix method . . . 233
A.3.4 Mode-matching method . . . 237

**B Details to the mode-matching computations 239**
B.1 Mode-matching for the glide-symmetric corrugated parallel-plate waveguide 239
B.2 Gradient theorem for the simplification of the dispersion equation . . . 244
B.3 Projected modal functions for canonical holes . . . 245
B.3.1 Mode-matching for rectangular holes . . . 245
B.3.2 Mode-matching for circular holes . . . 246

**C Details to the dispersion study computations 253**
C.1 Linearization of the reduced glide-symmetric dispersion equation . . . 253
C.1.1 Simplification of the dispersion matrix . . . 253
C.1.2 One mode: dismissal of all higher-harmonic terms . . . 255
C.1.3 Two modes: simplification of the dispersion matrix coefficients . . . 256
C.2 Equivalence of glide and non-glide corrugated parallel-plate waveguides . . . 257

**D Details to the quasi-static homogenization computations 259**
D.1 Quasi-static dispersion equation for the corrugated parallel-plate waveguide 259
D.2 Approximations of the refractive index for the corrugated waveguide . . . 260
D.2.1 Reduction to a diagonal matrix . . . 261
D.2.2 Reduction to an arrowhead matrix . . . 261
D.2.3 Numerical comparison of the derived low-frequency index formulas 263
D.3 Reducing the number of modes for canonical holes . . . 263
D.4 Homogenization for rectangular and circular holes . . . 265
D.4.1 Homogenization for rectangular holes . . . 265
D.4.2 Homogenization for circular holes . . . 267
D.5 Finite element method for cylindrical waveguide . . . 269

**E Details to the quasi-static properties of glide-symmetric waveguides 275**
E.1 Constitutive parameter retrieval from the S-parameters . . . 275
E.2 Study of the Bloch impedance for square holes . . . 277
E.2.1 TEM fields in the integration plane for square holes . . . 277
E.2.2 Bloch voltage impact of odd-order harmonics . . . 278

**F Design considerations for the feed of the phase-shifter 281**

**Notations, conventions and acronyms 287**

**References 291**

# List of figures


1.1 Examples of artificial periodic surfaces found in literature. . . . . 3
1.2 Examples of reconfigurable metasurfaces found in literature. . . . . 8
1.3 Periodicity and information available in the Brillouin diagram. . . . . 10
1.4 Top view of different types of glide-symmetric metasurface waveguides. . . . . 13
1.5 Examples of planar glide symmetry. . . . . 14
1.6 Models of periodically-loaded coaxial lines with different higher symmetries. . 16
1.7 Magnetic field profile for different glide shifts in a dented transmission line. . 19
1.8 Prototypes of glide-symmetric electromagnetic bandgap devices designed at KTH Royal Institute of Technology. . . . . 20
1.9 Concept and prototype of a planar Luneburg lens made of holey glide-symmetric metasurfaces. . . . . 23

2.1 Metallic corrugated parallel-plate waveguides. . . . . 28
2.2 Colormap of the number of corrugations modes required for the convergence of the glide-symmetric dispersion curve. . . . . 34
2.3 Brillouin diagrams for corrugated parallel-plate waveguides, computed with CST or with the mode-matching method. . . . . 36
2.4 Holey glide-symmetric parallel-plate waveguide under study. . . . . 38
2.5 Holey glide-symmetric parallel-plate waveguide with rectangular holes. . . . . 45
2.6 Brillouin diagrams of parallel-plate waveguides with different rectangular holes, computed with CST or with the mode-matching method. . . . . 47
2.7 Holey glide-symmetric parallel-plate waveguide with circular holes. . . . . 48
2.8 Brillouin diagrams of glide-symmetric parallel-plate waveguides with circular holes, computed with CST or with the mode-matching method. . . . . 49

3.1 Linearization index to reflect the dispersive behavior of a waveguide. . . . . 53
3.2 Comparison of the dispersive behavior of non-glide-symmetric and glide-symmetric structures. . . . . 54
3.3 Comparison of the terms associated to different Floquet harmonics, in the 1-mode dispersion equation of a corrugated parallel-plate waveguide. . . . . 58
3.4 Equivalent glide-symmetric and non-glide-symmetric corrugated parallel-plate waveguides. . . . . 60
3.5 Brillouin diagrams of the equivalent corrugated parallel-plate waveguides. . . 61

3.6 Brillouin diagram for the glide-symmetric structure, comparing the dispersion curves obtained with CST, the 2-mode and 1-mode models, and the linearized models. . . . 68
3.7 Impact of the odd-order harmonics on the Brillouin diagram of glide-symmetric parallel-plate waveguides with square holes. . . . 71

4.1 Parametric study of the low-frequency effective refractive index as a function of the corrugation width. . . . 79
4.2 Frequency validity of the quasi-static refractive index of a glide-symmetric corrugated parallel-plate waveguide. . . . 80
4.3 Comparison of the glide-symmetric and non-glide-symmetric low-frequency effective refractive index as a function of the corrugation width. . . . 81
4.4 Quasi-static Floquet harmonics in the spectral domain. . . . 84
4.5 Holey glide-symmetric parallel-plate waveguides with canonical holes. . . . 89
4.6 Refractive index convergence as the number of modes increases for glide-symmetric parallel-plate waveguides with rectangular holes. . . . 91
4.7 Computation time of the quasi-static refractive index as a function of the number of modes, comparing the quasi-static closed-form formula with the mode-matching method approximation. . . . 92
4.8 Low-frequency refractive index for glide-symmetric parallel-plate waveguides with rectangular holes, as function of the hole dimensions, computed with the closed-form formula or with CST. . . . 94
4.9 Low-frequency refractive index for parallel-plate waveguides with square holes, computed with the closed-form formula as a function of the propagation direction and the hole size. . . . 95
4.10 Low-frequency refractive index for glide-symmetric parallel-plate waveguides with rectangular holes, as function of the propagation direction, computed with the closed-form formula or with CST. . . . 95
4.11 Low-frequency refractive index for glide-symmetric parallel-plate waveguides with circular holes, as function of the hole dimensions, computed with the closed-form formula or with CST. . . . 96
4.12 Low-frequency refractive index for parallel-plate waveguides with circular holes, as function of the propagation direction, computed with the closed-form formula. . . . 97
4.13 Maximizing the effective refractive index of a glide-symmetric parallel-plate waveguide by varying the square hole size. . . . 98
4.14 Maximizing the effective refractive index of a glide-symmetric parallel-plate waveguide by varying the circular hole size. . . . 99
4.15 Maximizing the anisotropy of a holey glide-symmetric parallel-plate waveguide by varying the dimensions of the rectangular holes. . . . 101
4.16 Quasi-static refractive index as a function of the square hole size, computed with the FEM-based modal study. . . . 103

4.17 Quasi-static refractive index as a function of the circular hole radius, computed with the FEM-based modal study. . . . 104
4.18 Normalized error for the quasi-static projected modal functions computed with the FEM, for the first TM mode of a square hole. . . . 105
4.19 Different cases of super-ellipses. . . . 106
4.20 Quasi-static refractive index of holey glide-symmetric parallel-plate waveguides with super-elliptic holes, as function of the super-ellipse order. . . . 107
4.21 Eigensolutions of the square holes with an inner square pin, computed with the two-dimensional FEM. . . . 109
4.22 Quasi-static refractive index of a holey glide-symmetric parallel-plate waveguide with square pins, computed with the FEM-based modal study. . . . 110
4.23 Eigensolutions of the 10-branch star-shaped holes, computed with the two-dimensional FEM. . . . 111
4.24 Quasi-static refractive index of a holey glide-symmetric parallel-plate waveguide with star-shaped holes, computed with the FEM-based modal study. . . . 112
4.25 Frequency-dependent error between the quasi-static refractive index computed with the closed-form formula or with CST. . . . 114
4.26 Brillouin diagrams of glide-symmetric parallel-plate waveguides with square holes, computed with the full mode-matching method, the quasi-static formula, and the frequency-improved formula. . . . 118
4.27 Brillouin diagrams of glide-symmetric parallel-plate waveguides with circular holes, computed with the full mode-matching method, the quasi-static formula, and the frequency-improved formula. . . . 119

5.1 Coefficients of the most excited hole modes in the quasi-static regime of holey parallel-plate waveguides with canonical hole shapes. . . . 123
5.2 Two-modes quasi-static refractive index of holey parallel-plate waveguides, as function of the hole size. . . . 124
5.3 Quasi-static refractive index of holey parallel-plate waveguides depending on the gap and hole dielectrics. . . . 128
5.4 Quasi-static refractive index of holey parallel-plate waveguides, varying both gap and hole dielectrics. . . . 129
5.5 Glide-symmetric vs. non-glide-symmetric quasi-static effective refractive index computed for extreme gap values and overlapping holes. . . . 130
5.6 Glide-symmetric quasi-static effective refractive index computed for zero gap values and overlapping holes. . . . 131
5.7 Glide-symmetric quasi-static effective refractive index computed for extreme gap values and almost-overlapping holes. . . . 132
5.8 Impedance matching of a dielectric slab with holey metasurfaces. . . . 134
5.9 Transmission line model of the simulated CST waveguide. . . . 135
5.10 Line impedance of the holey parallel-plate waveguide computed from CST with the reflection technique. . . . 136

5.11 CST-simulated unit cell of a holey glide-symmetric parallel-plate waveguide with square holes. . . . 137
5.12 Constitutive parameter retrieval from the transfer-matrix of holey parallel-plate waveguides with square holes. . . . 140
5.13 Refractive index and impedance convergence for different number of cells, from the transfer-matrix of holey parallel-plate waveguides with square holes. 141
5.14 Effective impedance of holey parallel-plate waveguides as function of the hole size, comparing the reflection method and the transfer-matrix method. . . . 142
5.15 Fields of the glide-symmetric holey parallel-plate waveguide, computed analytically or with CST. . . . 149
5.16 Impedance integration paths in the holey glide-symmetric parallel-plate waveguide with square holes. . . . 150
5.17 Fields in one unit cell of the glide-symmetric holey parallel-plate waveguide with square holes, computed analytically in the quasi-static regime. . . . 152
5.18 Fields in one unit cell of the non-glide-symmetric holey parallel-plate waveguide with square holes, computed analytically in the quasi-static regime. . . . 153
5.19 Fields in one unit cell of the glide-symmetric holey parallel-plate waveguide with circular holes, computed analytically in the quasi-static regime. . . . 154
5.20 Fields in one unit cell of the non-glide-symmetric holey parallel-plate waveguide with circular holes, computed analytically in the quasi-static regime. . . 155
5.21 Constitutive parameter retrieval for holey parallel-plate waveguides with square holes, computed in the quasi-static framework or with CST. . . . 156
5.22 Constitutive parameter retrieval for holey parallel-plate waveguides with circular holes, computed in the quasi-static framework or with CST. . . . 157
5.23 CST models for the impedance matching simulations with holey glide-symmetric parallel-plate waveguides. . . . 159
5.24 Impedance-matching by means of non-glide-symmetric square holes. . . . 160
5.25 Impedance-matching by means of glide-symmetric square holes. . . . 160
5.26 Impedance-matching by means of glide-symmetric circular holes. . . . 161
5.27 Quasi-static reflection coefficient as function of the feeding dielectric parameters. 162
5.28 Two-modes quasi-static Bloch impedance of holey parallel-plate waveguides as function of the hole size. . . . 163
5.29 Quasi-static fields in the impedance integration plane for a holey parallel-plate waveguide with square holes. . . . 169

6.1 Sensitivity of the refractive index to the hole depth of glide-symmetric parallel-plate waveguides with different shapes and fillings. . . . 176
6.2 Holey glide-symmetric parallel-plate waveguides unit cells, PEC or SIH. . . . 178
6.3 Refractive index as a function of frequency, for different hole depths of glide-symmetric parallel-plate waveguides with circular holes (PEC or SIH). . . . 179
6.4 Refractive index variation of holey glide-symmetric parallel-plate waveguides when changing the hole depth from $h = 0.5\,\mathrm{mm}$ to $h = 2.5\,\mathrm{mm}$. . . . 181

6.5 Refractive index as a function of frequency, for different hole depths of glide-symmetric parallel-plate waveguides with square substrate-integrated holes with or without pin. . . . 182
6.6 Refractive index variation of SIH parallel-plate waveguides when changing the hole depth from $h = 0.5\,\text{mm}$ to $h = 2.5\,\text{mm}$, glide-symmetric vs. non-glide-symmetric designs. . . . 183
6.7 Impedance matching by means of substrate-integrated holes. . . . 184
6.8 Illustration of the contactless reconfiguration concept. . . . 186
6.9 CST capture of the high-impedance surface mushroom unit cell. . . . 187
6.10 Brillouin diagram of the mushroom high-impedance surface for different air layers. . . . 188
6.11 Brillouin diagram of the mushroom high-impedance surface for different substrate thicknesses. . . . 188
6.12 Brillouin diagram of the mushroom high-impedance surface for different patch sizes. . . . 189
6.13 Brillouin diagram of the mushroom high-impedance surface for different via radii. . . . 189
6.14 Brillouin diagram of the mushroom high-impedance surface for different substrate permittivities. . . . 190
6.15 Brillouin diagram of the mushroom high-impedance surface for different cell periodicities. . . . 190
6.16 Brillouin diagram of the high-impedance surface covered with a holey PEC plate, comparing shifted and aligned designs. . . . 192
6.17 Stopband of the high-impedance surface covered with a square SIH, as function of the air layer between the high-impedance surface and SIH substrates. 194
6.18 Brillouin diagram of the mushroom high-impedance surface. . . . 195
6.19 Brillouin diagram of the contactless reconfigurable unit cell tuned for operation in the Ku band. . . . 197
6.20 Concept of a reconfigurable phase-shifter in ridge gap waveguide technology. . 198
6.21 Ridge gap waveguide for lateral wave confinement. . . . 200
6.22 Dispersion diagram of the EBG mushroom unit cell, for different permittivities above the mushrooms. . . . 201
6.23 S-parameters of the ridge gap waveguide depending on the number of EBG mushroom rows. . . . 201
6.24 Magnitude of the electric field in the ridge gap waveguide simulated in CST. . 202
6.25 S-parameters of the ridge gap waveguide depending on the ridge via's distance from the edge. . . . 202
6.26 S-parameters of the ridge gap waveguide depending on the separation between ridge vias. . . . 203
6.27 Metallic and dielectric losses in the ridge gap waveguide. . . . 204
6.28 S-parameter of the reconfigurable waveguide with 8 tapered cells for impedance-matching. . . . 205
6.29 Metallic and dielectric losses of the reconfigurable waveguide with tapered holes. 206

6.30 Perpendicular transition from a standard rectangular waveguide to the ridge gap waveguide. . . . . 208
6.31 Metallic and dielectric losses of the rectangular waveguide to ridge gap waveguide transition. . . . . 209
6.32 Perspective views of the phase-shifter prototype modeled in CST. . . . . 211
6.33 Description of the different layers of the prototype. . . . . 212
6.34 Pictures of the coaxial-to-rectangular transition used to feed the prototype. . 216

D.1 Low-frequency effective refractive index as a function of the corrugation width, for different matrix inverse simplification methods. . . . . 264

F.1 Brillouin diagram of the EBG unit cell with glide-symmetric holes in metallic plates. . . . . 282
F.2 Leakage reduction in a rectangular waveguide made of two pieces with glide-symmetric holes. . . . . 283
F.3 Leakage reduction in the staircase feed made of two pieces, with glide-symmetric holes. . . . . 284
F.4 S-parameters of the feed, with holes and corrugations to prevent leakage, in the case of perfect contact. . . . . 285

# Chapter 1

# Glide-symmetric metasurface waveguides for modern communication systems

The topic of higher symmetries, and more specifically glide symmetry (GS), is bound to the larger subject of metasurfaces. This chapter gives an overview of what higher symmetric metasurfaces are, what they are being used for, and how they can be modeled.

First, metasurfaces are defined in section 1.1. A broad classification according to their applications is proposed. In order to lay the background for metasurface waveguides, the focus is put on metasurfaces used as a support for surface waves.

Then, the notion of higher symmetry is presented in section 1.2. The range of existing higher symmetries is rapidly covered. The study of the glide-symmetric (G-S) operator leads to a generalized version of the Floquet theorem. This theorem has direct consequences on the field symmetries and the dispersive properties of waveguides displaying these symmetries. These properties can be captured in the Brillouin diagram, which is one of the main visualization tools used throughout this report.

If higher symmetries have been such a hot topic of research in the last decade, it is because they offer a wide variety of enhanced propagation properties. Section 1.3 lists these different properties, combined with concrete application examples in microwave devices. Classical analysis methods of metasurfaces are shown to be limited when higher symmetries are implemented. Therefore, new methods have been developed to accelerate and improve the design of higher-symmetric structures. A more detailed review of existing modeling techniques for higher-symmetric waveguides is found in appendix A.3.

## 1.1 Metasurfaces in microwave devices

Metamaterials are a periodic arrangement of sub-wavelength elements that modify the electromagnetic field. The average phenomenon observable at a wavelength scale results in propagation features that are not found in nature, such as negative refractive index [46]

or double negative effective media [47]. Metamaterials such as split-ring resonator arrays, built with non-magnetic materials, can create magnetic responses by concentrating the field at critical locations [48]. Non-reciprocal media can be created for the design of isolators or circulators without being confronted to the challenge of ferrite integration [49]. For example, an external biasing field can be used to excite transistor-loaded ring resonators, thus simulating an artificial ferrite material, including its Faraday rotation features. Another application is the emulation of high refractive indexes without the use of lossy dielectrics [50]. Due to the shift between different layers, the geometry can be seen as higher-symmetric as defined in section 1.2. However, in the context of this thesis, higher symmetries will be considered only for waveguides made of metasurfaces.

Metasurfaces are the two-dimensional equivalent of these metamaterials, printed or embedded in a metallic or dielectric layer. The periodic arrangement is two-dimensional (2-D), or even one-dimensional (1-D). This arrangement enables the control of the tangential fields around the surface, and therefore offers full control of the total fields in the space around. Due to their reduced thickness, metasurfaces yield lower absorption than bulky metamaterials. They are conformable and can be easily integrated, ensuring a vast range of applications [51]. That is why the research of metasurfaces has kept growing, starting with periodic arrays of wires for reflectors and polarizers in the second half of the 20th century, metallic patches or slots arranged periodically for plane wave filters since the 2000s, and are now being extended towards reconfigurability [51].

In the following, some broad categories of metasurface applications are presented. Although multiple classifications are possible, one can distinguish between metasurfaces used for radiation and beam manipulation, in opposition to metasurfaces designed to guide waves. As such, here we divide metasurfaces more according to their applications than according to their nature. The goal is not to draw an extended review of metasurface applications, but rather to give some insight about how metasurfaces can be used, and to focus on surface-wave metasurfaces. More extensive reviews can be found in [52], [51], [53] or [47].

### 1.1.1 Reflection, transmission, and radiation

**Frequency-selective surfaces** Frequency-selective surface (FSS) are a well-known example of 2-D arrangements of periodic elements. A combination of resonant components, coming in all sorts of shapes, filters or transmits the incident waves at particular frequencies. Equivalent circuit models show that metallic patches offer capacitive responses (low-pass), whereas slots offer inductive responses (high-pass). They can be arranged in single-layer or multi-layer structures. Techniques such as fractal patterns have been researched for multi-band uses and size reduction of these FSSs [53], as illustrated in Fig. 1.1a. This diversity of designs have made FSSs good candidates for filters, polarizers, beam splitters, and semi-reflective mirrors. Antenna reflectors can be made more efficient by using FSSs: two separate feeds at different frequencies use the FSS either in reflection or in transmission to aim at the reflector with the same direction [58]. FSSs are also used as filters to build narrow bandpass radomes [59].

(a) Fractal frequency-selective surface [54].

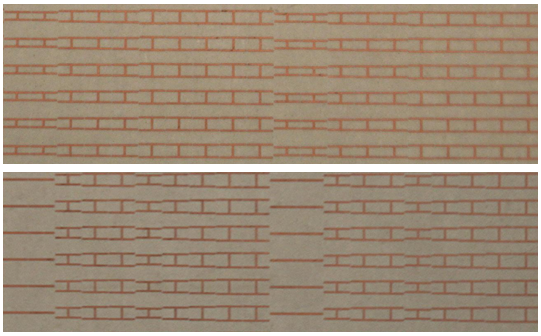

(b) Top and bottom of a reflectionless bian-isotropic Huygen's metasurface [55].

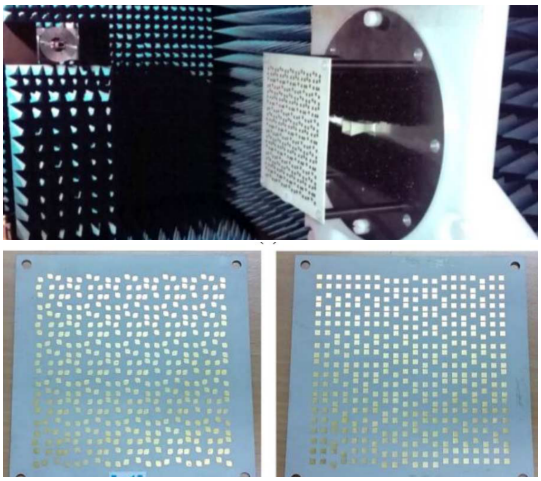

(c) Top and bottom of a circular-polarizing transmit-array with measurement setup [56].

(d) Endfire repeater reflect-array [57].

Figure 1.1: Examples of artificial periodic surfaces found in literature.

In FSSs, the periodic elements have dimensions of the order of the wavelength, which creates strong resonances. It can thus be argued that FSSs are not metasurfaces in the sense that they do not exhibit effective bulk behavior due to subwavelength elements [26].

**Huygen's metasurfaces** When illuminating a metasurface with a given source, the incident wave excites subwavelength magnetic and/or electric dipoles on the metasurface, creating a determined current density distribution. Arbitrary current distributions can be obtained with distributed metallic loops or strips, which create the required surface reactance, as illustrated in Fig. 1.1b. Applying Huygen's principle, the reflected or transmitted wave can be shaped arbitrarily. That is why such applications are named Huygen's metasurfaces [60]. They can be used for reflectionless refraction at extreme angles, bi-anisotropic responses, gain enhancement of antennas (similarly to a lens), or

arbitrary radiation patterns. The metasurface is then described with an effective surface impedance tensor, or with a dimensionless susceptibility tensor. Surface impedance tensors relate the electric and magnetic tangential field components on the metasurface. From this, an effective homogeneous media can be defined, which corresponds to the reflected or transmitted wave when the metasurface is illuminated by a plane wave [47].

**Transmit and reflect arrays** The combination of several layers of metasurfaces offers further degrees of freedom to tune the transmission properties. As an example, an artificial dielectric layer of high density can be obtained with a 2-D array of metallic patches, which is low-loss due to the absence of actual high-density dielectric materials. When several layers are placed in front of an antenna, the resulting field concentration of the transmitted wave improves its front-to-back ratio [61]. More generally, the behavior of antennas can be tuned by so-called transmit-arrays. The idea is to link the unit cells of two stacked metasurfaces with tunable phase-shifters, such that the phase distribution at the aperture is completely controlled. By illuminating such a metasurface with the antenna feed, one can shape the direction and the polarization of the radiation at will in a very directive way [62]. Compact transmit-arrays have been presented for linear-to-circular polarizers [56] (shown in Fig. 1.1c) and multi-beam radiation [63], [64]. Compared to classical phased arrays, transmit-arrays offer compact wide-aperture solutions for the purpose of portable localisation [65]. They also enable larger power-handling with lower insertion losses in the phase-shifting network [18],with all-metallic layers avoiding the use of dielectrics [66].

Conversely, a metasurface can change the radiation pattern of a feeder by using its reflective properties. Reflect-arrays combine the advantages of phased arrays and reflectors, by having a simple low-loss feed illuminate a metasurface with locally-controllable reflection phase. For example, highly-directive dual-polarized reflection is achieved in [67], or a linear-to-circular polarizer in [68]. The reflection can even be totally cancelled, like in the repeater built in [57] (shown in Fig. 1.1d). It is made of a metallic metasurface with uneven grooves, yielding endfire reflection for indoor signal transmission.

Designing such reflect-arrays presents important challenges, notably avoiding abrupt geometrical changes between adjacent cells to reduce losses [69], [70]. In [71], a unit cell is presented that comes back to its initial form after a 360° cycle, avoiding such geometrical changes throughout the reflect-array, and also exhibiting a large operating bandwidth. Moreover, several designs offering the same phase profile may be possible, making it difficult to efficiently synthesize the "best" reflect-array design [72]. Updated models that take into account the varying coupling between adjacent unit cells are needed, especially in the case of reconfigurability [73]. Equivalent circuit models are an efficient way to accelerate the design of particular cells [74]. Artificial neural networks can also be used, but they require large training databases [75], [76].

Another interesting reflective metasurface design involves placing a high-impedance surface (HIS) in the ground plane of an integrated antenna. The HIS simulates an artificial magnetic conductor, that is a surface where the tangential magnetic component vanishes. Replacing the perfectly electrically conducting (PEC) of the ground plane with

perfectly magnetically conducting (PMC) enables to reduce the slab thickness by image theory, and thus to increase the bandwidth of the antenna [47]. However, in practice the HIS has its own additional thickness. More importantly, its elements are not resonant over an infinite band, and so it behaves as a magnetic conductor in limited ranges of frequency and incident angles. This illustrates how, on top of the challenge of creating an arbitrary current density pattern, metasurfaces are subjected to a bandwidth problem due to the resonant nature of its periodic elements [52, Chap. 3].

Bandwidth issues can be tackled by building active metasurfaces, which are not bound by Foster's reactance theorem – which states that reactance must increase with frequency in passive media. A metasurface whose reactance decreases with frequency can be built with active elements. Then, when coupled with the increasing reactance of a passive element, it can reduce the radar scattering of this element over a large bandwidth, acting as a cloak [77].

**Radiating metasurfaces** Instead of having the waves being transmitted in a single refraction process, a partially-reflective metasurface can be used to confine the waves in a resonant cavity. The waves propagate along the leaky metasurface in a multiple reflection process with low attenuation, such that a large aperture is created from a small non-directive feeding point, yielding high directive antennas. The resulting antenna is called Fabry-Perot cavity antenna [47]. The thickness of the Fabry-Perot cavity can be reduced by combining the partially-reflective metasurface with a HIS instead of the metallic ground plane. High directivity with increased bandwidth is achievable when the cavity is closed with several FSSs with different resonance frequencies [78]. The shape of the radiated beam can be shaped by the spatial control of the metasurface leakage, for example to obtain conical beams, Bessel beams, or a focused focal point. Given that these antennas make use of leaky waves, they are often used for beam-steering by means of frequency-scanning. However, beam-steering at a single frequency can also be achieved with tunable partially-reflection surfaces (mechanically, electronically, or with variable bias field).

Another type of metasurface-based radiators are holographic antennas. Here, the feeding point is conceived to directly excite a surface-wave along the metasurface. The surface impedance of this metasurface is then modulated. This creates an effective magnetic current distribution, which is optimized to generate an arbitrary radiation pattern aperture field. For example, circularly polarized beams can be obtained with a spiral modulation of the metasurface impedance. But linear polarizations are possible too, dual-polarized antennas, or multiple beams at different frequencies [47]. However, such antennas have a bandwidth problem, because the designed radiation properties occur when the wavelength of the cylindrical surface wavefront matches the modulation period of the surface impedance. Bandwidth can be increased with a non-uniform modulation period, such that it fits different frequencies at different locations [79].

### 1.1.2 Surface-wave metasurfaces

In the previous paragraphs, metasurfaces have been used with normal or oblique field incidence for their particular transmission of reflection features. In the case of holographic metasurfaces, surface waves were used, but with the aim of radiation. In this section, metasurfaces are designed such that the waves are guided along the surface without radiation. Special propagation features can be obtained, such as negative-index surfaces [46], illusion of surface deformations [80], or perfect absorbers with zero reflection [81]. Metasurfaces make it even possible to confine surface waves along a single propagation path [82]. The use of metasurfaces as surface waveguides notably offers the possibility of index-grading for conformable microwave devices [83]. The use of transformation optics makes it possible to combine surface deformations with isotropic low-profile index-grading, to create effective index profiles not achievable in practice, such as index singularities [84]. With this technique, devices such as Eaton's lens [84], Maxwell Fish-eye lens [85], or cloaking domes [86] have been designed. Such designs can be applied to large low-profile planar antennas deformed for reasons of aerodynamics or manufacturing.

Index-grading is the main motivation for the structures studied in this thesis. In the following, fundamental notions of surface-wave metasurfaces related to this topic are broadly presented.

**Surface waves** Surface waves have been a long-studied topic, independently of metasurfaces, given that a non-radiating wave propagating at the interface between different media is useful for the transmission of electromagnetic (EM) energy and information. For example, Zenneck and Sommerfeld-Goubau waves have been studied since the beginning of the 20th century, as well as their relation to wave incidence with no reflection (Brewster angle) [87]. The higher the reactance of the surface, the more confined the transverse magnetic (TM) fields at the surface [87]. Adding corrugations is shown to be a way to increase the reactance without the use of dielectric coating, and thus with reduced losses. In [88], Brillouin illustrates this by creating such a boundary condition with thin corrugations, motivated by the need of slow waves for linear electron accelerators. The phenomena of guiding wave by means of metasurfaces are often described with concepts inherited from optics or acoustics. Some of those main concepts are addressed next.

**Spoof surface plasmon polaritons** The use of metallic periodic metasurfaces instead of dielectric interfaces to guide surface waves has been put in relation with the optical theory of surface plasmon polaritons (SPPs). SPPs have been originally studied at optical frequencies, enabling surface waves at a simple metal-air interface [89]. SPPs are surface waves which interact with the free electrons of a conducting surface, usually metal. The surface charges become resonant as they interact with the wave. This leads to field concentration at the surface, and thus to the channelling of the wave. The SPP wavenumber becomes larger than in free-space, hence an exponential decrease of the field perpendicularly to the surface, as it lives outside the light cone. For this phenomenon to occur, the interface must be between media of opposite permittivity [90].

At the interface between air and smooth PEC, no surface waves are possible. Nonetheless, adding sub-wavelength periodic alterations can lead to the appearance of bound states that are similar to SPPs. The propagation features of these states are controlled by the periodic alterations, e.g., holes or corrugations. These alterations can be shown to be equivalent to an effective dielectric layer, whose homogenized constitutive parameters enable SPPs. That is why these emulations of SPPs are called spoof SPPs [91].

**Hard and soft surfaces** The concept of hard and soft surfaces comes from acoustics in order to describe particular boundary conditions for waves propagating along a considered surface. Implementing such boundary conditions with metasurfaces makes it possible to extend these notions to electromagnetic theory [92]. Given a particular propagation direction, one defines the transverse and the longitudinal tangential field components. On the one hand, for a soft boundary condition, both transverse field components are ideally zero. In terms of surface impedance, this is equivalent to a longitudinal impedance $Z_\mathrm{l} \to \infty$ – such that there are no longitudinal currents (i.e. no transverse magnetic component $H_\mathrm{t} = 0$) – and a transverse impedance $Z_\mathrm{t} = 0$ – such that $E_\mathrm{t} = 0$. On the other hand, a surface is hard if the longitudinal field are null. This implies that the longitudinal impedance $Z_\mathrm{l} = 0$ and the transverse impedance $Z_\mathrm{t} \to \infty$.

A corrugated surface with sub-wavelength corrugations and thin walls between the corrugations can be used to create an anisotropic boundary condition, such that for propagation along the corrugations, the surface is hard, whereas for propagation perpendicular to the corrugations, the surface is soft. Hard surfaces favor straight transversal field lines, and therefore transverse electric magnetic (TEM) modes, which can be useful to design high-gain antennas [92].

**All-metallic antennas** While at low frequencies, dielectric metasurfaces using patches and slots can be used to tune the effective propation features of waveguides and antennas, the losses become prohibitive at higher frequencies. Therefore, all-metallic devices are preferable [47]. As explained in the previous paragraphs, metasurfaces become central to these designs, in order to benefit from the properties of spoof SPP at air/metal interfaces. A good example of the application of such all-metallic metasurfaces are for lens antennas, where the waves are reshaped into the desired beam by changes of the effective refractive index [20], [93]. Lens antennas are “aperture antennas”, because they change the phase distribution at the radiation aperture. Transformation optics can be used to compress lenses without affecting the radiation pattern [22], [94]. Beyond the issue of losses, metasurfaces are good alternative to dielectrics for planar lenses: one is not limited to commercially available dielectrics, and no index discretization is necessary. But the challenge is obtaining simultaneously a low dispersion and a high-enough refractive index. Indeed, getting a high index typically requires being close to a high-impedance band, where the dispersion of metasurfaces is high. These issues can be solved with higher symmetries, as presented in section 1.2.

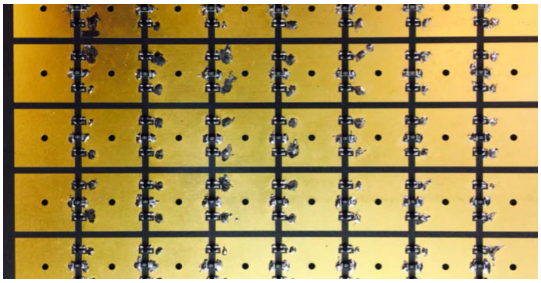

(a) Reconfigurable surface wave absorber made of transistor-connected mushrooms [95].

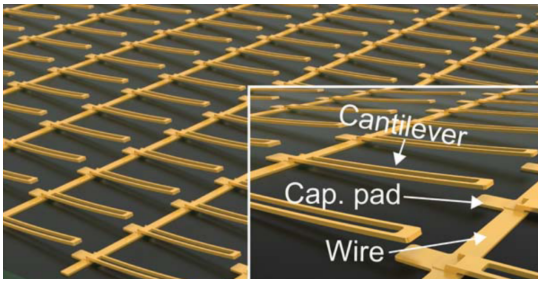


(b) Reconfigurable polarizer based on voltage-biased cantilevers [96].

Figure 1.2: Examples of reconfigurable metasurfaces found in literature.

### 1.1.3 Towards reconfigurability

Before addressing the central topic of higher symmetries, a few words about reconfigurability are essential. The reconfiguration of metasurfaces is a challenge, because of the many sub-wavelength elements, hence complex control circuitry [52, Chap. 1]. Pin or varactor diodes control the capacitance between adjacent unit cells, or even within a unit cell, e.g., to change the electric length of the resonant elements [97]. They can be controlled either through control wires, or activated by the incident field, e.g., diodes or transistors that change state depending on the incoming energy. An example of a transistor-based metasurface is shown in Fig. 1.2a. However, circuit components face scaling and cost constraints due to the high number of elements. Moreover, high-power handling is a problem, due to the breakdown or non-linearity of the components [52, Chap. 6]. Alternately, liquid crystal layers are promising, but they have a relatively slow switching time [98]. Another possibility is to integrate thermally-responsive materials in metasurfaces, such as superconductors or phase change materials (e.g. vanadium dioxide). It is also possible to use photoconductive semiconductors, whose conductivity can be controlled at optical speed by photo-excitation. Mechanical options include deformable cantilevers [96] (illustrated in Fig. 1.2b), piezoelectric actuators [99] or microfluidic technology [100].

As an example, a reconfigurable transmit-array is presented in [101], with a 1-bit unit cell enabling two phase states. The reconfiguration happens through a control bias that steers two pin diodes. Although two phase states lead to discretization losses (due to the lower directivity and aperture efficiency), the insertion loss is significantly reduced and more stable throughout the different states, and the design and integration of the transmit-array are less difficult. This unit cell is used in [102] for a monopulse radar, or in [103] for a switchable circular polarizer with reconfigurable beam-steering.

## 1.2 Fundamental concepts of higher symmetries

In this section, the dispersive properties of periodic waveguides and metasurfaces are extended to higher symmetries. Floquet's theorem is used to express the fields at the surface of a periodic structure as a sum of harmonics. When higher symmetries are

introduced, they impact the symmetries of the Floquet harmonics propagating in the structure, with consequences on the dispersive behavior of the waveguide. This is described by a generalization of Floquet's theorem.

The notion of higher symmetries encompass a wide range of structures with interesting features, some of which are mentioned in this section. Nonetheless, our focus lies on GS, which is the higher symmetry used in our studies.

### 1.2.1 Periodicity and Floquet condition

When a structure is spatially periodic, with period $p$, this periodicity has consequences on the dispersive properties along the direction of periodicity, independently of the structure geometry. A cartesian coordinate system is defined, i.e., every point is defined by $\boldsymbol{r} = (x, y, z)$. The spatial translation operator $\boldsymbol{T}_p$ is defined such that

$$\boldsymbol{T}_p \{\boldsymbol{r}\} = \boldsymbol{r} + p\boldsymbol{e}_z \,, \tag{1.1}$$

where $\boldsymbol{e}_z$ is the unit vector in the $z$-direction. A structure is called *periodic* along the $z$-direction if it is invariant under the translation (1.1). Its period is $p > 0$. The restriction of the structure to a single period $p$ is called a *unit cell*. From this translation operator acting on spatial coordinates, another operator $\boldsymbol{\mathcal{T}}_p$ acting on the field can be defined as

$$\boldsymbol{\mathcal{T}}_p \{\boldsymbol{E}(\boldsymbol{r})\} = \boldsymbol{E}\left(\boldsymbol{T}_p \{\boldsymbol{r}\}\right) = \boldsymbol{E}\left(\boldsymbol{r} + p\boldsymbol{e}_z\right) \,. \tag{1.2}$$

The Floquet boundary condition expresses the field in one cell of the structure as a function of the field in the adjacent cell. Considering the electric field $\boldsymbol{E}$ at a point $\boldsymbol{r}$, Floquet's boundary condition yields

$$\boldsymbol{\mathcal{T}}_p \{\boldsymbol{E}(\boldsymbol{r})\} = \boldsymbol{E}(\boldsymbol{r}) \mathrm{e}^{-\mathrm{j}k_z p} \,, \tag{1.3}$$

where $k_z$ is the wavenumber in the $z$-direction.

Expression (1.3) can be interpreted as an eigenvalue problem, stating that the field propagating in the periodic structure is an eigenvector of the translation operator $\boldsymbol{\mathcal{T}}_p$, with eigenvalue $t = \mathrm{e}^{-\mathrm{j}k_z p}$. Indeed,

$$\left[\boldsymbol{\mathcal{T}}_p - t\right] \boldsymbol{E}(\boldsymbol{r}) = 0 \,. \tag{1.4}$$

At a given frequency $\omega$ corresponding to a free-space wavenumber $k$, the set of possible eigenvalues $t(k)$ is called the spectrum of the translation operator $\boldsymbol{\mathcal{T}}_p$ [104]. For a given eigenvalue $t$, there exist infinitely many possible wavenumbers $k_z$, as adding multiples of $2\pi$ does not change the value of the complex exponential function. A fundamental wavenumber $k_z$ can be defined in an arbitrary interval e.g., $k_z \in [0, 2\pi/p[$. Then, higher harmonics can be defined as having wavenumbers $k_z^{(s)} = k_z + s2\pi/p$, with $s$ an integer. One can verify that for any integer $s$,

$$\mathrm{e}^{-\mathrm{j}k_z^{(s)} p} = \mathrm{e}^{-\mathrm{j}\left(k_z + s\frac{2\pi}{p}\right)p} = \mathrm{e}^{-\mathrm{j}k_z p} = t \,. \tag{1.5}$$

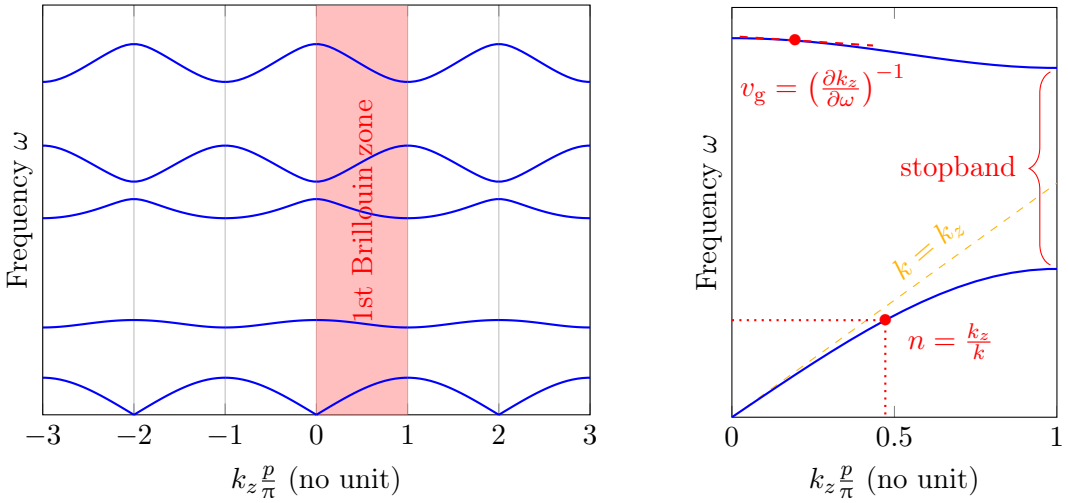


(a) Periodicity of the Brillouin diagram.

(b) First Brillouin zone: stopbands/passbands, mode velocities.

Figure 1.3: Periodicity and information available in the Brillouin diagram. The line of light (dashed yellow) separates the slow and fast wave regions.

All $k_z$ and related harmonics $k_z^{(s)}$ which are solution of (1.3) form the wavenumber spectrum of the considered $p$-periodic structure. This spectrum is displayed in the Brillouin diagram which is described in the following paragraph 1.2.2.

It is important to note that even though a specific $k_z$ may be such that $\mathrm{e}^{-\mathrm{j}k_z p} = t$, with $t$ an eigenvalue of the translation operator $\boldsymbol{\mathcal{T}}_p$, it does not imply that it belongs to the wavenumber spectrum of the structure. Indeed, for $k_z$ to be in the spectrum of the structure, it must be a solution of (1.3). Not only does that mean that it must be associated to a particular eigenvalue $t$, but it must also allow a non-zero eigenfield $\boldsymbol{E}$ to exist within the considered structure i.e., a non-zero field satisfying the other boundary conditions within a cell. Such a field may not exist for a specific structure at a particular frequency. Consequently the Floquet condition implies that the smallest possible periodicity of the wavenumber spectrum is $2\pi/p$, but it is not necessarily the periodicity of the spectrum, which can be larger in practice, due to specific boundary conditions removing certain modes. To illustrate this, the example of multiple periodic cells is detailed in appendix A.1.

### 1.2.2 Brillouin diagram

The Brillouin diagram, also called dispersion diagram, is an important display tool when it comes to wave propagation in any structure, and particularly when it comes to periodic waveguides. Many fundamental propagation features are easily highlighted in the Brillouin diagram, as shown in Fig. 1.3. The latter is a chart of frequency as a function of the propagation constant $k_z$. For a given frequency, it gives the propagation constants of

all the modes that can propagate in the structure at this given frequency. The horizontal axis is usually normalized by the structure period $p/\pi$, so that one reads $k_z p/\pi$ – that is the number of half-wavelengths per cell.

The Brillouin diagram is a practical tool when it comes to the representation of propagation velocities. Indeed, the refractive index is defined by $n = c_0/v_p = k_z/k$. Therefore, each point in the dispersion diagram corresponds to a specific refractive index, which can be found as the slope of a line between the origin of the diagram and the considered point. Similarly, the group velocity is the derivative of the frequency with respect to wavenumber $k_z$. Therefore, the slope of the dispersion curve is proportional to this phase velocity.

Moreover, the Brillouin diagram shows at which frequencies the structure can be operated in a passband or in a stopband. When the real part of $k_z$ is zero of a multiple of $\pi/p$, then the attenuation constant is different from zero, and so the wave is attenuated.

The result in (1.5) means that the Brillouin diagram associated to the $p$-periodic structure has a minimum periodicity of 2 along the $k_z p/\pi$ axis.

### 1.2.3 Floquet harmonics and Floquet theorem

The field $\boldsymbol{E}$ in a periodic waveguide can be seen as a periodic standing wave $\boldsymbol{E}^{(\mathrm{sw})}$ with a phase-shift due to propagation. Therefore

$$\boldsymbol{E}^{(\mathrm{sw})}(\boldsymbol{r}) = \boldsymbol{E}(\boldsymbol{r})\mathrm{e}^{\mathrm{j}k_z z}\,, \tag{1.6}$$

where the exponential term cancels the propagation term in $\boldsymbol{E}$. One can note that $\boldsymbol{E}^{(\mathrm{sw})}$ is indeed $p$-periodic, given that

$$\boldsymbol{E}^{(\mathrm{sw})}(\boldsymbol{r}+p\boldsymbol{e}_z) = \boldsymbol{E}(\boldsymbol{r}+p\boldsymbol{e}_z)\mathrm{e}^{\mathrm{j}k_z(z+p)} = \boldsymbol{E}(\boldsymbol{r})\mathrm{e}^{-\mathrm{j}k_z p}\mathrm{e}^{\mathrm{j}k_z z}\mathrm{e}^{\mathrm{j}k_z p} = \boldsymbol{E}^{(\mathrm{sw})}(\boldsymbol{r})\,, \tag{1.7}$$

where (1.3) is inserted in (1.6). Because of its peridocity, $\boldsymbol{E}^{(\mathrm{sw})}$ can be expressed as the Fourier series

$$\boldsymbol{E}^{(\mathrm{sw})}(\boldsymbol{r}) = \sum_{s=-\infty}^{+\infty} \boldsymbol{e}_s(x,y)\mathrm{e}^{-\mathrm{j}s\frac{2\pi}{p}z}\,, \tag{1.8}$$

where $\boldsymbol{e}_s$ is the transverse field vector associated to the $s$-th longitudinal harmonic of the Fourier series.

Inserting (1.8) in (1.6) leads to an expression of the field $\boldsymbol{E}$ as a sum of so-called *Floquet harmonics*, namely

$$\boldsymbol{E}(\boldsymbol{r}) = \boldsymbol{E}^{(\mathrm{sw})}(\boldsymbol{r})\mathrm{e}^{-\mathrm{j}k_z z} = \sum_{s=-\infty}^{+\infty} \boldsymbol{e}_s(x,y)\mathrm{e}^{-\mathrm{j}s\frac{2\pi}{p}z}\mathrm{e}^{-\mathrm{j}k_z z} = \sum_{s=-\infty}^{+\infty} \boldsymbol{e}_s(x,y)\mathrm{e}^{-\mathrm{j}k_z^{(s)} z}\,, \tag{1.9}$$

where $k_z^{(s)} = k_z + s\frac{2\pi}{p}$ is the wave number of the $s$-th Floquet harmonic in the $z$-direction. This proves Floquet's theorem for periodic structures: the field in an infinite periodic structure consists of an infinite sum of spatial harmonics.

### 1.2.4 Higher symmetries

A periodic structure is said to be higher-symmetric when it is defined by more than one symmetry operator. This means that on top of the translation operator defining periodicity, there is another redundancy within the unit cell. Such redundancies have consequences on the field symmetries and the dispersive behavior of the structure. Most notably, higher symmetries are a solution to the narrow-band problem of metasurfaces, inherent to their resonant nature [105]. In the following paragraphs, some examples of such higher symmetries are described, with emphasis put on GS, which is the object of this thesis.

**Parity time-reverse duality symmetry (PTD)** A structure is PTD-symmetric when it is invariant after the composition of the parity operator, time-reversal, and the duality operator. It can then be shown that the corresponding scattering matrix is antisymmetric, which yields a "scattering anomaly". This anomaly implies that there are no back reflections along the propagation path, independently of the geometry of the propagation path [106]. Therefore, PTD-symmetric structure are particularly interesting when it comes to waveguiding along complicated paths or for matching of radiators. It is notable that for a passive lossless structure to be PTD-symmetric, the time-reversal constraint is not required anymore, and the structure needs simply be invariant for parity and duality operations. For example, a confined wave can be guided in a parallel-plate waveguide (PPW) exhibiting PTD symmetry along an arbitrarily complicated path, by using PEC and PMC boundary conditions [107]. On the upper plate, the left side of the path is PEC, whereas the right side is PMC. The opposite is true for the lower plate. The guided wave is confined at the interface between the boundary conditions, and is not reflected even at the sharpest bends. Effective absorbers can be designed applying this concept within rectangular waveguides (RWs) [108]. In order to approach PMC boundary conditions in practice, HIS metasurface such as mushrooms can be used [109]. Theoretically, when lossy material are used, there must be a balance between lossy and gain elements, such that when inverting time and space, the system is invariant [52, Chap. 8].

**Glide symmetry** GS is one of the simplest higher symmetries, because it is purely geometrical. A G-S structure is invariant when shifting it by half a period in the propagation direction, and then by mirroring it with respect to the propagation plane, as illustrated in Fig. 1.4a. It is found in nature (fossils, worms, plants), in our footsteps, in art [110]. It has been studied in the 1960s-70s in its 1-D form [38], [39], [104] – there is only one direction of periodicity – but until the 21st century, research about GS stagnated. With the development of computers and growing research about metasurfaces, interest in GS has resurfaced, mostly in its 2-D form. A waveguide is built with two metasurfaces facing each other, and the upper metasurface is shifted by half a period in both orthogonal propagation directions, creating GS in both directions, as illustrated in Fig. 1.4c. Another 2-D version of GS is possible, called braided GS, which interleaves two 1-D GSs as shown in Fig. 1.4b. In [111], holes are drilled in the top and bottom faces of a

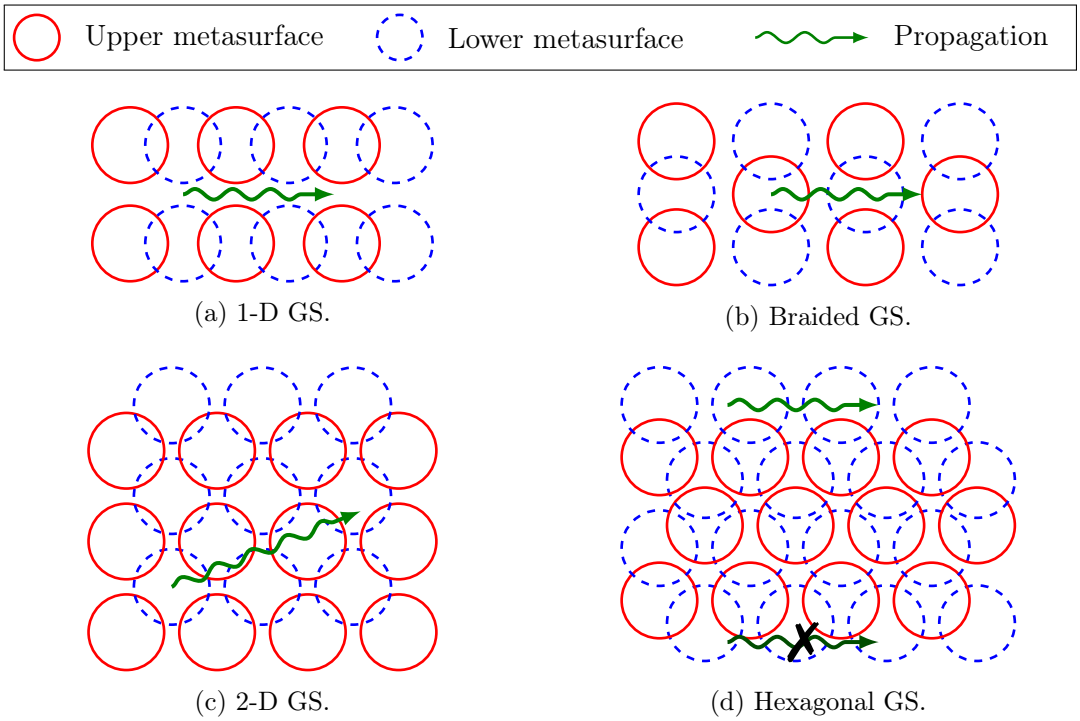


(a) 1-D GS. (b) Braided GS.

(c) 2-D GS. (d) Hexagonal GS.

Figure 1.4: Top view of different types of G-S metasurface waveguides. The propagation plane is in the page. The metasurface elements are pictured as circular holes, but they can be any periodic variation of the geometry.

RW. Along the propagation direction, each row of holes forms 1-D GS. In the transverse direction, each column of holes forms GS too, but with a different period, creating this braided GS.

A cylindrical version of GS has been presented in [117] and called *polar* GS. Is not much different from classical GS, except that it is applied in a waveguide with cylindrical geometry, usually a coaxial cable. The mirroring operation is performed with respect to a cylindrical surface that encompasses the inner conductor. The coaxial cable can be loaded periodically with metallic rings, as illustrated in Fig. 1.6a taken from [117] or with transverse corrugations [118].

A constraint of GS is the need for two metasurfaces, with risks of misalignment. Therefore, another type of GS has recently been implemented, where the mirroring plane is orthogonal to the propagation plane. For example in [112], a transmission line is created by slotting a metallic plate. In order to close the stopband of this line, G-S notches are made on both sides of the slot, as shown in Fig. 1.5a. The complementary G-S structure shown in Fig. 1.5b is studied in [113]. This leads to a frequency-scanning leaky-wave antenna with dual-beam radiation, where the leakage is accurately controlled by the dimensions of the G-S dents. Moreover, GS prevents some of the stopbands that would have limited the operating band of this antenna. In [114], a partially-dielectric-

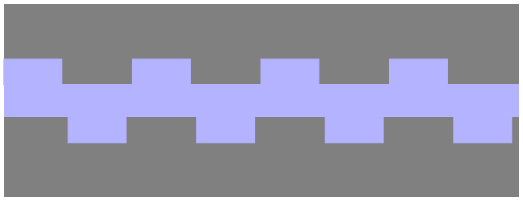

(a) Dented slot [112].

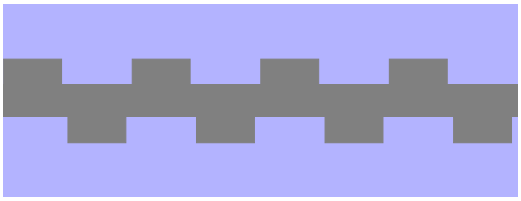

(b) Dented microstrip [113].

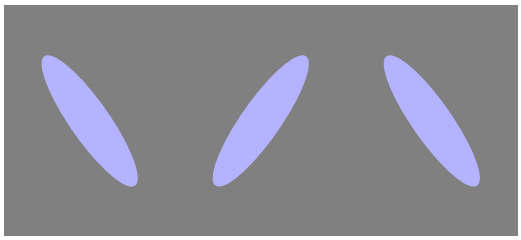

(c) Slotted filter with single row GS [114].

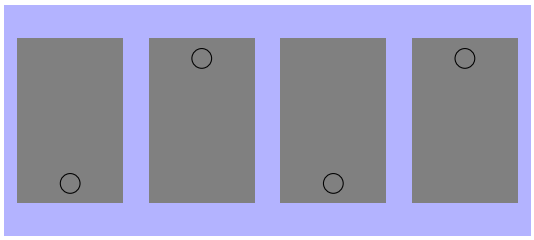

(d) Mushroom ground for microstrip filter [115].

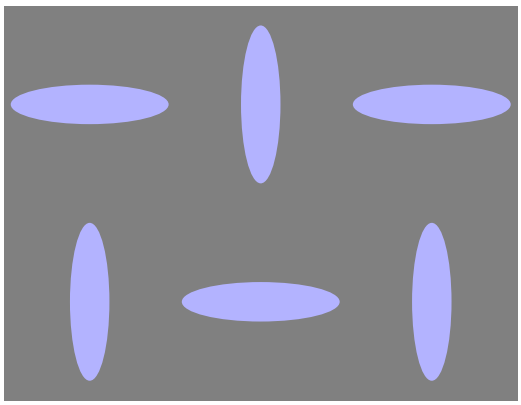

(e) Slotted filter with double row GS [114].

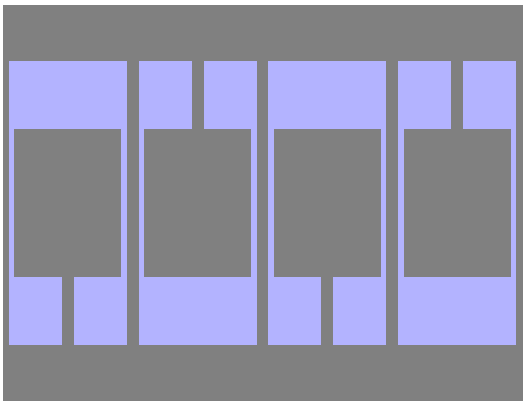

(f) Defected ground for microstrip filter [116].

Figure 1.5: Examples of planar GS, illustrating the top view of a dielectric layer (in blue) with G-S metallization (in gray).

filled PPW yields planar GS on the metallization between the air and dielectric layers, by rotating elliptic slots as illustrated in Fig. 1.5c. If the ellipses are rotated further, there is no more planar GS, but it can be reformed by adding a second row of these slots, as shown in Fig. 1.5e. Planar GS can also be used for integrated filters, for example by etching G-S patterns in the ground plane of a microstrip filter [116] (an example is shown in Fig. 1.5f), or by modifying the via positions in a mushroom metasurface [115], as illustrated in Fig. 1.5d. This improves the stopband of such filters.

Changing the alignment between the G-S metasurfaces can be used as an additional degree of freedom to control the stopbands of waveguides and filters [111], [119], [120]. In the metasurface lens designed in [121], three different focal points can be reconfigured by breaking the GS, such that the focal point moves between the different locations. But

the breaking of GS is also achievable by changing the dimensions of the GS elements [122].

In some systems exhibiting lower symmetries such as a mirror plane, it might be unsuitable to implement GS. For example, for a coplanar waveguide, breaking the mirror symmetry would change the radiative behavior of even and odd modes. The effects of higher symmetries can be obtained nonetheless. In [123], each slot of the coplanar line is dented in a G-S way, yielding two parallel dented slots like the one pictured in Fig. 1.5a. The mirror symmetry is maintained by making the dents in the left slot the reflection of the dents in the right slot with respect to the central axis of the waveguide. Therefore, the overall waveguide is not G-S. However, when breaking the local GS of each slot by lengthening only the external dents, it is possible to re-create the dispersive behavior of a G-S transmission line. This example shows that a mirrored broken GS can effectively behave as classical GS.

GS has since been studied in other fields, such as acoustics, in order to create low-dispersive waveguides [124] or to create edge modes exploiting the bandgap features of the symmetry [125]. Similarly in photonics, silicon-based waveguides implement GS to close some bandgaps, or special crystal arrangements are formed to guide the light only between the atomic rows displaying GS [126].

Section 1.3 is dedicated to the applications of GS in electromagnetics. The implications of GS regarding the dispersion diagram are detailed in paragraph 1.2.5.

**Hexagonal glide symmetry** The 2-D GS described above is based on a rectangular lattice i.e., each metasurface is made of an array of unit cells. However, more complex unit cell arrangements can be designed, with extended degrees of freedom. Recently, a hexagonal GS has been presented [105]. Circular copper patches are printed on a dielectric layer, forming a triangular lattice. Two such layers form a waveguide, and a shift between them creates hexagonal GS. Indeed, when viewing the total unit cell from above, the patches form a hexagon, where the corners are patches that are alternately in the upper or in the lower layer, as illustrated in Fig. 1.4d. One layer is enough to support a surface mode, but two G-S layers confine the fields more, yielding a denser effective propagation medium. Moreover, edge modes can be controlled in this way depending on how the G-S geometry is ended at the borders of the metasurfaces. This is visible in Fig. 1.4d when considering the circles to be metallic patches: edge modes can propagate at edges where the patches overlap only with one other patch, because then isolated charges are necessary to restore the charge neutrality of these patches. This is not the case on the edges with two patch overlaps.

**Glide-time symmetry** The different higher symmetries presented above can be combined. For example, [127] presents a structure that is both PTD-symmetric (alternating gain and loss elements) and G-S. The resulting transmission line displays additional degeneracy points i.e., frequencies at which several propagating modes have the same phase velocity.

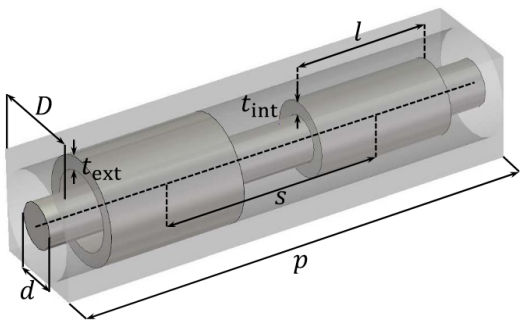


(a) Polar-glide symmetry [117]. After each half-period translation, the load is mirrored with respect to a cylindrical surface.

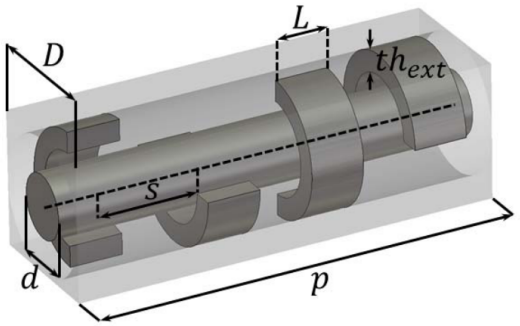


(b) 4-fold twist symmetry [128]. After each half-period translation, the load is rotated around the central axis.

Figure 1.6: Models of periodically-loaded coaxial lines with different higher symmetries.

**Twist symmetry** Twist symmetry has been described in [38], [104]. Like GS, it is a purely geometrical symmetry, but it is adapted to cylindrical waveguides. The translation operator is not associated to a mirroring operation, but to a rotation. Twist symmetry can be $N$-fold, with $N$ an integer. An $N$-fold twist-symmetric waveguide is invariant after a translation of $p/N$, $p$ being the total period, and a rotation of angle $2\pi/N$ around the central waveguide axis.

[32] implements 4-fold twist symmetry in a coaxial line, where bolts are screwed in the inner conductor to act as metallic pins that rotate around the inner conductor with an angle of $\pi/2$. This closes the three first stopbands of the structure, making it wideband. Similarly, [128] adds twist-symmetric elements in a coaxial cable, but on the outer conductor, in the form of half-rings rotated by an angle of $\pi/2$. The 4-fold twist symmetric structure of this article is shown in Fig. 1.6b. When cut along a longitudinal plane, these rings look like corrugations in the outer conductor, offering many tuning parameters. In [118], transverse slots are made in the inner conductor, such that a cross-section of the inner conductor at the position of a slot pictures a half-circle. It is notable that for simple elements such as pins or half-rings, a two-fold twist symmetry is equivalent to classical GS, because rotating the element by 180° is equivalent to mirroring it with respect to a plane that cuts the waveguide in half longitudinally. Twist symmetries can also be implemented in cylindrical waveguides (no inner conductor), with asymmetrical irises that are rotated along the propagation direction. Twist-symmetric perforated irises prevent the propgation of the first transverse electric (TE) mode of a classical cylindrical waveguide, increasing the operating band of the TM mode [129]. Irises in the shape of split-ring resonators are used in [130] : a multi-layered lens is built of metallic plates with split-ring resonator slots. Twist symmetry is implemented between the resonators that are aligned across the layers. Changing the order of the twist symmetry from one line of resonators to the other is an effective way of changing the phase delay, and so the desired phase pattern is obtained at the lens aperture in order to create plane waves.

Similarly to GS, twist symmetry can be broken in many different ways in order

to reconfigure the dispersive properties [131]: changing the angle of rotation between adjacent elements, changing the geometry of these elements within a unit cell,... Twist symmetry can also be combined with polar GS, yielding a higher symmetry with three operators. The elements are translated by $p/N$, rotated by $2\pi/N$, and every other time they are mirrored with respect to the cylindrical plane between the conductors. Such an example of a polar-twist-symmetric coaxial waveguide with metallic pins placed alternately on the inner and outer conductors is examined in [32]. In such structures, the symmetry can easily be broken by rotating the inner conductor with respect to the outer conductor, which changes the angles between adjacent polar elements [118].

That $N$ should be an integer is the condition for the structure to be periodic. However, a generalization of this symmetry is possible, where the rotation angle is arbitrary, but constant throughout the structure. In [132], a metamaterial of this kind is analyzed by means of transfer matrices.

### 1.2.5 Generalized Floquet theorem for glide symmetry

Let us consider a G-S structure with period $p$. Each unit cell can be divided in two subcells: from one subcell to the next one, there is not just a translation $p/2$, but also a mirror-reflection with respect to the propagation plane. The G-S operator $\boldsymbol{\mathcal{G}}$ considers the field that is shifted by half a cell and mirrored with respect to the plane $y = 0$, yielding

$$\boldsymbol{\mathcal{G}}\left\{\boldsymbol{E}(\boldsymbol{r})\right\} = \boldsymbol{E}(x, -y, z + \frac{p}{2})\,. \tag{1.10}$$

This means that composing two times the operator $\boldsymbol{\mathcal{G}}$ corresponds to the translation operator i.e.,

$$(\boldsymbol{\mathcal{G}})^2 = \boldsymbol{\mathcal{T}}_p\,. \tag{1.11}$$

Let us consider a *non-degenerate* non-zero eigenmode $\boldsymbol{E}$ of the G-S waveguide. Then, according to the generalized Floquet theorem [104], $\boldsymbol{E}$ must be an eigenmode of both the translation operator $\boldsymbol{\mathcal{T}}_p$ (with eigenvalue $t$) and the G-S operator $\boldsymbol{\mathcal{G}}$ (with eigenvalue $\ell$). This can be expressed as

$$\exists\, t \in \mathbb{C} \text{ s.t. } \left[\boldsymbol{\mathcal{T}}_p - t\right]\boldsymbol{E}(\boldsymbol{r}) = 0 \quad \Longleftrightarrow \quad \exists\, \ell \in \mathbb{C} \text{ s.t. } \left[\boldsymbol{\mathcal{G}} - \ell\right]\boldsymbol{E}(\boldsymbol{r}) = 0\,. \tag{1.12}$$

A proof of this theorem can be found in appendix A.2.

According to the Floquet theorem (1.3), for a closed and lossless structure, the eigenvalue of the translation operator is $t = \mathrm{e}^{-\mathrm{j}k_z p}$. Given (1.11), this means that the two possible eigenvalues of $\boldsymbol{\mathcal{G}}$ are $\ell = \pm\mathrm{e}^{-\mathrm{j}k_z \frac{p}{2}}$, yielding

$$\boldsymbol{\mathcal{G}}\left\{\boldsymbol{E}(\boldsymbol{r})\right\} = \pm\mathrm{e}^{-\mathrm{j}k_z \frac{p}{2}}\boldsymbol{E}(\boldsymbol{r})\,. \tag{1.13}$$

It can be shown that these two eigenvalues are equivalent. Inserting the harmonic decomposition (1.9) in (1.13) yields

$$\sum_{s=-\infty}^{+\infty} \boldsymbol{e}_s(x, -y)\mathrm{e}^{-\mathrm{j}k_z^{(s)}\left(z+\frac{p}{2}\right)} = \pm\mathrm{e}^{-\mathrm{j}k_z \frac{p}{2}} \sum_{s=-\infty}^{+\infty} \boldsymbol{e}_s(x, y)\mathrm{e}^{-\mathrm{j}k_z^{(s)} z}\,, \tag{1.14}$$

which is equivalent, for each harmonic order $s$, to

$$(-1)^s \boldsymbol{e}_s(x,-y) = \pm \boldsymbol{e}_s(x,y)\,. \tag{1.15}$$

This means that half of the harmonics are antisymmetric with respect to the propagation plane, whereas the other half is symmetric. Changing the sign of the eigenvalue is equivalent to re-ordering the harmonics differently. Therefore, it is sufficient to consider the generalized Floquet theorem (1.13) with an arbitrary sign.

## 1.3 Properties and applications of glide-symmetric metasurfaces

As presented in the previous section, GS is one of the higher symmetries that is simplest to implement given its geometrical nature, but it also offers many degrees of freedom and many variants. That is why it has been extensively explored in the last decade. In this section, the features of GS are presented in relation to its concrete applications. More extensive reviews of the uses of GS can be found in [133], [134] or [110].

### 1.3.1 Electromagnetic bandgap applications

#### 1.3.1.1 Closing the first stopband

In a periodic structure, there is typically a stopband between the first and second modes, at the right-end of the first Brillouin zone. This stopband phenomenon is well-known for SPPs, and is quite intuitive in the case of corrugations [89, Box. 3]. When the wavelength is equal to half-the-period of a metasurface – that is at the right-end of the Brillouin diagram – two standing waves are possible at the surface of the corrugations. But these waves resonate at different frequencies due to disparity of the charge distributions. The mode with the largest distance between the charges and highest field distorsion contains the most EM energy, and therefore corresponds to the highest frequency. Between these two resonating frequencies, waves cannot propagate, yielding a stopband.

When it comes to G-S waveguides, the stopband between these two modes is closed. In [135], the fields of the modes are shown for two corrugated lines of finite thickness facing each other. Some of these field images are shown in Fig. 1.7. The corrugated lines can be seen as two infinite combs between which the waves are guided. Each of these combs supports spoof SPPs, which couple when the gap between the combs is small. Two possible modes are possible: the anti-bonding combination and the bonding combinations of the upper and lower spoof SPPs. When the upper and lower corrugations are aligned, the bonding mode leads to a symmetric magnetic field distribution with respect to the symmetry plane. On the other hand, the anti-bonding mode is antisymmetric. At the right-end of the Brillouin zone, the anti-bonding mode has a nodal line in the symmetry plane, and so its resonance frequency is higher than the bonding mode's frequency. When the upper comb is shifted in the propagation direction, the fields of the bonding mode get more distorted, and so its resonance frequency increases. On the contrary, the field

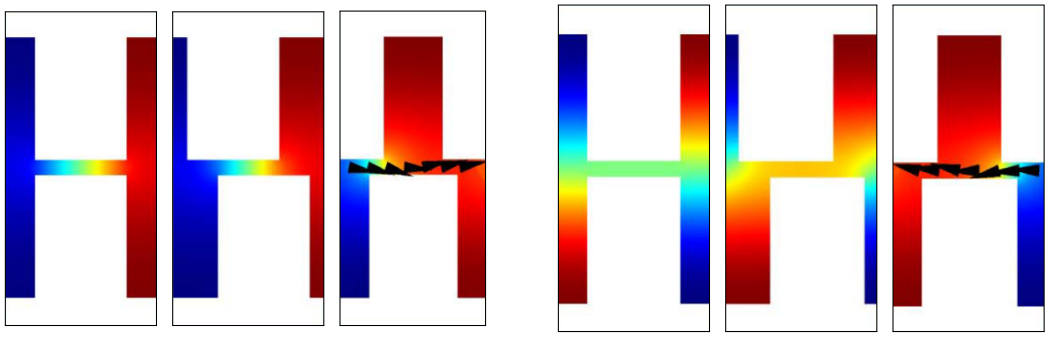

(a) Bonding mode [135].

(b) Antibonding mode [135].

Figure 1.7: Transverse magnetic field profile in the G-S dented transmission line presented in [135], at the end of the first Brillouin zone. For each mode, the upper metasurface is successively aligned with the lower metasurface, shifted by a fifth of the period, and G-S.

distorsion of the anti-bonding mode is decreased, and so is its resonance frequency. When a shift of half a period is reached, both modes have exactly the same field distribution, but opposite Poynting vectors (and group velocities), as illustrated in the third clip in Figs. 1.7a and 1.7b. This means that a mode degeneracy is achieved at the right end of the Brillouin zone. The stopband is closed with GS. Moreover, a stronger lateral field confinement is obtained when GS is implemented. Increasing the thickness of the comb further increases the negative-group-velocity of the second band, with a maximum achieved for an infinite structure, i.e., a structure invariant along the corrugations.

Closing the stopband can also be explained by showing that the two space harmonics that cross at the right-end of the Brillouin zone do not couple, and that this lack of interaction means that they cross without influencing each other [136]. Removing this stopband is an interesting way of controlling the bandwidth of filters and transmission lines. In [137] a spoof SPP propagates within a groove made in a metal plate. The side walls of the groove are modulated with periodic diaphragms. GS is added by alternating diaphragms on either side of the groove. This closes the bandgap between the first two modes, which are shown to have the same field distribution like in [135]. Therefore, the bandwidth of the waveguide is increased. Similarly, closing the stopband between first and second modes can be used to increase the passband of some filters. In the substrate-integrated waveguide (SIW) filter designed in [138], split-ring resonators are etched in the upper and lower metallization in a G-S layout, thus increasing the passband of the filter.

Broken GS offers good control on the width of the passbands and stopbands of such filters and waveguides. Loading a RW with periodic ridges makes it possible to create a stopband for the first RW mode, at frequencies where the second RW mode still propagates [120]. When shifting the ridges on one side of the waveguide, transforming the structure towards GS, the stopband becomes narrower, thus controlling the monomodal regime. A similar reconfigurable filter design is presented in [139].

Another example where closing the stopband is useful is for leaky-wave antennas

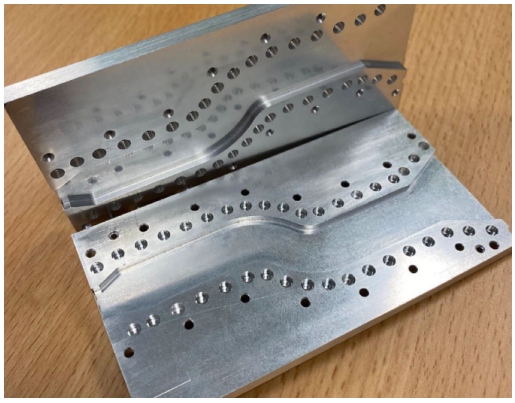

(a) Mode converter in gap-waveguide technology [110], [142].

(b) Waveguide flanges with G-S leakage repression [110], [143].

Figure 1.8: Prototypes of microwave devices designed at KTH Royal Institute of Technology, making use of the enlarged stopband of G-S holes.

(LWAs). [136] presents a LWA made of a planar corrugated Goubau line. In order to have a high frequency-scanning rate, the group velocity of the leaky mode must be high. This is true near the stopband, but the stopband also limits the operation band. GS closes this stopband, while maintaining a high group velocity. In order to further increase the radiation efficiency of the LWA, the Goubau line is periodically loaded with G-S metallic patches.

#### 1.3.1.2 Stretching the second stopband

A direct consequence of closing the first stopband with GS is the widening of the next stopband, between the second and third modes. This is studied in [140] for a PPW unit cell with G-S cylindrical holes. The impact of the different geometrical parameters on the electromagnetic bandgap (EBG) is explored in [141]. In [34], holes of different shapes are compared.

**Gap waveguides** This increased stopband between the second and third modes of G-S waveguides is interesting for EBG waveguides and to avoid leakages. For example, in order to reduce the manufacturing costs of a RW, it can be made of two separate metallic plates. Grooves are made in each plate, such that the RW is re-created when assembling the plates. However, the roughness of the plates and manufacturing imperfections can create a small gap between the plates, causing energy leakage. Drilling G-S EBG holes in the plates on both sides of the RW is a low-cost solution to prevent this leakage from happening [144]. If the holes are placed in a G-S way, not only is the bandwidth of this solution increased, but also the attenuation factor in the stopband is larger. It appear that very few rows of holes are required to repress most of the energy leakage [37]. This method is robust to bends in the waveguide, as shown in [37] for two 90° bends. By

changing the width of the waveguides at such carefully designed bends, mode converters can be easily manufactured [142], [145], with an example pictured in Fig. 1.8.

**Multi-layered structures** This method can be extended to multi-layered waveguides. Instead of building a RW with two plates, [146] stacks multiple metallic layers to create a high waveguide with thin metallic sheets. In order to avoid leakage between these multiple sheets, G-S holes are drilled between all the layers. The stacked holey G-S unit cell yields a huge stopband in all propagation directions (between 100 and 200 GHz). The multi-layer design allows for a simple transition design for a RW feed arriving perpendicularly. This technology is robust to bends too, and can be extended to all kinds of microwave devices, e.g., feeding networks for antenna arrays. In [147], a multi-layered antenna array is designed and the different layers are manufactured by means of 3D printing based on stereolithography combined with subsequent metal plating. The G-S EBG holes double the efficiency of the waveguide compared to the case where nothing prevents the waves from leaking in the gap between the layers.

**Phase-shifters** Building waveguides in two separate plates, assembled without leakage thanks to G-S holes, is interesting for the design of phase-shifters. The 90° phase-shifter in [145] is built as a RW with G-S holes. The phase-shift is achieved by inserting a dielectric slab in the RW, which can be easily opened. The G-S holes also make it easy to widen the waveguide aroung the position of the slab, in order to increase the bandwidth of operation. A similar design is presented in [148], where two rows of holes are used to repress all leakage. But G-S metasurfaces can also be used in the propagation region to create a phase-shift, as illustrated in [36], where G-S holes are used to guide the waves, and where G-S pins change the propagation constant to tune the phase-shift.

**Filters** This increase of the stopband between second and third modes is a powerful tool for microwave filters. The filter designed in [149] not only uses G-S holes to avoid leakage on the sides of a RW filter, but also in the propagation region of the waveguide to increase the range of the filtered frequencies. [111] conceives a similar RW filter for satellite applications. The longer the filter, the higher the total attenuation, which is increased by GS. By breaking GS, additional control of the stopband width is obtained. These features can also be applied to microstrip filters by means of planar GS. Instead of drilling holes or vias, periodic slots can be etched in the ground plane below the strip, creating a defected ground structure. Adding planar GS to this pattern enhances the width and the rejection level of the filter stopband [116]. Note that the manufacturing effort is the same, the pattern is just reversed every second time. Similarly, [115] and [150] add planar GS to a mushroom EBG filter by moving the mushroom vias to the side of the patches, and changing the side of the vias from one patch to the next. The mushroom metasurface is placed below a microstrip line to implement the filtering properties. The stopband is shown to be widened with GS by up to 80%.

**Waveguide flanges** EBG structures are not only useful to guide waves, but also to improve waveguide flanges. Despite screwing two flanges tight together, leakage can happen if the two flanges are not perfectly planar. [143] adds a row of G-S holes in a circle all around the RW, in the flanges, to avoid leakage, as illustrated in Fig. 1.8. One row is enough for small gaps. There is no need for additional components, it is enough to drill holes in existing flanges. The diameter of the holes is larger than the accuracy needed with metallic pins that would achieve the same result, which alleviates manufacturing constraints. If holes are deep enough, the stopband is not sensitive to the drilling depth accuracy. Moreover, if the flange surfaces happen to be perfectly smooth, then there is no gap at all, contrarily to an EBG design with pins. This design has been patented in [151]. In [152], another interesting extension of GS is presented to reduce the thickness of an EBG layer for contactless flanges, where a snake-like metasurface is built from two compacted bed of nails.

**Leaky-wave antennas** LWAs can also be implemented in this EBG G-S technology. A leaky RW can be implemented with G-S holes, such that leakage is completely suppressed on one side of the waveguide with only one row of holes [153]. On the other side, G-S holes with different dimensions offer a precise control of the leakage, in order to create an aperture illumination that reduces the side-lobes of the radiated beam [154]. In [155], it is shown that GS offers a wider range of attenuation constants than non-glide-symmetric (nGS) holes, and so the leakage rate can be tuned more efficiently.

### 1.3.2 Increased refractive index and low dispersion

**Metamaterials** The maximum refractive index of a given medium is bound to its atomic polarizability and spatial arrangement. It can be increased by working near the resonances of the atomic grid, but this increases the frequency dispersion of the medium, given that the refractive index varies strongly around resonances. Therefore, increasing the refractive index by keeping a low dispersion is a challenge of metamaterials and metasurfaces. GS is a solution to this challenge. A giant-index metamaterial is designed in [50]. Metallic patches in a multi-layered metamaterial are arranged such that the layers are G-S with respect to each other, meaning that the patches are shifted from one layer to the next. Then, a wave that propagates through the layers sees a giant refractive index of the order of $10^3$. The reason is that the field perturbation by the G-S path leads to a decrease of the effective electric field and an increase of the effective displacement field, that would not happen if the patches were aligned.

**One-dimensional glide symmetry** Not only is this density increase happening for 1-D GS too, but it is also combined with a reduction of the frequency dispersion. In a mictrostrip antenna made of a dented strip, the stopband between the first and second modes is closed when the dents are G-S on both sides of the strip [113]. Closing this stopband appears to straighten the dispersion curve of the first mode, thus reducing its frequency dispersion. The dispersion is even further reduced when adding a second

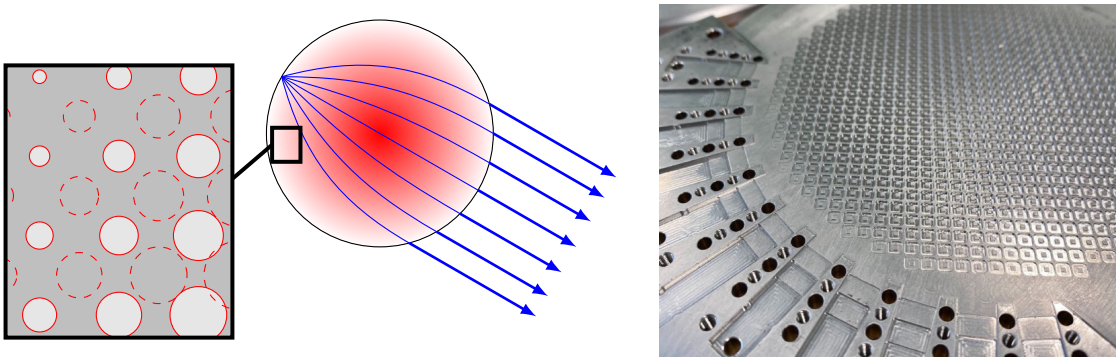

(a) Top view of the lens concept, with inset of the index grading.

(b) Prototype lens built at KTH Royal Institute of Technology [110], [157].

Figure 1.9: Concept and prototype of a planar Luneburg lens made of holey G-S metasurfaces [157]. The index grading is controlled by the hole radius.

dented strip on the other side of the substrate, shifted in the propagation direction in order to create a second dimension of GS. Moreover, the fields are more confined around the strips when GS is added, hinting towards a denser effective medium. Similar features are observed in [119], for a transmission line made of printed double-sided parallel-strip lines. Each line is corrugated on both sides. GS is introduced by shifting the upper line in the propagation direction with respect to the lower line. This reduces the dispersion of the first mode and closes the first stopband, enabling a large increase of the band of operation of this transmission line. Moreover, the refractive index is increased. This design is used is [156] for a wideband bandpass filter.

These features are exploited for the design of a phase-shifter [36]. Bed of nails are added within a RW. Adding pins lowers the first mode of the RW, showing an increase of propagation constant. This effect is stronger with GS. Moreover, the strong decrease of the cut-off frequency makes it possible to scale the waveguide down for a given operation band. This cut-off lowering is sensitive to the period of the unit cell, but only when the pins are GS. This is because the coupling of adjacent pins is stronger in the G-S configuration, and can thus be tuned by changing the distance between the pins. GS increases the operating band of such microwave devices. A similar phase-shifter is designed in [149], but the pins are replaced with two rows of circular holes.

**Two-dimensional glide symmetry** One of the first papers bringing to light the benefits of GS for metasurface waveguides is [33]. The dispersion diagram of a PPW unit cell with G-S metallic pins shows the increased refractive index and the reduced frequency dispersion of this waveguide. The same is true for holey metasurfaces. By changing the depth of the square holes, the refractive index can be varied from 1 to $\sqrt{2}$. This is the maximum index needed to build a planar Luneburg lens, which transforms a non-directive source into a plane wave, as outlined in Fig. 1.9a. Simulations show that such a lens can be operated over an extremely large band (from 4 to 18 GHz) due to the low

dispersion offered by these G-S metasurfaces. If nGS metasurfaces were used, not only would the bandwidth be smaller, but also the gap between the metasurfaces would need to be smaller to reach the required maximum index. A similar design is presented in [158], where an even larger gap is made possible by putting a dielectric layer between G-S bed of nails metasurfaces. Transformation optics are used to convert the focal point of the lens into a flattened line, fitting the feed profile. Dispersion is reduced by GS, yielding a stable index from 4 to 16 GHz. Other designs using dielectrics are possible, such as a substrate where G-S circular metallic patches are printed on both sides of the slab[159]. Parametric studies show that this design is low-dispersive too, and that it offers an index range large enough to build graded-index lenses. Designs with dielectric unit cells are also possible [160]. However, fully-metallic lenses are preferable at higher frequencies because of the increased dielectric losses. In order to relieve the constraint on the gap between the metasurfaces, the refractive index of all-metallic G-S metasurfaces can be increased by adding metallic pins inside the square holes [157]. The pins increase the effective index, allowing for a larger gap between the metasurfaces, and therefore a larger bandwidth of operation. A wideband low-loss Luneburg lens is manufactured, including a staircase feed and a flare for impedance matching at the lens borders. A picture of the finished prototype is shown in Fig. 1.9b. Similarly, [161] presents a Luneburg lens where the GS holes are hexagonal and are also combined with a central pin. Nevertheless, manufacturing all-metallic metasurfaces is costly. [162] presents a way to build a Luneburg lens in fully-integrated substrate layers. These holes are called substrate-integrated holes (SIHs), and are discussed in more details in section 6.1.

Other lens profiles can be realized with G-S metasurfaces. A Maxwell fish-eye lens transforms one source point into another focal point at the opposite lens border. [163] designs such a lens in a dielectric PPW, with G-S slots in the shape of Jerusalem crosses. GS suppresses the first stopband, reduces the dispersion, and increases the refractive index of the waveguide. Without GS, a denser or thiner substrate would be required for such a lens. Likewise, a Gutman lens can be designed in a PPW with G-S pins [164]. A Gutman lens is a modified Luneburg lens, where the focal circle has a smaller radius, making it possible to put the source closer to the center, thus reducing the overall lens size. But this requires a higher refractive index, enabled by GS. It is to be noted that the smaller focal circle implies that the different feed are more tightly packed. A similar planar lens with G-S pins is created in [165] to improve the increase directivity of a Ku horn antenna. Given that GS increases the refractive index, and thiner lens can be built.

Finally, 2-D G-S waveguides can also be combined with LWAs to reduce beam-squinting. In [154], a prism made of a holey G-S PPW is placed at the radiation edge of the LWA. The frequency dispersion of the prism is complementary to the frequency-scanning behavior of the LWA, and so the radiation becomes stable over a wide band. Compared to nGS holes of same size, a higher refractive index is achieved by G-S holes. Therefore, for the same result, the size of the holes can be increased. In the resulting prism, the total number of holes is reduced by three quarters, which is a big manufacturing gain. On the contrary, for backward radiation, such a dispersive prism can be used to increase the frequency beam-scanning. In this case, to suppress unwanted beams due

to other harmonics in the operating band, G-S pins can be added in the LWA waveguide. They offer more control over the dispersion of the harmonics, for better mode selection and improved beam-scanning [166].

### 1.3.3 Isotropic and anisotropic behavior

A direct consequence of closing the first stopband and reducing the dispersion is that G-S metasurface waveguides can be isotropic over a wider band. This is illustrated in [34], for a holey G-S PPW where the holes have the shape of equilateral triangles. Equilateral triangular holes yield isotropic behavior with or without GS, but the stopband between the first and second modes limits this isotropy in the nGS configuration. [34] also show that G-S triangular holes reach a maximum refractive index larger than with circular holes, and almost as large as with square holes, but on a wider frequency band than square holes. Still, circular holes are best in terms of dispersion and wideband isotropy.

Depending on the shape of the unit cell, metasurface waveguides may be anisotropic. This means that the refractive index changes depending on the propagation direction. For example, anisotropic behavior is observed for a G-S holey PPW with rectangular holes [167]. In [35], a metallized PPW with etched holes is shown to display anisotropy for elliptic holes or for meandered lines. A higher level of anisotropy is achieved with GS. This means that for a given performance, smaller variations of the unit cell parameters are necessary, and so the operation band remains larger. Using elliptic holes and transformation optics, a wideband Luneburg lens is compressed by 30%. A similar lens compression is achieved in [168] with elliptical holes for a wideband Maxwell fish-eye lens and in [162] with SIHs.

### 1.3.4 Effective magnetic response

In the metallized PPW with etched ellipses in [35], the effective constitutive parameters of the unit cell have been extracted in order to retrieve the relative permittivity and permeability of the waveguide. When the waveguide is excited with a PPW mode, it appears that a higher effective permeability is achieved with GS. This is confirmed in [44] for circular holes etched in the metallizations of a metallic slab. It is observed that G-S holes yield a higher permeability than nGS holes. Moreover, when changing the dielectric permittivity of the slab, the effective permeability remains constant, whereas the effective permittivity changes, and much more so with G-S holes. Therefore, by etching G-S holes in metallization of dielectric slab, one can tune its effective constitutive parameters in order to match this substrate to another medium. Additionally, given the higher permeability, the range of effective densities achievable with GS is higher than without GS, and so a wider range of substrates can be matched. On top of that, the bandwidth of these effective parameters is much larger with GS.

[44] illustrates these features by making a dielectric slab invisible when inserted in a dielectric PPW, over a wide band. Following the same idea, reflections at the border of a planar lenses can be avoided. In [44], wideband matching is obtained for a hyperbolic dielectric lens, such that the antenna beam is directive without reflections.

Finally, [168] studies the anisotropy of these effective constitutive parameters. Using the scattering parameters of the unit cell, the effective constitutive parameters are extracted for GS elliptical holes. The effective permittivity appears to be isotropic, meaning that the anisotropy of the G-S unit cell is mainly due to its strong magnetic response.

### 1.3.5 The challenge of modeling glide-symmetric metasurface waveguides

The simulation of G-S metasurface waveguides is a challenge. The special features listed in the previous paragraphs are the consequence of large geometrical disparities, interactions between the metasurfaces, and multi-modal coupling between adjacent unit cells. This makes existing simulation methods either very slow or inaccurate.

Commercial solvers are very slow when the distance between the metasurfaces is small. They do not compute the imaginary part of the wavenumber for complex modes [169]. Analytic models for metasurfaces such as homogenization [91], [170] fail to capture the multi-modal coupling between adjacent elements in the G-S configuration [41]. The derivation of equivalent circuits [171] becomes difficult for non-canonical metasurfaces, especially when it comes to include the coupling due to the misalignment between the metasurfaces [41].

In recent years, new modeling techniques have been developed with higher-symmetric structures in mind. While the single-mode transfer matrix method [17] does not take into account the multi-modal coupling between adjacent unit cells, a multi-modal extension of this technique is derived in [43] for G-S waveguides. It is based on the computation of the multi-modal transfer matrix of one unit cell in a commercial solver. combined with the general Floquet theorem, the resulting eigenvalue problem is the dispersion equation of the waveguide, which can be solved numerically. Most importantly, it includes higher symmetries in the eigenvalue problem, making it possible to simulate only a fraction of the unit cell in the commercial solver. It also yields the attenuation information of the waveguide [172]. This method works for 2-D and three-dimensional (3-D) periodic materials as well [169], and since its publication it has been used for the design of many G-S devices [149], [173]–[175].

Another method well-suited to G-S waveguides is mode-matching [42], [167], [176], [177]. Like the multi-modal transfer matrix method, it yields the dispersion equation of the waveguide. While it is less flexible than the transfer matrix method, it has the advantage of requiring no information computed with commercial solvers. This method is presented in detail in chapter 2.

A more extensive review of the computation methods for metasurface waveguides can be found in appendix A.3.

# Chapter 2

# Mode-matching method and dispersion equation of glide-symmetric waveguides

The mode-matching method (MMM) consists in enforcing boundary conditions at discontinuities between different regions, where the fields are decomposed as sums of orthogonal modes. It has been used for many decades for the study of metasurface waveguides, for example in [88], where the dispersion diagram of a slotted waveguide is found by decomposing the fields in orthogonal modes. As such, the MMM has become a textbook fundamental [17, pp. 203-9] to study waveguide discontinuities. However, it is only recently that the glide-symmetric (G-S) properties have been used with a specific MMM formulation. In [176], the dispersion equations of G-S and non-glide-symmetric (nGS) (that is, mirror-symmetric) corrugated parallel-plate waveguides (PPWs) are derived. Only propagation perpendicular to the corrugations is considered, and so this method is generalized in [42] for arbitrary propagation directions. Corrugated waveguides are invariant along the corrugations, and so these structures implement one-dimensional (1-D) glide symmetry (GS). The MMM is applied to two-dimensional (2-D) GS in [167], which analyzes metasurface waveguides pierced with rectangular holes. The generalization for arbitrary hole shapes is found in [45], with specific application to circular holes.

Given that the MMM yields an accurate dispersion equation for a wide range of metasurface waveguides, it is chosen as this thesis' starting point for the analysis of GS.

In this chapter, we develop the works presented in [176] and [45], for corrugated and holey PPWs, respectively. A corrugated PPW yields the simplest form of 1-D GS. In section 2.1, its dispersion equation is derived for both G-S and nGS designs. The theoretical properties of the dispersion equation are validated, and it is solved to compare the G-S and nGS Brillouin diagrams.

The case of 2-D GS is then considered with a holey PPW in section 2.2. The most general case is considered, where the shape of the periodic cavities are simply required to be invariant in the depth direction. For example, additional pins may be present at the

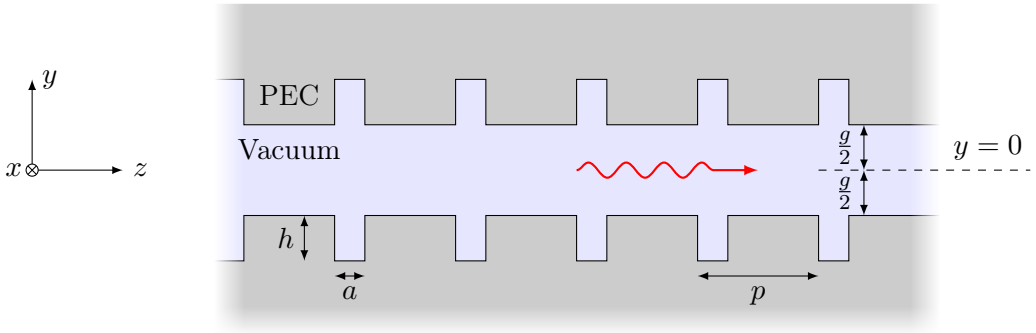


(a) Mirror-symmetric i.e., nGS, design.

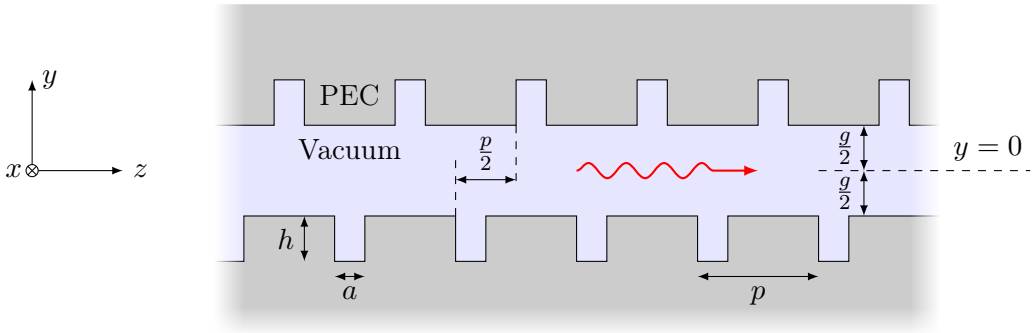


(b) G-S design.

Figure 2.1: Metallic corrugated PPWs. The structures are invariant in the $x$-direction. The red arrow indicates the propagation direction.

center of the holes. In the following, *holes* and *holey* metasurfaces are used to designate this very loose meaning of invariant cavities. As such, this chapter generalizes the MMM presented in [45] slightly further, although it must be noted that in fact the equations are barely changed by this generalization. At the end of section 2.2, the MMM is applied to the examples of rectangular and circular holes.

In order to ease the reading of the mode-matching process, most of the mathematical derivations are left out, with only the main steps remaining. However, more detailed derivations can be found in appendix B.

## 2.1 Corrugated parallel-plate waveguide

### 2.1.1 Mirrored and glide-symmetric corrugated PPWs

The structure under study in this section is a periodic PPW with corrugations perpendicular to the propagation direction, shown in Fig. 2.1. Both perfectly electrically conducting (PEC) plates are parallel to the $xz$-plane, and are separated by a gap $g$. The corrugations are parallel to the $x$-direction, with a width $a$ and a depth $h$. The origin

of the coordinate system is located in-between the two plates, such that the lower plate is located at $y = -g/2$, and right above the beginning of a corrugation, such that there is a corrugation in the lower plate between $0 < z < a$. Modes propagating in the $z$-direction are considered. Given that the corrugations are perpendicular to this direction and spaced by a distance $p$, the waveguide is $p$-periodic along the $z$-axis and invariant along the $x$-axis.

Here, the simple case of vacuum-filled waveguides. In practice, this enables low-loss devices. Section 2.2 will take dielectric fillings into account for the study of holey PPWs, in order to generalize the MMM.

Both the upper and lower PEC plates are corrugated. When the corrugation of the upper plate are at the same $z$-coordinates than the corrugations of the lower plate, the structure is symmetric with respect to the plane $y = 0$, at half-distance between the corrugated planes. The resulting nGS structure is shown in Fig. 2.1a, and displays no higher symmetries.

A higher symmetry is added for the structure presented in Fig. 2.1b. Shifting the upper plate by $p/2$ (half the cell length) in the propagation direction introduces GS.

In the next paragraphs, the MMM is applied to such corrugated PPWs, as described in [42].

### 2.1.2 Modal decomposition of the fields

Given that the structure is invariant along the $x$-direction, the structure can be studied in the $yz$-plane. Moreover, due to the periodicity of the metasurface waveguide, it is sufficient to consider the fields within one unit cell. Fields in subsequent cells are related using the Floquet theorem presented in section 1.3.

Only transverse magnetic (TM) modes are considered in both the corrugations and in the gap between the metasurfaces. It should be noted that the MMM can be applied similarly to transverse electric (TE) modes. This would result in different eigensolutions of the PPW, which are not of interest here.

**Modes in the corrugations** In the lower corrugations, the fields in the corrugations are a sum of parallel-plate TM modes propagating in the $y$-direction [17, pp.104-108]. These modes satisfy the PEC boundary conditions at $y = -g/2 - h$ and at $z = 0, a$, yielding

$$\begin{cases} H_x^{(\mathrm{cor})} = \mathrm{j}\omega\epsilon \sum_{m=0}^{+\infty} c_m \frac{1}{k_{y,m}} \cos\left(k_{z,m} z\right) \cos\left(k_{y,m}\left[y + \frac{g}{2} + h\right]\right) \\ E_y^{(\mathrm{cor})} = -\sum_{m=0}^{+\infty} c_m \frac{k_{z,m}}{k_{y,m}} \sin\left(k_{z,m} z\right) \cos\left(k_{y,m}\left[y + \frac{g}{2} + h\right]\right) \\ E_z^{(\mathrm{cor})} = \sum_{m=0}^{+\infty} c_m \cos\left(k_{z,m} z\right) \sin\left(k_{y,m}\left[y + \frac{g}{2} + h\right]\right) \\ E_x^{(\mathrm{cor})} = H_y^{(\mathrm{cor})} = H_z^{(\mathrm{cor})} = 0 \end{cases}, \tag{2.1}$$

where each integer index $m$ corresponds to one TM mode with coefficient $c_m$ and cutoff wavenumber $k_{z,m} = m\pi/a$. The wavenumber in the corrugation depth direction is defined by $k_{y,m} = \sqrt{k_0^2 - (k_{z,m})^2}$, with $k_0$ the free-space wavenumber. In the following, all terms having the order $m$ written as a subscript correspond to quantities related to the corrugations (fields coefficients, wavenumbers,...)

**Floquet harmonics between the corrugated surfaces** The corrugated PPW is $p$-periodic. Therefore, according to (1.9), the field that propagates in the waveguide can be expressed as a sum of Floquet harmonics. These harmonics satisfy the wave equation in the gap. Considering TM modes ($H_z^{(\text{gap})} = 0$) for propagation in a waveguide without $x$-variation, the fields can be expressed as

$$\begin{cases} E_y^{(\text{gap})} = \sum\limits_{s=-\infty}^{+\infty} \mathrm{j}\frac{k_z^{(s)}}{k_y^{(s)}} \left[ -X^{(s)} \cos\left(k_y^{(s)} y\right) + Y^{(s)} \sin\left(k_y^{(s)} y\right) \right] \mathrm{e}^{-\mathrm{j}k_z^{(s)} z} \\ E_z^{(\text{gap})} = \sum\limits_{s=-\infty}^{+\infty} \left[ X^{(s)} \sin\left(k_y^{(s)} y\right) + Y^{(s)} \cos\left(k_y^{(s)} y\right) \right] \mathrm{e}^{-\mathrm{j}k_z^{(s)} z} \\ H_x^{(\text{gap})} = \sum\limits_{s=-\infty}^{+\infty} \mathrm{j}\frac{\omega\epsilon}{k_y^{(s)}} \left[ X^{(s)} \cos\left(k_y^{(s)} y\right) - Y^{(s)} \sin\left(k_y^{(s)} y\right) \right] \mathrm{e}^{-\mathrm{j}k_z^{(s)} z} \\ E_x^{(\text{gap})} = H_y^{(\text{gap})} = H_z^{(\text{gap})} = 0 \end{cases}, \tag{2.2}$$

where each order $s$ corresponds to one Floquet harmonic, with $k_z^{(s)} = k_z + s\frac{2\pi}{p}$ the wavenumber in the $z$-direction. In the $y$-direction, the fields are confined between the metasurfaces, with the vertical wavenumber $k_y^{(s)} = \sqrt{k_0^2 - (k_z^{(s)})^2}$. The fields can be either symmetric or antisymmetric with respect to the propagation plane, with corresponding coefficients $X^{(s)}$ and $Y^{(s)}$.

### 2.1.3 Mode-matching in the glide-symmetric PPW

We enforce additional boundary conditions on the corrugated plates. On the one hand, the electric field tangential to PEC surfaces must vanish between the corrugations. On the other hand, at the frontier between the gap region and the corrugated regions, the $x$-component of the magnetic field and the $z$-component of the electric field must match.

A *first set of equations* is obtained by matching the electric fields on the lower corrugation. The harmonic coefficients $X^{(s)}$ and $Y^{(s)}$, as well as all the corrugation mode coefficients $c_m$, are unknowns of this equation. Doing the same at the upper corrugation surface yields a *second set of equations*. Thanks to the generalized Floquet theorem (1.13), the field in the upper corrugation are known to be equal to the field in the lower corrugation, with an additional phase-shift of $k_z\frac{p}{2}$ or $k_z\frac{p}{2} + \pi$, i.e.,

$$E_z(z + \tfrac{p}{2})\big|_{y=\frac{g}{2}} = \pm \mathrm{e}^{-\mathrm{j}k_z\frac{p}{2}}\, E_z(z)\big|_{y=-\frac{g}{2}} \,. \tag{2.3}$$

Consequently, an additional modal decomposition like (2.1) for the upper corrugation is not necessary. The unknowns of the second set of equations are still the coefficients $c_m$, $X^{(s)}$ and $Y^{(s)}$, as shown in appendix B.1.

After the matching of the electric field components, each harmonic order $s$ is associated to two equations involving these coefficients. Linearly combining these two equations leads to independent expressions for $X^{(s)}$ and $Y^{(s)}$, derived in appendix B.1. For each harmonic $s$,

$$X^{(s)} = -\frac{1 \mp (-1)^s}{2\sin\left(k_y^{(s)}\frac{g}{2}\right)} \mathrm{j}\frac{k_z^{(s)}}{p} \sum_{m=0}^{+\infty} c_m \sin\left(k_{y,m}h\right) \frac{1-(-1)^m \mathrm{e}^{\mathrm{j}k_z^{(s)}a}}{{k_z^{(s)}}^2 - \left(\frac{m\pi}{a}\right)^2}, \tag{2.4}$$

$$\text{and} \quad Y^{(s)} = \frac{1 \pm (-1)^s}{2\cos\left(k_y^{(s)}\frac{g}{2}\right)} \mathrm{j}\frac{k_z^{(s)}}{p} \sum_{m=0}^{+\infty} c_m \sin\left(k_{y,m}h\right) \frac{1-(-1)^m \mathrm{e}^{\mathrm{j}k_z^{(s)}a}}{{k_z^{(s)}}^2 - \left(\frac{m\pi}{a}\right)^2}. \tag{2.5}$$

The choice of the sign depends on the sign in (2.3). As explained in section 1.2.5, it reorders the Floquet harmonics, but results in the same dispersion diagram.

Finally, a *third set of equations* is obtained by matching the coefficients of the magnetic field ($x$-component) at the lower corrugation. The projection basis is the basis of corrugation modes, as illustrated in appendix B.1. For each corrugation mode $m'$, this leads to the equation

$$\begin{aligned} &-\sum_{s=-\infty}^{+\infty} \frac{1}{k_y^{(s)}} \left[X^{(s)} \cos\left(k_y^{(s)}\frac{g}{2}\right) + Y^{(s)} \sin\left(k_y^{(s)}\frac{g}{2}\right)\right] \mathrm{j}k_z^{(s)} \frac{1-(-1)^{m'}\mathrm{e}^{-\mathrm{j}k_z^{(s)}a}}{{k_z^{(s)}}^2 - \left(\frac{m'\pi}{a}\right)^2} \\ &= \frac{a}{2^{\min\{1,m'\}}} c_{m'} \frac{1}{k_{y,m'}} \cos\left(k_{y,m'}h\right), \end{aligned} \tag{2.6}$$

Inserting expressions (2.4) and (2.5) into (2.6), the gap coefficients $X^{(s)}$ and $Y^{(s)}$ can be totally removed, such that only one set of equations is left, involving the corrugation coefficients $c_m$. Appendix B.1 shows how this set of equations can be formalized as the matrix equation

$$\underline{\boldsymbol{M}} \cdot \boldsymbol{c}' = \boldsymbol{0}, \tag{2.7}$$

where the vector of unknown $\boldsymbol{c}'$ is made of the normalized corrugation coefficients $c'_m = \sin\left(k_{y,m}h\right)c_m$, and where the square matrix $\underline{\boldsymbol{M}}$ has elements $M_{m'm}$ of the form

$$\begin{aligned} M_{m'm} = {} & \delta_{m'm} \frac{pa}{2^{\min\{1,m\}}} \frac{\cot(k_{y,m}h)}{k_{y,m}} \\ & + \sum_{s=-\infty}^{+\infty} \begin{bmatrix} \cot\left(k_y^{(s)}\frac{g}{2}\right)\frac{1\mp(-1)^s}{2} \\ -\tan\left(k_y^{(s)}\frac{g}{2}\right)\frac{1\pm(-1)^s}{2} \end{bmatrix} \frac{{k_z^{(s)}}^2}{k_y^{(s)}} \frac{f_{m'm}^{(s)}}{\left[{k_z^{(s)}}^2 - \left(\frac{m\pi}{a}\right)^2\right]\left[{k_z^{(s)}}^2 - \left(\frac{m'\pi}{a}\right)^2\right]}, \end{aligned} \tag{2.8}$$

where it is reminded that $k_{y,m} = \sqrt{k_0^2 - \left(\frac{m\pi}{a}\right)^2}$, $k_y^{(s)} = \sqrt{k_0^2 - {k_z^{(s)}}^2}$, $k_z^{(s)} = k_z + s\frac{2\pi}{p}$, and where one defines the term

$$f_{m'm}^{(s)} = \begin{cases} 4\sin^2\left(k_z^{(s)}\frac{a}{2}\right), & \text{if } m' \text{ and } m \text{ are both even,} \\ 4\cos^2\left(k_z^{(s)}\frac{a}{2}\right), & \text{if } m' \text{ and } m \text{ are both odd,} \\ \mathrm{j}(-1)^{m'} 4\sin\left(k_z^{(s)}\frac{a}{2}\right)\cos\left(k_z^{(s)}\frac{a}{2}\right), & \text{if } m'+m \text{ is odd.} \end{cases} \tag{2.9}$$

The tangent and cotangent functions in the square brackets of (2.8) result from the symmetry of the harmonics as a function of their order $s$.

In a numerical framework, the infinite sums would need to be truncated, so that the vector of unknows and the matrix are of finite size. In this case, the size of the vector $\boldsymbol{c'}$ corresponds to the number of TM modes retained in the corrugations for the computation. This is physically justified, as shown in section 2.1.6.

### 2.1.4 Mode-matching in the mirror-symmetric PPW

The MMM can be applied in a similar way to the nGS corrugated PPW displayed in Fig. 2.1a. The structure is still $p$-periodic, but the nGS geometry is symmetric regarding the plane $y = 0$, unlike the G-S structure. As a consequence, the field of the propagating harmonics is either symmetric or antisymmetric regarding this plane. Both cases can be studied separately by reducing the problem to the lower half of the structure [17, p. 42].

The upper half can be replaced by an infinite plane at $y = 0$. In order to derive an antisymmetric longitudinal electric field, this infinite plane is PEC, whereas for a symmetric longitudinal electric field, the infinite plane is perfectly magnetically conducting (PMC). For the PEC case, boundary conditions then imply that the electric field between the corrugated plates is antisymmetric regarding the plane $y = 0$ i.e., $Y^{(s)} = 0$ in (2.2). For the PMC case, boundary conditions then imply that the electric field between the corrugated plates is symmetric regarding the plane $y = 0$ i.e., $X^{(s)} = 0$ in (2.2).

Mode-matching leads to two sets of equations involving the corrugation coefficients $c_m$ and the gap coefficients ($X^{(s)}$ or $Y^{(s)}$, depending on whether the PMC or the PEC case is considered).

Given that the PMC and the PEC cases are considered separately, these two sets of equations are enough to isolate the normalized corrugation coefficients $c'_m = \sin(k_{y,m}h)c_m$ into a matrix equation similar to (2.7). In the PEC case, the square matrix $\underline{\boldsymbol{M}}$ has coefficients

$$M_{m'm} = \delta_{m'm}\frac{pa}{2^{\min\{1,m\}}}\frac{\cot(k_{y,m}h)}{k_{y,m}} + \sum_{s=-\infty}^{+\infty}\cot\left(k_y^{(s)}\frac{g}{2}\right)\frac{{k_z^{(s)}}^2}{k_y^{(s)}}\frac{f_{m'm}^{(s)}}{\left[{k_z^{(s)}}^2 - \left(\frac{m\pi}{a}\right)^2\right]\left[{k_z^{(s)}}^2 - \left(\frac{m'\pi}{a}\right)^2\right]}, \tag{2.10}$$

whereas in the PMC case, the coefficients are

$$M_{m'm} = \delta_{m'm} \frac{pa}{2^{\min\{1,m\}}} \frac{\cot(k_{y,m}h)}{k_{y,m}} - \sum_{s=-\infty}^{+\infty} \tan\left(k_y^{(s)} \frac{g}{2}\right) \frac{{k_z^{(s)}}^2}{k_y^{(s)}} \frac{f_{m'm}^{(s)}}{\left[k_z^{(s)\,2} - \left(\frac{m\pi}{a}\right)^2\right]\left[k_z^{(s)\,2} - \left(\frac{m'\pi}{a}\right)^2\right]}\,, \tag{2.11}$$

where $\delta_{m'm}$ is the Kroenecker symbol, $k_{y,m} = \sqrt{k_0^2 - \left(\frac{m\pi}{a}\right)^2}$, $k_y^{(s)} = \sqrt{k_0^2 - {k_z^{(s)}}^2}$ and $k_z^{(s)} = k_z + n\frac{2\pi}{p}$, and $f_{m'm}^{(s)}$ is defined as in (2.9).

### 2.1.5 Dispersion equations

In order to have non-trivial solutions, the determinant of the matrix $\underline{\boldsymbol{M}}$ in (2.7) must be equal to zero. This condition yields the dispersion equation relating the wavenumber $k_z$ of the waves propagating with the free-space wavenumber $k_0$,

$$|\underline{\boldsymbol{M}}|(k_0, k_z) = 0\,, \tag{2.12}$$

with the matrix coefficients (2.8) in the G-S case, and (2.10) or (2.11) in the nGS case. We refer to $\underline{\boldsymbol{M}}$ as the dispersion matrix.

Whether the G-S or the nGS waveguide is considered, previous derivations have lead to two possible dispersion equations. In the nGS case, antisymmetric and symmetric modes have been decoupled in (2.10) and (2.11). In the G-S case, depending on the phase-shift used when applying the generalized Floquet theorem, two set of signs can appear in (2.8). In practice, only one equation may be used in order to find the total Brillouin diagram, because changing the sign is equivalent to reordering the Floquet harmonics in the modal decomposition. In the following, we consider only the dispersion equation where the minus sign is chosen is (2.3).

### 2.1.6 Numerical solution: truncation of higher modes and harmonics

#### 2.1.6.1 Truncation of corrugation modes

The size of the dispersion matrix in (2.12) is dependent on the number of corrugation modes. In order to solve the dispersion equation numerically, the infinite amount of modes in the corrugations must be truncated to a finite number. Such a number exists, as matrix coefficients for higher modes tend to be negligible compared to lower modes, as can be seen easily in (2.12) when increasing the mode orders $m'$ and $m$.

When the width of the corrugations is very small compared to the wavelength, as is usually the case for metasurfaces, the field variability on the corrugated plate is small. Consequently, few modes are necessary to capture this variability. That is why it is reasonable to truncate (2.12) to a finite number of corrugation modes. In chapter 3, to simplify the dispersive study of the waveguide with thin corrugations, it is even acceptable to keep only the transverse electric magnetic (TEM) mode.

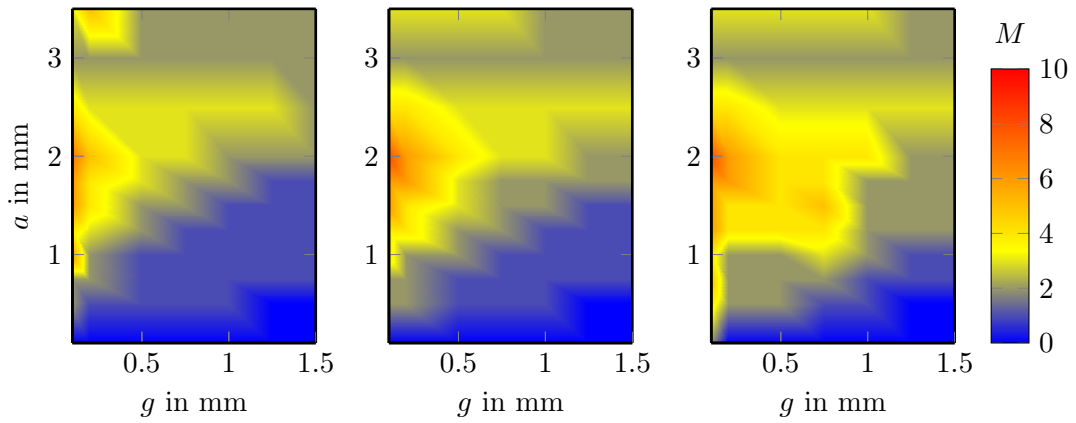


(a) $h = 0.5\,\text{mm}$ (b) $h = 1\,\text{mm}$ (c) $h = 1.5\,\text{mm}$

Figure 2.2: Colormap of the number of corrugations modes $M$ required for the convergence of the G-S dispersion curve for $k < \pi/p$, depending on the gap $g$ and the corrugation width $a$. 37 frequency points are computed for each curve, which is considered to converge when there is less than a 1% variation in $k_z$ for all observation points. The cell width is $p = 4\,\text{mm}$.

In Fig. 2.2, the number of modes for convergence of the Brillouin curve is estimated for different geometrical parameters of the G-S structure. In order to do so, the dispersion equation is solved for 37 points linearly placed between $k = 0$ and $k = \pi/p$, with a cell-length $p = 4\,\text{mm}$. 61 harmonics are considered, that is $s \in [\![-30, 30]\!]$, which is observed to be enough to accurately describe the fields in the gap between the metasurfaces. The number of modes $M$ is increased until convergence of the curve. Convergence is considered to be reached for a number of modes $M$ when for all observation points, there is less than 1% variation between the computed $k_z$ for $M$ and $M - 1$.

The general observation is that the larger $g$, the fewer modes are necessary for convergence. This is expectable, because the coupling between the metasurfaces decreases, and so the field variations are less constrained at the surface of the corrugations. Moreover, for small corrugation widths $a$, very few modes are necessary, which is coherent with the fact that higher modes cannot propagate in thin corrugations. Medium corrugations (around half-a-cell) require the most modes: if $a = p/2$, then the corrugation edges of opposite metasurfaces are the closest, resulting in strong field concentrations. Finally, when increasing the corrugation depth $h$, the number of modes must be increased as well.

#### 2.1.6.2 Truncation of Floquet harmonics

Similarly, the propagation of the Floquet harmonics is also impacted if $\lambda \gg p$. This is usually the case, given that for metasurfaces, the cell length shall be small compared to

the wavelength. The transverse propagation constant of the $s$-th harmonic is

$$k_y^{(s)} = \sqrt{k_0^2 - {k_z^{(s)}}^2} = k_0\sqrt{1 - \left(\frac{k_z^{(s)}}{k_0}\right)^2} = k_0\sqrt{1 - \left(\frac{k_z}{k_0} + s\frac{\lambda}{p}\right)^2}. \tag{2.13}$$

For slow waves, i.e., $k_z/k_0 > 1$, and when $\lambda \gg p$, no harmonics have a real propagation constant in the $y$-direction. Therefore, these modes are attenuated in the $y$-direction. On the one hand, this means that the corresponding $k_z^{(s)}$ is real, meaning that the $s$-th Floquet mode can propagate between the plates. On the other hand, the vertical attenuation gets stronger with increasing order $s$, and so these modes are likely not to "see" both plates simultaneously, meaning that they propagate as if only one corrugated plate was present. These waves do not reflect the complex coupling mechanism that yield the special dispersion behavior of the G-S structure for lower modes. Therefore, a truncation of the number of Floquet harmonics to simplify the expression of (2.12) is justified as well.

### 2.1.7 Validity of the mode-matching method for corrugated PPWs

In this section, the accuracy of the MMM is validated by comparing the computed Brillouin diagrams with the results obtained in the commercial electromagnetic (EM) eigenmode solver of CST. The nGS and the G-S structure displayed in Fig. 2.1 are modeled in CST.

The MMM dispersion equations (2.8) and (2.10) are solved in Matlab using 61 harmonics and 16 modes. In order to solve the dispersion equation, the root-finding algorithm presented in [178] is used. It is based on a local approximation of the underlying complex function by a Padé approximant of type II [179, p. 53]. If the initial guesses do not lie too far away from the root, this algorithm yields exponential convergence. Given the non-linearity of the dispersion equation, the initial guess fed to the algorithm is influent. Given three initial guesses $x_{n-2}$, $x_{n-1}$ and $x_n$ at the $n$-th iteration of the algorithm, the newest guess for the root of a function $f$ is computed as

$$x_{n+1} = \frac{x_1\frac{x_3-x_2}{f(x_1)} + x_2\frac{x_1-x_3}{f(x_2)} + x_3\frac{x_2-x_1}{f(x_3)}}{\frac{x_3-x_2}{f(x_1)} + \frac{x_1-x_3}{f(x_2)} + \frac{x_2-x_1}{f(x_3)}}. \tag{2.14}$$

This algorithm must be applied for each observation frequency. The initial guesses for the newer frequency point can be taken close to the previous result. In doing so, one increases the chances that the same mode is tracked from one frequency point to the other, resulting in a continuous Brillouin curve.

The computed dispersion curves are plotted in Fig. 2.3. For all structures, the cell length is $p = 4\,\text{mm}$ and the gap between the plates $g = 0.1\,\text{mm}$. Each subfigure corresponds to different corrugation widths $a$ and depths $h$.

Fig. 2.3 shows that the MMM accurately renders the Brillouin diagram of these structures. The comparison of the nGS with G-S dispersion curves confirms that GS reduces the dispersion of the first mode, and closes the stopband between the first two modes.

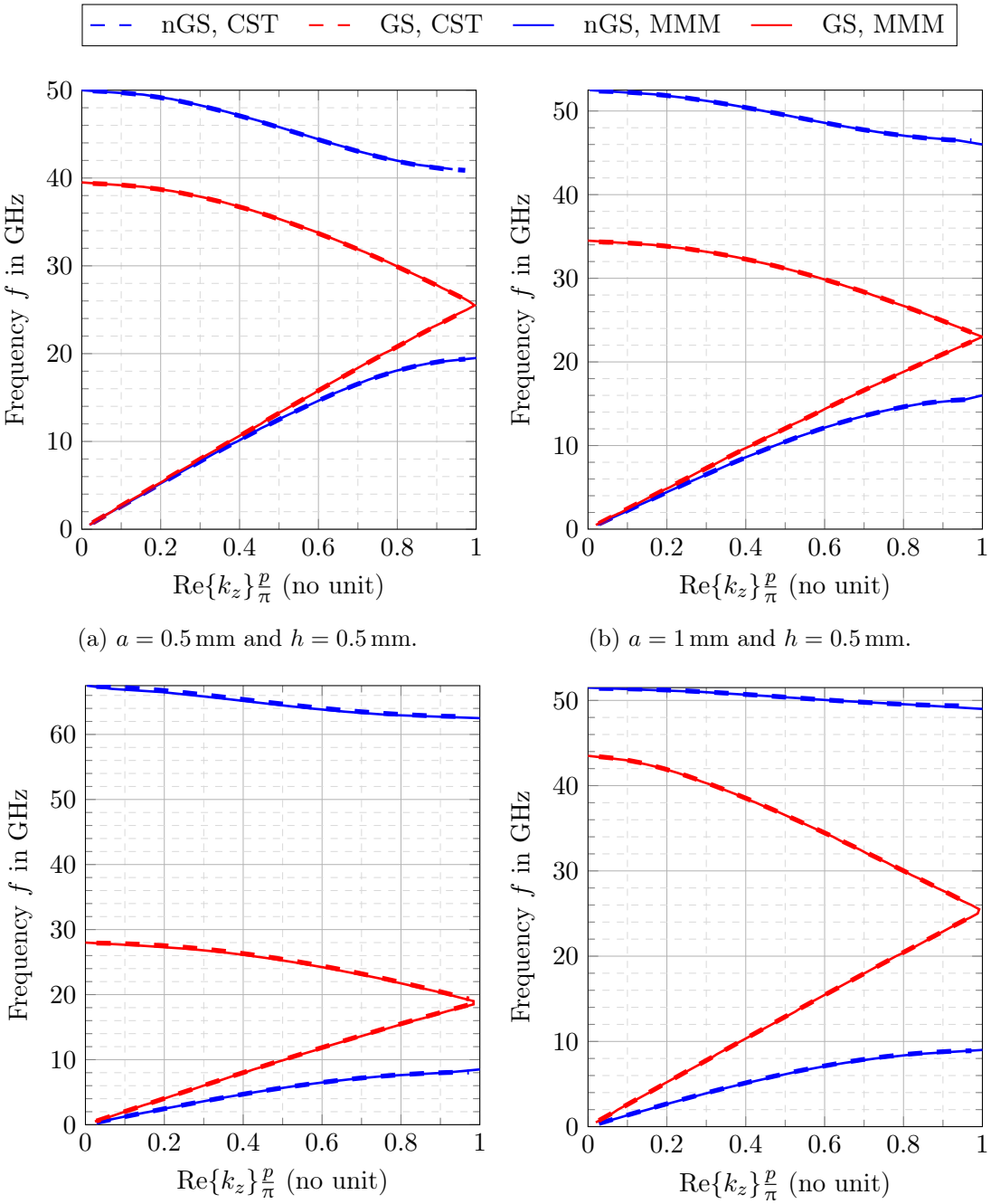


(a) $a = 0.5\,\text{mm}$ and $h = 0.5\,\text{mm}$.

(b) $a = 1\,\text{mm}$ and $h = 0.5\,\text{mm}$.

(c) $a = 2\,\text{mm}$ and $h = 1.5\,\text{mm}$.

(d) $a = 3\,\text{mm}$ and $h = 1.5\,\text{mm}$.

Figure 2.3: Brillouin diagrams for the corrugated PPW, with corrugations of width $a$ and depth $h$. Both G-S and nGS curves are computed with CST or with the MMM. The MMM is applied with 16 modes and 61 harmonics. All structures have $p = 4\,\text{mm}$ and $g = 0.1\,\text{mm}$.

## 2.2 Holey parallel-plate waveguide

While the corrugated PPW is a 1-D G-S waveguide, in this section, a more general example is studied: the holey PPW, which can bear 2-D GS. The focus is placed on the G-S design, but the study of the counterpart nGS structure follows the same steps. Notable changes in the nGS equation are given as side-notes.

### 2.2.1 Holey glide-symmetric PPW

The structure under study is a PPW, where both PEC plates are normal to the $y$-direction and are separated by a gap $g$, filled with a medium 1 with relative permittivity $\epsilon_{\mathrm{r}1}$ and permeability $\mu_{\mathrm{r}1}$. Each plate is pierced with an array of cylindrical holes of depth $h$, filled with a medium 2 with constitutive parameters $(\epsilon_{\mathrm{r}2}, \mu_{\mathrm{r}2})$. The cross-section $S$ of these holes is invariant in the $y$-direction. These holes are repeated periodically in the $x$- and $z$-directions, with the resulting unit cell having a length $p_z$ in the $z$-direction and $p_x$ in the $x$-direction. The upper plate is shifted in both directions by half a unit cell, such that GS is introduced in both $x$- and $z$-directions. The origin of the cartesian coordinate system is placed at mid-distance between the metasurfaces.

The cross-section $S$ of the holes does not need to have a unique closed contour. It can be completely arbitrary, for example allowing isolated pins to be present in the hole. In the following, the word *hole* is used under this loose definition.

Fig. 2.4 illustrates a structure with potato-shaped holes enclosing a single metallic pin. The red arrow in the perspective view indicates the wave propagation plane. In the top view, one unit cell is framed, and the G-S shift between the upper and the lower plates is highlighted. The angle between the propagation direction and the $z$-axis, in the propagation plane, is called $\theta$.

### 2.2.2 Modal decomposition of the fields

#### 2.2.2.1 Modes in the holes

Each hole can be seen as a cylindrical waveguide of cross-section $S$ parallel to the $y$-direction. Fields in the holes can be decomposed as sums of waveguide modes: TM, TE, and TEM modes. In the following, the mode type is identified with the superscript $\mathrm{i} = \mathrm{e}, \mathrm{h}, \mathrm{t}$, respectively. For each mode, the longitudinal $y$-component of the field (subscript $y$) is separated from the transverse field (subscript t), which is a 2-D vector in the $zx$-plane. The electric transverse component of the $m$-th mode can be written as

$$\boldsymbol{E}^{\mathrm{i}}_{\mathrm{t},m}(x,y,z) = \mathrm{j}\boldsymbol{e}^{\mathrm{i}}_{\mathrm{t},m}(z,x)\sin\left(k^{\mathrm{i}}_{y,m}\left[y+h+\tfrac{g}{2}\right]\right)\,, \tag{2.15}$$

where the longitudinal wavenumber $k^{\mathrm{i}}_{y,m} = \sqrt{k_0^2\epsilon_{\mathrm{r}2}\mu_{\mathrm{r}2} - {k^{\mathrm{i}}_m}^2}$ is related to the vacuum free-space wavenumber $k_0$ and the cut-off wavenumber $k^{\mathrm{i}}_m$ of the mode. The two-dimensional field $\boldsymbol{e}^{\mathrm{i}}_{\mathrm{t},m}$ is the $m$-th modal function that characterizes the mode at the surface of the hole. It depends only on the cross-section of the hole, and is independent of the frequency and the hole depth. The sine term in (2.15) is due to the reflection of

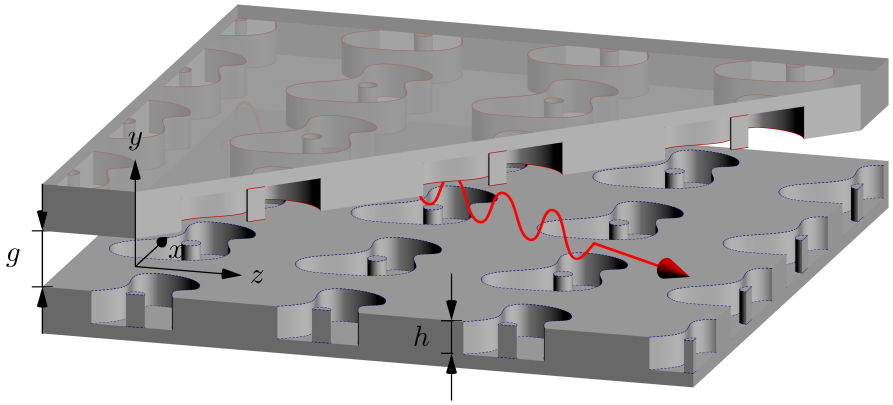


(a) Perspective view. The red arrow indicates the propagation plane.

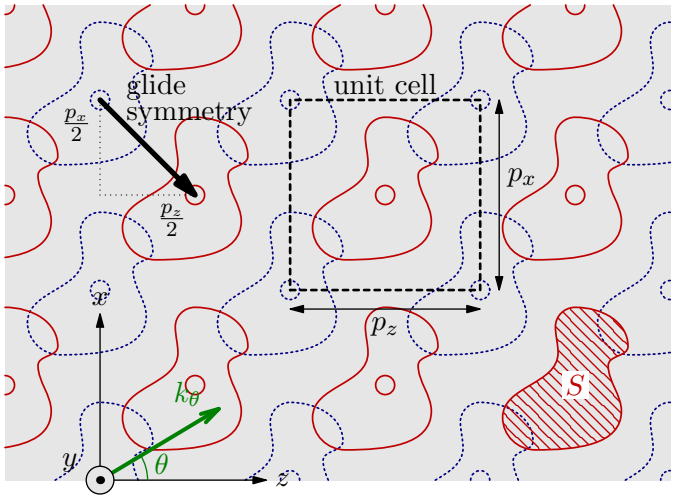


(b) Top view. The G-S shift between upper holes (red) and lower holes (blue) creates GS.

Figure 2.4: Holey G-S PPW under study.

the waves at the bottom of the holes, resulting in a standing wave. The corresponding magnetic transverse field is

$$\boldsymbol{H}^{\mathrm{i}}_{\mathrm{t},m}(x,y,z) = -Y^{\mathrm{i}}_m \left(\hat{\boldsymbol{y}} \times \boldsymbol{e}^{\mathrm{i}}_{\mathrm{t},m}(z,x)\right) \cos\left(k^{\mathrm{i}}_{y,m}\left[y+h+\tfrac{g}{2}\right]\right) . \tag{2.16}$$

The cut-off wavenumber $k^{\mathrm{i}}_m$ must be defined for each mode. Note that for TEM modes, $k^{\mathrm{t}}_m = 0$, and so $k^{\mathrm{t}}_{y,m} = k_0\sqrt{\epsilon_{\mathrm{r}2}\mu_{\mathrm{r}2}} = k_2$. From cylindrical waveguide theory [17, pp.99-101], the wave admittances are

$$Y^{\mathrm{e}}_m = \frac{k_0\epsilon_{\mathrm{r}2}}{\eta_0\sqrt{k_0^2\epsilon_{\mathrm{r}2}\mu_{\mathrm{r}2} - {k^{\mathrm{e}}_m}^2}}, \quad Y^{\mathrm{h}}_m = \frac{\sqrt{k_0^2\epsilon_{\mathrm{r}2}\mu_{\mathrm{r}2} - {k^{\mathrm{h}}_m}^2}}{\eta_0 k_0 \mu_{\mathrm{r}2}} \quad \text{and} \quad Y^{\mathrm{t}}_m = \frac{1}{\eta_2}, \tag{2.17}$$

where $\eta_2 = \eta_0\sqrt{\mu_2/\epsilon_{\mathrm{r}2}}$, with $\eta_0 \simeq 377\,\Omega$ the intrinsic vacuum impedance.

As such, the total transverse fields in the holes are weighted sums of these modes,

$$\boldsymbol{E}_{\mathrm{t}}^{\mathrm{i}}(x,y,z) = \mathrm{j}\sum_m C_m^{\mathrm{i}}\boldsymbol{e}_{\mathrm{t},m}^{\mathrm{i}}(z,x)\sin\left(k_{y,m}^{\mathrm{i}}\left[y+h+\tfrac{g}{2}\right]\right)\,, \tag{2.18}$$

and

$$\boldsymbol{H}_{\mathrm{t}}^{\mathrm{i}}(x,y,z) = -\sum_m C_m^{\mathrm{i}}Y_m^{\mathrm{i}}\left(\hat{\boldsymbol{y}}\times\boldsymbol{e}_{\mathrm{t},m}^{\mathrm{i}}(z,x)\right)\cos\left(k_{y,m}^{\mathrm{i}}\left[y+h+\tfrac{g}{2}\right]\right)\,. \tag{2.19}$$

**Longitudinal field components** From Maxwell's equations, the longitudinal component of each TM mode is found as

$$E_{y,m}^{\mathrm{e}} = \frac{\eta_0}{\mathrm{j}k_0\epsilon_{\mathrm{r}2}}\left[\frac{\partial H_{x,m}^{\mathrm{e}}}{\partial z}-\frac{\partial H_{z,m}^{\mathrm{e}}}{\partial x}\right] = \frac{\mathrm{j}\cos\left(k_{y,m}^{\mathrm{e}}\left[y+h+\frac{g}{2}\right]\right)}{\sqrt{k_0^2\epsilon_{\mathrm{r}2}\mu_{\mathrm{r}2}-{k_m^{\mathrm{e}}}^2}}\left(\frac{\partial e_{z,m}^{\mathrm{e}}}{\partial z}+\frac{\partial e_{x,m}^{\mathrm{e}}}{\partial x}\right)\,, \tag{2.20}$$

with $\eta_0$ the intrinsic vacuum impedance. Similarly, the longitudinal TE magnetic component is

$$H_{y,m}^{\mathrm{h}} = \frac{1}{\mathrm{j}k_0\eta_0\mu_{\mathrm{r}2}}\left[\frac{\partial E_{z,m}^{\mathrm{h}}}{\partial x}-\frac{\partial E_{x,m}^{\mathrm{h}}}{\partial z}\right] = \frac{\sin\left(k_{y,m}^{\mathrm{h}}\left[y+h+\frac{g}{2}\right]\right)}{k_0\eta_0\mu_{\mathrm{r}2}}\left[\frac{\partial e_{z,m}^{\mathrm{h}}}{\partial x}-\frac{\partial e_{x,m}^{\mathrm{h}}}{\partial z}\right]\,. \tag{2.21}$$

Obviously, TEM modes have no longitudinal field components.

#### 2.2.2.2 Floquet harmonics between the holey metasurfaces

Due the periodicity of the structure, the fields between the metasurfaces are expressed as a sum of Floquet harmonics. Each harmonic of orders $(s,\ell)$, $s\in\mathbb{Z}$ and $\ell\in\mathbb{Z}$, has components parallel to the propagation plane $zx$ that can be expressed as

$$\boldsymbol{E}_{\mathrm{t}}^{(s\ell)} = \left[\,\boldsymbol{a}^{(s\ell)}\sin\left(k_y^{(s\ell)}y\right)+\boldsymbol{b}^{(s\ell)}\cos\left(k_y^{(s\ell)}y\right)\right]\mathrm{e}^{-\mathrm{j}k_x^{(\ell)}x-\mathrm{j}k_z^{(s)}z}\,, \tag{2.22a}$$

$$\boldsymbol{H}_{\mathrm{t}}^{(s\ell)} = \underline{\boldsymbol{Y}}^{(s\ell)}\cdot\left[\,\boldsymbol{a}^{(s\ell)}\cos\left(k_y^{(s\ell)}y\right)-\boldsymbol{b}^{(s\ell)}\sin\left(k_y^{(s\ell)}y\right)\right]\mathrm{e}^{-\mathrm{j}k_x^{(\ell)}x-\mathrm{j}k_z^{(s)}z}\,, \tag{2.22b}$$

with the vertical wavenumber $k_y^{(s\ell)} = \sqrt{k_0^2\epsilon_{\mathrm{r}1}\mu_{\mathrm{r}1}-{k_x^{(\ell)}}^2-{k_z^{(s)}}^2}$, and the Floquet wavenumbers $k_z^{(s)}$ and $k_x^{(\ell)}$ being

$$k_z^{(s)} = k_z + s\frac{2\pi}{p_z} \quad\text{and}\quad k_x^{(\ell)} = k_x+\ell\frac{2\pi}{p_x}\,. \tag{2.23}$$

Given the Maxwell-Faraday equation, the admittance matrix in (2.22b) is equal to

$$\underline{\boldsymbol{Y}}^{(s\ell)} = \frac{\mathrm{j}}{k_0\eta_0\mu_{\mathrm{r}1}k_y^{(s\ell)}}\begin{bmatrix}-k_x^{(\ell)}k_z^{(s)} & {k_z^{(s)}}^2-k_0^2\epsilon_{\mathrm{r}1}\mu_{\mathrm{r}1}\\ k_0^2\epsilon_{\mathrm{r}1}\mu_{\mathrm{r}1}-{k_x^{(\ell)}}^2 & k_x^{(\ell)}k_z^{(s)}\end{bmatrix}\,, \tag{2.24}$$

where the transverse two-dimensional basis is $(z,x)$.

As such, the total fields is the propagation plane between the metasurfaces are

$$\boldsymbol{E}_{\mathrm{t}} = \sum_{s=-\infty}^{+\infty} \sum_{\ell=-\infty}^{+\infty} \left[ \boldsymbol{a}^{(s\ell)} \sin\left(k_y^{(s\ell)} y\right) + \boldsymbol{b}^{(s\ell)} \cos\left(k_y^{(s\ell)} y\right) \right] F^{(s\ell)}\,, \tag{2.25a}$$

$$\boldsymbol{H}_{\mathrm{t}} = \sum_{s=-\infty}^{+\infty} \sum_{\ell=-\infty}^{+\infty} \underline{\boldsymbol{Y}}^{(s\ell)} \left[ \boldsymbol{a}^{(s\ell)} \cos\left(k_y^{(s\ell)} y\right) - \boldsymbol{b}^{(s\ell)} \sin\left(k_y^{(s\ell)} y\right) \right] F^{(s\ell)}\,, \tag{2.25b}$$

where $F^{(s\ell)} = \mathrm{e}^{-\mathrm{j}k_x^{(\ell)}x - \mathrm{j}k_z^{(s)}z}$. In the following, the double sum $\sum_{s=-\infty}^{+\infty} \sum_{\ell=-\infty}^{+\infty}$ is written $\sum_{s,\ell}$ for conciseness.

**Transverse field components** From the Maxwell-Gauss equation, the transverse field components of each harmonic are

$$E_y^{(s\ell)} = \mathrm{j}\frac{F^{(s\ell)}}{k_y^{(s\ell)}} \begin{bmatrix} k_z^{(s)} \\ k_x^{(\ell)} \end{bmatrix}^{\mathrm{T}} \cdot \left[ \boldsymbol{b}^{(s\ell)} \sin\left(k_y^{(s\ell)} y\right) - \boldsymbol{a}^{(s\ell)} \cos\left(k_y^{(s\ell)} y\right) \right]\,, \tag{2.26}$$

and

$$H_y^{(s\ell)} = \frac{F^{(s\ell)}}{k_1\eta_1} \begin{bmatrix} -k_x^{(\ell)} \\ k_z^{(s)} \end{bmatrix}^{\mathrm{T}} \cdot \left[ \boldsymbol{a}^{(s\ell)} \sin\left(k_y^{(s\ell)} y\right) + \boldsymbol{b}^{(s\ell)} \cos\left(k_y^{(s\ell)} y\right) \right]\,. \tag{2.27}$$

### 2.2.3 Mode-matching in the GS holey PPW

#### 2.2.3.1 Mode-matching: electric field continuity on the holes

First, the electric fields are projected onto the basis of Floquet harmonics, both in the gap and in the holes, such that their coefficients can be equated at the surface of the holes. The Floquet harmonics are already expressed in this basis. However, the change of basis for the fields in the holes results in the series of terms called projected modal functions (PMFs), defined for each modal function $\boldsymbol{e}_{\mathrm{t},m}^{\mathrm{i}}$ as

$$\tilde{\boldsymbol{e}}_{\mathrm{t},m}^{\mathrm{i}(s\ell)} = \iint_S \boldsymbol{e}_{\mathrm{t},m}^{\mathrm{i}} F^{(s\ell)} \mathrm{d}S\,. \tag{2.28}$$

These PMFs can be seen as the 2-D Fourier transforms of the modal functions, evaluated at the pair of Floquet wavenumbers $(k_z^{(s)}, k_x^{(\ell)})$.

Matching the fields at the lower hole ($y = -g/2$) yields a first set of equations with the unknown field coefficients $C_m^{\mathrm{i}}$, $\boldsymbol{a}^{(s\ell)}$ and $\boldsymbol{b}^{(s\ell)}$. According to the generalized Floquet theorem (1.13), the fields at the surface of the upper hole have a phase-shift of $\pm\mathrm{e}^{-\mathrm{j}k_x\frac{p_x}{2}}\mathrm{e}^{-\mathrm{j}k_z\frac{p_z}{2}}$ with respect to the fields at the lower hole, meaning that

$$\boldsymbol{E}\left(x, \tfrac{g}{2}, z\right) = \pm\mathrm{e}^{-\mathrm{j}k_x\frac{p_x}{2}}\mathrm{e}^{-\mathrm{j}k_z\frac{p_z}{2}}\boldsymbol{E}\left(x - \tfrac{p_x}{2}, -\tfrac{g}{2}, z - \tfrac{p_z}{2}\right)\,. \tag{2.29}$$

Therefore, at the upper hole ($y = g/2$), the projection of the hole modes onto the Floquet harmonics yields a second set of equations, involving the same unknowns. Combining these two equations yields the Floquet coefficients as functions of the hole mode coefficients,

$$\boldsymbol{a}^{(s\ell)} = \frac{\mathrm{j}}{p_x p_z} \frac{-1 \pm (-1)^{s+\ell}}{2 \sin\left(k_y^{(s\ell)} \frac{g}{2}\right)} \sum_m C_m^{\mathrm{i}} \sin\left(k_{y,m}^{\mathrm{i}} h\right) \tilde{\boldsymbol{e}}_{\mathrm{t},m}^{\mathrm{i}(s\ell)*}, \tag{2.30a}$$

$$\boldsymbol{b}^{(s\ell)} = \frac{\mathrm{j}}{p_x p_z} \frac{1 \pm (-1)^{s+\ell}}{2 \cos\left(k_y^{(s\ell)} \frac{g}{2}\right)} \sum_m C_m^{\mathrm{i}} \sin\left(k_{y,m}^{\mathrm{i}} h\right) \tilde{\boldsymbol{e}}_{\mathrm{t},m}^{\mathrm{i}(s\ell)*}. \tag{2.30b}$$

Note that these equations are vectorial, given that the PMFs have two components along the $z$- and the $x$-direction.

**NGS configuration** If the holes of the upper and lower metasurfaces are aligned, then the structure has mirror symmetry. Using image theory, half of the structure can be filled with PEC. The magnetic fields are symmetric with respect to the middle propagation plane, and the electric fields are antisymmetric. Therefore, for all $(s, \ell)$, $\boldsymbol{b}^{(s\ell)} = 0$, and

$$\boldsymbol{a}^{(s\ell)} = -\frac{\mathrm{j}}{p_x p_z \sin\left(k_y^{(s\ell)} \frac{g}{2}\right)} \sum_m C_m^{\mathrm{i}} \sin\left(k_{y,m}^{\mathrm{i}} h\right) \tilde{\boldsymbol{e}}_{\mathrm{t},m}^{\mathrm{i}(s\ell)*}. \tag{2.31}$$

#### 2.2.3.2 Mode-matching: magnetic field continuity on the holes

The boundary conditions require the tangential magnetic fields to be continuous along the boundary between the holes and the PPW gap. In order to enforce this condition, the magnetic fields in the gap are projected onto the basis of vectorial hole modes. The resulting modal coefficients can then be equated along the hole surface.

We introduce the squared norm of the real modal functions

$$I_m^{\mathrm{i}} = \iint_S \boldsymbol{e}_{\mathrm{t},m}^{\mathrm{i}} \cdot \boldsymbol{e}_{\mathrm{t},m}^{\mathrm{i}} \mathrm{d}S. \tag{2.32}$$

Because of the orthogonality of the modes in the holes, the projection of one mode onto the other is always null, unless the mode is projected onto itself, yielding $I_m^{\mathrm{i}}$.

For a given mode of type $\mathrm{i}'$ and order $m'$, the projection of the total tangential magnetic field on the modal function $\boldsymbol{e}_{\mathrm{t},m'}^{\mathrm{i}'}$ yields

$$-C_{m'}^{\mathrm{i}'} Y_{m'}^{\mathrm{i}'} I_{m'}^{\mathrm{i}'} \cos\left(k_{y,m'}^{\mathrm{i}'} h\right) = \sum_{s,\ell} \underline{\boldsymbol{Y}}^{(s\ell)} \begin{bmatrix} \boldsymbol{a}^{(s\ell)} \cos\left(k_y^{(s\ell)} \frac{g}{2}\right) \\ + \boldsymbol{b}^{(s\ell)} \sin\left(k_y^{(s\ell)} \frac{g}{2}\right) \end{bmatrix} \cdot \left(\hat{\boldsymbol{y}} \times \tilde{\boldsymbol{e}}_{\mathrm{t},m'}^{\mathrm{i}'(s\ell)}\right). \tag{2.33}$$

#### 2.2.3.3 Matrix equation of the holey glide-symmetric PPW

The expressions of Floquet coefficients (2.30) can be inserted in (2.33). We choose the negative signs in (2.30). This yields an equation that only involves the hole mode coefficients, that is

$$\begin{aligned}
&-C^{\mathrm{i}'}_{m'} Y^{\mathrm{i}'}_{m'} I^{\mathrm{i}'}_{m'} \cos\left(k^{\mathrm{i}'}_{y,m'} h\right) \\
&= -\frac{\mathrm{j}}{p_x p_z} \sum_m C^{\mathrm{i}}_m \sin\left(k^{\mathrm{i}}_{y,m} h\right) \sum_{s,\ell} f^{(s\ell)} \underline{\boldsymbol{Y}}^{(s\ell)} \tilde{\boldsymbol{e}}^{\mathrm{i}(s\ell)*}_{\mathrm{t},m} \cdot \left(\hat{\boldsymbol{y}} \times \tilde{\boldsymbol{e}}^{\mathrm{i}'(s\ell)}_{\mathrm{t},m'}\right),
\end{aligned} \tag{2.34}$$

where we call the *vertical spectral function*

$$f^{(s\ell)} = \begin{cases} \cot\left(k_y^{(s\ell)} \frac{g}{2}\right), & \text{if } s+\ell \text{ is even,} \\ -\tan\left(k_y^{(s\ell)} \frac{g}{2}\right), & \text{if } s+\ell \text{ is odd.} \end{cases}. \tag{2.35}$$

To simplify the equations, we introduce the scaled mode coefficients $c^{\mathrm{i}}_m = C^{\mathrm{i}}_m \sin\left(k^{\mathrm{i}}_{y,m} h\right)$. Developing the admittance matrix $\underline{\boldsymbol{Y}}^{(s\ell)}$ finally yields the mode-matching equations, for each mode of order $m'$,

$$\begin{aligned}
&-k_0 \eta_0 \mu_{\mathrm{r}1} p_x p_z c^{\mathrm{i}'}_{m'} Y^{\mathrm{i}'}_{m'} I^{\mathrm{i}'}_{m'} \cot\left(k^{\mathrm{i}'}_{y,m'} h\right) \\
&= \sum_m c^{\mathrm{i}}_m \sum_{s,\ell} \frac{f^{(s\ell)}}{k_y^{(s\ell)}} \left[ \begin{array}{l} k_0^2 \epsilon_{\mathrm{r}1} \mu_{\mathrm{r}1} \left( \tilde{e}^{\mathrm{i}'(s\ell)}_{z,m'} \tilde{e}^{\mathrm{i}(s\ell)*}_{z,m} + \tilde{e}^{\mathrm{i}'(s\ell)}_{x,m'} \tilde{e}^{\mathrm{i}(s\ell)*}_{x,m} \right) \\ - \left( k_z^{(s)} \tilde{e}^{\mathrm{i}'(s\ell)}_{x,m'} - k_x^{(\ell)} \tilde{e}^{\mathrm{i}'(s\ell)}_{z,m'} \right) \left( k_z^{(s)} \tilde{e}^{\mathrm{i}(s\ell)}_{x,m} - k_x^{(\ell)} \tilde{e}^{\mathrm{i}(s\ell)}_{z,m} \right)^* \end{array} \right].
\end{aligned} \tag{2.36}$$

Equation (2.36) can be reformulated into a matrix equation $\underline{\boldsymbol{M}} \cdot \boldsymbol{c} = 0$, with $\boldsymbol{c}$ the vector of unknown normalized mode coefficients $c^{\mathrm{i}}_m$, and where each row and each column of the matrix $\underline{\boldsymbol{M}}$ corresponds to hole modes of orders $m'$ and $m$ and types i′ and i′. The coefficients of this matrix are

$$\begin{aligned}
M^{\mathrm{i}'\mathrm{i}}_{m'm} &= \delta_{\mathrm{i}'\mathrm{i}} \delta_{m'm} k_0 \eta_0 \mu_{\mathrm{r}1} p_x p_z Y^{\mathrm{i}}_m I^{\mathrm{i}}_m \cot\left(k^{\mathrm{i}}_{y,m} h\right) \\
&\quad + \sum_{s,\ell} \frac{f^{(s\ell)}}{k_y^{(s\ell)}} \left[ \begin{array}{l} k_0^2 \epsilon_{\mathrm{r}1} \mu_{\mathrm{r}1} \left( \tilde{e}^{\mathrm{i}'(s\ell)}_{z,m'} \tilde{e}^{\mathrm{i}(s\ell)*}_{z,m} + \tilde{e}^{\mathrm{i}'(s\ell)}_{x,m'} \tilde{e}^{\mathrm{i}(s\ell)*}_{x,m} \right) \\ - \left( k_z^{(s)} \tilde{e}^{\mathrm{i}'(s\ell)}_{x,m'} - k_x^{(\ell)} \tilde{e}^{\mathrm{i}'(s\ell)}_{z,m'} \right) \left( k_z^{(s)} \tilde{e}^{\mathrm{i}(s\ell)}_{x,m} - k_x^{(\ell)} \tilde{e}^{\mathrm{i}(s\ell)}_{z,m} \right)^* \end{array} \right].
\end{aligned} \tag{2.37}$$

The truncation of the number of hole modes and harmonics can be justified like for the corrugated structure in section 2.1.6.

**NGS configuration** In the nGS case, the mode-matching equations are the same, except for the vertical spectral function, which is a cotangent for all harmonics (not just for even-order harmonics like in the G-S case).

### 2.2.4 Dispersion equation

The dispersion matrix $\underline{\boldsymbol{M}}$ can be subdivided according to the type of modes involved. As such, the matrix equation can be rewritten as

$$\begin{bmatrix} \underline{\boldsymbol{M}}^{\mathrm{e/e}} & \underline{\boldsymbol{M}}^{\mathrm{e/h}} \\ \left(\underline{\boldsymbol{M}}^{\mathrm{e/h}}\right)^{\mathrm{H}} & \underline{\boldsymbol{M}}^{\mathrm{h/h}} \end{bmatrix} \begin{bmatrix} \boldsymbol{c}^{\mathrm{e}} \\ \boldsymbol{c}^{\mathrm{h}} \end{bmatrix} = \boldsymbol{0}\,, \tag{2.38}$$

where the hole modes have been regrouped such that the first row/columns correspond to TM modes (all terms with an 'e' superscript), whereas the last rows/columns correspond to TE modes and TEM modes (all terms with an 'h' superscript). The choice of regrouping TE and TEM modes is motivated in paragraph 2.2.4.1.

The coefficients of the resulting submatrices are

$$\begin{aligned} M^{\mathrm{e/e}}_{m'm} = {} & \delta_{m'm} k_0^2 \frac{\mu_{\mathrm{r}1}\epsilon_{\mathrm{r}2}}{\sqrt{k_0^2\epsilon_{\mathrm{r}2}\mu_{\mathrm{r}2} - {k_m^{\mathrm{e}}}^2}} p_x p_z I_m^{\mathrm{e}} \cot\left(h\sqrt{k_0^2\epsilon_{\mathrm{r}2}\mu_{\mathrm{r}2} - {k_m^{\mathrm{e}}}^2}\right) \\ & + \sum_{s,\ell} \frac{f^{(s\ell)}}{k_y^{(s\ell)}} \begin{bmatrix} k_0^2\epsilon_{\mathrm{r}1}\mu_{\mathrm{r}1}\left(\tilde{e}^{\mathrm{e}(s\ell)}_{z,m'}\tilde{e}^{\mathrm{e}(s\ell)*}_{z,m} + \tilde{e}^{\mathrm{e}(s\ell)}_{x,m'}\tilde{e}^{\mathrm{e}(s\ell)*}_{x,m}\right) \\ -\left(k_z^{(s)}\tilde{e}^{\mathrm{e}(s\ell)}_{x,m'} - k_x^{(\ell)}\tilde{e}^{\mathrm{e}(s\ell)}_{z,m'}\right)\left(k_z^{(s)}\tilde{e}^{\mathrm{e}(s\ell)}_{x,m} - k_x^{(\ell)}\tilde{e}^{\mathrm{e}(s\ell)}_{z,m}\right)^* \end{bmatrix}, \end{aligned} \tag{2.39}$$

given the wave impedance of TM modes, and

$$\begin{aligned} M^{\mathrm{h/h}}_{m'm} = {} & \delta_{m'm} \frac{\mu_{\mathrm{r}1}\sqrt{k_0^2\epsilon_{\mathrm{r}2}\mu_{\mathrm{r}2} - {k_m^{\mathrm{h}}}^2}}{\mu_{\mathrm{r}2}} p_x p_z I_m^{\mathrm{h}} \cot\left(h\sqrt{k_0^2\epsilon_{\mathrm{r}2}\mu_{\mathrm{r}2} - {k_m^{\mathrm{h}}}^2}\right) \\ & + \sum_{s,\ell} \frac{f^{(s\ell)}}{k_y^{(s\ell)}} \begin{bmatrix} k_0^2\epsilon_{\mathrm{r}1}\mu_{\mathrm{r}1}\left(\tilde{e}^{\mathrm{h}(s\ell)}_{z,m'}\tilde{e}^{\mathrm{h}(s\ell)*}_{z,m} + \tilde{e}^{\mathrm{h}(s\ell)}_{x,m'}\tilde{e}^{\mathrm{h}(s\ell)*}_{x,m}\right) \\ -\left(k_z^{(s)}\tilde{e}^{\mathrm{h}(s\ell)}_{x,m'} - k_x^{(\ell)}\tilde{e}^{\mathrm{h}(s\ell)}_{z,m'}\right)\left(k_z^{(s)}\tilde{e}^{\mathrm{h}(s\ell)}_{x,m} - k_x^{(\ell)}\tilde{e}^{\mathrm{h}(s\ell)}_{z,m}\right)^* \end{bmatrix}, \end{aligned} \tag{2.40}$$

given the wave impedance of TE modes. For TEM modes, the definition (2.40) is still valid, given that the wave impedance of TE modes is a generalization of the TEM impedance for a non-zero cut-off wavenumber. Note that there are diagonal matrix terms in $\underline{\boldsymbol{M}}^{\mathrm{h/h}}$ only when the orders $m'$ and $m$ are equal, and both correspond to the same mode type (TE or TEM). Finally, the non-diagonal submatrix $\underline{\boldsymbol{M}}^{\mathrm{e/h}}$ has coefficients

$$M^{\mathrm{e/h}}_{m'm} = \sum_{s,\ell} \frac{f^{(s\ell)}}{k_y^{(s\ell)}} \begin{bmatrix} k_0^2\epsilon_{\mathrm{r}1}\mu_{\mathrm{r}1}\left(\tilde{e}^{\mathrm{e}(s\ell)}_{z,m'}\tilde{e}^{\mathrm{h}(s\ell)*}_{z,m} + \tilde{e}^{\mathrm{e}(s\ell)}_{x,m'}\tilde{e}^{\mathrm{h}(s\ell)*}_{x,m}\right) \\ -\left(k_z^{(s)}\tilde{e}^{\mathrm{e}(s\ell)}_{x,m'} - k_x^{(\ell)}\tilde{e}^{\mathrm{e}(s\ell)}_{z,m'}\right)\left(k_z^{(s)}\tilde{e}^{\mathrm{h}(s\ell)}_{x,m} - k_x^{(\ell)}\tilde{e}^{\mathrm{h}(s\ell)}_{z,m}\right)^* \end{bmatrix}, \tag{2.41}$$

where there is no diagonal term because the matrix $\underline{\boldsymbol{M}}^{\mathrm{e/h}}$ represents the TM interactions with TE or TEM modes.

In order for (2.38) to yield a non-trivial solution, the determinant of the matrix must be zero. This yields the dispersion equation of the structure,

$$\begin{vmatrix} \underline{\boldsymbol{M}}^{\mathrm{e/e}} & \underline{\boldsymbol{M}}^{\mathrm{e/h}} \\ \left(\underline{\boldsymbol{M}}^{\mathrm{e/h}}\right)^{\mathrm{H}} & \underline{\boldsymbol{M}}^{\mathrm{h/h}} \end{vmatrix} = 0\,. \tag{2.42}$$

This dispersion equation can be solved numerically for any frequency $f$ in order to obtain the Brillouin diagram of the structure, as explained for the corrugated structure in section 2.1.7.

#### 2.2.4.1 Reduced dispersion matrix coefficients

When TM modes are involved in (2.38), the matrix coefficients can be simplified, due to the relation between the cartesian components of the transverse electric field. From waveguide field theory [17, p. 100], the TM modal functions satisfy

$$\begin{bmatrix} e^{\mathrm{e}}_{z,m}(z,x) \\ e^{\mathrm{e}}_{x,m}(z,x) \end{bmatrix} = \frac{1}{k^{\mathrm{e}}_m} \nabla_{\mathrm{t}} e_{y,m}(z,x)\,, \tag{2.43}$$

where $e_{y,m}$ is the longitudinal electric field of the TM modal function. The superscript 'e' is omitted, given that only TM modes have an electric $y$-component. The PMFs defined in (2.28) are linked to the longitudinal field component with

$$\begin{aligned} \begin{bmatrix} \tilde{e}^{\mathrm{e}(s\ell)}_{z,m} \\ \tilde{e}^{\mathrm{e}(s\ell)}_{x,m} \end{bmatrix} &= \iint_S \left[ \nabla_{\mathrm{t}} \left\{ \frac{e_{y,m}}{k^{\mathrm{e}}_m} F^{(s\ell)} \right\} - \frac{e_{y,m}}{k^{\mathrm{e}}_m} \nabla_{\mathrm{t}} \left\{ F^{(s\ell)} \right\} \right] \mathrm{d}S \\ &= \oint_{\partial S} \frac{e_{y,m}}{k^{\mathrm{e}}_m} F^{(s\ell)} \boldsymbol{n} \mathrm{d}\ell + \mathrm{j} \begin{bmatrix} k^{(s)}_z \\ k^{(\ell)}_x \end{bmatrix} \iint_S \frac{e_{y,m}}{k^{\mathrm{e}}_m} F^{(s\ell)} \mathrm{d}S \\ &= \frac{\mathrm{j}}{k^{\mathrm{e}}_m} \begin{bmatrix} k^{(s)}_z \\ k^{(\ell)}_x \end{bmatrix} \iint_S e_{y,m} F^{(s\ell)} \mathrm{d}S\,. \end{aligned} \tag{2.44}$$

The first line comes from the gradient product rule. The second line is derived from Green's theorem [180, p. 431]. Indeed, appendix B.2 shows that

$$\iint_S \nabla_{\mathrm{t}} e_{y,m}(z,x) \mathrm{d}z\mathrm{d}x = \oint_{\partial S} e_{y,m}(z,x) \boldsymbol{n} \mathrm{d}\ell\,, \tag{2.45}$$

where $\partial S$ is the hole contour and $\boldsymbol{n}$ is the exterior normal at each contour point. Finally, the last line is obtained considering that the longitudinal electric field vanishes on the hole contour.

From (2.44), it comes that

$$k^{(\ell)}_x \tilde{e}^{\mathrm{e}(s\ell)}_{z,m} = k^{(s)}_z \tilde{e}^{\mathrm{e}(s\ell)}_{x,m}\,, \tag{2.46}$$

This is true for all TM modes, for arbitrary holes. Consequently, the matrix coefficients (2.39) and (2.41), which involve TM modes, can be simplified as

$$\begin{aligned} M^{\mathrm{e/e}}_{m'm} = {} & \delta_{m'm} k_0^2 \frac{\mu_{\mathrm{r}1}\epsilon_{\mathrm{r}2}}{\sqrt{k_0^2 \epsilon_{\mathrm{r}2}\mu_{\mathrm{r}2} - {k^{\mathrm{e}}_m}^2}} p_x p_z I^{\mathrm{e}}_m \cot\left( h \sqrt{k_0^2 \epsilon_{\mathrm{r}2}\mu_{\mathrm{r}2} - {k^{\mathrm{e}}_m}^2} \right) \\ & + k_0^2 \epsilon_{\mathrm{r}1}\mu_{\mathrm{r}1} \sum_{s,\ell} \frac{f^{(s\ell)}}{k^{(s\ell)}_y} \frac{\tilde{e}^{(s\ell)}_{y,m'} \tilde{e}^{(s\ell)*}_{y,m}}{k^{\mathrm{e}}_{m'} k^{\mathrm{e}}_m} \left( {k^{(s)}_z}^2 + {k^{(\ell)}_x}^2 \right)\,. \end{aligned} \tag{2.47}$$

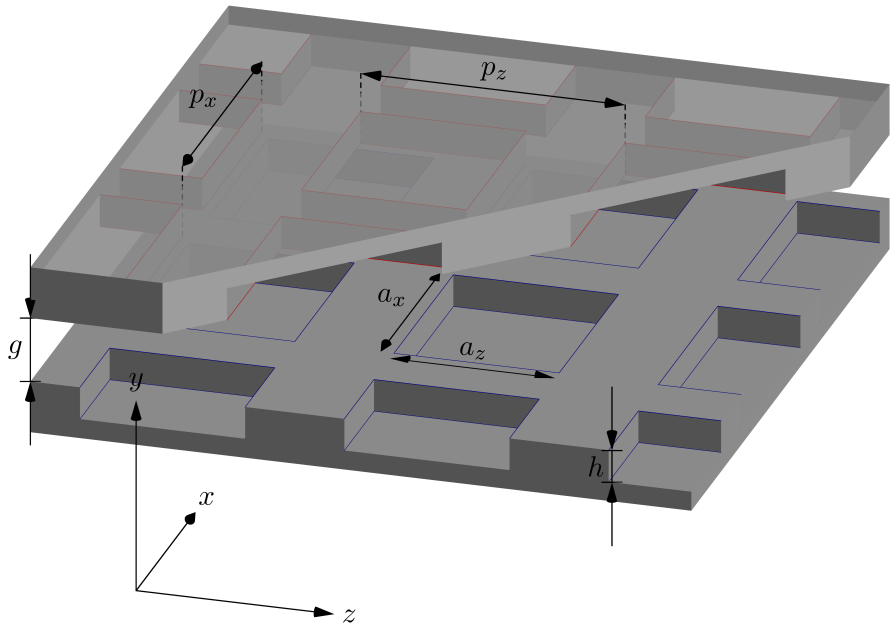


Figure 2.5: Holey G-S PPW with rectangular holes of size $a_z \times a_x$.

and

$$M^{\mathrm{e/h}}_{m'm} = \mathrm{j}k_0^2\epsilon_{\mathrm{r1}}\mu_{\mathrm{r1}} \sum_{s,\ell} \frac{f^{(s\ell)}}{k_y^{(s\ell)}} \frac{\tilde{e}^{(s\ell)}_{y,m'}}{k^{\mathrm{e}}_{m'}} \left( k_z^{(s)} \tilde{e}^{\mathrm{h}(s\ell)}_{z,m} + k_x^{(\ell)} \tilde{e}^{\mathrm{h}(s\ell)}_{x,m} \right)^* , \tag{2.48}$$

where the PMF for the longitudinal component is defined as

$$\tilde{e}^{(s\ell)}_{y,m} = \iint_S e_{y,m} F^{(s\ell)} \mathrm{d}S \,. \tag{2.49}$$

As such, the only information that is required for TM modes is the longitudinal component $e_{y,m}$. The squared norm (2.32) can be reformulated for each mode as

$$I^{\mathrm{e}}_m = \iint_S \frac{1}{{k^{\mathrm{e}}_m}^2} \left[ \left( \frac{\partial e_{y,m}}{\partial z} \right)^2 + \left( \frac{\partial e_{y,m}}{\partial x} \right)^2 \right] \mathrm{d}S \,. \tag{2.50}$$

No such simplification can be done for TE or TEM modes. Indeed, the TE longitudinal magnetic field component does not vanish on the hole contour, which prevents the simplifications done in (2.44) for TM modes. The same is true for the scalar potential of the TEM modes.

### 2.2.5 Example: rectangular holes

The MMM presented in the previous paragraphs is applicable for any holey metasurfaces. However, canonical hole shapes such as rectangles or circles have closed-form expressions for their modal functions, and so the PMFs (2.28) can be found analytically.

As an example, a GS PPW with empty rectangular holes is considered, as illustrated in Fig. 2.5. For holes of size $a_z \times a_x$, each modal function is defined by two integer orders $q$ and $m$. TM modes with $m > 0$ and $q > 0$ have the longitudinal electric modal function [17, p. 117]

$$e_{y,qm}(z,x) = \sin\left(\frac{m\pi}{a_z}z\right)\sin\left(\frac{q\pi}{a_x}x\right), \tag{2.51}$$

which is defined such that the corner of the hole is located at $(z,x) = (0,0)$. TE modes have $(q,m) \neq (0,0)$, and the transverse modal functions are

$$\begin{bmatrix} e^{\mathrm{h}}_{z,qm} \\ e^{\mathrm{h}}_{x,qm} \end{bmatrix} = \begin{bmatrix} \dfrac{q\pi}{a_x k_{qm}}\cos\left(\frac{m\pi}{a_z}z\right)\sin\left(\frac{q\pi}{a_x}x\right) \\ -\dfrac{m\pi}{a_z k_{qm}}\sin\left(\frac{m\pi}{a_z}z\right)\cos\left(\frac{q\pi}{a_x}x\right) \end{bmatrix}, \tag{2.52}$$

where $k_{qm}$ is the cut-off wavenumber of the mode.

The PMFs corresponding to these modes are computed in appendix B.3.1, yielding (B.33) for TM modes, and (B.36) and (B.37) for TE modes, as well as their squared norms (B.32) and (B.35). These terms are sufficient to fill out all the matrix coefficients in the dispersion equation (2.42). This dispersion equation can then be solved numerically to draw the Brillouin diagram of the structure under study.

This is done in Fig. 2.6 for different geometries of holey PPWs. G-S and nGS designs are compared in each subfigure. All structures have square periodicities $p_z = p_x = 4\,\mathrm{mm}$ and a gap between the metasurfaces $g = 0.1\,\mathrm{mm}$. The holes of size $a_z \times a_x$ and depth $h$ are filled with vacuum, and are squares or rectangles depending on the subfigures.

Two modeling techniques are used in Fig. 2.6 to compute the Brillouin diagrams. The reference curves are obtained with the eigenmode solver of CST. They are compared to the curves obtained by means of the MMM, as described in the previous paragraphs. The dispersion matrix is truncated to 150 TM and 150 TE modes. Each matrix coefficient takes 1681 harmonics into account, which correspond to harmonic orders $s$ and $\ell$ both ranging from -20 to 20.

Both techniques appear to match, showing that the MMM is an accurate alternative to commercial solvers, and that it can be taken as a basis for all subsequent studies of holey metasurface waveguides.

### 2.2.6 Example: circular holes

A second canonical example is developed here, where circular holes of radius $a$ are drilled in the metasurfaces. For generality, these holes can be filled with a dielectric of arbitrary permittivity $\epsilon_\mathrm{r}$, as illustrated in Fig. 2.7.

Circular hole modes involve Bessel functions of the first kind [17, pp. 124-126]. Therefore, the derivations of the PMFs are more demanding than for rectangular holes. These derivations are given in appendix B.3.2.

Each circular waveguide mode depends on two positive integer orders $q$ and $m$, and on a third index $t = 1, 2$. For $t = 1$, $q > 0$ and $m > 0$, whereas for $t = 2$, the only

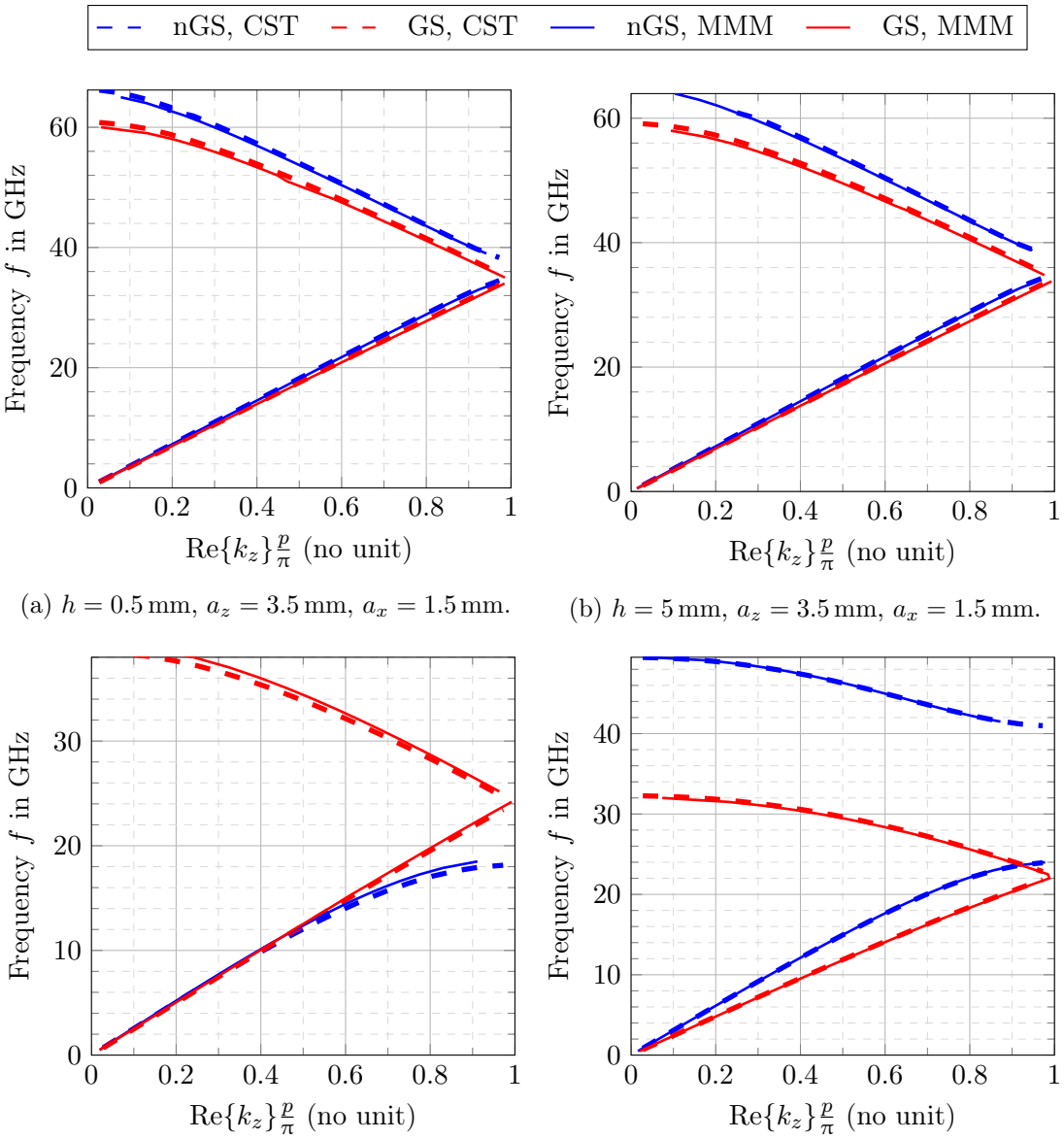


(a) $h = 0.5\,\text{mm}$, $a_z = 3.5\,\text{mm}$, $a_x = 1.5\,\text{mm}$.

(b) $h = 5\,\text{mm}$, $a_z = 3.5\,\text{mm}$, $a_x = 1.5\,\text{mm}$.

(c) $h = 5\,\text{mm}$, $a_z = 1.5\,\text{mm}$, $a_x = 3.5\,\text{mm}$.

(d) $h = 5\,\text{mm}$, $a_z = a_x = 3\,\text{mm}$.

Figure 2.6: Brillouin diagrams of PPWs with different rectangular holes of size $a_z \times a_x$ and depth $h$. G-S and nGS curves are computed with CST or with the MMM. The MMM is applied with 150 TM modes, 150 TE modes, and 1681 harmonics. All structures have $p_z = p_x = 4\,\text{mm}$ and $g = 0.1\,\text{mm}$.

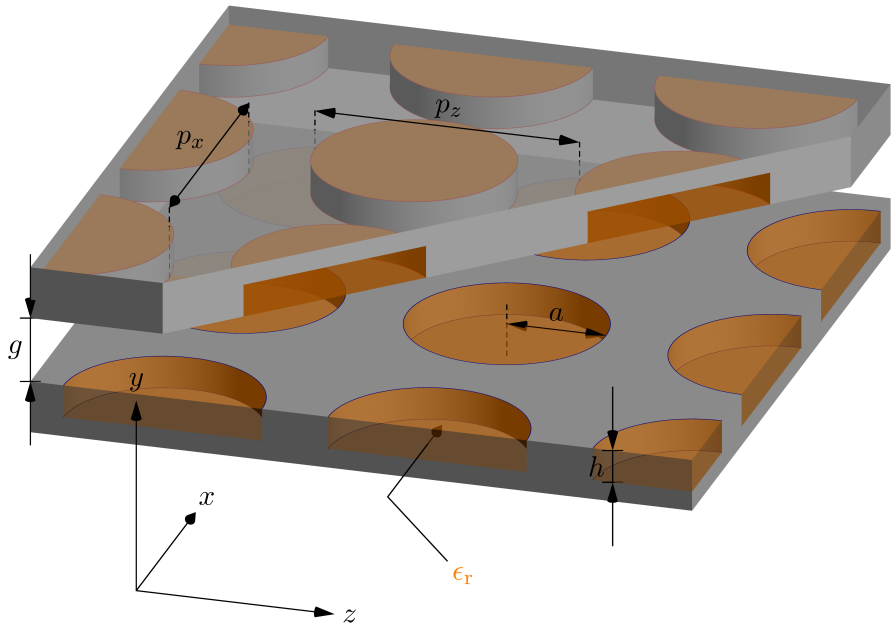


Figure 2.7: Holey G-S PPW with circular holes of radius $a$, filled with a dielectric of relative permittivity $\epsilon_r$.

restriction is $m > 0$. The longitudinal TM modal functions are

$$e_{y,qm1}(\rho,\phi) = \sin(q\phi)\, J_q(k_{qm}\rho) \tag{2.53}$$

$$\text{and} \quad e_{y,qm2}(\rho,\phi) = \cos(q\phi)\, J_q(k_{qm}\rho)\ , \tag{2.54}$$

where $t = 1$ in the first case, and $t = 2$ in the second case. The cut-off wavenumber is named $k_{qm}$. For TE modes, the modal functions are

$$\begin{bmatrix} e^{\mathrm{h}}_{\rho,qm1} \\ e^{\mathrm{h}}_{\phi,qm1} \end{bmatrix} = \begin{bmatrix} -\cos(q\phi)\, \frac{q}{k'_{qm}\rho} J_q\left(k'_{qm}\rho\right) \\ \sin(q\phi)\, J'_q\left(k'_{qm}\rho\right) \end{bmatrix}, \tag{2.55}$$

$$\text{and} \quad \begin{bmatrix} e^{\mathrm{h}}_{\rho,qm2} \\ e^{\mathrm{h}}_{\phi,qm2} \end{bmatrix} = \begin{bmatrix} \sin(q\phi)\, \frac{q}{k'_{qm}\rho} J_q\left(k'_{qm}\rho\right) \\ \cos(q\phi)\, J'_q\left(k'_{qm}\rho\right) \end{bmatrix}, \tag{2.56}$$

with $k'_{qm}$ the cut-off wavenumber.

The PMFs corresponding to these modes are computed in appendix B.3.2, yielding (B.53) for TM modes, (B.68) and (B.69) for TE modes, as well as their squared norms (B.55) and (B.70). Fig. 2.8 illustrates the validity of the MMM applied to G-S PPWs with circular holes. The holey metasurfaces have periodicities $p_z = p_x = 4\,\mathrm{mm}$ and are separated by an air gap $g = 0.1\,\mathrm{mm}$. The holes of depth radius $a = 1.5\,\mathrm{mm}$ have variable depths $h$ and are filled either by Rogers dielectric RO3003 ($\epsilon_r = 3$) or RO3010 ($\epsilon_r = 11.2$). The dispersion curves obtained with the eigensolver of CST are compared with the MMM. For the latter, 150 TM and 150 TE modes are kept, as well as 1681 Floquet harmonics. All MMM curves match the CST results.

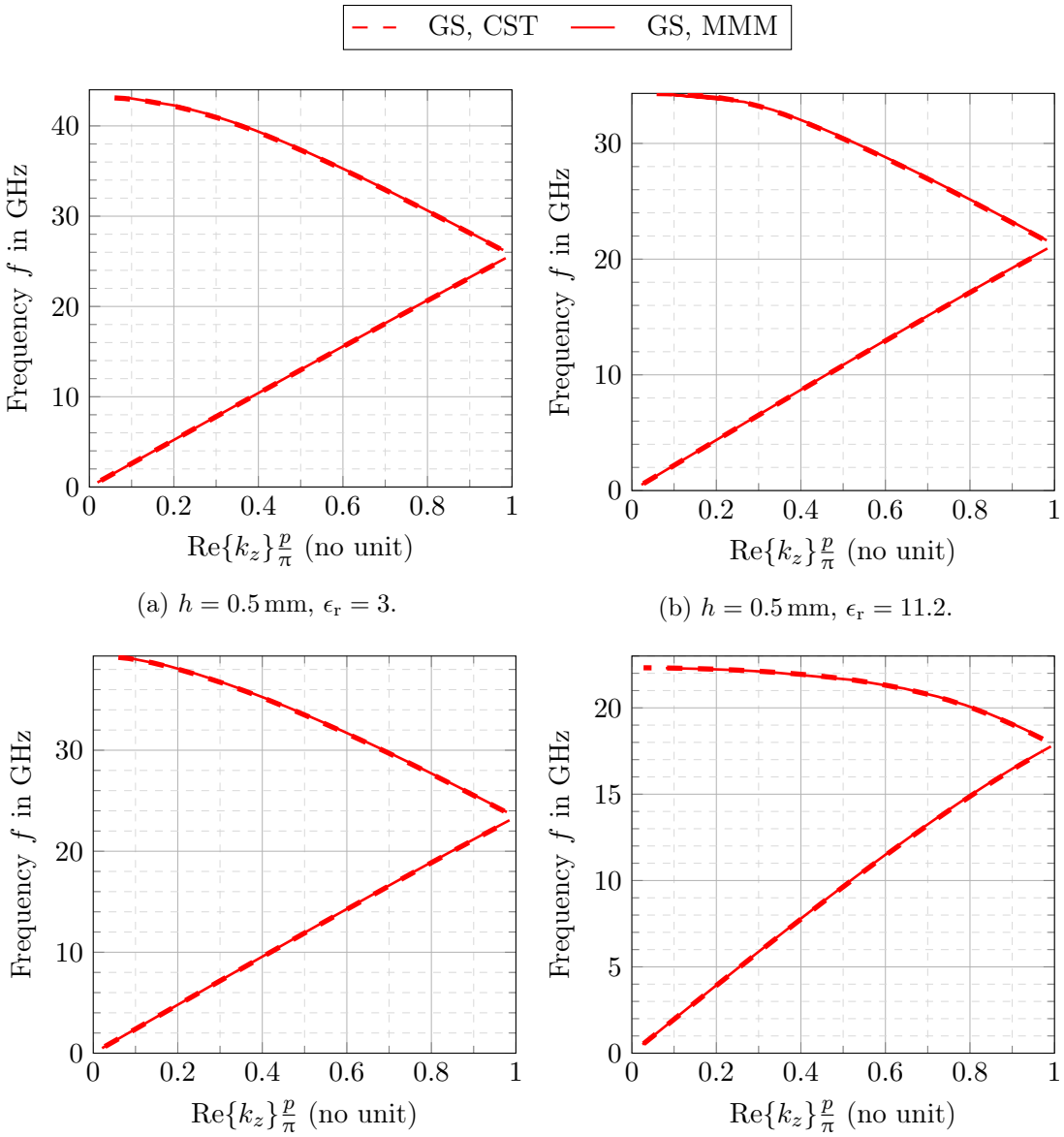


(a) $h = 0.5\,\mathrm{mm}$, $\epsilon_\mathrm{r} = 3$.

(b) $h = 0.5\,\mathrm{mm}$, $\epsilon_\mathrm{r} = 11.2$.

(c) $h = 3\,\mathrm{mm}$, $\epsilon_\mathrm{r} = 3$.

(d) $h = 3\,\mathrm{mm}$, $\epsilon_\mathrm{r} = 11.2$.

Figure 2.8: Brillouin diagrams of G-S PPWs with circular holes, computed with CST or with the MMM. The MMM is applied with 150 TM modes, 150 TE modes, and 1681 harmonics. The waves propagate along the $z$-axis i.e., $\theta = 0$. All structures have $p_z = p_x = 4\,\mathrm{mm}$, $g = 0.1\,\mathrm{mm}$. The holes have a radius $a = 1.5\,\mathrm{mm}$, a depth $h$ and are filled with a relative permittivity $\epsilon_\mathrm{r}$.

## Chapter landmarks

The mode-matching procedures described in literature for G-S metasurface waveguides have been rendered in details in this chapter, both for 1-D GS and 2-D GS. This is motivated by the resulting dispersion equations, which act as a starting point for the studies in this thesis. The modal functions used subsequently can thus be related to the total fields propagating in the waveguide. Moreover, explicit details are given on the practical implementation of the method, so that the algorithm can be used as a reference when compared to the performances of the novel techniques presented thereafter.

For corrugated PPWs in section 2.1, numerical simulations are used to illustrate the impact of the waveguide geometry onto the number of required modes for the MMM to yield accurate results. This provides us with preliminary insight about the coupling mechanisms between the metasurfaces.

For the holey metasurface waveguides studied in section 2.2, the MMM is generalized to holes that can be excited with TEM modes, which has not been explicitly published before. Most importantly, the proper separation of the different hole modes makes it possible to simplify the coefficients of the dispersion matrix. For TM modes, the matrix coefficients are expressed in terms of the longitudinal modal functions instead of the transverse fields. This simplification is essential for the quasi-static homogenization process in chapter 4.

Finally, it is notable that the dispersion diagrams in this chapter were obtained quite faster by means of the MMM than with the eigensolver of CST. Given the various parameters involved for each method, it is difficult to make precise quantitative comparisons. However, for practical accuracy of the effective wavenumber in holey metasurface waveguides (within 1% of the true value), CST requires around one minute to find the eigenvalue at a given frequency, whereas directly solving the dispersion equation requires only several seconds. These rough estimates can serve as references to assess subsequent techniques.

# Chapter 3

# Study of the low-dispersive behavior of glide symmetry from the mode-matching formulation

One of the most commented properties of glide symmetry (GS) is its ability to reduce the dispersive behavior of the waveguide [32], [33], [157]. In chapter 2, the dispersion diagrams of different glide-symmetric (G-S) waveguides are obtained by means of the mode-matching method (MMM). The corrugated parallel-plate waveguide (PPW) examples presented in Fig. 2.3 illustrate the differences between G-S and non-glide-symmetric (nGS) waveguides. GS closes the stopband between the first and second modes, at the right-end of the Brillouin diagram i.e., at $k_z = \pi/p_z$. This reduces the dispersion in the first Brillouin zone ($k_z < \pi/p$). Thereby, the first dispersion curve of the G-S structure is almost linear, whereas the first curve of the nGS structure bends towards the right of the first Brillouin zone, where the group velocity vanishes. The same behavior is notable for two-dimensional (2-D) GS, as shown for holey PPWs with rectangular holes in Fig. 2.6. This seems to be particularly true when the effective density of the waveguide is high. The aim of this chapter is the dispersive study of these G-S waveguides. A better physical understanding of the difference between G-S and nGS waveguides is sought, as well as elements of analytical proof for the reduction of dispersion.

The Brillouin diagrams for corrugated and holey PPWs are obtained by solving the dispersion equations (2.12) and (2.42), respectively. At each frequency point $f$, the dispersion equation is solved by means of iterative numerical solvers to obtain the corresponding effective propagation constants $k_z$ and $k_x$. Given the strong non-linearity of these dispersion equations in both G-S and nGS cases, it is a difficult task to show that the G-S structure is low-dispersive compared to the nGS structure. Ideally, one would like to show that the dispersion equation of the G-S structure can be written as a function of the effective refractive index with no frequency dependency, while the nGS dispersion equation cannot. Unfortunately, doing that in the general case is not achieved in this work. Nevertheless, some particular cases give fruitful insights about the dispersion, and different techniques are applied to extend our understanding of GS.

Most of this chapter focuses on the corrugated PPW, presented in section 2.1. The linearization of the G-S dispersion curves is highlighted in section 3.1, and is shown to be particularly strong when the gap between the metasurfaces is small. This is explained by analyzing the dispersion equation: decreasing the gap leads to the dismissal of all harmonics with symmetric longitudinal electric fields in the G-S structure. This strongly influences the coupling of the harmonics, and is the source of the dispersive disparities between the two structures, as shown in section 3.2. Based on this, an equivalence between a given G-S waveguide and a scaled nGS structure is derived, yielding new physical insight about the linearity of the G-S dispersion curves. Then, section 3.4 attempts to prove the linearity of the G-S dispersion curve analytically. The dispersion equation of the G-S structure is linearized and an analytical refractive index is derived, but only under certain geometrical restrictions on the corrugations. Indeed, this derivation is valid only for one or two modes in the corrugations, which is not enough to accurately describe wave propagation for certain geometries, as shown in Fig. 2.2. Details to these computations are gathered in appendix C. Finally, the impact of the harmonics is generalized to holey PPWs. Unfortunately, the complexity of 2-D GS makes it more difficult to get simple dispersion studies for holey PPWs than for the corrugated PPW.

## 3.1 Low-dispersive behavior enabled by glide symmetry

GS leads to a reduction of lower dispersion of the first mode i.e., the dispersion curve is not "bent" as it is in the nGS case. Visually, the G-S dispersion curve seems linearized in the first Brillouin zone i.e., for $k_z < \pi/p_z$. In this paragraph, a way to quantify this linearization is sought. The ratio of the group velocity at $k_z = \pi/p$ over the group velocity at $k_z = 0$ is not a good indicator of this linearization, because in the nGS case, it is always zero (as the group velocity at $k_z = \pi/p$ is zero). Moreover, the dispersion curves of both GS and nGS structures could be linear over most of the first Brillouin zone, and then the nGS curve could bend only at the end, close to $k_z = \pi/p$, in which case there is low dispersion over most of the first Brillouin zone for both structures. One would want to distinguish this case from the situation where the nGS curve bends progressively over the whole Brillouin zone, whereas the G-S curve remains linear.

In order to compute a *linearization indicator* that captures these differences, a reference curve is needed. This reference is the zero-dispersive curve, which is tangential to the true dispersion curve at $f \to 0$, but which remains linear in the Brillouin diagram. If there is low dispersion over the whole Brillouin zone, then the true dispersion curve should be close to this tangential curve. The tangential reference curve and the abscissa axis of the Brillouin diagram form a triangle, with area $\mathcal{A}_t$. When the true dispersion curve bends, the area under this curve is smaller than $\mathcal{A}_t$, and is called $\mathcal{A}_d$. The ratio $(\mathcal{A}_d - \mathcal{A}_d)/\mathcal{A}_t$ is the area between the two curves, normalized by $\mathcal{A}_t$. It is always smaller than 1, and is a good indicator of the linearity of the dispersion curve. When it is equal to 0, the dispersion curve is perfectly linear. The computation of this linearization index

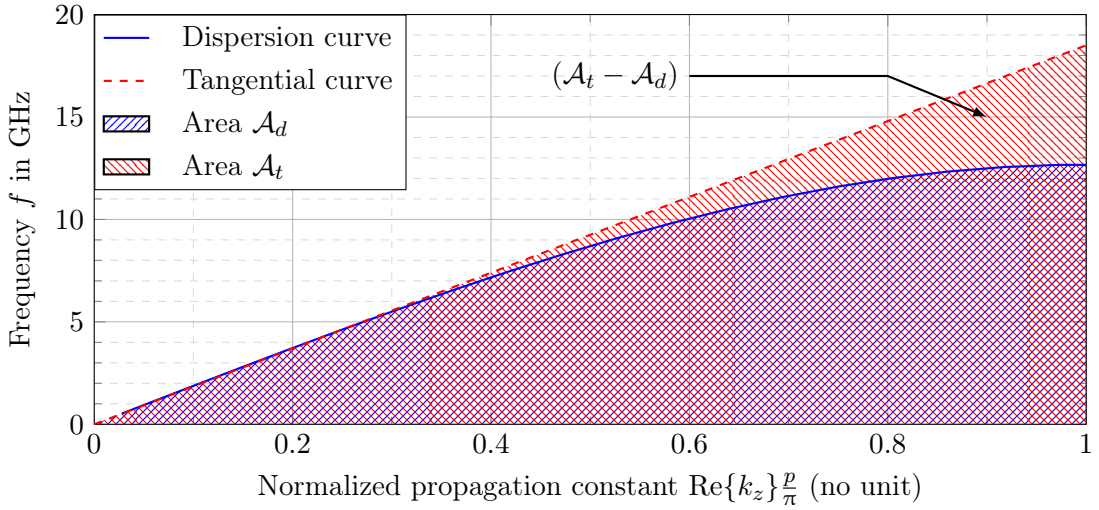


Figure 3.1: Illustration of the computation of the linearization index: the dispersion curve demarcates the area $\mathcal{A}_d$, whereas its tangent at $k_z = 0$ demarcates the area $\mathcal{A}_t$. The larger the normalized difference $(\mathcal{A}_t - \mathcal{A}_d)/\mathcal{A}_t$ between the two, the more dispersive is the propagation of the corresponding mode.

is illustrated in Fig. 3.1, where one can see the tangential curve corresponding to a dispersion curve, and both areas.

This linearization index is computed as a function of geometry for corrugated PPWs. Each plot in Fig. 3.2 corresponds to a different corrugation depth $h$, and maps the linearization index in percent as function of the corrugation width $a$ and the gap $g$ between the metasurfaces. All structures have a periodicity $p = 4\,\mathrm{mm}$. Fig. 3.2 highlights how the nGS structure (all the right subfigures) is more dispersive than the GS structure (all the left subplots): for equivalent dimensions, the linearization index of the nGS structure is always much higher than for the GS structure. This confirms the interest of GS for wide-band low-dispersive waveguides.

It is notable that this difference is particularly remarkable for a small gap $g$ between the metasurfaces, where the nGS structure tends to be particularly dispersive, while the G-S curves remain quite linear. Moreover, one should also take into account the fact that even for GS, the dispersion curve is not perfectly linear, especially for medium corrugation widths (approx. $a = p/2$) and deeper corrugations. This will make it more difficult to prove the dispersion reduction between GS and nGS structures. Indeed, it will not be possible to prove that the G-S dispersion equation is frequency-independent, because this is obviously not the case. Therefore, we will either focus on particular cases where linear approximations can be made, or we will rely on other arguments to explain the difference between G-S and nGS waveguides.

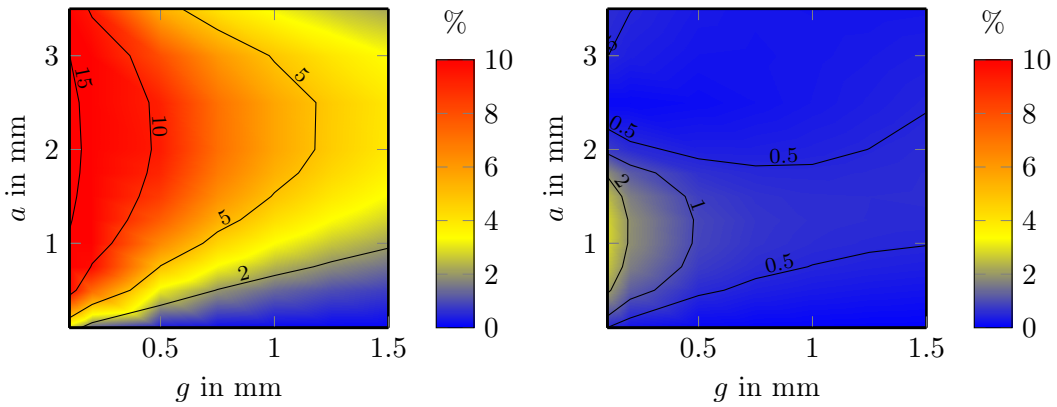


(a) $h = 0.5\,\text{mm}$, nGS. (b) $h = 0.5\,\text{mm}$, G-S.

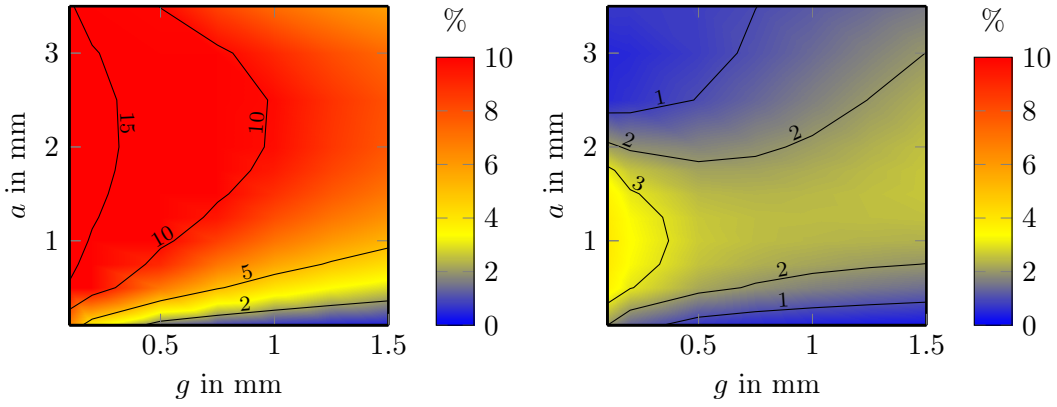


(c) $h = 1\,\text{mm}$, nGS. (d) $h = 1\,\text{mm}$, G-S.

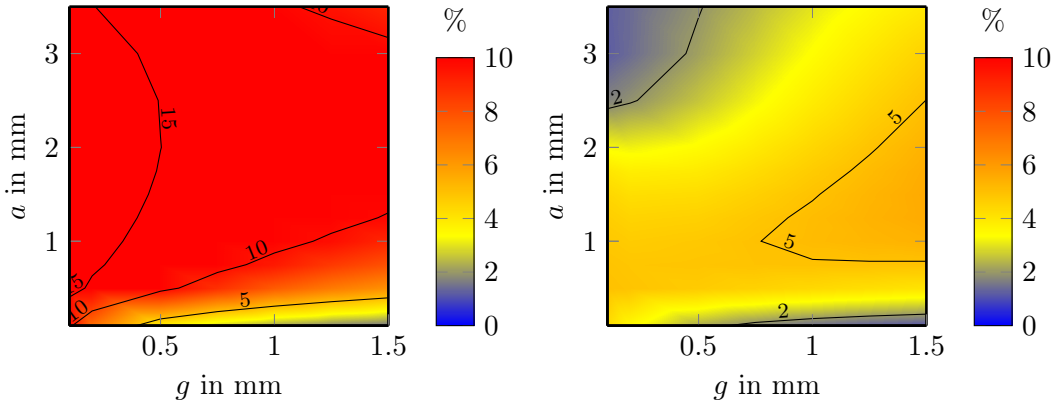


(e) $h = 1.5\,\text{mm}$, nGS. (f) $h = 1.5\,\text{mm}$, G-S.

Figure 3.2: Comparison of the dispersive behavior of nGS and G-S structures. The linearization indicator is plotted as a percentage, depending on the gap $g$ and the corrugation width $a$. The cell width is $p = 4\,\text{mm}$, for different corrugation widths $h$.

## 3.2 Impact of the harmonics in the parallel-plate waveguide with small gap

In section 2.1, the MMM derives the dispersion equation (2.12) for corrugated PPWs. This dispersion equation is solved when the determinant of the matrix $\underline{\boldsymbol{M}}$ vanishes. In the following, we refer to this matrix as the dispersion matrix. This matrix is defined by (2.8) in the G-S case, and by (2.10) in the nGS case.

### 3.2.1 Dismissal of odd-order harmonics

According to (2.2), (2.4) and (2.5), even-order harmonics have an antisymmetric longitudinal electric field, whereas odd-order harmonics are symmetric. Although in the G-S structure, (3.1) indicates that both even and odd harmonics have an impact on wave propagation, it can be shown that under certain conditions, only the harmonics with antisymmetric fields are dominant. This means that all harmonics with odd orders $s$ can be dismissed.

It appears that for a small gap $g$ between the metasurfaces, the even-order harmonics are dominant. Indeed, according to (2.8), the dispersion matrix of the G-S corrugated PPW has coefficients

$$\begin{aligned} M_{m'm} = \delta_{m'm}\frac{pa}{2^{\min\{1,m\}}}\frac{\cot(k_{y,m}h)}{k_{y,m}} + \cot\Big(k_y\frac{g}{2}\Big)\frac{k_z^2}{k_y}\frac{f^{(0)}_{m'm}}{\Big[k_z^2-\big(\frac{m\pi}{a}\big)^2\Big]\Big[k_z^2-\Big(\frac{m'\pi}{a}\Big)^2\Big]} \\ - \sum_{\substack{s=-\infty \\ s\text{ even}\neq 0}}^{+\infty} \coth\left(\frac{g}{2}\sqrt{\Big(k_z^{(s)}\Big)^2-k^2}\right)\frac{{k_z^{(s)}}^2}{k_y^{(s)}}\frac{f^{(s)}_{m'm}}{\Big[{k_z^{(s)}}^2-\big(\frac{m\pi}{a}\big)^2\Big]\Big[{k_z^{(s)}}^2-\Big(\frac{m'\pi}{a}\Big)^2\Big]} \\ - \sum_{\substack{s=-\infty \\ s\text{ odd}}}^{+\infty} \tanh\left(\frac{g}{2}\sqrt{\Big(k_z^{(s)}\Big)^2-k^2}\right)\frac{{k_z^{(s)}}^2}{k_y^{(s)}}\frac{f^{(s)}_{m'm}}{\Big[{k_z^{(s)}}^2-\big(\frac{m\pi}{a}\big)^2\Big]\Big[{k_z^{(s)}}^2-\Big(\frac{m'\pi}{a}\Big)^2\Big]}\,, \end{aligned} \tag{3.1}$$

where the function $f^{(s)}_{m'm}$ is defined in (2.9), and where the term $s = 0$ is isolated. The wavenumber $k_y^{(s)}$ is imaginary, and so the trigonometric functions are rewritten as hyperbolic functions of a real variable. The hyperbolic cotangent function is strictly larger than the hyperbolic tangent. This is not enough to state that all the odd-order harmonics can be dismissed, as both hyperbolic tangent and cotangent converge to one for higher-order harmonics. However, if the cotangent is much smaller than the tangent for all the harmonics to be retained, then odd-order harmonics can be neglected.

This depends on the number of harmonics that have an impact in the dispersion equation (see the truncation of the harmonics in section 2.1.6). Let $S > 0$ be the highest harmonic order to be considered. In the first Brillouin zone (that is for $k_0 < k_z < \pi/p$), the higher-order harmonic wavenumbers are approximately frequency-independent,

$$k_z^{(s)} = k_z + s\frac{2\pi}{p} \simeq s\frac{2\pi}{p}\,, \tag{3.2}$$

where $S \geq s \gg 1$. For the highest order $S$,

$$\frac{\coth\left(\frac{g}{2}\sqrt{\left(k_z^{(S)}\right)^2 - k_0^2}\right)}{\tanh\left(\frac{g}{2}\sqrt{\left(k_z^{(S)}\right)^2 - k_0^2}\right)} \simeq \frac{\coth\left(S\pi\frac{g}{p}\right)}{\tanh\left(S\pi\frac{g}{p}\right)} = \frac{1}{\tanh^2\left(S\pi\frac{g}{p}\right)}. \tag{3.3}$$

If this ratio is large for the harmonic $S$, then this is the case for lower-order harmonic too, thus proving that all odd-order harmonics are negligible. For that to be true, $S\pi\frac{g}{p}$ must be small enough. In this case, the hyperbolic tangent function can be linearized, yielding the condition

$$\left(S\pi\frac{g}{p}\right)^2 \ll 1 \qquad \Longleftrightarrow \qquad g \ll \frac{p}{S\pi}. \tag{3.4}$$

The best-case scenario is when the maximum harmonic order is $S = 1$. Taking a threshold of 10 in the left condition of (3.4), with a cell-length $p = 4\,\text{mm}$, the maximum gap is $g = 0.4\,\text{mm}$. In the reverse logic, for $g = 0.1\,\text{mm}$ and a threshold of 10, there should be no relevant harmonics with orders higher than $S = 5$.

Unfortunately, the number of harmonics $S$ needed to obtain accurate dispersion curves can only be obtained by simulation, when the results converge. Nevertheless, it should also be noted that in all cases, the low-order harmonics have a larger impact on dispersion than high-order harmonics. Therefore, when $g$ is already smaller than a fraction of $p/\pi$, it is enough to say that the dispersion is mainly influenced by even-order harmonics.

On the other hand, the nGS matrix coefficients are defined in (2.10): all the harmonic terms are proportional to the cotangent, meaning that they all have an antisymmetric longitudinal electric field, independently of the order parity. Therefore, the odd-order harmonics cannot be dismissed from the dispersion equation, even for a small gap. As such, (3.4) gives a good insight about how small $g$ needs to be for the G-S waveguide to behave differently from its nGS counterpart. In the next section, it is shown how dismissing the odd-order harmonics impacts the dispersive behavior of the corrugated waveguide.

### 3.2.2 Coupling of symmetric and antisymmetric harmonics

In the previous paragraphs, it is shown that the harmonics with symmetric field can be dismissed in the G-S structure if the gap is small enough, whereas they are kept in the nGS structure. Therefore, twice as many harmonics are considered in the nGS structure as in the G-S structure. This leads to different harmonic couplings in both structures. Here, the effect of neglecting the symmetric harmonics is observed by plotting the corresponding terms in the dispersion equation. In order to do so, the simplified case with one corrugation mode is considered, so that the dispersion equations become scalar equations. This study does not prove the dispersive features of the structures, but it

hints on how the coupling of adjacent harmonics leads to the "bending" of the dispersion curve in the nGS case.

It is assumed that the gap $g$ is small enough so that only antisymmetric harmonics are relevant in the G-S structure. Moreover, it is assumed that only one mode propagates in the corrugations. Let us consider $M_{00}$, the dispersion matrix coefficient associated to the corrugation mode of order 0. The dispersion equation with one mode is of the form $M_{00} = 0$. According to (3.1) and (2.10), $M_{00}$ has the form

$$M_{00} = \gamma_0 + F_{00}^{(0)} + \sum_{\substack{s=-\infty \\ s \text{ even} \neq 0}}^{+\infty} F_{00}^{(s)} + \sum_{\substack{s=-\infty \\ s \text{ odd}}}^{+\infty} F_{00}^{(s)}\,, \tag{3.5}$$

where $\gamma_0$ can be identified as the term preceded by the Krœnecker symbol, and where for even-order G-S harmonics and all nGS harmonics,

$$F_{00}^{(s)} = -\frac{a^2}{\sqrt{{k_z^{(s)}}^2 - k_0^2}} \coth\left(\frac{g}{2}\sqrt{{k_z^{(s)}}^2 - k_0^2}\right) \operatorname{sinc}^2\left(k_z^{(s)}\tfrac{a}{2}\right), \tag{3.6}$$

with $k_z^{(s)} = k_z + s\frac{2\pi}{p}$. For G-S odd-order harmonics, the cotangent is replaced by a tangent. It is notable that these terms have a singularity at $k_z^{(s)} = \pm k_0$ i.e., at $k_z = s\frac{2\pi}{p} \mp k_0$.

In Fig. 3.3, these harmonic terms are plotted for different frequencies over the interval $k_z \in [0, 2\pi/p]$. The five largest terms are kept ($|s| \leq 2$), but actually only the harmonics $s = 0$ and $s = -1$ are dominant in the first Brillouin zone. The dimensions of the structure are chosen so that the field variability at the corrugation surface is negligible, and so only one mode yields the true Brillouin diagram: $p = 4\,\text{mm}$, $a = 0.1\,\text{mm}$, $g = 0.1\,\text{mm}$ and $h = 0.5\,\text{mm}$.

In Fig. 3.3, the left subfigures cover the G-S case, whereas the right subfigures cover the nGS counterpart structure. The true propagation wavenumber $k_z$ is computed in both cases and is indicated by a red solid vertical line. All the solid curves correspond to harmonic terms with even orders. These terms represent antisymmetric harmonics (even orders $s$), and they are involved in both G-S and nGS dispersion equations. On the contrary, the dashed curves represent symmetric harmonics (odd orders $s$), and they are involved only in the nGS dispersion equation.

The behavior of the harmonics with increasing frequency in Fig. 3.3 gives an insight about how the presence of the symmetric harmonics influences the dispersive behavior of the nGS structure compared to the G-S structure. The fundamental harmonic has a singularity at $k_0$, which results in a peak in Fig. 3.3 for the curve $s = 0$. Given that the dispersion solution $k_z$ is larger than $k_0$ (slow wave), it is located right to the peak. Similarly, the harmonic $s = -1$ has a singularity at $2\pi/p - k_0$. At low frequencies, the harmonic term $s = 0$ is dominant. Therefore, G-S and nGS solutions are close. But the singularity of $s = 0$ increases linearly with the frequency, and so $k_z$ shifts to the right. On the contrary, the singularity of $s = -1$ shifts to the left, making the harmonic term

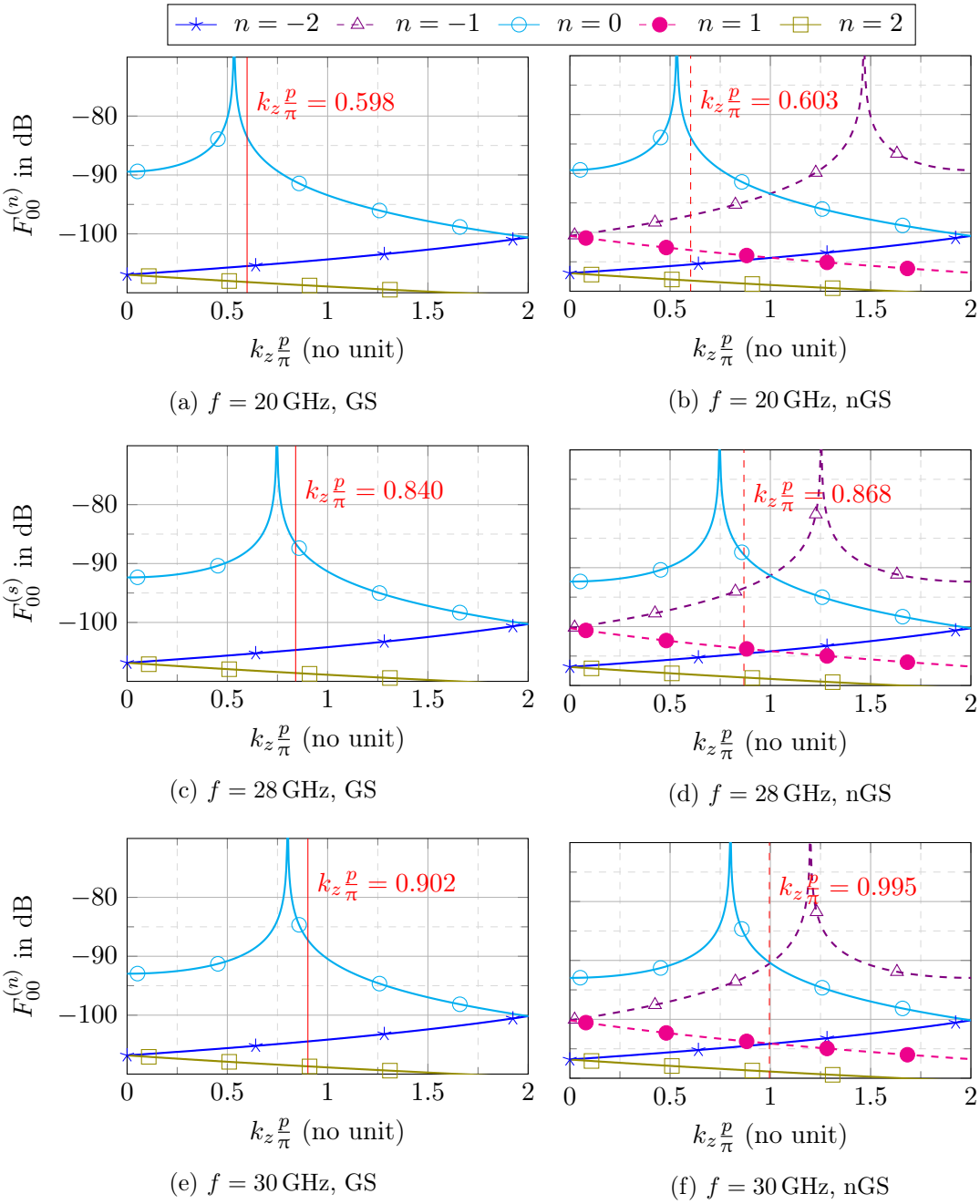


(a) $f = 20\,\text{GHz}$, GS (b) $f = 20\,\text{GHz}$, nGS

(c) $f = 28\,\text{GHz}$, GS (d) $f = 28\,\text{GHz}$, nGS

(e) $f = 30\,\text{GHz}$, GS (f) $f = 30\,\text{GHz}$, nGS

Figure 3.3: Dispersion terms $F_{00}^{(s)}$ associated to the Floquet harmonic of order $s$ in the dispersion equation $M_{00} = 0$ for the corrugated PPW. The vertical axis corresponds to the value of the harmonic term, and is expressed in dB ($10\log_{10}|F|$) as a function of $k_z$. Both G-S and nGS cases are compared a several observation frequencies. The true solution $k_z$ of the dispersion equation is indicated with a red vertical line. The structure parameters are: $p = 4\,\text{mm}$, $h = 0.5\,\text{mm}$, $g = 0.1\,\text{mm}$ and $a = 0.1\,\text{mm}$.

$s = -1$ larger at the true solution $k_z$. As the solution get closer to the right end of the first Brillouin zone, the harmonic terms $s = 0$ and $s = -1$ evolve to similar strengths, breaking the linearity of the equation in the nGS case. This does not happen for the G-S case, given that only antisymmetric harmonics (even order $s$) are present. Thereby, the GS dispersion curve stays more linear, keeping the dispersion low.

## 3.3 Equivalence of glide-symmetric and non-glide structures

In this section, we show that for a G-S corrugated PPW with a small gap, there exists a theoretical nGS structure that has the same dispersive properties. This equivalent structure gives additional insight about the linearity and the stopbands of the G-S dispersion curve.

The dispersion equation for the G-S structure is a mixture between even modes and odd modes of the nGS structure. Indeed, considering the $s$-th Floquet term in (2.8) for the eigenvalue $\ell_1$, if $s$ is even, then its behavior is like the $s$-th antisymmetric mode of the nGS structure i.e., the cotangent term in (2.10). On the contrary, when $s$ is odd, then the Floquet harmonic behaves like the $s$-th symmetric mode of the nGS structure i.e., the tangent term in (2.11).

According to paragraph 3.2.1, if the gap $g$ is small enough (it must satisfy (3.4)), then the symmetric harmonics of the G-S structure can be discarded. As such, the dispersion matrices of the G-S and the nGS structure (equations (2.8) and (2.10), respectively) are almost identical. The only difference is that the nGS structure has all harmonics, whereas the G-S structure only has harmonics with even order $s$. Therefore, it can be shown that the G-S corrugated PPW is equivalent to a scaled nGS structure in the first Brillouin zone. The periodicity $\hat{p}$ of this equivalent nGS structure must be half that of the G-S structure i.e., $\hat{p} = p/2$. Then, all the nGS harmonics $\hat{k}_z^{(s)}$ can be identified to one of the even-order harmonics of the GS structure, given that

$$\hat{k}_z^{(s)} = k_z + s\tfrac{2\pi}{\hat{p}} = k_z + s\tfrac{4\pi}{p} = k_z + (2s)\tfrac{2\pi}{p} = k_z^{(2s)}\,. \tag{3.7}$$

Moreover, the equivalent nGS structure has a double gap $\hat{g} = 2g$. The detailed proof of the proportionality of the resulting dispersion matrices can be found in appendix C.2. In the end, it comes that for any dispersion matrix coefficient,

$$\hat{M}_{m'm} = \frac{1}{2} M_{m'm}\,, \tag{3.8}$$

where $\underline{\hat{\boldsymbol{M}}}$ is the dispersion matrix of the equivalent nGS waveguide. The 1/2-factor can be factored out of the matrix determinant, and so both structures have the same dispersion equation. As such, the G-S and nGS structures sketched in Fig. 3.4 are equivalent in terms of dispersive behavior.

This equivalence may seem intuitive for a small corrugation width $a$. Indeed, in the G-S structure, every corrugation is faced with a perfectly electrically conducting (PEC)

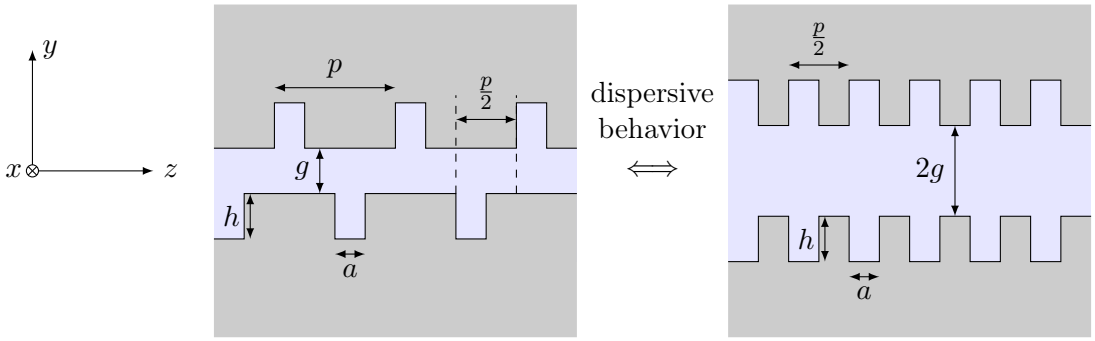


Figure 3.4: Equivalent G-S corrugated PPW (on the left) and nGS corrugated PPW with period $p/2$ (on the right). This equivalence is true in the first Brillouin zone under the conditions (3.4).

plate on the other side of the gap. If this PEC plate was infinite, it could be replaced by a symmetric corrugation at twice the gap, because of image theory. The idea of having a nGS equivalent structure with $p/2$ and $2g$ thus does not seem to come out of nowhere. Nevertheless, this equivalence is intriguing for $a > p/2$. Indeed, in this case, the equivalent nGS structure does not physically exist: the corrugation width $a$ is larger than the cell-length $\hat{p} = p/2$. The G-S PPW therefore embodies a non-physical nGS structure.

This explains why G-S dispersion curves seem more linear (and thus less dispersive) than nGS dispersion curves. The GS curve is the first half of a nGS curve, the more linear part, before the curve starts "bending". This equivalency also explains the vanishing of the stopband between the first and second modes in the G-S Brillouin diagram. A nGS structure of period $p$ has a stopband at $k_z = \pi/p$ between the first and second Brillouin modes. This means that a nGS structure of period $\hat{p} = p/2$ has a stopband at $k_z = \pi/\hat{p} = 2\pi/p$. This nGS structure is equivalent to the G-S structure of period $p$. As such, the G-S structure has its first stopband at $k_z = 2\pi/p$, and not at $k_z = \pi/p$. Taking into account the evenness and the $2\pi/p$-periodicity of the Brillouin diagram for the G-S structure, this stopband appears between the second and third Brillouin modes.

This is illustrated in Fig. 3.5: all curves with square markers correspond to the dispersion curves of nGS structures, whereas all curves with triangle markers correspond to G-S structures. The nGS structure with period $p/2$ has a first stopband at $k_z = 2\pi/p$. Given that this structure is equivalent to the G-S structure with period $p$, the same dispersion curve (solid red) belongs to the spectrum of the latter (so it has both triangle and square markers). The other eigenvalue of the G-S structure creates an additional dispersion curve, which is symmetric regarding the $k_z = \pi/p$ axis. This additional curve (dashed red with triangle markers) cuts the first one at $k_z = \pi/p$, and so there is no stopband there, contrarily to the nGS structure with period $p$.

It must be kept in mind that this equivalence is only proven here for the particular case of the corrugated PPW with small gap. As shown in section 3.2.1, a small gap is the condition for a notable difference between G-S and nGS waveguides. Nevertheless,

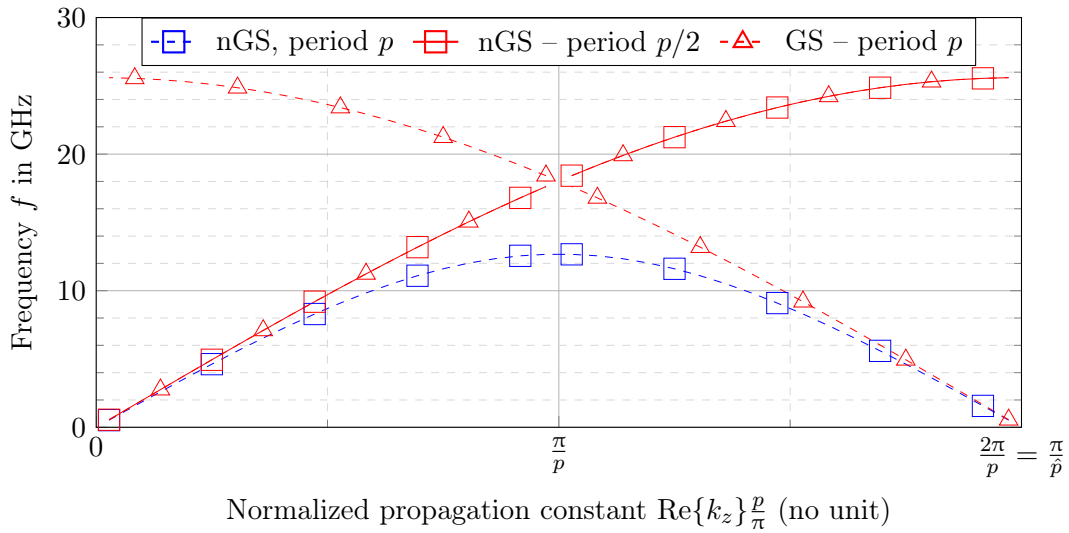


Figure 3.5: Brillouin diagrams for the corrugated PPWs shown in Fig. 3.4. The G-S waveguide (solid and dashed red curves) has dimensions $p = 4\,\mathrm{mm}$, $h = 1.5\,\mathrm{mm}$, $g = 0.2\,\mathrm{mm}$ and $a = 1\,\mathrm{mm}$. It is compared to a nGS structure with the same dimensions (dashed blue curve), but also to its equivalent nGS structure (solid red curve), which has half the periodicity and twice the gap.

it can not be taken as a justification for properties of GS in general. In future works, it would be interesting to see if a generalization of this equivalence is possible, notably for 2-D GS.

## 3.4 Linearization of the glide-symmetric dispersion equation for one or two modes

In this section the dispersion equation of the G-S corrugated parallel-plate waveguide is linearized, under certain geometrical restrictions. Linearizing the dispersion equation means that all frequency dependencies are simplified, resulting in a dispersion equation that only depends on the effective refractive index $n$. This proves that for such structures, there is no dispersion under the subwavelength condition.

### 3.4.1 Simplified G-S dispersion equation with small gap and small corrugations

The dispersion of the G-S corrugated PPW is of the form $|\underline{\boldsymbol{M}}| = 0$, where the coefficients of the dispersion matrix $\underline{\boldsymbol{M}}$ are given by (3.1). These coefficients are simplified under the following assumptions:

1. Subwavelength assumption: $p \leq \lambda_0/2$, with the free-space wavenumber $\lambda_0$.

2. Observation restricted to the first Brillouin zone: $0 \leq k_0 \leq k_z \leq \frac{\pi}{p}$.

The subwavelength assumption, as well as restricting the observation window, guarantees that all longitudinal dimensions are small compared to the wavelength, and so the harmonic fields can be considered to be constant over the range of a unit cell.

3. Shallow corrugations: $h \leq \frac{p}{8}$.

The restriction on the corrugation depth is necessary in order to approximate the field variation between the bottom and the surface of the holes as linear.

4. Small gap: $g \leq \frac{p}{4}$.

The small gap enables to dismiss all harmonics with odd order, as explained in section 3.2.1. Given that in the nGS case, these harmonics are not negligible, the following low-dispersive behavior cannot be proven without GS.

5. Thin corrugations: $a < p$.

The reason for the corrugation width restriction is two-fold. On the one hand, with thin corrugations, the oscillatory nature of $\mathrm{sinc}^2\left(k_z^{(s)}\frac{a}{2}\right)$ in the harmonic terms (3.6) can be removed: these terms are linearized for the fundamental harmonic and approximated by constants for higher harmonics. This approximation is tightly bound to how small $a$ is compared to $p$, and to which point the trigonometric functions may be linearized. In the first Brillouin zone, the biggest approximation happens at the right-end of the Brillouin diagram, accepting that $\sin\left(\frac{\pi}{2}\frac{a}{p}\right) \simeq \frac{\pi}{2}\frac{a}{p}$. The smaller $a$, the better this approximation.

On the other hand, small corrugations require fewer modes in the corrugations, as illustrated in Fig. 2.2. This reduces the size of the dispersion matrix, and thus makes an analytical linearization of the equation worth considering. Note that for wide corrugations, few modes are needed too. However, the trigonometric linearizations are rougher.

The details of all subsequent simplifications of (3.1) can be found in appendix C.1.1.

### 3.4.2 Linearization for 1 corrugation mode

It is assumed that only one mode in the corrugations is enough to yield a good approximate of the dispersion curve, that is one transverse electric magnetic (TEM) mode. The dispersion equation becomes scalar,

$$M_{00} = 0\,, \tag{3.9}$$

where $M_{00}$ is made of a sum of terms, each of which corresponds to one harmonic, according to (3.1). In the first Brillouin zone, if the gap and the corrugations are small, $M_{00}$ can be simplified according to appendix C.1.1. Moreover, appendix C.1.2 shows

that if the gap $g$ is small, then the fundamental-harmonic term is dominant. In the end, the dispersion term $M_{00}$ can be approximated by

$$M_{00} \simeq \frac{pa}{hk_0^2} - \frac{2a^2}{gk_0^2\left[n^2-1\right]}, \tag{3.10}$$

with the effective refractive index $n$. After factoring out the frequency dependency, the dispersion equation for 1 mode and 1 harmonic becomes

$$\frac{p}{h} - \frac{2a}{g\left[n^2-1\right]} = 0\,. \tag{3.11}$$

This equation depends only on $n$, which shows that the corresponding dispersion curve is linear. The analytical solution of this equation is

$$n = \pm\sqrt{1+\frac{2ha}{gp}}\,. \tag{3.12}$$

Although this solution is valid only under many geometrical restrictions, it has a simple form, and provides direct understanding about the influence of the various structure parameters on the refractive index. Notably, decreasing the gap further results in an increase of the refractive index. This does not break the restrictions on the validity of (3.12). Decreasing the period, or enlarging the corrugations increases $n$ as well, however this can only be done up to the limits set in 3.4.1.

### 3.4.3 Linearization for 2 corrugation modes

The problem is extended to 2 modes in the corrugations, in order to cover more structures. Consequently, the dispersion matrix $\underline{\boldsymbol{M}}$ becomes a $2\times 2$ matrix, and is made of matrix coefficients $M_{00}$, $M_{11}$, and $M_{01}=-M_{10}$. For a small gap, thin and shallow corrugations, and in the first Brillouin zone, these coefficients can be simplified according to appendix C.1.3.

The simplified 2-modes dispersion equation is

$$\frac{1}{k_0^2}\tilde{M}_{00}(n)\tilde{M}_{11} + \frac{1}{k_0^2}\tilde{M}_{01}^2(n) = 0\,, \tag{3.13}$$

where $\tilde{M}_{00}$ is defined in (3.10). Factoring out the frequency, and inserting the terms derived in appendix C.1.3, yields

$$\left\{\tfrac{pa}{h} - \tfrac{2a^2}{g[n^2-1]}\right\}\left\{\begin{array}{l} -\frac{pa^2\coth\left(\pi\frac{h}{a}\right)}{2\pi} - \frac{8a^4n^2}{g\pi^4[n^2-1]} \\ -\sum\limits_{\substack{s=2\\ s\text{ even}}}^{+\infty}\frac{8\cos^2\left(s\pi\frac{a}{p}\right)\left(s\frac{2\pi}{p}\right)\coth\left[s\pi\frac{g}{p}\right]}{\left[\left(s\frac{2\pi}{p}\right)^2-\left(\frac{\pi}{a}\right)^2\right]^2} \end{array}\right\} + \left\{\tfrac{\mathrm{j}4na^3}{g\pi^2[n^2-1]}\right\}^2 = 0\,, \tag{3.14}$$

which can be simplified as

$$\left\{\frac{p}{h}-\frac{2a}{g[n^2-1]}\right\}\left\{-\frac{pa^2\coth\left(\pi\frac{h}{a}\right)}{2\pi}-\sum_{\substack{s=2\\ s\text{ even}}}^{+\infty}\frac{8\cos^2\left(s\pi\frac{a}{p}\right)\left(s\frac{2\pi}{p}\right)\coth\left[s\pi\frac{g}{p}\right]}{\left[\left(s\frac{2\pi}{p}\right)^2-\left(\frac{\pi}{a}\right)^2\right]^2}\right\}-\frac{8pa^4n^2}{gh\pi^4[n^2-1]}=0\,. \tag{3.15}$$

This equation depends only on $n$, proving that the G-S structure has a low-dispersive behavior in the first Brillouin zone and under the given structural assumptions. If it is solved numerically, care must be given to the singularity in the denominator, dealt with in appendix C.1.3. Additionally, an analytical solution can be extracted from (3.14), namely

$$n=\pm\sqrt{\frac{gp+2ha}{gp+\frac{8}{\pi^4}pa^4\frac{1}{\frac{pa^2\coth\left(\pi\frac{h}{a}\right)}{2\pi}+\sum\limits_{\substack{s=2\\ s\text{ even}}}^{+\infty}\frac{8\cos^2\left(s\pi\frac{a}{p}\right)\left(s\frac{2\pi}{p}\right)\coth\left[s\pi\frac{g}{p}\right]}{\left[\left(s\frac{2\pi}{p}\right)^2-\left(\frac{\pi}{a}\right)^2\right]^2}}}}\,, \tag{3.16}$$

This analytical expression of the refractive index characterizes the waveguide over the whole first Brillouin zone, and it can be applied to a wider range of waveguides than (3.12), because two modes are considered in the corrugations.

Like for the 1-mode derivation in paragraph 3.4.2, the fundamental harmonic has a dominant impact on propagation. As such, if all high-order harmonic terms are neglected in the denominator, (3.16) can be further simplified as

$$n=\sqrt{1+\frac{2ha}{gp}}\Bigg/\sqrt{1+\frac{16}{\pi^3}\frac{a^2}{gp\coth\left(\pi\frac{h}{a}\right)}}\,. \tag{3.17}$$

This last expression of the linearized refractive index lays out a corrective term compared to the 1-mode formula (3.12). This corrective term contains the impact of the field interactions between the fundamental harmonic and the second corrugation mode.

### 3.4.4 Validity of linearized dispersion models

Fig. 3.6 displays the Brillouin diagram of the G-S structure for various corrugation widths $a$. The periodicity is $p = 4\,\text{mm}$. The corrugation depth $h = 0.5\,\text{mm}$ and the gap $g = 0.1\,\text{mm}$ are chosen so that they satisfy the geometrical restrictions 3.4.1.

The true dispersion curve obtained with CST is compared to the dispersion curve computed with one or two modes. These dispersion curves are obtained by solving the MMM dispersion equation with 50 harmonics. Moreover, the linearized dispersion curves obtained with (3.12) (1 mode) and (3.16) (2 modes) are also plotted (dashed curves).

First, it is notable that at low frequencies, the linearized dispersion curves (dashed line) are always tangent to the corresponding exact curves (solid line), whether for 1

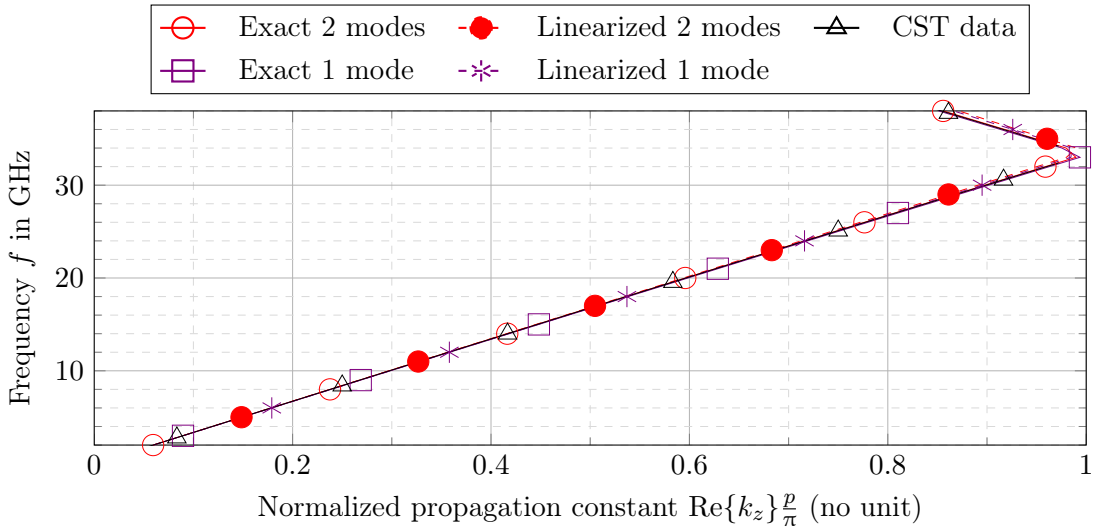


(a) $a = 0.1\,\mathrm{mm}$.

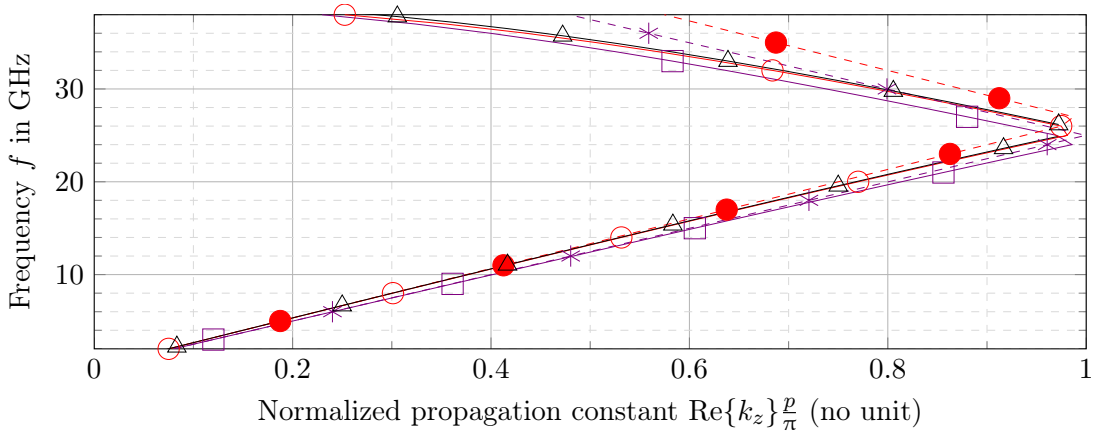


(b) $a = 0.5\,\mathrm{mm}$.

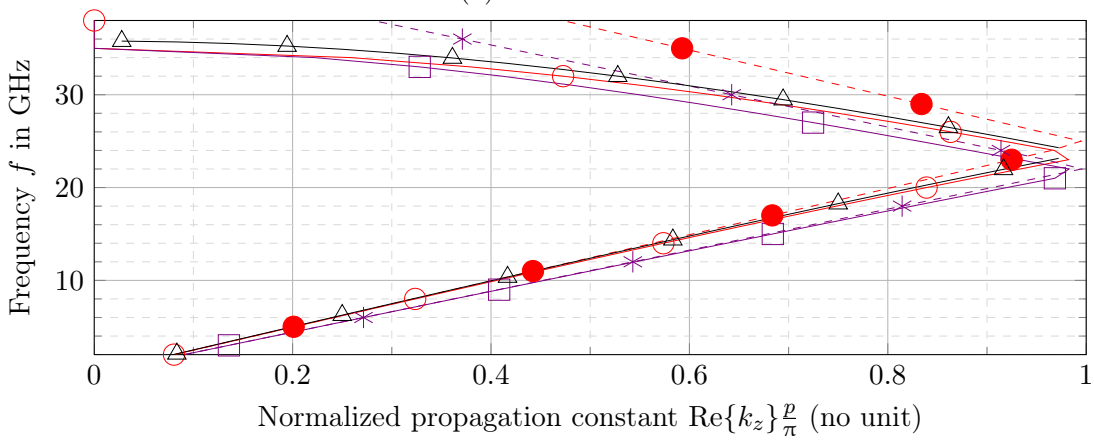


(c) $a = 0.75\,\mathrm{mm}$.

Figure 3.6: (Cont. – caption after last subfigure).

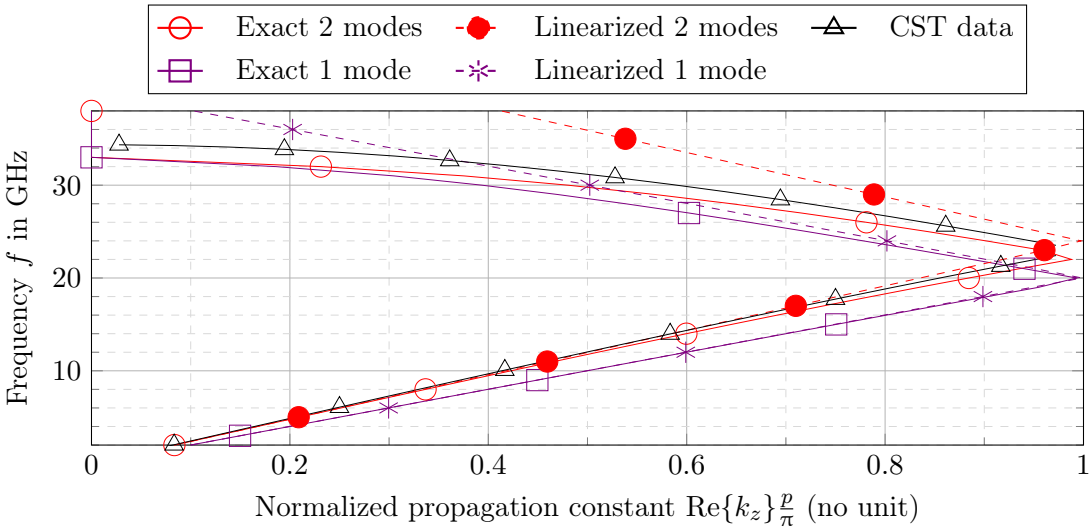


(d) $a = 1\,\mathrm{mm}$.

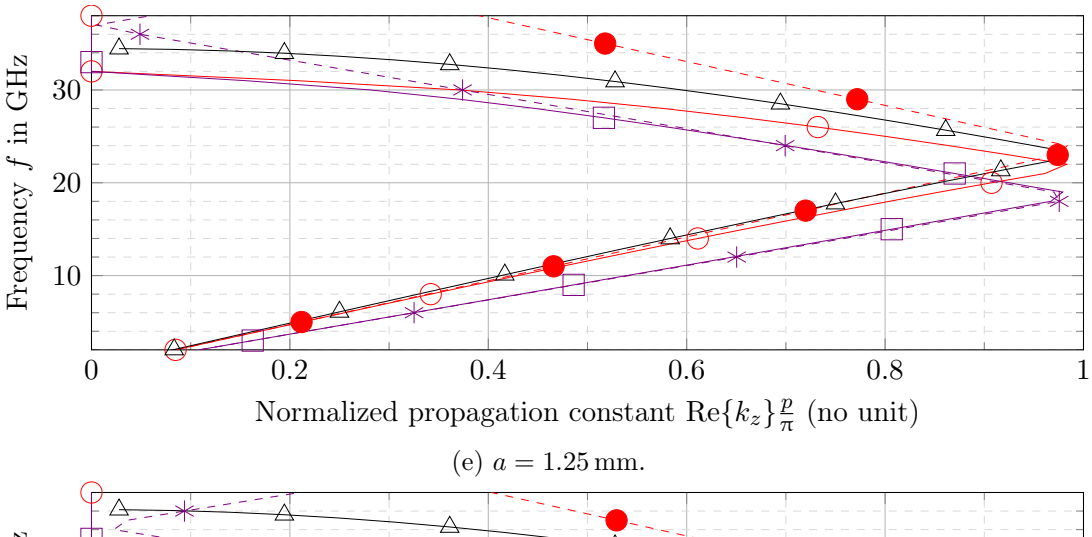


(e) $a = 1.25\,\mathrm{mm}$.

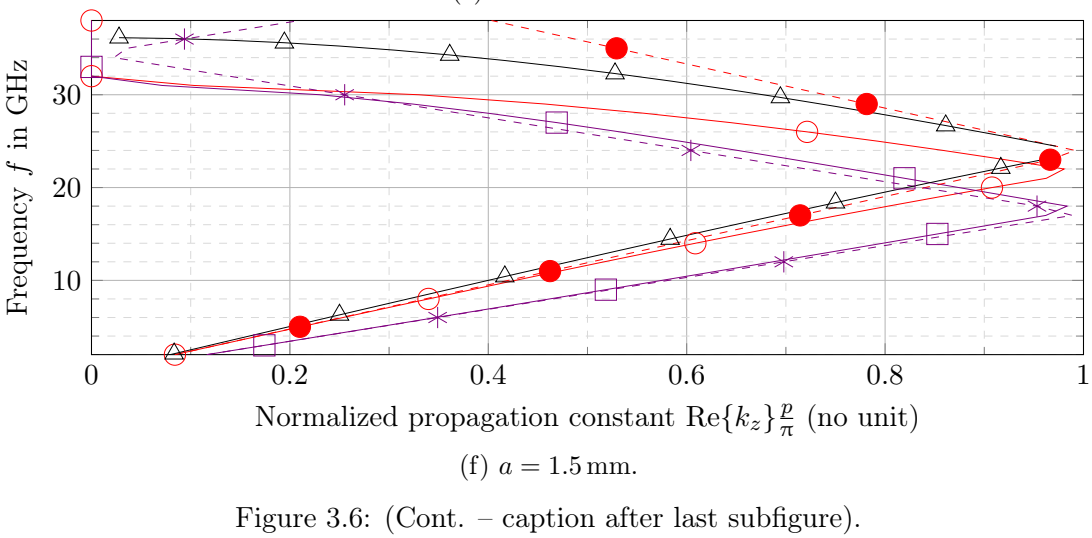


(f) $a = 1.5\,\mathrm{mm}$.

Figure 3.6: (Cont. – caption after last subfigure).

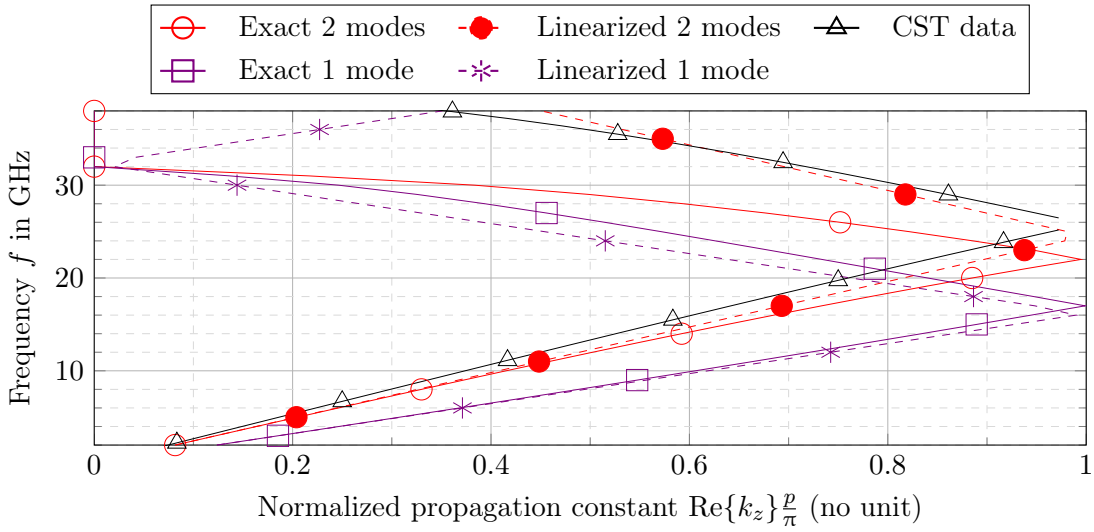


(g) $a = 1.75\,\mathrm{mm}$.

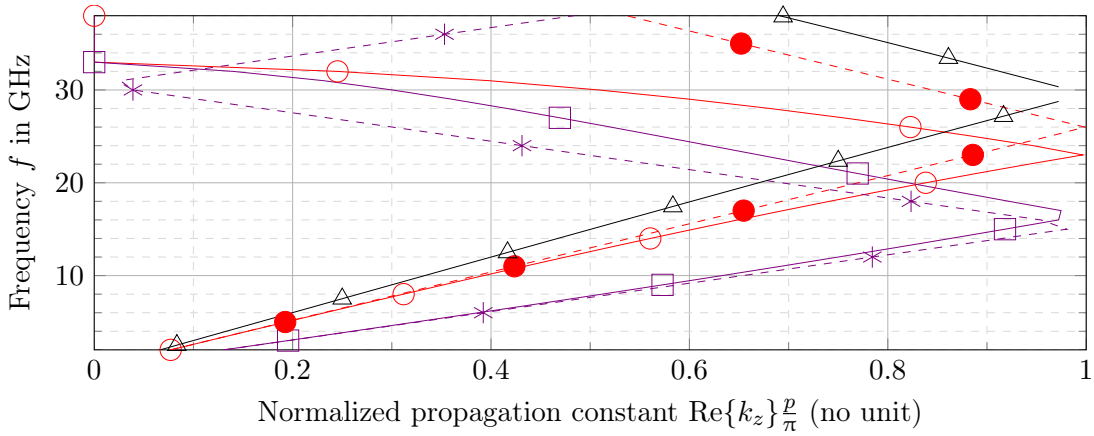


(h) $a = 2\,\mathrm{mm}$.

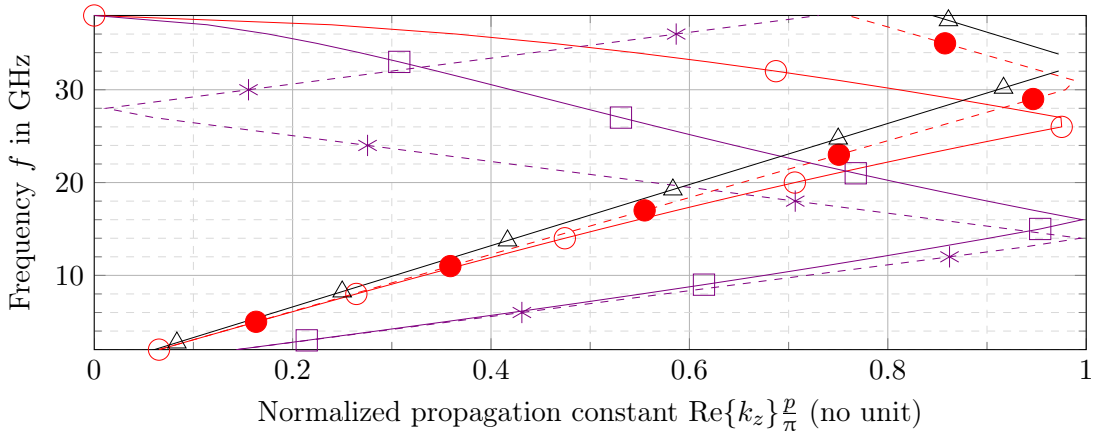


(i) $a = 2.5\,\mathrm{mm}$.

Figure 3.6: (Cont. – caption after last subfigure).

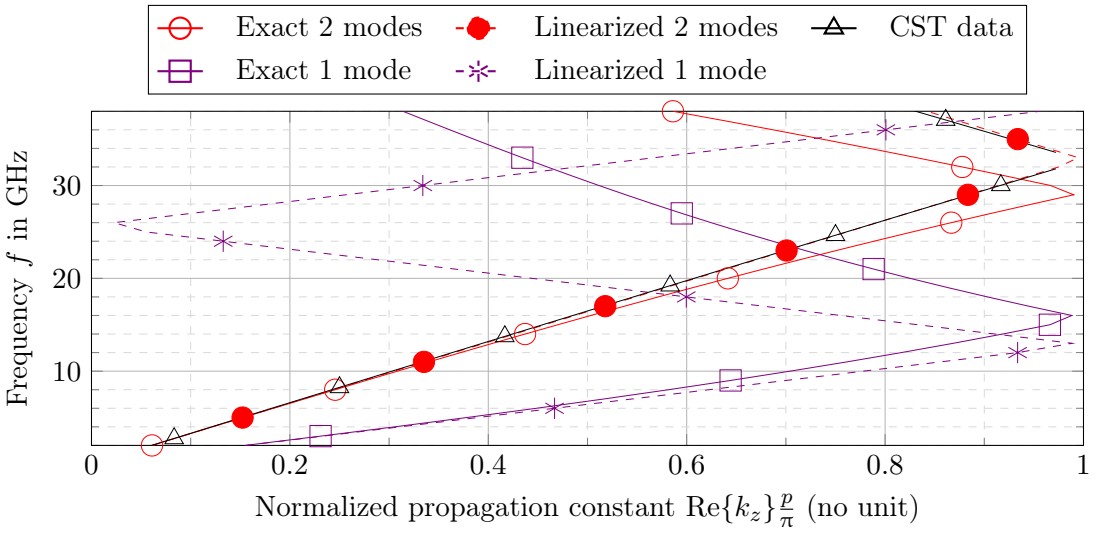


(j) $a = 3\,\mathrm{mm}$.

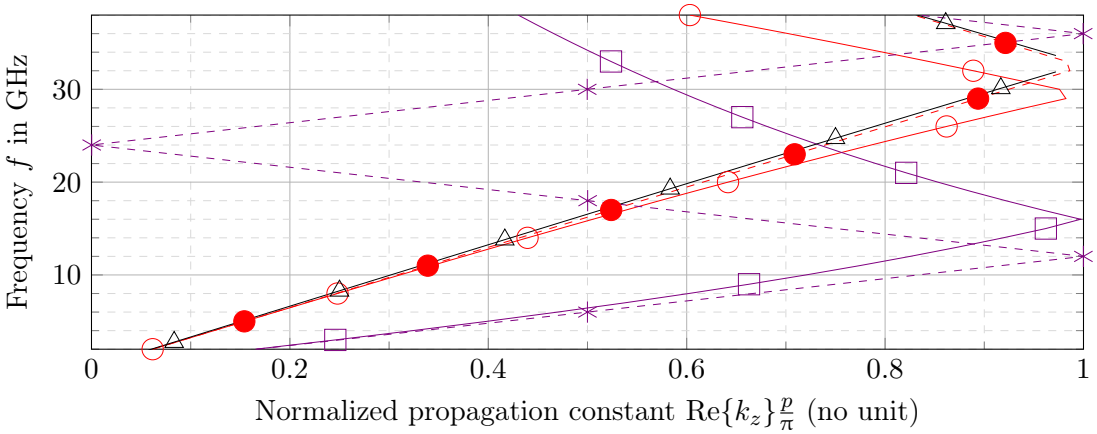


(k) $a = 3.5\,\mathrm{mm}$.

Figure 3.6: Brillouin diagram for the G-S structure with $p = 4\,\mathrm{mm}$, $h = 0.5\,\mathrm{mm}$, $g = 0.1\,\mathrm{mm}$ and varying corrugation width $a$. The dispersion curve obtained with CST is compared with the 2-mode and 1-mode models. For both models, the true dispersion curve is compared to its linearized version (3.12) or (3.16). 50 harmonics are considered for each model.

mode or for 2 modes, whatever the corrugation width. This is due to the fact that all the approximations become asymptotically accurate when $f \to 0$.

Secondly, Fig. 3.6 confirms that both linearizations (1 or 2 modes) are valid for small corrugations ($a \leq 0.5\,\text{mm}$), given that the resulting dispersion curves fit the CST results. However, with increasing corrugation width, the 1-mode model drifts away from the true dispersion curve, and so does its linearization. On the other hand, the 2-mode model quite fits the CST Brillouin diagram up to corrugations of medium width ($a \leq 1.5\,\text{mm}$). Up to these medium corrugations, the 2-mode linearization can be taken as proof that the corrugated G-S PPW is low-dispersive in the first Brillouin zone.

For wider corrugations, even the 2-mode model does not capture the exact dispersive properties of the waveguide. This is expected, because Fig. 2.2 shows that for $h = 0.5\,\text{mm}$, these medium corrugation widths require more modes to accurately characterize wave propagation.

Fig. 2.2 also shows that for larger corrugations, fewer modes are required. That is why for large corrugations ($a \leq 3\,\text{mm}$ and $a \leq 3.5\,\text{mm}$), the 2-mode linearization approaches the CST curve again. However, it is to be noted that the non-linearized 2-mode curves are less accurate at the right-end of the Brillouin diagram. This is because larger corrugations lead to bigger approximations with increasing frequency, even if 2 modes are enough, as explained at the end of 3.4.1. The index formula (3.16) is thus valid in the first half of the Brillouin diagram, but less so with increasing frequency.

## 3.5 Holey parallel-plate waveguides

The corrugated PPW is studied in the previous section, because its geometry makes it easier to analyze the impact of GS on the dispersion diagram. However, it only covers one-dimensional (1-D) GS. Ideally, these results about the dispersive behavior of GS should be generalized to two dimensions. This section studies the holey PPW with 2-D GS. Although linearization of the dispersion curves is not achieved, the impact of the Floquet harmonics in the G-S and nGS cases is analyzed.

The dispersion equation of holey G-S PPWs is given in (2.42), with matrix coefficients (2.40), (2.47) and (2.48) depending on the type of the modes in the holes. Each dispersion matrix coefficient is made of a sum of harmonic terms. All harmonic terms are proportional to the vertical spectral function $f^{(s\ell)} = c^{(s\ell)}/k_y^{(s\ell)}$. The term $c^{(s\ell)}$ is the only function that changes between G-S and nGS dispersion equations. It is either equal to $\tan\left(k_y^{(s\ell)}\frac{g}{2}\right)$ if $s+\ell$ is odd, or to $\cot\left(k_y^{(s\ell)}\frac{g}{2}\right)$ if $s+\ell$ is even. It can be shown that when the gap $g$ is sufficiently small, terms with $s+\ell$ even are dominant, making it possible to dismiss all harmonic terms where $s+\ell$ is odd.

It can be safely stated that $k_y^{(s\ell)} = \sqrt{k_0^2 - {k_z^{(s)}}^2 - {k_x^{(\ell)}}^2}$ is complex, given that the Floquet harmonics are guided within the PPW, meaning in particular that ${k_z}^2 + {k_x}^2 > k_0^2$. In the special case where $k_x = 0$ (main propagation along the $z$-direction), then $k_z > k_0$.

Consequently,

$$\begin{aligned} \cot\left(k_y^{(s\ell)}\tfrac{g}{2}\right) &= -\mathrm{j}\coth\left(\tfrac{g}{2}\sqrt{{k_z^{(s)}}^2+{k_x^{(\ell)}}^2-k_0^2}\right), \\ \text{and} \quad \tan\left(k_y^{(s\ell)}\tfrac{g}{2}\right) &= \mathrm{j}\tanh\left(\tfrac{g}{2}\sqrt{{k_z^{(s)}}^2+{k_x^{(\ell)}}^2-k_0^2}\right), \end{aligned} \tag{3.18}$$

and so

$$c^{(s\ell)} = \begin{cases} -\coth\left(\tfrac{g}{2}\sqrt{{k_z^{(s)}}^2+{k_x^{(\ell)}}^2-k_0^2}\right) & \text{if } s+\ell \text{ even}, \\ -\tanh\left(\tfrac{g}{2}\sqrt{{k_z^{(s)}}^2+{k_x^{(\ell)}}^2-k_0^2}\right) & \text{if } s+\ell \text{ odd}. \end{cases} \tag{3.19}$$

Let $S = \max[s,\ell]$ be the largest harmonic order for both $s$ and $\ell$. Then, in the first Brillouin zone,

$$\frac{g}{2}\sqrt{{k_z^{(s)}}^2+{k_x^{(\ell)}}^2-k_0^2} \leq \frac{g}{2}\sqrt{{k_z^{(s)}}^2+{k_x^{(s)}}^2} \leq \frac{g}{2}\frac{\pi}{p}\sqrt{2}\,[2S+1]\,, \tag{3.20}$$

where $p = \max[p_x, p_z]$. When a positive number $x \leq 1/2$, then $\coth(x) \simeq 1/x$ and $\tanh(x) \simeq x$ with an error of less than 3%. Consequently,

$$\text{if} \quad S \leq \frac{1}{2}\left(\frac{p}{g\pi\sqrt{2}}-1\right), \quad \text{then} \quad c^{(s\ell)} \simeq \begin{cases} -\frac{2}{g}\frac{1}{k_y^{(s\ell)}} & \text{if } s+\ell \text{ even}, \\ -\frac{g}{2}k_y^{(s\ell)} & \text{if } s+\ell \text{ odd}. \end{cases} \tag{3.21}$$

If the gap is small enough, simulations show this to be true, because $S$ is not very large. As an example, for $p/g = 40$, it can be shown that $S = 2$ is enough. The condition (3.21) requires $S \leq 4$, which is less restrictive.

Given that these simplifications are true when $\frac{g}{2}k_y^{(s\ell)} \leq \frac{1}{2}$, this means that the cotangent terms are at least 4 times as large as the tangent terms, in the worst case. Actually, in the previous numerical example with $p/g = 40$ and $S = 2$, the cotangent terms are at least 13 times as large as the tangent terms. Consequently, the harmonic terms with even $s+\ell$ are dominant with respect to the harmonic terms with odd $s+\ell$ for $g$ small enough.

This is illustrated in Fig. 3.7 for a G-S PPW with square holes of size $a = 3\,\mathrm{mm}$, depth $h = 5\,\mathrm{mm}$, and periodicity $p_z = p_x = 4\,\mathrm{mm}$. The Brillouin curve computed with all the harmonics is compared to the curve where only even-order harmonics are kept in the dispersion equation. A parametric study of this difference is made as function of the gap $g$. As expected, for small values of $g$, dismissing the odd-order harmonics has no impact on the accuracy of the MMM, because all relevant harmonics satisfy (3.21). When the gap increases, both odd- and even-order harmonics have an impact on dispersion, and so a disparity is observed between the dispersion curves, starting at higher frequencies.

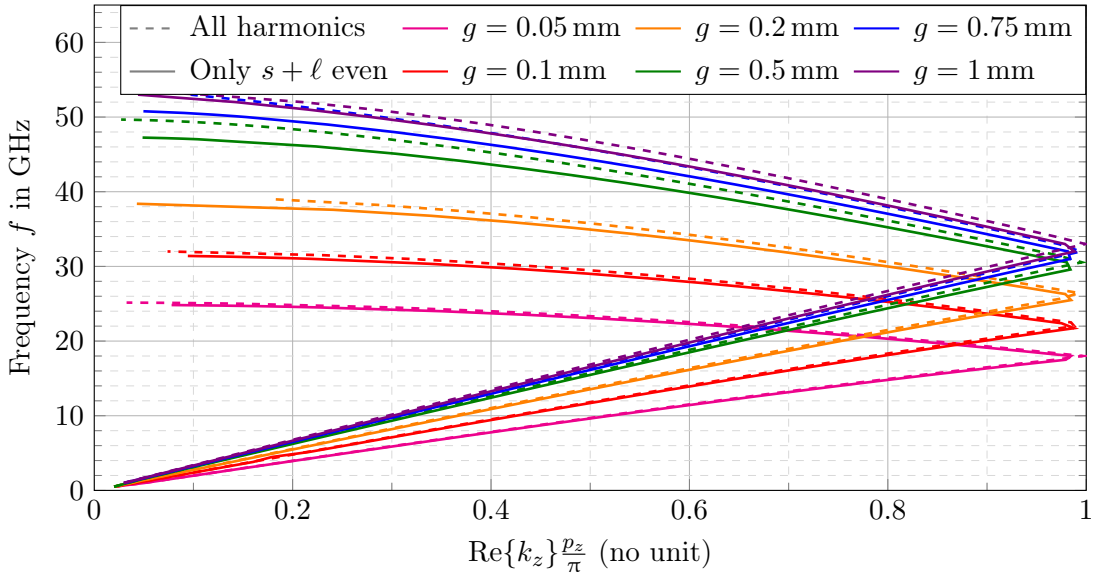


Figure 3.7: Brillouin diagram of G-S PPWs with square holes and different gaps $g$ between the metasurfaces. Depending on the gap, the impact of keeping the odd-order harmonics (dashed curves) or dismissing them (solid curves) is observed. In both cases, the MMM is applied with 150 transverse magnetic (TM) modes, 150 transverse electric (TE) modes, and harmonics orders $s$ and $\ell$ ranging from -20 to 20. All structures have $p_z = p_x = 4\,\mathrm{mm}$, $h = 5\,\mathrm{mm}$ and $a_z = a_x = 3\,\mathrm{mm}$. The waves propagate along the $z$-axis i.e., $\theta = 0$.

## Chapter landmarks

The aim of this chapter was to gain further understanding about the reduced dispersion of GS. Based on the dispersion equations obtained with the MMM, following findings are made:

- Parametric studies show that the smaller the gap $g$ between the metasurfaces, the lower the dispersion of G-S waveguides compared to nGS waveguides.

- The reduced dispersion is due to the dominance of harmonics with antisymmetric fields in the case of GS. A condition for this dominance is given in (3.4) for corrugated PPWs, and in (3.21) for holey PPWs. When these conditions are satisfied, the symmetric harmonics can be dismissed.

- In Fig. 3.3, it is shown that the low dispersion can be explained with a linear shift of a singularity in the fundamental harmonic with increasing frequency. In the nGS case, this linearity is broken by the symmetric harmonics, which are not dismissible.

- Under the geometrical restrictions listed in paragraph 3.4.1, the dispersion curve of G-S corrugated PPWs can be linearized, proving the low dispersion. For thin corrugations, a closed-form expression of the effective refractive index is found in (3.12). For medium corrugations, this index is given by (3.16). These formulas accurately describe the dispersive behavior of the waveguide over the first Brillouin zone.

- Under the assumption of a small gap (3.21), a G-S corrugated PPW is shown to yield the same dispersive behavior as a nGS waveguide with twice the gap and half the period. This nGS equivalent is not physical for large corrugations.

We have not been able to linearize the dispersion curve of corrugated and holey waveguides except in very particular cases. Other paths, involving a limited number of harmonics, have been pursued, but required numerical computations to show the linearity. In the 2-D case (holey PPW), mathematical relations between the G-S and nGS have been found, but do not give physical insight about the dispersion. Therefore, these results are not reported here. These difficulties are mostly due to the large number of parameters that impact the frequency dispersion. GS reduces the dispersion compared to its nGS counterpart, but the linearity of the first mode is not true in general. That is why particular cases have been taken as examples in this chapter. The main result is the impact of the harmonics with decreasing gap, which seems to be the physical difference between G-S and nGS propagation in all structures.

# Chapter 4

# Quasi-static homogenization of glide-symmetric parallel-plate waveguides

When the dispersion equation (2.42) is solved as a function of frequency, it yields the Brillouin diagram of the glide-symmetric (G-S) parallel-plate waveguide (PPW). However, this equation is non-linear, so finding its solution requires iterative numerical solvers. Therefore, the parametric studies required for the design of a G-S microwave device can become quite cumbersome.

In chapter 3, the dispersive study of G-S corrugated PPWs leads to closed-form formulas for the effective refractive index of these waveguides. However, (3.12) and (3.16) are derived only under certain geometrical restrictions, which enable to prove that the dispersion curve is linear in the first Brillouin zone. Nevertheless, results in the previous chapter have shown that glide symmetry (GS) reduces the dispersion of the first Brillouin mode beyond these geometrical restrictions. This means that the effective refractive index of the structure at a given frequency defines the propagation behavior of the waveguide over a wide band. As such, there is no particular need to obtain the complete Brillouin diagram of the structure. The almost-constant effective refractive index of the first mode is enough. If this low dispersion is accepted as true (with or without analytical proof), then it is sufficient to compute the effective refractive index at one particular frequency point. A good choice for this particular point is the quasi-static regime i.e., when frequency tends to zero. Indeed, we show here that it is possible to get a closed-form formula for the equivalent refractive index for arbitrary waveguide geometries when considering the structure at low frequencies.

Such a quasi-static homogenization implicitly relies on the principles of the multiple scales method, which is based on the theory of small perturbations [181]. The idea is to solve differential equations that describe phenomena operating at widely different scales. In order to do that, it assumes that the phenomena are uncorrelated. The power series of the perturbed signal become more complicated, but the resulting solution takes all the different scales into account. In the present case, wave propagation between holey meta-

surfaces combines two phenomena at different scales. On the one hand, the overall phase variation due to wave propagation in a PPW: due to the subwavelength assumption, these phase variations are slow compared to the metasurface's unit cells. On the other hand, the phase perturbations due to the metasurface geometry are fast, of the same scale as the periodicity. The spectral decomposition of the field into Floquet harmonics facilitates the separation of two types of field variations, particularly distinguishable at low frequencies. Indeed, the wavelength of the fundamental harmonic stretches to infinity in the quasi-static regime, as do the phase variation due to propagation, whereas the wavenumbers of the high-order harmonics become integer fractions of the unit cell, thus capturing the local phase disruptions. Therefore, in the quasi-static regime, the power series that describe the harmonic fields can be reduced to their fundamental terms without loss of accuracy, while the resulting simplified dispersion equation contains distinct terms to describe the different scales of phase variation.

This method is applied in section 4.1 of this chapter to the corrugated PPW, and in section 4.2 to the holey PPW. The quasi-static assumption as well as other relevant simplifications are applied to the true dispersion equation of the G-S structure, obtained with the mode-matching method (MMM) in chapter 2. The resulting matrix can be transformed into a scalar equation. This equation yields a closed-form solution for the effective refractive index of the waveguide.

This closed-form solution depends on the modal functions at the surface of the metasurface cavities (corrugations or holes). For canonical cavities such as corrugations or rectangular holes, these modal functions are known analytically. Therefore, the resulting refractive index has a purely analytical form, leading to very fast simulation and optimization of the metasurface waveguides. This is developed in section 4.3 for canonical holes. On the other hand, arbitrary hole shapes require the use of a numerical eigenmode solver, such as the finite element method (FEM). Section 4.4 shows how the closed-form formula can be associated to a two-dimensional (2-D) FEM to explore new hole shapes.

The wideband validity of these closed-form formulas is enabled by the low-dispersive GS. But it is only truly accurate in the quasi-static regime, contrarily to the formulas derived in chapter 3, which were derived as a consequence of the low-dispersive proof. Section 4.5 attemps to incorporate some frequency dependencies into the quais-static formulas to further improve the wideband accuracy of this technique.

## 4.1 Quasi-static formula for the effective refractive index of a corrugated parallel-plate waveguide

In this section, the dispersion equation (2.12) obtained by means of the MMM is considered. The dispersion matrix coefficients (2.8) are simplified in the quasi-static regime, in order to reformulate this equation and to solve it analytically.

### 4.1.1 Low-frequency reformulation of the dispersion equation

**Separation of fundamental vs. higher harmonics** If $k_0 \to 0$, then the effective fundamental wavenumber $k_z$ goes to zero as well. Therefore, in the quasi-static regime, the wavenumbers of the Floquet harmonics are reduced to

$$k_z^{(s)} = k_z + s\frac{2\pi}{p} \underset{k_0\to 0}{=} \begin{cases} nk_0 & \text{if } s = 0, \\ s\frac{2\pi}{p} & \text{else,} \end{cases} \tag{4.1}$$

The wavenumber of the fundamental harmonic goes to zero linearly with frequency, proportionally to the refractive index $n$. Therefore, the fundamental harmonic must be considered separately from the higher harmonics, whose wavenumbers become frequency-independent constants.

Given (2.8), we define a vertical spectral function, which characterizes the field distribution of the harmonics across the gap. It is defined as

$$\begin{aligned} f^{(s)} &= \begin{cases} \frac{{k_z^{(s)}}^2}{k_y^{(s)}}\cot\left(\frac{g}{2}k_y^{(s)}\right) & \text{if } s \text{ is even,} \\ -\frac{{k_z^{(s)}}^2}{k_y^{(s)}}\tan\left(\frac{g}{2}k_y^{(s)}\right) & \text{if } s \text{ is odd,} \end{cases} \\ &\underset{k_0\to 0}{=} \begin{cases} \frac{2n^2}{g(1-n^2)} & \text{if } s = 0, \\ \bar{f}^{(s)} & \text{if } s \neq 0, \end{cases} \end{aligned} \tag{4.2}$$

with the quasi-static higher-harmonic vertical spectral function

$$\bar{f}^{(s)} = \begin{cases} -s\frac{2\pi}{p}\coth\left(\frac{g}{2}s\frac{2\pi}{p}\right) & \text{if } s \text{ is even,} \\ -s\frac{2\pi}{p}\tanh\left(\frac{g}{2}s\frac{2\pi}{p}\right) & \text{if } s \text{ is odd,} \end{cases} \tag{4.3}$$

which is frequency-independent.

**Separation of TEM vs. TM modes** In the dispersion equation (2.12), the matrix $\underline{\boldsymbol{M}}$ can be subdivided according to the nature of the modes in the corrugations. When $m = 0$, the mode is transverse electric magnetic (TEM), whereas when $m \geq 1$, the modes are transverse magnetic (TM). Consequently, the dispersion matrix can be rewritten as

$$\underline{\boldsymbol{M}} = \begin{bmatrix} M_{00} & \boldsymbol{m}^{\mathrm{H}} \\ \boldsymbol{m} & \underline{\boldsymbol{M}}^{\mathrm{e}} \end{bmatrix}, \tag{4.4}$$

where the first row and column of the matrix represent mode interactions with the TEM mode, whereas the lower-right part of the matrix contains only TM modes. All these coefficients are defined in the following. It must be noted that $M_{00}$ and $\boldsymbol{m}$ have an additional $k_0$ factor compared to the matrix coefficients derived in (2.8). Indeed, the dispersion equation (2.12) is invariant if the determinant of the matrix $\underline{\boldsymbol{M}}$ is multiplied by any scalar, and so the first row and the first column of $\underline{\boldsymbol{M}}$ can be multiplied by $k_0$ without changing the equation. This modification helps solving the dispersion equation in the quasi-static regime.

The coefficients that express the interactions between TM modes can be written as

$$M^{\mathrm{e}}_{m'm} = \delta_{m'm}\gamma_m + f^{(0)} e^{(0)}_{m'} e^{(0)*}_{m} + \sum_{\substack{s=-\infty \\ s\neq 0}}^{+\infty} f^{(s)} e^{(s)}_{m'} e^{(s)*}_{m} \,. \tag{4.5}$$

where the vertical spectral functions are defined in (4.2). The term $\gamma_m$ represents the field distribution of the mode $m$ in the corrugations, and is easily identifiable in (2.8) as it is preceded by the Krœnecker function. The terms $e^{(s)}_m$ are the projections of the modes onto the Floquet harmonics on the corrugated surface. All these coefficients are defined in appendix D.1.

The scalar coefficient $M_{00}$ is purely TEM. Separating fundamental and higher-harmonic terms, it can be written as

$$M_{00} = k_0^2\gamma_0 + f^{(0)} k_0^2 \left| e^{(0)}_0 \right|^2 + \sum_{\substack{s=-\infty \\ s\neq 0}}^{+\infty} f^{(s)} k_0^2 e^{(s)}_0 e^{(s)*}_0 \,. \tag{4.6}$$

The $k_0^2$ factors are due to the multiplication of the first row and column of the dispersion matrix with $k_0$.

Finally, the coefficients of the vector $\boldsymbol{m}$ are mixed coefficients, relating the TM modes with the TEM mode. They are defined as

$$m_m = k_0 f^{(0)} e^{(0)}_m e^{(0)*}_0 + \sum_{\substack{s=-\infty \\ s\neq 0}}^{+\infty} f^{(s)} k_0 e^{(s)}_m e^{(s)*}_0 \,. \tag{4.7}$$

The $k_0$ factors are due to the multiplication of the first row of the dispersion matrix with $k_0$.

**Quasi-static simplification of the TEM coefficient** According to the quasi-static simplifications made in appendix D.1, the simplification of (4.6) in the quasi-static regime is

$$\begin{aligned} M_{00} &\underset{k_0\to 0}{=} \frac{pa}{h} + \frac{2a^2}{g\left(1-n^2\right)} + \sum_{\substack{s=-\infty \\ s\neq 0}}^{+\infty} \bar{f}^{(s)} k_0^2 \bar{e}^{(s)}_0 \bar{e}^{(s)*}_0 \\ &\underset{k_0\to 0}{=} \frac{pa}{h} + \frac{2a^2}{g\left(1-n^2\right)} \,, \end{aligned} \tag{4.8}$$

where the higher-harmonic terms disappear because of the $k_0^2$ factor.

**Quasi-static simplification of TM coefficients** According to the quasi-static simplifications made in appendix D.1, the simplification of (4.5) in the quasi-static regime

is

$$M^{\mathrm{e}}_{m'm} \underset{k_0\to 0}{=} \delta_{m'm}\bar{\gamma}_m + \frac{2n^2}{g\,(1-n^2)}\bar{e}^{(0)}_{m'}\bar{e}^{(0)*}_{m} + \sum_{\substack{s=-\infty \\ s\neq 0}}^{+\infty} \bar{f}^{(s)}\bar{e}^{(s)}_{m'}\bar{e}^{(s)*}_{m}\,. \tag{4.9}$$

where $\bar{\gamma}_m$, $\bar{f}^{(s)}$, $\bar{e}^{(0)}_m$ and $\bar{e}^{(s)}_m$ are frequency-independent.

**Quasi-static simplification of mixed coefficients** According to the quasi-static simplifications made in appendix D.1, the simplification of (4.7) in the quasi-static regime is

$$m_m \underset{k_0\to 0}{=} -\frac{2n}{g\,(1-n^2)}\mathrm{j}a\bar{e}^{(0)}_m\,. \tag{4.10}$$

where the higher-harmonic terms disappear because of the $k_0$ factor.

### 4.1.2 Analytic low-frequency refractive index

According to (4.8), (4.9) and (4.10), the dispersion matrix (4.4) is simplified in the quasi-static regime as

$$\underline{\boldsymbol{M}} \underset{k_0\to 0}{=} \begin{bmatrix} \frac{pa}{h} & \mathbf{0} \\ \mathbf{0} & \underline{\boldsymbol{\Sigma}} \end{bmatrix} + \frac{2}{g\,(1-n^2)} \begin{bmatrix} \mathrm{j}a \\ n\bar{\boldsymbol{e}}^{(0)} \end{bmatrix} \begin{bmatrix} \mathrm{j}a \\ n\bar{\boldsymbol{e}}^{(0)} \end{bmatrix}^{\mathrm{H}}\,. \tag{4.11}$$

All the fundamental-harmonic terms are isolated, because they are $n$-dependent, whereas the diagonal and higher-harmonic coefficients of the TM modes are regrouped in the matrix $\underline{\boldsymbol{\Sigma}}$, that is

$$\Sigma_{m'm} = \delta_{m'm}\bar{\gamma}_m + \sum_{\substack{s=-\infty \\ s\neq 0}}^{+\infty} \bar{f}^{(s)}\bar{e}^{(s)}_{m'}\bar{e}^{(s)*}_{m}\,. \tag{4.12}$$

The vector $\bar{\boldsymbol{e}}^{(0)}$ contains all the TM mode projections on the fundamental harmonic, that is $\bar{e}^{(0)}_m$ with $m > 0$.

If $\underline{\boldsymbol{\Sigma}}$ is assumed to be invertible (which is not proven here), then the determinant of $\underline{\boldsymbol{M}}$ in (4.11) can be reformulated as a scalar expression, making use of the so-called determinant lemma [182, p. 416]. The latter states that the determinant of $\underline{\boldsymbol{M}}$ can be written as

$$\begin{aligned} |\underline{\boldsymbol{M}}| &\underset{k_0\to 0}{=} \left| \begin{bmatrix} \frac{pa}{h} & \mathbf{0} \\ \mathbf{0} & \underline{\boldsymbol{\Sigma}} \end{bmatrix} + \frac{2}{g\,(1-n^2)} \begin{bmatrix} \mathrm{j}a \\ n\bar{\boldsymbol{e}}^{(0)} \end{bmatrix} \begin{bmatrix} \mathrm{j}a \\ n\bar{\boldsymbol{e}}^{(0)} \end{bmatrix}^{\mathrm{H}} \right| \\ &= \left( 1 + \frac{2}{g\,(1-n^2)} \begin{bmatrix} \mathrm{j}a \\ n\bar{\boldsymbol{e}}^{(0)} \end{bmatrix}^{\mathrm{H}} \begin{bmatrix} \frac{pa}{h} & \mathbf{0} \\ \mathbf{0} & \underline{\boldsymbol{\Sigma}} \end{bmatrix}^{-1} \begin{bmatrix} \mathrm{j}a \\ n\bar{\boldsymbol{e}}^{(0)} \end{bmatrix} \right) \left| \begin{bmatrix} \frac{pa}{h} & \mathbf{0} \\ \mathbf{0} & \underline{\boldsymbol{\Sigma}} \end{bmatrix} \right|\,. \end{aligned} \tag{4.13}$$

Given that $\Sigma$ is invertible, its determinant is non-zero. Consequently, the dispersion equation (2.12) is equivalent to

$$1 + \frac{2}{g\,(1-n^2)} \begin{bmatrix} \mathrm{j}a \\ n\bar{\boldsymbol{e}}^{(0)} \end{bmatrix}^{\mathrm{H}} \begin{bmatrix} \frac{pa}{h} & \mathbf{0} \\ \mathbf{0} & \underline{\boldsymbol{\Sigma}} \end{bmatrix}^{-1} \begin{bmatrix} \mathrm{j}a \\ n\bar{\boldsymbol{e}}^{(0)} \end{bmatrix} = 0\,. \tag{4.14}$$

Equation (4.14) can be reformulated as the second-order polynomial equation

$$n^2 \left( g - 2 \left[ \bar{\boldsymbol{e}}^{(0)} \right]^{\mathrm{T}} \underline{\boldsymbol{\Sigma}}^{-1} \bar{\boldsymbol{e}}^{(0)} \right) - g - 2\frac{ah}{p} = 0\,. \tag{4.15}$$

Note that the hermitian of $\bar{\boldsymbol{e}}^{(0)}$ is replaced by the transpose operator, given that $\bar{\boldsymbol{e}}^{(0)}$ is real according to (D.7).

Equation (4.15) is solved for the closed-form expression of the refractive index

$$n = \sqrt{\frac{g + 2\frac{ah}{p}}{g - 2\left[\bar{\boldsymbol{e}}^{(0)}\right]^{\mathrm{T}} \underline{\boldsymbol{\Sigma}}^{-1} \bar{\boldsymbol{e}}^{(0)}}}\,. \tag{4.16}$$

This formula is an accurate characterization of the effective medium in the quasi-static regime of the corrugated PPW. As such it establishes a very fast modeling method of these structures, without requiring full-wave commercial solvers such as CST. Note that when only the fundamental corrugation mode is considered, there are no vectorial terms in the denominator, yielding the linearized formula (3.12). However, the latter formula is valid only under strict geometrical restrictions in the first Brillouin zone, whereas (4.16) is accurate for any waveguides in the quasi-static regime.

Although the solution (4.16) is closed-form and fully analytical, it contains the inverse of $\underline{\boldsymbol{\Sigma}}$. A numerical approach is still necessary in order to compute its inverse if a large number of modes $M$ is considered. In appendix D.2, different options are presented to obtain more explicit expressions of the low-frequency equivalent index $n$, based on the sparsity of $\underline{\boldsymbol{\Sigma}}$ and on neglecting some of the reamining coefficients without affecting the precision of the results.

### 4.1.3 Numerical study of the low-frequency effective refractive index

The closed-form refractive index formula (4.16) is derived in the quasi-static regime for arbitrary sizes of corrugated PPWs. As such, it should match full-wave solvers for any geometry, assuming that enough modes and harmonics are considered in the MMM.

This is confirmed by Fig. 4.1, where the low-frequency refractive index is plotted as a function of the corrugation width $a$. The structure periodicity is $p = 4\,\mathrm{mm}$. Different corrugation depths $h$ and metasurface gaps $g$ are considered. In all cases, 10 modes and 50 harmonics are taken into account for the analytical index (4.16) (dashed curve). It is compared to the true index computed with CST (solid curve) at approximately 10 MHz.

Given that $n$ is almost constant in the first Brillouin zone, the index computed in the quasi-static regime remains valid up to a certain frequency, depending on the desired

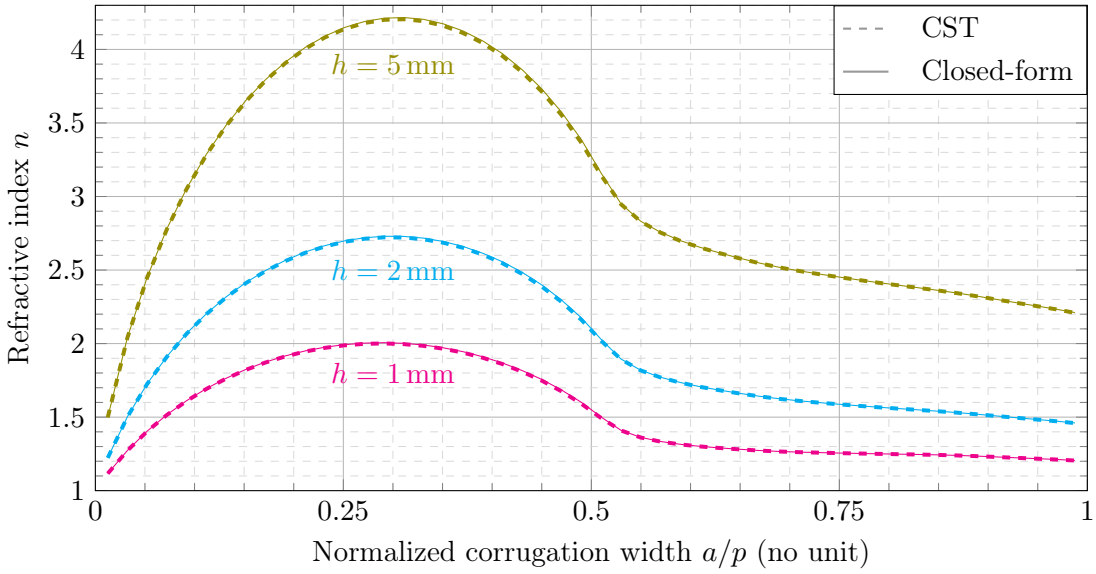


(a) $g = 0.1\,\mathrm{mm}$, varying the corrugation depth $h$.

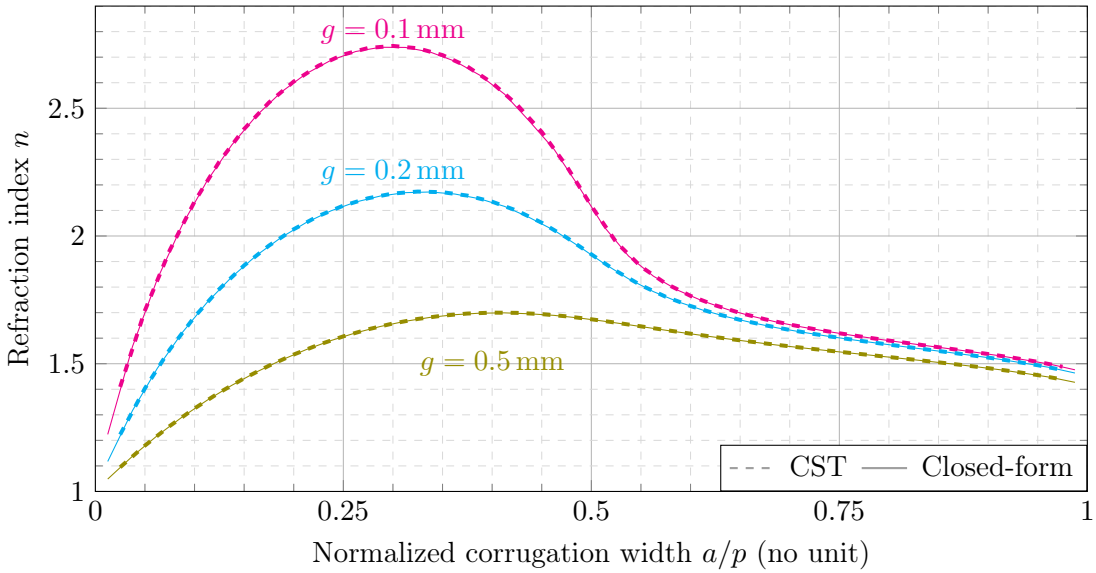


(b) $h = 0.5\,\mathrm{mm}$, varying the gap $g$.

Figure 4.1: Parametric study of the low-frequency effective refractive index $n$ as a function of the corrugation width $a$. The cell length is $p = 4\,\mathrm{mm}$. 10 modes and 50 harmonics are considered. The true refractive index computed with CST (solid) is compared to the analytic model (4.16).

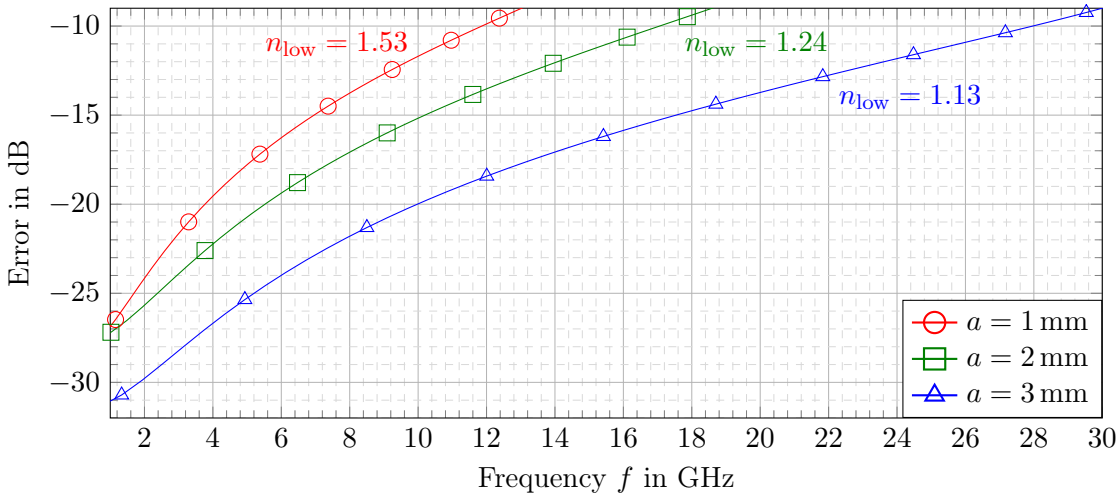


Figure 4.2: Frequency validity of the quasi-static refractive index $n$ computed with (4.16). The error $10\log_{10}|(n_{\text{low}} - n_{\text{CST}})/n_{\text{CST}}|$ between the quasi-static index $n_{\text{low}}$ and the true index computed with CST is plotted as a function of frequency. The G-S corrugated PPW has dimensions $p = 4\,\text{mm}$, $g = 0.1\,\text{mm}$ and $h = 2\,\text{mm}$. Different corrugations width $a$ are considered. In each case, the value of quasi-static index is indicated.

accuracy. This is illustrated in Fig. 4.2. The quasi-static index (4.16) is compared to the true frequency-dependent index computed with CST at 10 MHz for different structures. For all considered G-S structures, the periodicity is $p = 4\,\text{mm}$, the gap between the metasurfaces is $g = 0.1\,\text{mm}$, and the corrugation depth is $h = 2\,\text{mm}$. Three different corrugation widths $a$ are simulated, so that the frequency validity can be examined for different effective densities. The quasi-static index value is indicated in each case next to the corresponding curves.

As expected, the error is negligible at low frequencies, proving again the validity of the formula (4.16) in the quasi-static regime. Although the error increases with frequency, the formula can be used to characterize the waveguide over a wide frequency range, despite being derived in the quasi-static regime. The extend of this validity is correlated to the effective refractive index. Indeed, the study of G-S waveguides has highlighted the quasi-linearity of the propagating mode in the first Brillouin zone. However, the higher the effective refractive index of the waveguide, the lower the frequency at which the mode reaches the end of the first Brillouin zone. If the curve was perfectly linear, the frequency at $k_z = \pi/p$ would be $f = \frac{c_0}{2pn_{\text{low}}}$, with $c_0$ the speed of light in vacuum and $n_{\text{low}}$ the quasi-static refractive index. That explains why in Fig. 4.2, for $a = 3\,\text{mm}$, the frequency validity is larger than for $a = 1\,\text{mm}$. In the first case, $n_{\text{low}} = 1.13$, and so the right-end Brillouin frequency is approximately $f = 33\,\text{GHz}$. In the second case, with $n_{\text{low}} = 1.54$, this is reduced to $f = 24\,\text{GHz}$. Additionally, denser effective media seem to be more dispersive, meaning that the dispersion curve starts bending before reaching

the end of the first Brillouin zone. This explains the large disparities in the frequency validity in Fig. 4.2. Nevertheless, taking into account these limitations, the formula still gives a good approximation of the effective index over a large portion of the first Brillouin zone.

### 4.1.4 Quasi-static homogenization of non-glide PPWs

The effective refractive index at low frequencies can be computed for the non-glide-symmetric (nGS) structure too. All simplifications made for the G-S structure in section 4.1.1 and appendix D.1 can be made for the nGS structure. The resulting dispersion equation is almost exactly like (4.16), except that the coefficients of the matrix $\underline{\mathbf{\Sigma}}$ in (4.12) have the same terms for even- and odd-order harmonics. This means that in (4.3), the vertical spectral function is proportional to a hyperbolic cotangent for all $s$.

The low-frequency effective refractive index $n$ (4.16) is computed for both G-S and nGS PPWs, and is plotted in Fig. 4.3 as a function of the corrugation width $a$. The dimensions of the structure are $p = 4\,\text{mm}$, $h = 0.5\,\text{mm}$ and $g = 0.1\,\text{mm}$. 10 corrugation modes and harmonics with orders up to $|s| \leq 25$ are considered for all computations. The index $n$ computed with (4.16) is compared to the true index, computed with CST at approximately $f = 10\,\text{MHz}$.

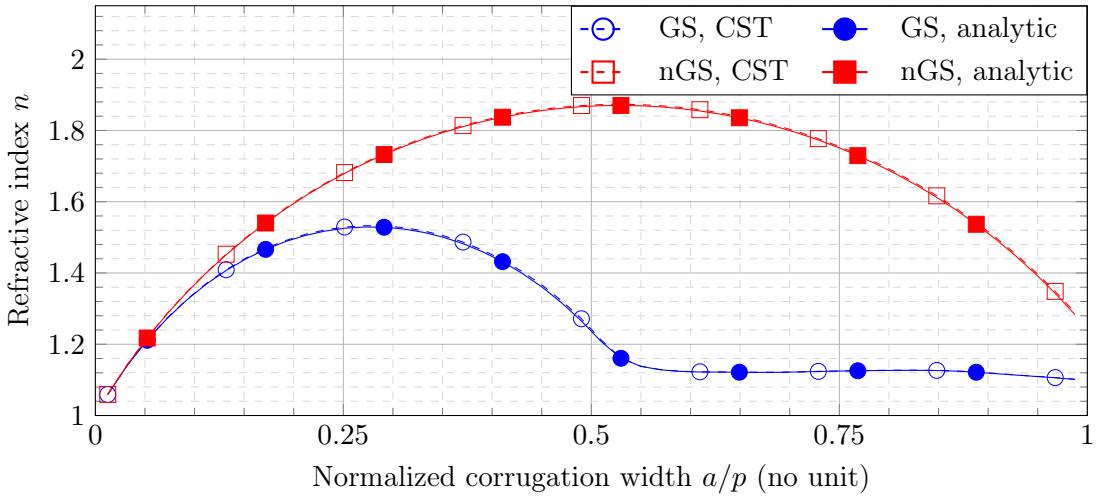


Figure 4.3: Comparison of the G-S and nGS low-frequency effective refractive index $n$, as a function of the corrugation width $a$. 10 modes and 50 harmonics are considered. Other structure parameters are $p = 4\,\text{mm}$, $h = 0.5\,\text{mm}$ and $g = 0.1\,\text{mm}$. The true refractive index computed at 10 MHz with CST corresponds to the dashed curves, whereas the analytic index computed with (4.16) is represented by solid curves.

For small corrugations, the G-S and the nGS PPW are asymptotically identical in terms of density. However, as the corrugations get wider, Fig. 4.3 shows that the nGS structure is denser, meaning that the phase velocity is smaller than in the G-S structure.

Additionally, the refractive index profiles in Fig. 4.3 withstand the equivalency between G-S and nGS structures with double-periodicity derived in section 3.3. Indeed, for $0 < a < p/2$, the index curve of the G-S structure has the same form as the nGS curve over the interval $0 < a < p$. Given that the G-S structure is equivalent to a scaled nGS structure with half cell-length, it makes sense that the refractive index has a similar $a$-dependency.

## 4.2 Quasi-static formula for the effective refractive index of holey parallel-plate waveguides

In this section, the quasi-static homogenization method previously derived for corrugated PPWs is extended to 2-D GS, as published in [183] by the authors. The holey PPWs studied in sections 2.2 and 3.5 are considered. The dispersion equation (2.42), with matrix coefficients (2.40), (2.47) and (2.48), is simplified when $k_0 \to 0$. Similarly to (4.16), the resulting closed-form formula for the effective refractive index depends only on the structure geometry. Additionally, this formula is a function of the main angle of propagation between the two metasurfaces.

### 4.2.1 Distinction between fundamental and higher harmonics

The wave propagating between the two holey metasurfaces is defined by its main propagation constant $\boldsymbol{k}_\theta = k_\theta \hat{\boldsymbol{u}}_\theta$. Its direction in the $zx$-plane can be characterized by the angle $\theta$ formed between the unitary propagation vector $\hat{\boldsymbol{u}}_\theta$ and the $z$-axis. Finding $k_\theta$ at a given frequency is equivalent to finding the effective refractive index $n_\theta = k_\theta/k_0$. As such, it is notable that the effective refractive index $n_\theta$ is direction-dependent in the general case, and so the holey metasurface waveguide may be anisotropic.

In the dispersion equation (2.42), the fundamental mode is not defined by $k_\theta$, but by the wavenumbers $k_z$ and $k_x$. These wavenumbers correspond to propagation in orthogonal directions. As such, they are the cartesian components of the propagation vector $\boldsymbol{k}_\theta$, such that they are related by

$$k_\theta = \sqrt{k_z^2 + k_x^2} = n_\theta k_0 \,. \tag{4.17}$$

When $k_0 \to 0$, (4.17) implies that $k_\theta \to 0$, $k_z \to 0$ and $k_x \to 0$. In the following, writing the condition $k_0 \to 0$ is thus synonymous of all fundamental harmonics going to zero as well. Therefore, in the quasi-static regime, the wavenumbers of all the Floquet harmonics defined in (2.23) become

$$\begin{bmatrix} k_z^{(s)} \\ k_x^{(\ell)} \end{bmatrix} \underset{k_0 \to 0}{=} \begin{cases} \begin{bmatrix} k_z \\ k_x \end{bmatrix} = \begin{bmatrix} k_0 n_\theta \cos\theta \\ k_0 n_\theta \sin\theta \end{bmatrix} & \text{for } s = \ell = 0, \\ \begin{bmatrix} \frac{s2\pi}{p_z} \\ \frac{\ell 2\pi}{p_x} \end{bmatrix} = \boldsymbol{\Gamma}^{(s\ell)} & \text{for } (s,\ell) \neq (0,0), \end{cases} \tag{4.18}$$

where $\mathbf{\Gamma}^{(s\ell)}$ can be understood as the quasi-static propagation vector of the harmonic $(s,\ell)$. As such, in the spectral domain, all Floquet harmonics are evaluated at the points $\mathbf{\Gamma}^{(s\ell)}$. Fundamental and higher-harmonic terms must be distinguished, given that in the former case, the spectral point $\mathbf{\Gamma}^{(00)} = (0,0)$ is approached from a direction which directly depends on $\theta$, at a speed that depends on $n_\theta$. This is illustrated in the spectral representation Fig. 4.4. That is why the occurrences of the fundamental harmonic are not dismissed yet, as they might lead to $n_\theta$-dependencies.

This happens in the vertical spectral function defined in (2.35). Considering (4.18), in the case of the fundamental harmonic, it can be shown that

$$\frac{f^{(00)}}{k_y^{(00)}} \underset{k_0\to 0}{=} \frac{2}{gk_0^2\left(\epsilon_{\mathrm{r}1}\mu_{\mathrm{r}1} - n_\theta^2\right)}\,, \tag{4.19}$$

whereas for higher harmonics

$$\frac{f^{(s\ell)}}{k_y^{(s\ell)}} \underset{k_0\to 0}{=} \bar{f}^{(s\ell)} = \begin{cases} -\tanh\left(\frac{g}{2}\Gamma^{(s\ell)}\right)/\Gamma^{(s\ell)} & \text{if } \ell+s \text{ odd},\\ -\coth\left(\frac{g}{2}\Gamma^{(s\ell)}\right)/\Gamma^{(s\ell)} & \text{if } \ell+s \text{ even}, \end{cases} \tag{4.20}$$

with the norm $\Gamma^{(s\ell)} = \left\|\mathbf{\Gamma}^{(s\ell)}\right\| = \sqrt{(\ell 2\pi/p_x)^2 + (s2\pi/p_z)^2}$.

This distinction between fundamental and higher harmonics is not necessary when it comes to the projected modal functions (PMFs) defined in (2.28), which are all simplified as

$$\bar{e}_m^{(s\ell)} = \iint\limits_S e_m \bar{F}^{(s\ell)}\mathrm{d}s\,, \tag{4.21}$$

where $e_m$ may be any of the three electric field components, and $\bar{F}^{(s\ell)} = \mathrm{e}^{-\mathrm{j}\frac{\ell 2\pi}{p_x}x - \mathrm{j}\frac{s2\pi}{p_z}z}$. For the fundamental harmonic, $\bar{F}^{(00)} = 1$, and so $\bar{e}_m^{(00)}$ is the average of the electric field component $e_m$ over the hole area. As such, all $\bar{e}_m^{(00)}$ are real coefficients.

Overall, (4.21) shows that the quasi-static dispersive behavior of the waveguide is related to the shape of the holes through the Fourier transform of their modal fields, evaluated periodically, as visualized by the blue points in Fig. 4.4.

### 4.2.2 Simplification of the matrix coefficients

In the dispersion equation (2.42), the modes are ordered according to type, such that $\underline{\boldsymbol{M}}$ can be subdivided in four submatrices. Different quasi-static simplifications are possible for the different submatrices, according to the mode type.

For ease of notation, we define the refractive index of the gap medium $n_1 = \sqrt{\epsilon_{\mathrm{r}1}\mu_{\mathrm{r}1}}$, the refractive index of the hole medium $n_2 = \sqrt{\epsilon_{\mathrm{r}2}\mu_{\mathrm{r}2}}$, and the corresponding free-space wavenumber $k_1 = k_0 n_1$.

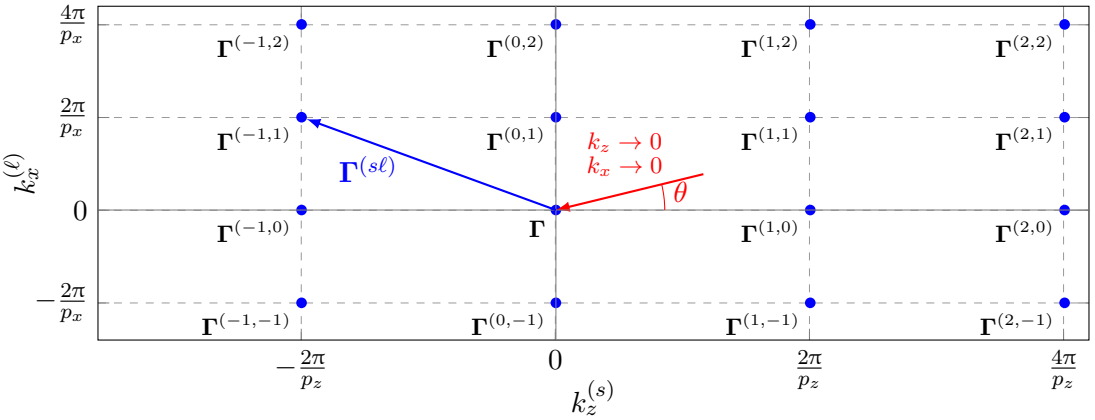


Figure 4.4: Spectral domain of the Floquet harmonics. During the homogenization process, the harmonics of orders $(s, \ell)$ are evaluated at the blue points, which are the periodic replicas of the $\mathbf{\Gamma}$-point $(k_z, k_x) = (0, 0)$. The latter is approached from the propagation direction $\theta$, as indicated by the red arrow.

**Diagonal terms** In (2.40) and (2.47), there is a term that exists only on the diagonal of the submatrix $\underline{\boldsymbol{M}}^{\mathrm{h/h}}$ and $\underline{\boldsymbol{M}}^{\mathrm{e/e}}$, respectively, because it is multiplied by the Krœnecker symbol $\delta_{m'm}$. In $\underline{\boldsymbol{M}}^{\mathrm{h/h}}$, the quasi-static approximation of this diagonal term depends on whether a transverse electric (TE) or a TEM mode is considered.

The cut-off wavenumber $k_m^{\mathrm{h}}$ of a TE mode is non-zero. Therefore, the frequency-dependencies vanish next to it, yielding $k_{y,m}^{\mathrm{h}} \to \mathrm{j}k_m^{\mathrm{h}}$. As such, the quasi-static diagonal term in (2.40) becomes

$$\frac{\mu_{\mathrm{r}1} k_m^{\mathrm{h}}}{\mu_{\mathrm{r}2}} p_x p_z I_m^{\mathrm{h}} \coth\left(k_m^{\mathrm{h}} h\right) , \tag{4.22}$$

where $\cot\left(\mathrm{j}k_m^{\mathrm{h}} h\right) = -\mathrm{j}\coth\left(k_m^{\mathrm{h}} h\right)$.

When the mode is TEM, then $k_m^{\mathrm{h}} = 0$, and so $k_{y,m}^{\mathrm{h}} \to k_0 n_2$. For $k_0 \to 0$, the cotangent term is approximated by the inverse function, and so the frequency dependencies cancel out. Therefore, for TEM modes, the diagonal term of $\underline{\boldsymbol{M}}^{\mathrm{h/h}}$ is

$$\frac{\mu_{\mathrm{r}1}}{\mu_{\mathrm{r}2}} \frac{p_x p_z}{h} I_m^{\mathrm{h}} . \tag{4.23}$$

For $\underline{\boldsymbol{M}}^{\mathrm{e/e}}$ in (2.47), the diagonal term becomes

$$-k_0^2 \frac{\mu_{\mathrm{r}1} \epsilon_{\mathrm{r}2}}{k_m^{\mathrm{e}}} p_x p_z I_m^{\mathrm{e}} \coth\left(k_m^{\mathrm{e}} h\right) , \tag{4.24}$$

where the quasi-static simplifications are the same as in (4.22). The wave admittance of TM modes (2.37) is used.

**Fundamental-harmonic terms** In (2.40), (2.47) and (2.48), the matrix coefficients contain a sum of terms, each of which corresponding to one Floquet harmonic. Due to the distinction made in (4.18), the term that corresponds to the fundamental harmonic is taken out of the sum and treated separately. The harmonic wavenumbers and the vertical spectral function are simplified according to (4.18) and (4.19).

In (2.47) for $\underline{\boldsymbol{M}}^{\mathrm{e/e}}$, the fundamental-harmonic term becomes

$$k_1^2 \frac{2n_\theta^2}{g\left(n_1^2-n_\theta^2\right)} \frac{\bar{e}_{y,m'}^{(00)} \bar{e}_{y,m}^{(00)}}{k_{m'}^{\mathrm{e}} k_m^{\mathrm{e}}}, \tag{4.25}$$

where the complex conjugate is removed because $\bar{e}_{y,m}^{(00)}$ is real, as defined in (4.21). In (2.48) for $\underline{\boldsymbol{M}}^{\mathrm{e/h}}$,

$$\mathrm{j}k_1 n_1 \frac{2n_\theta}{g\left(n_1^2-n_\theta^2\right)} \frac{\bar{e}_{y,m'}^{(00)}}{k_{m'}^{\mathrm{e}}} \left(\cos\theta \bar{e}_{z,m}^{\mathrm{h}(00)} + \sin\theta \bar{e}_{x,m}^{\mathrm{h}(00)}\right). \tag{4.26}$$

Finally, for $\underline{\boldsymbol{M}}^{\mathrm{h/h}}$ in (2.40), the fundamental term is simplified as

$$\frac{2}{g\left(n_1^2-n_\theta^2\right)} \begin{bmatrix} n_1^2 \left(\bar{e}_{z,m'}^{\mathrm{h}(00)} \bar{e}_{z,m}^{\mathrm{h}(00)} + \bar{e}_{x,m'}^{\mathrm{h}(00)} \bar{e}_{x,m}^{\mathrm{h}(00)}\right) \\ - n_\theta^2 \left(\cos\theta \bar{e}_{x,m'}^{\mathrm{h}(00)} - \sin\theta \bar{e}_{z,m'}^{\mathrm{h}(00)}\right) \left(\cos\theta \bar{e}_{x,m}^{\mathrm{h}(00)} - \sin\theta \bar{e}_{z,m}^{\mathrm{h}(00)}\right) \end{bmatrix}, \tag{4.27}$$

which can be reformulated as

$$\begin{aligned} &\frac{2}{g} \left(\cos\theta \bar{e}_{x,m'}^{\mathrm{h}(00)} - \sin\theta \bar{e}_{z,m'}^{\mathrm{h}(00)}\right) \left(\cos\theta \bar{e}_{x,m}^{\mathrm{h}(00)} - \sin\theta \bar{e}_{z,m}^{\mathrm{h}(00)}\right) \\ &+ \frac{2n_1^2}{g\left(n_1^2-n_\theta^2\right)} \left(\cos\theta \bar{e}_{z,m'}^{\mathrm{h}(00)} + \sin\theta \bar{e}_{x,m'}^{\mathrm{h}(00)}\right) \left(\cos\theta \bar{e}_{z,m}^{\mathrm{h}(00)} + \sin\theta \bar{e}_{x,m}^{\mathrm{h}(00)}\right), \end{aligned} \tag{4.28}$$

to isolate all $n_\theta$ dependencies. Note that there is no distinction needed between TE and TEM modes for the harmonic terms in $\underline{\boldsymbol{M}}^{\mathrm{h/h}}$.

**Higher-harmonic terms** The remaining terms in the sums of (2.40), (2.47), (2.48) are simplified as well. The harmonic wavenumbers and the vertical spectral functions are simplified according to (4.18) and (4.20). For $\underline{\boldsymbol{M}}^{\mathrm{h/h}}$, this yields

$$-\sum_{(s,\ell)\neq(0,0)} \bar{f}^{(s\ell)} \left(\tfrac{s2\pi}{p_z} \bar{e}_{x,m'}^{\mathrm{h}(s\ell)} - \tfrac{\ell 2\pi}{p_x} \bar{e}_{z,m'}^{\mathrm{h}(s\ell)}\right) \left(\tfrac{s2\pi}{p_z} \bar{e}_{x,m}^{\mathrm{h}(s\ell)} - \tfrac{\ell 2\pi}{p_x} \bar{e}_{z,m}^{\mathrm{h}(s\ell)}\right)^*, \tag{4.29}$$

where the terms proportional to $k_0^2$ are negligible compared to the remaining terms at low frequency. For $\underline{\boldsymbol{M}}^{\mathrm{e/e}}$, the higher-harmonic terms in (2.47) become

$$k_1^2 \sum_{(s,\ell)\neq(0,0)} \bar{f}^{(s\ell)} \frac{\bar{e}_{y,m'}^{(s\ell)} \bar{e}_{y,m}^{(s\ell)*}}{k_{m'}^{\mathrm{e}} k_m^{\mathrm{e}}} \Gamma^{(s\ell)\,2}. \tag{4.30}$$

Finally, for the coefficients of $\underline{\boldsymbol{M}}^{\mathrm{e/h}}$, the higher-harmonic terms are simplified similarly to $\underline{\boldsymbol{M}}^{\mathrm{e/e}}$ in (4.30). The resulting $k_0^2$ dependency makes these coefficients negligible compared to the fundamental-harmonic coefficient (4.26), which is proportional to $k_0$. As such, the low-frequency $\underline{\boldsymbol{M}}^{\mathrm{e/h}}$ only contains the fundamental-harmonic coefficients.

### 4.2.3 Total dispersion matrix

After the low-frequency simplifications detailed in the previous paragraphs, the dispersion matrix can be written as

$$\underline{\boldsymbol{M}} \underset{k_0\to 0}{=} \begin{bmatrix} k_1^2\left(\underline{\boldsymbol{\Sigma}}^{\mathrm{e}} + \frac{n_\theta^2}{n_1^2-n_\theta^2}\frac{2}{g}\boldsymbol{u}^{\mathrm{e}}[\boldsymbol{u}^{\mathrm{e}}]^{\mathrm{H}}\right) & \mathrm{j}k_1\frac{n_\theta n_1}{n_1^2-n_\theta^2}\frac{2}{g}\boldsymbol{u}^{\mathrm{e}}\left[\boldsymbol{u}^{\mathrm{h}}\right]^{\mathrm{H}} \\ -\mathrm{j}k_1\frac{n_\theta n_1}{n_1^2-n_\theta^2}\frac{2}{g}\boldsymbol{u}^{\mathrm{h}}[\boldsymbol{u}^{\mathrm{e}}]^{\mathrm{H}} & \underline{\boldsymbol{\Sigma}}^{\mathrm{h}} + \frac{n_1^2}{n_1^2-n_\theta^2}\frac{2}{g}\boldsymbol{u}^{\mathrm{h}}\left[\boldsymbol{u}^{\mathrm{h}}\right]^{\mathrm{H}} \end{bmatrix}. \tag{4.31}$$

The matrix $\underline{\boldsymbol{\Sigma}}^{\mathrm{e}}$ contains the diagonal and higher-harmonic terms for the TM modes, as defined in (4.24) and (4.30). The $k_1^2$-dependency is factored out of these terms. As such, its coefficients are

$$\Sigma^{\mathrm{e}}_{m'm} = -\delta_{m'm}\frac{\epsilon_{\mathrm{r}2}}{\epsilon_{\mathrm{r}1}k^{\mathrm{e}}_m}p_x p_z I^{\mathrm{e}}_m \coth\left(k^{\mathrm{e}}_m h\right) + \sum_{(s,\ell)\neq(0,0)} \bar{f}^{(s\ell)}\frac{\bar{e}^{(s\ell)}_{y,m'}\bar{e}^{(s\ell)*}_{y,m}}{k^{\mathrm{e}}_{m'}k^{\mathrm{e}}_m}\Gamma^{(s\ell)\,2}. \tag{4.32}$$

Similarly, $\underline{\boldsymbol{\Sigma}}^{\mathrm{h}}$ contains the diagonal and higher-harmonic terms of the remaining modes, as well as the part of the fundamental term that does not depend on $n_\theta$. For the TE modes, these terms are defined in (4.22), (4.28) and (4.29), yielding coefficients

$$\begin{aligned}\Sigma^{\mathrm{h}}_{m'm} = {}& \delta_{m'm}\frac{\mu_{\mathrm{r}1}k^{\mathrm{h}}_m}{\mu_{\mathrm{r}2}}p_x p_z I^{\mathrm{h}}_m \coth\left(k^{\mathrm{h}}_m h\right) \\ & + \frac{2}{g}\left(\cos\theta\bar{e}^{\mathrm{h}(00)}_{x,m'} - \sin\theta\bar{e}^{\mathrm{h}(00)}_{z,m'}\right)\left(\cos\theta\bar{e}^{\mathrm{h}(00)}_{x,m} - \sin\theta\bar{e}^{\mathrm{h}(00)}_{z,m}\right) \\ & - \sum_{(s,\ell)\neq(0,0)} \bar{f}^{(s\ell)}\left(\tfrac{s2\pi}{p_z}\bar{e}^{\mathrm{h}(s\ell)}_{x,m'} - \tfrac{\ell 2\pi}{p_x}\bar{e}^{\mathrm{h}(s\ell)}_{z,m'}\right)\left(\tfrac{s2\pi}{p_z}\bar{e}^{\mathrm{h}(s\ell)}_{x,m} - \tfrac{\ell 2\pi}{p_x}\bar{e}^{\mathrm{h}(s\ell)}_{z,m}\right)^*,\end{aligned} \tag{4.33}$$

whereas for TEM modes, according to the diagonal term (4.23), the matrix coefficients are

$$\begin{aligned}\Sigma^{\mathrm{h}}_{m'm} = {}& \delta_{m'm}\frac{\mu_{\mathrm{r}1}}{\mu_{\mathrm{r}2}}\frac{p_x p_z}{h}I^{\mathrm{h}}_m \\ & + \frac{2}{g}\left(\cos\theta\bar{e}^{\mathrm{h}(00)}_{x,m'} - \sin\theta\bar{e}^{\mathrm{h}(00)}_{z,m'}\right)\left(\cos\theta\bar{e}^{\mathrm{h}(00)}_{x,m} - \sin\theta\bar{e}^{\mathrm{h}(00)}_{z,m}\right) \\ & - \sum_{(s,\ell)\neq(0,0)} \bar{f}^{(s\ell)}\left(\tfrac{s2\pi}{p_z}\bar{e}^{\mathrm{h}(s\ell)}_{x,m'} - \tfrac{\ell 2\pi}{p_x}\bar{e}^{\mathrm{h}(s\ell)}_{z,m'}\right)\left(\tfrac{s2\pi}{p_z}\bar{e}^{\mathrm{h}(s\ell)}_{x,m} - \tfrac{\ell 2\pi}{p_x}\bar{e}^{\mathrm{h}(s\ell)}_{z,m}\right)^*,\end{aligned} \tag{4.34}$$

where only the diagonal term changes.

The remaining entries are the parts of the fundamental terms (4.25), (4.26) and (4.28) that have an $n_\theta$-dependency. They are all proportional to $2/g$, which is factored out. For the fundamental term of $\underline{\boldsymbol{M}}^{\mathrm{e/e}}$, when additionnally factoring $n_\theta^2/(n_1^2-n_\theta^2)$ out, the remaining elements can be written as the outer product of two vectors $\boldsymbol{u}^{\mathrm{e}}\boldsymbol{u}^{\mathrm{eH}}$. According to (4.25) , the vector $\boldsymbol{u}^{\mathrm{e}}$ has coefficients

$$u^{\mathrm{e}}_m = \frac{\bar{e}^{(00)}_{y,m}}{k^{\mathrm{e}}_m}. \tag{4.35}$$

Similarly, the $n_\theta$-dependent term of (4.28) is factored out, that is $n_1^2/(n_1^2 - n_\theta^2)$. The remaining part can be written as the outer product of a vector $\boldsymbol{u}^{\mathrm{h}}$ with its hermitian, with coefficients

$$u_m^{\mathrm{h}} = \cos\theta \bar{e}_{z,m}^{\mathrm{h}(00)} + \sin\theta \bar{e}_{x,m}^{\mathrm{h}(00)} \,. \tag{4.36}$$

The coefficients $u_m^{\mathrm{e}}$ and $u_m^{\mathrm{h}}$ can be identified in the fundamental term (4.26) of the submatrix $\underline{\boldsymbol{M}}^{\mathrm{e/h}}$. As such, the remaining terms are factored out, that is $\mathrm{j}k_1 n_\theta n_1/(n_1^2 - n_\theta^2)$.

### 4.2.4 Quasi-static homogenization

From the dispersion equation (2.42), the determinant of the dispersion matrix must be null. Considering the quasi-static simplification (4.31), the determinant of the matrix can be simplified by factoring out $1/(n_1^2 - n_\theta^2)$ from the total matrix. Moreover, $k_1 n_\theta$ can be factored out from the first row and the first column of the considered block-matrix. Similarly, $n_1$ can be factored out of the last row and the last column. This yields the reduced dispersion equation

$$\begin{vmatrix} \frac{n_1^2 - n_\theta^2}{n_\theta^2}\underline{\boldsymbol{\Sigma}}^{\mathrm{e}} + \frac{2}{g}\boldsymbol{u}^{\mathrm{e}}[\boldsymbol{u}^{\mathrm{e}}]^{\mathrm{H}} & \mathrm{j}\frac{2}{g}\boldsymbol{u}^{\mathrm{e}}\left[\boldsymbol{u}^{\mathrm{h}}\right]^{\mathrm{H}} \\ -\mathrm{j}\frac{2}{g}\boldsymbol{u}^{\mathrm{h}}[\boldsymbol{u}^{\mathrm{e}}]^{\mathrm{H}} & \frac{n_1^2 - n_\theta^2}{n_1^2}\underline{\boldsymbol{\Sigma}}^{\mathrm{h}} + \frac{2}{g}\boldsymbol{u}^{\mathrm{h}}\left[\boldsymbol{u}^{\mathrm{h}}\right]^{\mathrm{H}} \end{vmatrix} = 0 \,. \tag{4.37}$$

The determinant in (4.37) can be rewritten as the sum of a diagonal matrix that depends on $n_\theta$, summed with the outer product of two vectors,

$$\left| \left(n_1^2 - n_\theta^2\right) \begin{bmatrix} \frac{1}{n_\theta^2}\underline{\boldsymbol{\Sigma}}^{\mathrm{e}} & \boldsymbol{0} \\ \boldsymbol{0} & \frac{1}{n_1^2}\underline{\boldsymbol{\Sigma}}^{\mathrm{h}} \end{bmatrix} + \frac{2}{g} \begin{bmatrix} \mathrm{j}\boldsymbol{u}^{\mathrm{e}} \\ \boldsymbol{u}^{\mathrm{h}} \end{bmatrix} \begin{bmatrix} \mathrm{j}\boldsymbol{u}^{\mathrm{e}} \\ \boldsymbol{u}^{\mathrm{h}} \end{bmatrix}^{\mathrm{H}} \right| = 0 \,. \tag{4.38}$$

By using the determinant lemma [182, p. 416], (4.38) can be reformulated as the scalar equation

$$n_1^2 - n_\theta^2 + n_\theta^2 \frac{2}{g} \left[\boldsymbol{u}^{\mathrm{e}}\right]^{\mathrm{H}} \left[\underline{\boldsymbol{\Sigma}}^{\mathrm{e}}\right]^{-1} \boldsymbol{u}^{\mathrm{e}} + n_1^2 \frac{2}{g} \left[\boldsymbol{u}^{\mathrm{h}}\right]^{\mathrm{H}} \left[\underline{\boldsymbol{\Sigma}}^{\mathrm{h}}\right]^{-1} \boldsymbol{u}^{\mathrm{h}} = 0 \,, \tag{4.39}$$

which is a second order polynomial equation in $n_\theta$. Therefore, it is solved for

$$n_\theta = n_1 \sqrt{\frac{1 + \frac{2}{g}\left[\boldsymbol{u}^{\mathrm{h}}\right]^{\mathrm{H}} \left[\underline{\boldsymbol{\Sigma}}^{\mathrm{h}}\right]^{-1} \boldsymbol{u}^{\mathrm{h}}}{1 - \frac{2}{g}\left[\boldsymbol{u}^{\mathrm{e}}\right]^{\mathrm{H}} \left[\underline{\boldsymbol{\Sigma}}^{\mathrm{e}}\right]^{-1} \boldsymbol{u}^{\mathrm{e}}}} \,, \tag{4.40}$$

which is the effective refractive index of the G-S holey PPW in the quasi-static state. This homogenized index characterizes the waveguide over a wide frequency range, due to the low dispersion of G-S structures. It depends only on the waveguide geometry and materials. Specifically, the information about the shape of the holes is contained in the quasi-static PMFs $\bar{e}_m^{(s\ell)}$, which are the Fourier transforms of the hole modes evaluated

at the quasi-static harmonic wavenumbers. As such, getting the eigenmodes of the hole cross-section is the only prerequisite for (4.40) to be applicable.

This is illustrated in the following section by applying (4.40) to a series of examples. The validity of this formula is illustrated for holey G-S PPWs with canonical hole shapes in section 4.3, and for arbitrary hole shapes in section 4.4. Its limits in frequency are examined at the end of the chapter.

## 4.3 Canonical hole shapes

In the previous section, a closed-form solution of the effective refractive index is found for holey PPWs in the quasi-static regime. It depends only on the waveguide geometry. This includes the cross-section of the holes: the information about their eigenmodes must be incorporated in the formula. In the following, this procedure is applied to the example of canonical holes, for which the analytic expressions of the eigenmodes are known. It is shown that some of these eigenmodes do not impact the final refractive index, and so they can be dismissed. This accelerates the resulting closed-form formula even further, and so it can be used to perform fast parametric studies. It also opens the door to waveguide optimization.

### 4.3.1 Dismissal of the modes without dispersive effect

In the closed-form index formula (4.40), the size of the matrices $\underline{\boldsymbol{\Sigma}}^{\mathrm{e}}$ and $\underline{\boldsymbol{\Sigma}}^{\mathrm{h}}$ depends on the number of modes that are considered in the holes. When hundreds of TM and TE modes are needed to achieve a given accuracy for the refractive index, filling these matrices takes most of the algorithm's execution time, because they contain several tens of thousands of coefficients. Therefore, if the number of these modes can be reduced, the execution time can brought down even further.

From the closed-form solution of the refractive index (4.40), it is possible to identify some modes that have no influence on low-frequency propagation i.e., they do not change the value of the refractive index if they are kept in the formula (4.40). The conditions (D.17) and (D.18) derived in appendix D.3 are sufficient conditions for a mode to be dispensable. Roughly speaking, this happens when the field average at the hole surface of a mode is null. This is applied in appendix D.4.1.2 and D.4.2.2 for rectangular and circular holes, respectively.

### 4.3.2 Modal functions for rectangular and circular holes

**Rectangular holes** Holes with rectangular cross-section of size $a_z \times a_x$ are considered, as shown in Fig. 2.5. This yields a holey G-S PPW with the unit cell shown in Fig. 4.5a. Most of the hard work is already done in 2.2.5, that is deriving the Fourier transforms of the eigenmodes. The last step is simply to evaluate these expressions in the quasi-static regime. This is done in appendix D.4.1.

Added to the dimensions $p_z$, $p_x$, $h$, and $g$ of the holey PPW, equations (B.32), (B.35), (D.22), (D.24) and (D.25) are enough to fill out all the coefficients of the matrices $\underline{\boldsymbol{\Sigma}}^{\mathrm{e}}$

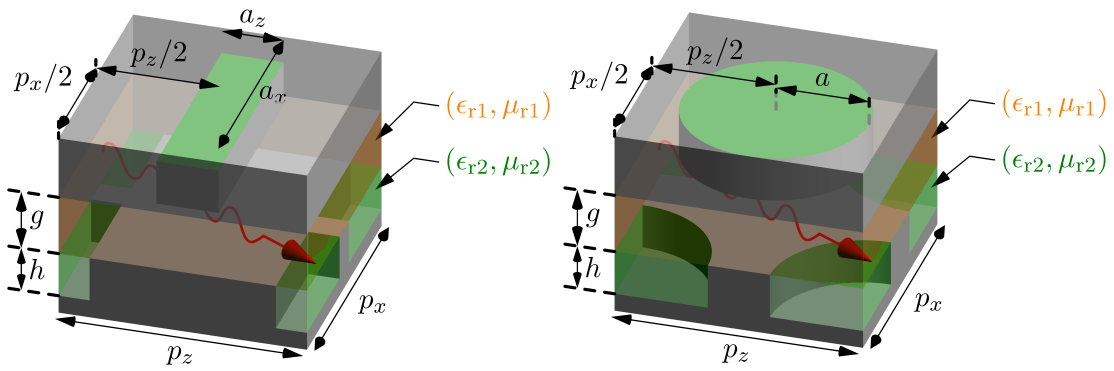


(a) Rectangular holes of size $a_z \times a_x$.

(b) Circular holes of radius $a$.

Figure 4.5: Holey G-S PPWs with canonical holes. The gap is filled with a dielectric $(\epsilon_{r1}, \mu_{r1})$, and the holes are filled with a dielectric $(\epsilon_{r2}, \mu_{r2})$. The red arrow indicates the wave propagation plane.

and $\underline{\boldsymbol{\Sigma}}^{h}$ in (4.32) and (4.34), as well as the coefficients of the vectors $\boldsymbol{u}^{e}$ and $\boldsymbol{u}^{h}$ in (4.35) and (4.36). As such, the refractive index formula (4.40) can be computed as function of the waveguide and hole dimensions.

Moreover, appendix D.4.1.2 shows that the index formula (4.40) is still accurate if one keeps only TM modes with both $q$ and $m$ are odd, and TE modes where $q+m$ is odd. This represents a reduction of the TM modes by half, and the TE modes by a quarter.

**Circular holes** For circular holes of radius $a$, the unit cell of the holey G-S PPW is illustrated in Fig. 4.5b, yielding the total structure shown in Fig. 2.7. In 2.2.6, the Fourier transforms of the circular eigenmodes are derived. The last step is simply to evaluate these expressions in the quasi-static regime. This is done is appendix D.4.2.

Inserting the quasi-static terms (D.30), (D.31), (D.32), (D.33), (D.34), and (D.35) into the matrix and vector coefficients (4.32), (4.34), (4.35) and (4.36) makes the formula (4.40) fully analytic, and so the effective refractive index can be computed directly as function of the geometry and the propagation direction.

Appendix D.4.2.2 shows that it is enough to keep only the TM modes with $t = 2$ and $q$ even, and the TE modes with $q$ odd are kept.

### 4.3.3 Convergence and time gain

The closed-form formula (4.40) yields the effective refractive index of the holey PPW as function of geometry and propagation direction. In this formula, the size of the different matrices depends on the number of modes considered in each hole. Moreover, each matrix coefficient (4.32) and (4.34) is dependent on the number of Floquet harmonics used in the MMM. Higher-order harmonics and modes have a reduced impact on the effective wave propagation, and can therefore be truncated, such that the dispersion matrix in (2.42) has a finite size [43].

However, this truncation depends on geometry and on the desired accuracy. In the following, we study the convergence of the low-frequency refractive index for increasingly many modes. This study is performed with two techniques in parallel. On the one side, the low-frequency refractive index is computed with the closed-form formula (4.40). On the other side, by solving the dispersion equation (2.42) at 1 MHz. We refer to this as the MMM approximation, for which around 20 iterations are performed to obtain an index convergence of $10^{-5}$. In order to avoid overflow when solving the dispersion equation (2.42), we consider the log-determinant of the dispersion matrix, and use a golden-section-search [184] to iteratively determine when the log-determinant tends towards $-\infty$. These adjustments highlight the gain in implementation complexity enabled by the closed-form formula (4.40), which requires no iterative tuning of any kind.

While the precision chosen in this comparison is much higher than the one required for applications, our aim is the rigorous validation of the accuracy of (4.40). Additionally, a CST simulation at around 10 MHz validates the convergence value of both methods. Holey GS PPWs with three different holes cross-sections and depth $h = 5\,\text{mm}$ are considered in Fig. 4.6. The metasurfaces have a periodicity $p_z = p_x = 4\,\text{mm}$ and are separated by a gap $g = 0.1\,\text{mm}$. No dielectrics are used in these examples. The waves propagate in the direction $\theta = 0°$.

In Fig. 4.6, the computed low-frequency refractive index is plotted as a function of the maximum mode order $m_{\max}$. The maximum mode order applies to both $q$ and $m$, for both TM and TE modes. As such, the total number of considered modes is $2m_{\max}(m_{\max}+1)$ – given that there no $\text{TE}_{00}$, $\text{TM}_{\text{q}0}$ nor $\text{TM}_{0\text{m}}$ modes. As such, the highest abscissa point in Fig. 4.6 i.e., $m_{\max} = 40$, corresponds to 3280 modes in the square holes. Additionally, each curve corresponds to a different number of Floquet harmonics, where orders $s$ and $\ell$ range within $\pm5$, $\pm20$ or $\pm80$. This latter case represents more than 25 000 Floquet harmonics.

**Time gain** The computation time for the three structures studied in Fig. 4.6 is compared between the closed-form formula (4.40) and the MMM approximation. The average time over the three considered structures is plotted in Fig. 4.7. A computer with a Quad-Core Intel Core i5 @2.4 GHz processor and with 8 GB of RAM is used, running the algorithms on Matlab without any parallelization effort. The total execution time to obtain the MMM curves up to $m_{\max} = 20$ for each structure is around 4 hours, whereas the closed-form formula requires only 106 seconds. The higher the number of modes, the higher the disparity in time between the two methods. That is why the MMM approximation was not computed for orders higher than $m_{\max} = 20$. In this latter case, with harmonics $\pm80$, the closed-form formula is 250 times faster then the MMM method.

There are several reasons for this speed-up. First, the MMM approximation is iterative, and must evaluate the matrix determinant several dozen times, depending on the search interval and the desired accuracy. Second, the low-frequency method developed in this paper enables the dismissal of many modes that have no impact on propagation, as explained in section 4.3.1. As such, for $2m_{\max}(m_{\max}+1)$ modes with the MMM approximation, only $\frac{3}{4}(m_{\max}+1)^2$ are kept for the closed-form formula. Finally, the matrices in

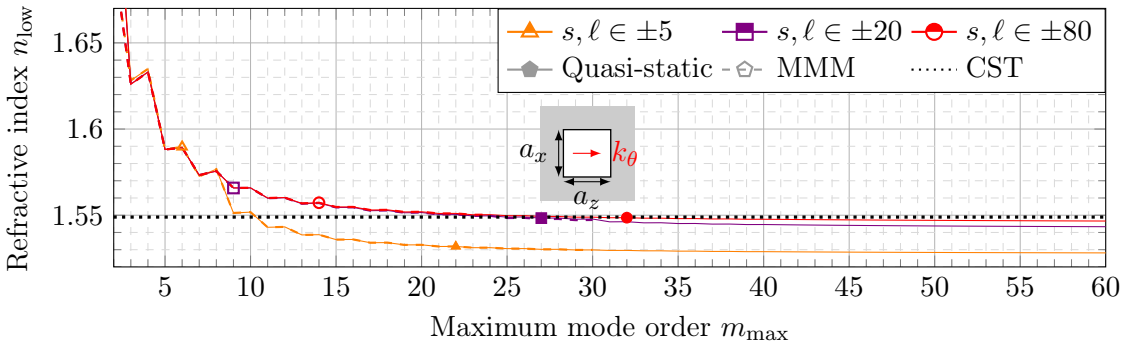


(a) $a_z = a_x = 3\,\text{mm}$.

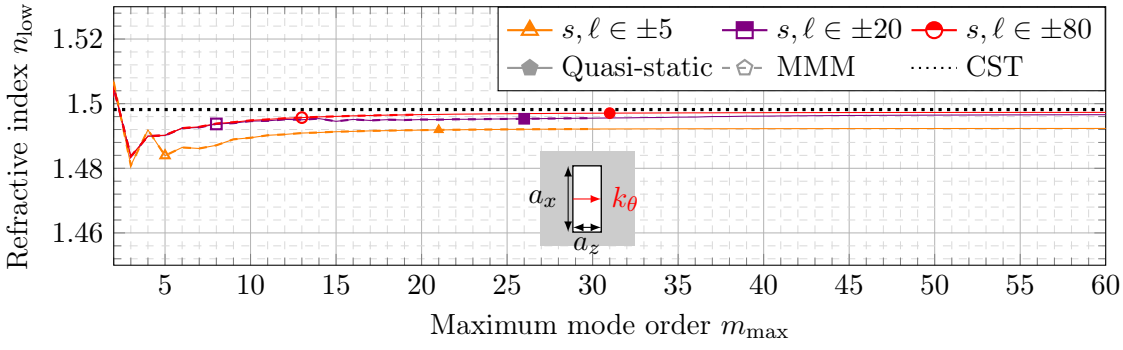


(b) $a_z = 1.5\,\text{mm}$, $a_x = 3.5\,\text{mm}$.

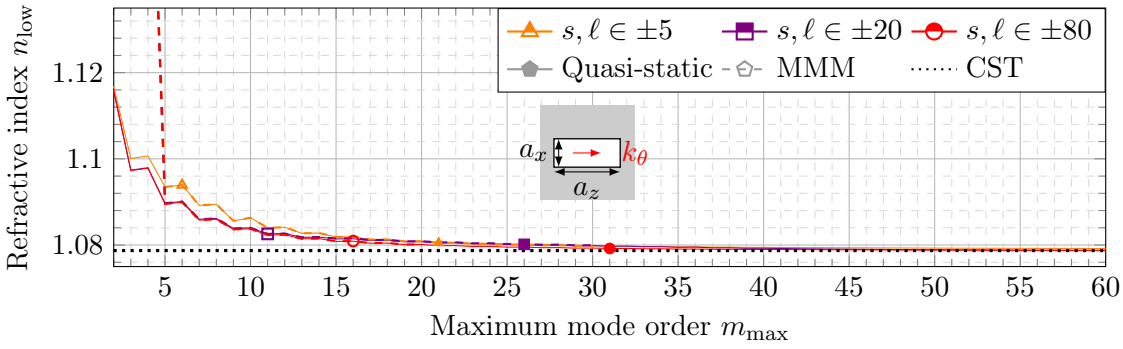


(c) $a_z = 3.5\,\text{mm}$, $a_x = 1.5\,\text{mm}$.

Figure 4.6: Refractive index convergence as the number of modes increases. The structures under study are G-S PPWs with rectangular holes, with periodicities $p_z = p_x = 4\,\text{mm}$, a gap $g = 0.1\,\text{mm}$ filled with vacuum, and empty rectangular holes of depth $h = 5\,\text{mm}$. The propagation direction is parallel to the $z$-axis. The low-frequency refractive index $n_{\text{low}}$ is computed with the MMM approximation and with the quasi-static closed-form formula (4.40). Each curve corresponds to a different number of Floquet harmonics. A reference result is also computed with CST.

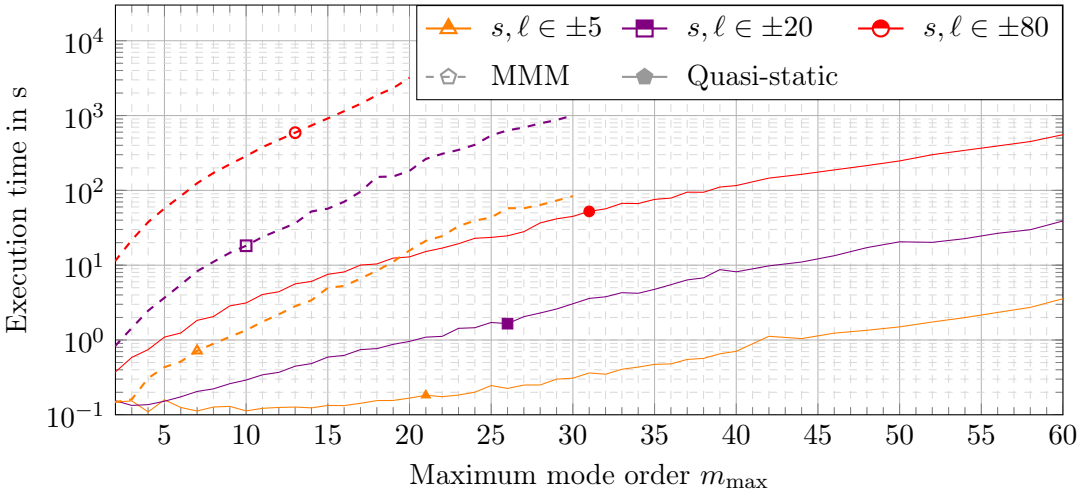


Figure 4.7: Computation time of the quasi-static refractive index as a function of the number of considered modes, comparing the quasi-static closed-form formula (4.40) (solid curves) with the MMM approximation (dashed curves). Different number of Floquet harmonics are used for each curve. The structure under study is the same as in Fig. 4.6, that is holey PPWs with $p_z = p_x = 4\,\text{mm}$, $g = 0.1\,\text{mm}$ and $h = 5\,\text{mm}$. The execution times are averaged over the three different rectangular hole cross-sections.

(4.40) have a much simpler form than the original dispersion matrix, and can be formed in more efficient ways. This is important, because most of the execution time comes from assembling the hundreds or thousands of harmonic terms inside the matrices, compared to which the time required to invert the matrices is negligible.

On top of the speed of execution, the implementation complexity is an other advantage of the closed-form formula. No iterative root-finding algorithm is involved, and so no parameters such as convergence limit or interval of search must be tuned. Additionally, no matrix determinants are computed, and so there are no problems with machine precision as with the direct MMM method.

No execution time information is given for the CST results. That is because a separate study would be necessary, with parameters such as the mesh grid refinement. Moreover, the CST licence at hand is run on a different computer, with higher computation capabilities. Nevertheless, from experience, in order to obtain refractive indexes with similar accuracy, the CST simulations last 20 to 100 times longer than the computation of the quasi-static formula (4.40), despite the larger computation capabilities.

### 4.3.4 Parametric studies

The quasi-static closed-form refractive index formula (4.40) enables fast and wideband characterization of holey G-S PPWs. In view of the considerable time gain illustrated in Fig. 4.7, this formula speeds up the otherwise cumbersome parametric studies that are required when designing metasurface microwave devices, such as lenses. In the following,

such parametric studies are performed for the canonical hole shapes considered in Fig. 4.5. Not only do they serve as examples, but they also validate the flexibility of the formula as a function of the structure's dimensions. Leaning on the results of the previous paragraph, the chosen number of modes and harmonics is high enough to achieve convergence of the effective refractive index.

#### 4.3.4.1 Rectangular holes: parametric studies

The low-frequency refractive index is computed with the closed-form formula (4.40) for G-S PPWs with rectangular holes. The quasi-static PMFs for rectangular holes have been derived in (D.22), (D.24) and (D.25). Only the relevant modes are kept, according to section 4.3.1.

For all parametric studies, the GS PPW has cells of size $p_z = p_x = 4\,\mathrm{mm}$, and it is not filled with any dielectrics. All results are compared to CST data, computed for $k_\theta = 0.4\,\mathrm{m}^{-1}$, which corresponds to a frequency of approximately 15 MHz. In Fig. 4.8, the propagation direction is $\theta = 0°$, and the holes are squares of size $a_z = a_x = a$. In each subfigure, the low-frequency refractive index is plotted as a function of a different geometrical parameter: the hole depth $h$ in 4.8a, and the hole size $a$ in 4.8b. The parametric curves depend on the gap $g$.

Fig. 4.8a shows that beyond a certain depth, $h$ does not impact the effective refractive index of the holey waveguide. Indeed, the hole's electrical size is tiny, therefore the rectangular waveguide modes are attenuated in the holes. The bottom of the holes barely interacts with the fields if it lies beyond a certain distance. This can be verified by considering the low-frequency matrices $\underline{\boldsymbol{\Sigma}}^{\mathrm{e}}$ in (4.32) and $\underline{\boldsymbol{\Sigma}}^{\mathrm{h}}$ in (4.34), which are the only $h$-dependent terms in the refractive index formula (4.40). Given $k_m$ the smallest cut-off wavenumber of the modes in the holes, the term $\coth\left(hk_m^{\mathrm{i}}\right)$ tends towards 1 when $h$ increases. This behavior does not depend on the hole cross-section. The impact of the hole size in Fig. 4.8b is more intricate, but a large range of refractive indexes can be achieved by changing the size of the holes. For a Luneburg lens, indexes up to $\sqrt{2}$ are needed, which can be achieved when $g = 0.1\,\mathrm{mm}$.

The closed-form formula (4.40) is a $\theta$-dependent function. As such, it can be used to study the isotropy of the holey GS PPW, by computing the low-frequency refractive index as a function of the propagation direction. This is done in Fig. 4.10 for two different structures: square holes of size $a = 3\,\mathrm{mm}$ in Fig. 4.10a, and rectangular holes with $a_z = 3.5\,\mathrm{mm}$ and $a_x = 1.5\,\mathrm{mm}$ in Fig. 4.10b. The hole depth is fixed at $h = 5\,\mathrm{mm}$. The same structure is studied in Fig. 4.9 with a gap $g = 0.1\,\mathrm{mm}$, where the isotropy is observed as a function of the square hole size $a$. G-S and nGS designs are compared.

Interestingly, the GS PPW with square holes is isotropic. This might seem counter-intuitive, given that the metasurface is made of a square lattice of holes. As such, the periodicity in different directions is not the same. Nevertheless, Fig. 4.10a displays a constant refractive index as function of the propagation angle. In chapter 5, it is shown how the closed-form formula (4.40) can reveal the isotropy of certain structures analytically. On the other hand, rectangular holes result in a $\theta$-dependent refractive index, as show in Fig. 4.10b, yielding an anisotropic waveguide. As such, the closed-form

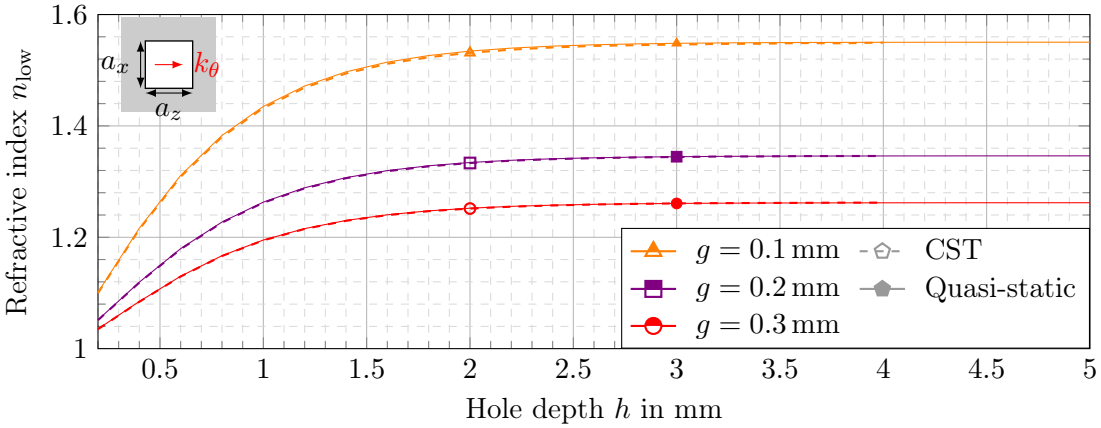


(a) As a function of $h$, with $a = 3\,\text{mm}$.

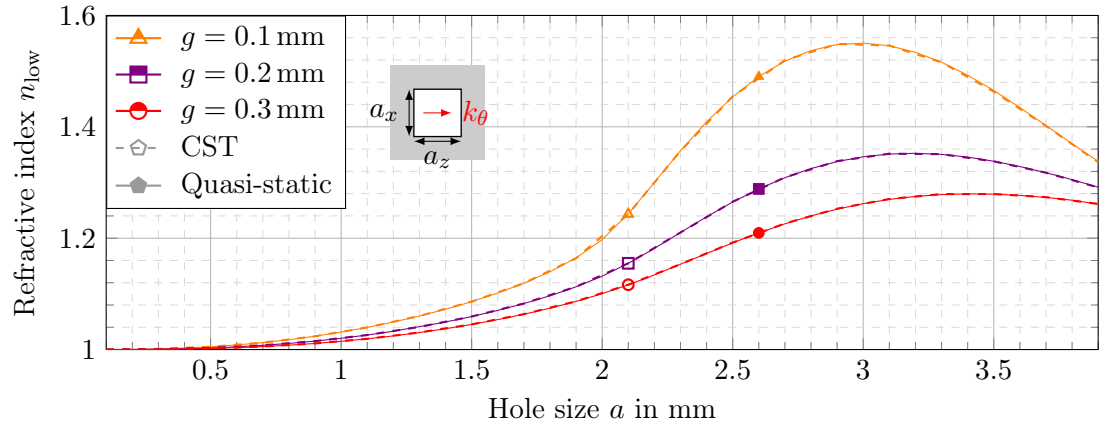


(b) As a function of $a$, with $h = 5\,\text{mm}$.

Figure 4.8: Parametric study of the low-frequency refractive index for G-S PPWs with rectangular holes. The low-frequency refractive index $n_{\text{low}}$ computed with the closed-form formula (4.40) (solid curves) is compared to CST data (dashed curves). All structures have $p_z = p_x = 4\,\text{mm}$, with propagation direction $\theta = 0°$.

index formula (4.40) enables the fast design of isotropic and anisotropic waveguides, for example for ultra-wideband compressed lenses as illustrated in [35].

#### 4.3.4.2 Circular holes: parametric studies

Additional parametric studies are performed in Fig. 4.11 for holes with circular cross-section of radius $a$, filled with a dielectric material of relative permittivity $\epsilon_{\text{r}2}$. The quasi-static PMFs for circular holes (D.30) to (D.35) are used in the closed-form formula (4.40) to compute the effective refractive index of the different structures. According to section 4.3.1, only the relevant modes are kept in (4.40). All results are compared to CST data computed at approximately 15 MHz.

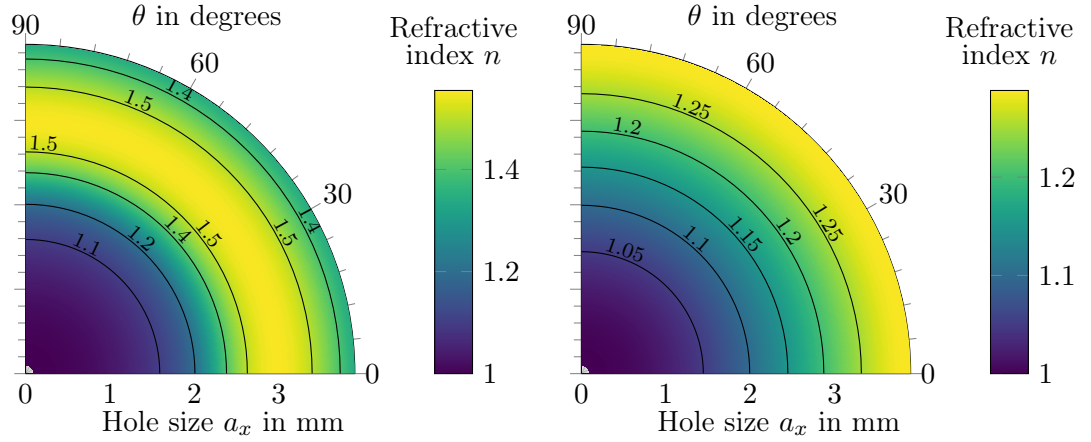


(a) G-S holes. (b) NGS holes.

Figure 4.9: Parametric study of the low-frequency refractive index for PPWs with square holes, computed with (4.40) as a function of the propagation direction $\theta$ and the hole size $a$. The waveguides have $p_z = p_x = 4\,\text{mm}$, $g = 0.1\,\text{mm}$, and $h = 5\,\text{mm}$.

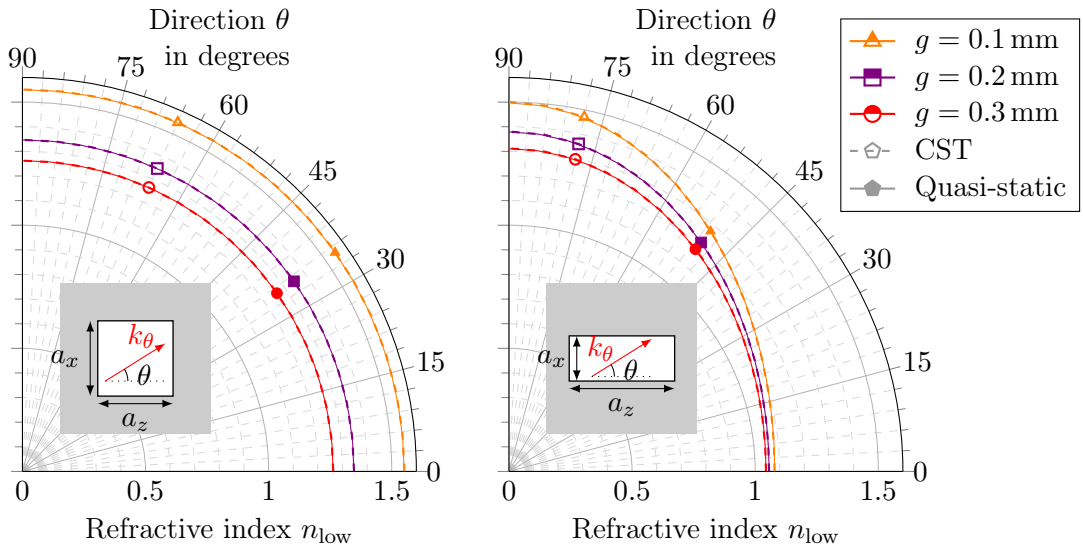


(a) $a_z = a_x = 3\,\text{mm}$. (b) $a_z = 3.5\,\text{mm}$, $a_x = 1.5\,\text{mm}$.

Figure 4.10: Study of the low-frequency refractive index as a function of the propagation direction $\theta$, for GS PPWs with rectangular holes. The shared dimensions are $p_z = p_x = 4\,\text{mm}$, $h = 5\,\text{mm}$. The low-frequency refractive index $n_{\text{low}}$ is computed with two techniques: CST's eigensolver and the closed-form formula (4.40).

In Fig. 4.11a the refractive index is plotted as a function of the hole depth $h$, and in Fig. 4.11b it is plotted as a function of the hole radius $a$. Each curve corresponds to a

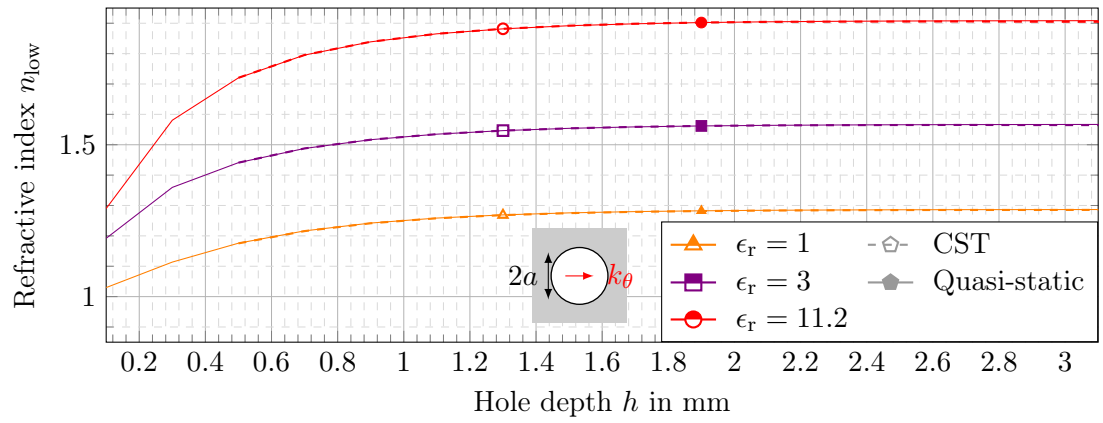


(a) For different hole depths $h$, with $a = 1.5\,\text{mm}$.

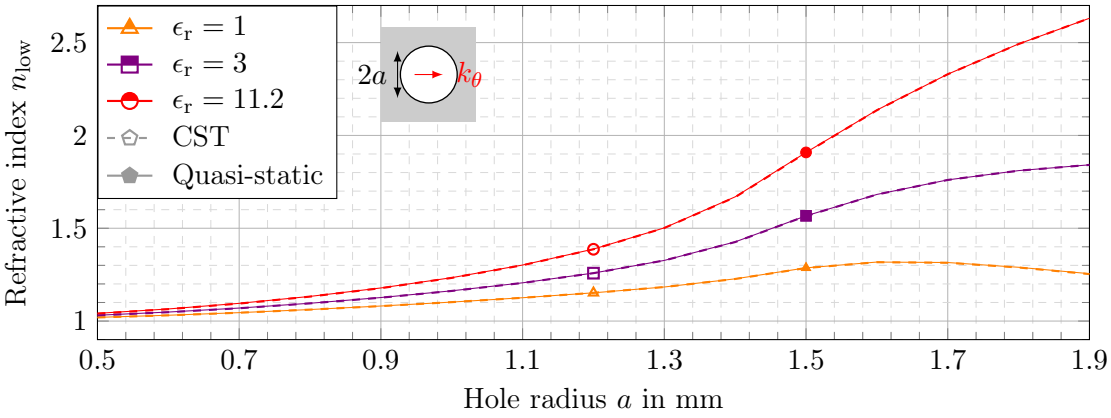


(b) For different hole radii $a$, with $h = 3\,\text{mm}$.

Figure 4.11: Parametric study of the low-frequency refractive index for circular holes. The low-frequency refractive index $n_{\text{low}}$ computed with the closed-form formula (4.40) is compared to CST data. The structure under study has dimensions $p_z = p_x = 4\,\text{mm}$, $g = 0.1\,\text{mm}$ and a propagation direction $\theta = 0°$.

different hole permittivity $\epsilon_{r2}$. As it did for rectangular holes, the closed-form formula matches CST data for all geometries, and for all hole fillings. In practice, circular holes are easier to drill than rectangular holes. The closed-form formula can be used to rapidly manufacture dense waveguides depending on the dielectric material that fills the holes. In Fig. 4.12, the isotropic behavior of circular holes is illustrated as a function of the hole radius, for both G-S and nGS designs.

### 4.3.5 Optimization of glide-symmetric holey parallel-plate waveguides

Considering a holey G-S PPWs, a closed-form formula for the effective refractive index has been found. In the previous sections, it is illustrated how this formula accelerates parametric studies, which consist in plotting the effective refractive index as a function

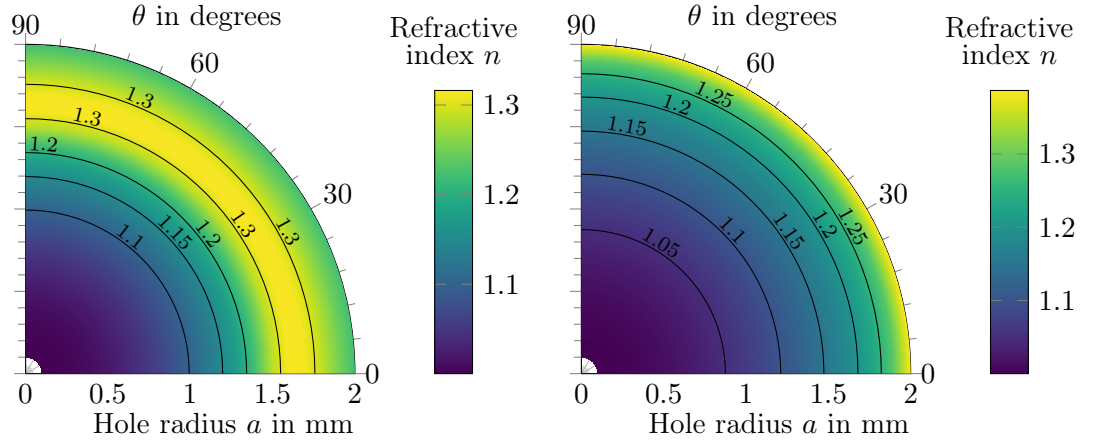


(a) G-S holes.

(b) NGS holes.

Figure 4.12: Parametric study of the low-frequency refractive index for PPWs with circular holes, computed with (4.40) as a function of the propagation direction $\theta$ and the hole radius $a$. The waveguides are filled with vacuul and have $p_z = p_x = 4\,\text{mm}$, $g = 0.1\,\text{mm}$, and $h = 5\,\text{mm}$.

one of the structure's dimensions. However, more complex information might be required when designing a metasurface microwave device. In the following, it is shown that the speed and closed form of (4.40) opens the door to direct optimization of the unit cell of holey G-S PPWs. Maximization of the refractive index and of the anisotropy are achieved.

#### 4.3.5.1 Square holes: maximum isotropic index

For square holes, the quasi-static PMFs are known analytically, as developed in section D.4.1. All following structures have square unit cells of size $p = 4\,\text{mm}$, hole depths $h = 5\,\text{mm}$, and have no dielectric fillings. The refractive index formula (4.40) is directly inserted into the optimizer, where the hole size $a$ is changed in order to maximize the refractive index. The algorithm used is the Matlab function `fmincon`, using an interior-point search method. It assumes convergence when the change rate is less than $1 \times 10^{-6}$.

In Fig. 4.13, the maximum refractive index is found for different gaps. Fig. 4.13b shows a classical parametric study for $g = 0.1\,\text{mm}$, where the refractive index is plotted as a function of the hole size $a$. The maximum index can be obtained in this way, nevertheless it is not very efficient in terms of number of evaluations of the formula (4.40). On the other hand, Figs. 4.13c and 4.13d are the result of an optimizing process. Fig. 4.13c plots the refractive index $n_{\max}$ as a function of $g$, where each $g$ point is the result of an optimization over $a$. Fig. 4.13d yields the corresponding hole size $a_{\max}$ for which $n_{\max}$ is found. The peak of Fig. 4.13b can be read directly in Figs. 4.13c and 4.13d. Interestingly, for smaller gaps, the maximum refractive index is not obtained for holes of maximum area.

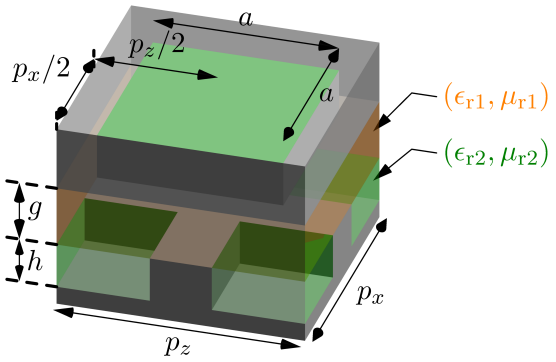


(a) Unit cell under study.

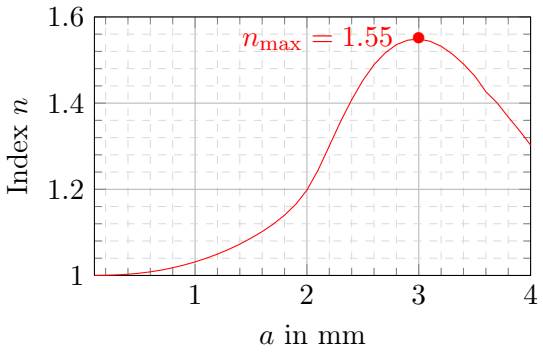


(b) Parametric curve for $g = 0.1\,\text{mm}$.

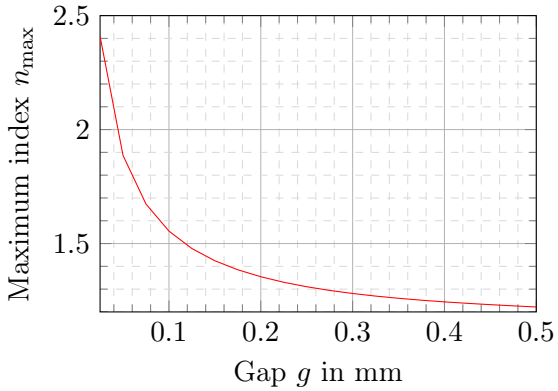


(c) Maximum achievable index as function of $g$.

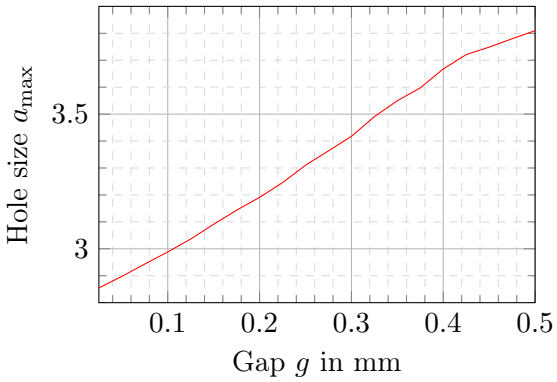


(d) Corresponding hole size $a_{max}$.

Figure 4.13: Maximizing the effective refractive index $n_{max}$ of a holey G-S PPW by varying the square hole size $a$, for arbitrary gaps $g$. Other structure dimensions are: $p = 4\,\text{mm}$ and $h = 5\,\text{mm}$. There are no dielectrics in the structure.

Obtaining Fig. 4.13d can be quite helpful when designing a lens antenna. For a given lens layout, the metasurface waveguide must be capable of yielding a maximum refractive index, for example $\sqrt{2}$ for a Luneburg lens. At the same time, the thinner the gap between the metasurfaces, the more difficult the manufacturing of the lens. Fig. 4.13d gives the maximum gap that is acceptable while preserving the necessary index range. For a Luneburg lens with square holey G-S metasurfaces, the maximum possible gap is $g = 0.16\,\text{mm}$. At the center of the lens, where the refractive index profile reaches its peak, the corresponding hole size is approximately $a = 3.1\,\text{mm}$.

#### 4.3.5.2 Circular holes: maximum isotropic index

The maximization of the refractive index can be performed for circular holes too. The refractive index formula (4.40) is applied using the quasi-static PMFs derived for circular holes in section D.4.2. The holey G-S PPW has square unit cells of size $p = 4\,\text{mm}$, holes of depth $h = 5\,\text{mm}$, and is not filled with any dielectrics.

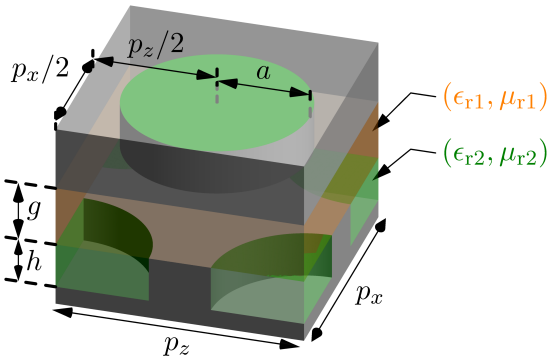


(a) Unit cell under study.

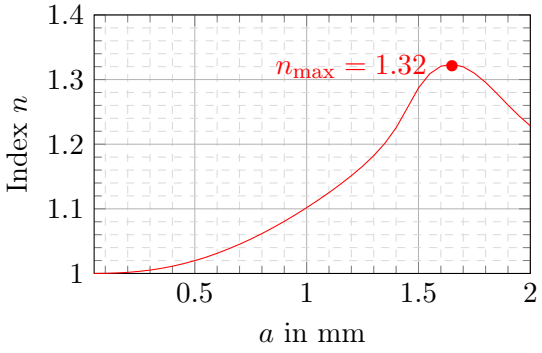


(b) Parametric curve for $g = 0.1\,\text{mm}$.

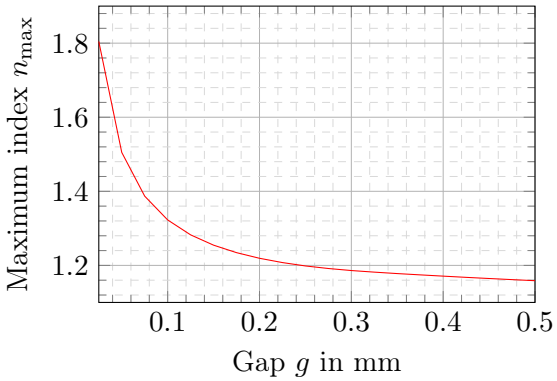


(c) Maximum achievable index as function of $g$.

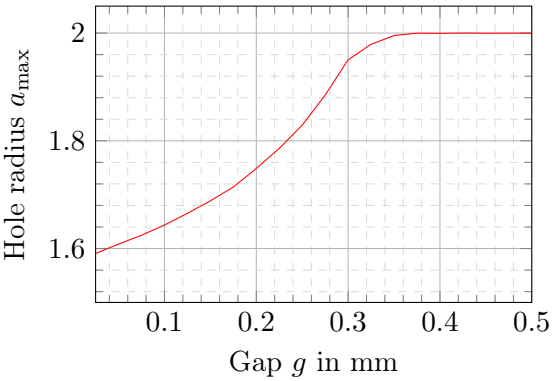


(d) Corresponding hole radius $a_{max}$.

Figure 4.14: Maximizing effective refractive index $n_{max}$ of a holey G-S PPW by varying the circular hole radius $a$, for arbitrary gaps $g$. Other structure dimensions are: $p = 4\,\text{mm}$ and $h = 5\,\text{mm}$. There are no dielectrics in the structure.

Similarly to the example in Fig. 4.13, a classical parameter sweep of the hole radius $a$ is first performed in Fig. 4.14b, for a gap $g = 0.1\,\text{mm}$. It leads to a maximum index $n = 1.32$ for $a = 1.65\,\text{mm}$. This value can be obtained more directly by inserting (4.40) into an optimizer algorithm. In Fig. 4.14c, the maximum refractive index is found for different gaps, where the varying parameter is the radius $a$ of the circular holes. Fig. 4.14d plots the corresponding hole radius $a_{max}$ for which $n_{max}$ is found.

It is notable that circular holes do not reach effective densities as high as square holes. For example, in order to design a Luneburg lens with circular holey metasurfaces, the maximum gap is $g = 0.07\,\text{mm}$, less than half the maximum gap enabled by square holes.

#### 4.3.5.3 Rectangular holes: maximum anisotropic index

In the previous paragraphs, the maximum refractive index is maximized for both square and circular holes, which yield isotropic behavior in the waveguide. However, if rectangular holes are used, the refractive index is different depending on the propagation

direction, as illustrated in the parametric study in Fig. 4.10b. The refractive index has extremas in the two directions aligned with the rectangle, that is for propagation angles $\theta = 0°$ and $\theta = 90°$. For some structures, maximizing the ratio between these extremas might be of interest, for example when compressing lenses. A search on the rectangular hole dimensions $a_z$ and $a_x$ must be performed to maximize the refractive index ratio $n_0/n_{90}$ between the two orthogonal directions.

For this optimization, performing a classical parameter sweep becomes quite cumbersome, given the 2-D search space. The colormap in Fig. 4.15b illustrates such a search for $p = 4\,\text{mm}$, $h = 5\,\text{mm}$, $g = 0.1\,\text{mm}$ and no dielectrics. Given that (4.40) yields a closed-form expression for the refractive index, the ratio $n_0/n_{90}$ can be computed in a closed form too. As such, it can be directly inserted in an optimizer algorithm, with two degrees of freedom: $a_z$ and $a_x$. Because the search space is two-dimensional, and to avoid non-convexity pitfalls, a global optimizing algorithm is used. The interior-point Matlab function `fmincon` is initialized at 10 random points, which lead to parallel searchs. This is handled automatically by Matlab's `createOptimProblem` framework.

The ratio $n_0/n_{90}$ is maximized for different gaps between the metasurfaces, yielding Fig. 4.15c. The corresponding hole dimensions are plotted in Fig. 4.15d. In order to obtain these curves, where 20 different gaps are considered, the closed-form formula (4.40) was called almost 13 000 times, for a total simulation time of approximately half-an-hour. Even if CST needed only one minute per structure simulation, the optimization of the anisotropy would have lasted 9 full days. Such optimization processes would be unrealistic without the speed-up of the quasi-static homogenization presented in this chapter.

## 4.4 Arbitrary hole shapes

### 4.4.1 Numerical extension with finite-element method

A closed-form formula for the effective refractive index of a G-S holey PPW has been found, for arbitrary hole shapes, yielding an homogenization of these waveguides. In order to apply this formula to a given structure, information about the hole modes is required. For rectangular or circular holes, these modes are known analytically, and so their norm, cut-off wavenumber and Fourier transform expressions can be embedded directly into the homogenization code. Once the analytical expressions are known, the quasi-static formula is very fast.

Nevertheless, computing all mode information analytically can be quite cumbersome, and prone to errors. Moreover, this approach is limited to very basic hole shapes, like rectangles and ellipses. That is why a numerical implementation of this homogenization technique is interesting. We have developed an in-house 2-D FEM that yields the eigenvalues and eigenmodes of the hole cross-section [185, chap. 9]. For TE and TM modes, a generalized eigenvalue problem must be solved, yielding the cut-off frequencies of the modes. The corresponding eigenmodes are the longitudinal fields of the modes i.e., electric for TM modes and magnetic for TE modes. For TEM modes, the scalar

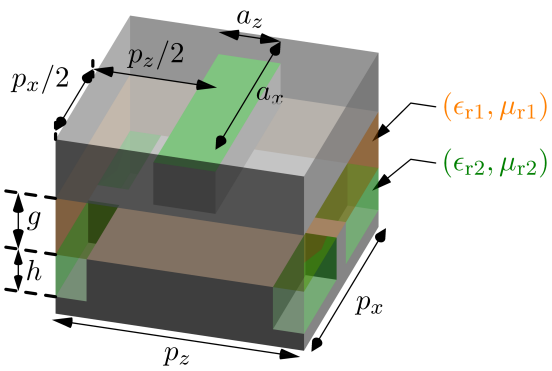


(a) Unit cell under study.

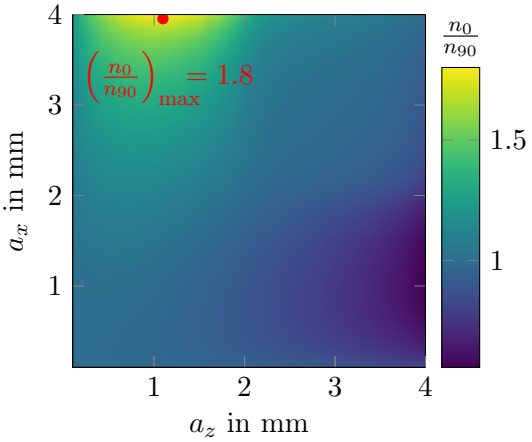


(b) Parametric ratio for $g = 0.1\,\text{mm}$.

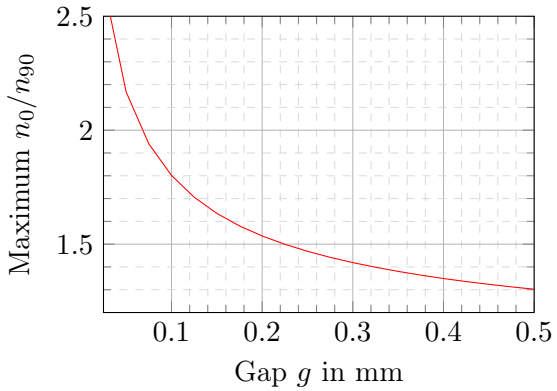


(c) Maximum achievable ratio as function of $g$.

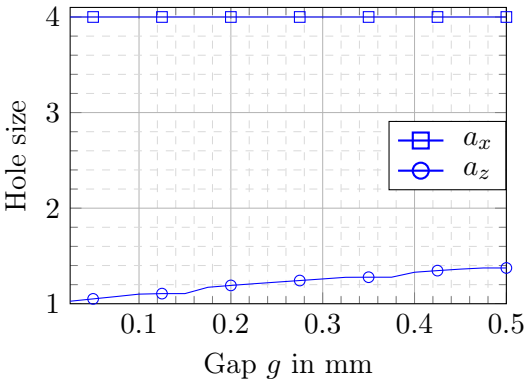


(d) Corresponding dimensions $a_z \times a_x$.

Figure 4.15: Maximizing the anisotropic ratio $n_0/n_{90}$ of a holey G-S PPW by varying the dimensions $a_z \times a_x$ of the rectangular holes, for arbitrary gaps $g$. Other structure dimensions are: $p = 4\,\text{mm}$ and $h = 5\,\text{mm}$. There are no dielectrics in the structure.

potential is found in a similar way. The transverse field components and the mode norms are obtained with numerical differentiation and integration, respectively.

The detailed FEM process is derived in appendix D.5, which yields the eigenmodes of a given hole. Its particular use for the homogenization of holey PPWs is detailed in the following paragraphs.

#### 4.4.1.1 Numerical computation of the quasi-static coefficients

**Field sampling and quasi-static projected modal functions** The interior surface of the hole cross-section is meshed in Matlab. The FEM matrices $\boldsymbol{S}$ and $\boldsymbol{R}$ are built for the TM and TE modes, and the generalized eigenvalue problem (D.43) is solved using the Matlab function `eig`. This function yields the set of the squared cut-off frequencies $k_m^{\text{e}}$

and $k_m^{\mathrm{h}}$. Each cut-off wavenumber is associated to a set of basis function weights $\{\alpha_{m,i}^{\mathrm{i}}\}$, with $\mathrm{i} = \mathrm{e}, \mathrm{h}$, which are the represent the eigenmodes of the problem. Additionnally, the number of inner conductors is detected, and equation (D.54) is solved for each resulting TEM mode. As such, by combining the obtained weights $\alpha_i$ in the approximations (D.37) and (D.52), the fields $e_{y,m}$, $h_{y,m}$ and $\Phi_m$ can be computed at all points of the hole cross-section.

The information needed in the quasi-static refractive index formula (4.40) is the Fourier transforms of the eigenmodes, evaluated at periodic points $(s\frac{2\pi}{p_z}, \ell\frac{2\pi}{p_x})$, as defined in (4.21). From a judicious sampling of the FEM fields, these Fourier coefficients can be obtained directly by applying a fast Fourier transform (FFT) algorithm. When applying the FFT on $N$ samples spaced by step $t$ in the spatial domain ($N$ odd), the resulting $N$ spectral points are spaced by steps $\frac{2\pi}{(N-1)t}$, covering a spectral range $\pm\frac{\pi}{t}$. Calling the maximum required harmonic order $s_{\max}$, we can define the required sampling step $t = \frac{p_z}{2s_{\max}}$, such that the highest spectral point is at $s_{\max}\frac{2\pi}{p_z}$. In order for the spectral points to fall at multiples of $\frac{2\pi}{p_z}$, it implies field sampling must be so that $N_z = 2s_{\max} + 1$.The same is true for the sampling in the $x$-direction, with the number of samples $N_x$ and the maximum harmonic order $\ell_{\max}$.

It must be noted that the FFT of the samples is not accurate for the highest harmonic orders, close to $\pm s_{\max}$ or $\pm\ell_{\max}$. The phase of the quasi-static PMFs is particularly affected. This is understandable, because a finer field sampling is required to accurately capture higher spatial frequencies. That is why in practice, $s_{\max}$ and $\ell_{\max}$ must be chosen larger than the harmonic orders that will be used in the quasi-static formula (4.40).

**Transverse TE and TM field components** Directly sampling the field component $e_{y,m}$ and applying the FFT, as described, yields the TM coefficients $\bar{e}_{y,m}^{(s\ell)}$ needed in the index formula (4.40). For TE modes, the transverse components are the derivates of $h_{y,m}$. For TEM modes, (D.50) computes these field components from the scalar potential.

These derivatives must be computed numerically, using finite difference approximations. Special care must be given to points lying in the contour. Notably for TE modes, there is a field discontinuity of $h_{y,m}$ at the hole contour, given that the magnetic field is not zero on the perfectly electrically conducting (PEC) walls. As such, the numerical differentiation must not incorporate the field points outside the hole, otherwise very large derivative points are obtained. Moreover, in geometries such as circular hole shapes, some points of the sampling grid may be isolated, that is they are neither preceded nor followed by another sampling point. The field derivatives can not be computed at such points, especially for TE modes.

Once the transverse field components are obtained, the FFT can be applied to yield all the quasi-static coefficients $\bar{e}_{z,m}^{(s\ell)}$ and $\bar{e}_{x,m}^{(s\ell)}$ needed to compute the effective refractive index.

**Squared norm of the modes** The cut-off wavenumbers and the quasi-static PMFs of the modes are computed. The last missing element for (4.40) to be computed is the squared norm (2.32) of each mode. From the sampled field component, this norm

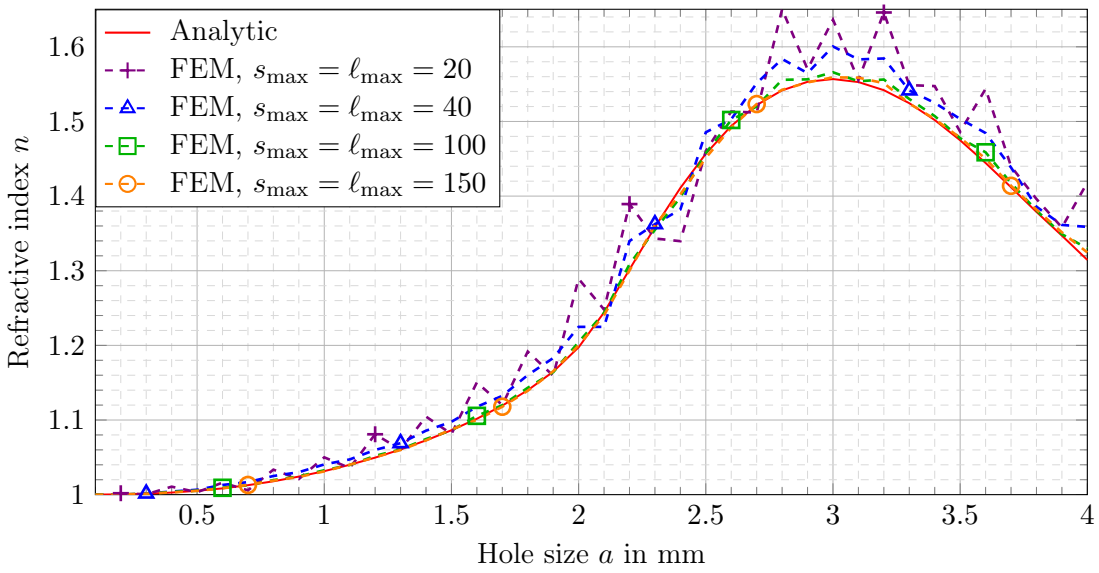


Figure 4.16: Quasi-static refractive index $n$ as a function of the square hole size $a$. Structure dimensions are: $p = 4\,\text{mm}$, $h = 5\,\text{mm}$ and $g = 0.1\,\text{mm}$. The curves are computed with the closed-form formula (4.40), comparing the case where the modes are obtained analytically or by means of the FEM-based modal study.

is computed using a numerical integration technique. Given the periodic sampling, we choose to implement the Newton-Cotes integration rules [186, p.148]. Inside the holes, the Newton-Cotes integration of fifth order (also known as Boole's rule) is applied. When getting close to the hole borders, rules of decreasing order are applied.

#### 4.4.1.2 Validation of the quasi-static homogenization with finite element method

In practice, the 2-D numerical study of the holes described in the previous paragraphs enables to generalize the refractive index formula (4.40) to arbitrary hole shapes. Before doing that, we consider canonical hole shapes in order to illustrate the effectiveness of the code. The index computed with the analytical index derived in section 4.3 is compared to the index obtained from the FEM modes.

In Fig. 4.16, a G-S holey PPW with square holes is considered. The structure has a gap $g = 0.1\,\text{mm}$, periodicities $p_z = p_x = 4\,\text{mm}$, and holes of depth $h = 5\,\text{mm}$. The quasi-static refractive index is plotted as function of the hole size $a$, filled with vacuum. In the index formula (4.40), 150 TE and 150 TM modes are considered, as well as harmonics with orders $s$ and $\ell$ in the range $\pm 20$. In the numerical modal study, the field sampling is done with different number of points, yielding different maximum harmonic ranges $s_{\max}$ and $\ell_{\max}$. The FEM meshing is fine enough not to influence these results. The same is done in Fig. 4.17, for a G-S holey PPW with circular holes.

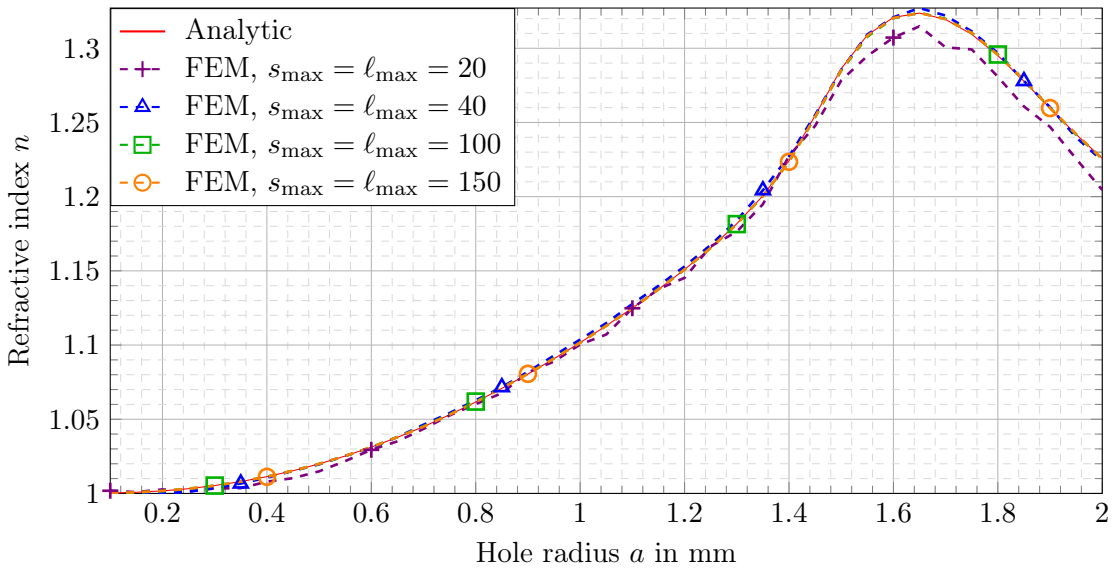


Figure 4.17: Quasi-static refractive index $n$ as a function of the circular hole radius $a$. Structure dimensions are: $p = 4\,\text{mm}$, $h = 3\,\text{mm}$ and $g = 0.1\,\text{mm}$. The curves are computed with the closed-form formula (4.40), comparing the case where the modes are obtained analytically or by means of the FEM-based modal study.

For both square and circular holes, the numerically-computed index matches the analytical results. This is provided that the number of samples is high enough i.e., that $s_{\max}$ and $\ell_{\max}$ are large enough. It appears that $s_{\max}$ and $\ell_{\max}$ need to be at least four times larger than the maximum harmonic order used in (4.40). Indeed, the FFT needs a fine sampling rate in order to retrieve the phase of the PMFs. In Fig. 4.18, the particular case of the first TM mode of a square hole with size $a = 3\,\text{mm}$ is considered, that is the mode $\text{TM}_{11}$. The TM field is sampled at different rates, such that different $s_{\max}$ and $\ell_{\max}$ are obtained when applying the FFT. The resulting PMFs $\bar{e}_{y,\text{FEM}}^{(s\ell)}$ are compared to the analytical PMFs $\bar{e}_{y,\text{ana.}}^{(s\ell)}$, computed according to the analytical expressions from section 4.3. The normalized error is computed in decibels as $10\log_{10}\left|\frac{\bar{e}_{y,\text{FEM}}^{(s\ell)}}{\max\{\bar{e}_{y,\text{FEM}}\}} - \frac{\bar{e}_{y,\text{ana.}}^{(s\ell)}}{\max\{\bar{e}_{y,\text{ana.}}\}}\right|$, where the PMFs are normalized with respect to their maximum, which is the fundamental PMF $\bar{e}_y^{(00)}$. This error is plotted in the spectral region $s = \pm 20$ and $\ell = \pm 20$, which corresponds to the coefficients that are used in the index formula for the curves in Fig. 4.16. Different sampling rates, corresponding to different $s_{\max}$ and $\ell_{\max}$, are considered.

The error study in Fig. 4.18 corroborates the results in Fig. 4.16, where $s_{\max}$ and $\ell_{\max}$ are increased to at least 5 times the number of harmonics considered in the index formula (4.40). This seems to limit the error to around 1% for all PMFs. Further reducing the error requires a huge increase of the sampling, with only limited accuracy improvements in the effective refractive index formula. In practice, a quick study of the convergence of

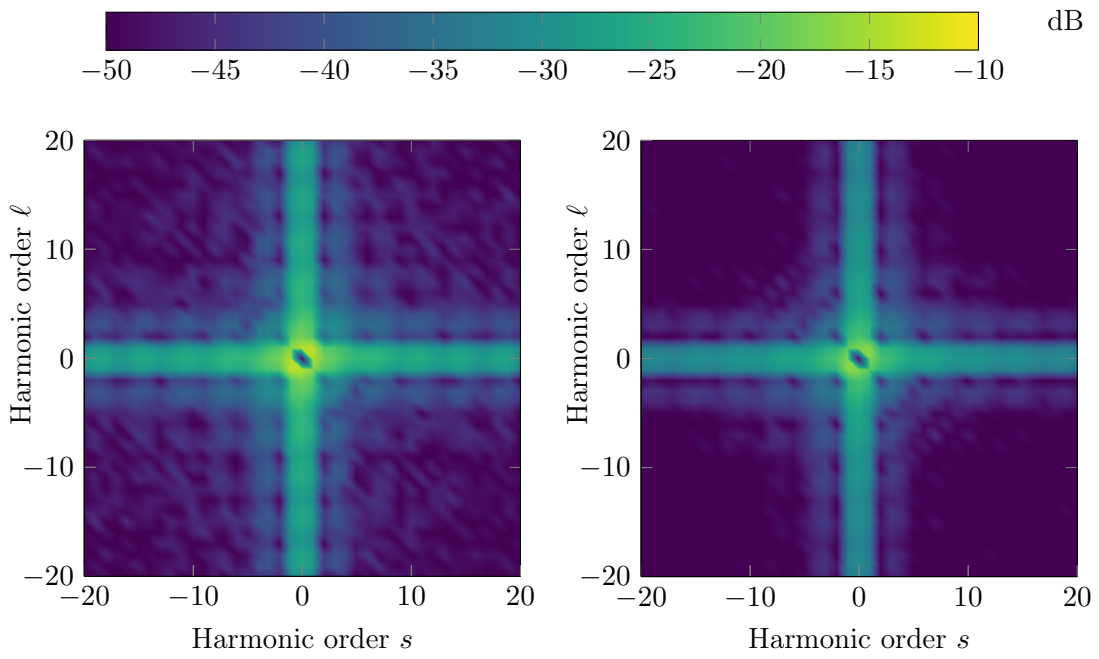


(a) $s_{\max} = \ell_{\max} = 20$.




(b) $s_{\max} = \ell_{\max} = 40$.

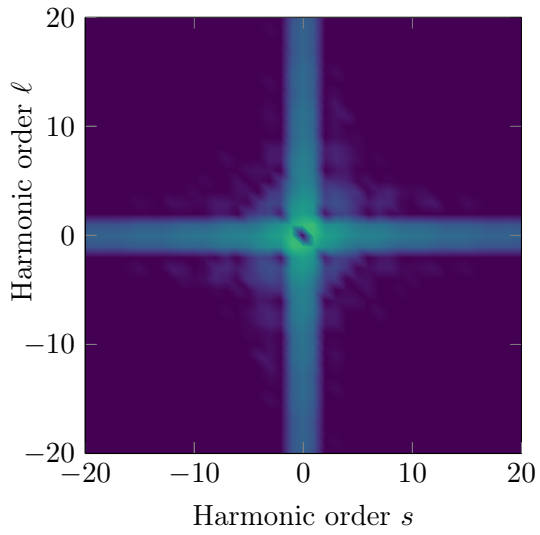


(c) $s_{\max} = \ell_{\max} = 150$.

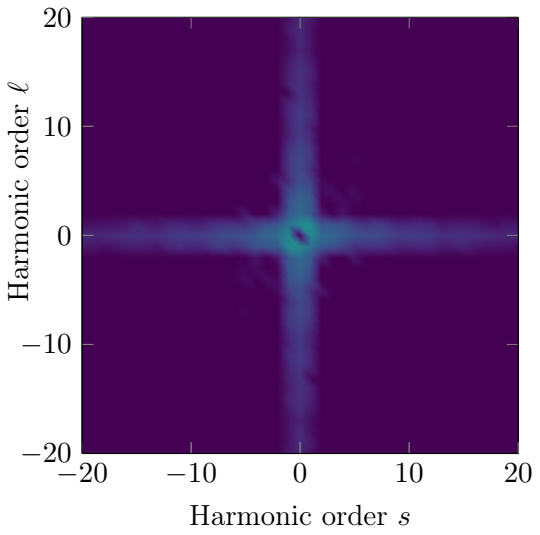


(d) $s_{\max} = \ell_{\max} = 1000$.

Figure 4.18: Normalized error for the quasi-static PMFs, computed with the FEM for the mode $\mathrm{TM}_{11}$ of a square hole with $a = 3\,\mathrm{mm}$. It is compared to the analytical PMFs. Only the spectral domain $(\pm 20\frac{2\pi}{p_z}, \pm 20\frac{2\pi}{p_x})$ is shown. Each subfigure corresponds to a different number of sampling points.

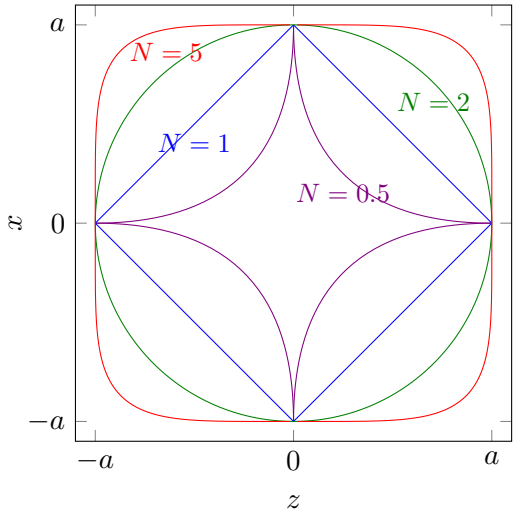


Figure 4.19: Different cases of super-ellipses, with varying order $N$.

the results is the best way to choose $s_{\max}$ and $\ell_{\max}$ for a given hole cross-section.

### 4.4.2 Shape optimization

The shape of the holes has an important impact on the effective properties of the holey G-S PPW. For example, in section 4.3.5, it appears that a higher refractive index can be achieved with square holes than with circular holes. If the cross-section is described by analytic curves, then the hole shape can be studied in a parametric way, same as the other dimensions of the metasurface waveguide. This study is made accessible by the index formula (4.40), leaning on the numerical modal study described in the previous paragraphs.

As an example, in this paragraph the description of the hole shape is generalized, in order to encompass both the square and the circle. A category of shapes that achieves that is called the super-ellipse. A super-ellipse of order $N$ and semi-axis $a_z$ and $a_x$ is defined by all the points satisfying the equation

$$\left|\frac{z}{a_z}\right|^N + \left|\frac{x}{a_x}\right|^N = 1\,. \tag{4.41}$$

Some particular super-ellipses are drawn in Fig. 4.19. When $N = 1$, the super-ellipse is a rhombus. When $N = 2$, a circle is obtained, and when $N \to \infty$, it approaches a square. When $N \ll 1$, the area of the resulting 4-branched star becomes asympotically small, and so in all following studies are limited to $N > 0.5$.

The super-elliptic hole is implemented with the numerical modal study, in order to compute the effective refractive index (4.40) as a function of the parameter $N$. In order to do that, particular care must be given to the meshing process. Indeed, for $N < 1$ or for very large $N$, the parametrization of the curve is not linear, meaning that the same

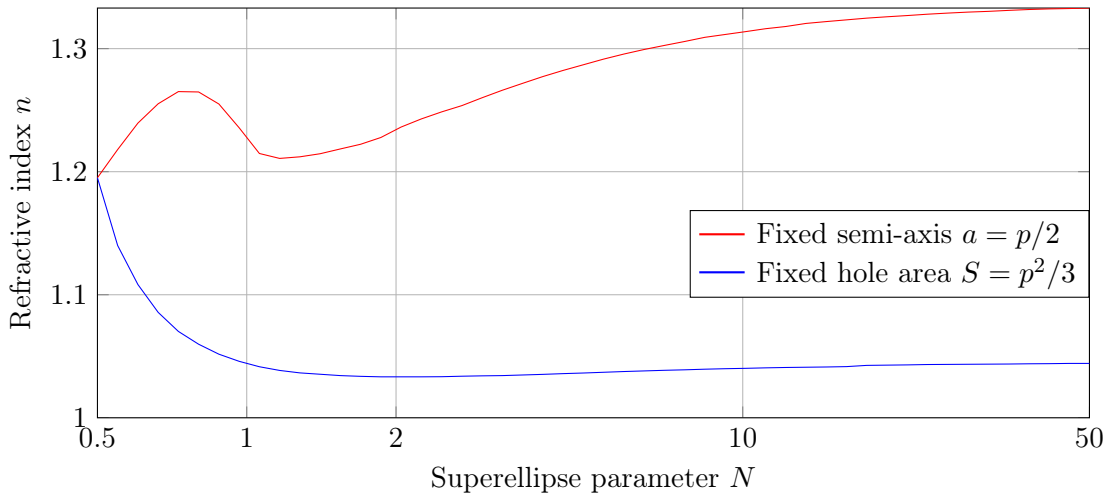


Figure 4.20: Quasi-static refractive index (4.40) of holey G-S PPWs with super-elliptic holes, as function of the super-ellipse order $N$. The structure dimensions are $p_z = p_x = 4\,\text{mm}$, $g = 0.1\,\text{mm}$ and $h = 5\,\text{mm}$. The shape semi-axis is constant at $a_z = a_x = 2\,\text{mm}$ for the red curve. For the blue curve, a constant hole area of $S = p^2/3$ is maintained.

variation in coordinates results in different lengths changes depending on the part of the super-ellipse. Depending on the meshing algorithm, this may result in an irregular mesh.

In Fig. 4.20, the quasi-static refractive index computed with (4.40) is plotted as a function of the super-elliptic parameter $N$, for a holey G-S PPW of periodicities $p_z = p_x = 4\,\text{mm}$, gap $g = 0.1\,\text{mm}$, and hole depth $h = 5\,\text{mm}$. Two setups are observed. In the first one, the semi-axis $a_z = a_x = 2\,\text{mm}$ are kept constant when changing $N$. Although this implies that the super-ellipse takes the maximum available area in the unit cell, it also means that different orders $N$ result in different hole areas. In this case, the square hole with $N \to \infty$ yields a much higher index than other configurations, given that it has the largest area. The red curve could therefore be increasing as a function of $N$ only because the hole area increases, and not due to a change of shape. That is why another setup is presented with the blue curve. There, the super-ellipse semi-axis are varied as a function of $N$, so that the hole area remains constant, here at $p^2/3$. In this case, it seems that concave shapes such as stars yield higher refractive index than convex shapes. Still, for both curves, square holes increase the effective refractive index of the waveguide compared to circular holes.

More complicated shape parametrization could be explored. For example, the so-called *superformula* is a further generalization of the super-ellipse, and it covers other shapes such as triangles and stars.

### 4.4.3 Exploration of imaginative shapes

The quasi-static homogenization is not limited to conventional hole shapes such as circles, squares, or even super-ellipses. Any hole shape can be used. As such, the homogenization technique coupled to the finite-element method opens the door to the exploration of more imaginative shapes, whose study would be cumbersome with commercial solvers.

In this section, some examples of such shapes are presented. First, it is shown that adding metallic pins in the hole increases the achievable effective refractive index. This also illustrates the robustness of our algorithm for holes with TEM eigenmodes. Then, a series of star-shaped holes is presented, which achieve high indexes too, but without the use of inner pins.

#### 4.4.3.1 Inner pins for TEM propagation

When the unit cell of the periodic PPW is made of holes, only TE and TM modes are excited at the surface of the holes. Because of the subwavelength regime in which the metasurface waveguide is used, the cutoff frequencies of these modes is much larger than the operating frequency. As such, the waves are attenuated when entering the holes. Therefore, increasing the hole depth has a limited impact on the refractive index of the waveguide, because the modes do not reach the bottom of the holes.

It has been shown [187], [188] that an increased refractive index can be achieved by adding pins in the holes. These pins act like inner conductors in a coaxial-like transmission line. Consequently, not only TE and TM modes are excited in the holes, but TEM modes too : one per inner conductor. Because these TEM modes have no cut-off frequency, an improved hole depth dependency is gained for the refractive index.

This is illustrated for a square hole with one inner square pin. The cross-section of the hole is shown in Fig. 4.21b, where the meshing used by the FEM is drawn. Here, the square holes have a size of $a_\mathrm{h} = 3.5\,\mathrm{mm}$, and the pins have a size of $a_\mathrm{p} = 0.5\,\mathrm{mm}$. In order to compute the eigenmodes with the FEM, this is the only information needed. It results in one TEM mode, because of the two conductors involved. The scalar potential of this TEM mode is shown in Fig. 4.21c. TE and TM modes are then obtained in the order of increasing cut-off frequencies. The longitudinal field distributions for six modes of each type are shown in Fig. 4.21.

The holes are repeated periodically with $p_z = p_x = 4\,\mathrm{mm}$ to create the two metasurfaces, separated by a gap $g = 0.1\,\mathrm{mm}$. The variation of the effective refractive index as a function of the hole depth $h$ is plotted in Fig. 4.22. Not only does it illustrate that the quasi-static homogenization+FEM method fits the CST results well. This particular example also shows that the addition of a simple pin increases the maximum achievable index compared to conventional holes. In Fig. 4.8b, the maximum index that can be achieved with square holes is $n = 1.55$. Here, after a sufficient increase of $h$, the index converges towards $n = 1.75$.

In terms of computational cost, a study such as Fig. 4.22 benefits hugely from the quasi-static homogenization presented here. Indeed, not only is the numerical discretization reduced to the 2-D hole cross-section, but the eigenproblem associated to the cross-

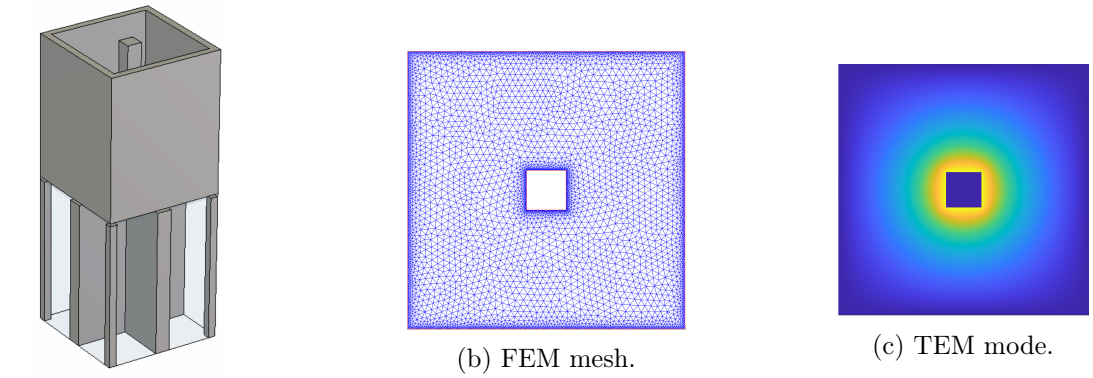

(a) Unitcell in CST. (b) FEM mesh. (c) TEM mode.

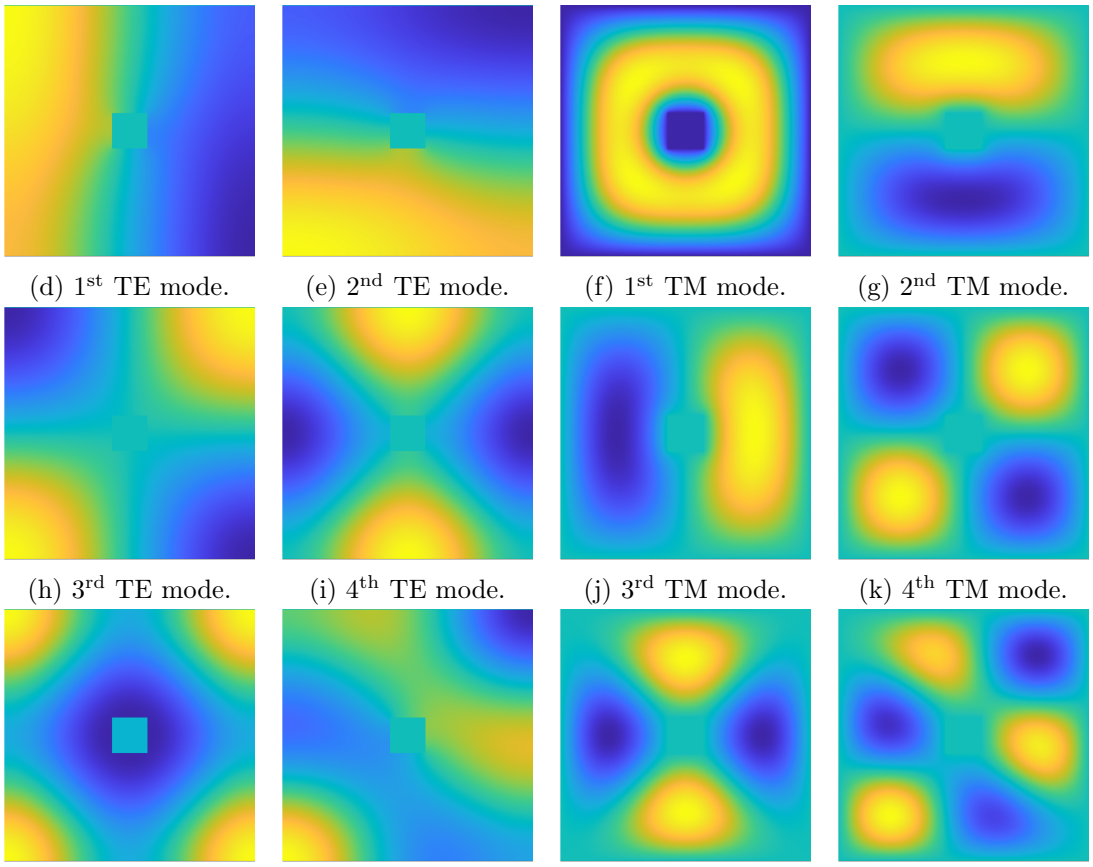

(d) 1st TE mode. (e) 2nd TE mode. (f) 1st TM mode. (g) 2nd TM mode.

(h) 3rd TE mode. (i) 4th TE mode. (j) 3rd TM mode. (k) 4th TM mode.

(l) 5th TE mode. (m) 6th TE mode. (n) 5th TM mode. (o) 6th TM mode.

Figure 4.21: Study of the eigensolutions of the square holes with an inner square pin. The corresponding G-S holey PPW unit cell is shown in (a), as modeled in CST. The modes are obtained by means of the custom 2-D FEM, whose meshing is shown in (b). Subfigure (c) plots the scalar potential $\Phi_m$ of the only TEM mode. The remaining subfigures plot the 6 first propagating modes of each type. For TE and TM modes, the longitudinal field component is represented: $h_{y,m}$ and $e_{y,m}$,respectively.

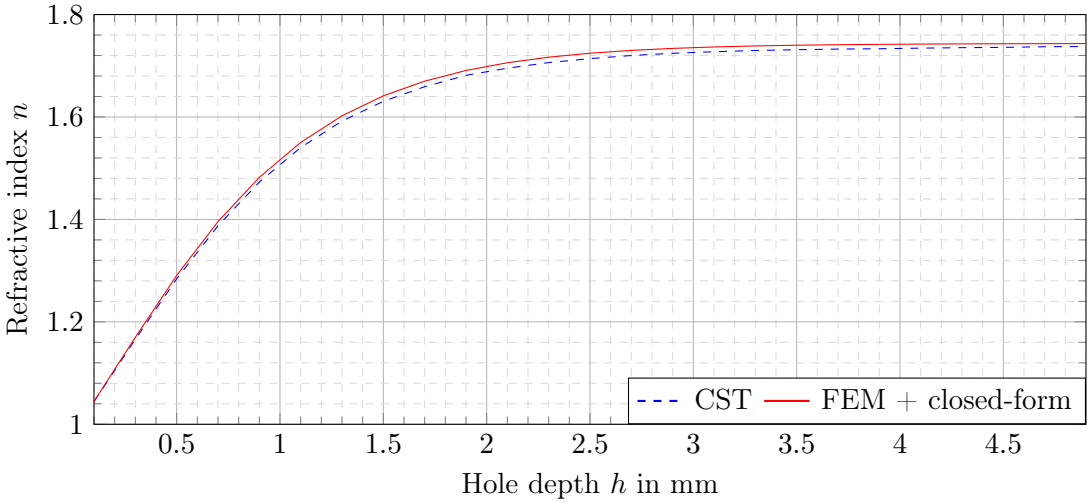


Figure 4.22: Quasi-static refractive index of a holey G-S PPW with square pins centered in the square holes, as a function of the hole depth $h$. The quasi-static formula (4.40), coupled with the FEM, is compared to the CST results, computed at approximately 10 MHz. The structure dimensions are $p_z = p_x = 4\,\text{mm}$, $g = 0.1\,\text{mm}$, with square holes of size $a_\text{h} = 3.5\,\text{mm}$ and pins of size $a_\text{p} = 0.5\,\text{mm}$.

section needs only be solved once. Given that the varying parameter is the hole depth $h$, each point of the curve in Fig. 4.22 uses the same hole cross-section. The field dependencies with respect to all the other unit cell dimensions are analytically embedded in the closed-from formula (4.40). As such, the FEM problem is solved once for the first index point, and then the quasi-statc index formula can be applied for as many geometries as required within a fraction of a second.

#### 4.4.3.2 Large index with star-shaped holes

Adding pins in the holes is not the only option in order to increase the effective refractive index. The 2-D FEM and the closed-form formula (4.40) open the door to the exploration of an infinite variety of hole shapes. An example is shown in Fig. 4.23, which leads to quite complicated unit cells, as shown in Fig. 4.23a. These star-shaped holes are characterized by three numbers: the radius of the outer circle $a_\text{out}$ which circumvents the shape, the radius of the inner circle $a_\text{in}$, which connects all the inner branch points, and the number $N$ of branches. In the following, $a_\text{in} = 1\,\text{mm}$, and $a_\text{out} = 2\,\text{mm}$, such that the star takes the maximum area inside a unit cell with $p_z = p_x = 4\,\text{mm}$. A selection of TE and TM modes that result from the 2-D FEM are illustrated in Fig. 4.23, in the case where $N = 10$.

The gap between the metasurfaces is $g = 0.1\,\text{mm}$, and the hole depth is $h = 5\,\text{mm}$. In Fig. 4.24, the effect of an increase of the number of branches is observed on the effective refractive index, by applying the homogenization formula (4.40) for different $N$.

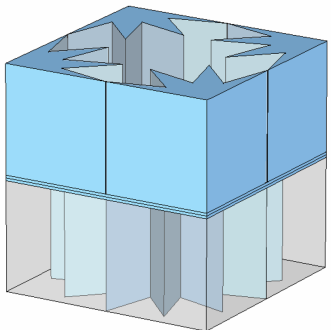

(a) Unitcell in CST.

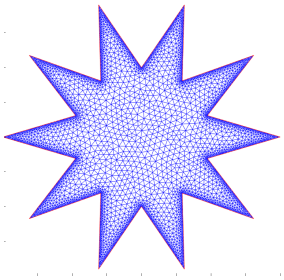

(b) FEM mesh.

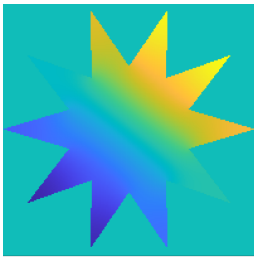

(c) 1st TE mode.

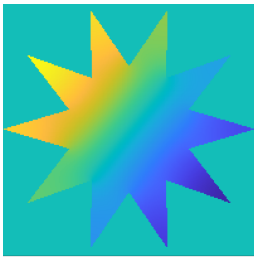

(d) 2nd TE mode.

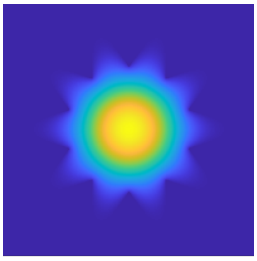

(e) 1st TM mode.

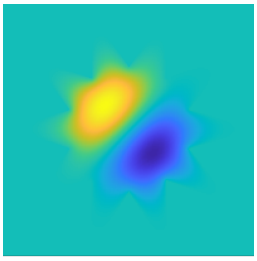

(f) 2nd TM mode.

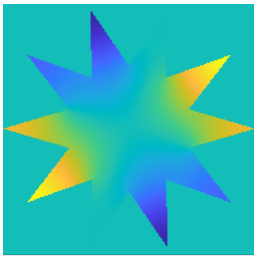

(g) 3rd TE mode.

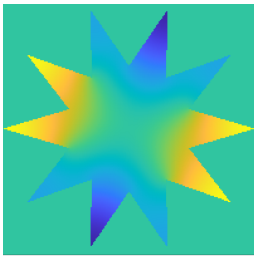

(h) 4th TE mode.

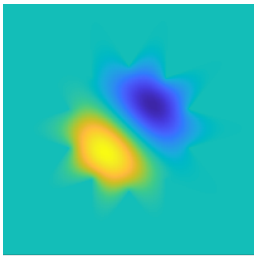

(i) 3rd TM mode.

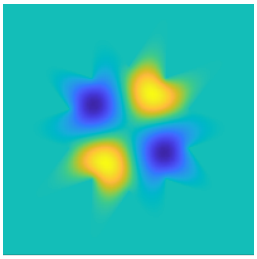

(j) 4th TM mode.

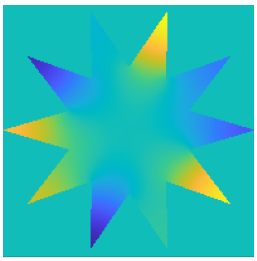

(k) 5th TE mode.

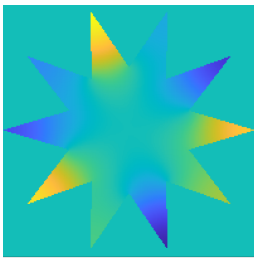

(l) 6th TE mode.

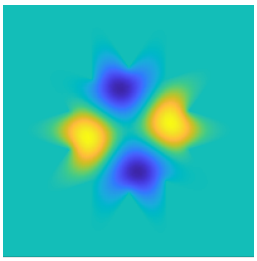

(m) 5th TM mode.

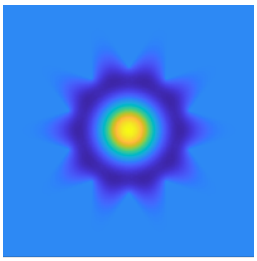

(n) 6th TM mode.

Figure 4.23: Study of the eigensolutions of the star-shaped holes with 10 branches. The corresponding G-S holey PPW unit cell is shown in (a), as modeled in CST. The modes are obtained by means of the custom 2-D FEM, whose meshing is shown in (b). The remaining subfigures plot the 6 first propagating modes of each type. For TE and TM modes, the longitudinal field component is represented: $h_{y,m}$ and $e_{y,m}$,respectively.

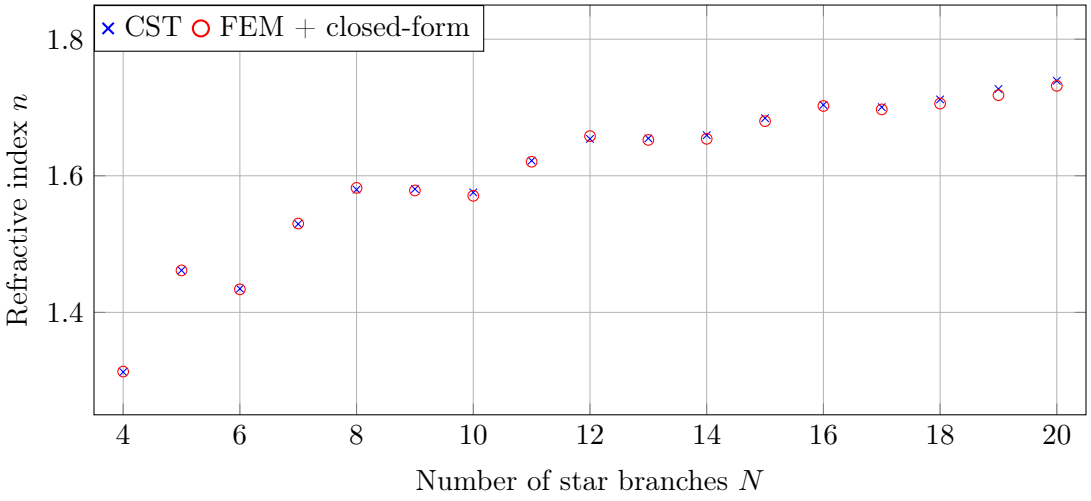


Figure 4.24: Quasi-static refractive index of a holey G-S PPW with star-shaped holes, as a function of the number of star branches $N$. The quasi-static formula (4.40), coupled with the FEM, is compared to the CST results, computed at approximately 10 MHz. The structure dimensions are $p_z = p_x = 4\,\text{mm}$, $g = 0.1\,\text{mm}$, $h = 5\,\text{mm}$, $a_{\text{in}} = 1\,\text{mm}$ and $a_{\text{out}} = 2\,\text{mm}$.

The quasi-static index computed with (4.40) and the FEM matches the index obtained with CST. Here too, it appears that a high refractive index can be achieved with a large number of branches. For example, with 20 branches, an index $n = 1.74$ is achieved, which is similar to the maximum index convergence with a pin in Fig. 4.22.

While manufacturing metasurfaces with such complex hole shapes may be difficult, these results show that concave hole shapes, with our without interior pins, can yield interesting effective features.

## 4.5 Frequency validity

### 4.5.1 Dependency on the frequency dispersion and the effective density

The frequency validity of the closed-form formula (4.40) is not inherent to its derivation, but is a consequence of the low-dispersive behavior of holey G-S waveguides. These structures have a dispersion curve which is close to linear in the first Brillouin zone. Consequently, the frequency at which the first mode exits the Brillouin zone could be taken as an upper bound of the validity of (4.40). Once $n_{\text{low}}$ is computed, a rough estimate of the frequency validity is thus given by

$$k_z \leq \frac{\pi}{p_z} \quad \Longleftrightarrow \quad f_{\text{max}} \leq \frac{c_0}{2 p_z n_{\text{low}}}\,, \tag{4.42}$$

which corresponds to the frequency at the right-end of the first Brillouin zone. Still, this limit presumes a quasi-linear dispersion curve in the first Brillouin zone. For some structures, this limit is underestimated, because the dispersion is very low. In other cases, the dispersion curve starts bending before it reaches the end of the first Brillouin zone. In Fig. 4.25, several examples of holey PPWs are studied, both G-S and nGS designs. The error between the quasi-static index (4.40) and the frequency-depend index computed with CST is plotted as function of frequency. The quasi-static index $n_{\text{low}}$ is indicated next to the corresponding curve.

All structures have unit cells of size 4 mm. Tolerating a relative error of less than 1%, this index can be used up to 31 GHz, 12 GHz, 8 GHz and 7 GHz for the G-S structures in (a), (b) (c) and (d), respectively. If an error or 10% is acceptable, this range rises up to 58 GHz, 34 GHz, 25 GHz and 13 GHz. In all cases, this is larger than for the nGS counterpart structure, which reaches a stopband at the end of the first Brillouin zone. As expected with (4.42), the larger the effective refractive index, the smaller the valid frequency range.

Fig. 4.25 also illustrates that when the effective density of the waveguide increases, the frequency dispersion is higher, and therefore the accuracy of (4.40) at $f_{\max}$ is reduced. If high accuracy is of importance for a given application, the validity of the closed-form formula should be checked with numerical analyses in the band of operation, especially for dense effective media, as (4.40) does not bear information about the frequency dispersion.

### 4.5.2 Improving the frequency validity

The quasi-static formula (4.40) is a zero-order approximation of the frequency-dependent dispersion equation, and as such its frequency validity is bound to the low-dispersive behavior of the waveguide. This not a problem in practice, because the foremost advantage of G-S waveguides is their low dispersion, and so they are used at frequencies where the effective refractive index is almost constant. Still, in order to improve the accuracy of the index formula, frequency dependencies must be retained in the derivation process. Keeping first-order terms is not difficult in itself. The difficulty lies in keeping the dispersion equation simple enough so that a closed-form solution $n_\theta$ can be found.

In the following, we examine which frequency dependencies can be kept, without preventing the simplification process described in section 4.2. Notably, all frequency dependencies related to the harmonic wavenumbers $k_z$ ans $k_x$ cannot be considered, because they involve the refractive index $n_\theta$. As such, it must be kept in mind that the subsequent closed-form formula, although frequency-dependent, has no guarantee of improving the results at higher frequencies. Indeed, while some frequency dependencies are kept, others are dismissed because they would disrupt the simplification process. The overall frequency balance of the dispersion equation may not be maintained, if the frequency terms retained are not the dominant ones.

**Frequency dependencies of the mode admittances** The terms where the frequency dependency is simplest to keep are the admittances of the hole modes, described

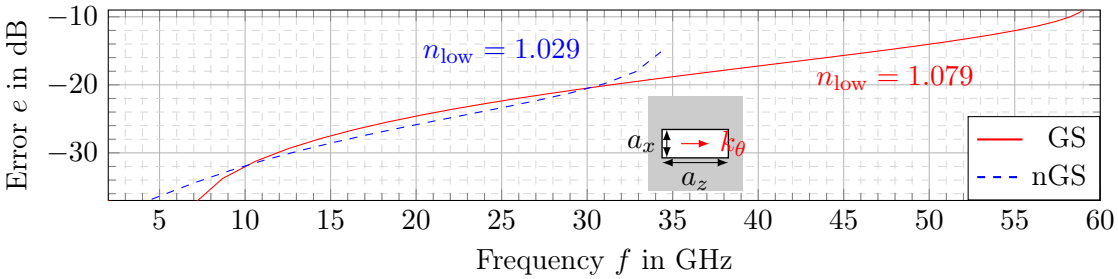


(a) Rectangular holes: $h = 5\,\text{mm}$, $a_z = 3.5\,\text{mm}$, $a_x = 1.5\,\text{mm}$.

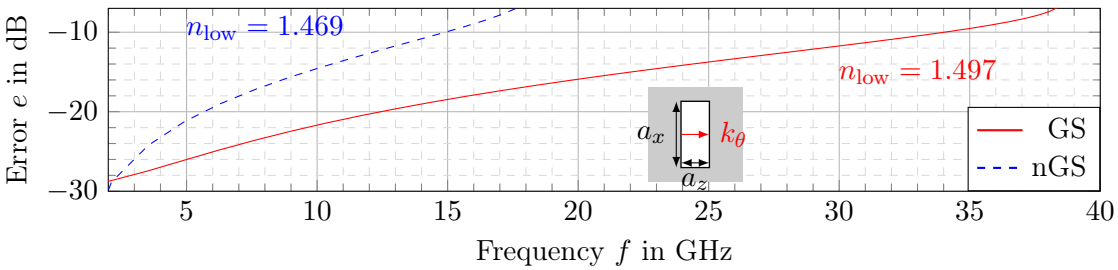


(b) Rectangular holes: $h = 5\,\text{mm}$, $a_z = 1.5\,\text{mm}$, $a_x = 3.5\,\text{mm}$.

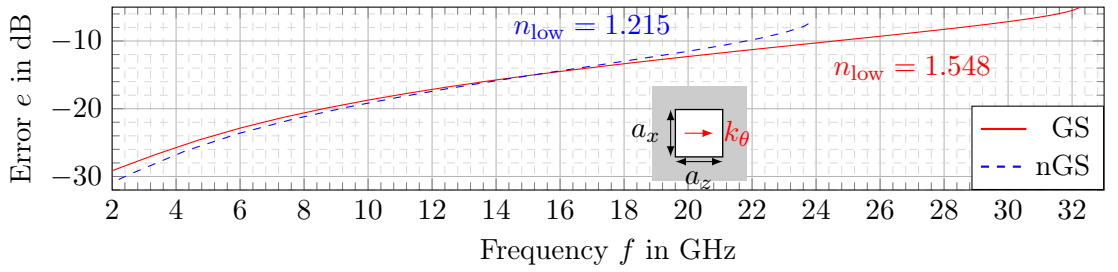


(c) Square holes: $h = 5\,\text{mm}$, $a_z = a_x = 3\,\text{mm}$.

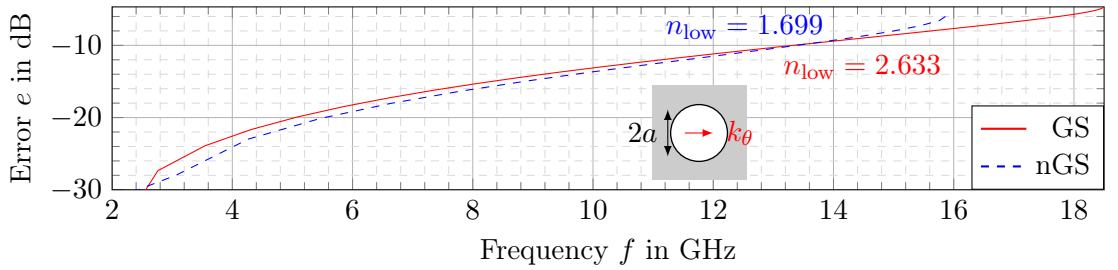


(d) Circular holes: $h = 3\,\text{mm}$, $a = 1.9\,\text{mm}$, $\epsilon_{\text{r}} = 11.2$.

Figure 4.25: Error between the low-frequency refractive index $n_{\text{low}}$ – computed with the closed-form formula (4.40) – and the refractive index obtained with CST as a function of frequency. The error is normalized and given in dB i.e., $e = 10 \log \left| \frac{n(f) - n_{\text{low}}}{n(f)} \right|$. The refractive indexes are computed for both G-S and nGS holey PPWs. All structures have cells of size of $p_z = p_x = 4\,\text{mm}$, $g = 0.1\,\text{mm}$, and a propagation direction $\theta = 0°$.

in (2.17). In the coefficients (2.40), (2.47) and (2.48) of the dispersion equation, these admittances appear in the diagonal terms of the submatrices $\underline{\boldsymbol{M}}^{\mathrm{e/e}}$ and $\underline{\boldsymbol{M}}^{\mathrm{h/h}}$. In the former case, keeping the frequency-dependent TM admittance yields the diagonal term

$$\frac{\mu_{\mathrm{r}1}\epsilon_{\mathrm{r}2}}{\sqrt{k_0^2\epsilon_{\mathrm{r}2}\mu_{\mathrm{r}2}-{k_m^{\mathrm{e}}}^2}}p_x p_z I_m^{\mathrm{e}}\cot\left(h\sqrt{k_0^2\epsilon_{\mathrm{r}2}\mu_{\mathrm{r}2}-{k_m^{\mathrm{e}}}^2}\right), \tag{4.43}$$

instead of the quasi-static term (4.24). Similarly, keeping the frequency-dependent TE admittance yields the diagonal term

$$\frac{\mu_{\mathrm{r}1}\sqrt{k_0^2\epsilon_{\mathrm{r}2}\mu_{\mathrm{r}2}-{k_m^{\mathrm{h}}}^2}}{\mu_{\mathrm{r}2}}p_x p_z I_m^{\mathrm{h}}\cot\left(h\sqrt{k_0^2\epsilon_{\mathrm{r}2}\mu_{\mathrm{r}2}-{k_m^{\mathrm{h}}}^2}\right), \tag{4.44}$$

instead of the quasi-static term (4.22).

**Frequency dependencies in the higher-harmonic terms** When simplifying the higher-harmonic terms of the matrix $\underline{\boldsymbol{M}}^{\mathrm{h/h}}$ from (2.40) to (4.29), the terms proportional to $k_0^2$ are dismissed in front of frequency-independent terms. These terms can be kept without disrupting the closed-form formula simplifications. Therefore, the higher-harmonic terms of $\underline{\boldsymbol{M}}^{\mathrm{h/h}}$ with $(s,\ell)\neq(0,0)$ become

$$\sum_{(s,\ell)\neq(0,0)}\bar{f}^{(s\ell)}\begin{bmatrix}k_0^2\epsilon_{\mathrm{r}1}\mu_{\mathrm{r}1}\left(\bar{e}_{z,m'}^{\mathrm{h}(s\ell)}\bar{e}_{z,m}^{\mathrm{h}(s\ell)*}+\bar{e}_{x,m'}^{\mathrm{h}(s\ell)}\bar{e}_{x,m}^{\mathrm{h}(s\ell)*}\right)\\ -\left(\frac{s2\pi}{p_z}\bar{e}_{x,m'}^{\mathrm{h}(s\ell)}-\frac{\ell 2\pi}{p_x}\bar{e}_{z,m'}^{\mathrm{h}(s\ell)}\right)\left(\frac{s2\pi}{p_z}\bar{e}_{x,m}^{\mathrm{h}(s\ell)}-\frac{\ell 2\pi}{p_x}\bar{e}_{z,m}^{\mathrm{h}(s\ell)}\right)^*\end{bmatrix}. \tag{4.45}$$

The higher-harmonic terms (2.39) in $\underline{\boldsymbol{M}}^{\mathrm{e/e}}$ that are proportional to $k_0^2$ do not need to be considered, because they are cancelled out independently of frequency, as shown in section 2.2.4.1, yielding (2.47).

Although a similar simplification was made in (2.48) for the higher-harmonic terms of $\underline{\boldsymbol{M}}^{\mathrm{e/h}}$, these higher-harmonic terms were dismissed altogether in the quasi-static simplification process, because they were proportional to $k_0^2$. When keeping these terms, the block-matrix reformulation of the dispersion equation in (4.37) has more than just the fundamental-harmonic terms in the non-diagonal submatrices, yielding

$$\begin{vmatrix}\frac{n_1^2-n_\theta^2}{n_\theta^2}\underline{\boldsymbol{\Sigma}}^{\mathrm{e}}+\frac{2}{g}\boldsymbol{u}^{\mathrm{e}}[\boldsymbol{u}^{\mathrm{e}}]^{\mathrm{H}} & \mathrm{j}\frac{2}{g}\boldsymbol{u}^{\mathrm{e}}\left[\boldsymbol{u}^{\mathrm{h}}\right]^{\mathrm{H}}+\mathrm{j}k_0\frac{n_1^2-n_\theta^2}{n_\theta}\underline{\boldsymbol{X}}\\ -\mathrm{j}\frac{2}{g}\boldsymbol{u}^{\mathrm{h}}[\boldsymbol{u}^{\mathrm{e}}]^{\mathrm{H}}-\mathrm{j}k_0\frac{n_1^2-n_\theta^2}{n_\theta}\underline{\boldsymbol{X}} & \frac{n_1^2-n_\theta^2}{n_1^2}\underline{\boldsymbol{\Sigma}}^{\mathrm{h}}+\frac{2}{g}\boldsymbol{u}^{\mathrm{h}}\left[\boldsymbol{u}^{\mathrm{h}}\right]^{\mathrm{H}}\end{vmatrix}=0, \tag{4.46}$$

with $\underline{\boldsymbol{X}}$ a matrix holding the simplified higher-harmonic terms of $\underline{\boldsymbol{M}}^{\mathrm{e/h}}$, with coefficients defined as

$$X_{m'm}=\sum_{(s,\ell)\neq(0,0)}\bar{f}^{(s\ell)}\frac{\bar{e}_{y,m'}^{(s\ell)}}{k_{m'}^{\mathrm{e}}}\left(\frac{s2\pi}{p_z}\bar{e}_{z,m}^{\mathrm{h}(s\ell)}+\frac{\ell 2\pi}{p_x}\bar{e}_{x,m}^{\mathrm{h}(s\ell)}\right)^*. \tag{4.47}$$

This means that (4.38) becomes

$$\left| \left(n_1^2 - n_\theta^2\right) \begin{bmatrix} \frac{1}{n_\theta^2}\underline{\boldsymbol{\Sigma}}^{\mathrm{e}} & \mathrm{j}\frac{k_0}{n_\theta}\underline{\boldsymbol{X}} \\ -\mathrm{j}\frac{k_0}{n_\theta}\underline{\boldsymbol{X}} & \frac{1}{n_1^2}\underline{\boldsymbol{\Sigma}}^{\mathrm{h}} \end{bmatrix} + \frac{2}{g} \begin{bmatrix} \mathrm{j}\boldsymbol{u}^{\mathrm{e}} \\ \boldsymbol{u}^{\mathrm{h}} \end{bmatrix} \begin{bmatrix} \mathrm{j}\boldsymbol{u}^{\mathrm{e}} \\ \boldsymbol{u}^{\mathrm{h}} \end{bmatrix}^{\mathrm{H}} \right| = 0\,. \tag{4.48}$$

and so the matrix containing the $\underline{\boldsymbol{\Sigma}}$ matrices is not block-diagonal anymore. Therefore, computing its inverse is more complicated with the determinant lemma, as done in (4.39). Assuming that $\mathrm{j}\frac{k_0}{n_\theta}\underline{\boldsymbol{X}}$ is small compared to the other matrix coefficients, which is true at low frequencies, the first-order approximation of the inverse of a matrix with small perturbations can be applied [189, p. 126], that is

$$\begin{aligned} \begin{bmatrix} \underline{\boldsymbol{A}} & \boldsymbol{\delta a} \\ \boldsymbol{\delta a}^{\mathrm{H}} & \underline{\boldsymbol{B}} \end{bmatrix}^{-1} &\simeq \begin{bmatrix} \underline{\boldsymbol{A}} & \boldsymbol{0} \\ \boldsymbol{0}^{\mathrm{H}} & \underline{\boldsymbol{B}} \end{bmatrix}^{-1} - \begin{bmatrix} \underline{\boldsymbol{A}} & \boldsymbol{0} \\ \boldsymbol{0}^{\mathrm{H}} & \underline{\boldsymbol{B}} \end{bmatrix}^{-1} \begin{bmatrix} \boldsymbol{0} & \boldsymbol{\delta a} \\ \boldsymbol{\delta a}^{\mathrm{H}} & \boldsymbol{0} \end{bmatrix} \begin{bmatrix} \underline{\boldsymbol{A}} & \boldsymbol{0} \\ \boldsymbol{0}^{\mathrm{H}} & \underline{\boldsymbol{B}} \end{bmatrix}^{-1} \\ &\simeq \begin{bmatrix} \underline{\boldsymbol{A}}^{-1} & -\underline{\boldsymbol{A}}^{-1}\boldsymbol{\delta a}\underline{\boldsymbol{B}}^{-1} \\ -\underline{\boldsymbol{B}}^{-1}\boldsymbol{\delta a}^{\mathrm{H}}\underline{\boldsymbol{A}}^{-1} & \underline{\boldsymbol{B}}^{-1} \end{bmatrix}, \end{aligned} \tag{4.49}$$

where $\underline{\boldsymbol{A}}$ and $\underline{\boldsymbol{B}}$ are invertible, and where in comparison $\boldsymbol{\delta a}$ has small coefficients. Making use of (4.49) when applying the determinant lemma to (4.48) leads to the second-order polynomial equation

$$\begin{aligned} n_\theta^2 \left[1 - \frac{2}{g}\boldsymbol{u}^{\mathrm{eH}}\underline{\boldsymbol{\Sigma}}^{\mathrm{e}-1}\boldsymbol{u}^{\mathrm{e}}\right] + n_\theta k_0 n_1^2 \frac{4}{g}\mathrm{Re}\left\{\boldsymbol{u}^{\mathrm{eH}}\underline{\boldsymbol{\Sigma}}^{\mathrm{e}-1}\underline{\boldsymbol{X}}\underline{\boldsymbol{\Sigma}}^{\mathrm{h}-1}\boldsymbol{u}^{\mathrm{h}}\right\} \\ -n_1^2\left[1 + \frac{2}{g}\boldsymbol{u}^{\mathrm{h}\mathrm{H}}\underline{\boldsymbol{\Sigma}}^{\mathrm{h}-1}\boldsymbol{u}^{\mathrm{h}}\right] = 0\,, \end{aligned} \tag{4.50}$$

Introducing

$$\begin{aligned} \Delta = k_0^2 n_1^4 \frac{4}{g^2}\mathrm{Re}\left\{\boldsymbol{u}^{\mathrm{eH}}\underline{\boldsymbol{\Sigma}}^{\mathrm{e}-1}\underline{\boldsymbol{X}}\underline{\boldsymbol{\Sigma}}^{\mathrm{h}-1}\boldsymbol{u}^{\mathrm{h}}\right\}^2 \\ +n_1^2\left[1 - \frac{2}{g}\boldsymbol{u}^{\mathrm{eH}}\underline{\boldsymbol{\Sigma}}^{\mathrm{e}-1}\boldsymbol{u}^{\mathrm{e}}\right]\left[1 + \frac{2}{g}\boldsymbol{u}^{\mathrm{h}\mathrm{H}}\underline{\boldsymbol{\Sigma}}^{\mathrm{h}-1}\boldsymbol{u}^{\mathrm{h}}\right] \end{aligned} \tag{4.51}$$

leads to the closed-form refractive index solution

$$n_\theta = \frac{-k_0 n_1^2 \frac{2}{g}\mathrm{Re}\left\{\boldsymbol{u}^{\mathrm{eH}}\underline{\boldsymbol{\Sigma}}^{\mathrm{e}-1}\underline{\boldsymbol{X}}\underline{\boldsymbol{\Sigma}}^{\mathrm{h}-1}\boldsymbol{u}^{\mathrm{h}}\right\} + \sqrt{\Delta}}{1 - \frac{2}{g}\boldsymbol{u}^{\mathrm{eH}}\underline{\boldsymbol{\Sigma}}^{\mathrm{e}-1}\boldsymbol{u}^{\mathrm{e}}}\,. \tag{4.52}$$

One can easily verify that when $k_0 \to 0$, (4.52) becomes (4.40).

**Numerical validity** As stated earlier in this section, the validity of the closed-form formula (4.52) is not guaranteed when incorporating all the frequency dependencies described in the previous paragraphs. The wave admittances in the diagonal terms (4.43) and (4.44) may help to capture the frequency-dispersion of the waveguide, but this effect may be insufficient or excessive. This can only be assessed with examples.

The Brillouin diagram of holey G-S PPWs is plotted in Fig. 4.26 and Fig. 4.27, for square and circular holes, respectively. All structures have periodicities $p_z = p_x = 4\,\text{mm}$ and a gap $g = 0.1\,\text{mm}$. The square holes have a size $a = 3\,\text{mm}$ and depth $h = 5\,\text{mm}$, whereas the circular holes have a radius $a = 1.5\,\text{mm}$ and $h = 3\,\text{mm}$. Different dielectric fillings are considered in the gap and the holes for each subfigure. In each case, the dispersion curves are computed in three different ways. The reference curve is given by solving the full MMM dispersion equation (2.42). This method has been shown to be accurate in section 2.2, and has the advantage of yielding results much faster than CST. The MMM curves are compared on the one hand to the quasi-static curve (4.40), which is the line tangent to the MMM curve at $k_0 \to 0$, and on the other hand to the improved formula (4.52), which is frequency-dependent. For all curves, 150 TM and 150 TE modes are used, as well as harmonic orders $s$ and $\ell$ in the range $\pm 30$.

Fig. 4.26 and Fig. 4.27 show that the added frequency dependencies (4.43) and (4.44), in the generalized formula (4.52), seem to be indeed an enhancement of the frequency range of the homogenization technique. In almost all cases, the enhanced curve better fits the reference curve in most of the first Brillouin zone, thus estimating the effective refractive index of the waveguide with better accuracy than with the purely quasi-static approach. This is particularly true when the structures are filled with vacuum, in which case the frequency validity is almost doubled.

However, these frequency enhancement are not enough to accurately describe the first mode, especially for dielectric-filled waveguides. One case where the frequency dependency seems to be too strong is for magnetic circular holes in Fig. 4.27d, where the quasi-static homogenization better follows the linear dispersion curve.

## Chapter landmarks

In this chapter, based on the dispersion equations obtained with the MMM in chapter 2, new modeling techniques have been developed for G-S PPWs:

- A closed-form solution of the quasi-static refractive index is found in (4.16) for corrugated PPW. It is accurate for both G-S and nGS designs. The frequency validity of this formula is observed in Fig. 4.2.
- Similarly, a closed-form formula of the quasi-static refractive index is found for holey G-S PPWs in (4.40). It is valid for arbitrary hole shapes and propagation directions.
- For canonical hole shapes with analytical knowledge of the modal functions, (4.40) can be accelerated by dismissing the modes that have no impact in the formula. On top of making parametric studies much faster, this opens the door to heavy optimization processes, for example to maximize the anisotropy of a rectangular hole.
- The index formula (4.40) is extended to arbitrary hole shapes by combining it to a 2-D FEM method. Unusual hole shapes can be explored, such as concave

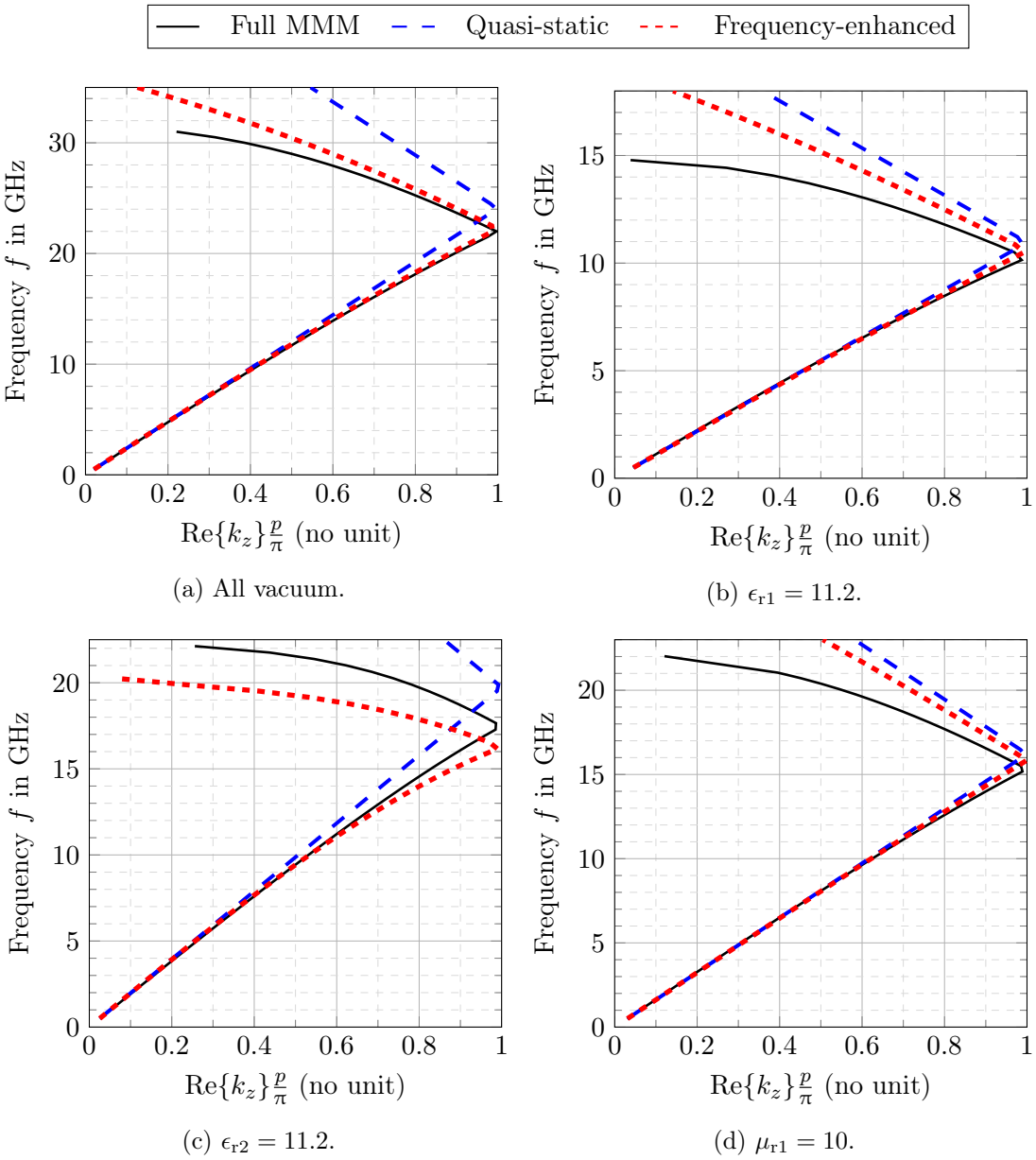


(a) All vacuum.

(b) $\epsilon_{r1} = 11.2$.

(c) $\epsilon_{r2} = 11.2$.

(d) $\mu_{r1} = 10$.

Figure 4.26: Brillouin diagrams of G-S PPWs with square holes, computed with the full MMM, the quasi-static formula (4.40), and the frequency-improved formula (4.52). All three methods use 150 TM modes, 150 TE modes, and 1681 harmonics. The structures have $p_z = p_x = 4\,\text{mm}$, $g = 0.1\,\text{mm}$, a hole size $a = 3\,\text{mm}$, and a hole depth $h = 5\,\text{mm}$. The waves propagate along the $z$-axis i.e., $\theta = 0$. Different gap and hole fillings are considered. Unless stated otherwise, the permittivities and permeabilities are like in vacuum.

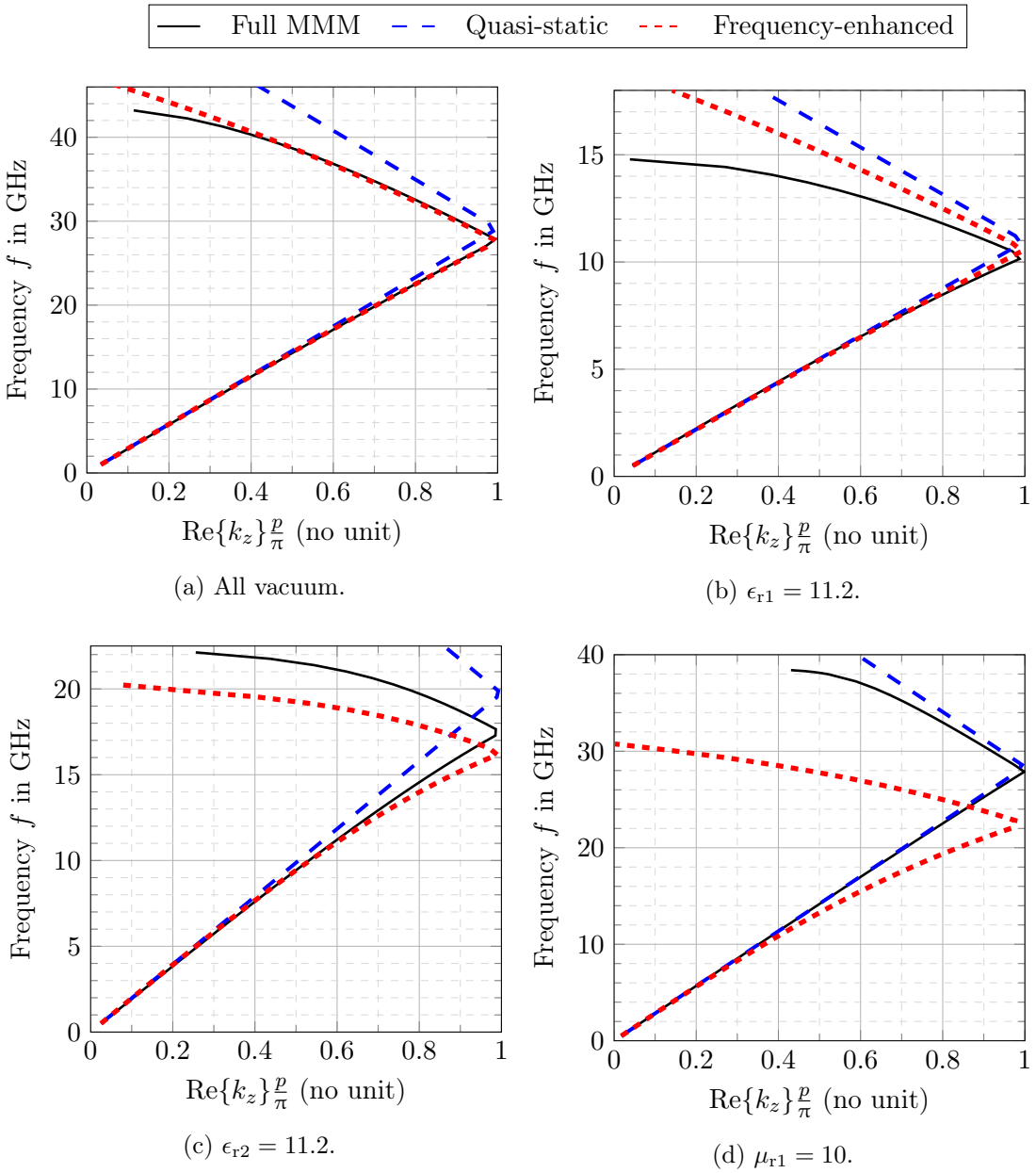


(a) All vacuum.

(b) $\epsilon_{r1} = 11.2$.

(c) $\epsilon_{r2} = 11.2$.

(d) $\mu_{r1} = 10$.

Figure 4.27: Brillouin diagrams of G-S PPWs with circular holes, computed with the full MMM, the quasi-static formula (4.40), and the frequency-improved formula (4.52). All three methods use 150 TM modes, 150 TE modes, and 1681 harmonics. The structures have $p_z = p_x = 4\,\text{mm}$, $g = 0.1\,\text{mm}$, a hole radius $a = 1.5\,\text{mm}$, and a hole depth $h = 3\,\text{mm}$. The waves propagate along the $z$-axis i.e., $\theta = 0$. Different gap and hole fillings are considered. Unless stated otherwise, the permittivities and permeabilities are like in vacuum.

holes or super-ellipses. These examples are not thought as applicable designs ready for implementation, but as illustrations of how the quasi-static homogenization method can efficiently highlight engaging propagation features through the fast study of creative geometries.

- The frequency-validity of (4.40) can be slightly improved by keeping some frequency-dependencies in the formula. Nevertheless, the benefits of these changes depend on each particular structure.

The main result of this chapter is the formula (4.40) for the refractive index of holey G-S PPWs. It is the first time that closed-form information is available for such G-S structures. Not only does it make the design of G-S devices much easier, but it also offers a unique opportunity to better understand the effects of the structure parameters on wave propagation. This is pursued in the next chapter.

# Chapter 5

# Quasi-static analysis of the properties of glide symmetry

In chapter 4, the dispersion equation obtained by means of the mode-matching method (MMM) is simplified in the quasi-static regime. This simplification yields the closed-form solution (4.40), which accurately describes the effective refractive index of holey glide-symmetric (G-S) parallel-plate waveguides (PPWs). This formula is particularly useful when it comes to the practical design of G-S waveguides, because it accelerates the required parametric studies.

Having a closed-form expression of the refractive index also opens the door to a better understanding of the structure's behavior. The impact of the different parameters on the refractive index can be studied analytically. For example, it can be used to prove that there are no $\theta$-dependencies for square or circular holes, proving the isotropy of these waveguides.

Most examples in chapter 4 illustrate the application of this formula to G-S waveguides, but it can be applied to non-glide-symmetric (nGS) structures too. Indeed, the MMM in chapter 2.2 has shown that the derivation of the dispersion equation follows the same steps for G-S and nGS waveguides, with only some particular terms changing. The wide-band accuracy of (4.40) for nGS waveguides is reduced, but the differences between G-S and nGS waveguides can be studied with this formulation. Section 5.1 isolates these differences in (4.40) in order to prove analytically if the effective refractive index is increased by glide symmetry (GS), as often observed in literature [33], [163].

A similar goal is pursued in section 5.2, namely the study of the increase in effective permeability observed with GS [35], [44]. Different methods to retrieve the constitutive parameters of the waveguide are considered. It comes out that an equivalent Bloch impedance can be defined analytically in the quasi-static regime with the help of (4.40) and the MMM field expressions. As such, the effective medium of the waveguide is fully characterized, and the constitutive parameters of G-S and nGS can be compared without resorting to commercial solvers.

In terms of practical application, one of the strengths of the index formula (4.40) is its generality, as it can be applied to any holey metasurface PPW. Unfortunately, the

presence of products between large matrices prevents a simple visualization of the role of geometrical and physical parameters. In the following sections, simplifications are made, mostly based on heuristic findings for a particular hole shape and reduction of the number of modes, simplifying the formula. The physical insight given with these particular cases can be extended to other structures, with caution.

## 5.1 Effective refractive index

This section puts under scrutiny the observation that GS increases the effective refractive index, as observed in literature [190] or in Fig. 4.25. The idea is to see if the differences brought by GS in the closed-form index formula (4.40) indeed lead to an increase of the refractive index. In order to do that, the formula is reduced to the main hole modes, which are shown to be sufficient to describe the overall behavior of the waveguide. This leads to a clear identification of the terms that differ with and without GS. Consequently, the impact of parameters such as the dielectric densities are highlighted.

### 5.1.1 Dominant modes in the quasi-static regime

The mode-matching process theoretically involves an infinite number of harmonics in the gap, and an infinite number of modes in the holes. However, hole modes with increasing cut-off frequency are expected to have little impact on the mode-matching procedure, especially in the quasi-static regime. This can be verified by finding the nullspace of the quasi-static dispersion matrix (4.31) [1]. This yields the coefficients of the excited hole modes: for transverse magnetic (TM) modes, the mode coefficients[2] are $c_m^{\mathrm{e}} = C_m^{\mathrm{e}} \sin\left(k_{y,m}^{\mathrm{e}} h\right)$, and for TE modes $c_m^{\mathrm{h}\,\prime} = C_m^{\mathrm{h}\,\prime} \sin\left(k_{y,m}^{\mathrm{h}} h\right)$.

The magnitude of the coefficients $c_m^{\mathrm{e}}$ and $c_m^{\mathrm{h}\,\prime}$ can be plotted to observe which modes are excited in a particular configuration at low frequency. This is done in Figs. 5.1a and 5.1b for a holey PPW with dimensions $p = 4\,\mathrm{mm}$, $g = 0.1\,\mathrm{mm}$, $h = 5\,\mathrm{mm}$, and square holes of size $a = 3\,\mathrm{mm}$. The structure is filled with vacuum. For each mode, the magnitude of the mode is plotted in blue for the nGS configuration, and in red for the G-S configuration. Only the 8 most-excited modes are plotted, and their magnitudes are normalized with respect to the strongest mode. Examining the coefficients of the hole modes, one TM mode and one TE mode are dominant, especially in the G-S case.

The same is done in Figs. 5.1c and 5.1d for circular holes of radius $a = 1.7\,\mathrm{mm}$ filled with a dielectric $(\epsilon_{\mathrm{r}2}, \mu_{\mathrm{r}2}) = (3, 4)$, while the gap is filled with $(\epsilon_{\mathrm{r}1}, \mu_{\mathrm{r}1}) = (2, 1.5)$. For TE modes, there is a dominance of one mode too. On the other hand, for TM modes, several modes have a comparable strength.

[1] The dispersion matrix needs to be modified in the quasi-static regime in order to find the coefficients of the modes. This process is described in section 5.2.2.

[2] As will be derived in section 5.2.2, the prime notation in the transverse electric (TE) case corresponds to a frequency-normalization in the field expressions, according to (5.21): in the quasi-static regime, the TE electric field vanishes, whereas the TM magnetic field vanishes.

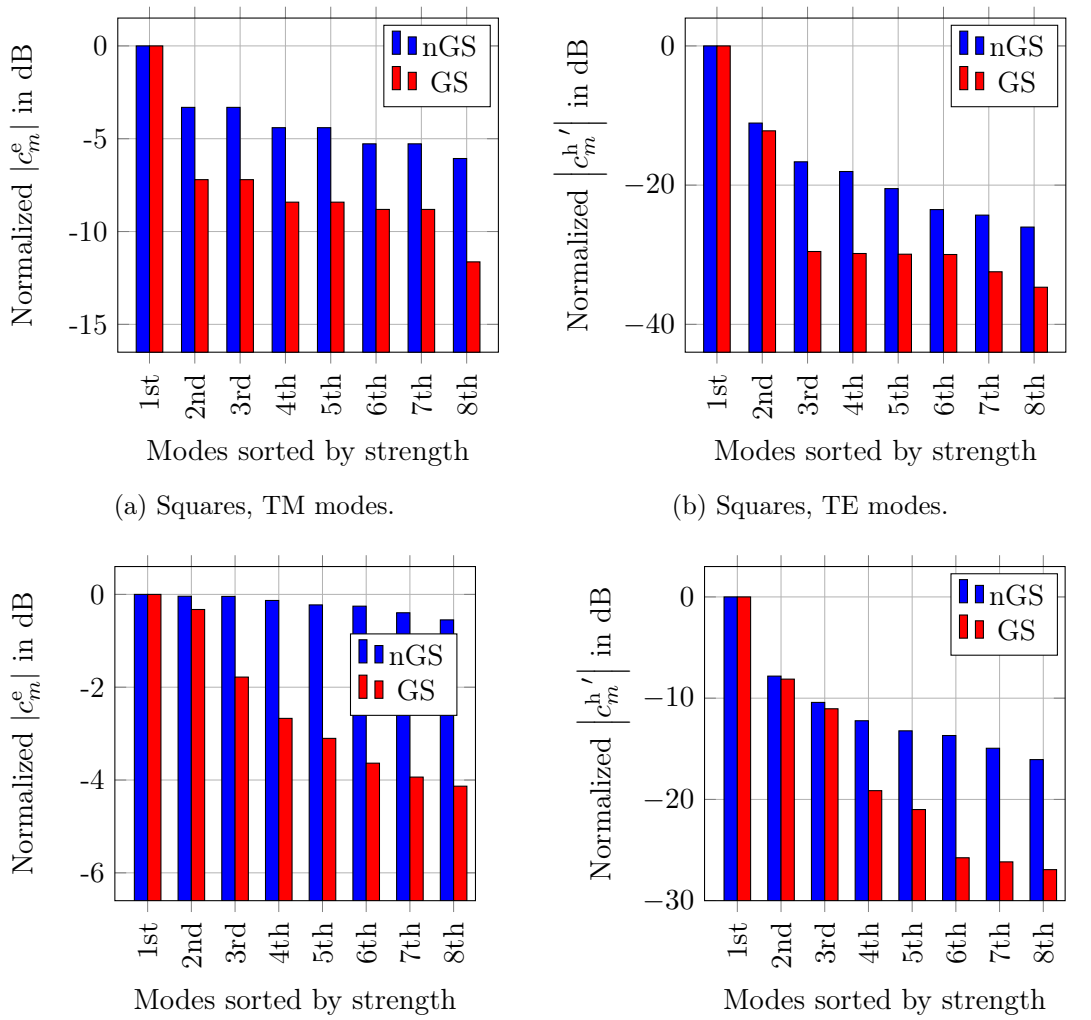


(a) Squares, TM modes.

(b) Squares, TE modes.

(c) Circles, TM modes.

(d) Circles, TE modes.

Figure 5.1: Coefficients of the most excited hole modes in the quasi-static regime of holey PPWs with canonical hole shapes: squares of size $a = 3\,\mathrm{mm}$ and circles of radius $a = 1.7\,\mathrm{mm}$. G-S and nGS cases are compared, with dimensions $p = 4\,\mathrm{mm}$, $h = 5\,\mathrm{mm}$ and gap $g = 0.1\,\mathrm{mm}$. For square holes, no dielectrics are used. Circular holes are filled with a dielectric $(\epsilon_{\mathrm{r}2}, \mu_{\mathrm{r}2}) = (3, 4)$, and in this case the gap is filled with a dielectric $(\epsilon_{\mathrm{r}1}, \mu_{\mathrm{r}1}) = (2, 1.5)$.

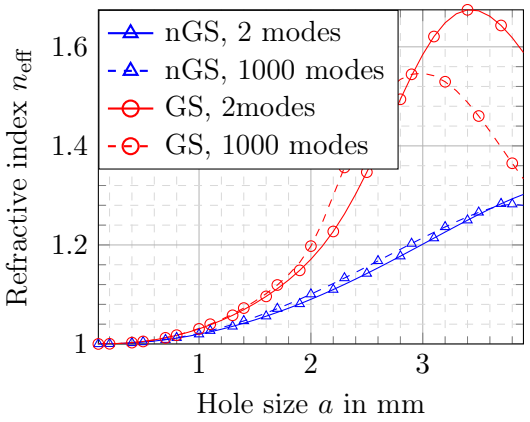


(a) Square holes of size $a$, no dielectrics.

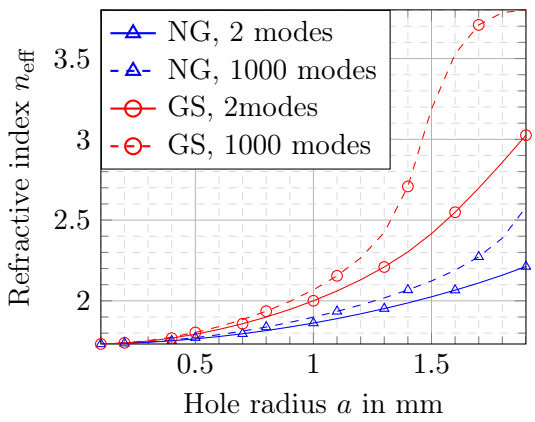


(b) Circular holes of radius $a$ filled with $(\epsilon_{r2}, \mu_{r2}) = (3, 4)$, and gap filled with $(\epsilon_{r1}, \mu_{r1}) = (2, 1.5)$.

Figure 5.2: Quasi-static effective refractive index of holey PPWs, as function of the hole size. The case with only 2 hole modes is compared with the converge value of the quasi-static framework. The structures have dimensions $p = 4\,\text{mm}$, $h = 5\,\text{mm}$, and $g = 0.1\,\text{mm}$. G-S and nGS configurations are compared.

In the following sections, our hypothesis is that the first TE and the first TM mode are enough to describe the overall effective properties of G-S versus nGS designs. This is confirmed by plotting the refractive index with the homogenized formula (4.40), keeping only two hole modes, and comparing it with the true index value. This is done in Figs. 5.2a and 5.2b for square and circular holes, respectively. The dimensions and dielectrics are the same as for Fig. 5.1. Only the hole size is varied.

Although in most cases shown in Fig. 5.2, two modes in the holes are not enough to precisely yield the effective propagation properties in the holey metasurface PPWs, they seem enough to capture the overall behavior of these structures, most notably the difference between GS and nGS designs. This is true even in the case of circular holes, where the hypothesis of two dominant modes is arguably wrong with respect to TM modes.

### 5.1.2 Does glide symmetry systematically increase the refractive index?

In previous papers, GS has been presented as a way to increase the refractive index of the waveguide. Is this always true? The impact of GS on the refractive index can be studied analytically from the quasi-static formula (4.40). This formula involves matrices and vectors whose size depends on the number of modes considered in the holes. This complicates any analytic study. However, as seen in paragraph 5.1.1, keeping only one TM and one TE mode yields acceptable results about the general behavior of the refractive index.

**Analytical study of the 2-modes quasi-static index formula** When keeping only these two modes, the effective index formula becomes

$$n_{\text{2modes}} = n_1 \sqrt{\frac{1 + \frac{2}{g}\left|u^{\text{h}}\right|^2 / \Sigma^{\text{h}}}{1 - \frac{2}{g}\left|u^{\text{e}}\right|^2 / \Sigma^{\text{e}}}}\,, \tag{5.1}$$

with the TM-related terms

$$\Sigma^{\text{e}} = -\frac{\epsilon_{\text{r2}}}{\epsilon_{\text{r1}} k^{\text{e}}} p_x p_z I^{\text{e}} \coth\left(k^{\text{e}} h\right) + \sum_{(s,\ell)\neq(0,0)} \bar{f}^{(s\ell)} \frac{\left|\bar{e}_y^{(s\ell)}\right|^2}{k^{\text{e}2}} \Gamma^{(s\ell)2}\,, \tag{5.2}$$

$$\text{and} \qquad u^{\text{e}} = \frac{\bar{e}_y^{(00)}}{k^{\text{e}}}\,, \tag{5.3}$$

and the TE-related terms

$$\Sigma^{\text{h}} = \frac{\mu_{\text{r1}} k^{\text{h}}}{\mu_{\text{r2}}} p_x p_z I^{\text{h}} \coth\left(k^{\text{h}} h\right) + \frac{2}{g}\left(\cos\theta \bar{e}_x^{\text{h}(00)} - \sin\theta \bar{e}_z^{\text{h}(00)}\right)^2 - \sum_{(s,\ell)\neq(0,0)} \bar{f}^{(s\ell)} \left|\tfrac{s2\pi}{p_z} \bar{e}_x^{\text{h}(s\ell)} - \tfrac{\ell 2\pi}{p_x} \bar{e}_z^{\text{h}(s\ell)}\right|^2\,, \tag{5.4}$$

$$\text{and} \qquad u^{\text{h}} = \cos\theta \bar{e}_z^{\text{h}(00)} + \sin\theta \bar{e}_x^{\text{h}(00)}\,. \tag{5.5}$$

The projected modal functions are the same for G-S and nGS designs, because they do not depend on the position of the holes, only on their shape. Therefore, $u^{\text{e}}$ and $u^{\text{h}}$ are equal for both designs. It is the terms $\Sigma^{\text{e}}$ and $\Sigma^{\text{h}}$ that change, because they contain $\bar{f}^{(s\ell)}$, defined in (4.20). It is reminded that the low-frequency vertical spectral functions are defined for each harmonic $(s,\ell)$, in the G-S case as

$$\bar{f}^{(s\ell)} = \begin{cases} -\tanh\left(\frac{g}{2}\Gamma^{(s\ell)}\right)/\Gamma^{(s\ell)} & \text{if } \ell + s \text{ odd}, \\ -\coth\left(\frac{g}{2}\Gamma^{(s\ell)}\right)/\Gamma^{(s\ell)} & \text{if } \ell + s \text{ even}, \end{cases} \tag{5.6}$$

and in the nGS case as

$$\bar{f}^{(s\ell)} = -\coth\left(\frac{g}{2}\Gamma^{(s\ell)}\right)\Big/\Gamma^{(s\ell)}\,. \tag{5.7}$$

These vertical spectral functions are the only terms that change between the G-S and nGS designs. For harmonics with $\ell + s$ odd, the magnitude of the G-S vertical spectral function is smaller than the nGS function: hyperbolic tangent versus cotangent of the same argument. With increasing harmonic orders, this difference decreases, as the tangent and the cotangent both tend to 1. The smaller the gap $g$, the higher this difference for more harmonics. Therefore, the comparison between G-S and nGS terms yields

$$\left|\Sigma^{\text{i}}_{\text{GS}}\right| < \left|\Sigma^{\text{i}}_{\text{nGS}}\right|\,, \qquad \text{with} \qquad \begin{cases} \Sigma^{\text{e}} < 0\,, \\ \Sigma^{\text{h}} > 0\,. \end{cases} \tag{5.8}$$

Given that in (5.1) these terms are inverted, we then have the numerators

$$\sqrt{1+\frac{2}{g}\left|u^{\mathrm{h}}\right|^2/\Sigma^{\mathrm{h}}_{\mathrm{GS}}} > \sqrt{1+\frac{2}{g}\left|u^{\mathrm{h}}\right|^2/\Sigma^{\mathrm{h}}_{\mathrm{nGS}}}\,, \tag{5.9}$$

and the denominators

$$\sqrt{1-\frac{2}{g}\left|u^{\mathrm{e}}\right|^2/\Sigma^{\mathrm{e}}_{\mathrm{GS}}} > \sqrt{1-\frac{2}{g}\left|u^{\mathrm{e}}\right|^2/\Sigma^{\mathrm{e}}_{\mathrm{NS}}}\,. \tag{5.10}$$

(5.9) shows that TE modes have an increasing effect on the G-S index with respect to the nGS index, whereas (5.10) shows that TM modes have a decreasing effect on the G-S index with respect to the nGS index.

At this point, we cannot state whether the refractive index of a G-S structure is higher than the index of its nGS counterpart. There is a balance between the effect of the numerator – GS increases $n$ – and the denominator – GS decreases $n$. However, by looking closer at the terms $1/\Sigma^{\mathrm{e}}$ and $1/\Sigma^{\mathrm{h}}$, it appears that the balance between these TE and TM terms can be willingly controlled through the dielectric constitutive parameters. Indeed, we can rewrite the refractive index (5.1) as

$$n_{2\mathrm{modes}} = n_1\sqrt{\frac{1+\frac{2}{g}\dfrac{\left|u^{\mathrm{h}}\right|^2}{\frac{\mu_{\mathrm{r}1}}{\mu_{\mathrm{r}2}}C^{\mathrm{h}}+X^{\mathrm{h}}_{\mathrm{GS/nGS}}}}{1+\frac{2}{g}\dfrac{\left|u^{\mathrm{e}}\right|^2}{\frac{\epsilon_{\mathrm{r}2}}{\epsilon_{\mathrm{r}1}}C^{\mathrm{e}}+X^{\mathrm{e}}_{\mathrm{GS/nGS}}}}}\,. \tag{5.11}$$

The terms $C^{\mathrm{i}}$ and $X^{\mathrm{i}}_{\mathrm{GS/nGS}}$ can be identified from the two terms in the sums $\Sigma^{\mathrm{e}}$ and $\Sigma^{\mathrm{h}}$ in (5.2) and (5.4). On the one hand, the real positive coefficients $C^{\mathrm{i}}$ are the same for G-S and nGS designs. On the other hand, the real positive coefficients $X^{\mathrm{i}}_{\mathrm{GS/nGS}}$ are smaller in the G-S case than in the nGS case. If the ratio $\epsilon_{\mathrm{r}2}/\epsilon_{\mathrm{r}1}$ is very large, then $\frac{\epsilon_{\mathrm{r}2}}{\epsilon_{\mathrm{r}1}}C^{\mathrm{e}}$ become large in front of $X^{\mathrm{e}}_{\mathrm{GS/nGS}}$, and so the changes in $X^{\mathrm{e}}_{\mathrm{GS/nGS}}$ (containing TM modes) have less effect on the overall index. Similar mechanisms are at work in the numerator. Overall,

1. if $\dfrac{\epsilon_{\mathrm{r}2}}{\epsilon_{\mathrm{r}1}}\uparrow$, then $\dfrac{n_{\mathrm{GS}}}{n_{\mathrm{nGS}}}\uparrow$ (less impact of the denominator term $X^{\mathrm{e}}_{\mathrm{GS/nGS}}$),

2. if $\dfrac{\epsilon_{\mathrm{r}2}}{\epsilon_{\mathrm{r}1}}\downarrow$, then $\dfrac{n_{\mathrm{GS}}}{n_{\mathrm{nGS}}}\downarrow$ (more impact of the denominator term $X^{\mathrm{e}}_{\mathrm{GS/nGS}}$),

3. if $\dfrac{\mu_{\mathrm{r}1}}{\mu_{\mathrm{r}2}}\uparrow$, then $\dfrac{n_{\mathrm{GS}}}{n_{\mathrm{nGS}}}\downarrow$ (less impact of the numerator term $X^{\mathrm{h}}_{\mathrm{GS/nGS}}$),

4. if $\dfrac{\mu_{\mathrm{r}1}}{\mu_{\mathrm{r}2}}\downarrow$, then $\dfrac{n_{\mathrm{GS}}}{n_{\mathrm{nGS}}}\uparrow$ (more impact of the numerator term $X^{\mathrm{h}}_{\mathrm{GS/nGS}}$).

This can be summarized by saying that the denser the hole dielectric compared to the gap dielectric, the larger the ratio between the G-S and the nGS refractive indexes.

Considering asymptotic cases of the dielectric constitutive paramerers shows that $n_{\mathrm{GS}}$ is not necessarily larger than $n_{\mathrm{nGS}}$. If $\epsilon_{\mathrm{r}2} \to 0$ or $\epsilon_{\mathrm{r}1} \to \infty$, then $n_{\mathrm{GS}} < n_{\mathrm{nGS}}$.

**Examples of the dielectric control over the index ratio** To illustrate this control over the difference between G-S and nGS, we compute the quasi-static effective refractive index of G-S and nGS designs with (4.40), for a metasurface PPW with square holes and dimensions $p = 4\,\mathrm{mm}$, $h = 5\,\mathrm{mm}$, $g = 0.1\,\mathrm{mm}$ and $a = 3\,\mathrm{mm}$. Initially, holes and gap are filled with vacuum. The indexes are computed with enough modes and harmonics to achieve convergence. In Fig. 5.3a, the relative gap permittivity $\epsilon_{\mathrm{r}1}$ is increased to increase the impact of $X^{\mathrm{e}}_{\mathrm{GS/nGS}}$. In Fig. 5.3b, the hole permittivity $\epsilon_{\mathrm{r}2}$ is increased to reduce the impact of $X^{\mathrm{e}}_{\mathrm{GS/nGS}}$. In Fig. 5.3c, the gap permeability $\mu_{\mathrm{r}1}$ is increased to reduce the impact of $X^{\mathrm{h}}_{\mathrm{GS/nGS}}$. Finally, in Fig. 5.3d, the hole permeability $\mu_{\mathrm{r}2}$ is increased to increase the impact of $X^{\mathrm{h}}_{\mathrm{GS/nGS}}$.

In Fig. 5.3, only one dielectric constitutive parameter is changed at a time, to illustrate the individual impact of each parameter. But their effects can be combined, to reach very large or very small index ratios between G-S and nGS waveguides. In Fig. 5.4, the same structure are used as in Fig. 5.3, but this time two parameters are increased simultaneously (while the two others are kept at 1): $\epsilon_{\mathrm{r}1}$ and $\mu_{\mathrm{r}1}$ in Fig. 5.4a, and $\epsilon_{\mathrm{r}2}$ and $\mu_{\mathrm{r}2}$ in Fig. 5.4b. For a very dense gap, the nGS design is effectively much denser than the G-S design, whereas for very dense holes, it is the other way around.

These figures confirm the impact of the different dielectric parameters on the ratio between G-S and nGS refractive indexes. When the gap dielectric gets denser, the ratio decreases (Figs. 5.3a, 5.3c and 5.4a), with even some cases where $n_{\mathrm{nGS}} < n_{\mathrm{GS}}$. On the other hand, when the hole dielectric gets denser, the ratio increases (Figs. 5.3b, 5.3d and 5.4b), with some cases where the G-S index is multiple times larger than the nGS index. This can be interpreted in terms of path length of the wave propagation. When the dielectric in the holes becomes denser, it concentrates the fields. In the nGS waveguide, this does not change the overall path length, because the upper and lower holes are symmetric with respect to the propagation plane. On the other hand, when the waves propagate in a GS structure, they alternatively meet a hole in the upper metasurface and a hole in the lower metasurface. As such, the overall field propagation path could be described as a snake which penetrates further in the holes when the hole density in increased. This creates a longer path length, which results in an apparent speed reduction of the effective wave. Equivalently, the effective refractive index of the structure increases.

**General effect of glide symmetry on the refractive index** Does GS systematically increase the refractive index? These studies show that the answer is no. Instead of an increase of the refractive index, the effect of GS can be defined with respect to the dielectrics in the structure. When the density of the dielectric of the holes and the gap are very different, then it can be expected that the effective density of the waveguide lies somewhere in-between the two, like a weighted average of these densities. *GS tends to*

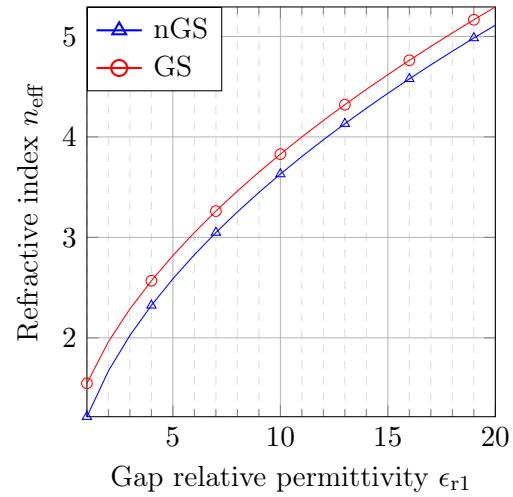


(a) Increasing impact of $X^{\text{e}}_{\text{GS/nGS}}$.

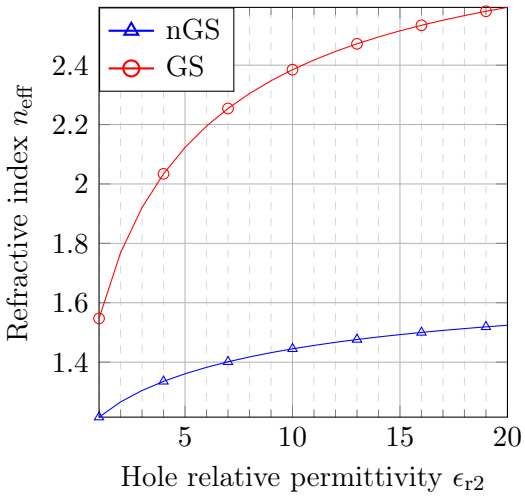


(b) Decreasing impact of $X^{\text{e}}_{\text{GS/nGS}}$.

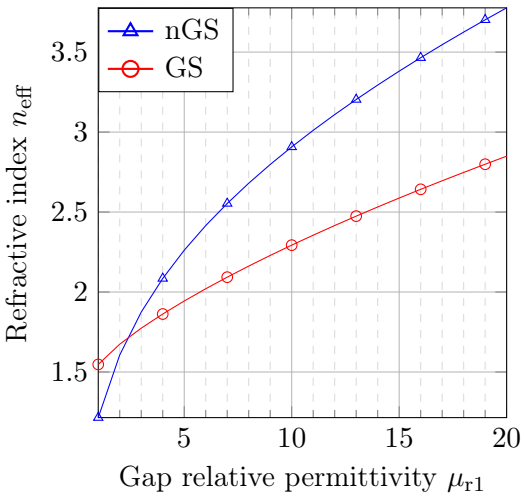


(c) Decreasing impact of $X^{\text{h}}_{\text{GS/nGS}}$.

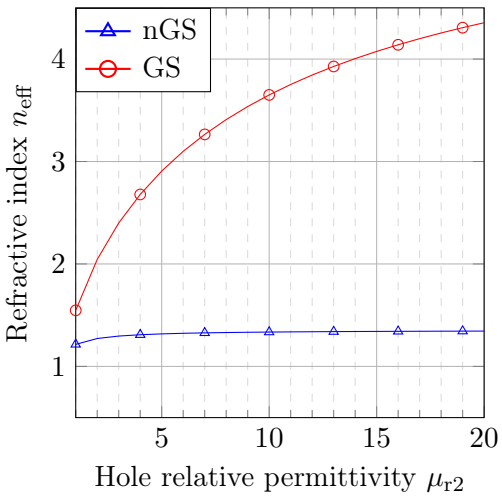


(d) Increasing impact of $X^{\text{h}}_{\text{GS/nGS}}$.

Figure 5.3: Quasi-static effective refractive index of holey PPWs, computed with (4.40), depending on the gap and hole dielectrics. The structures have dimensions $p = 4\,\text{mm}$, $h = 5\,\text{mm}$, $g = 0.1\,\text{mm}$ and square holes of size $a = 3\,\text{mm}$. G-S and nGS configurations are compared. The structures are initially empty ($\epsilon_{\text{r1}} = \epsilon_{\text{r2}} = \mu_{\text{r1}} = \mu_{\text{r2}} = 1$), with only one dielectric parameter changing in each subfigure.

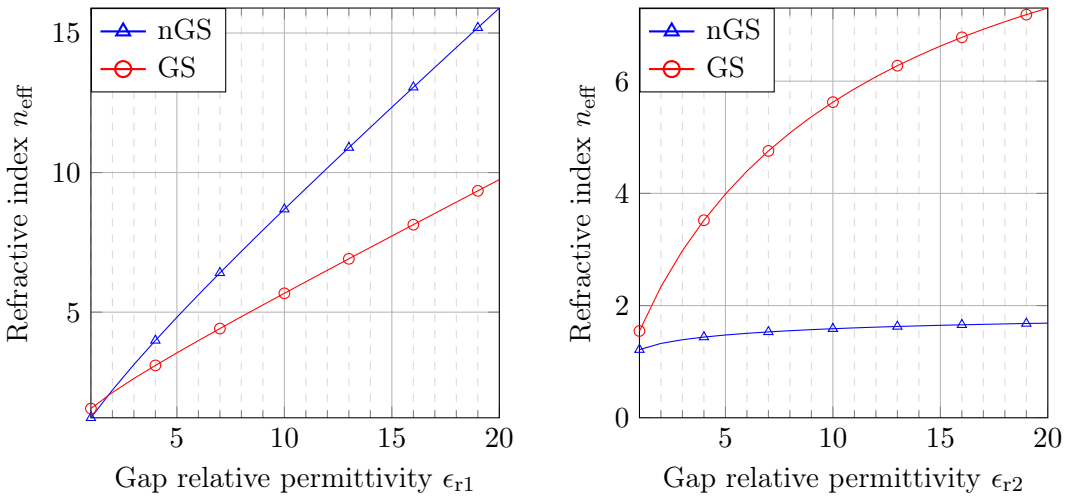


(a) Empty holes, increasing gap density.

(b) Empty gap, increasing hole density.

Figure 5.4: Quasi-static effective refractive index of holey PPWs, computed with (4.40), depending on the gap and hole dielectrics. The structures have dimensions $p = 4\,\text{mm}$, $h = 5\,\text{mm}$, $g = 0.1\,\text{mm}$ and square holes of size $a = 3\,\text{mm}$. G-S and nGS configurations are compared.

*give more weight to the hole dielectric than nGS*. If the hole density is larger than the gap density, then indeed GS increases the refractive index compared to nGS. But if the hole density is smaller than the gap density, the nGS index will remain closer to the gap density than GS, meaning that GS will bring the effective index lower – that is closer to the hole density.

What about gap and holes having the same density? How is the influence of GS being interpreted then, given that there is no density range in which GS and nGS would give different weights? In this case, each metasurface can still be seen as a somehow denser medium than the gap, because it is a mixture of dielectric and perfectly electrically conducting (PEC) plates. The latter can be seen as an infinitely dense medium. Therefore, GS will still pull the effective density closer to the metasurface effective density, which is larger then the gap density. That is why in this case GS increases the refractive index.

### 5.1.3 Giant refractive index for asymptotically small gap

In section 3.1, it is highlighted that the differences between G-S and nGS waveguides are particularly remarkable when the gap $g$ between the metasurfaces is small compared to the metasurface periodicity. When the metasurfaces are brought closer, their mutual coupling gets stronger. As such, studying the quasi-static refractive index at the limit when $g \to 0$ is revealing of the differences between structures with or without GS.

In Fig. 5.5, the effective refractive index is computed with (4.40) for gaps getting exponentially smaller. The considered holey PPW has periodicities $p_z = p_x = 4\,\text{mm}$, with square holes of size $a = 3\,\text{mm}$ and depth $h = 5\,\text{mm}$. No dielectrics are used. In

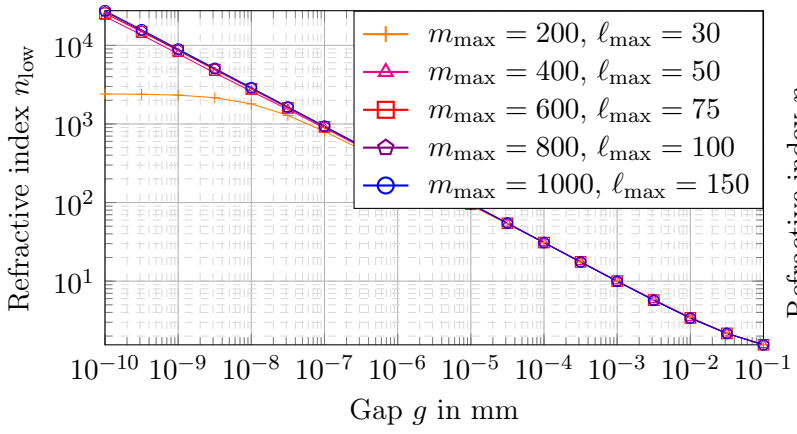


(a) G-S waveguide.

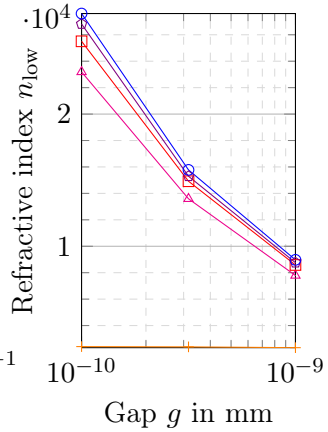


(b) Inset for GS.

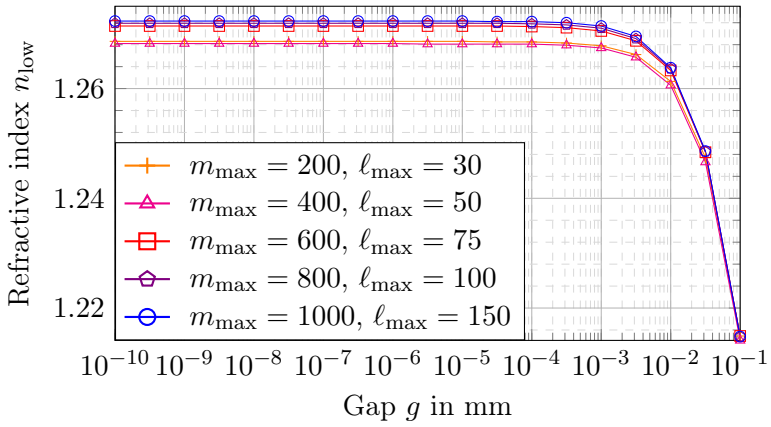


(c) NGS waveguide.

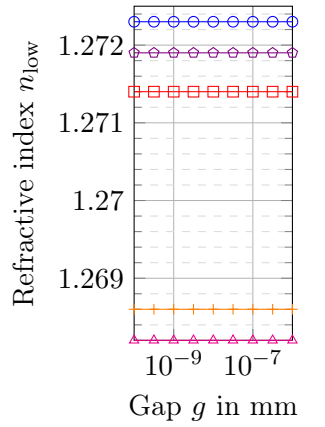


(d) Inset for nGS.

Figure 5.5: Quasi-static effective refractive index computed with (4.40) as function of the gap $g$, for a holey PPW with $p = 4\,\text{mm}$, and square holes of size $a = 3\,\text{mm}$ and depth $h = 5\,\text{mm}$. For each curve, the number $m_{\max}$ of TM and TE modes is indicated, and the maximum harmonic order $\ell_{\max}$, such that $s = \pm\ell_{\max}$ and $\ell = \pm\ell_{\max}$.

Fig. 5.5a, the G-S refractive index is plotted in logarithmic scale, with linear details in the inset 5.5b. The same is done in Figs. 5.5c and 5.5d for the nGS counterpart structure. Each curve corresponds to an increased number of modes and harmonics to ensure convergence of the results.

In Fig. 5.5a, it appears that the G-S refractive index does not converge when $g \to 0$. Moreover, the smaller the gap, the larger the number of modes required to get the correct refractive index. This illustrates that the smaller the gap between the metasurfaces, the stronger the coupling between the holes. To confirm that for the G-S structure, the refractive index does not converge with decreasing gap, the extreme case $g = 0$ is considered in Fig. 5.6. It appears that the refractive index can be made arbitrarily large

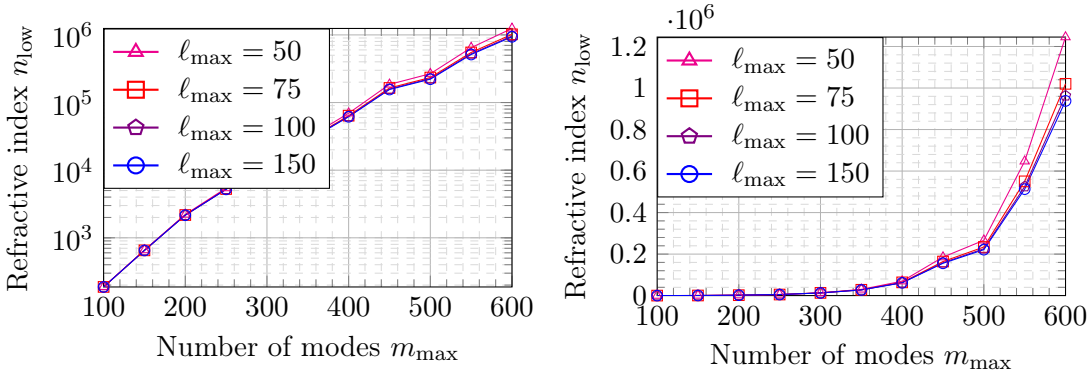


(a) Logarithmic scale.

(b) Linear scale.

Figure 5.6: Quasi-static refractive index (4.40) at $g = 0$, as function of the number of modes considered in the holes. The structure under study is a holey G-S PPW with $p = 4\,\text{mm}$, and square holes of size $a = 3\,\text{mm}$ and depth $h = 5\,\text{mm}$. The abscissa $m_{\max}$ corresponds to both the number of TE and TM modes. Each curve corresponds to a different number of harmonics $(s, \ell)$ with $s = \pm\ell_{\max}$ and $\ell = \pm\ell_{\max}$.

depending on the number of modes that are used. This means that $g \to 0$ leads to $n \to \infty$ and to $m_{\max} \to \infty$ – $m_{\max}$ being the number of modes that captures the coupling.

Evidently, the giant refractive index observed for this G-S structure has no practical implications. Not only would a waveguide with such a small gap yield huge losses, but also the passband of the waveguide would be extremely small. However, this asymptotic behavior can be put in parallel to the asymptotic behavior of the nGS structure in Fig. 5.5c. Here, the refractive index converges rapidly. This convergence value is very small compared to the values obtained with the G-S structure. It shows that the coupling is very different in the two designs. Most importantly, because the G-S structure tends to an infinite index when $g \to 0$, it is understandable that already at practical gap sizes its index becomes much larger than the nGS index.

The lack of convergence of a G-S structure's refractive index – and therefore its ability to reach large indexes at small gaps – depends on whether or not its holes are overlapping. In the example of Fig. 5.5 the hole size is $a = 3\,\text{mm}$, and so the holes have an overlap of $1 \times 1\,\text{mm}$. In Fig. 5.7a, a holey G-S PPW with smaller holes $a = 1.5\,\text{mm}$ is considered, so that that they do not overlap. The effective refractive index is computed with (4.40) for exponentially decreasing gaps. As expected, the G-S structure has a convergent refractive index when the gap goes to zero. This works up the to limiting case of $a = p/2$, as illustrated in Fig. 5.7c. But if the hole size is increased just a bit more, for example $a = 2.1\,\text{mm}$ in Fig. 5.7e, then the emerging overlap prevents the convergence in the G-S structure. Here the overlapping is very small, and so the increase of the refractive index is much more modest than in Fig. 5.5a, but it shows no signs of convergence despite the already very large number of modes that are used.

In conclusion, the refractive index formula (4.40) opens an unprecedented window onto the coupling mechanism between the metasurfaces. It was observed that the re-

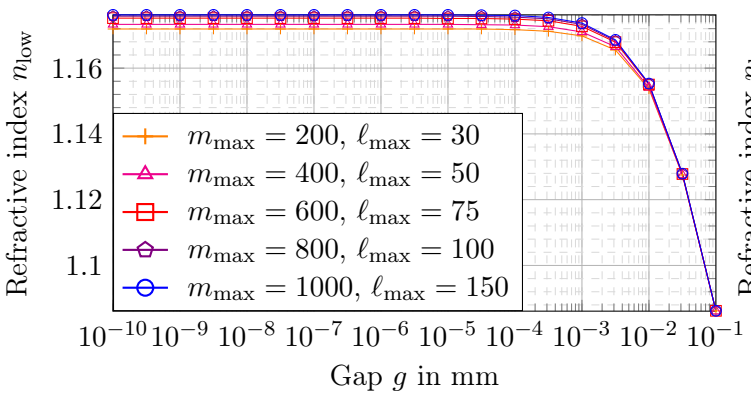


(a) Not-overlapping holes: $a = 1.5\,\text{mm}$.

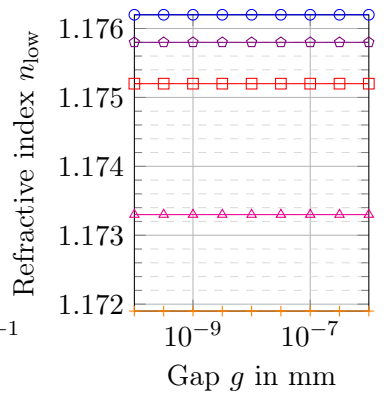


(b) Inset of (a).

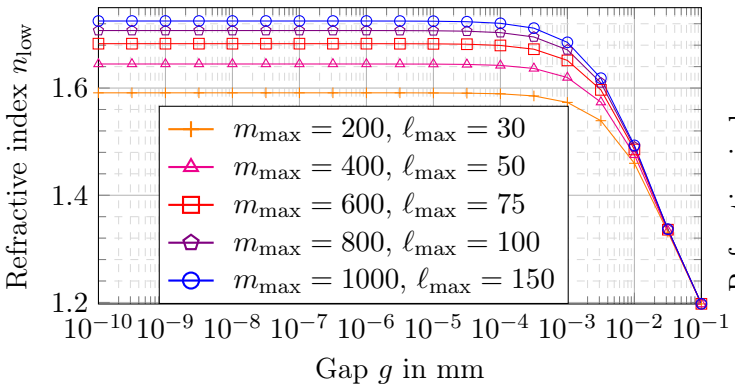


(c) Quasi-overlapping holes: $a = 2\,\text{mm}$.

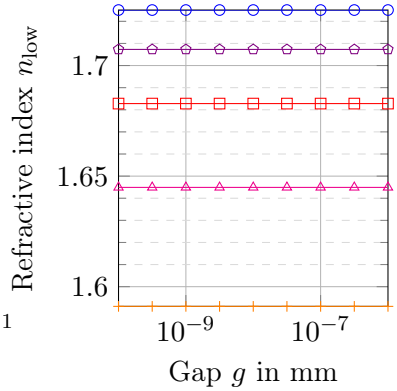


(d) Inset of (c).

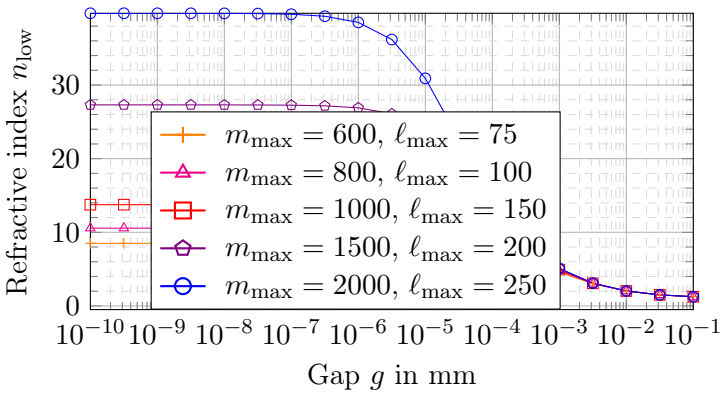


(e) Barely-overlapping holes: $a = 2.1\,\text{mm}$.

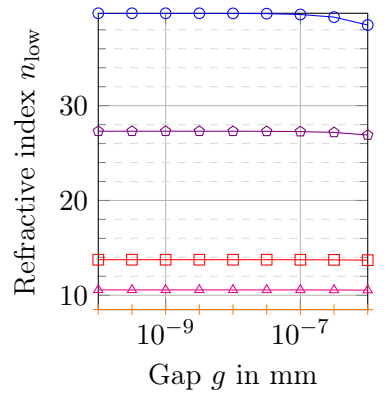


(f) Inset of (e).

Figure 5.7: Quasi-static effective refractive index computed with (4.40) as function of the gap $g$, for holey G-S PPWs with $p = 4\,\text{mm}$, and square holes of size $a$ and depth $h = 5\,\text{mm}$. For each curve, the number $m_{\max}$ of TM and TE modes is indicated, and the maximum harmonic order $\ell_{\max}$, such that $s = \pm\ell_{\max}$ and $\ell = \pm\ell_{\max}$.

fractive index difference between G-S and nGS waveguides is particularly high when the holes are overlapping, because in this case the G-S index is unbounded when $g \to 0$. With previous simulation methods such as commercial solvers, driving the gap to such small fractions of the unit cell length would be very challenging, and so to our knowledge, this difference in terms of convergence was never highlighted before.

## 5.2 Effective constitutive material parameters

In the context of impedance-matching of a dielectric slab, it has been shown that G-S waveguides yield a higher magnetic response than nGS waveguides [44]. The range of matchable dielectrics is broadened thanks to the higher permeability enabled by GS. This implies that for a given propagating mode, G-S waveguides can be modeled as an equivalent dielectric material, with effective impedance and refractive index. In this section, we describe how the effective constitutive parameters of the waveguide are computed. From the consistency of results between different techniques, it is found that the effective impedance can be computed directly from the quasi-static Bloch mode that propagates between the metasurfaces. Using the quasi-static framework developed in chapter 4, this effective Bloch impedance is computed without resorting to commercial solvers. Finally, closed-form expressions of this Bloch impedance are obtained in simplified cases, which leads to an analytic proof of GS's increased permeability.

### 5.2.1 Impedance matching by means of holey metasurfaces

A transverse electric magnetic (TEM) mode propagates in a PPW filled with a dielectric $(\epsilon_{\mathrm{rL}}, \mu_{\mathrm{rL}})$. At some point, a dielectric slab $(\epsilon_{\mathrm{r1}}, \mu_{\mathrm{r1}})$ is put in the way of the wave, such that it penetrates and exits the slab with normal incidence, as shown in the side view Fig. 5.8. In order to avoid refections at the dielectric interfaces, the PEC plates on both sides of the dielectric slab are transformed into metasurfaces, by means of periodic holes – which may be filled with a dielectric $(\epsilon_{\mathrm{r2}}, \mu_{\mathrm{r2}})$. When it comes to the incident TEM mode, the resulting metasurface waveguide portion is to be modeled by an equivalent effective dielectric PPW $(\epsilon_{\mathrm{eff}}, \mu_{\mathrm{eff}})$. If the equivalent effective impedance $Z_{\mathrm{eff}}$ matches the TEM impedance $Z_{\mathrm{TEM}}$, then reflections are avoided at the dielectric interfaces.

Retrieving the effective constitutive parameters of a waveguide from its S-parameters is a well-known process [191]. The idea is to first retrieve the effective refractive index and line impedance of the waveguide, from which the effective relative permittivity $\epsilon_{\mathrm{eff}}$ and relative permeability $\mu_{\mathrm{eff}}$ are computed. However, the notion of line impedance becomes a gray area when considering periodic structures. Indeed, the characteristic impedance of a transmission line is uniquely defined only for TEM modes, and, more importantly, it is directly related to the intrinsic impedance of the effective medium only for TEM modes. It is the intrinsic impedance that is related to the propagation medium parameters [17, p. 171]. As such, computing the line impedance to obtain constitutive parameters is theoretically only justified for TEM transmission lines. In

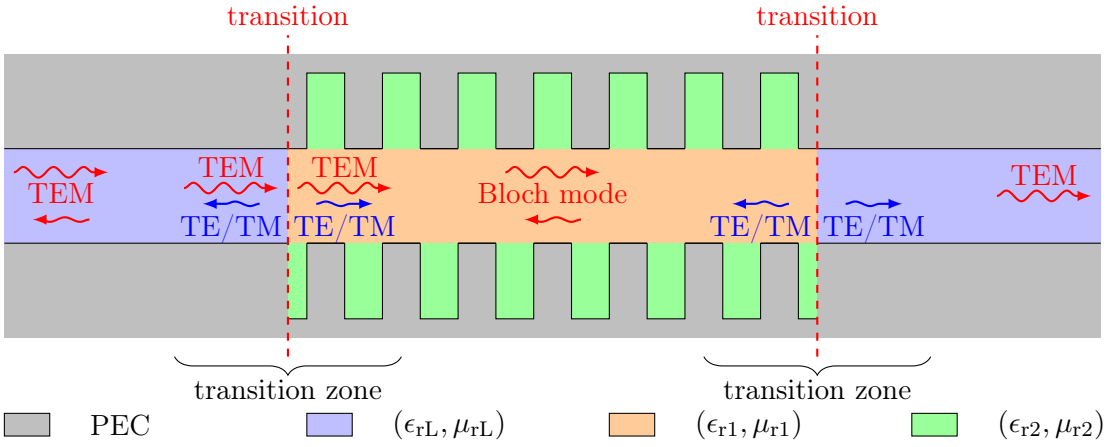


Figure 5.8: Impedance matching of a dielectric slab with holey metasurfaces. The gap is made exagerratedly large to better visualize the propagating modes.

periodic structures, Bloch modes are not necessarily TEM, and therefore the notion of line impedance and constitutive parameters is debatable.

Moreover, it is important to understand that the effective impedance $Z_{\text{eff}}$ does not completely represent the metasurface waveguide. It is only a simplification of how it appears to the TEM mode. Additional resonances in the metasurface waveguide may create a non-zero input reactance. At the dielectric interface, the fields are disrupted by the closest holes, resulting in a variation of the fields along the interface. This leads to the excitation of other modes (TE, TM), which are are evanescent in the quasi-static regime, and are therefore concentrated around the interface.

In the following, we will show that these effects can be neglected. For the aim of our analysis, i.e., the matching of the PPW in Fig. 5.8, the concept of effective medium is defined in order to accurately describes the reflective and transmissive properties of the waveguide. The effective constitutive parameters are directly linked to the notion of characteristic impedance, with no relation to the intrinsic impedance.

The following paragraphs present two numerical techniques to obtain the effective impedance $Z_{\text{eff}}$ in CST. On the one hand, $Z_{\text{eff}}$ is computed by considering the reflection coefficient of the structure drawn in Fig. 5.8. This is the reference impedance considered in this section, because the resulting impedance is representative of the practical behavior of the waveguide, that is its ability to avoid reflections at dielectric interfaces. On the other, $Z_{\text{eff}}$ is obtained by considering the transfer-matrix of one unit cell of the metasurface waveguide. These two methods are then compared, leading to a discussion about how to use the quasi-static modal fields to define a Bloch impedance.

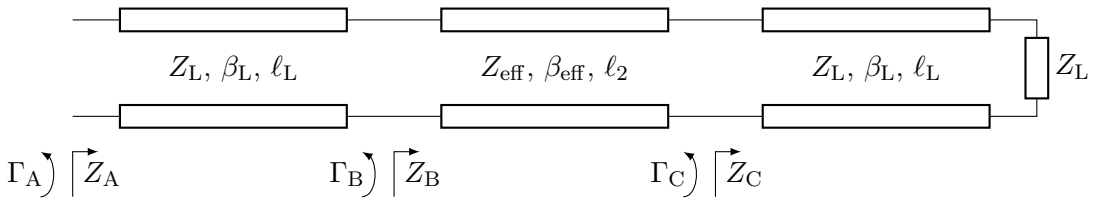


Figure 5.9: Transmission line model of the simulated CST waveguide.

#### 5.2.1.1 Effective impedance: CST reflection set-up

The definition of an effective impedance must embody the reflective properties of the metasurface waveguide. Here, the line impedance of the waveguide is directly derived from its reflective properties, by simulating the structure seen in Fig. 5.8 in its entirety. If the metasurface is built such that this reflective impedance matches the impedance of the feeding dielectric PPW, then it is certain that the reflections are repressed. That is why the impedance obtained by this reflection measure is used as the reference value for all subsequent computation methods.

In CST, $N$ successive unit cells of the holey metasurface waveguide are simulated. Instead of putting the waveguide ports directly at the end cells, two PPWs of length $\ell_\mathrm{L}$ and relative permittivity $\epsilon_\mathrm{rL}$ are added to feed both sides of the metasurface waveguide. This is important, as it guarantees that the measured reflection coefficient corresponds to the TEM mode of a simple PPW. Therefore, the total structure can be modeled as three transmission lines put in series, as pictured in Fig. 5.9. The propagation constant in the PPW is the TEM wavenumber $\beta_\mathrm{L} = \frac{2\pi f}{c_0}\sqrt{\epsilon_\mathrm{rL}}$, with $c_0$ the speed of light in vacuum.

CST builds waveguide ports that perfectly match parallel-plate waveguides. This ensures that no waves are reflected at the output port. Therefore, the output port impedance is equivalent to a $Z_\mathrm{L}$ load, $Z_\mathrm{L}$ being the line impedance of the PPW. This impedance is known analytically as $Z_\mathrm{L} = \frac{\eta_0}{\sqrt{\epsilon_\mathrm{rL}}}\frac{g}{p}$, where $g$ is the gap between the metasurfaces as well as the PPW height, $p$ is the cell periodicity as well as the width of the simulated PPW portion, and $\eta_0$ is the vacuum intrinsic impedance.

Given the absence of reflection at the output port, $Z_\mathrm{C} = Z_\mathrm{L}$. Then, using transmission line theory [17, p. 59], this impedance is transformed by the metasurface waveguide into

$$Z_\mathrm{B} = Z_\mathrm{eff}\frac{Z_\mathrm{C} + \mathrm{j}Z_\mathrm{eff}\tan\left(\beta_\mathrm{eff}\ell_2\right)}{Z_\mathrm{eff} + \mathrm{j}Z_\mathrm{C}\tan\left(\beta_\mathrm{eff}\ell_2\right)} = Z_\mathrm{eff}\frac{Z_\mathrm{L} + \mathrm{j}Z_\mathrm{eff}\tan\left(\beta_\mathrm{eff}\ell_2\right)}{Z_\mathrm{eff} + \mathrm{j}Z_\mathrm{L}\tan\left(\beta_\mathrm{eff}\ell_2\right)}, \tag{5.12}$$

where $\ell_2 = Np$ is the total length of the $N$ unit cells.

At the input side, the reflection coefficient $\Gamma_\mathrm{A}$ is the S-parameter $S_{11}$ given by CST at the input port. It can be propagated forwards along the input PPW, yielding $\Gamma_B = S_{11}\mathrm{e}^{\mathrm{j}2\ell_\mathrm{L}\beta_\mathrm{L}}$ (this can be done directly in CST using the de-embeding function). Given the relation

$$Z_\mathrm{B} = Z_\mathrm{L}\frac{1+\Gamma_B}{1-\Gamma_B} = Z_\mathrm{L}\frac{1+S_{11}\mathrm{e}^{\mathrm{j}2\ell_\mathrm{L}\beta_\mathrm{L}}}{1-S_{11}\mathrm{e}^{\mathrm{j}2\ell_\mathrm{L}\beta_\mathrm{L}}} \tag{5.13}$$

between the reflection coefficient and the impedance at the input of the metasurface waveguide, the latter can be computed from the S-parameters of CST.

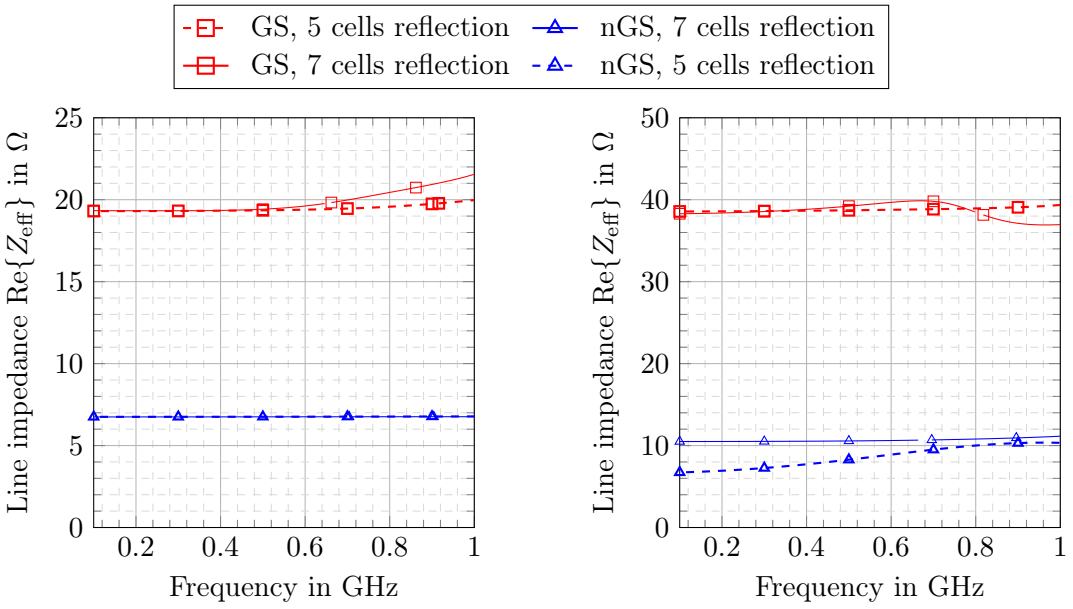


(a) $a = 3\,\text{mm}$. (b) $a = 3.5\,\text{mm}$.

Figure 5.10: Line impedance of the holey PPW, computed with the reflection technique (5.14) in CST. G-S (red) and nGS (blue) configurations are compared. The feeding PPWs have $\ell_{\text{L}} = 15\,\text{mm}$. The metasurface dimensions are $p = 4\,\text{mm}$, $h = 3\,\text{mm}$, $g = 0.1\,\text{mm}$, $\epsilon_{\text{r1}} = 10.7$, and different square hole sizes. The number of cells between the feeding PPWs is either $N = 5$ or $N = 7$.

Once $Z_{\text{B}}$ is known, (5.12) can be solved for $Z_{\text{eff}}$. For this to be possible, $\beta_{\text{eff}}$ must be computed from the transmission coefficient of the waveguide. Then, (5.12) is a second-order polynomial equation in $Z_{\text{eff}}$, solved for

$$Z_{\text{eff}} = \frac{-\left(Z_1 - Z_{\text{B}}\right) \pm \sqrt{\left(Z_1 - Z_{\text{B}}\right)^2 - 4\tan^2\left(\beta_{\text{eff}}\ell_2\right) Z_{\text{B}} Z_1}}{2\text{j}\tan\left(\beta_{\text{eff}}\ell_2\right)}\,. \tag{5.14}$$

The sign in (5.14) must be chosen so that the result is physical. Notably, when $Z_{\text{B}}$ tends to $Z_1$, then $Z_{\text{eff}}$ must tend to $Z_1$ too.

**Numerical validation** This process is executed for holey metasurfaces with $p = 4\,\text{mm}$, $h = 3\,\text{mm}$, and a gap $g = 0.1\,\text{mm}$ filled with a dielectric with $\epsilon_{\text{r1}} = 10.7$. The feeding PPWs are filled with a dielectric with $\epsilon_{\text{rL}} = 2$ and length $\ell_{\text{L}} = 15\,\text{mm}$. To verify the coherence of the process, two different number of cells are compared: $N = 5$, and $N = 7$. Fig. 5.10 plots the line impedance computed with (5.14). In the left subfigure, the square holes of the metasurfaces have a size $a = 3\,\text{mm}$, whereas in the right subfigure, $a = 3.5\,\text{mm}$. Both cases are simulated in G-S and nGS configurations.

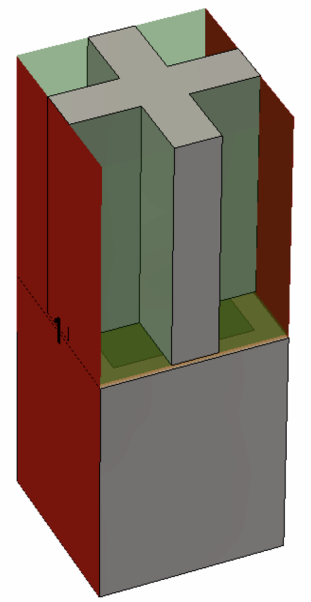

(a) Model of the unit cell.

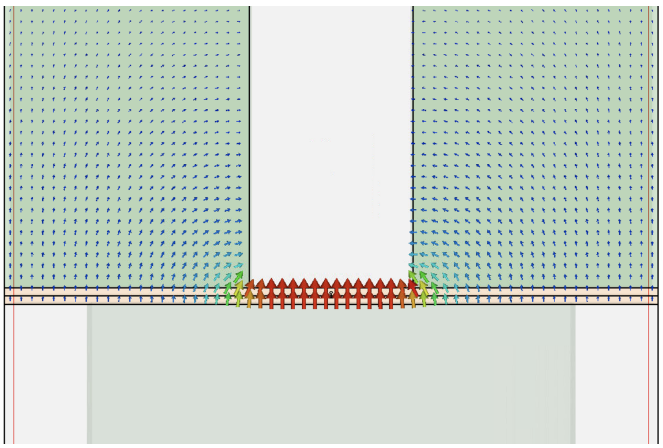

(b) Electric field of the excited mode at the waveguide port.

Figure 5.11: Capture of the CST-simulated unit cell of a holey G-S PPW with square holes. The waveguide ports are represented by the red surfaces.

Fig. 5.10 shows that the low-frequency line impedance of the metasurface waveguide is approximately the same for both numbers of cells $N$. The quasi-static value is not quite convergent yet, and so in the following even more unit cells are used to ensure the validity of this technique. But even though the present example in not completely accurate, it captures the general behavior between different geometries and between the G-S and nGS configurations. The impedance of the holey PPWs is much increased with GS.

#### 5.2.1.2 Effective impedance: CST unit cell simulation

One of the main disadvantages of the reflection technique is the execution time. Simulating tens of unit cells with enough accuracy can become tedious. Therefore, one might wonder whether computing the transfer-matrix of just one unit cell is enough to capture the effective impedance of the periodic waveguide. In the general case of G-S waveguides, this is not true, as explained in [43], because of the multimodal coupling between adjacent unit cells. A special multi-modal transfer-matrix technique must be used, as described in appendix A.3.3. However, we are interested in the quasi-static regime of holey PPWs. We show here that by choosing the cutting plane wisely, the single-modal transfer-matrix of a unit cell is sufficient to obtain a good approximation of the effective impedance in the quasi-static regime.

We consider the unit cell of a holey metasurface waveguide. The first step is the

retrieval of the S-parameters of this unit cell. One cell is modeled in the frequency solver of CST, such that the lower hole is in the middle of the lower plate, and quarters of the upper holes are dispatched at each corner of the unit cell, as pictured in the CST capture Fig. 5.11a. Two waveguide ports are placed at each end of the waveguide (at $z = 0$ and $z = p$), covering the total side of the unit cell with open boundary conditions. The lateral boundary conditions are periodic (at $x = \pm p/2$).

After running the simulation, the solver yields the frequency-dependent S-parameters $S_{21}$ and $S_{11}$. These parameters are normalized with the line impedance of the waveguide ports. This port impedance corresponds to the TEM mode of a waveguide that would have the same cross-section as the unit cell at the waveguide port, but with no variation in the propagation direction. The electric field of this port mode is captured in Fig. 5.11b. However, for periodic structures, CST may struggle to compute the reference port impedance, because the periodic boundary conditions force CST to consider a Bloch mode. Therefore, the port impedance must be computed directly from the excitation fields.

Since the metasurfaces create a system of two metallic conductors, the first excited mode at the port is ensured to be TEM. That is why the port impedance can be characterized by integrating the fields between the two conductors in the plane of the waveguide port. The resulting current and voltage are uniquely defined for a TEM mode [17, p. 166-7]. From the CST simulation, the electric and magnetic fields at the input port are collected. The equivalent voltage is defined as

$$V_{\text{port}} = \int_{-g/2}^{g/2} E_y|_{z=0,x=0} \, \mathrm{d}y \,, \tag{5.15}$$

such that the vertical electric field component is integrated along across the gap separating the metasurfaces. Given the chosen unit cell in Fig. 5.11a, it appears that the linear path defined by $z = 0$ and $x = 0$ had no holes at its ends. Similarly, the equivalent current is defined as

$$I_{\text{port}} = \int_{-p/2}^{p/2} H_x|_{z=0,y=-g/2} \, \mathrm{d}x \,, \tag{5.16}$$

such that the integration path follows the surface of the lower metasurface. From these equivalent values, a reference port impedance is defined as

$$Z_{\text{port}} = V_{\text{port}}/I_{\text{port}} \,. \tag{5.17}$$

This can be done in both G-S and nGS cases.

The retrieval of the normalized impedance $z_{\text{eff}}$ from the simulated S-parameters of the unit cell is described in appendix E.1. Then, the de-normalized line impedance of the waveguide is

$$Z_{\text{eff}} = z_{\text{eff}} Z_{\text{port}} \,. \tag{5.18}$$

This de-normalized line impedance is related to the relative constitutive parameters $\mu_{\text{eff}}$ and $\epsilon_{\text{eff}}$ of an effective dielectric-filled PPW of height $g$ [17, p. 104] with

$$Z_{\text{eff}} = \eta_{\text{eff}} \frac{g}{p} = \eta_0 \sqrt{\frac{\mu_{\text{eff}}}{\epsilon_{\text{eff}}}} \frac{g}{p} \,. \tag{5.19}$$

where $\eta_{\text{eff}}$ would be the effective intrinsic impedance of the equivalent PPW, and where $\eta_0 = \sqrt{\mu_0/\epsilon_0} \simeq 376.7\,\Omega$ is the vacuum impedance.

Once $z_{\text{eff}}$ is found, the effective refractive index can be computed as well, as explained in appendix E.1. According to [191], correctly choosing the sign of $z_{\text{eff}}$ enforces $\text{Im}\{n\} \leq 0$, as required for passive structures. However, this procedure leads to different candidates for $n_{\text{eff}}$, because of the branch points in the formula. In the following, the correct branch point is chosen as the most likely, given our experience of holey metasurface waveguides. For unknown structures, different numbers of unit cells should be simulated in order to find the true index.

In the end, given that the effective refractive index is defined as $n_{\text{eff}} = \sqrt{\mu_{\text{eff}} \epsilon_{\text{eff}}}$, the constitutive parameters are computed as

$$\mu_{\text{eff}} = n_{\text{eff}} Z_{\text{eff}} \frac{p}{g\eta_0} \quad \text{and} \quad \epsilon_{\text{eff}} = \frac{n_{\text{eff}}}{Z_{\text{eff}}} \frac{g\eta_0}{p} \,. \tag{5.20}$$

**Numerical validation** A holey PPW is considered, with dimensions $p = 4\,\text{mm}$, $h = 3\,\text{mm}$, a gap $g = 0.1\,\text{mm}$ filled with a dielectric $\epsilon_{\text{r1}} = 10.7$, and square holes of size $a = 3\,\text{mm}$. G-S and nGS configurations are compared. The unit cell is simulated in CST from 0 to 10 GHz to extract the S-parameters and port fields. Fig. 5.12 shows the simulation results for the S-parameters, the computed Bloch impedance (5.18), the corresponding effective refractive index, and the resulting constitutive parameters (5.20).

The port impedance, computed according to (5.17) and used to de-normalize the line impedance in Fig. 5.12c, has a value of $9.1\,\Omega$ for the G-S structure, and $3.0\,\Omega$ for the nGS structure.

It is notable that this process is not numerically stable when $S_{21} \simeq 1$ and $S_{11} \simeq 0$. This corresponds to frequencies where the first mode reaches the end of the Brillouin zone – that is a stopband for the nGS structure and a mode degeneracy for the GS structure. The formulas for the impedance and the refractive index become undefined in these cases. Therefore, the unit cell transfer-matrix method can only be uses at frequencies yielding stable parameters.

One might wonder whether simulating one single unit cell is enough to display the effective propagation properties of the periodic waveguide. One way to verify this is to simulate more than one cell, and check if the resulting S-parameters yield converging $n_{\text{eff}}$ and $Z_{\text{eff}}$. In Fig. 5.13, the computed refractive index and the line impedance are plotted for different numbers of G-S or nGS cells. Only the real parts are plotted, for clarity.

When considering the effective parameters in Fig. 5.13, the overall behavior of the waveguide is captured by any number of simulated unit cells. However, not only is simulating one single cell faster, but it also yields S-parameters that are better suited for numerical processing. Indeed, the larger the number of cells, the more often $S_{11} =$

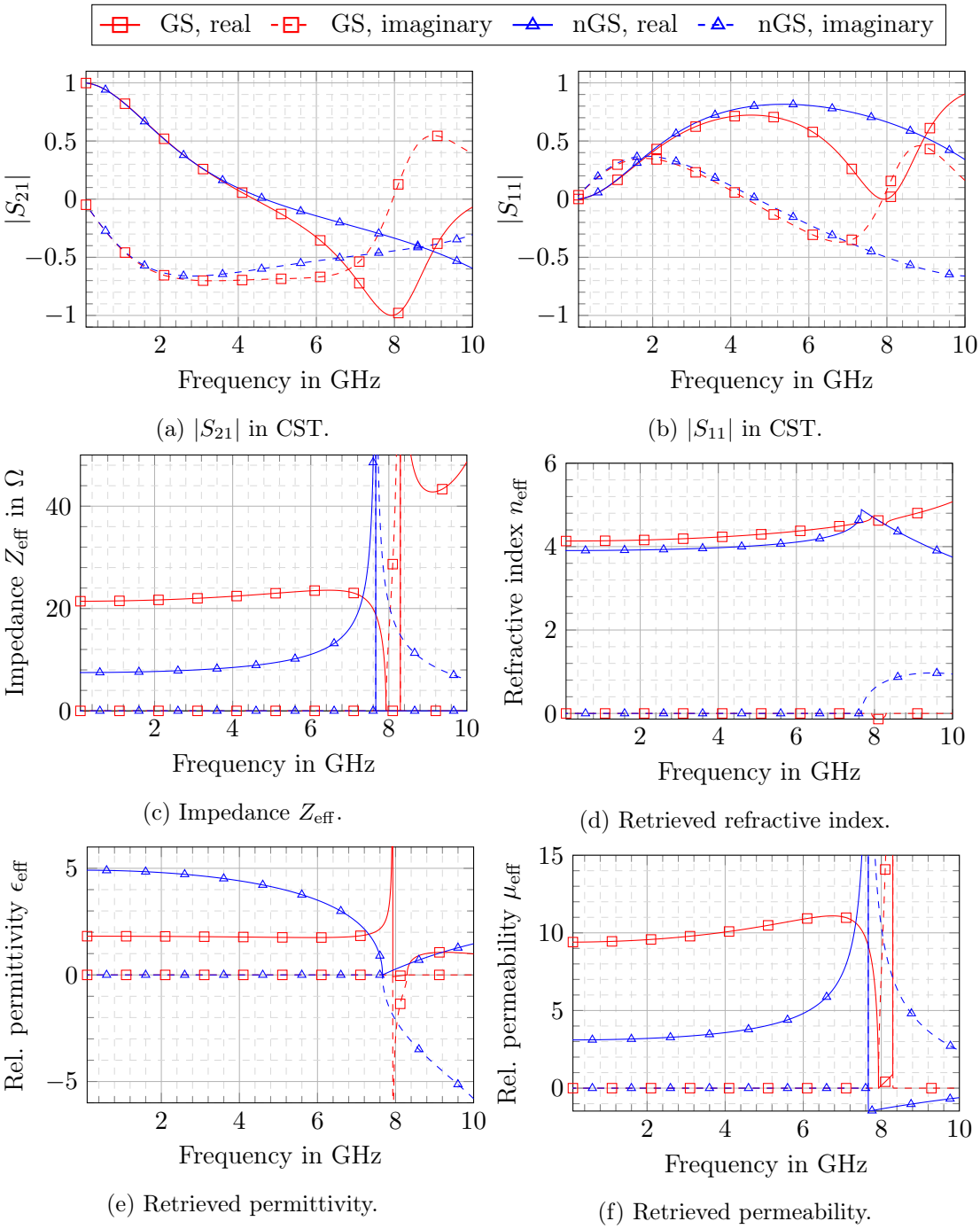


(a) $|S_{21}|$ in CST.

(b) $|S_{11}|$ in CST.

(c) Impedance $Z_{\text{eff}}$.

(d) Retrieved refractive index.

(e) Retrieved permittivity.

(f) Retrieved permeability.

Figure 5.12: Constitutive parameter retrieval for holey PPWs with square holes, from the transfer-matrix of its unit cell obtained with CST. The dimensions are $p = 4\,\text{mm}$, with empty square holes of size $a = 3\,\text{mm}$ and depth $h = 3\,\text{mm}$. The gap between the metasurfaces $g = 0.1\,\text{mm}$ is filled with a dielectric $\epsilon_{\text{r1}} = 10.7$.

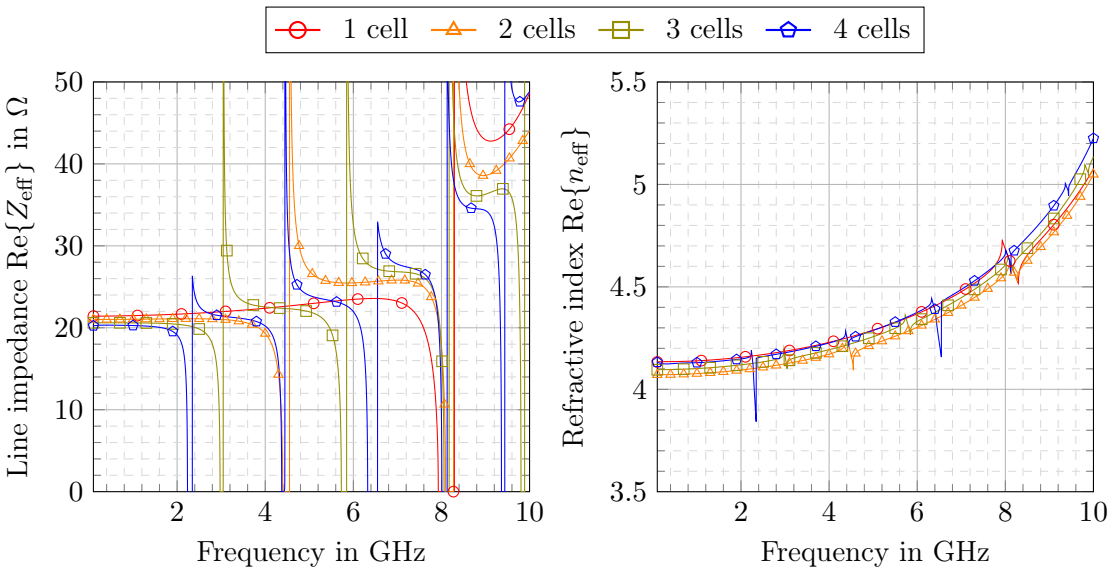


(a) GS, impedance.

(b) GS, refractive index.

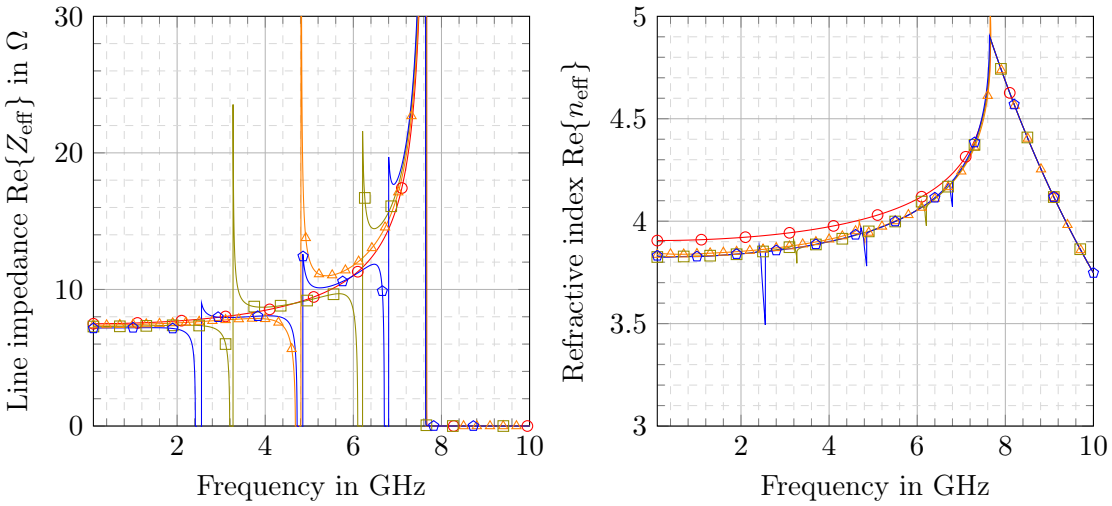


(c) nGS, impedance.

(d) nGS, refractive index.

Figure 5.13: Constitutive parameter retrieval of holey PPWs with square holes, from the transfer-matrix of the unit cell obtained in CST. The curves show the convergence of the effective refractive index and impedance when increasing the number of simulated unit cells. The dimensions are $p = 4\,\text{mm}$, $h = 3\,\text{mm}$, $g = 0.1\,\text{mm}$, and $a = 3\,\text{mm}$. The gap is filled with a dielectric $\epsilon_{\text{r1}} = 10.7$.

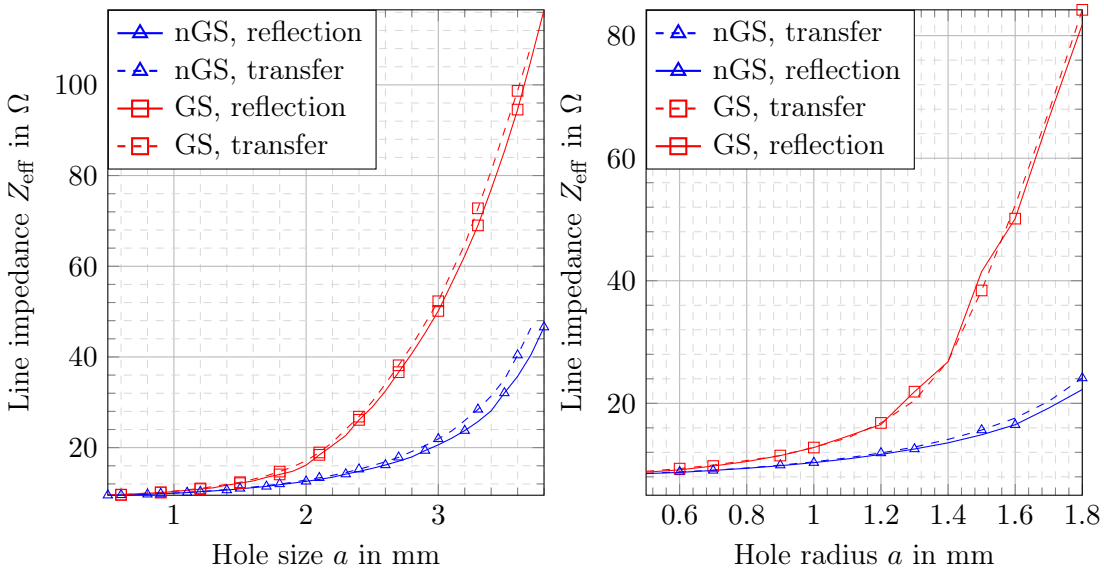


(a) Square holes of size $a$, no dielectrics.

(b) Circular holes of radius $a$ and $(\epsilon_{r2}, \mu_{r2}) = (3, 4)$, gap $(\epsilon_{r1}, \mu_{r1}) = (2, 1.5)$.

Figure 5.14: Effective impedance of holey PPWs as function of the hole size. The impedances are computed in CST, comparing the reflection method and the transfer-matrix method. All structures have dimensions $p = 4\,\text{mm}$, $h = 5\,\text{mm}$, and $g = 0.1\,\text{mm}$, and the nGS design is compared to the G-S design.

0, leading to numerical instabilities that are particularly visible for the impedance in Fig. 5.13a or Fig. 5.13c. Nevertheless, in the prospect of using the homogenized mode-matching method, we are particularly interested in low-frequency results. There, the numerical simulations are stable overall.

#### 5.2.1.3 Consistency of reflection and transfer-matrix methods

When comparing the computed impedances in Fig. 5.10 and in Fig. 5.12, it appears that similar effective impedances are computed with the reflection method and with the transfer-matrix of one unit cell. In these figures, the holey PPW has a periodicity $p = 4\,\text{mm}$, square holes of depth $h = 3\,\text{mm}$ and size $a = 3\,\text{mm}$, and a gap $g = 0.1\,\text{mm}$ filled with a dielectric $\epsilon_{r1} = 10.7$. In the G-S case, both techniques yield $Z_{\text{eff}} \simeq 20\,\Omega$, whereas in the nGS design, $Z_{\text{eff}} \simeq 7\,\Omega$. The comparison between both techniques can be pushed further by varying the shape and the size of the holes.

In Fig. 5.14, the quasi-static impedance $Z_{\text{eff}}$ is computed in CST using the two methods described above: the reflection method of paragraph 5.2.1.1, and the transfer-matrix (with one unit cell) of paragraph 5.2.1.2. For the reflection method, the reflection coefficient is measured at 50 MHz. The S-parameters and the port impedance required for the transfer-matrix method are obtained at the same frequency. In Fig. 5.14a, $Z_{\text{eff}}$ is plotted as a function of the size of the square holes. No dielectrics are used in the

structure. On the other hand, the impedance in Fig. 5.14b corresponds to circular holes filled with a dielectric $(\epsilon_{r2}, \mu_{r2}) = (3, 4)$, whereas the gap is filled with a dielectric $(\epsilon_{r1}, \mu_{r1}) = (2, 1.5)$. Both G-S and nGS are handled, with all structures having dimensions $p = 4\,\text{mm}$, $h = 5\,\text{mm}$, and $g = 0.1\,\text{mm}$.

As hinted by the simulations in the previous sections, the results from the reflection and transfer-matrix methods match quite well. The precision is not very stable, but this was to be expected given how these methods are unsuited for the computation of the effective refractive impedance in the quasi-static regime[3]. Still, both methods characterize the overall behavior of these holey PPWs with canonical hole shapes in the same way, notably the difference between G-S and nGS waveguides.

This is truly interesting, because it opens the door to the definition of a Bloch impedance without the use of commercial solvers. First, it must be understood that both methods are quite different in nature:

- On the one hand, the reflection method yields the impedance that is representative of a PPW TEM mode exciting the Bloch mode of a holey PPW. This impedance also contains the parasitic effects due to the transitions – that is the interaction between the incident TEM mode and the evanescent modes at the transition discontinuity. It gives a good estimation of the Bloch impedance if this discontinuity effect is negligible.

- On the other hand, the transfer-matrix method computes the impedance seen by the port mode loaded with the unit cells of the metasurface waveguide. It gives a good estimation of the Bloch impedance if the Bloch mode is close to the port mode, since higher-order port modes which could play a role are neglected.

The fact that the transfer-matrix impedance is similar to the reflection impedance means that the first excited port mode is sufficient to describe the Bloch mode in the plane chosen for the transfer-matrix method. More precisely, this mode has fields that are proportional to the fields of the Bloch mode in the same plane. This first port mode is TEM, as illustrated in Fig. 5.11b. Therefore, in this plane, the Bloch mode is TEM too. And so, the fields of the Bloch modes can be integrated in this plane in order to yield an effective Bloch impedance that should characterize the waveguide, same as the reflection method and the transfer-matrix method.

If the fields are known analytically in the unit cell, then this integration may be performed without use of a commercial solver, making the effective impedance of the holey PPW much more accessible. This can be done in the quasi-static framework derived in chapter 4.

[3]During simulations, CST issues several warnings about the lower limit of the solvers being reached, and how this affects the precision of the results. This makes sense, given that the dimensions of the unit cell are very small compared to the wavelength. Therefore, a small propagation error across the unit cell has a large impact at a wavelength scale.

### 5.2.2 Quasi-static fields

Having expressions for the fields in the holey PPW unit cell opens the door to the computation of the Bloch impedance by integrating these fields. In this section, the quasi-static electric and magnetic fields are derived from the MMM expressions of section 2.2. However, the MMM expressions need to be simplified with care in the quasi-static regime in order to yield the correct fields.

#### 5.2.2.1 Hole mode coefficients

Homogenizing the dispersion equation (2.42) in the quasi-static regime yields the closed-form formula (4.40) for the effective refractive index. Once this is done, the matrix equation of the MMM (2.38) must be solved to obtain the coefficients $\boldsymbol{c}^{\mathrm{e}}$ and $\boldsymbol{c}^{\mathrm{h}}$ of the hole modes. These coefficients are the nullspace of the dispersion matrix.

In the quasi-static state, the dispersion matrix has the form (4.31). Therefore, we cannot look for the nullspace of the matrix directly, because most of the matrix coefficients vanish when $k_0 \to 0$. This means that the field coefficients must be re-defined, by multiplying or dividing them by $k_0$. This is also motivated by the fact that under their current expressions (2.18), (2.19), (2.20) and (2.21), some of the field components go to infinity when $k_0 \to 0$, which is unphysical.

When $k_0 \to 0$, the electric field components of TM modes in (2.18) and (2.20) become constants with respect to frequency. The magnetic field in (2.19) and (2.21) vanishes. On the other hand, for TE modes, the electric field is constant with respect to frequency, but the magnetic field blows up if $k_0 \to 0$. That is why for TE modes, the mode coefficients are replaced by

$$C_m^{\mathrm{h}} = k_0 C_m^{\mathrm{h}\,\prime}\,. \tag{5.21}$$

If the coefficients $C_m^{\mathrm{h}\,\prime}$ are finite, then when $k_0 \to 0$, the TE electric field vanishes, and the magnetic components are constants with respect to frequency[4]. It is reminded that $c_m^{\mathrm{i}} = C_m^{\mathrm{i}} \sin\left(k_{y,m}^{\mathrm{i}} h\right)$, hence in the following $c_m^{\mathrm{i}\,\prime} = C_m^{\mathrm{i}\,\prime} \sin\left(k_{y,m}^{\mathrm{i}} h\right)$, with $c_m^{\mathrm{h}} = k_0 c_m^{\mathrm{h}\,\prime}$.

With the coefficients change (5.21), the dispersion equation (2.38) with the quasi-static matrix (4.31) is equivalent to

$$\begin{bmatrix} k_1^2 \left(\underline{\boldsymbol{\Sigma}}^{\mathrm{e}} + \frac{n_\theta^2}{n_1^2 - n_\theta^2} \frac{2}{g} \boldsymbol{u}^{\mathrm{e}} [\boldsymbol{u}^{\mathrm{e}}]^{\mathrm{H}}\right) & \mathrm{j}k_1 \frac{n_\theta n_1}{n_1^2 - n_\theta^2} \frac{2}{g} \boldsymbol{u}^{\mathrm{e}} \left[\boldsymbol{u}^{\mathrm{h}}\right]^{\mathrm{H}} \\ -\mathrm{j}k_1 \frac{n_\theta n_1}{n_1^2 - n_\theta^2} \frac{2}{g} \boldsymbol{u}^{\mathrm{h}} [\boldsymbol{u}^{\mathrm{e}}]^{\mathrm{H}} & \underline{\boldsymbol{\Sigma}}^{\mathrm{h}} + \frac{n_1^2}{n_1^2 - n_\theta^2} \frac{2}{g} \boldsymbol{u}^{\mathrm{h}} \left[\boldsymbol{u}^{\mathrm{h}}\right]^{\mathrm{H}} \end{bmatrix} \begin{bmatrix} \boldsymbol{c}^{\mathrm{e}} \\ k_0 \boldsymbol{c}^{\mathrm{h}\prime} \end{bmatrix} = \boldsymbol{0}\,. \tag{5.22}$$

In order to find the coefficients $\boldsymbol{c}^{\mathrm{e}}$ and $\boldsymbol{c}^{\mathrm{h}\prime}$, the $k_0$ factor of the latter can be re-distributed in the second column of the matrix. This leads to a $k_0^2$ factor in the first row, and a

[4]Changing the field coefficients at this point may seem tedious. It could have been done earlier in the MMM process in chapter 4. However, the definitions in chapter 4 allow to keep the same formalism for TE and TM modes during the MMM. Otherwise, the field expressions would be different for each kind of mode, complicating all previous sections.

$k_0$ factor in the second row. All these factors can be removed without changing the nullspace of the matrix. In the end, the equation to be solved is

$$\begin{bmatrix} n_1^2\left(\underline{\boldsymbol{\Sigma}}^{\mathrm{e}} + \frac{n_\theta^2}{n_1^2-n_\theta^2}\frac{2}{g}\boldsymbol{u}^{\mathrm{e}}[\boldsymbol{u}^{\mathrm{e}}]^{\mathrm{H}}\right) & \mathrm{j}n_1\frac{n_\theta n_1}{n_1^2-n_\theta^2}\frac{2}{g}\boldsymbol{u}^{\mathrm{e}}\left[\boldsymbol{u}^{\mathrm{h}}\right]^{\mathrm{H}} \\ -\mathrm{j}n_1\frac{n_\theta n_1}{n_1^2-n_\theta^2}\frac{2}{g}\boldsymbol{u}^{\mathrm{h}}[\boldsymbol{u}^{\mathrm{e}}]^{\mathrm{H}} & \underline{\boldsymbol{\Sigma}}^{\mathrm{h}} + \frac{n_1^2}{n_1^2-n_\theta^2}\frac{2}{g}\boldsymbol{u}^{\mathrm{h}}\left[\boldsymbol{u}^{\mathrm{h}}\right]^{\mathrm{H}} \end{bmatrix} \begin{bmatrix} \boldsymbol{c}^{\mathrm{e}} \\ \boldsymbol{c}^{\mathrm{h}\prime} \end{bmatrix} = \boldsymbol{0}\,, \tag{5.23}$$

which is totally independent of the frequency, and so none of the coefficients in (5.23) vanish when $k_0 \to 0$.

#### 5.2.2.2 Gap harmonic coefficients

The harmonic fields in the gap depend on the hole mode coefficients, as expressed by (2.30). However, TE and TM modes have a different impact depending on the symmetry of the gap harmonics. This is developed in the following paragraphs, where we define the coefficients

$$\bar{d}^{\mathrm{e}(s\ell)} = -\mathrm{j}\sum_m \frac{c_m^{\mathrm{e}}}{k_m^{\mathrm{e}}}\bar{e}_{y,m}^{(s\ell)*} \quad \text{and} \quad \bar{\boldsymbol{d}}^{\mathrm{h}(s\ell)} = \sum_m c_m^{\mathrm{h}\,\prime}\bar{\boldsymbol{e}}_{\mathrm{t},m}^{\mathrm{h}(s\ell)*}\,. \tag{5.24}$$

In the following, the term $\bar{\boldsymbol{d}}^{\mathrm{h}(s\ell)}$ represent the influence of the TE hole modes onto the harmonic fields. On the other hand, $\bar{\boldsymbol{d}}^{\mathrm{e}(s\ell)}$ holds the TM influence of the hole modes.

**Fundamental harmonic** For the fundamental harmonic, $\boldsymbol{b}^{(00)} = 0$ as defined in (2.30b), but according to (2.30a),

$$\begin{aligned} \boldsymbol{a}^{(00)} &= \frac{-\mathrm{j}}{p_x p_z}\frac{1}{\sin\left(k_y^{(00)}\frac{g}{2}\right)}\left(\sum_m c_m^{\mathrm{e}}\tilde{\boldsymbol{e}}_{\mathrm{t},m}^{\mathrm{e}(00)*} + \sum_m c_m^{\mathrm{h}}\tilde{\boldsymbol{e}}_{\mathrm{t},m}^{\mathrm{h}(00)*}\right) \\ &\underset{k_0\to 0}{=} \frac{-\mathrm{j}}{p_x p_z}\frac{2}{gk_0\sqrt{n_1^2-n_\theta^2}}\left(\sum_m c_m^{\mathrm{e}}\frac{-\mathrm{j}n_\theta k_0}{k_m^{\mathrm{e}}}\begin{bmatrix}\cos\theta\\ \sin\theta\end{bmatrix}\bar{e}_{y,m}^{(00)*} + \sum_m k_0 c_m^{\mathrm{h}\,\prime}\bar{\boldsymbol{e}}_{\mathrm{t},m}^{\mathrm{h}(00)*}\right) \\ &\underset{k_0\to 0}{=} \frac{-2\mathrm{j}}{p_x p_z g\sqrt{n_1^2-n_\theta^2}}\left(n_\theta\begin{bmatrix}\cos\theta\\ \sin\theta\end{bmatrix}\bar{d}^{\mathrm{e}(00)} + \bar{\boldsymbol{d}}^{\mathrm{h}(00)}\right)\,. \end{aligned} \tag{5.25}$$

For the magnetic field (2.25b), these coefficients are multiplied by the admittance matrix (2.24). At low frequency and for $(s,\ell) = (0,0)$, the latter can be written as

$$\underline{\boldsymbol{Y}}^{(00)} \underset{k_0\to 0}{=} \frac{\mathrm{j}}{\eta_0\mu_{\mathrm{r}1}\sqrt{n_1^2-n_\theta^2}}\left(n_\theta^2\begin{bmatrix}\cos\theta\\ \sin\theta\end{bmatrix}\begin{bmatrix}-\sin\theta\\ \cos\theta\end{bmatrix}^{\mathrm{T}} - n_1^2\begin{bmatrix}0 & 1\\ -1 & 0\end{bmatrix}\right)\,. \tag{5.26}$$

Therefore, both $\boldsymbol{a}^{(00)}$ and $\underline{\boldsymbol{Y}}^{(00)}$ are frequency-independent constants at low frequency. Therefore, from (2.25), (2.26) and (2.27), the low-frequency field components of the

fundamental harmonic are

$$\boldsymbol{E}_{\mathrm{t}}^{(00)} = \boldsymbol{a}^{(00)} \sin\left(k_y^{(00)} y\right) F^{(00)} \underset{k_0 \to 0}{=} 0\,, \tag{5.27a}$$

$$\boldsymbol{H}_{\mathrm{t}}^{(00)} = \underline{\boldsymbol{Y}}^{(00)} \boldsymbol{a}^{(00)} \cos\left(k_y^{(00)} y\right) F^{(00)} \underset{k_0 \to 0}{=} \underline{\boldsymbol{Y}}^{(00)} \boldsymbol{a}^{(00)}\,, \tag{5.27b}$$

$$E_y^{(00)} = -\mathrm{j} \frac{F^{(00)}}{k_y^{(00)}} \begin{bmatrix} k_z \\ k_x \end{bmatrix}^{\mathrm{T}} \boldsymbol{a}^{(00)} \cos\left(k_y^{(00)} y\right) \underset{k_0 \to 0}{=} \frac{-\mathrm{j} n_\theta}{\sqrt{n_1^2 - n_\theta^2}} \begin{bmatrix} \cos\theta \\ \sin\theta \end{bmatrix}^{\mathrm{T}} \boldsymbol{a}^{(00)}\,, \tag{5.27c}$$

$$H_y^{(00)} = \frac{F^{(00)}}{k_1 \eta_1} \begin{bmatrix} -k_x \\ k_z \end{bmatrix}^{\mathrm{T}} \boldsymbol{a}^{(00)} \sin\left(k_y^{(00)} y\right) \underset{k_0 \to 0}{=} 0\,, \tag{5.27d}$$

since at low frequency $\sin\left(k_y^{(00)} y\right) \to 0$, $\cos\left(k_y^{(00)} y\right) \to 1$, and $F^{(00)} \to 1$. As such, both TM and TE modes contribute to the field of the fundamental harmonic, because $\boldsymbol{a}^{(00)}$ defined in (5.25) contains both $\bar{\boldsymbol{d}}^{\mathrm{h}(s\ell)}$ and $\bar{\boldsymbol{d}}^{\mathrm{e}(s\ell)}$.

**Even-order higher harmonics** When $s + \ell$ is even and $(s, \ell) \neq (0, 0)$, $\boldsymbol{b}^{(s\ell)} = 0$, but according to (2.30a),

$$\begin{aligned} \boldsymbol{a}^{(s\ell)} &= \frac{-\mathrm{j}}{p_x p_z} \frac{1}{\sin\left(k_y^{(s\ell)} \frac{g}{2}\right)} \left( \sum_m c_m^{\mathrm{e}} \tilde{\boldsymbol{e}}_{\mathrm{t},m}^{\mathrm{e}(s\ell)*} + \sum_m c_m^{\mathrm{h}} \tilde{\boldsymbol{e}}_{\mathrm{t},m}^{\mathrm{h}(s\ell)*} \right) \\ &\underset{k_0 \to 0}{=} \frac{-\mathrm{j}}{p_x p_z} \frac{1}{\sin\left(\mathrm{j}\Gamma^{(s\ell)} \frac{g}{2}\right)} \left( \sum_m c_m^{\mathrm{e}} \frac{-\mathrm{j}}{k_m^{\mathrm{e}}} \begin{bmatrix} \frac{s2\pi}{p_z} \\ \frac{\ell 2\pi}{p_x} \end{bmatrix} \bar{e}_{y,m}^{(s\ell)*} + \sum_m k_0 c_m^{\mathrm{h}\,\prime} \bar{\boldsymbol{e}}_{\mathrm{t},m}^{\mathrm{h}(s\ell)*} \right) \\ &\underset{k_0 \to 0}{=} \frac{-\mathrm{j}}{p_x p_z \sin\left(\mathrm{j}\Gamma^{(s\ell)} \frac{g}{2}\right)} \left( \boldsymbol{\Gamma}^{(s\ell)} \bar{d}^{\mathrm{e}(s\ell)} + k_0 \bar{\boldsymbol{d}}^{\mathrm{h}(s\ell)} \right)\,, \end{aligned} \tag{5.28}$$

where it is reminded that $\boldsymbol{\Gamma}^{(s\ell)} = [s2\pi/p_z, \ell 2\pi/p_x]^{\mathrm{T}}$ and $\Gamma^{(s\ell)} = ||\boldsymbol{\Gamma}^{(s\ell)}||$. One could be tempted to simplify the expression further: the TE term seems negligible with respect to the TM term, due to a $k_0$ factor. However, this is not true for some of the harmonic field components. Indeed, for the magnetic field (2.25b), these coefficients are multiplied by the admittance matrix (2.24). At low frequency, the latter can be written as

$$\underline{\boldsymbol{Y}}^{(s\ell)} \underset{k_0 \to 0}{=} \frac{1}{k_0 \eta_0 \mu_{\mathrm{r}1} \Gamma^{(s\ell)}} \left( \boldsymbol{\Gamma}^{(s\ell)} \left[ \hat{\boldsymbol{y}} \times \boldsymbol{\Gamma}^{(s\ell)} \right]^{\mathrm{T}} - k_1^2 \begin{bmatrix} 0 & 1 \\ -1 & 0 \end{bmatrix} \right)\,. \tag{5.29}$$

This matrix is proportional to $1/k_0$. When it is multiplied to $\boldsymbol{a}^{(s\ell)}$, the cancelling of some TM terms and the division by $k_0$ causes the TE terms of $\boldsymbol{a}^{(s\ell)}$ to be necessary. Taking this into account, from (2.25), (2.26) and (2.27), the low-frequency field components of

the higher even-order harmonics are

$$\boldsymbol{E}_{\mathrm{t}}^{(s\ell)} = \boldsymbol{a}^{(s\ell)} \sin\left(k_y^{(s\ell)} y\right) F^{(s\ell)}\,, \tag{5.30a}$$

$$\boldsymbol{H}_{\mathrm{t}}^{(s\ell)} = \underline{\boldsymbol{Y}}^{(s\ell)} \boldsymbol{a}^{(s\ell)} \cos\left(k_y^{(s\ell)} y\right) F^{(s\ell)}\,, \tag{5.30b}$$

$$E_y^{(s\ell)} = -\mathrm{j}\frac{F^{(s\ell)}}{k_y^{(s\ell)}} \begin{bmatrix} k_z^{(s)} \\ k_x^{(\ell)} \end{bmatrix}^{\mathrm{T}} \boldsymbol{a}^{(s\ell)} \cos\left(k_y^{(s\ell)} y\right), \tag{5.30c}$$

$$H_y^{(s\ell)} = \frac{F^{(s\ell)}}{k_1 \eta_1} \begin{bmatrix} -k_x^{(\ell)} \\ k_z^{(s)} \end{bmatrix}^{\mathrm{T}} \boldsymbol{a}^{(s\ell)} \sin\left(k_y^{(s\ell)} y\right), \tag{5.30d}$$

and so, in the quasi-static regime,

$$\boldsymbol{E}_{\mathrm{t}}^{(s\ell)} \underset{k_0\to 0}{=} -\frac{\mathrm{j}\bar{F}^{(s\ell)} \sin\left(\mathrm{j}\Gamma^{(s\ell)} y\right)}{p_x p_z \sin\left(\mathrm{j}\Gamma^{(s\ell)} \frac{g}{2}\right)} \boldsymbol{\Gamma}^{(s\ell)} \bar{d}^{\mathrm{e}(s\ell)}\,, \tag{5.31a}$$

$$\boldsymbol{H}_{\mathrm{t}}^{(s\ell)} \underset{k_0\to 0}{=} -\frac{\mathrm{j}\bar{F}^{(s\ell)} \cos\left(\mathrm{j}\Gamma^{(s\ell)} y\right)}{\eta_0 \mu_{\mathrm{r}1} p_x p_z \Gamma^{(s\ell)} \sin\left(\mathrm{j}\Gamma^{(s\ell)} \frac{g}{2}\right)} \boldsymbol{\Gamma}^{(s\ell)} \left[\hat{\boldsymbol{y}} \times \boldsymbol{\Gamma}^{(s\ell)}\right]^{\mathrm{T}} \bar{\boldsymbol{d}}^{\mathrm{h}(s\ell)}\,, \tag{5.31b}$$

$$E_y^{(s\ell)} \underset{k_0\to 0}{=} \frac{\mathrm{j}\bar{F}^{(s\ell)} \Gamma^{(s\ell)} \cos\left(\mathrm{j}\Gamma^{(s\ell)} y\right)}{p_x p_z \sin\left(\mathrm{j}\Gamma^{(s\ell)} \frac{g}{2}\right)} \bar{d}^{\mathrm{e}(s\ell)}\,, \tag{5.31c}$$

$$H_y^{(s\ell)} \underset{k_0\to 0}{=} -\frac{\mathrm{j}\bar{F}^{(s\ell)} \sin\left(\mathrm{j}\Gamma^{(s\ell)} y\right)}{\eta_0 \mu_{\mathrm{r}1} p_x p_z \sin\left(\mathrm{j}\Gamma^{(s\ell)} \frac{g}{2}\right)} \left[\hat{\boldsymbol{y}} \times \boldsymbol{\Gamma}^{(s\ell)}\right]^{\mathrm{T}} \bar{\boldsymbol{d}}^{\mathrm{h}(s\ell)}\,. \tag{5.31d}$$

Therefore, in the gap, the low-frequency electric field of the higher harmonics depends only on the TM hole modes, whereas the magnetic field depends only on the TE hole modes.

Note that when the structure is nGS, then these are the expressions for all the harmonics, not just the even-order harmonics.

**Odd-order harmonics** When $s+\ell$ is odd, $\boldsymbol{a}^{(s\ell)} = 0$, but

$$\begin{aligned} \boldsymbol{b}^{(s\ell)} &= \frac{\mathrm{j}}{p_x p_z} \frac{1}{\cos\left(k_y^{(s\ell)} \frac{g}{2}\right)} \left( \sum_m c_m^{\mathrm{e}} \tilde{\boldsymbol{e}}_{\mathrm{t},m}^{\mathrm{e}(s\ell)*} + \sum_m c_m^{\mathrm{h}} \tilde{\boldsymbol{e}}_{\mathrm{t},m}^{\mathrm{h}(s\ell)*} \right) \\ &\underset{k_0\to 0}{=} \frac{\mathrm{j}}{p_x p_z \cos\left(\mathrm{j}\Gamma^{(s\ell)} \frac{g}{2}\right)} \left( \boldsymbol{\Gamma}^{(s\ell)} \bar{d}^{\mathrm{e}(s\ell)} + k_0 \bar{\boldsymbol{d}}^{\mathrm{h}(s\ell)} \right). \end{aligned} \tag{5.32}$$

Like for even-order harmonics, the dominance of TM or TE hole modes on the gap fields cannot be decided yet. At low-frequency, the admittance matrix of odd-order harmonics has the same form as in (5.29). Consequently, the fields of odd-order harmonics

are

$$\boldsymbol{E}_{\mathrm{t}}^{(s\ell)} = \boldsymbol{b}^{(s\ell)} \cos\left(k_y^{(s\ell)} y\right) F^{(s\ell)}\,, \tag{5.33a}$$

$$\boldsymbol{H}_{\mathrm{t}}^{(s\ell)} = -\underline{\boldsymbol{Y}}^{(s\ell)} \boldsymbol{b}^{(s\ell)} \sin\left(k_y^{(s\ell)} y\right) F^{(s\ell)}\,, \tag{5.33b}$$

$$E_y^{(s\ell)} = \mathrm{j}\frac{F^{(s\ell)}}{k_y^{(s\ell)}} \begin{bmatrix} k_z^{(s)} \\ k_x^{(\ell)} \end{bmatrix}^{\mathrm{T}} \boldsymbol{b}^{(s\ell)} \sin\left(k_y^{(s\ell)} y\right), \tag{5.33c}$$

$$H_y^{(s\ell)} = \frac{F^{(s\ell)}}{k_1 \eta_1} \begin{bmatrix} -k_x^{(\ell)} \\ k_z^{(s)} \end{bmatrix}^{\mathrm{T}} \boldsymbol{b}^{(s\ell)} \cos\left(k_y^{(s\ell)} y\right), \tag{5.33d}$$

yielding, in the quasi-static regime,

$$\boldsymbol{E}_{\mathrm{t}}^{(s\ell)} \underset{k_0\to 0}{=} \frac{\mathrm{j}\bar{F}^{(s\ell)} \cos\left(\mathrm{j}\Gamma^{(s\ell)} y\right)}{p_x p_z \cos\left(\mathrm{j}\Gamma^{(s\ell)} \frac{g}{2}\right)} \boldsymbol{\Gamma}^{(s\ell)} \bar{d}^{\mathrm{e}(s\ell)}\,, \tag{5.34a}$$

$$\boldsymbol{H}_{\mathrm{t}}^{(s\ell)} \underset{k_0\to 0}{=} -\frac{\mathrm{j}\bar{F}^{(s\ell)} \sin\left(\mathrm{j}\Gamma^{(s\ell)} y\right)}{\eta_0 \mu_{\mathrm{r}1} p_x p_z \Gamma^{(s\ell)} \cos\left(\mathrm{j}\Gamma^{(s\ell)} \frac{g}{2}\right)} \boldsymbol{\Gamma}^{(s\ell)} \left[\hat{\boldsymbol{y}} \times \boldsymbol{\Gamma}^{(s\ell)}\right]^{\mathrm{T}} \vec{\boldsymbol{d}}^{\mathrm{h}(s\ell)}\,, \tag{5.34b}$$

$$E_y^{(s\ell)} \underset{k_0\to 0}{=} \frac{\mathrm{j}\bar{F}^{(s\ell)} \Gamma^{(s\ell)} \sin\left(\mathrm{j}\Gamma^{(s\ell)} y\right)}{p_x p_z \cos\left(\mathrm{j}\Gamma^{(s\ell)} \frac{g}{2}\right)} \bar{d}^{\mathrm{e}(s\ell)}\,, \tag{5.34c}$$

$$H_y^{(s\ell)} \underset{k_0\to 0}{=} \frac{\mathrm{j}\bar{F}^{(s\ell)} \cos\left(\mathrm{j}\Gamma^{(s\ell)} y\right)}{\eta_0 \mu_{\mathrm{r}1} p_x p_z \cos\left(\mathrm{j}\Gamma^{(s\ell)} \frac{g}{2}\right)} \left[\hat{\boldsymbol{y}} \times \boldsymbol{\Gamma}^{(s\ell)}\right]^{\mathrm{T}} \vec{\boldsymbol{d}}^{\mathrm{h}(s\ell)}\,. \tag{5.34d}$$

Similarly to even-order harmonics, the electric components are related to the TM hole modes, whereas the magnetic components are related to the TE modes.

#### 5.2.2.3 Numerical computation of the modal fields in the gap

After computing the effective refractive index with (4.40), and finding the mode coefficients by solving (5.23), the fields in the gap can be computed with (5.27), (5.31), and (5.34). As an example, we simulate a holey PPW of periods $p_z = p_x = 4\,\mathrm{mm}$ and gap $g = 0.1\,\mathrm{mm}$. The holes are squares of size $a = 3\,\mathrm{mm}$, and have a depth $h = 5\,\mathrm{mm}$. The gap and the holes are filled with vacuum. Both G-S and nGS configurations are considered. The waves propagate in the plane $zx$ along the $z$-axis, which corresponds to $\theta = 0°$. Fig. 5.15 compares the fields computed with our quasi-static homogenization framework (top subfigures (a) to (c)) with the fields simulated with CST's eigenmode solver at approximately 10 MHz (bottom subfigures (d) to (f)). The magnitude of all field components is plotted.

The fields computed with the quasi-static framework match the CST-simulated fields for all components, up to a scaling factor. The differences come from the need of an even finer mesh in CST, which leads to extended execution times. Even with the rough mesh used in Fig. 5.15, computing the fields with CST is still slower than the quasi-static analytic computation by several orders of magnitude.

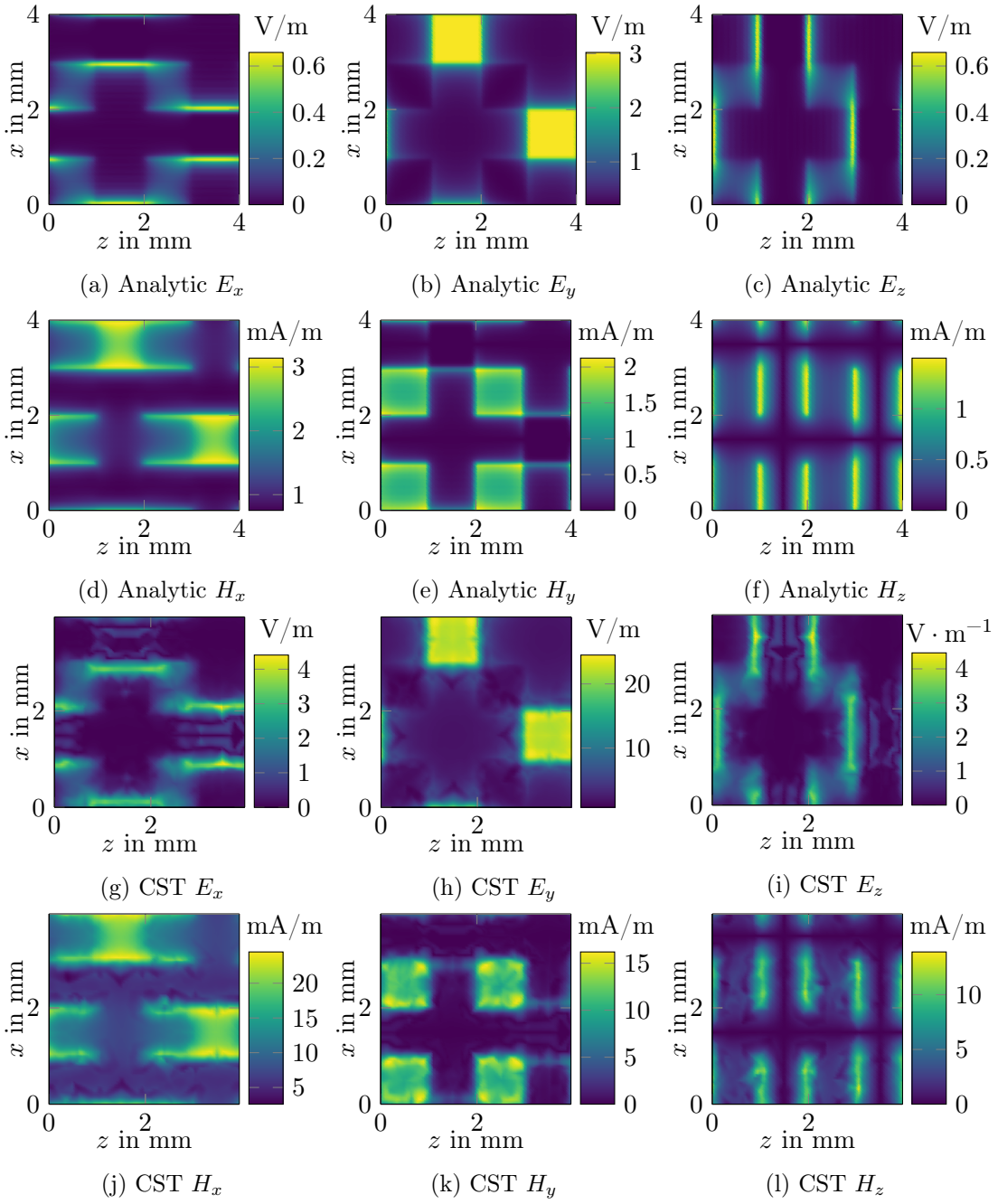


(a) Analytic $E_x$ (b) Analytic $E_y$ (c) Analytic $E_z$

(d) Analytic $H_x$ (e) Analytic $H_y$ (f) Analytic $H_z$

(g) CST $E_x$ (h) CST $E_y$ (i) CST $E_z$

(j) CST $H_x$ (k) CST $H_y$ (l) CST $H_z$

Figure 5.15: Fields of the G-S holey PPW, computed analytically in the quasi-static regime as described in paragraph 5.2.2.2, or with CST at approx. 10 MHz. The cutting plane is $y = 0$ – that is in-between the two metasurfaces – and the waves propagate in the $z$-direction. The structure has $p_z = p_x = 4\,\text{mm}$, $g = 0.1\,\text{mm}$, $a = 3\,\text{mm}$, $h = 5\,\text{mm}$, and is filled with vacuum.

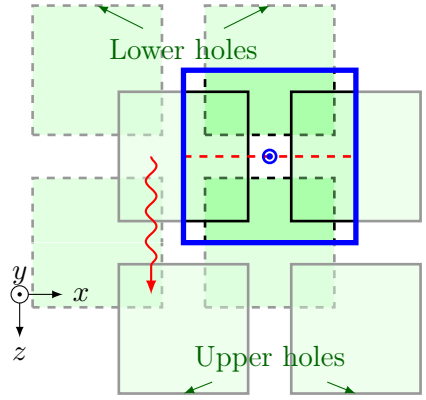


(a) View of the $zx$-plane. The propagation direction is indicated by the red arrow.

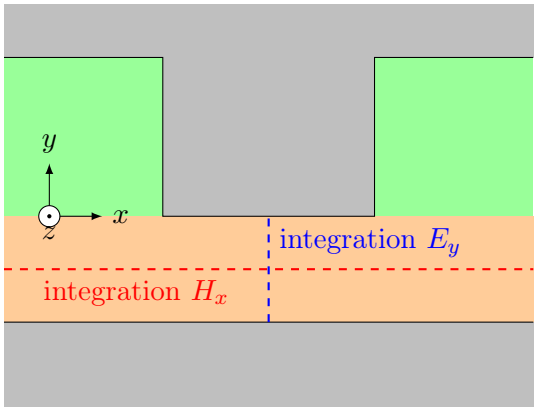


(b) View of the $xy$-plane, normal to the propagation direction.

Figure 5.16: Holey G-S PPW with square holes, as considered for the definition of the Bloch impedance. The propagation direction is the $z$-axis. The unit cell is framed in blue. The fields are integrated in the $xy$-plane between the metasurfaces, as indicated by the dashed red and blue paths – for magnetic and electric field integration, respectively.

### 5.2.3 Bloch impedance and impedance matching

In section 5.2.1.3, the CST-computated impedance is the same with the reflection method or with the transfer-matrix method. This means that if the fields of the Bloch mode are available, the effective impedance can be computed by integrating these fields. Indeed, in the port plane of the transfer-matrix simulation, the Bloch mode should be quasi-TEM. Therefore, the integration of the electric and magnetic fields in this plane does not depend on the the integration path, defining a unique Bloch impedance. Note that these observations are made only for canonical hole shapes, that is square and circular.

The quasi-static fields of holey PPWs have been derived analytically in section 5.2.2. Therefore, for a given waveguide geometry, the effective refractive index is computed with (4.40). This value can then be inserted in the quasi-static expression (5.27), (5.31), (5.34), which yield the electric and magnetic fields in the gap between the metasurfaces. Then, these fields can be integrated in the unit cell in order to yield effective Bloch voltages and currents. The integration paths are shown in Fig. 5.16 for square holes. The integration plane is the same as CST's waveguide port in Fig. 5.11a. It is placed such that it is normal to the propagation direction and between two holes of the lower metasurface (or the upper metasurface). The magnetic field is integrated in this plane across the total width of the unit cell. The electric field is integrated at the point where there is no upper hole, along a path binding the two conductors without entering the holes. According to this, the Bloch voltage and current are defined as

$$V_\mathrm{B} = \int_{y=-\frac{g}{2}}^{\frac{g}{2}} E_y|_{\substack{z=z_0\\x=x_0}} \,\mathrm{d}y\,, \quad \text{and} \quad I_\mathrm{B} = \int_{x=0}^{p_x} H_x|_{\substack{z=z_0\\y=y_0}} \,\mathrm{d}x\,, \tag{5.35}$$

where $(z_0, x_0, y_0)$ is a point in the integration plane in-between holes. Finally, the effective Bloch impedance is computed as

$$Z_{\mathrm{B}} = \frac{V_{\mathrm{B}}}{I_{\mathrm{B}}}\,. \tag{5.36}$$

To illustrate the validity of this procedure, the quasi-static fields in the unit cell of different holey PPWs are plotted in Figs. 5.17, 5.18, 5.19 and 5.20, respectively for G-S square holes, nGS square holes, G-S circular holes, and nGS circular holes. All the structures in these examples have square periodicities $p_z = p_x = 4\,\mathrm{mm}$, a gap $g = 0.1\,\mathrm{mm}$ and a hole depth $h = 5\,\mathrm{mm}$. PPWs with square holes do not use dielectrics, and the hole size is $a = 3\,\mathrm{mm}$. On the other hand, the circular holes of radius $a = 1.7\,\mathrm{mm}$ are filled with a dielectric $(\epsilon_{\mathrm{r}2}, \mu_{\mathrm{r}2}) = (3, 4)$, combined with a gap dielectric $(\epsilon_{\mathrm{r}1}, \mu_{\mathrm{r}1}) = (2, 1.5)$. For each waveguide, four field components are plotted. Subfigures (a) and (b) represent the magnitude of the longitudinal field electric and magnetic components $|E_z|$ and $|H_z|$. These components are of interest, because they must be zero for the Bloch mode to be quasi-TEM in the integration plane. Subfigures (c) and (d) represent the magnitude of the transverse field components parallel to the integration paths. For the electric field integration, the shortest path binding the two metasurfaces is aligned with the $y$-axis, and the the field $|E_y|$ is plotted in (c). Similarly, the straightest path crossing the unit cell is the $x$-axis, and so in (d) the magnetic component of interest is $|H_x|$. For better visualization, each field component is plotted in the plane $y = 0$ (in-between the metasurfaces), as well as in the integration plane $z = p/2$.

For square and circular holes, Figs. 5.17 to 5.20 confirm that in the chosen plane, there are no longitudinal field components, whether the structure is G-S or not. Thus, the transverse fields can be integrated along the represented paths in order to yield the Bloch voltage and current (5.35). In the next section, the resulting Bloch impedance (5.36) is compared to the reference impedance computed in CST.

#### 5.2.3.1 Comparison with the CST reflection method

In the following, a holey PPW is considered, with $p_z = p_x = 4\,\mathrm{mm}$, $g = 0.1\,\mathrm{mm}$, and holes of depth $h = 5\,\mathrm{mm}$. The quasi-static effective refractive index is computed with (4.40), and then the Bloch impedance is computed with (5.36). With these two pieces of information, the waveguide can be fully homogenized, retrieving effective constitutive permittivities and permeabilities. In Figs. 5.21 and 5.22, the effective media parameters are plotted as functions of the hole size $a$, for both G-S and nGS configurations. They are compared to the value obtained from the reflection method described in section 5.2.1.1, with CST simulations at 0.1 GHz. In Fig. 5.21, the holes are square, and the structure is filled with vacuum. In Fig. 5.22, the circular holes are filled with a dielectric $(\epsilon_{\mathrm{r}2}, \mu_{\mathrm{r}2}) = (3, 4)$, and the gap is filled with a dielectric $(\epsilon_{\mathrm{r}1}, \mu_{\mathrm{r}1}) = (2, 1.5)$.

The results in Figs. 5.21 and 5.22 show good agreement between the quasi-static Bloch impedance (5.36) and the reference impedance computed in CST, for square and circular holes, and for G-S and nGS waveguides. One could even be tempted to trust the

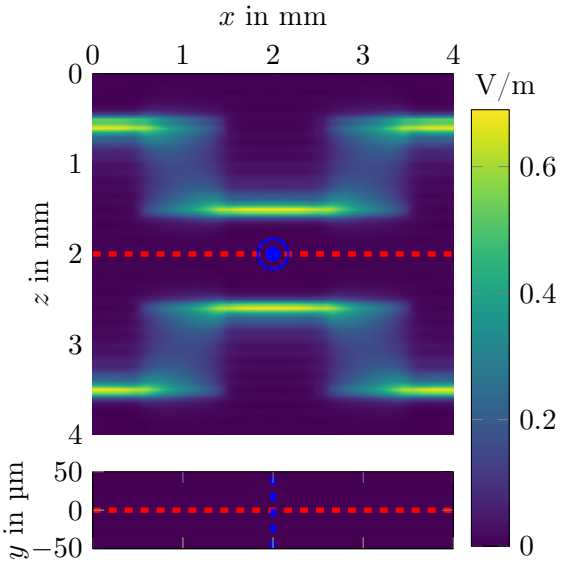


(a) $|E_z|$ (top and cross views).

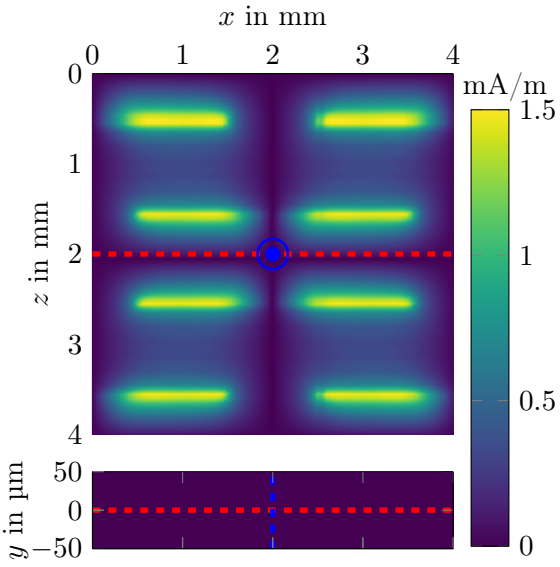


(b) $|H_z|$ (top and cross views).

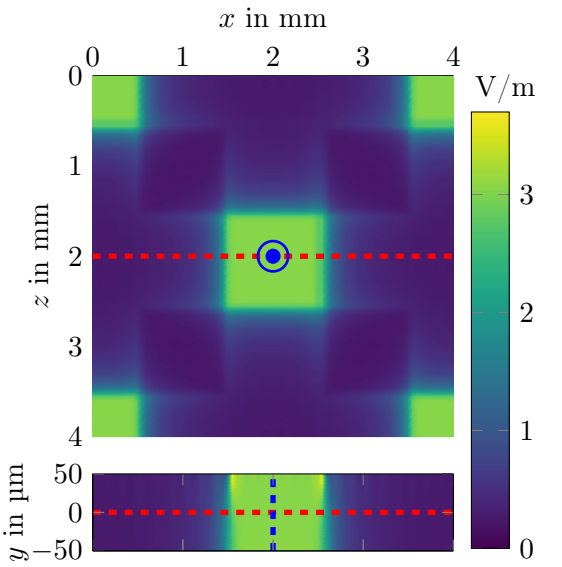


(c) $|E_y|$ (top and cross views).

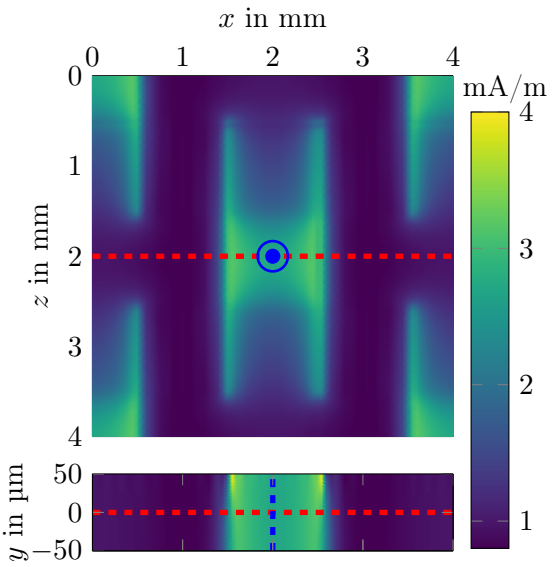


(d) $|H_x|$ (top and cross views).

Figure 5.17: Fields in one unit cell of the G-S holey PPW with square holes, computed analytically in the quasi-static regime as described in paragraph 5.2.2.2. The waves propagate in the $z$-direction. The structure has $p_z = p_x = 4\,\text{mm}$, $g = 0.1\,\text{mm}$, $a = 3\,\text{mm}$, $h = 5\,\text{mm}$, and is filled with vacuum. The integration paths described in Fig. 5.16 are indicated by the dashed lines. For each filed component, two cuts are shown in the unit cell: a top view in the cutting plane $y = 0$, and a cross view in the cutting plane $z = p/2$.

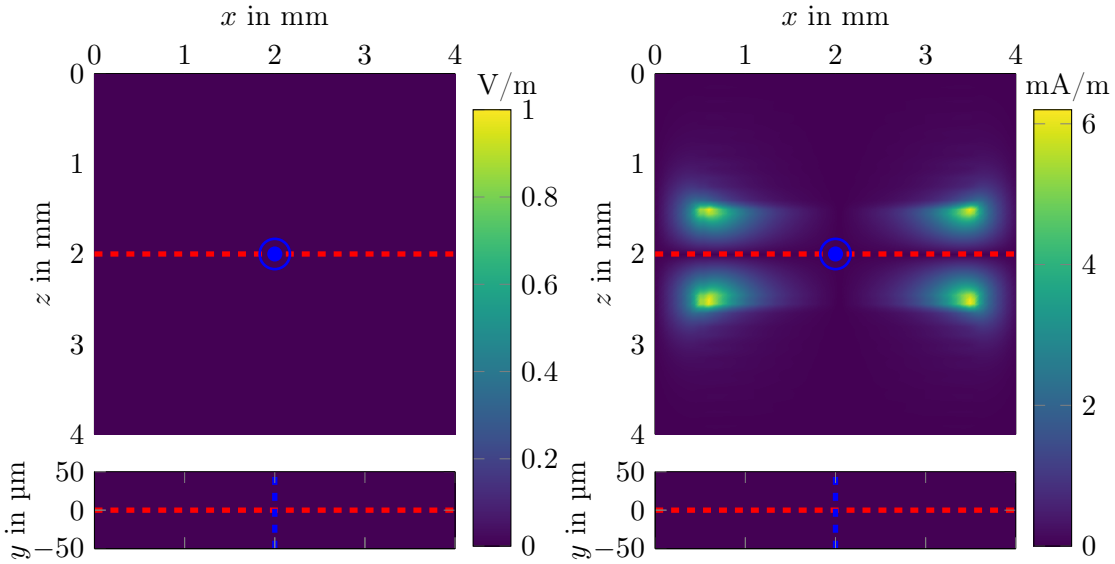


(a) $|E_z|$ (top and cross views).

(b) $|H_z|$ (top and cross views).

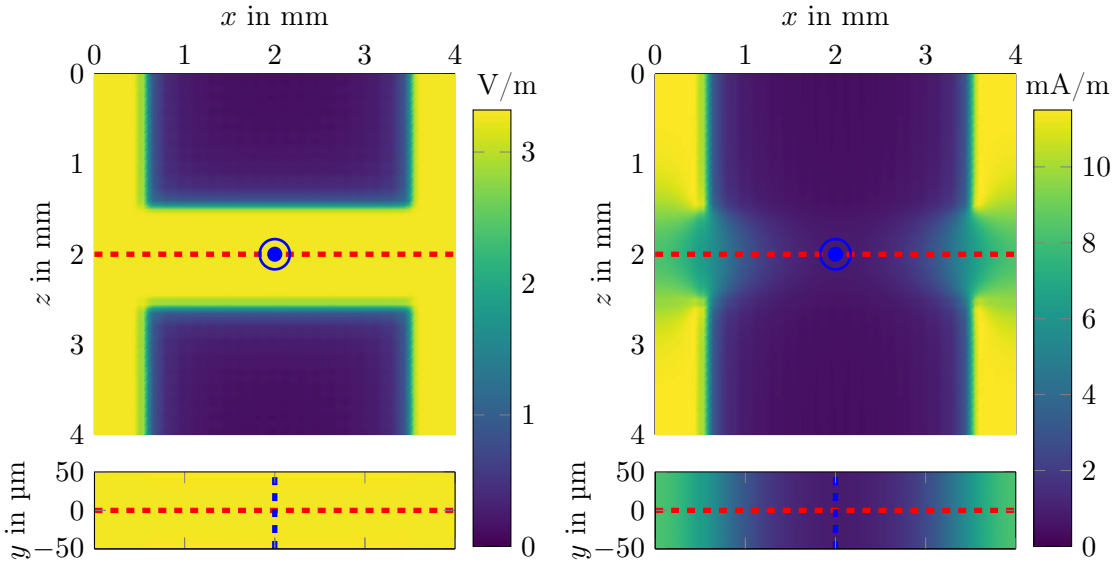


(c) $|E_y|$ (top and cross views).

(d) $|H_x|$ (top and cross views).

Figure 5.18: Fields in one unit cell of the nGS holey PPW with square holes, computed analytically in the quasi-static regime as described in paragraph 5.2.2.2. The waves propagate in the $z$-direction. The structure has $p_z = p_x = 4\,\text{mm}$, $g = 0.1\,\text{mm}$, $a = 3\,\text{mm}$, $h = 5\,\text{mm}$, and is filled with vacuum. The integration paths described in Fig. 5.16 are indicated by the dashed lines. For each filed component, two cuts are shown in the unit cell: a top view in the cutting plane $y = 0$, and a cross view in the cutting plane $z = p/2$.

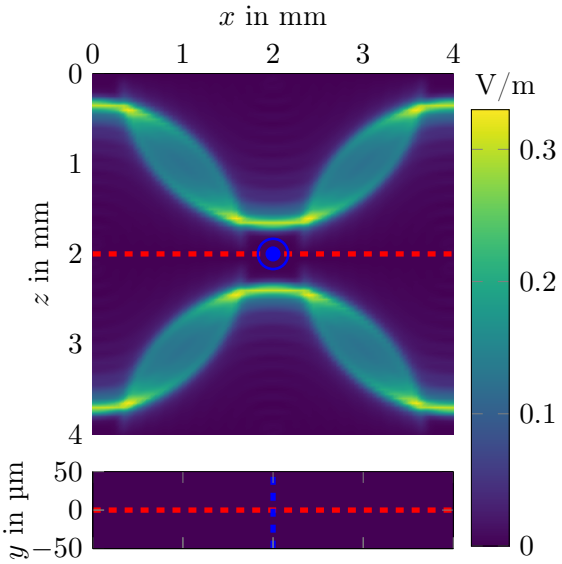


(a) $|E_z|$ (top and cross views).

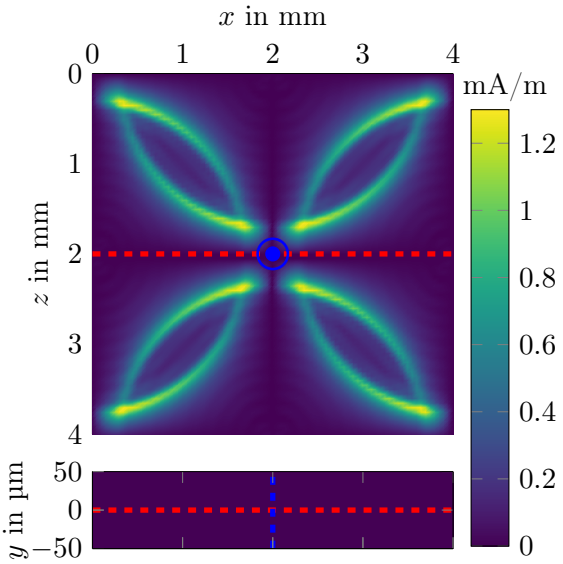


(b) $|H_z|$ (top and cross views).

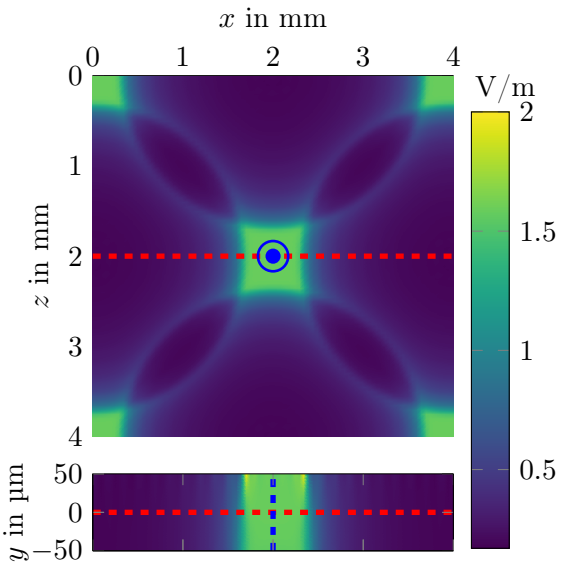


(c) $|E_y|$ (top and cross views).

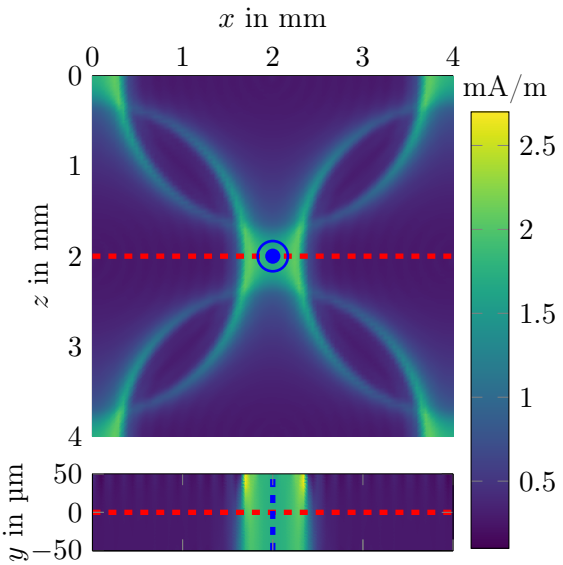


(d) $|H_x|$ (top and cross views).

Figure 5.19: Fields in one unit cell of the G-S holey PPW with circular holes, computed analytically in the quasi-static regime as described in paragraph 5.2.2.2. The waves propagate in the $z$-direction. The structure has periodicities $p_z = p_x = 4\,\text{mm}$, a gap $g = 0.1\,\text{mm}$ filled with $(\epsilon_{r1}, \mu_{r1}) = (2, 1.5)$, and holes of radius $a = 1.7\,\text{mm}$ and depth $h = 5\,\text{mm}$, filled with $(\epsilon_{r2}, \mu_{r2}) = (3, 4)$. The integration paths described in Fig. 5.16 are indicated by the dashed lines. For each filed component, two cuts are shown in the unit cell: a top view in the cutting plane $y = 0$, and a cross view in the cutting plane $z = p/2$.

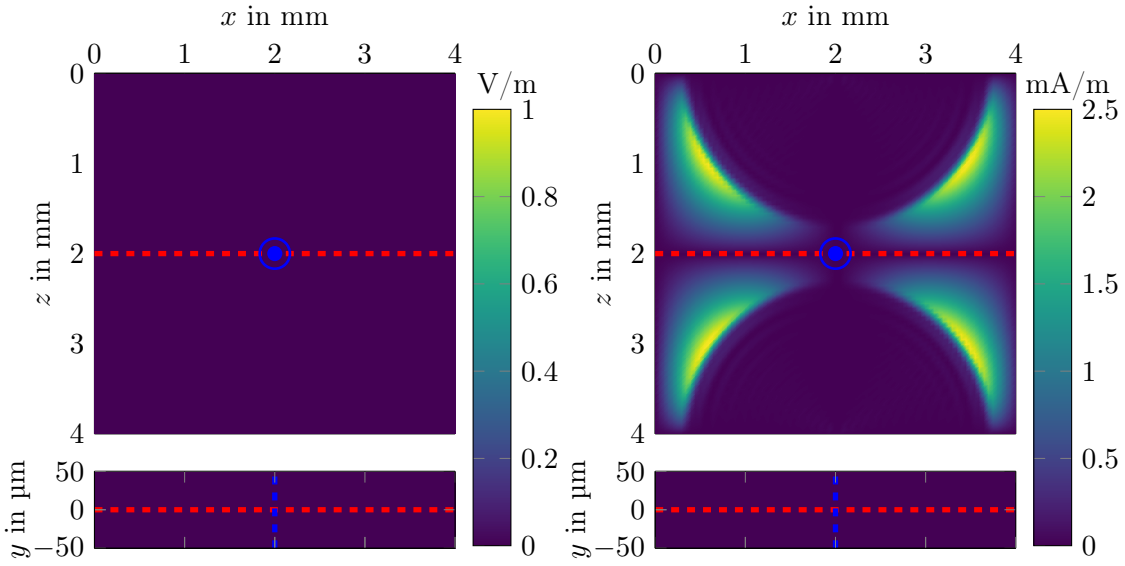


(a) $|E_z|$ (top and cross views).

(b) $|H_z|$ (top and cross views).

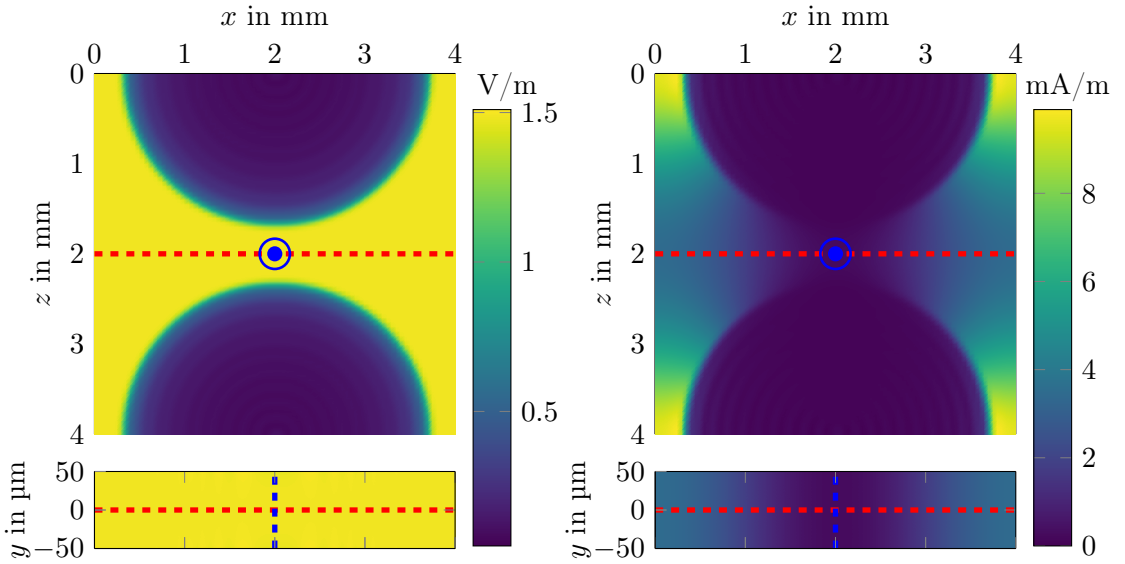


(c) $|E_y|$ (top and cross views).

(d) $|H_x|$ (top and cross views).

Figure 5.20: Fields in one unit cell of the nGS holey PPW with circular holes, computed analytically in the quasi-static regime as described in paragraph 5.2.2.2. The waves propagate in the $z$-direction. The structure has periodicities $p_z = p_x = 4\,\text{mm}$, a gap $g = 0.1\,\text{mm}$ filled with $(\epsilon_{\text{r}1}, \mu_{\text{r}1}) = (2, 1.5)$, and holes of radius $a = 1.7\,\text{mm}$ and depth $h = 5\,\text{mm}$, filled with $(\epsilon_{\text{r}2}, \mu_{\text{r}2}) = (3, 4)$. The integration paths described in Fig. 5.16 are indicated by the dashed lines. For each filed component, two cuts are shown in the unit cell: a top view in the cutting plane is $y = 0$, and a cross view in the cutting plane is $z = p/2$.

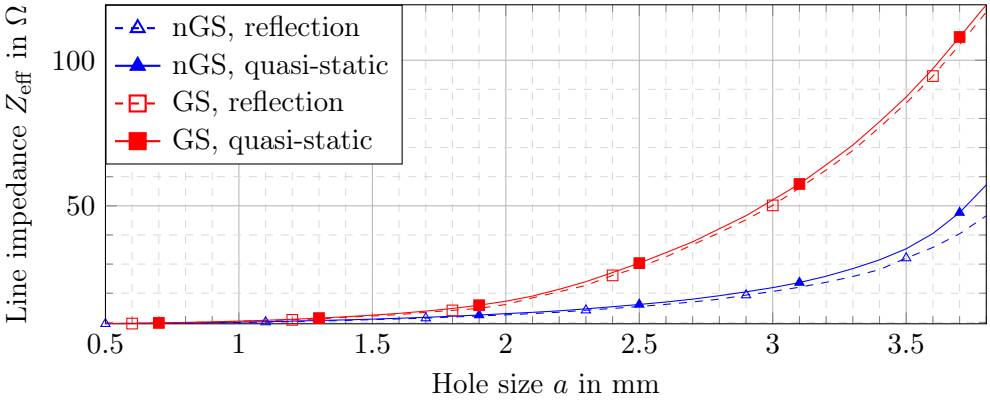


(a) Bloch impedance.

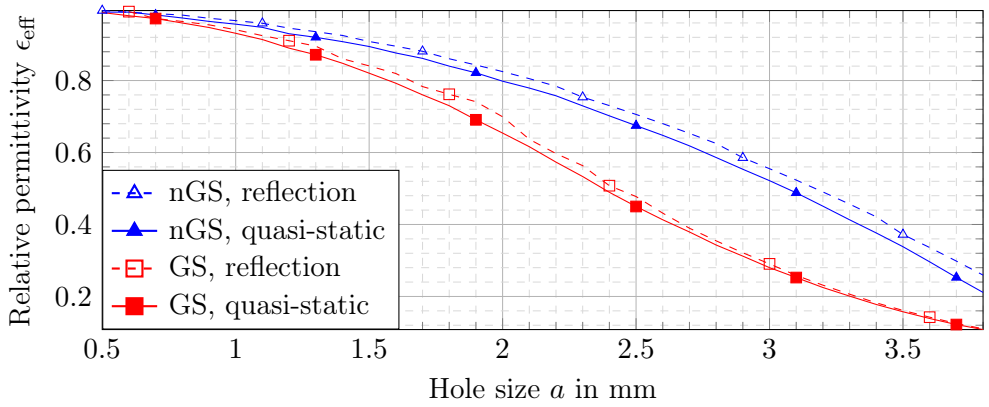


(b) Relative permittivity.

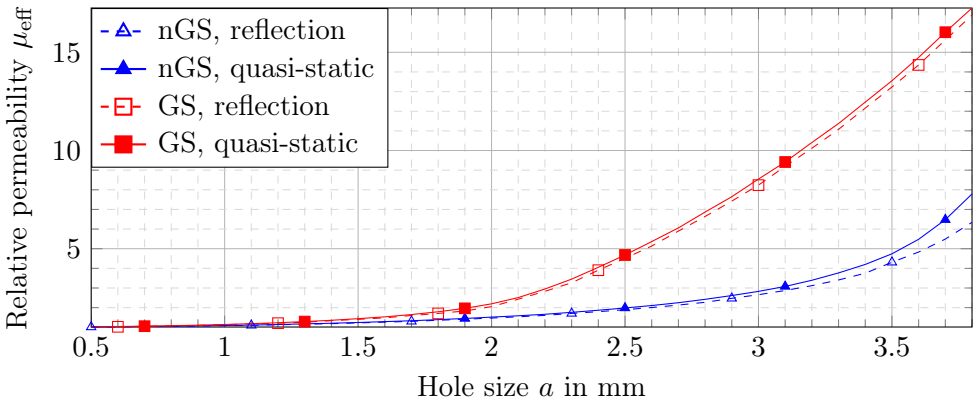


(c) Relative permeability.

Figure 5.21: Constitutive parameter retrieval for holey PPWs, as function of the square hole size $a$. The parameters are computed in the quasi-static analytic framework with (4.40) and (5.36), and compared with the CST reflection method.The structure is filled with vacuum, with dimensions $p = 4\,\text{mm}$, $h = 5\,\text{mm}$, and $g = 0.1\,\text{mm}$. G-S and nGS configurations are compared.

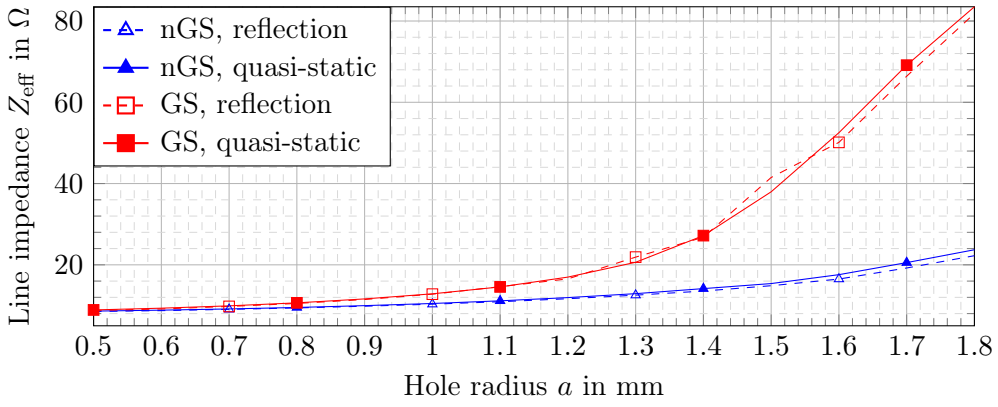


(a) Bloch impedance.

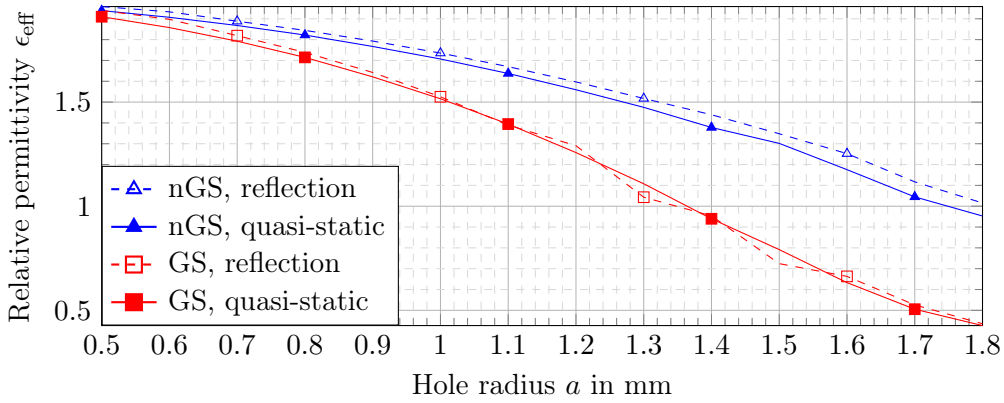


(b) Relative permittivity.

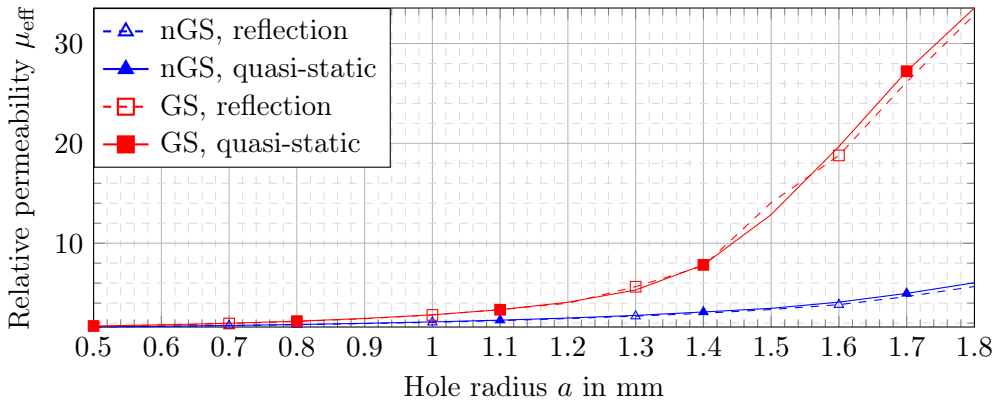


(c) Relative permeability.

Figure 5.22: Constitutive parameter retrieval for a holey PPW, as function of the circular hole radius $a$. The parameters are computed in the quasi-static analytic framework with (4.40) and (5.36), and compared with the CST reflection method. The structure dimensions are $p = 4\,\text{mm}$, $h = 5\,\text{mm}$, and $g = 0.1\,\text{mm}$. It uses gap and hole dielectrics $(\epsilon_{\text{r1}}, \mu_{\text{r1}}) = (2, 1.5)$ and $(\epsilon_{\text{r2}}, \mu_{\text{r2}}) = (3, 4)$.G-S and nGS configurations are compared.

analytic curves more than the CST results, because the latter have a somehow erratic behavior, whereas the quasi-static curves seem much smoother.

A comment can be made when comparing square holes in Fig. 5.21 and circular holes in Fig. 5.22. Retrieving the constitutive parameters of these holey PPWs offers further insight about the differences between different hole shapes. In the case of square hole, the relative permittivity is smaller than one, whereas for circular holes, except for very large holes, the permittivity is between 1 and 2. The quasi-static impedance makes such comparisons more more accessible.

It must be highlighted that the effective impedance is derived in the quasi-static regime. As such, it is to be expected that at higher frequencies, the validity of $Z_{\text{eff}}$ worsens. Nevertheless, the quasi-static characterization can likely be used up to higher frequencies for G-S waveguides, given the low frequency dispersion.

#### 5.2.3.2 Impedance matching with the Bloch impedance

In order to further validate the effective constitutive parameters obtained in our quasi-static framework, we consider a PPW with a change of dielectric, as illustrated by the CST models pictured in Fig. 5.23. The waves propagate in a dielectric medium $(\epsilon_{\text{rL}}, \mu_{\text{rL}})$ (red in the CST model). In the middle of the structure, a dielectric slab $(\epsilon_{\text{r1}}, \mu_{\text{r1}})$ of length $L_{\text{s}}$ is inserted, creating an obstacle with normal wave incidence (blue in the CST model). In order to avoid reflections, holes are drilled in the metal around the dielectric slab in order to achieve impedance matching (green in the CST model). If the dimension of these holes creates the right effective impedance $Z_{\text{eff}}$, then the slab should be reflectionless for the incident wave.

In practice, given the dielectrics, one would have to perform parametric studies to find the unit cells that have the desired effective properties. Here, we are rather interested in validating the effective properties obtained in the quasi-static framework, and so we have more of a reverse-engineering approach. For a given G-S holey PPW unit cell, we compute the quasi-static effective properties from (4.40) and (5.36). Then, the computed constitutive parameters are used for the dielectric of the feeding PPWs (in red in Fig. 5.23). If the matching works, it indicates that our quasi-static framework is indeed able to predict the effective parameters of our holey PPW in the context of dielectric waveguides matching, and that (5.36) can be used for the subsequent parametric studies. For each example, two structures are compared. On the one hand, the unmatched structure, where an air slab is placed in-between the two feeding slabs, creating reflections. On the other hand, the (theoretically) matched structure, where holey metasurfaces are placed on both sides of the center dielectric slab. This is supposed to suppress the reflections at low frequencies.

First, an example with nGS square holes is examined Fig. 5.24. According to Fig. 5.21, square holes of size $a = 3\,\text{mm}$ yield an effective permittivity $\epsilon_{\text{eff}} = 0.52$, and an effective permeability $\mu_{\text{eff}} = 2.83$. These are the constitutive parameters chosen for the feeding dielectric PPW $(\epsilon_{\text{rL}}, \mu_{\text{rL}})$, of length $L_{\text{f}} = 20\,\text{mm}$. It is followed by a slab of air of length $L_{\text{s}} = 40\,\text{mm}$ (which corresponds to 10 metasurface unit cells). Finally, another feeding

(a) No matching holes.

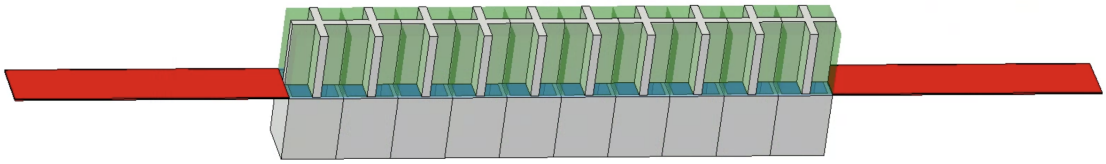

(b) Square holes.

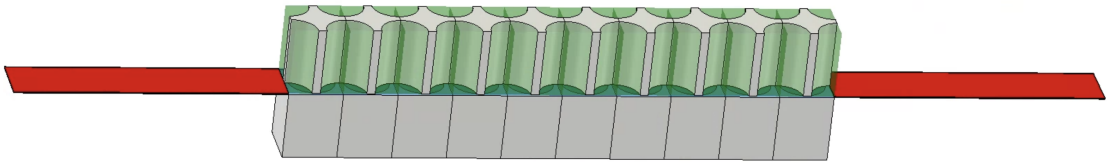

(c) Circular holes.

Figure 5.23: CST models for the impedance matching simulations with holey G-S PPWs. The waveguide ports are placed at the ends of the feeding PPWs (red dielectrics). The structures are periodic in the $x$-direction (perpendicular to the propagation direction), which is made possible by the hexahedral mesh of CST's frequency solver.

dielectric of $L_\mathrm{f} = 20\,\mathrm{mm}$ is placed at the end of the waveguide. CST's frequency solver is used to compute the S-parameters of the structure between 0 and 20 GHz.

The same configuration is used in Fig. 5.25 for the G-S vacuum filled structure from Fig. 5.21, with holes of size $a = 3\,\mathrm{mm}$, yielding $\epsilon_\mathrm{eff} = 0.28$ and $\mu_\mathrm{eff} = 8.55$.

Finally, impedance matching is achieved with G-S circular holes in Fig. 5.26. The setup is the same as in Figs. 5.24 and 5.25, except that the dielectrics are changed. The center dielectric is $(\epsilon_\mathrm{r1}, \mu_\mathrm{r1}) = (2, 1.5)$, and holes of radius $a = 1.7\,\mathrm{mm}$ are drilled along this center slab, forming a G-S PPW. The holes are filled with a dielectric $(\epsilon_\mathrm{r2}, \mu_\mathrm{r2}) = (3, 4)$. According to the quasi-static parametric study in Fig. 5.22, such a holey G-S PPW yields effective constitutive parameters $(\epsilon_\mathrm{reff}, \mu_\mathrm{reff}) = (0.52, 27.22)$. This values are thus used for the feeding dielectric PPWs of length $L_\mathrm{s} = 40\,\mathrm{mm}$.

From Figs. 5.24 to 5.26, it appears that the effective material properties defined in the quasi-static framework are quite accurate. Without the metasurfaces, most of the power is reflected at the dielectric interfaces, which was predictable. Adding the holey metasurfaces enables good impedance matching between the different dielectric PPWs. Although derived in the quasi-static regime, the effective properties of the metasurface waveguides suppress more than 99% of the reflections up to 12 GHz for the square holes, and more than 90% up to almost 20 GHz. The G-S design enables matching to even higher frequencies, due to the low frequency-dispersion of G-S waveguides. In the example of the

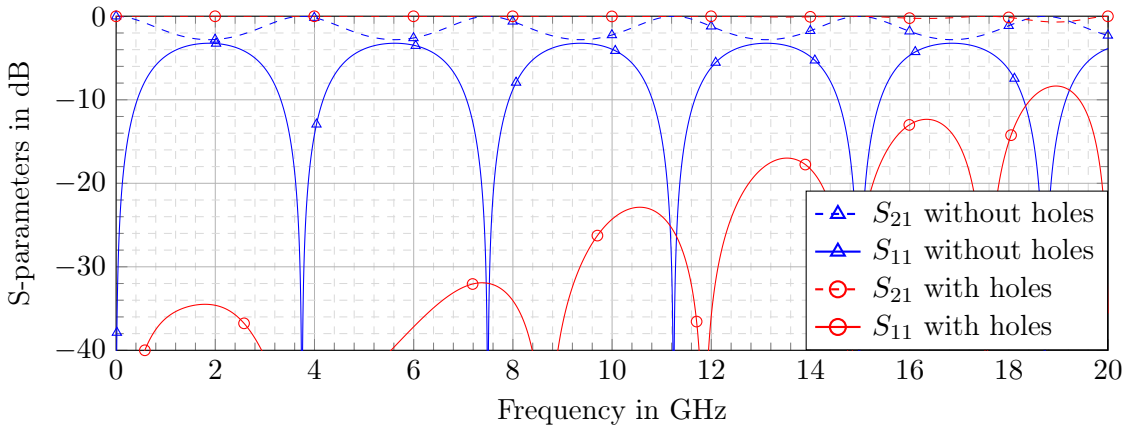


Figure 5.24: S-parameters of a dielectric PPW $(\epsilon_{\mathrm{rL}}, \mu_{\mathrm{rL}}) = (0.52, 2.83)$ of height $g = 0.1\,\mathrm{mm}$, blocked by a vacuum slab of length $L_{\mathrm{s}} = 40\,\mathrm{mm}$, in line with the simulation model of Fig. 5.23. Results without impedance-matching are compared to the case where square holes are drilled in the plates of the PPW along the slab, creating a nGS holey PPW with dimensions $p = 4\,\mathrm{mm}$, $h = 5\,\mathrm{mm}$, and $a = 3\,\mathrm{mm}$.

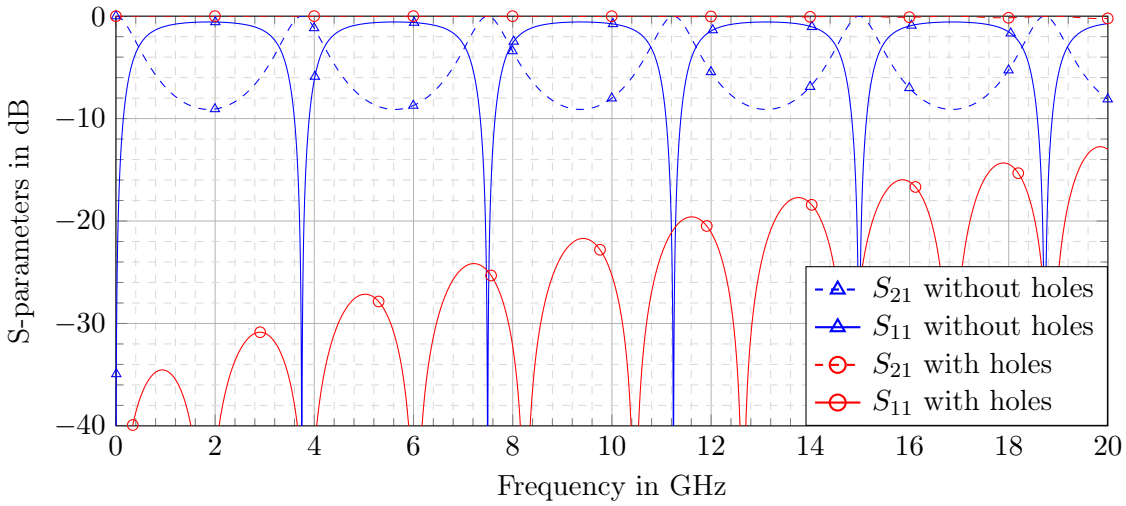


Figure 5.25: S-parameters of a dielectric PPW $(\epsilon_{\mathrm{rL}}, \mu_{\mathrm{rL}}) = (0.28, 8.55)$ of height $g = 0.1\,\mathrm{mm}$, blocked by a vacuum slab of length $L_{\mathrm{s}} = 40\,\mathrm{mm}$, in line with the simulation model of Fig. 5.23. Results without impedance-matching are compared to the case where square holes are drilled in the plates of the PPW along the slab, creating a G-S holey PPW with dimensions $p = 4\,\mathrm{mm}$, $h = 5\,\mathrm{mm}$, and $a = 3\,\mathrm{mm}$.

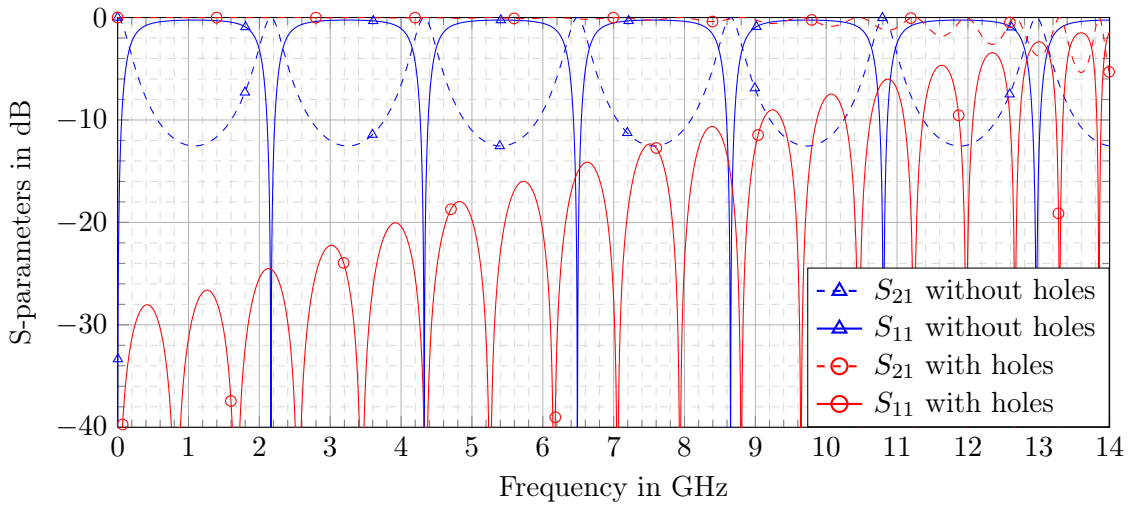


Figure 5.26: S-parameters of a dielectric PPW $(\epsilon_{\mathrm{rL}}, \mu_{\mathrm{rL}}) = (0.52, 27.22)$ of height $g = 0.1\,\mathrm{mm}$, blocked by a dielectric slab $(\epsilon_{\mathrm{r1}}, \mu_{\mathrm{r1}}) = (2, 1.5)$ of length $L_{\mathrm{s}} = 40\,\mathrm{mm}$, in line with the simulation model of Fig. 5.23. Results without impedance-matching are compared to the case where circular holes are drilled in the plates of the PPW along the slab and filled with a dielectric $(\epsilon_{\mathrm{r2}}, \mu_{\mathrm{r2}}) = (3, 4)$, creating a G-S holey PPW with dimensions $p = 4\,\mathrm{mm}$, $h = 5\,\mathrm{mm}$, and $a = 1.7\,\mathrm{mm}$.

circular holes with dense dielectrics, the band of validity is smaller, as could be expected for such dense structures (as explained section 4.5.1). Still, less than 10% of the incident power is reflected up to 9 GHz.

The effective constitutive parameters obtained in the quasi-static framework are good. But are they the best? The structure with G-S empty square holes in Fig. 5.25 is considered again. The permittivity $\epsilon_{\mathrm{rL}}$ and the permeability $\mu_{\mathrm{rL}}$ of the feeding dielectrics are tuned around the effective values $(\epsilon_{\mathrm{eff}}, \mu_{\mathrm{eff}}) = (0.28, 8.55)$, computed in the quasi-static regime. In Fig. 5.27, the maximum value of $S_{11}$ between 0 and 2 GHz is considered in the $(\epsilon_{\mathrm{rL}}, \mu_{\mathrm{rL}})$-plane. This shows if the theoretically computed values yield the best possible impedance matching.

Fig. 5.27 shows that there remains a small difference between the "best" effective parameters and the quasi-static parameters. In Fig. 5.25 slightly better impedance matching would have been achieved by tuning the feeding dielectrics. This is understandable, given that our quasi-static parameters describe an infinitely periodic holey PPW, whereas in the mode-matching situation, the metasurface waveguide is finite (here, only 10 unit cells). The field variation caused by the holes at the boundary between the two gap dielectrics excites higher modes, which are reflected at the boundary, neglected in the homogenized model. Yet, even for such a small structure, the holey metasurfaces suppress most of the reflections, and the quasi-static refractive index and Bloch impedance are fast and accurate techniques to achieve that.

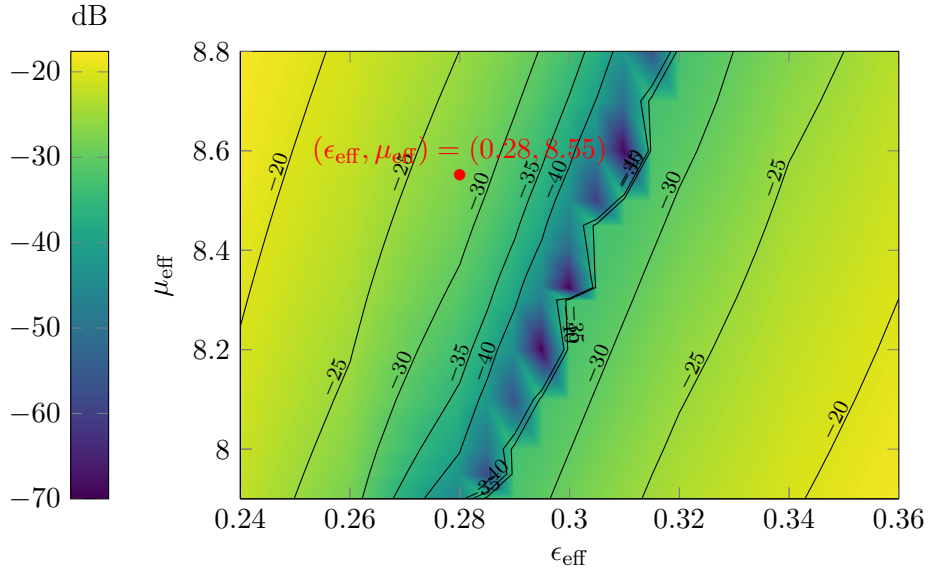


Figure 5.27: Quasi-static reflection $S_{11}$ as function of the feeding dielectric parameters $(\epsilon_{\text{rL}}, \mu_{\text{rL}})$. The feeding waveguides of length $L_{\text{s}} = 40\,\text{mm}$ are on either side of the center holey G-S PPW made of 10 unit cells, with empty square holes of size $a = 3\,\text{mm}$ and depth $h = 5\,\text{mm}$. The unit cell periodicity is $p = 4\,\text{mm}$, and the gap between the metallic plates is $g = 0.1\,\text{mm}$. The effective constitutive parameters of the center holey structure computed in the quasi-static regime are pointed out.

### 5.2.4 Effects of glide symmetry on the constitutive parameters

In Figs. 5.21 and 5.22, it appears clearly that GS increases the Bloch impedance. Combining the Bloch impedance with the effective refractive index (4.40) also highlights the higher magnetic density enabled by GS. In this section, the quasi-static framework is used to analytically prove these features of GS.

Unfortunately, without simplifications, analytical demonstrations are not possible, because the Bloch impedance computation relies on the nullspace of the dispersion matrix $\underline{\boldsymbol{M}}$ in (5.23). For accurate computations, a large number of modes must be considered in the holes, leading to a large matrix $\underline{\boldsymbol{M}}$: the nullspace can only be computed numerically.

Nevertheless, relying on the findings in paragraph 5.1.1, the physical behavior of these waveguides is captured when the number of modes is reduced to the two most excited ones: one TM and one TE mode. Fig. 5.28 shows the impact of keeping only two modes on the accuracy of the Bloch impedance. In Fig. 5.28a, empty G-S square holes of varying sizes are considered, with $p = 4\,\text{mm}$, $h = 5\,\text{mm}$, and $g = 0.1\,\text{mm}$. Waveguides with the same dimensions are studied in Fig. 5.28b, with G-S circular holes of varying radius, and dielectric fillings $(\epsilon_{\text{r1}}, \mu_{\text{r1}}) = (2, 1.5)$ and $(\epsilon_{\text{r2}}, \mu_{\text{r2}}) = (3, 4)$. These studies show that although accuracy is lost when keeping only two modes, the overall qualitative differences between G-S and nGS waveguides are contained in the two-modes Bloch impedance.

By keeping only one TE and one TM mode, the dispersion matrix $\underline{\boldsymbol{M}}$ becomes a $2 \times 2$

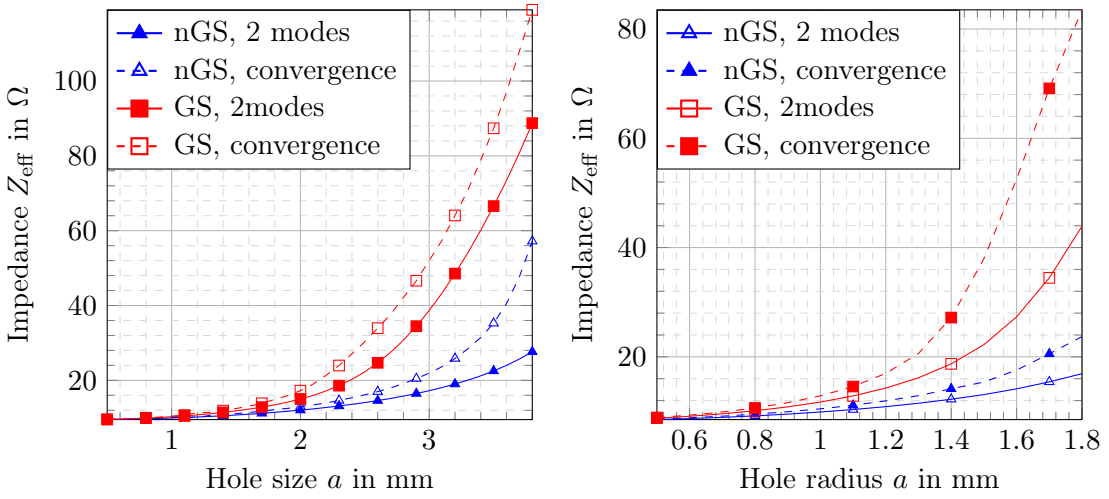


(a) Square holes of size $a$, no dielectrics.

(b) Circular holes of radius $a$ with $(\epsilon_{\text{r}2}, \mu_{\text{r}2}) = (3, 4)$, and gap with $(\epsilon_{\text{r}1}, \mu_{\text{r}1}) = (2, 1.5)$.

Figure 5.28: Quasi-static effective Bloch impedance of holey PPWs, as function of the hole size. The case with only 2 hole modes is compared with the converge value of the quasi-static framework. The structures have dimensions $p = 4\,\text{mm}$, $h = 5\,\text{mm}$, and $g = 0.1\,\text{mm}$. G-S and nGS configurations are compared.

matrix, and the resulting 2-modes matrix equation is of the form

$$\begin{bmatrix} A & B \\ B^* & D \end{bmatrix} \begin{bmatrix} c^{\text{e}} \\ c^{\text{h}\prime} \end{bmatrix} = \mathbf{0}\,, \tag{5.37}$$

with, according to (5.23),

$$A = n_1^2 \left( \Sigma^{\text{e}} + \frac{n_\theta^2}{n_1^2 - n_\theta^2} \frac{2}{g} \left| u^{\text{e}} \right|^2 \right)\,, \tag{5.38}$$

$$B = \text{j} n_1 \frac{n_\theta n_1}{n_1^2 - n_\theta^2} \frac{2}{g} u^{\text{e}} \left[ u^{\text{h}} \right]^*\,, \tag{5.39}$$

$$\text{and} \quad D = \Sigma^{\text{h}} + \frac{n_1^2}{n_1^2 - n_\theta^2} \frac{2}{g} \left| u^{\text{h}} \right|^2\,. \tag{5.40}$$

Assuming that the nullspace of this matrix is not empty i.e., $AD - |B|^2 = 0$, the solutions of (5.37) are proportional to

$$\begin{bmatrix} c^{\text{e}} \\ c^{\text{h}\prime} \end{bmatrix} = \begin{bmatrix} -B \\ A \end{bmatrix} = \begin{bmatrix} -\text{j} n_1 \frac{n_\theta n_1}{n_1^2 - n_\theta^2} \frac{2}{g} u^{\text{e}} \left[ u^{\text{h}} \right]^* \\ n_1^2 \left( \Sigma^{\text{e}} + \frac{n_\theta^2}{n_1^2 - n_\theta^2} \frac{2}{g} \left| u^{\text{e}} \right|^2 \right) \end{bmatrix}\,, \tag{5.41}$$

with, according to (4.32), (4.35) and (4.36),

$$\Sigma^{\mathrm{e}} = -\frac{\epsilon_{\mathrm{r}2}}{\epsilon_{\mathrm{r}1}k^{\mathrm{e}}}p_x p_z I^{\mathrm{e}}\coth\left(k^{\mathrm{e}}h\right) + \sum_{(s,\ell)\neq(0,0)} \bar{f}^{(s\ell)}\frac{\left|\bar{e}_y^{(s\ell)}\right|^2}{k^{\mathrm{e}2}}\Gamma^{(s\ell)2}\,, \tag{5.42}$$

$$u^{\mathrm{e}} = \frac{\bar{e}_y^{(00)}}{k^{\mathrm{e}}}, \quad \text{and} \quad u^{\mathrm{h}} = \cos\theta\bar{e}_z^{\mathrm{h}(00)} + \sin\theta\bar{e}_x^{\mathrm{h}(00)}\,. \tag{5.43}$$

Note that in section 5.2.3, the impedances are computed for a propagation direction aligned with the grid i.e., $\theta = 0$. This is taken as an assumption in the following, simplifying $u^{\mathrm{h}}$ accordingly.

In section 5.2.2.2, the quasi-static fields are expressed as functions of the mode coefficients. Inserting the two-modes coefficients (5.41), the intermediary terms $\bar{d}^{\mathrm{i}(s\ell)}$ in (5.24) become

$$\bar{d}^{\mathrm{e}(s\ell)} = -\mathrm{j}\frac{c^{\mathrm{e}}}{k^{\mathrm{e}}}\bar{e}_y^{(s\ell)*} = -\frac{n_\theta n_1^2}{n_1^2 - n_\theta^2}\frac{2}{gk^{\mathrm{e}2}}\bar{e}_y^{(00)}\bar{e}_z^{\mathrm{h}(00)*}\bar{e}_y^{(s\ell)*}\,, \tag{5.44}$$

and

$$\bar{\boldsymbol{d}}^{\mathrm{h}(s\ell)} = c^{\mathrm{h}\prime}\bar{\boldsymbol{e}}_{\mathrm{t}}^{\mathrm{h}(s\ell)*} = n_1^2\bar{\boldsymbol{e}}_{\mathrm{t}}^{\mathrm{h}(s\ell)*}\begin{pmatrix} -\frac{\epsilon_{\mathrm{r}2}}{\epsilon_{\mathrm{r}1}k^{\mathrm{e}}}p_x p_z I^{\mathrm{e}}\coth\left(k^{\mathrm{e}}h\right) \\ +\sum_{(s,\ell)\neq(0,0)} \bar{f}^{(s\ell)}\frac{\left|\bar{e}_y^{(s\ell)}\right|^2}{k^{\mathrm{e}2}}\Gamma^{(s\ell)2} + \frac{n_\theta^2}{n_1^2-n_\theta^2}\frac{2}{g}\frac{\left|\bar{e}_y^{(00)}\right|^2}{k^{\mathrm{e}2}} \end{pmatrix}\,, \tag{5.45}$$

with $\bar{e}_y^{\mathrm{e}(s\ell)}$ and $\bar{\boldsymbol{e}}_{\mathrm{t}}^{\mathrm{h}(s\ell)*}$ the projected modal functions (PMFs) of the TM and TE modes.

In the following, it is reminded that the differences between G-S and nGS waveguides are located in the vertical spectral functions of the harmonics, defined in (4.20) as

$$\bar{f}^{(s\ell)} = \begin{cases} -\tanh\left(\frac{g}{2}\Gamma^{(s\ell)}\right)/\Gamma^{(s\ell)} & \text{if G-S and } \ell+s \text{ odd,} \\ -\coth\left(\frac{g}{2}\Gamma^{(s\ell)}\right)/\Gamma^{(s\ell)} & \text{if G-S and } \ell+s \text{ even, or if nGS.} \end{cases} \tag{5.46}$$

Before computing the Bloch current and voltage, a preliminary term useful for the following is studied, namely the sum $n_\theta\bar{d}^{\mathrm{e}(00)} + \bar{d}_z^{\mathrm{h}(00)}$. From (5.44) and (5.45), the sum can be simplified as

$$\begin{aligned} n_\theta\bar{d}^{\mathrm{e}(00)} + \bar{d}_z^{\mathrm{h}(00)} &= -\frac{n_\theta^2 n_1^2}{n_1^2 - n_\theta^2}\frac{2}{gk^{\mathrm{e}2}}\bar{e}_z^{\mathrm{h}(00)*}\left|\bar{e}_y^{(00)}\right|^2 - \frac{\epsilon_{\mathrm{r}2}n_1^2}{\epsilon_{\mathrm{r}1}k^{\mathrm{e}}}p_x p_z I^{\mathrm{e}}\coth\left(k^{\mathrm{e}}h\right)\bar{e}_z^{\mathrm{h}(00)*} \\ &\quad + n_1^2\bar{e}_z^{\mathrm{h}(00)*}\sum_{(s,\ell)\neq(0,0)} \bar{f}^{(s\ell)}\frac{\left|\bar{e}_y^{(s\ell)}\right|^2}{k^{\mathrm{e}2}}\Gamma^{(s\ell)2} + \frac{n_\theta^2 n_1^2}{n_1^2-n_\theta^2}\frac{2}{g}\frac{\left|\bar{e}_y^{(00)}\right|^2}{k^{\mathrm{e}2}}\bar{e}_z^{\mathrm{h}(00)*} \\ &= n_1^2\bar{e}_z^{\mathrm{h}(00)*}\left(-\frac{\epsilon_{\mathrm{r}2}}{\epsilon_{\mathrm{r}1}k^{\mathrm{e}}}p_x p_z I^{\mathrm{e}}\coth\left(k^{\mathrm{e}}h\right) + \sum_{(s,\ell)\neq(0,0)} \bar{f}^{(s\ell)}\frac{\left|\bar{e}_y^{(s\ell)}\right|^2}{k^{\mathrm{e}2}}\Gamma^{(s\ell)2}\right)\,. \end{aligned} \tag{5.47}$$

According to the vertical spectral function definitions in (5.46), the terms in the sum are negative, and the absolute value of the total sum is smaller in the G-S case. Therefore,

$$\left|n_\theta\bar{d}^{\mathrm{e}(00)} + \bar{d}_z^{\mathrm{h}(00)}\right|_{\mathrm{GS}} < \left|n_\theta\bar{d}^{\mathrm{e}(00)} + \bar{d}_z^{\mathrm{h}(00)}\right|_{\mathrm{nGS}}\,. \tag{5.48}$$

#### 5.2.4.1 Effective Bloch current

The Bloch current is defined in (5.35) as

$$I_{\mathrm{B}} = \int_{x=0}^{p_x} H_x \mathrm{d}x = \int_{x=0}^{p_x} \sum_{(s,\ell)} H_x^{(s\ell)} \mathrm{d}x = \sum_{(s,\ell)} I_{\mathrm{B}}^{(s\ell)}\,, \tag{5.49}$$

where the magnetic field is the sum of the components of all the Floquet harmonics according to (2.25). In the following, these harmonics are considered according to their parity.

**Even-order harmonics** For even-order harmonics except $(s,\ell) = (0,0)$, the transverse magnetic field $H_x$ is defined in (5.31) as

$$\boldsymbol{H}_{\mathrm{t}}^{(s\ell)} \underset{k_0\to 0}{=} -\frac{\mathrm{j}\bar{F}^{(s\ell)} \cos\left(\mathrm{j}\Gamma^{(s\ell)} y\right)}{\eta_0 \mu_{\mathrm{r}1} p_x p_z \Gamma^{(s\ell)} \sin\left(\mathrm{j}\Gamma^{(s\ell)} \frac{g}{2}\right)} \boldsymbol{\Gamma}^{(s\ell)} \left[\hat{\boldsymbol{y}} \times \boldsymbol{\Gamma}^{(s\ell)}\right]^{\mathrm{T}} \bar{\boldsymbol{d}}^{\mathrm{h}(s\ell)}\,, \tag{5.50}$$

and therefore

$$H_x^{(s\ell)} \underset{k_0\to 0}{=} -\frac{\mathrm{j}\bar{F}^{(s\ell)} \cos\left(\mathrm{j}\Gamma^{(s\ell)} y\right)}{\eta_0 \mu_{\mathrm{r}1} p_x p_z \Gamma^{(s\ell)} \sin\left(\mathrm{j}\Gamma^{(s\ell)} \frac{g}{2}\right)} \left[\frac{s2\pi}{p_z}\frac{\ell 2\pi}{p_x} \bar{d}_x^{\mathrm{h}(s\ell)} - \left(\frac{\ell 2\pi}{p_x}\right)^2 \bar{d}_z^{\mathrm{h}(s\ell)}\right]. \tag{5.51}$$

The only $x$-dependency is in the exponential term $\bar{F}^{(s\ell)} = \mathrm{e}^{-\mathrm{j}\frac{\ell 2\pi}{p_x}x - \mathrm{j}\frac{s2\pi}{p_z}z}$. Therefore, when integrating the magnetic field across the unit cell, the integral term is reduced to

$$\int_{x=0}^{p_x} \mathrm{e}^{-\mathrm{j}\frac{\ell 2\pi}{p_x}x} \mathrm{d}x = 0 \quad \text{if} \quad l \neq 0\,. \tag{5.52}$$

In the case where $\ell = 0$, the magnetic field component in (5.51) is null anyway, because of the $\ell$-proportionality. This means that in the effective Bloch current (5.49), all even-order harmonics have no contribution, given that their integral across the unit cell is zero.

**Odd-order harmonics** The transverse magnetic field component of odd-harmonics is defined in (5.34) as

$$H_x^{(s\ell)} \underset{k_0\to 0}{=} -\frac{\mathrm{j}\bar{F}^{(s\ell)} \sin\left(\mathrm{j}\Gamma^{(s\ell)} y\right)}{\eta_0 \mu_{\mathrm{r}1} p_x p_z \Gamma^{(s\ell)} \cos\left(\mathrm{j}\Gamma^{(s\ell)} \frac{g}{2}\right)} \left[\frac{s2\pi}{p_z}\frac{\ell 2\pi}{p_x} \bar{d}_x^{\mathrm{h}(s\ell)} - \left(\frac{\ell 2\pi}{p_x}\right)^2 \bar{d}_z^{\mathrm{h}(s\ell)}\right]. \tag{5.53}$$

The only difference with the even-order case is that these fields are antisymmetric with respect to $y$. The integral along $x$ is zero too. This means that in the effective Bloch current (5.49), all odd-order harmonics have no contribution.

**Fundamental harmonic** Given the two previous paragraphs, the Bloch current is defined only from the fundamental Floquet harmonic, which is constant in the integration plane. Indeed, from (5.27),

$$\begin{aligned}\boldsymbol{H}_{\mathrm{t}}^{(00)} &\underset{k_0\to 0}{=} \underline{\boldsymbol{Y}}^{(00)}\boldsymbol{a}^{(00)} \\ &= \frac{2\left(n_\theta^2\begin{bmatrix}\cos\theta\\ \sin\theta\end{bmatrix}\begin{bmatrix}-\sin\theta\\ \cos\theta\end{bmatrix}^{\mathrm{T}} - n_1^2\begin{bmatrix}0 & 1\\ -1 & 0\end{bmatrix}\right)\left(n_\theta\begin{bmatrix}\cos\theta\\ \sin\theta\end{bmatrix}\bar{d}^{\mathrm{e}(00)} + \bar{\boldsymbol{d}}^{\mathrm{h}(00)}\right)}{\eta_0\mu_{\mathrm{r}1}p_xp_zg\left(n_1^2-n_\theta^2\right)}\,. \end{aligned} \tag{5.54}$$

For $\theta = 0$, this yields

$$\boldsymbol{H}_{\mathrm{t}}^{(00)} \underset{k_0\to 0}{=} \frac{2}{\eta_0\mu_{\mathrm{r}1}p_xp_zg\left(n_1^2-n_\theta^2\right)}\begin{bmatrix}0 & n_\theta^2-n_1^2\\ n_1^2 & 0\end{bmatrix}\left(\begin{bmatrix}n_\theta\bar{d}^{\mathrm{e}(00)}\\ 0\end{bmatrix} + \bar{\boldsymbol{d}}^{\mathrm{h}(00)}\right), \tag{5.55}$$

and so the fundamental-harmonic contribution to the Bloch current is

$$I_{\mathrm{B}}^{(00)} = p_xH_x^{(00)} \underset{k_0\to 0}{=} \frac{2n_1^2}{\eta_0\mu_{\mathrm{r}1}p_zg\left(n_1^2-n_\theta^2\right)}\left(n_\theta\bar{d}^{\mathrm{e}(00)} + \bar{d}_z^{\mathrm{h}(00)}\right). \tag{5.56}$$

In parentheses, we recognize the expression studied in (5.48), which is smaller in the G-S case. However, this is not enough to state that the Bloch current is smaller in the G-S case, because in (5.56) $H_x^{(00)}$ also depends on $n_1^2 - n_\theta^2$. The magnitude of this term is different between G-S and nGS configurations because of $n_\theta$, but it is not obvious here in which case the magnitude is larger.

Nevertheless, the fundamental harmonic being the only contribution to the current in (5.49),

$$I_{\mathrm{B}} = \int_{x=0}^{p_x} H_x^{(00)}\mathrm{d}x = p_xH_x^{(00)} = I_{\mathrm{B}}^{(00)}\,, \tag{5.57}$$

with $I_{\mathrm{B}}^{(00)}$ defined in (5.56).

#### 5.2.4.2 Effective Bloch voltage

Similarly, to the current, the Bloch voltage is defined in (5.35) as

$$V_{\mathrm{B}} = \int_{y=-g/2}^{g/2} E_y\mathrm{d}y = \int_{y=-g/2}^{g/2}\sum_{(s,\ell)} E_y^{(s\ell)}\mathrm{d}y = \sum_{(s,\ell)} V_{\mathrm{B}}^{(s\ell)}\,, \tag{5.58}$$

where the integration path binds the two metasurfaces across the gap.

**Glide odd-order harmonics** In the case of a G-S structure, according to (5.34), harmonics with odd $s+\ell$ have an electric field

$$E_y^{(s\ell)} \underset{k_0\to 0}{=} \frac{\mathrm{j}\bar{F}^{(s\ell)}\Gamma^{(s\ell)}\sin\left(\mathrm{j}\Gamma^{(s\ell)}y\right)}{p_x p_z \cos\left(\mathrm{j}\Gamma^{(s\ell)}\frac{g}{2}\right)}\bar{d}^{\mathrm{e}(s\ell)}\,. \tag{5.59}$$

Given this antisymmetric field distribution along the gap because of the sinus function, the integral contribution of this field is null. Therefore, in the G-S case, none of the odd-order harmonics impact the Bloch voltage.

**Glide even-order or nGS harmonics** For G-S harmonics with $s+\ell$ even and not null, and for all higher harmonics of the nGS case, according to (5.31) the electric field has the form

$$E_y^{(s\ell)} \underset{k_0\to 0}{=} \frac{\mathrm{j}\bar{F}^{(s\ell)}\Gamma^{(s\ell)}\cos\left(\mathrm{j}\Gamma^{(s\ell)}y\right)}{p_x p_z \sin\left(\mathrm{j}\Gamma^{(s\ell)}\frac{g}{2}\right)}\bar{d}^{\mathrm{e}(s\ell)}\,. \tag{5.60}$$

The only field variation along $g$ is located in the cosine function. The integral comes down to

$$\int_{y=-g/2}^{g/2}\cos\left(\mathrm{j}\Gamma^{(s\ell)}y\right)\mathrm{d}y = \frac{2\sin\left(\mathrm{j}\Gamma^{(s\ell)}\frac{g}{2}\right)}{\mathrm{j}\Gamma^{(s\ell)}}\,. \tag{5.61}$$

Therefore

$$V_{\mathrm{B}}^{(s\ell)} = \frac{2\bar{F}^{(s\ell)}}{p_x p_z}\bar{d}^{\mathrm{e}(s\ell)} = -\frac{4\bar{F}^{(s\ell)}}{p_x p_z g k^{\mathrm{e}2}}\frac{n_\theta n_1^2}{n_1^2-n_\theta^2}\bar{e}_y^{(00)}\bar{e}_z^{\mathrm{h}(00)*}\bar{e}_y^{(s\ell)*}\,. \tag{5.62}$$

Note that this voltage depends on the position $(z_0, x_0)$ of the integration path in the propagation plane, because of the term $\bar{F}^{(s\ell)}$. In the following, this position is chosen so that the Bloch fields are in-between two holes, that is $z_0 = a/2 - p/2$. Appendix E.2.1 proves that the fields are TEM in this plane. However, more in-depth studies should consider how the effective impedance is impacted by the chosen position.

**Fundamental harmonic** According to (5.27), for $\theta = 0$ the fundamental electric field has the form

$$E_y^{(00)} \underset{k_0\to 0}{=} -\frac{2n_\theta}{p_x p_z g\left(n_1^2-n_\theta^2\right)}\left(n_\theta\bar{d}^{\mathrm{e}(00)} + \bar{d}_z^{\mathrm{h}(00)}\right)\,. \tag{5.63}$$

As such, it is constant along the integration path, and $V_{\mathrm{B}}^{(00)} = gE_y^{(00)}$. We recognize the term studied in (5.48).

#### 5.2.4.3 Bloch impedance

**With only the fundamental harmonic** This case is not accurate, because one harmonic is not enough to properly describe the field behavior in the waveguide. However, its simplicity is noteworthy. From (5.56) and (5.63), the Bloch impedance (5.36) for the fundamental harmonic is defined as

$$Z_{\mathrm{B}}^{(00)} = \left| \frac{V_{\mathrm{B}}^{(00)}}{I_{\mathrm{B}}^{(00)}} \right| = \frac{g \frac{2n_\theta}{p_x p_z g\left(n_1^2 - n_\theta^2\right)} \left( n_\theta \bar{d}^{\mathrm{e}(00)} + \bar{d}_z^{\mathrm{h}(00)} \right)}{p_x \frac{2n_1^2}{\eta_0 \mu_{\mathrm{r}1} p_x p_z g\left(n_1^2 - n_\theta^2\right)} \left( n_\theta \bar{d}^{\mathrm{e}(00)} + \bar{d}_z^{\mathrm{h}(00)} \right)} = \eta_0 \frac{g}{p_x} \frac{n_\theta}{\epsilon_{\mathrm{r}1}} \,. \tag{5.64}$$

The Bloch impedance for one harmonic is proportional to the impedance of a parallel-plate waveguide of gap $g$ and width $p_x$. It is also proportional to the effective refractive index $n_\theta$. If the latter is larger in the G-S case, then the Bloch impedance is larger as well. Note that decreasing the gap density makes the impedance larger, and much more so in the G-S case, because then the G-S index become larger than the nGS index (as shown in section 5.1.2).

**General case** When all the harmonics are considered,

$$Z_{\mathrm{B}} = \left| \frac{\sum\limits_{(s,\ell)} V_{\mathrm{B}}^{(s\ell)}}{I_{\mathrm{B}}^{(00)}} \right| = \eta_0 \frac{g}{p_x} \frac{n_\theta}{\epsilon_{\mathrm{r}1}} - \frac{\sum\limits_{(s,\ell)\neq(0,0)} V_{\mathrm{B}}^{(s\ell)}}{I_{\mathrm{B}}^{(00)}} \,. \tag{5.65}$$

In the G-S case, this yields

$$\begin{aligned} Z_{\mathrm{B,GS}} = \quad & \eta_0 \frac{g}{p_x} \frac{n_\theta}{\epsilon_{\mathrm{r}1}} + \sum_{s+\ell \,\mathrm{even}} \frac{2 n_\theta \eta_0 \mu_{\mathrm{r}1} \bar{F}^{(s\ell)} \bar{e}_y^{(00)} \bar{e}_z^{\mathrm{h}(00)*} \bar{e}_y^{(s\ell)*}}{p_x k^{\mathrm{e}2} \left( n_\theta \bar{d}^{\mathrm{e}(00)} + \bar{d}_z^{\mathrm{h}(00)} \right)} \\ = n_\theta \eta_0 & \left[ \frac{g}{p_x} \frac{1}{\epsilon_{\mathrm{r}1}} + \sum_{s+\ell \,\mathrm{even}} \frac{2 \mu_{\mathrm{r}1} \bar{F}^{(s\ell)} \bar{e}_y^{(00)} \bar{e}_z^{\mathrm{h}(00)*} \bar{e}_y^{(s\ell)*}}{p_x k^{\mathrm{e}2} \left( n_\theta \bar{d}^{\mathrm{e}(00)} + \bar{d}_z^{\mathrm{h}(00)} \right)} \right] , \end{aligned} \tag{5.66}$$

whereas in the nGS case,

$$\begin{aligned} Z_{\mathrm{B,nGS}} = \quad & \eta_0 \frac{g}{p_x} \frac{n_\theta}{\epsilon_{\mathrm{r}1}} + \sum_{(s,\ell)\neq(0,0)} \frac{2 n_\theta \eta_0 \mu_{\mathrm{r}1} \bar{F}^{(s\ell)} \bar{e}_y^{(00)} \bar{e}_z^{\mathrm{h}(00)*} \bar{e}_y^{(s\ell)*}}{p_x k^{\mathrm{e}2} \left( n_\theta \bar{d}^{\mathrm{e}(00)} + \bar{d}_z^{\mathrm{h}(00)} \right)} \\ = n_\theta \eta_0 & \left[ \frac{g}{p_x} \frac{1}{\epsilon_{\mathrm{r}1}} + \sum_{(s,\ell)\neq(0,0)} \frac{2 \mu_{\mathrm{r}1} \bar{F}^{(s\ell)} \bar{e}_y^{(00)} \bar{e}_z^{\mathrm{h}(00)*} \bar{e}_y^{(s\ell)*}}{p_x k^{\mathrm{e}2} \left( n_\theta \bar{d}^{\mathrm{e}(00)} + \bar{d}_z^{\mathrm{h}(00)} \right)} \right] . \end{aligned} \tag{5.67}$$

As shown in (5.48), the term in the denominator of the sum is smaller for GS. This means that if we consider the Bloch impedances corresponding to each of the even-order harmonics, the G-S impedance is larger. However, this does not yet mean that the overall sum leads to a smaller G-S Bloch impedance. Indeed, in the nGS case, there are twice as

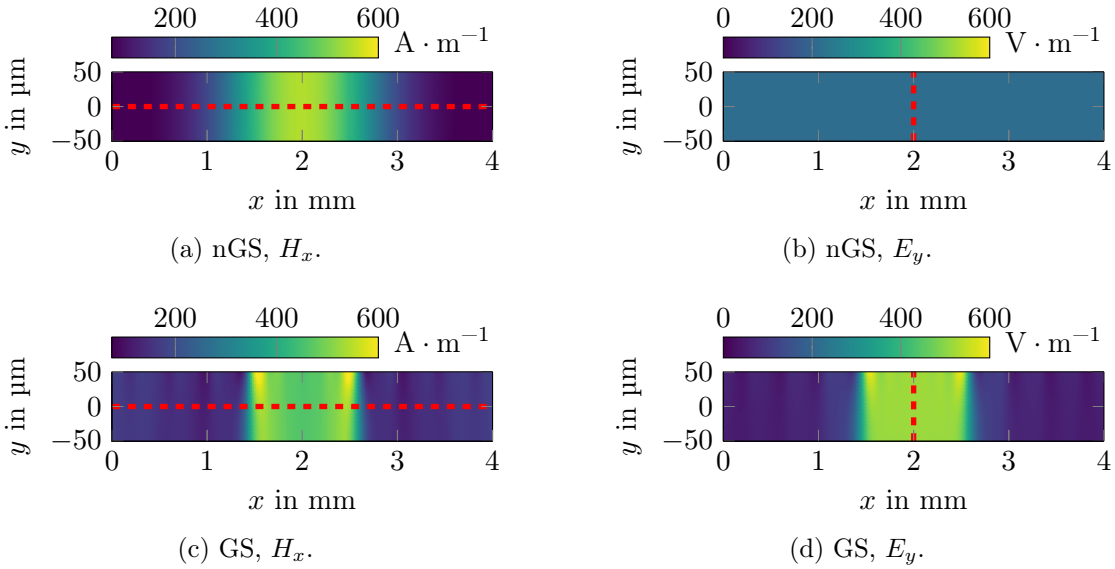


(a) nGS, $H_x$.

(b) nGS, $E_y$.

(c) GS, $H_x$.

(d) GS, $E_y$.

Figure 5.29: Quasi-static fields in the impedance integration plane for a holey PPW with square holes, computed as described in paragraph 5.2.2.2. The integration paths are indicated in dashed red. G-S and nGS configurations are compared. The fields are normalized such that the effective Bloch current is 1 A in both configurations. The structure is filled with vacuum and has dimensions $p = 4\,\text{mm}$, $h = 5\,\text{mm}$, $g = 0.1\,\text{mm}$ and $a = 3\,\text{mm}$.

many terms in the sum, due to all the odd-order harmonics. Appendix E.2.2 holds the proofs that the odd-order harmonics have no impact in (5.67) for square holes. Under this condition, these equations show that the 2-mode Bloch impedance can be written as

$$Z_\text{B} = n_\theta X\,, \quad \text{with} \quad X_\text{GS} > X_\text{nGS}\,, \tag{5.68}$$

where the terms $X_\text{GS}$ and $X_\text{nGS}$ can be identified from (5.66) and (5.67). The impact of GS on $n_\theta$ depending on the dielectrics must be taken into account, as described in paragraph 5.1.2. Since such waveguides are mostly used in a context where the refractive index is increased by GS, (5.68) shows that

$$Z_\text{B,GS} > Z_\text{B,nGS}\,, \tag{5.69}$$

as observed in Figs. 5.21a and 5.22a.

When visualizing the transverse fields in the integration plane, this impedance difference takes on a more physical meaning. Fig. 5.29 plots the magnetic field $H_x$ and the electric field $E_y$ for both G-S and nGS configurations with square holes. The fields are normalized such that the effective Bloch current is the same for both configurations. It appears that in the nGS design, the electric field is almost constant across the unit cell, whereas in the G-S design, it is concentrated in the center, between the two upper holes where it reaches higher values. This increases the Bloch voltage, and the G-S Bloch impedance is larger than the nGS impedance.

This has immediate consequences on the effective constitutive material parameters of the waveguide. The relative permittivity of the waveguide is proportional to the ratio between the refractive index and the impedance i.e., $\epsilon_{\text{eff}} = \eta_0 n_\theta / Z_{\text{B}}$. Considering (5.68), this implies that

$$\epsilon_{\text{eff}} = \frac{\eta_0}{X}, \quad \text{with} \quad X_{\text{GS}} > X_{\text{nGS}}. \tag{5.70}$$

Therefore, (5.70) shows that

$$\epsilon_{\text{eff,GS}} < \epsilon_{\text{eff,nGS}}, \tag{5.71}$$

as observed in Figs. 5.21b and 5.22b. Similarly, the permeability is proportional to the product of the refractive index and the impedance, that is $\mu_{\text{eff}} = n_\theta Z_{\text{B}} / \eta_0$. Therefore, according to (5.68),

$$\mu_{\text{eff}} = \frac{1}{\eta_0} n_\theta^2 X, \quad \text{with} \quad X_{\text{GS}} > X_{\text{nGS}}. \tag{5.72}$$

Assuming that we consider a case where the refractive index is increased by GS, then

$$\mu_{\text{eff,GS}} \gg \mu_{\text{eff,nGS}}, \tag{5.73}$$

as observed in Figs. 5.21c and 5.22c. Note that while (5.69) and (5.73) rely on the assumption that the refractive index is increased by GS, the expression (5.71) is true independently of $n_\theta$. This shows that GS reduces the permittivity of a waveguide even in cases where the G-S refractive index is smaller.

In the end, the quasi-static framework developed in chapters 4 and 5 makes it possible to prove some of the effective material properties of GS. Combined with the refractive index formula (4.40), the Bloch impedance (5.36) gives access to the full characterization of holey PPWs with canonical hole shapes. At the cost of some accuracy, these expressions can be made fully analytical when keeping only the dominant modes, such that the differences between G-S and nGS waveguides are visible in the formulas. This gives elements of analytical proof for the observations made with G-S structures, most notably the increase of the permeability.

## Chapter landmarks

The closed-form formula (4.40) for the refractive index of holey PPWs accelerates the design of metasurface waveguides. But it is also a powerful analysis tool for the properties of G-S structures:

- The impact of the dielectrics in the waveguide is brought to light. The formula (4.40) shows in which cases the G-S refractive index is larger than the nGS index, but also that for some dielectrics this is not the case, contrarily to all the examples shown in literature until now.

- The coupling between upper and lower holes is observed when the gap becomes asymptotically small. When G-S holes are overlapping, a much higher refractive index can be obtained than in the nGS case.

- From (4.40), expressions for the quasi-static fields of the unit cell are derived. By integrating the transverse and magnetic fields in a particular cutting plane, a Bloch impedance is defined. In the case of square and circular holes, this Bloch impedance accurately describes the behavior of the Bloch mode, without the use of commercial solvers. It can be used to achieve impedance matching, or to compute the effective material properties of the waveguide.

- When reducing the field expressions to two modes, the effective material expressions are simplified such that the differences between G-S and nGS waveguides are analytically highlighted. When the G-S refractive index is higher, then so are its impedance and its permeability. The G-S permittivity is always smaller than the nGS permittivity.

These studies are concentrated on the canonical cases of square and circular holes, which are the most commonly used shapes. The definition of the Bloch impedance is based on heuristic observations. Future research should focus on understanding the limits of this impedance's validity, in order to generalize the results derived in this chapter.

# Chapter 6

# Substrate-integrated reconfigurable glide-symmetric phase-shifter

In the previous chapters, holey glide-symmetric (G-S) parallel-plate waveguides (PPWs) are analyzed and modeled in the quasi-static regime. The homogenization of wideband metasurface waveguides not only increases the analytic understanding of glide symmetry (GS), but it also opens the door to the accelerated design of microwave devices, such as lenses. Depending on the expected features of these devices, more complex metasurfaces may be needed. This is particularly true when reconfigurability is sought.

Reconfigurability has become an attractive feature for modern communication systems. Therefore, it is relevant to explore how holey PPWs may be designed to include this feature. As an extension to the theoretical work lead during this thesis, this last chapter proposes the design of a reconfigurable prototype. The complexity of the design puts the developed quasi-static homogenization to the test, and illustrates how GS is an asset for reconfigurability.

Previous reconfigurable devices have benefited from the stopband features of GS. A reconfigurable filter is designed in [139] by breaking the GS, which re-opens the stopband between the first and second modes. On the other hand, [192] exploits the giant stopband that is created between the second and third modes by GS. Changing the gap between the metasurfaces shifts this stopband, such that the operating frequency finds itself either in a passband or in the stopband, creating a high-power-handling switch. In line with the previous chapters, we are more interested in the propagation band of GS, which can be described in the quasi-static regime using the developed framework. That is why we naturally drifted towards the idea of a reconfigurable phaseshifter, with the refractive index being controlled by changing the geometry of the metasurfaces. In the following paragraphs, the inherent advantages of holey G-S PPWs for phase-shifters are presented, as well as the existing possibilities to add reconfigurability to these structures.

**Phase-shifters in gap-waveguide technology** Phase-shifters are needed in many microwave devices, such as phased arrays [193], power dividers [194], magic Ts [195] or phase discriminators. As an alternative to lossy and unshielded microstrip delay-lines,

many phase-shifter concepts in substrate-integrated waveguide (SIW) technology have been developed: changing the width of the waveguide [196], adding inductive posts [197], integrating ferrite materials [198], or creating density changes [199], [200].

However, at millimeter waves, dielectric losses limit the power handling of these designs. Partially air-filled phase-shifters have been presented [201]. But hollow metallic waveguides are the preferred alternative to drive the losses down [202]. Furthermore, gap-waveguide technology avoids the need for contact between upper and lower waveguide parts [203]. Therefore, it has been developed in many microwave applications due to its high power handling abilities [204]. Having two independent metallic layers facilitates the insertion of phase-shifting artefacts within the waveguide, such as ferrite slabs [205]. Additionally, the use of high-impedance surfaces like bed of nails to guide the waves facilitates width variation to change the phase [206]. In [145], a 90°-phase-shifter in gap-waveguide technology is presented, combining the use of a dielectric slab and an increase of the waveguide width to change both the phase and the impedance.

Phase-shifters depending on the length or the width of the waveguide can be difficult to implement in complex microwave devices such as beam-forming networks. Another option to vary the phase is to use metasurfaces. A 90°-phaseshifter is implemented in a square hollow waveguide using corrugated walls [207]. Split-ring resonators of optimized sizes are used in [208] to obtain a set a phase-shifters of same length. In gap-waveguide technology, bed of nails tailored to tune the effective refractive index can be added within the waveguide [209]. The larger the refractive index variation enabled by the pins, the shorter the phase-shifter for a required phase-shift. This motivates the use of GS. In the case of phase-shifters, G-S electromagnetic bandgap (EBG) structures [37] can be used to guide the waves in the gap waveguide more efficiently, but also to improve the effective properties of the waveguide [190]. In [36], a phase-shifter using non-glide-symmetric (nGS) bed of nails is compared with a phase-shifter where the nails on the upper plate are shifted by half a unit cell in the propagation direction, creating GS. This considerably increases the refractive index range, thus leading to a more compact phase-shifter. A similar result can be obtain by replacing the pins with holes [149], which makes the design easier to manufacture.

**Reconfigurable phase-shifters** Most of the previously cited phase-shifter designs offer a fixed phase-shift at a given frequency, but some applications require a reconfigurable phase. Reconfigurable phase-shifters using active components, such as an externally biased ferrite slab [210], or electrically controlled diodes [211]–[213], are power consuming to remain in a given state. Liquid crystals as propagation media are easily electrically reconfigurable, but yield high insertion losses [174], [214]. In [148], it is suggested that the use of gap-waveguide technology makes it easy to replace the inserted slab to change the phase. However, this implies discrete values of the phase, and demands opening the waveguide. Alternatively in [215], a flexible metallic strip is controlled by an external screw to change the inner waveguide width. The groove gap waveguide can also be slotted, such that the phase-shift is externally controlled by moving a high-density dielectric slab over the slots [216]. In [217], a gap waveguide with holey G-S metasurfaces is re-

configured by changing the effective depth of the holes with screws. However, not only does each screw need to be tuned separately, but there must be perfect contact between the screws and the metallic metasurfaces. The resulting manufacturing accuracy would be released if reconfiguration was achieved without contact between the mechanically moving components. Recent designs exploit the interesting contactless property of gap waveguides to change the waveguide dimensions without the leakage that would occur between sliding components [218]. The upper metasurface can be shifted with respect to the lower metasurface to dynamically change the length of the transmission lines, thus changing the phase-shift [219]. Similarly, the width can also be changed by shifting the laterally guiding pins closer [220].

In this chapter, we combine the advantages of contactless high-impedance surface (HIS) and G-S metasurfaces to create a reconfigurable phase-shifter of fixed length and width. Similarly to [217], the idea is to vary the propagation constant in a holey G-S PPW by changing the effective depth of the holes.

This working principle needs a holey PPW that is sensitive to the hole depth. In section 6.1, preliminary studies in the quasi-static regime improve this sensitivity not only through GS, but also by choosing a substrate-integrated technology to integrate the metasurfaces. Reproducing the holes directly in the substrate using metallic vias improves the impact of the hole depth on the refractive index. The validity of the quasi-static homogenization techniques developed in chapter 4 is studied for these substrate-integrated hole (SIH) metasurface PPWs. The reconfigurable unit cell based on these SIHs is then developed in section 6.2. In order to make the reconfigurability possible, HIS metasurfaces are designed such that they offer a stopband at the operating frequencies. Finally, the resulting reconfigurable contactless unit cell is incorporated in the design of a phase-shifter. Section 6.3 presents several leads for the manufacturing of a prototype. CST simulations are presented to validate all the steps of the design, while the device is currently being manufactured and will be measured as soon as it is available.

## 6.1 Preliminary quasi-static studies for reconfiguration

### 6.1.1 Refractive index sensitivity to the hole depth

In order to design a reconfigurable holey PPW whose refractive index changes with the hole depth, the unit cell must be designed such that it is as sensitive as possible to the depth of the holes. At first, in order to design such a cell, we study the sensitivity of different holey surfaces with respect to the hole depth when the hole is closed with perfectly electrically conducting (PEC) plates, as seen in previous chapters. Later on, we will replace the PEC with movable HISs.

The sensitivity of the unit cell to the hole depth is expected to be mostly related to the hole itself – its shape, size, filling – and the dimensions of the basic unit cell such as the gap between the metasurfaces. When opening the holes and loading them capacitively with the HIS, the accurate value of the effective refractive index will probably change compared to holes closed with PEC. However, the sensitivity to the hole depth should

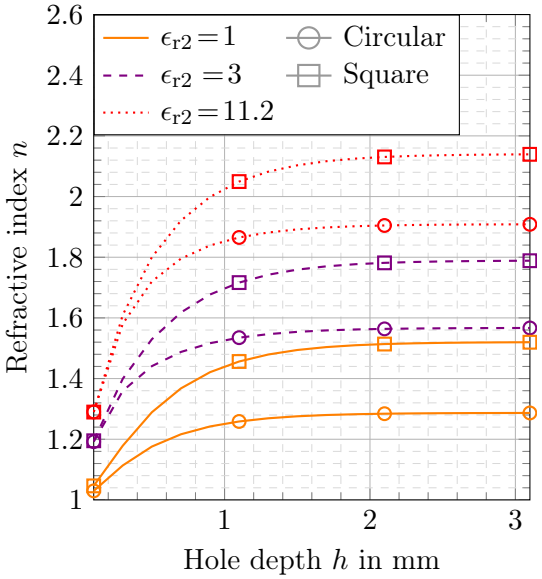


(a) Refractive index as a function of the hole depth.

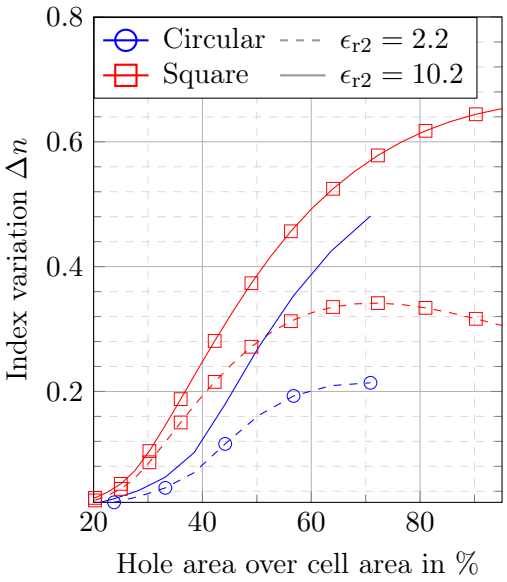


(b) Refractive index variation when changing the hole depth from 0.5 mm to 2.5 mm.

Figure 6.1: Sensitivity of the refractive index to the hole depth of holey G-S PPWs. All waveguides have $p = 4\,\text{mm}$ and $g = 0.1\,\text{mm}$. The holes of depth $h$ are filled with different permittivities $\epsilon_{r2}$. Square and circular holes are compared.

be qualitatively preserved.

In order to accelerate these qualitative preliminary studies, the closed-form formula (4.40) for the quasi-static refractive index makes it very easy to observe the sensitivity to the hole depth for different unit cell designs. As described in the previous chapters, the accuracy of this formula deteriorates with increasing frequency. However this is not a problem here, given that the point of interest is not the exact value of the refractive index, but its quantitative variation with the hole depth. The formula (4.40) is thus well-suited for this kind of studies.

The holey G-S PPWs under study do not have a dielectric filling in the gap $g$ between the holey metasurfaces. Indeed, in order to build a loss-less reconfigurable waveguide, it is preferable that most of the energy be located in air. Therefore, all the following structures have the gap medium $(\epsilon_{r1}, \mu_{r1}) = (1, 1)$. On the other hand, the holes may be filled with a dielectric with permittivity $\epsilon_{r2}$ in order to increase the available refractive index range. This should not affect the losses much, as the waves mainly propagate in the gap. Only non-magnetic substrates are considered, so $\mu_{r1} = 1$. In Fig. 6.1a, the quasi-static refractive index is computed as function of the hole depth $h$. The unit cell has a square periodicity $p = 4\,\text{mm}$ and a gap $g = 0.1\,\text{mm}$. First, circular holes of radius $a = 1.5\,\text{mm}$ are considered.

As observed previously with holey metallic metasurfaces, the refractive index sensitivity to the hole depth is limited. Beyond a certain depth, the refractive index saturates

at a maximum value. This is due to the fact the all the hole modes are excited below their cut-off frequencies, and so the waves have a limited penetration in the holes. A better penetration is achieved when increasing the density of the hole filling, as shown in Fig. 6.1a for permittivities $\epsilon_{r2} = 1$, $\epsilon_{r2} = 3$ and $\epsilon_{r2} = 11.2$. A denser dielectric lowers the cut-off frequencies of the excited modes, and so the sensitivity to the hole depth is increased. Therefore, the convergence value of the refractive index is higher for a denser dielectric.

Increasing the maximum achievable refractive index as function of the hole depth is of foremost importance for the reconfigurable unit cell. Indeed, the higher the maximum index value, the larger the available range of reconfigurable indexes. Moreover, Fig. 6.1a shows that the refractive index is most sensitive when the hole depth is small, meaning that most of the index reconfiguration is only possible when the holes are shallow. This is an important limiting factor given that the unit cell can not be reconfigured starting at $h = 0$: the hole depth is lower-bounded by the thickness of the metallic plates that constitute the PPW. The hole depth can then only be increased by moving the HIS further away of the central PPW. This is illustrated in Fig. 6.1b, which plots the index variation when changing the depth from $h = 0.5\,\text{mm}$ to $h = 2.5\,\text{mm}$. This variation is much smaller than the maximum refractive index that can be achieved by increasing the hole depth, given that the index variation is considered only starting at $h = 0.5\,\text{mm}$, which is assumed to be the thickness of the PEC plate here.

On top of increasing the hole density, another improvement of the depth sensitivity can be achieved by changing the hole shape. Fig. 6.1a shows that square holes yield larger refractive indexes than circular holes with the same area – here, a square size $a = 2.7\,\text{mm}$. Consequently, the possible index variation is larger as well, as illustrated in Fig. 6.1b.

Therefore, these preliminary studies motivate the use of holey PPWs with square holes filled with a dense dielectric, which yield a good sensitivity of the refractive index to the hole depth. Moreover, the thinner the PEC plates of the PPW, the larger the available index variation.

Unfortunately, holey metasurface with dense square holes are difficult to manufacture. It is more expensive to mill square holes compared to the simply drilling circular holes. But most importantly, filling each hole with the required dielectric substrate is particularly challenging. That is why in the next paragraphs, an alternative is sought to facilitate the manufacturing of the reconfigurable unit cell.

### 6.1.2 Improved sensitivity with substrate-integrated holes

The manufacturing of holey metasurface waveguides can be facilitated by using metallized substrate layers instead of fully metallic plates. The resulting waveguides are made of so-called SIHs, which were first introduced in [221]. The idea is to recreate the holes in the dielectric substrate layer by etching the copper on top and bottom metallization away in the desired hole shape, and then by adding metallic vias around the hole. The resulting unit cells are pictured in Fig. 6.2 for circular and square holes, to recreate the PEC-based holes shown above. In [221], the modes that propagate in the recreated holes are

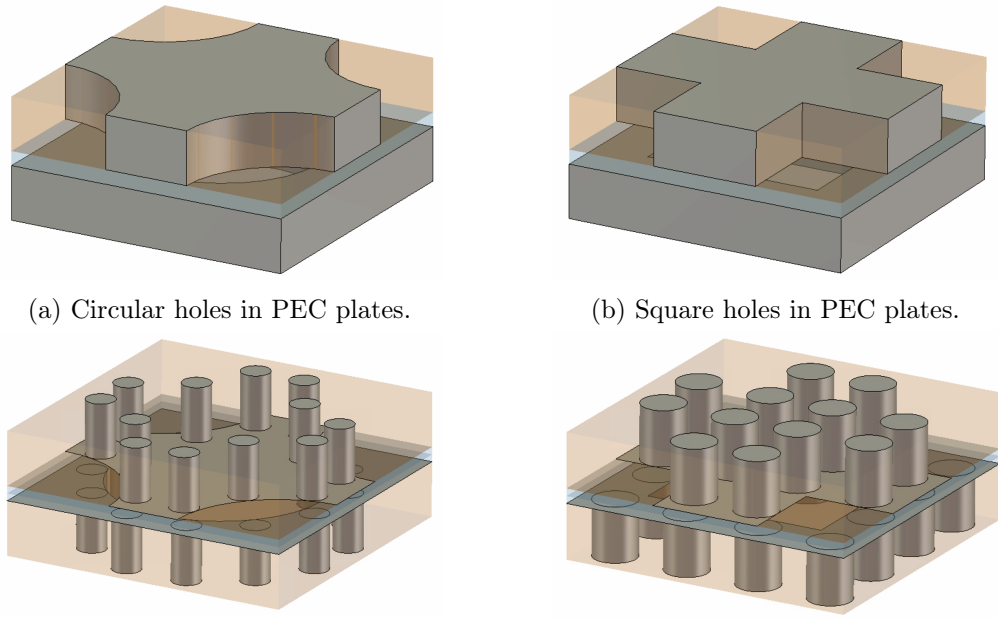

(a) Circular holes in PEC plates.

(b) Square holes in PEC plates.

(c) Circular SIHs.

(d) Square SIHs.

Figure 6.2: Holey G-S PPWs unit cells, as simulated in the eigenmode solver of CST.

observed. It appears that on top of the evanescent transverse electric (TE) and transverse magnetic (TM) modes that slightly penetrate the PEC-based holes, additional modes are able to propagate along the multi-conductor transmission lines created by the metallic vias, which are not limited by their cut-off frequencies. Moreover, additional resonances appear in in the dielectric cavities, leading to narrow stopbands with high rejection. Such SIH metasurfaces are implemented in [222] to build a cost-effective Luneburg lens, where two layers of SIHs form a GS low-loss waveguide. In order to design such a lens and to validate it experimentally [162], [223], the required parametric studies show that SIHs lead to an increased refractive index compared to PEC-based holes, but also to an increased frequency dispersion. SIH waveguides are different from SIWs, where the wave propagates within the substrate through the lateral guiding of the vias [224]. Here, most of the electromagnetic energy is in the empty space between the holey metasurfaces, so the overall structure is low-loss in spite of the dielectric layers. This technique is thus suited for any millimeter-wave device, such as leaky-wave antennas (LWAs), where the beam-correcting prism can be built with SIHs [155].

As such, replacing PEC-based holey metasurfaces with SIHs has several advantages:

- Ease of the manufacturing: PCB layers can be etched and metallic vias formed, which is much simpler than milling metal. This also gives more flexibility for the hole shape, because the latter simply depends on the position of the vias. As an example, [173] builds a compressed Luneburg lens with elliptical SIHs. This is not more complicated than manufacturing circular SIHs, whereas elliptical PEC

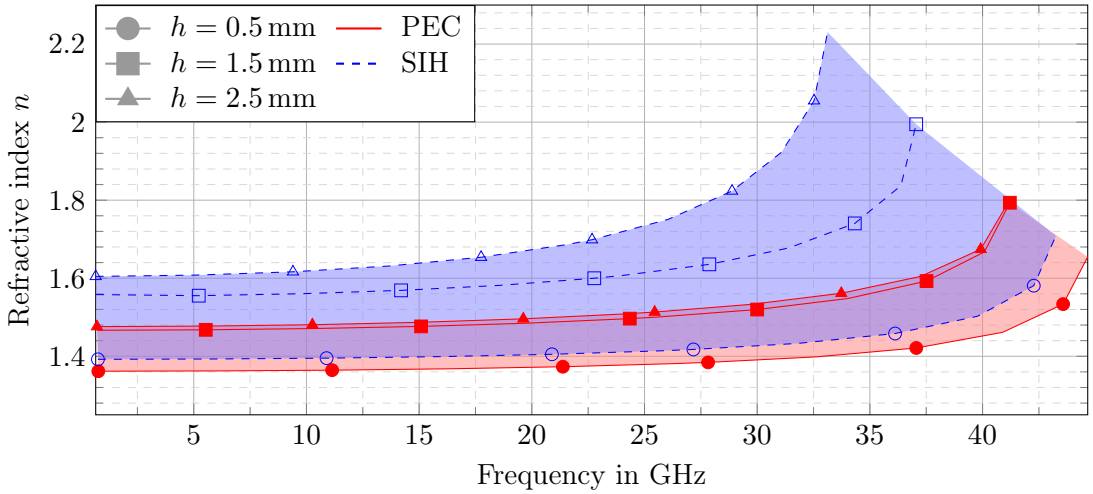


Figure 6.3: Refractive index as a function of frequency, for different hole depths of G-S PPWs with circular holes. PEC-based holes and SIHs designs are compared. The structures have $p = 4\,\text{mm}$, $g = 0.1\,\text{mm}$, and hole of radius $a = 1.5\,\text{mm}$ with $\epsilon_{r2} = 2.2$. For each SIH, 12 vias of radius $r = 0.2\,\text{mm}$ are used.

holes would have required upgraded manufacturing techniques compared to circular holes.

- The use of dielectrics enables higher refractive indexes, thus making possible a larger range of variation. Dielectric-filled holes is in the nature of SIHs, as the dielectric in the holes is the same as the substrate layer. Previously, in order to achieve sufficiently high indexes, a very small gap between the metasurfaces would have been required. The increase of refractive index with SIHs releases this constraint, which facilitating the assembling of prototypes.

- The increase of the possible refractive index range is not only due to the dielectric filling, but also to the increased sensitivity to the hole depth with SIHs. Indeed, the additional modes that propagate along the metallic vias increase the depth beyond which the refractive index saturates. This is particularly useful in regard to our application, given that it extends the portion of the index variation that is available beyond the lower depth bound due to the plate thickness.

This last point is particularly visible in Fig. 6.3, where the refractive index of a holey PPW with circular holes is plotted as a function of frequency. Two designs are compared: PEC-based holes, and SIHs. In each case, the three index curves are plotted: for a hole depth $h = 0.5\,\text{mm}$, for $h = 1.5\,\text{mm}$ and for $h = 2.5\,\text{mm}$. The structures have periodicities $p = 4\,\text{mm}$ and a gap $g = 0.1\,\text{mm}$ between the metasurfaces. Whether PEC-based or substrate-integrated, the holes have a radius $a = 1.5\,\text{mm}$, and are filled with a dielectric with $\epsilon_{r2} = 2.2$ (which is the permittivity of the substre layer used for the SIHs). For each SIH, 12 vias of radius $r = 0.2\,\text{mm}$ give form to the hole.

It appears that for PEC-base holes, the refractive index almost reaches its maximum value at $h = 1.5\,\text{mm}$, and that adding an extra millimeter in depth does not increase the refractive index much more. On the other hand, for SIHs, rising the depth from $h = 0.5\,\text{mm}$ to $h = 1.5\,\text{mm}$ already yields a larger index variation than for PEC holes, and that pursuing up to $h = 2.5\,\text{mm}$ adds another considerable index change.

In Fig. 6.4, the comparison between PEC-based holes and SIHs is developed, with focus on the achievable refractive index variation. The refractive index is plotted as function of the frequency, and each curve corresponds to the index variation when changing the hole depth from $h = 0.5\,\text{mm}$ to $h = 2.5\,\text{mm}$. All the considered structures have periodicities $p = 4\,\text{mm}$ and a metasurface gap $g = 0.1\,\text{mm}$. Square holes of size $a = 2.5\,\text{mm}$ are compared to circular holes of radius $a = 1.5\,\text{mm}$. PEC-based holes are compared to SIHs, where hole shapes are created with 12 vias of radius $r = 0.2\,\text{mm}$. Each subfigure corresponds to a different dielectric filling: $\epsilon_{\text{r}2} = 2.2$, $\epsilon_{\text{r}2} = 4$ or $\epsilon_{\text{r}2} = 10.2$.

These studies confirm the qualitative studies executed with (4.40). Square holes yield a larger hole sensitivity, and the denser the hole dielectric the better. Moreover, the use of SIHs can even double the index variation compared to PEC-based holes.

Nevertheless, (6.4) also confirms that SIHs yield a larger frequency dispersion than PEC holes. If a stable variation of the refraction index is sought over a given bandwidth, then it requires a trade-off with the index variation.

**Substrate-integrated holes with central pin** In [187], [188], it is highlighted that an increased refractive index can be achieved by adding a metallic pin inside the holes, because then a transverse electric magnetic (TEM) mode can penetrate further in the holes. This is confirmed in the numerical application of the quasi-static index formula in section 4.4.3.1. Nevertheless, one of the downsides of this idea is its manufacturing cost, because it demands milling the holes around the central pin.

With SIH technology, adding a central pin does not add any manufacturing complexity to the design, because an additional metallic via is simply added in the middle of the holes. Therefore, it is of interest to see if even more refractive index sensitivity to the hole depth can be achieved with this central via.

In Fig. 6.5, the refractive index of G-S PPWs with square SIHs is plotted as a function of frequency, for different hole depths $h$. The case with an additional central via, enabling the propagation of a TEM mode, is compared to the case without this via. The central via has a radius of 0.4 mm. All waveguides have periodicities $p = 4\,\text{mm}$, the gap between the metasurfaces is $g = 0.1\,\text{mm}$. The square SIHs have a size $a = 2.5\,\text{mm}$. They are made in a substrate $\epsilon_{\text{r}2} = 2.2$ with 12 vias of radius $r = 0.2\,\text{mm}$.

Without the central via, the refractive index variation from $h = 0.5\,\text{mm}$ to $h = 2.5\,\text{mm}$ is approximately 0.33 at low frequencies. When adding the central pin, it rises up to 0.45. This confirms that a larger index variation can be obtained by enabling the propagation of TEM modes in the holes. However, this design is not pursued in the rest of this chapter. The reason is the increased frequency dispersion. SIHs are already responsible for a rise of the dispersive behavior, limiting the bandwidth in which the refractive index variation is stable. In Fig. 6.5 this phenomenon is accentuated by the central pin. The

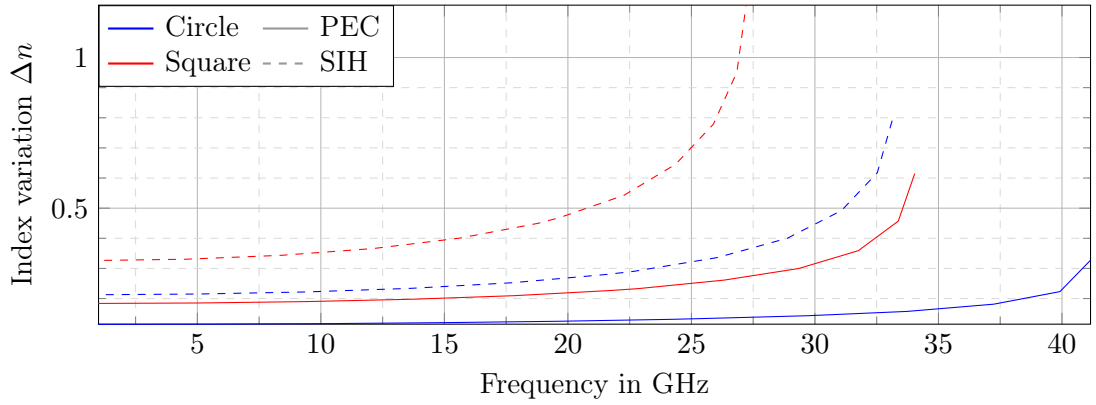


(a) $\epsilon_{r2} = 2.2$.

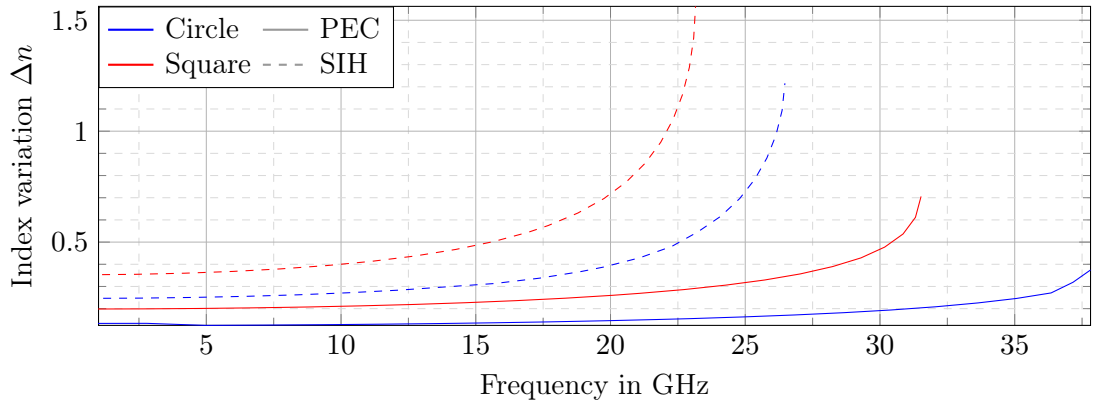


(b) $\epsilon_{r2} = 4$.

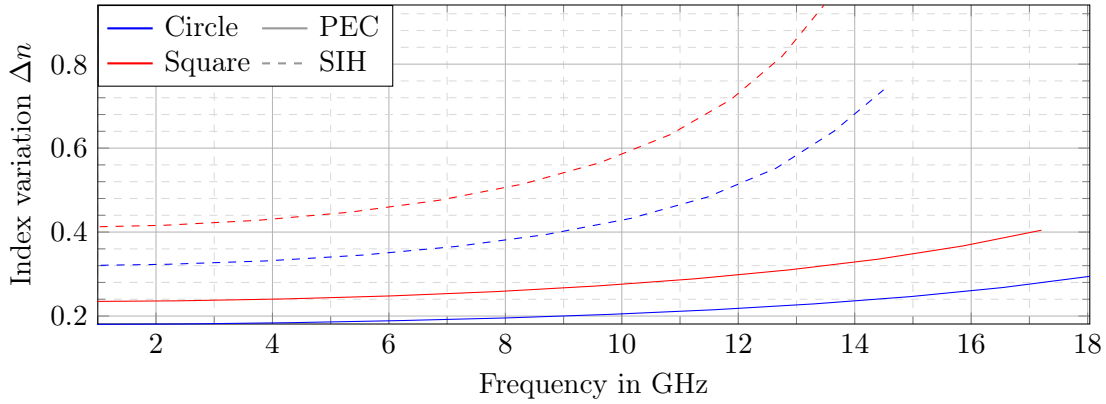


(c) $\epsilon_{r2} = 10.2$.

Figure 6.4: Refractive index variation of holey G-S PPWs when changing the hole depth from $h = 0.5\,\text{mm}$ to $h = 2.5\,\text{mm}$. All waveguides have $p = 4\,\text{mm}$ and $g = 0.1\,\text{mm}$. Square holes have $a = 2.5\,\text{mm}$, whereas circular holes have $a = 1.5\,\text{mm}$. SIHs have 12 vias of radius $r = 0.2\,\text{mm}$.

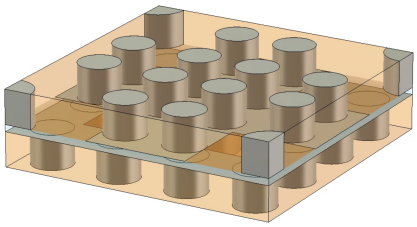

(a) CST unit cell model.

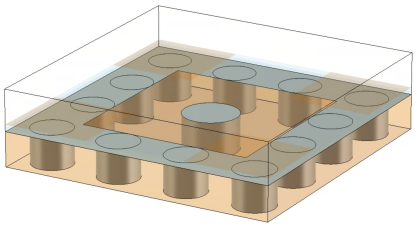

(b) View of the lower substrate.

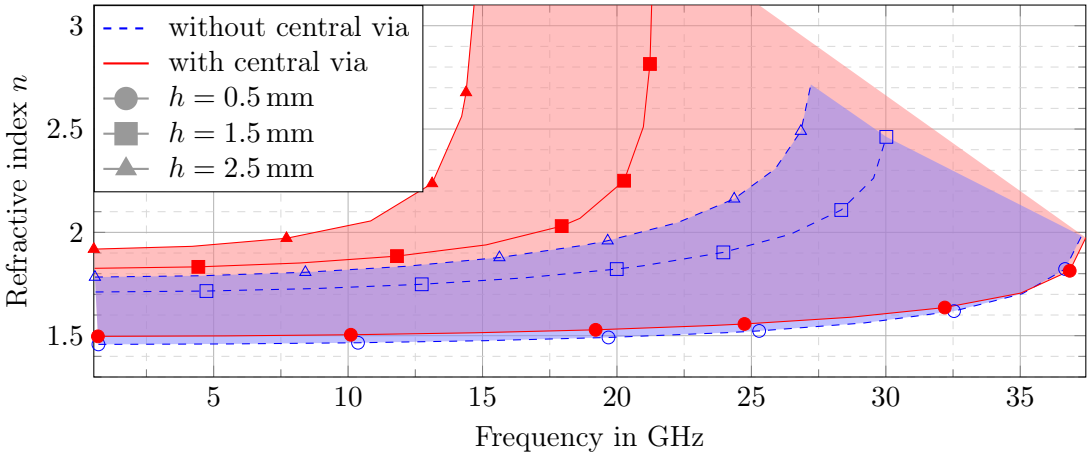


(c) Refractive index.

Figure 6.5: Refractive index as a function of frequency, for different hole depths of G-S PPWs with square SIHs, with or without central via. The structures have $p = 4\,\text{mm}$, $g = 0.1\,\text{mm}$, and SIHs of size $a = 2.5\,\text{mm}$ with $\epsilon_{r2} = 2.2$, and 12 vias of radius $r = 0.2\,\text{mm}$. The central pin has a radius of $0.4\,\text{mm}$.

trade-off between dispersion and index variation favors the design without the central pin, at the expense of some index range.

### 6.1.3 Necessity of glide symmetry for hole depth impact

In the previous paragraphs, all the considered structures are G-S, both for PEC-based holes and SIHs. A first reason is that GS reduces the frequency dispersion compared to its nGS counterpart structure. Given that the frequency dispersion has been observed to be a potential issue, this is already a valid motivation for the use of GS.

But in Fig. 6.6, a more irrevocable argument in favor of GS is observed. The refractive index variation as a function of frequency is plotted again, but this time comparing a SIH G-S PPW with its nGS counterpart. The structures have periodicities $p = 4\,\text{mm}$, the gap between the metasurfaces is $g = 0.1\,\text{mm}$, the square SIHs have a size $a = 2.5\,\text{mm}$ and are made in a substrate $\epsilon_{r2} = 10.2$ with 12 vias of radius $r = 0.2\,\text{mm}$. The hole depth is changed from $h = 0.5\,\text{mm}$ to $h = 2.5\,\text{mm}$.

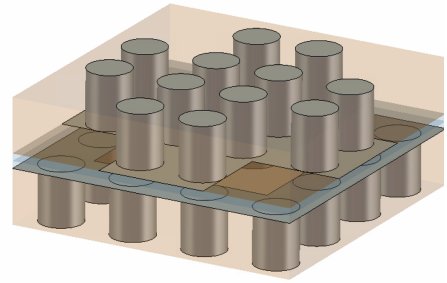

(a) G-S SIHs.

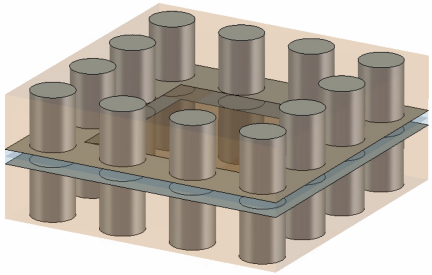

(b) NGS SIHs.

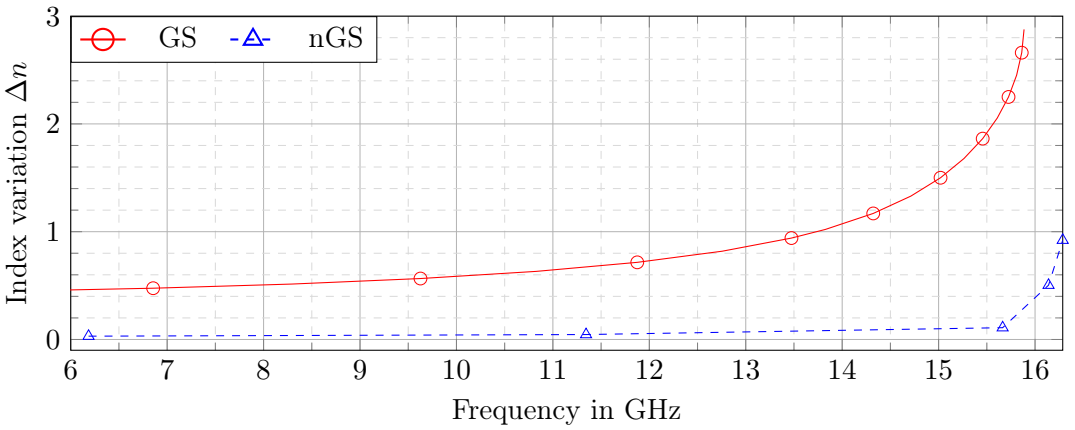


(c) Refractive index variation.

Figure 6.6: Refractive index variation of SIH PPWs when changing the hole depth from $h = 0.5\,\text{mm}$ to $h = 2.5\,\text{mm}$. The G-S design is compared to the nGS design. The waveguides have $p = 4\,\text{mm}$ and $g = 0.1\,\text{mm}$. The square SIHs have $a = 2.5\,\text{mm}$, 12 vias of radius $r = 0.2\,\text{mm}$, and $\epsilon_{r2} = 10.2$.

It appears that the nGS design has almost no sensitivity to the hole depth: changing the depth from $h = 0.5\,\text{mm}$ to $h = 2.5\,\text{mm}$ leads to a refractive index variation of 0.03 at low frequencies, whereas the same depth change increases the G-S index by 0.42. This difference makes the nGS design unsuitable for the considered reconfigurable unit cell. Therefore, without GS, changing the hole depth in order to control the effective refractive index of the waveguide would be much more challenging.

In light of manufacturing issues, the power of GS is even more appreciable, because adding GS to a design does not increase the manufacturing complexity one bit. One just needs to shift the upper metasurface by half a cell length with respect to the lower metasurface. The only constraint is that one should be careful with the alignment of the metasurfaces in order to maintain the $p/2$-shift.

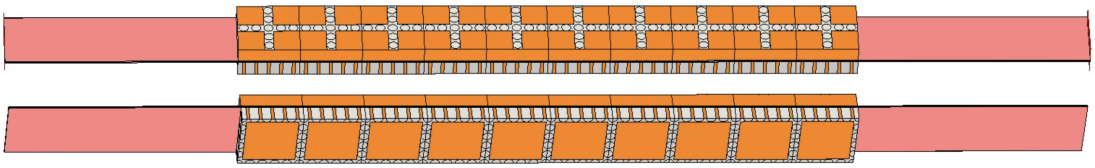

(a) CST model for impedance-matching with SIHs.

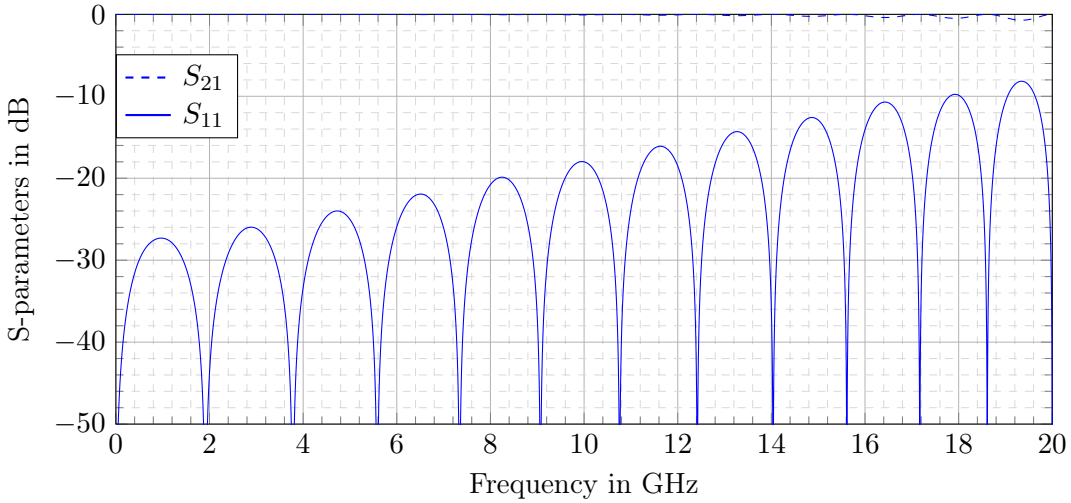


(b) Resulting S-parameters.

Figure 6.7: Impedance matching of a dielectric PPW $(\epsilon_{\mathrm{rL}}, \mu_{\mathrm{rL}}) = (0.52, 27.22)$ of height $g = 0.1\,\mathrm{mm}$, blocked by 10 cells of a SIH G-S PPW. Each feeding dielectric is 15 mm long. The metasurface waveguide has $p = 4\,\mathrm{mm}$, and square SIHs of size $a = 3.4\,\mathrm{mm}$, filling $\epsilon_{\mathrm{r2}} = 6.5$ and depth $h = 1\,\mathrm{mm}$.

### 6.1.4 Extension of the Bloch impedance to substrate-integrated holes

Paragraph 6.1.2 shows that the quasi-static refractive index formula (4.40) can be used to gain preliminary knowledge about structures that are more complex than holey metasurface PPWs, namely for SIHs metasurface waveguides. We investigate here whether the other characterization tool developed for holey PPWs in the quasi-static regime can be used for PPWs, that is the Bloch impedance computed analytically in section 5.2. The purpose of this impedance is to avoid reflections at the transition between different dielectric PPWs by adding holey metasurfaces on both sides of the new dielectric. In section 5.2.3.2, in order to evaluate the validity of the computed impedance, the effective permittivity and permeability of the holey PPW is computed analytically in the quasi-static regime. A portion of this metasurface waveguide is then placed between two dielectric PPWs, tuned to match the corresponding effective constitutive parameters. Observing that the reflections at the waveguide transitions are indeed suppressed confirms that the computed effective parameters are indeed valid.

The same procedure is applied for G-S PPW with SIHs. A waveguide with periodicity $p = 4\,\text{mm}$ and gap $g = 0.1\,\text{mm}$ is considered. The gap is empty, and the metasurfaces are made of square holes of size $a = 3.4\,\text{mm}$ and depth $h = 1\,\text{mm}$, filled with a dielectric $\epsilon_{\text{r2}} = 6.5$. The Bloch impedance and the effective refractive index are computed for these dimensions, yielding $\epsilon_{\text{eff}} = 0.52$ and $\mu_{\text{eff}} = 27.22$. This would be an accurate characterization of the waveguide for PEC-based holes. However, the simulation setup to validate this characterization is applied to a SIH waveguide with the same dimensions. As illustrated in Fig. 6.7a, 10 unit cells of the metasurface waveguide are placed in-between two dielectric PPWs of length 15 mm, with the computed constitutive parameters. The S-parameters of the resulting structure are then plotted in Fig. 6.7b.

The matching with SIHs is surprisingly good, most of the reflections being avoided. This means that the Bloch impedance computed for the metallic holey PPW is a good approximation of the reflective behavior of the SIH waveguide. An explanation for this could be that the SIHs do not impact the shape of the fields in the gap much, where the fields are integrated to define the Bloch impedance.

It has been observed that SIHs increase the effective refractive index. If the Bloch impedance is approximately constant with or without SIHs, it means that the effective constitutive parameters of the PEC-based waveguide are both multiplied by the same factor when implementing SIHs. Although we leave these findings open to deeper studies, they are an additional illustration of how the quasi-static analysis of holey PPWs opens the door to the simulation and understanding of waveguides that can be much more complex than metallic metasurfaces.

## 6.2 Design of the reconfigurable unit cell

### 6.2.1 Reconfiguring the substrate-integrated hole depth with high-impedance metasurfaces

In the G-S-waveguide studied in section 6.1, the depth $h$ of the holes is fixed, whether the holes are formed in a PEC or in a substrate layer. Indeed, the bottom of the holes is closed by metal. In order to reconfigure this depth, one could insert metallic cylinders in the holes, that would slide to change the depth, as is done in [217]. The advantage of this technique is that the holes can be completely filled with the metallic cylinder, offering a large range of depth variation. However, it requires perfect contact between the cylinders and the holes to avoid leaks, which leads to manufacturing complications.

In this work, we aim at contactless reconfiguration of the hole depth. In order to do so, the holes are completely going through the layer (metallic or dielectric), such that they are opened to the outside of the holey G-S PPW. However, the waves should not escape the waveguide through the holes. In order to prevent this leakage, HISs are placed on both sides of the PPW, as illustrated in red in Fig. 6.8. These HIS are designed to yield a stopband for surface waves at the operating frequency. Therefore, the waves that try to escape the PPW through the holes are confined in the region between the holes and the HIS, without being able to propagate outside of the PPW. This confinement can be seen

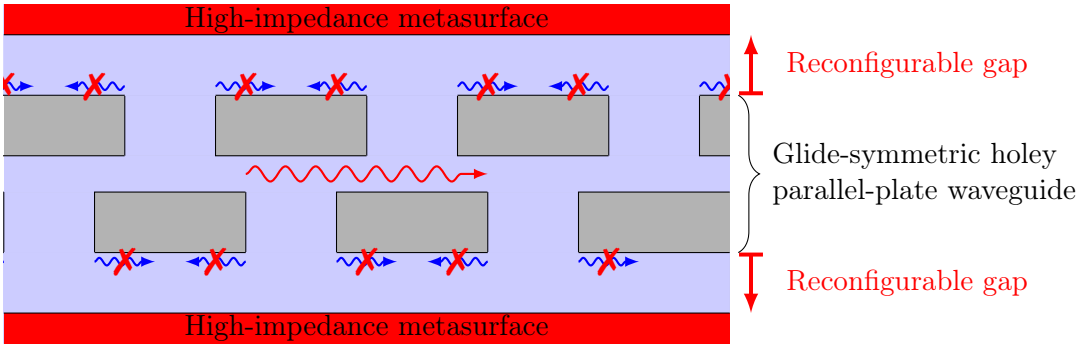


Figure 6.8: Illustration of the contactless depth reconfiguration concept, for a holey G-S PPW.

as a capacitive cavity that extends the hole, effectively lengthening its depth. Therefore, when moving the HISs closer or further away from the central PPW, this effective depth is changed, impacting the refractive index according to its depth sensitivity, as described in section 6.1.

In order for this process to be effective, there are two distinct requirements:

- First, the reconfiguration of the HIS position must cause a variation of the effective refractive index. For this to be true, the central holey PPW must be designed such that it is sensitive to the hole depth. Moreover, the central layers must be thin enough that the waves can see the movement of the HISs on the other side of the holes. These aspect have been explored in section 6.1, where SIHs with square holes stand out as a good candidate.

- Second, the HISs must prevent the propagation of surface waves within the complete operation band. This means that its stopband must be large enough such that it covers the operation band even when moving the HISs further away from the central PPW.

In the following paragraphs, the HIS is designed independently of the central waveguide.

### 6.2.2 High-impedance metasurfaces

The HIS should be substrate-integrable to ease the final manufacturing. Therefore, high-impedance mushroom metasurfaces are used, as presented in [225]. These metasurfaces are made of a dielectric layer with a ground metallization on one side, whereas the other side is covered with a periodic array of metallic patches. Each patch is linked to the ground with a metallic via that goes through the dielectric. The unit cell of this structure looks like a mushroom, as shown in Fig. 6.9.

Such a mushroom HIS is convenient in terms of manufacturing, because it does not require more techniques than for the realization of the SIH layers of the central waveguide. Mushrooms also appear to be particularly effective when it comes to the width of the

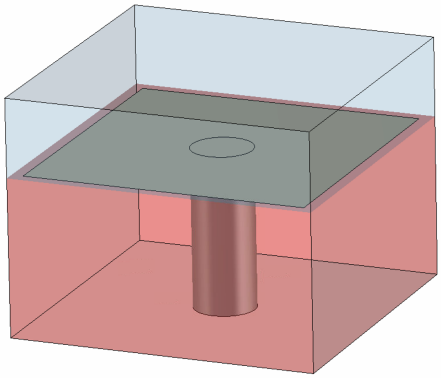

Figure 6.9: CST capture of the HIS mushroom unit cell. The structure is periodic in $z$- and $x$-directions, and closed with PEC boundaries at the top and bottom. The layer is filled with vacuum, whereas the area below the mushroom is a dielectric.

achievable stopband, because of their particular resonances. Moreover, mushrooms offer a large number of dimensional parameters, which can be tuned to obtain the desired stopband. Parametric studies are undertaken next to observe how the stopband can be adjusted.

#### 6.2.2.1 Parametric study of an EBG mushroom metasurface

The EBG behavior of the mushroom metasurface is described in [225]. In this section, similar designs are studied in CST from a parametric point of view, in order to understand the impact of the dimensions of the structure on the bandgap. In the following, each cell of the metasurface has a size $p_{\text{HIS}} \times p_{\text{HIS}}$. The dielectric substrate of relative permittivity $a_{\text{HIS}}$ has a thickness $h_{\text{HIS}}$. It is grounded by a PEC boundary, and covered by a small air layer of thickness $g_{\text{HIS}}$, which is the parameter that varies in the final reconfigurable structure. Contrarily to the structure in [225], the waveguide is closed on its top by a PEC plate, creating a PPW partly filled with dielectric. The PEC mushrooms are embedded in the dielectric layer, and are formed by a square patch at the surface of the dielectric of size $a_{\text{HIS}} \times a_{\text{HIS}}$. Its thickness is ideally assumed to be zero. The patch is then shorted to the ground plane by a metallic via, placed in the middle of each patch, with radius $r_{\text{HIS}}$.

The impact of each of these parameters is considered in Figs. 6.10 to 6.15. In each case, the Brillouin diagram of the unit cell is plotted for two or three modes, in order to highlight the stopband after the first mode. The propagation direction is aligned with the mushroom array. The structures are simulated in CST with the dimensions listed in the caption of each figure.

**Impact of the air layer** Fig. 6.10 shows that a larger air layer leads to a smaller bandgap. This is understandable, because the larger the layer, the smaller the impact of the boundary conditions at a given frequency, and so the HIS filters less and less

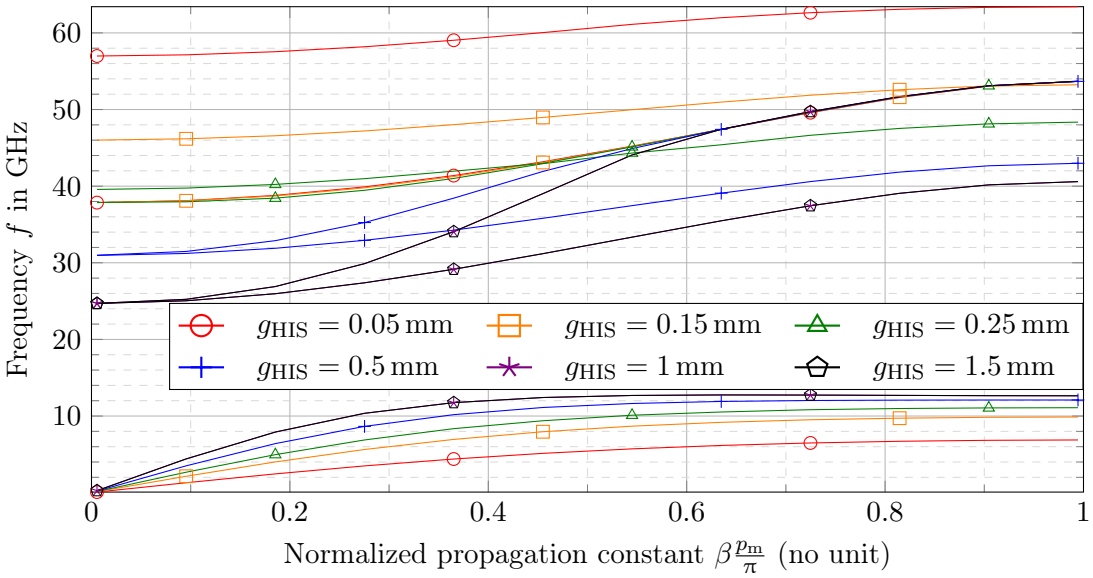


Figure 6.10: Brillouin diagram of the mushroom HIS, for different air layers $g_{HIS}$, and with $p_{HIS} = 2\,mm$, $r_{HIS} = 0.2\,mm$, $a_{HIS} = 1.85\,mm$, $h_{HIS} = 1.6\,mm$, and $\epsilon_{HIS} = 2.2$.

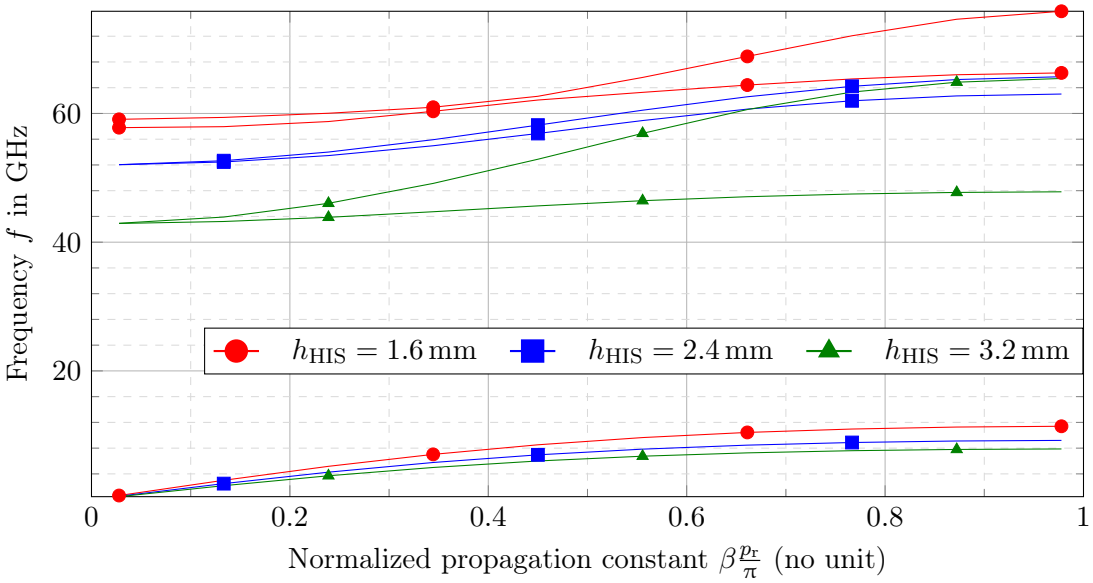


Figure 6.11: Brillouin diagram of the mushroom HIS, for different substrate thicknesses $h_{HIS}$, and with $p_{HIS} = 2\,mm$, $g_{HIS} = 0.15\,mm$, $r_{HIS} = 0.2\,mm$, $a_{HIS} = 1.85\,mm$, and $\epsilon_{HIS} = 1$.

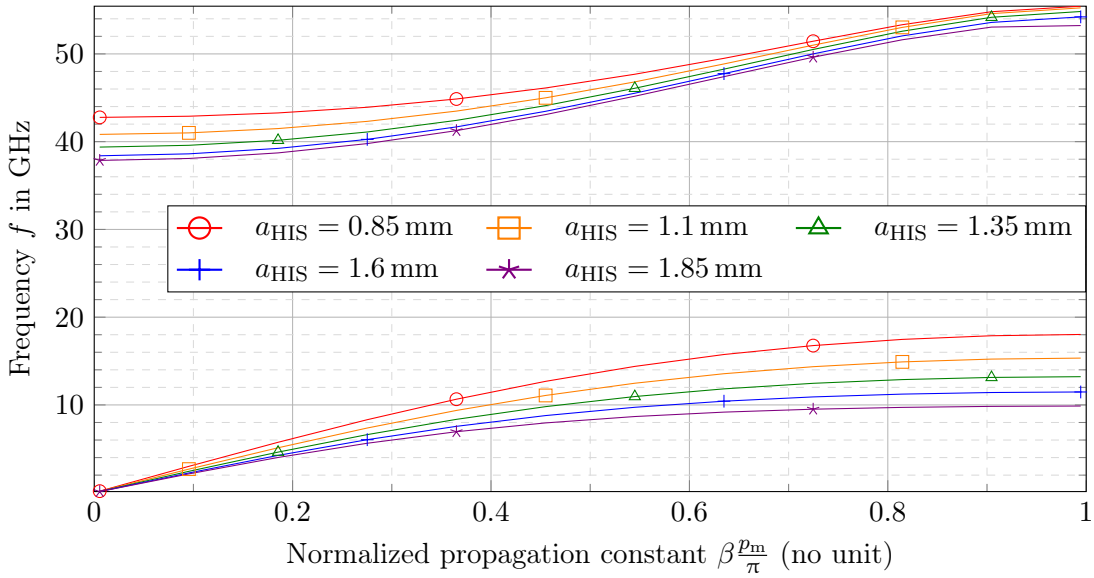


Figure 6.12: Brillouin diagram of the mushroom HIS, for different patch sizes $a_\mathrm{HIS}$, and with $p_\mathrm{HIS} = 2\,\mathrm{mm}$, $g_\mathrm{HIS} = 0.15\,\mathrm{mm}$, $r_\mathrm{HIS} = 0.2\,\mathrm{mm}$, $h_\mathrm{HIS} = 1.6\,\mathrm{mm}$, and $\epsilon_\mathrm{HIS} = 2.2$.

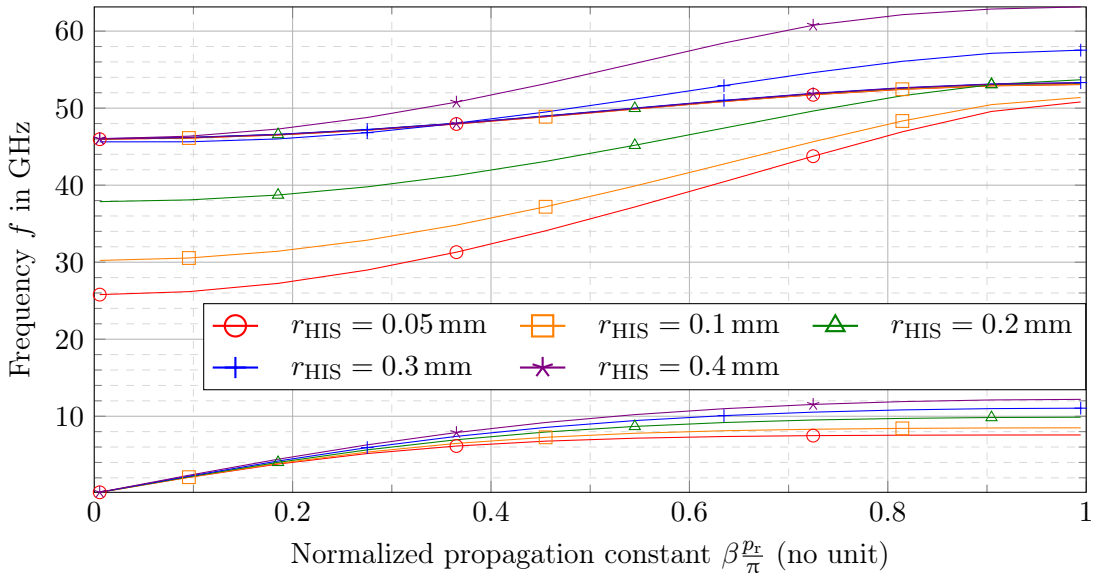


Figure 6.13: Brillouin diagram of the mushroom HIS, for different via radii $r_\mathrm{HIS}$, and with $p_\mathrm{HIS} = 2\,\mathrm{mm}$, $g_\mathrm{HIS} = 0.15\,\mathrm{mm}$, $a_\mathrm{HIS} = 1.85\,\mathrm{mm}$, $h_\mathrm{HIS} = 1.6\,\mathrm{mm}$, and $\epsilon_\mathrm{HIS} = 2.2$.

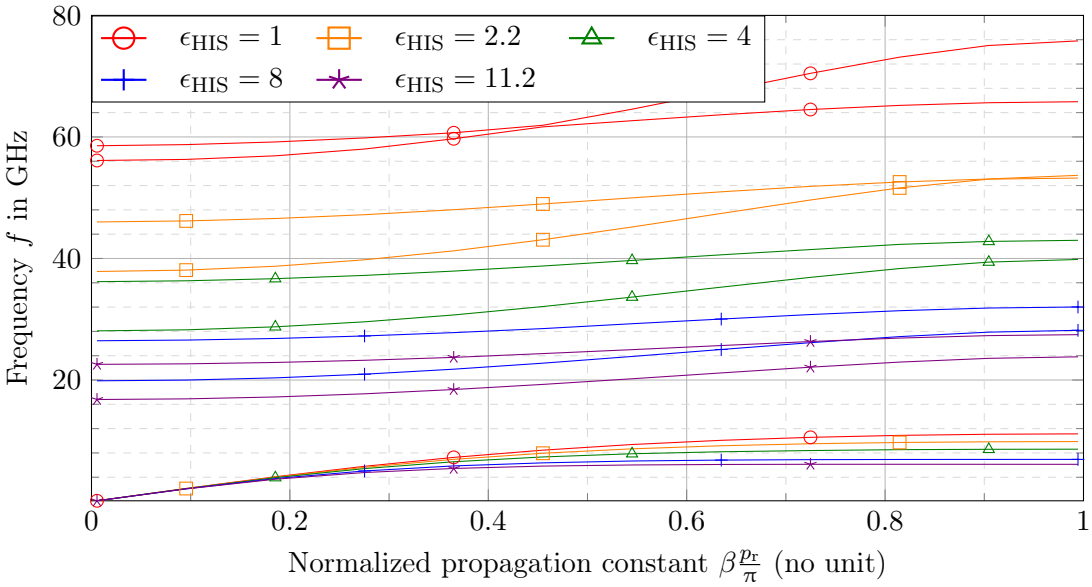


Figure 6.14: Brillouin diagram of the mushroom HIS, for different substrate permittivities $\epsilon_{\mathrm{HIS}}$, and with $p_{\mathrm{HIS}} = 2\,\mathrm{mm}$, $g_{\mathrm{HIS}} = 0.15\,\mathrm{mm}$, $r_{\mathrm{HIS}} = 0.2\,\mathrm{mm}$, $a_{\mathrm{HIS}} = 1.85\,\mathrm{mm}$, and $h_{\mathrm{HIS}} = 1.6\,\mathrm{mm}$.

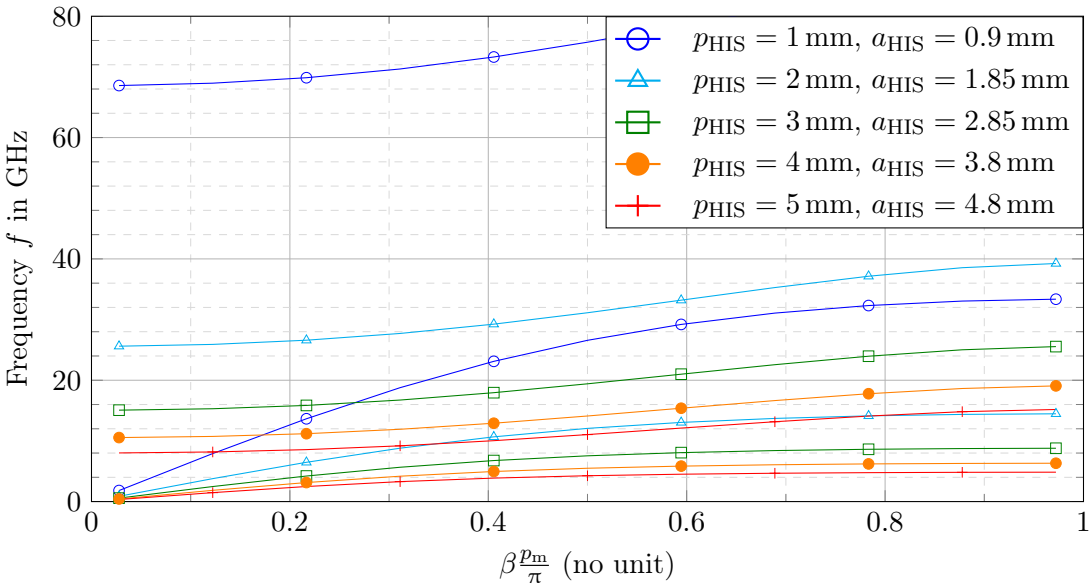


Figure 6.15: Brillouin diagram of the mushroom HIS, for different cell periodicities $p_{\mathrm{HIS}}$ and corresponding $a_{\mathrm{HIS}}$, and with $g_{\mathrm{HIS}} = 0.05\,\mathrm{mm}$, $r_{\mathrm{HIS}} = 0.2\,\mathrm{mm}$, $\epsilon_{\mathrm{HIS}} = 4$, and $h_{\mathrm{HIS}} = 0.25\,\mathrm{mm}$.

frequencies with increasing layer. This reduction of the stopband happens both at the lower and the upper frequency bounds.

**Impact of the dielectric tickness** When the dielectric layer gets thicker, the stopband shifts towards lower frequencies, as illustrated in Fig. 6.11. Indeed, increasing the dielectric thickness lenghtens the metallic via, and therefore lowers the resonance of the mushroom. If this parameter is controlled to tune the position of the stopband, it must be kept in mind that the HIS layer is mechanically moved in order to reconfigure the waveguide. Therefore, this layer should not be too thin, otherwise it could be not sufficiently rigid, and this might impact the accuracy of the reconfiguration.

**Impact of the patch size** In Fig. 6.12, the size of the square patches has a similar effect as the dielectric height, because increasing the patch size shifts the resonance frequency of the mushroom down. Nevertheless, the patch size has a strong impact on the lower bound of the stopband. In terms of relative bandwidth, a large patch achieves a better stopband than a small patch. Therefore, it is advisable to maximize the patch size for a given unit cell area.

**Impact of the via radius** The radius of the via might seem to be a parameter of secondary importance. However, Fig. 6.12 shows that it has a strong impact on the stopband as well. The thicker the via, the higher the stopband. Also, the relative bandwidth of the stopband increases slightly with the radius. Therefore, it appears that a large via is preferable.

**Impact of the substrate permittivity** The impact of the substrate permittivity in Fig. 6.14 is similar to the effect of the via radius. The denser the dielectric, the lower the stopband, but also the smaller its relative bandwidth. Ideally, the mushrooms would be just PEC in air to maximize the stopband. However, in order to make the integrated manufacturing possible, some kind of substrate must be chosen as a support for the mushrooms.

**Impact of the unit cell periodicity** From Fig. 6.15, it appears that the period of the unit cell remains the main lever to shift the stopband around a desired frequency. In this figure, the size of the patches is changed along with the unit cell, such that it covers most of the cell area. A period $p_{\mathrm{HIS}} = 1\,\mathrm{mm}$ yields a stopband between 33 GHz and 68 GHz, whereas a period of $p_{\mathrm{HIS}} = 5\,\mathrm{mm}$ yields a stopband between 4.5 GHz and 8 GHz. The relative bandwidth is not strongly affected.

In order to satisfy the stopband requirements of a given application, the HIS mushroom has many parameters that can be tuned. If possible, a dense substrate and large vias should be used. The cell periodicity controls the overall location of the stopband. Then, the size of the mushroom can be optimized such that they yield the best upper and lower frequency bounds. The patch size has a strong control on the lower frequency bound, whereas the substrate thickness has more control on the upper bound. Finally,

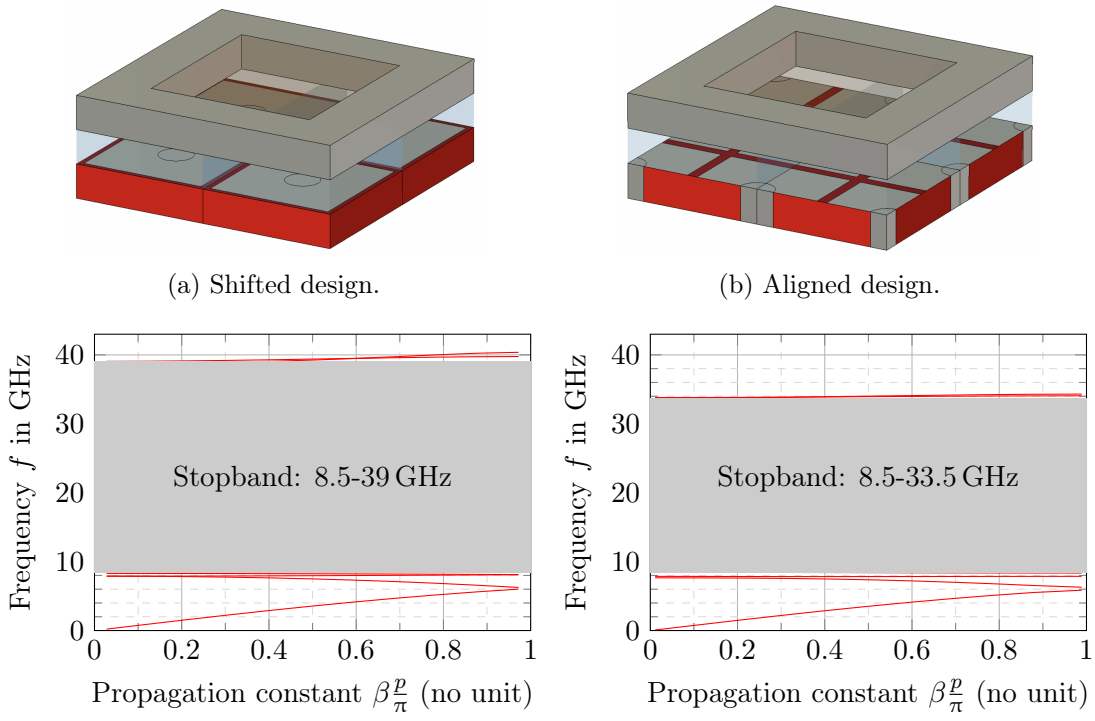


(a) Shifted design.

(b) Aligned design.

(c) Shifted design.

(d) Aligned design.

Figure 6.16: Brillouin diagram of the HIS covered with a holey PEC plate. Shifted and aligned designs are compared. The mushroom layer built in a substrate $a_{\text{HIS}} = 2.2$ has dimensions $p_{\text{HIS}} = 2\,\text{mm}$, $h_{\text{HIS}} = 1.6\,\text{mm}$, $a_{\text{HIS}} = 1.85\,\text{mm}$, $r_{\text{HIS}} = 0.2\,\text{mm}$ and $g_{\text{HIS}} = 0.1\,\text{mm}$. The holey PEC layer has $p = 4\,\text{mm}$, $a = 2.5\,\text{mm}$, $h = 0.25\,\text{mm}$ and $\epsilon_{\text{r2}} = 11.2$.

this optimization process should be fulfilled with the maximum air layer used in the final application, because it is the worst case in terms of stopband.

#### 6.2.2.2 Influence of the holey plate on the high-impedance metasurface

In the previous section, the mushroom metasurface is covered with a simple PEC plate. However, in the final structure, the holey GS PPW that is layered above the mushrooms does not offer an infinite PEC surface, but a holey PEC plate or SIHs. In order for the dimensions of the HIS to be better adjusted, we simulated a waveguide as presented in Fig. 6.16a: the mushroom metasurface is faced with a hole, like in the final structure. The hole is closed with PEC. In the following, the mushroom period is half that of the hole period, meaning that four mushrooms face each hole. These studies hint on how the center waveguide influences the stopband of the HIS.

When looking at Fig. 6.16a, it appears that two designs are possible: the “shifted”

version, where the center of the hole is aligned with the intersection of four adjacent patches, and the "aligned" version, where the hole axis is aligned with the axis one of the mushroom patches, as illustrated in Fig. 6.16b. The Brillouin diagrams of the modes in the HIS corresponding to Figs. 6.16a and 6.16b are plotted in Figs. 6.16c and 6.16d, respectively. The mushrooms have a period $p_{\mathrm{HIS}} = 2\,\mathrm{mm}$. There are embedded in a dielectric substrate $a_{\mathrm{HIS}} = 2.2$ of thickness $h_{\mathrm{HIS}} = 1.6\,\mathrm{mm}$. The square patch size is $a_{\mathrm{HIS}} = 1.85\,\mathrm{mm}$, and the metallic vias have a radius $r_{\mathrm{HIS}} = 0.2\,\mathrm{mm}$. The layer between the HIS and the covering PEC is $g_{\mathrm{HIS}} = 0.1\,\mathrm{mm}$. The holey metallic metasurface has a period $p = 4\,\mathrm{mm}$ and square holes of size $a = 2.5\,\mathrm{mm}$ and depth $h = 0.25\,\mathrm{mm}$, filled with a dielectric of permittivity $\epsilon_{\mathrm{r}2} = 11.2$.

Fig. 6.16 shows that the alignment of the mushrooms with the holes has an impact on the stopband. If a large stopband is sought, then the shifted design is preferable – that is when the center axis of the hole is aligned with the intersection between four mushrooms. The aligned design reduces the upper bound of the stopband by several gigahertz.

It appears that the holes in the upper plate have an impact on the stopband of the HIS. The influence of each parameter of these holes must be studied. This is done in Fig. 6.17, where the stopband of structures similar to Fig. 6.16a is studied as a function of the layer $g_{\mathrm{HIS}}$ between the HIS and the central holey layer. This time, SIH layers are used, with permittivity $\epsilon_{\mathrm{r}2}$ and thickness $h$. The square SIHs of size $a$ are made of 12 vias of radius $r = 0.3\,\mathrm{mm}$, forming an array of periodicity $p = 4\,\mathrm{mm}$. The parameters $\epsilon_{\mathrm{r}2}$, $h$ and $a$ are varied in Figs. 6.17a, 6.17b and 6.17c, respectively. For all structures, the mushrooms are the same, with dimensions $p_{\mathrm{HIS}} = 2\,\mathrm{mm}$, $h_{\mathrm{HIS}} = 0.5\,\mathrm{mm}$, $a_{\mathrm{HIS}} = 1.85\,\mathrm{mm}$, and $r_{\mathrm{HIS}} = 0.25\,\mathrm{mm}$.

Fig. 6.17 shows that when the layer $g_{\mathrm{HIS}}$ is large, the stopband is independent of the SIH parameters. According to these findings, the alignment of the layers described in Fig. 6.16 is not restrictive either, because it loses its influence with large $g_{\mathrm{HIS}}$. Nevertheless, in the following, the shifted design is chosen by default.

### 6.2.3 Reconfigurable unit cell in the Ku band

In sections 6.1.2 and 6.2.2, both elements of the reconfigurable unit cell are studied: the SIH central waveguide, and the mushroom HIS. These elements can be designed separately in order to achieve the best results in a given stopband.

The stopband of the HIS must include the operation band of the application. While sat-com and 5G applications of interest would require a prototype working in the Ka frequency band, in this chapter we propose a preliminary design in the Ku band for a proof of concept, in order to take advantage of fabrication tolerances that are less strict.

#### 6.2.3.1 High-impedance metasurface in the Ku band

For the Ku band, the mushrooms can be tuned to yield the Brillouin diagram in Fig. 6.18a. The periodicity is $p_{\mathrm{HIS}} = 2\,\mathrm{mm}$, the mushrooms are integrated in a dielectric layer of permittivity $\epsilon_{\mathrm{HIS}} = 3$ and thickness $h_{\mathrm{HIS}} = 1.52\,\mathrm{mm}$. The square patches have a size $a_{\mathrm{HIS}} = 1.85\,\mathrm{mm}$, and are grounded with vias of radius $r_{\mathrm{HIS}} = 0.2\,\mathrm{mm}$. Two layers between

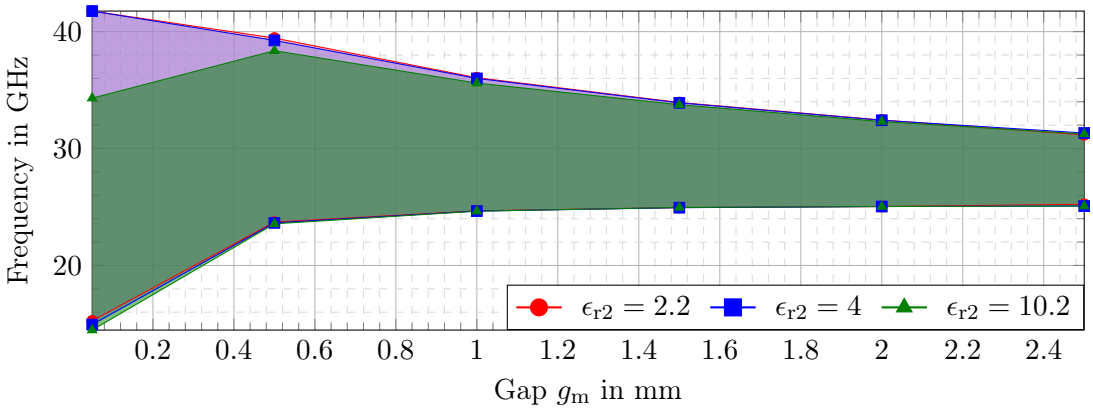


(a) Different SIH permittivities $\epsilon_{r2}$.

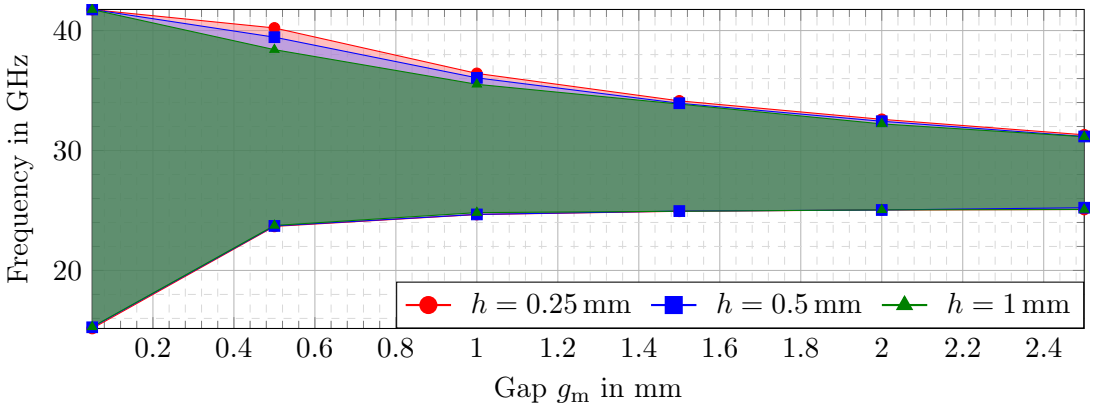


(b) Different SIH depths $h$.

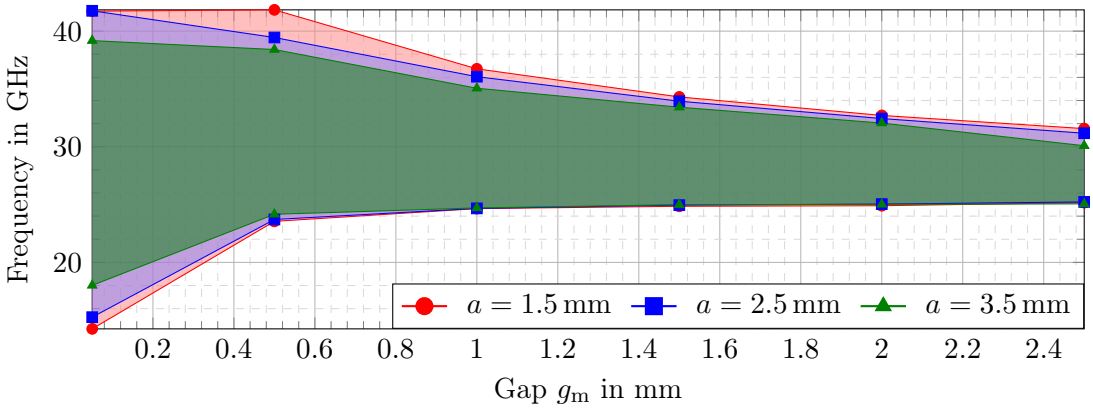


(c) Different SIH sizes $a$.

Figure 6.17: Stopband of the HIS covered with a square SIH, as function of the air layer $g_{\text{HIS}}$ between the HIS and SIH substrates. Each SIH cell $p = 4\,\text{mm}$ covers four mushroom cells $p_{\text{HIS}} = 2\,\text{mm}$. The mushrooms have $a_{\text{HIS}} = 2.2$, $h_{\text{HIS}} = 0.5\,\text{mm}$, $a_{\text{HIS}} = 1.85\,\text{mm}$, and $r_{\text{HIS}} = 0.25\,\text{mm}$.

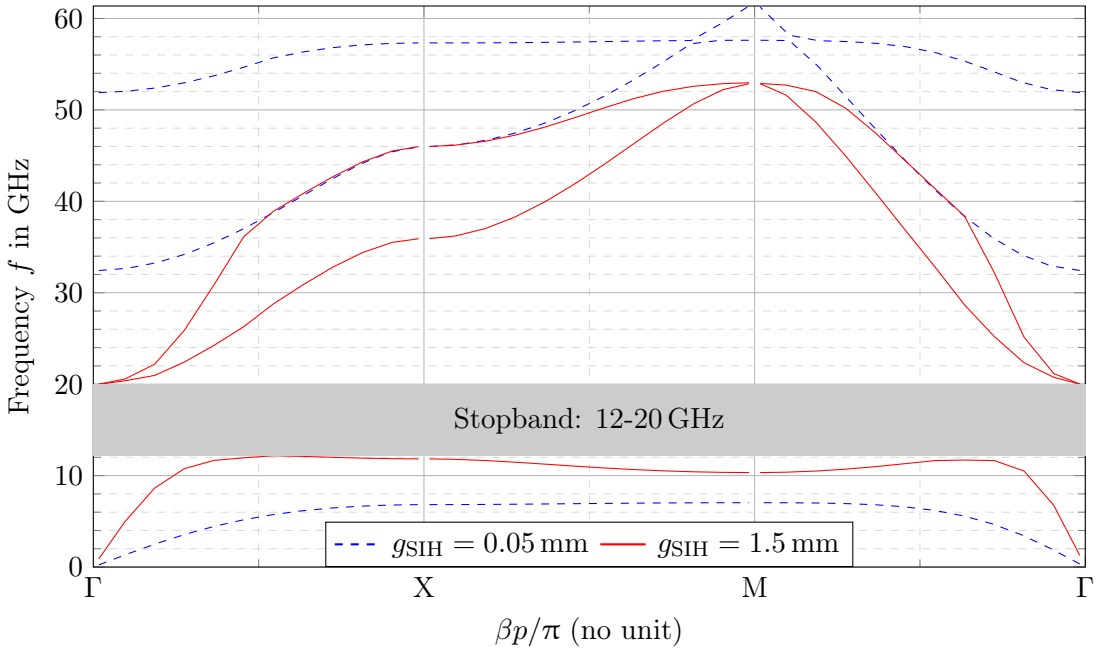


(a) Layer $g_{\mathrm{HIS}}$ filled with $\epsilon_{\mathrm{rs}} = 1$.

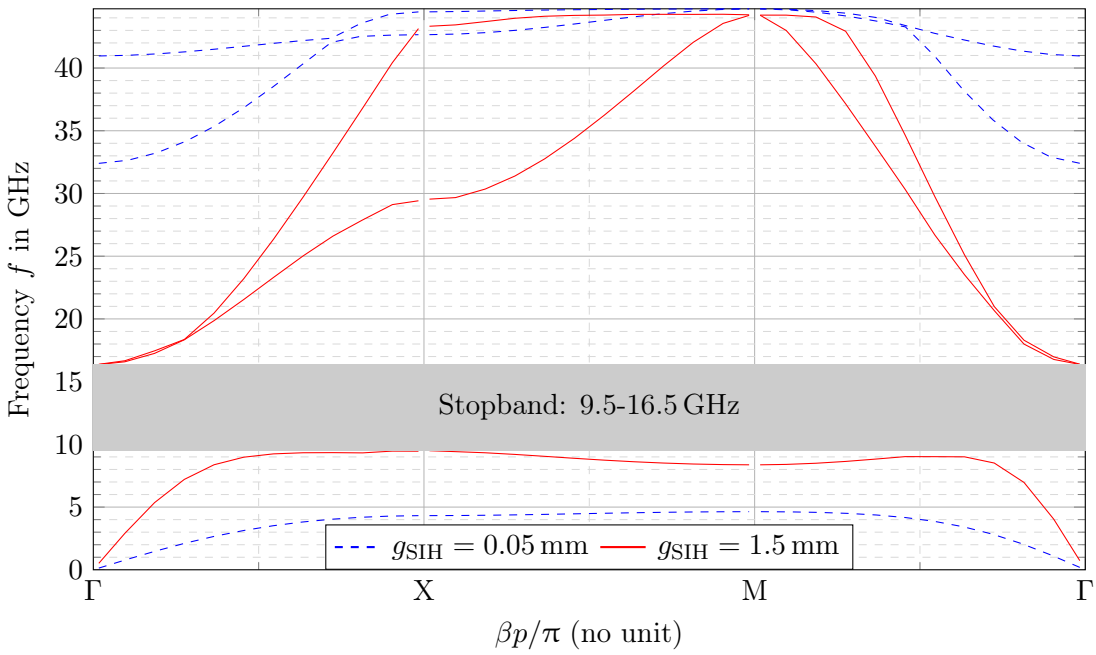


(b) Layer $g_{\mathrm{HIS}}$ filled with $\epsilon_{\mathrm{rs}} = 3$.

Figure 6.18: Brillouin diagram of the mushroom HIS, with $p_{\mathrm{HIS}} = 2\,\mathrm{mm}$, $a_{\mathrm{HIS}} = 3$, $h_{\mathrm{HIS}} = 1.52\,\mathrm{mm}$, $a_{\mathrm{HIS}} = 1.85\,\mathrm{mm}$, and $r_{\mathrm{HIS}} = 0.2\,\mathrm{mm}$.

the HIS and the upper metallic plate are considered: $g_{\text{HIS}} = 0.05\,\text{mm}$ and $g_{\text{HIS}} = 1.5\,\text{mm}$. Only the latter case truly matters, given that it yields the most restrictive stopband, that is from 12 to 20 GHz. This fits the Ku-band. Increasing the layer $g_{\text{HIS}}$ would close the stopband further. Therefore $g_{\text{HIS}} = 1.5\,\text{mm}$ is the most extreme reconfiguration that is possible for this waveguide.

The layer $g_{\text{HIS}}$ is naturally filled with air, given that the HIS are moved closer or further away from the central waveguide. Nonetheless, Fig. 6.18b computes the Brillouin diagram for the same structure as in Fig. 6.18a, except that the layer is filled with a dielectric of permittivity $\epsilon_{\text{rs}} = 3$. The subscripts `rs` stands for *reconfigurable separator*. The reason for this study will be elaborated in section 6.3. In short, in order to maintain the layer $g_{\text{HIS}}$ at fixed values, separators made of dielectric material are used between the layers. Therefore, the stopband of the HIS must be preserved even in the presence of this dielectric layer placed in-between. Although the stopband slightly shifts to lower frequencies, it still covers most of the Ku band.

Note that the Brillouin diagrams in Fig. 6.18 are more complete than in the previous figures, because different propagation directions are considered at the surface of the HIS. The direction Γ-X corresponds to propagation along the $z$-axis i.e., $\beta_x = 0$. Γ-M is the diagonal direction, with $\beta_x = \beta_z$. Finally, the variation along X-M closes the triangle in the wavenumber domain, with $\beta_z = \pi/p$ and varying $\beta_x$. Considering the dispersion curves along this spectral path increases the chances that the stopband is valid for all propagation directions.

#### 6.2.3.2 Total unit cell in the Ku-band

The HIS presented in Fig. 6.18 is combined to a G-S SIH waveguide. The latter is tuned to have its first mode in the Ku band and to yield a high sensitivity to the hole depth, as explained in section 6.1. The resulting waveguide has a periodicity $p = 4\,\text{mm}$ and a gap $g = 0.25\,\text{mm}$ where most of the energy propagates. The SIH layers have a thickness $h = 0.25\,\text{mm}$ and a permittivity $\epsilon_{\text{r2}} = 6.5$. The square holes of size $a = 3.4\,\text{mm}$ are created with 16 vias of radius $r = 0.3\,\text{mm}$.

The operating band of this unit cell matches the Ku band. In the center frequency, that is 15 GHz, the variation of the refractive index when changing the layer $g_{\text{HIS}}$ from 0.05 mm to 1.5 mm is $\Delta n = 0.36$.

From the images of the CST model in Fig. 6.19, it is notable that only one layer of metallic vias is used between adjacent SIH. This is suggested in [222], [223], in order to get larger hole sizes, but also to maintain the mechanical integrity of substrate layer.

The central gap $g$ between the SIH layers is quite large compared to the examples studied in section 6.1, which reduces the available refractive index variation. Nevertheless, keeping this gap not too small makes the assembling process less prone to inaccuracies. This is compensated by using SIH dielectric layers with a thickness $h = 0.25\,\text{mm}$, such that an important index variation with the hole depth is available. Such thin dielectric layers become rather flexible, and so the final benchmark must ensure that all layers are flat.

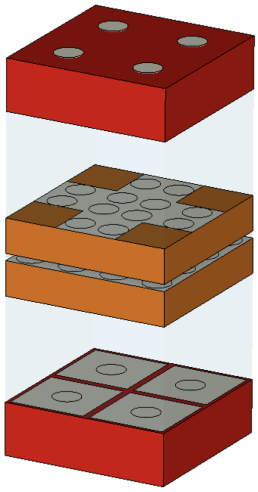

(a) CST unit cell model.

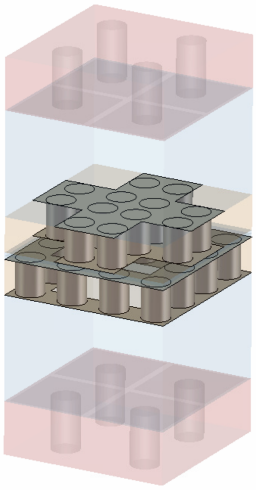

(b) CST unit cell model.

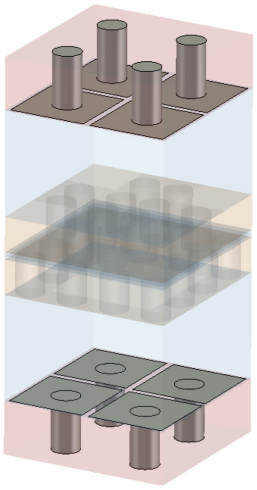

(c) CST unit cell model.

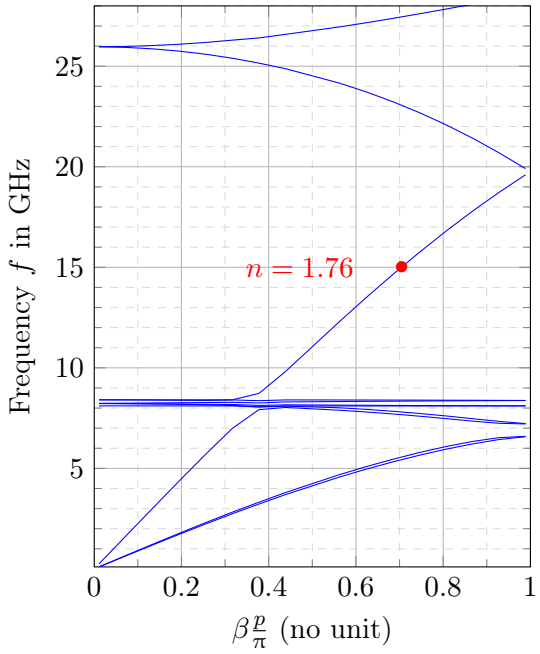


(d) Brillouin diagram for $g_{\text{HIS}} = 0.05\,\text{mm}$.

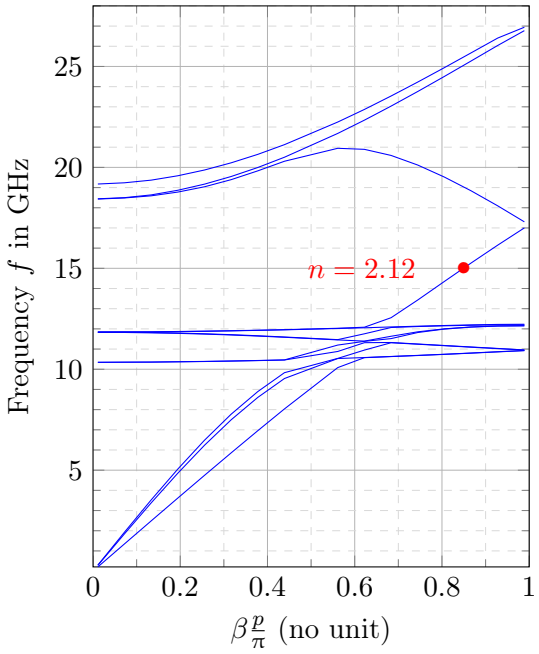


(e) Brillouin diagram for $g_{\text{HIS}} = 1.5\,\text{mm}$.

Figure 6.19: Contactless reconfigurable unit cell tuned for operation in the Ku band. The central G-S SIH waveguide has $p = 4\,\text{mm}$, $g = 0.25\,\text{mm}$ $a = 3.4\,\text{mm}$, $h = 0.25\,\text{mm}$, $\epsilon_{\text{r2}} = 6.5$ and 16 vias $r = 0.3\,\text{mm}$. The mushroom HIS has $p_{\text{HIS}} = 2\,\text{mm}$, $a_{\text{HIS}} = 3$, $h_{\text{HIS}} = 1.52\,\text{mm}$, $a_{\text{HIS}} = 1.85\,\text{mm}$, and $r_{\text{HIS}} = 0.2\,\text{mm}$.

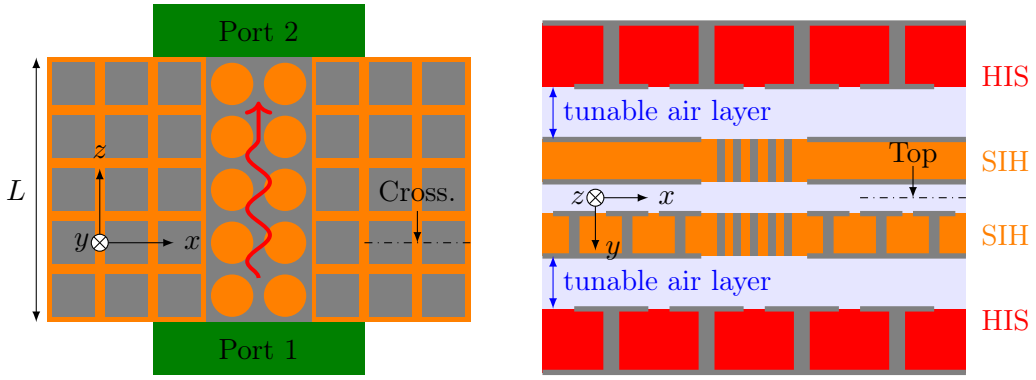


(a) Top view, in the central propagation gap. (b) Cross view, normal to propagation.

Figure 6.20: Reconfigurable phase-shifter in ridge gap waveguide (RGW) technology. The waves propagate at the center of the structure, within a holey G-S PPW, as indicated by the red array in the top view. Wave confinement is obtained with mushroom HIS. The effective depth of the holes is changed by tuning the air gap between the middle (orange) and external (red) layers.

## 6.3 Design of a reconfigurable phase-shifter

Here we use the unit cell designed in section 6.2 for the design of a reconfigurable phase-shifter. The idea is simply to let the waves propagate through a given number of unit cells, and to change the refractive index of the waveguide by moving the HISs on either side. This changes the phase-shift throughout the waveguide. In the following, this prototype is thus characterized as a phase-shifter, although it relates more to a reconfigurable delay-line.

Fig. 6.20 illustrates the overall concept of the phase-shifter. In the top view Fig. 6.20a, the waves propagate from one feeding port to the other, in the gap between the G-S SIH layers (in orange). In order to confine the waves in the region where the SIHs are located, HISs with mushrooms are placed on either side of the propagation region. These mushrooms are integrated in the same substrate layer as the lower SIHs. As such, the center waveguide can be seen as a ridge gap waveguide (RGW), where the refractive index of the ridge is modified with G-S SIHs. For an effective refractive index $n$ in the propagation region, the phase-shift between the two ports at a frequency $f$ is $\theta = n\frac{2\pi f}{c_0}L$, with $L$ the waveguide length and $c_0$ the speed of light in vacuum.

The cross view of the waveguide in Fig. 6.20b shows how the different layers of the structure are arranged. The waves mainly propagate in the vacuum at the center of the cross-section, between the SIH layers (in orange). On either side of these central layers, the HIS layers (in red) are moved closer or further away from the central layers. This changes the effective depth of the SIHs. The mushrooms embedded in these outer layers prevent the waves from propagating between the SIH and HIS layers. The resulting

change $\Delta n$ of the effective refractive index leads to the phase-shift

$$\Delta\theta = \Delta n \frac{2\pi f}{c_0} L\,. \tag{6.1}$$

Therefore, in order to achieve a phase-shift up to $2\pi$ at a frequency $f$, the phase-shifter must have a minimum length $L = \lambda_0/\Delta n$, with $\lambda_0$ the free-space wavelength. The larger the refractive index variation enabled by the reconfigurable unit cell, the more compact the total phase-shifter.

A candidate for the reconfigurable SIH unit cell is already designed in section 6.2. Additional designs are required for

- the RGW: suitable EBG mushrooms must be placed on either side of the central ridge to guide the waves laterally;
- the impedance matching between the SIH waveguide and the feeding ports;
- the feeding ports: a transition towards classical waveguides must be made to enable lab measurements of the phase-shift;
- the mounting structure for the overall prototype built in the lab, to assemble all the layers and the feeds.

Each of these parts is addressed in the following paragraphs.

### 6.3.1 Holey ridge gap waveguide

One of the fundamental concepts of the current design is the lack of contact between the different parts. This is true for the mechanically moving parts – the HIS layers – but for the SIH layers too. Following the concept of gap waveguides [203], [226], the guiding structure is closed laterally by using high-impedance metasurfaces, which act as perfectly magnetically conducting (PMC) boundary conditions. Given that the gap between the layers is smaller than a quarter wavelength, the waves cannot cross these HIS. Consequently, a quasi-TEM mode propagates in the air gap between the ridge and the metallization of the upper layer. As for the reconfigurable HIS layers studied in section 6.2, integrated mushrooms are used to yield the desired stopband.

An illustration of the resulting RGW is drawn in Fig. 6.21, as well as pictures of the model simulated in CST. The lower substrate layer contains the central ridge and the lateral high-impedance mushrooms. The upper substrate layer is completely metallized, and so the air gap is closed by a metal plate from above. Note that at this point, no SIHs are considered.

Fig. 6.22 plots the dispersion diagram of the EBG mushrooms used to guide the waves laterally. According to the unit cell designed in paragraph 6.2.3.2, the mushrooms are integrated in a layer of permittivity $\epsilon_{r2} = 6.5$ and thickness $h = 0.25\,\text{mm}$. The gap between the SIH layers is $g = 0.25\,\text{mm}$, which corresponds to the space between the mushroom and the upper metal sheet. Therefore, the only parameters left to tune


(a) CST structure: top view.

(b) CST structure: perspective view.

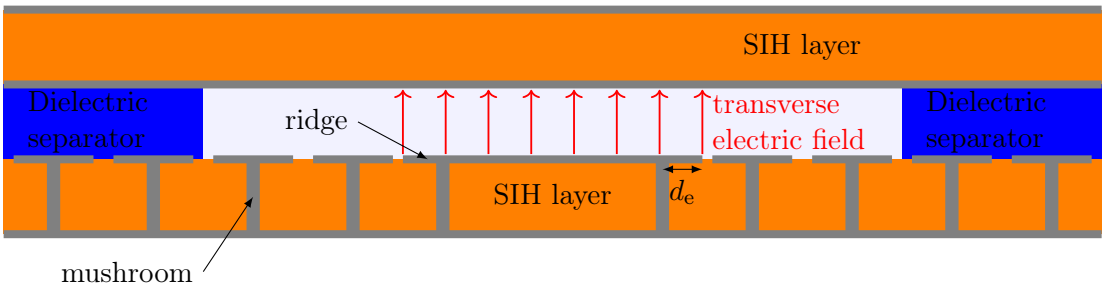


(c) Schematic cross-section of the RGW.

Figure 6.21: Ridge gap waveguide used to confine the waves laterally and between the two substrate layers.

the stopband are the metasurface periodicity $p_{\text{lat}}$ and the patch size $a_{\text{lat}}$. A satisfying stopband at Ku frequencies is obtained for $p_{\text{lat}} = 2.4\,\text{mm}$ and $a_{\text{lat}} = 2.3\,\text{mm}$. The mushroom vias have a radius $r_{\text{lat}} = 0.2\,\text{mm}$.

In Fig. 6.22, different relative permittivities $\epsilon_{\text{sep}}$ are considered for the medium above the mushrooms. This is because in the final prototype, separators are needed to maintain the gap between the different layers. The central gap between the SIH layers is particularly small (0.25 mm), and so these separators must be brought as close as possible to the central ridge where the waves propagate. These separators are shown in blue in Fig. 6.21c. Therefore, the mushrooms must be designed such that they yield a stopband with or without the presence of these dielectric separators. In the final design, the central separators are manufactured with Rogers RO3003 or RO3006, depending on the available substrates, and so $\epsilon_{\text{sep}} = 3$ or $\epsilon_{\text{sep}} = 6.5$, respectively. According to Fig. 6.22, in both cases the resulting stopband confines the waves for frequencies in the Ku band.

The lateral confinement is confirmed by simulating a section of the RGW of length 12 mm. The central ridge has a width of 16.6 mm, which corresponds to four SIH unit

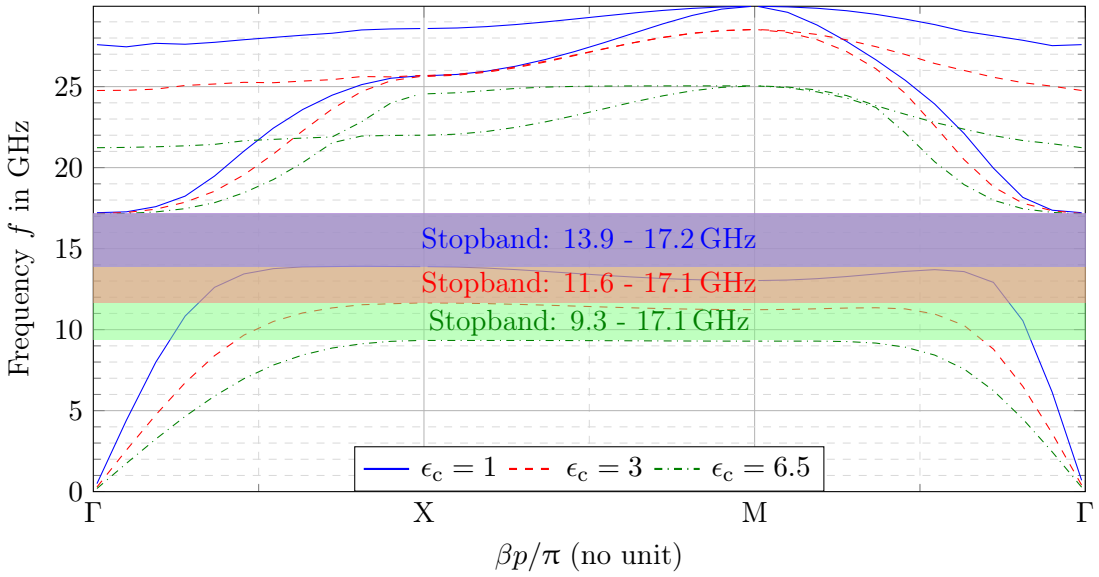


Figure 6.22: Dispersion diagram of the EBG mushroom unit cell, for different permittivities $\epsilon_{sep}$ above the mushrooms. The mushrooms have dimensions $p_{lat} = 2.4\,mm$, $a_{lat} = 2.3\,mm$, $r_{lat} = 0.2\,mm$, and are integrated in a dielectric layer with $\epsilon_{r2} = 6.5$ and $h = 0.25\,mm$. The gap is $g = 0.25\,mm$.

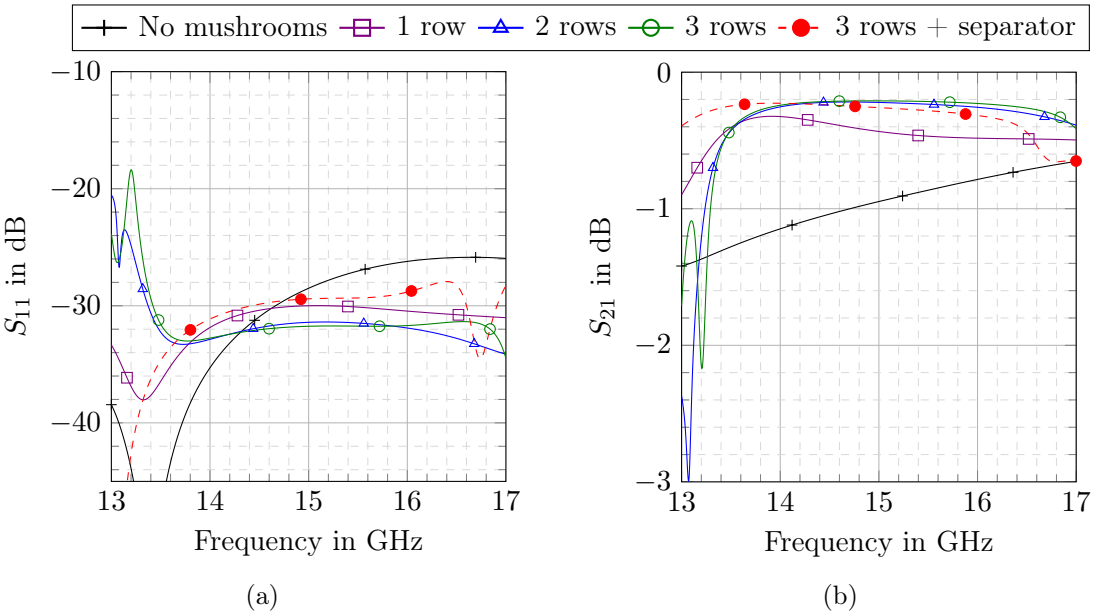


Figure 6.23: S-parameters of a RGW of length 12 mm. The ridge has a width 16.6 mm, and $\epsilon_{r2} = 6.5$, $h = 0.25\,mm$ and $g = 0.25\,mm$. Different numbers of mushrooms rows guide the waves, with $p_{lat} = 2.4\,mm$, $a_{lat} = 2.3\,mm$ and $r_{lat} = 0.2\,mm$. The last case covers the mushrooms with $\epsilon_{sep} = 3$.

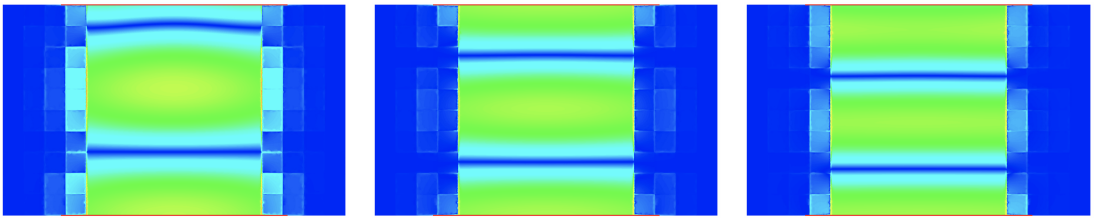

(a) 13 GHz. (b) 15 GHz. (c) 17 GHz.

Figure 6.24: Magnitude of the electric field at the surface of the RGW simulated in CST, with the same dimensions as in Fig. 6.23, at different frequencies.

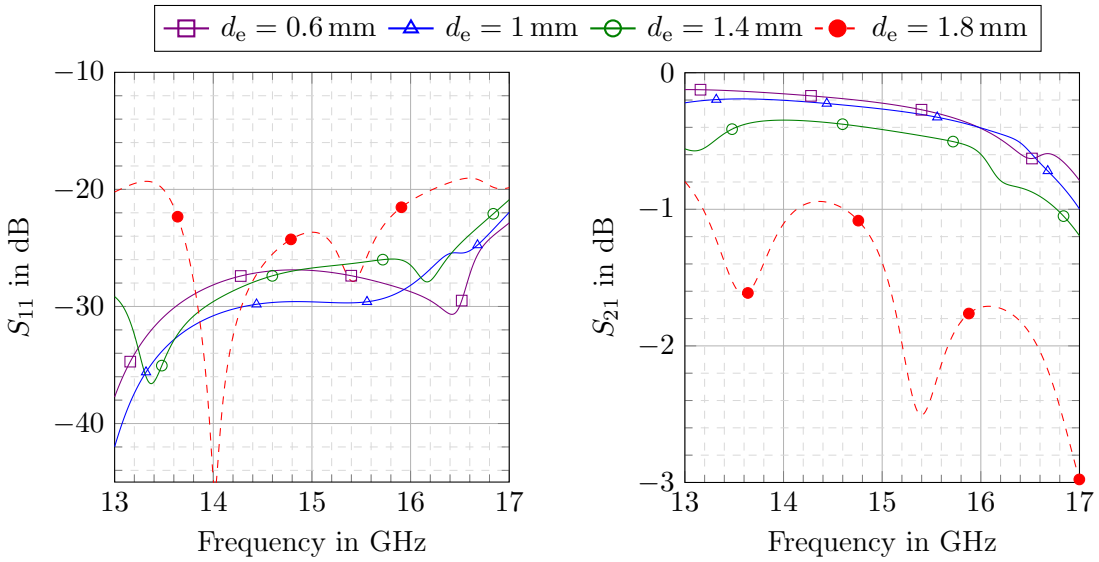


(a) (b)

Figure 6.25: S-parameters of the same RGW as in Fig. 6.23, with 3 mushrooms rows, a separator $\epsilon_{sep} = 6.5$, and for different distances $d_e$ between the vias and the edge of the ridge. The inter-via distance is $d_v = 2.4\,\text{mm}$.

cells. The feeding port excites the fields above the ridge, as visible in the CST capture in Fig. 6.21b. The mushrooms are as designed in Fig. 6.22. Different numbers of mushrooms are simulated, in order to know how many rows are necessary to confine the waves. The resulting S-parameters are plotted in Fig. 6.23. It appears that one row of mushrooms is enough to confine most of the energy along the ridge. Two or three rows slightly improve the transmission between the two ports. An additional case where the mushrooms are completely covered with a separator of permittivity $\epsilon_{sep} = 3$ is also considered, and shows similar performances. The resulting fields are shown at different frequencies of the Ku band in Fig. 6.24. The confinement of the waves is clearly visible.

The RGW simulated in Fig. 6.23 is designed such that the waves do not propagate in the substrate layers. In order to achieve that, the dielectric area below the ridge must

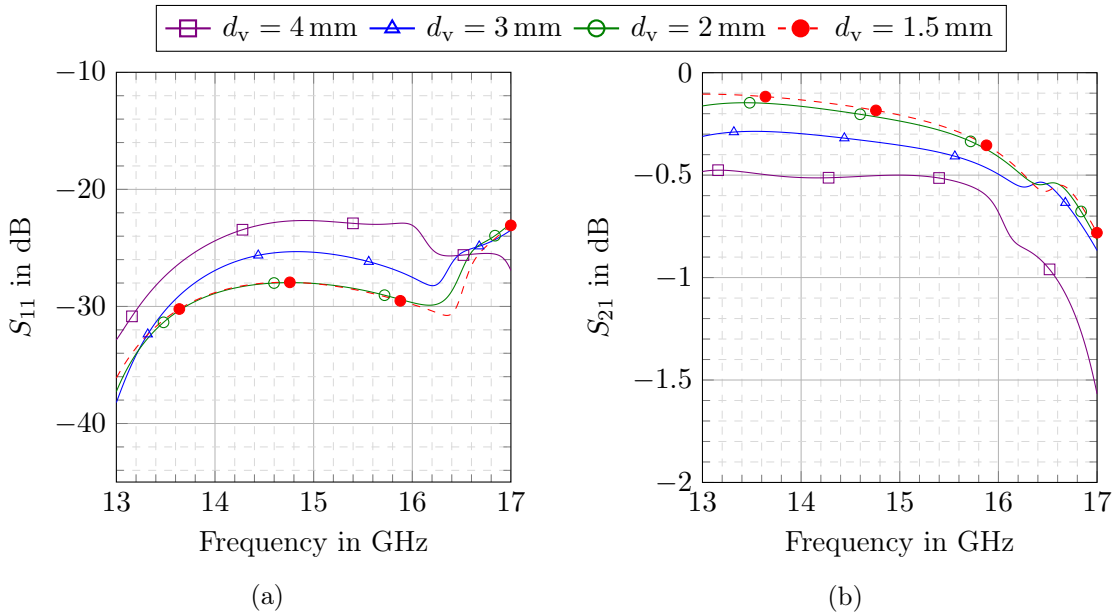


(a) (b)

Figure 6.26: S-parameters of the same RGW as in Fig. 6.23, with 3 mushrooms rows, a separator $\epsilon_{sep} = 6.5$, and for different distances $d_v$ between two successive vias. The distance between the vias and the ridge edge is $d_e = 1\,mm$.

be closed off with metallic vias. The position and periodicity of the vias have a limited but non-negligible impact on the performance of the RGW, and are characterized by the distances $d_e$ and $d_v$, as illustrated in Fig. 6.21. In Fig. 6.25, the distance $d_e$ between the vias and the ridge edge is changed for the same RGW as in Fig. 6.23 – except that a separator of permittivity $\epsilon_{sep} = 6.5$ is used. It appears that the waves are well-transmitted as long as the vias are close enough to the edge. Moreover, fewer reflections are achieved when the vias are not too close to the edge. In the following, $d_e = 1\,mm$.

In Fig. 6.26, the same structure is simulated with different distances $d_v$ between the ridge vias. The only requirement is that the vias must no be too spaced out. When $d_v \leq 2\,mm$, good transmission is achieved. In the following, $d_v = 1.5\,mm$.

Finally, the metallic and dielectric losses are observed in Fig. 6.27. All PEC surfaces are replaced with copper metallizations of thickness $17\,\mu m$ and $\sigma = 5.8 \times 10^7\,S \cdot m^{-1}$. The Rogers RO3006 slabs are modeled in their lossy version, with loss tangent $\tan\delta = 0.002$. For a waveguide of length $12\,mm$, that is 5 lateral mushrooms in length, dielectric losses have a reduced impact on the transmission. Most of the losses happen in the metal sheets. Yet, less than $0.1\,dB$ are lost in transmission when all the losses are accounted for, that is $0.16\,dB$ per wavelength at $15\,GHz$.

### 6.3.2 Variable phase-shift

Once the RGW is designed, G-S SIHs can be integrated in the lower and upper layer to change the effective refractive index, and control it by moving the outer HIS layers.

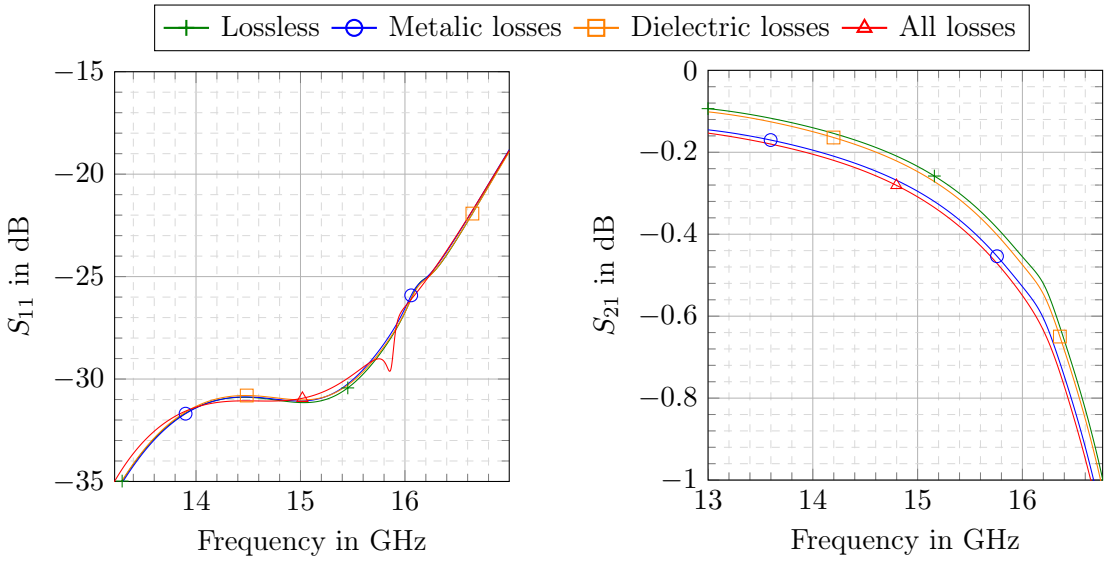


(a) $S_{11}$ (b) $S_{21}$

Figure 6.27: S-parameters of the same RGW as in Fig. 6.23, with 3 mushrooms rows, a separator $\epsilon_{\text{sep}} = 6.5$, vias with $d_{\text{v}} = 1.5\,\text{mm}$ and $d_{\text{e}} = 1\,\text{mm}$. Lossy substrates have $\tan\delta = 0.002$, and lossy metals have $\sigma = 5.8 \times 10^7\,\text{S} \cdot \text{m}^{-1}$.

| **Upper hole nb.** | 1 | 2 | 3 | 4 | 5 | 6 | 7 |
|---|---|---|---|---|---|---|---|
| **Size (in mm)** | 0.5 | 0.85 | 1.2 | 1.65 | 2.15 | 2.65 | 3.15 |
| **Size (in mm)** | 0.25 | 0.65 | 1 | 1.4 | 1.9 | 2.4 | 2.9 | 3.4 |
| **Lower hole nb.** | 0.5 | 1.5 | 2.5 | 3.5 | 4.5 | 5.5 | 6.5 | 7.5 |

Table 6.1: Dimensions of an 8-cell tapering of the SIH sizes, for the impedance matching of the reconfigurable waveguide. The alternating upper and lower hole dimensions reflect the G-S configurations between the two SIH layers.

However, when a wave propagate along the RGW, it is reflected when it first meets the SIHs, because the impedance of the SIH waveguide is not adapted to the feed of the RGW. In order to solve this problem, the SIHs must be introduced with a gradual increase of the refractive index. This means that the size of the SIHs has to be tapered at the waveguide feeds.

This tapering must be robust enough that it matches the impedance for the most extreme configuration, that is when the HIS layers are the furthest away from the central layers. Then, the refractive index in the SIH waveguide is maximal, and so the hole size tapering must be very smooth. Such a tapering is proposed in Tab. 6.1, where eight cells are needed to change from the smallest to the largest hole size. Due to the G-S configuration of the SIHs, this represents 15 different hole sizes. Naturally, the number of metallic vias surrounding each SIH must be changed accordingly to the hole size.

In order to validate this tapering, one row of phase-shifter is simulated in CST, as

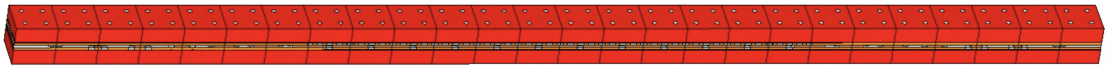

(a) CST model: all substrate-integrated layers.

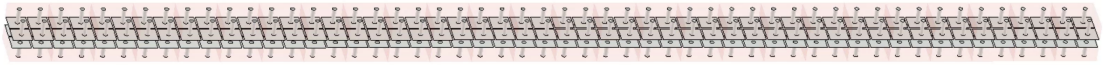

(b) CST model: mushrooms of the reconfigurable HIS layers.

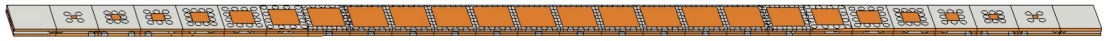

(c) CST model: top view of the G-S SIH waveguide layers.

(d) CST model: bottom view of the G-S SIH waveguide layers.

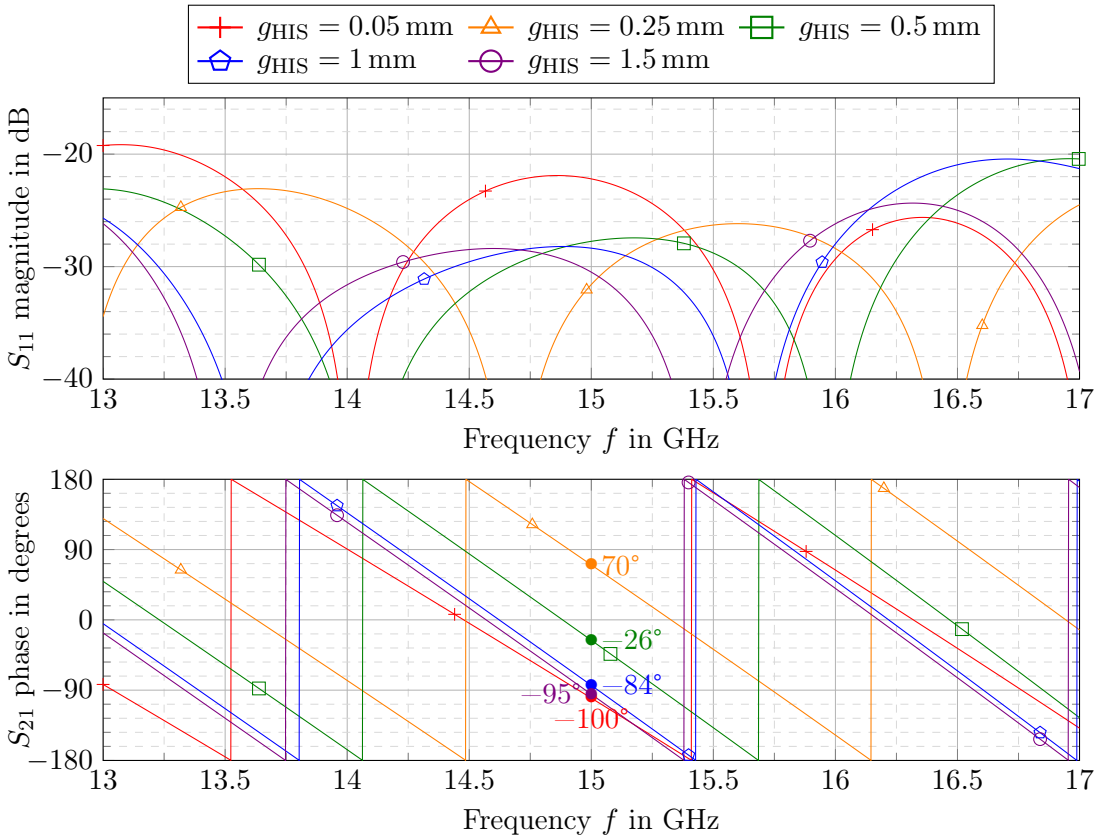


(e) Reflection coefficient $S_{11}$ and phase of the transmission coefficient $S_{21}$.

Figure 6.28: S-parameter of 10 chained unit cells as described in Fig. 6.19, with 8 tapered cells with the dimensions in Tab. 6.1. The waveguide is reconfigured by changing the gap $g_{\mathrm{HIS}}$ for both outer HIS layers.

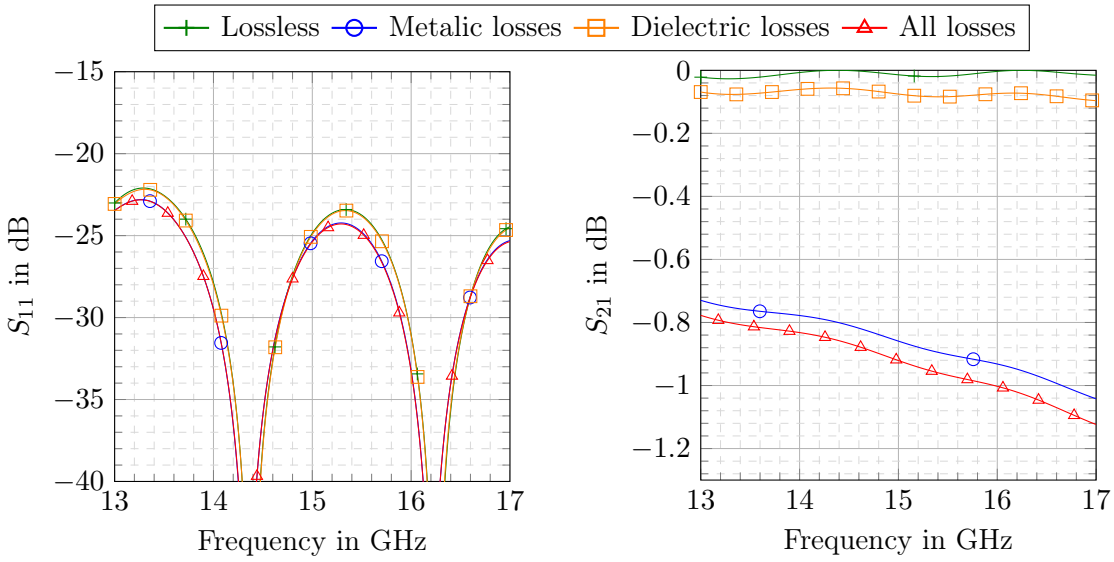


(a) $S_{11}$. (b) $S_{21}$.

Figure 6.29: S-parameter of 10 chained unit cells as described in Fig. 6.19, with 8 tapered cells with the dimensions in Tab. 6.1. The reconfigurable air layer has $g_{\mathrm{HIS}} = 0.05\,\mathrm{mm}$. Lossy RO3003 and RO3006 layers have $\tan\delta = 0.001$ and $\tan\delta = 0.002$, respectively, and lossy metals have $\sigma = 5.8 \times 10^7\,\mathrm{S \cdot m^{-1}}$.

shown in Figs. 6.28a to 6.28d. This structure can be seen as a chain of the unit cell of Fig. 6.19, except that it contains only 10 cells with maximal SIH size. On each side, 8 additional unit cells are added, with the tapering described in Tab. 6.1. Laterally, periodic boundary conditions are enforced. The reason why only one such row is simulated is the size of the problem. In order to obtain accurate S-parameters in CST, the mesh of the discretized model yields several millions of cells, depending on the air layer $g_{\mathrm{HIS}}$ between the SIH and HIS layers. If more rows are added laterally to recreate the hole ridge – not to mention the laterally guiding mushrooms – the available computer memory saturates. Therefore, this is the closest observation of the phase-shifting process that we can achieve in simulation.

In Fig. 6.28, the space between the SIH and HIS layers is reconfigured up to $g_{\mathrm{HIS}} = 1.5\,\mathrm{mm}$, which is the maximum gap that maintains a stopband at Ku frequencies, according to Fig. 6.18. Good impedance matching is achieved in the Ku band, with $S_{11} \leq -20\,\mathrm{dB}$ for all configurations. Fig. 6.28e also shows the phase of the transmission coefficient $S_{21}$. It appears that when moving the HIS layers away from the center waveguide, the phase-shift between the two feeding ports can be changed over a range $\Delta\theta = 2\pi$. With this design, any phase-shift can thus be achieved by tuning the gap appropriately.

Finally, the losses in the phase-shifting row of unit cells are observed in Fig. 6.29. In order to perform such a simulation in CST, a tetrahedral mesh has to be used to allow

| **Step** | 1 | 2 | 3 | 4 | 5 | 6 |
|---|---|---|---|---|---|---|
| **Height (in mm)** | 1.57 | 5.51 | 4.93 | 2.71 | 4.13 | $\infty$ |
| **Width (in mm)** | 0.25 | 0.35 | 0.8 | 2.58 | 4.65 | 7.9 |

Table 6.2: Staircase dimensions for the rectangular transition of the feed.

metallic losses. However, this prevents the use of periodic lateral boundary conditions in the frequency solver. Therefore, the structure shown in Figs. 6.28a is simulated with PMC boundary conditions. The configuration with an air layer $g_{\mathrm{HIS}} = 0.05\,\mathrm{mm}$ is chosen, because the fields are more concentrated, maximizing the losses. The Rogers RO3003 layers (for the HIS) have a loss tangent $\tan\delta = 0.001$, while the Rogers RO3006 layers (for the SIH) have a loss tangent $\tan\delta = 0.002$. All metallizations are made of copper sheets of thickness $17\,\mu\mathrm{m}$, and $\sigma = 5.8 \times 10^7\,\mathrm{S \cdot m^{-1}}$. In the Ku band, the total losses correspond to an attenuation of approximately $-0.2\,\mathrm{dB}$ per wavelength.

### 6.3.3 Feed

In the reconfigurable waveguide, the waves propagate between the two SIH layers, that is in a gap of 0.25 mm. In order to feed such a waveguide for in-lab measurements, a proper waveguide transition must be designed. Given the manufacturing possibilities at hand, we chose to make a transition from a rectangular waveguide (RW) adapted to the Ku band. According to the Electronic Industries Alliance standard, a WR62 waveguide is fitting, where a width $w_{\mathrm{r}} = 15.8\,\mathrm{mm}$ and a height $h_{\mathrm{r}} = 7.9\,\mathrm{mm}$ yield a recommended operating band of 12.4 to 18 GHz.

On the one hand, the width of the ridge in the RGW can be increased to the width of the feeding waveguide. That is why in the simulation of section 6.3.1, the ridge has $w_{\mathrm{r}} = 16.6\,\mathrm{mm}$, which is close to the RW width $w_{\mathrm{r}}$, and corresponds to an integer number of SIH unit cells. On the other hand, the transition must go from a height $h_{\mathrm{r}} = 7.9\,\mathrm{mm}$ to a gap $g = 0.25\,\mathrm{mm}$. This is possible, without impedance mismatch, using a staircase transition. However, placing this staircase transition in the alignment of the phase-shifter would extend an already very long prototype[1] – the design in Fig. 6.28 has 16 cells, yielding a total length of 84 mm. That is why a transition with perpendicular feed is designed, as illustrated in Fig. 6.30.

The rectangular staircase is milled inside a metal bulk. The dimensions of the different steps are optimized and given in Tab. 6.2. This feed is placed on the upper SIH layer, where a slot is made in the upper metallization to let the waves enter. In order to guide the waves through this layer, a dielectric cavity is created with metallic vias. A second slot is made in the inner metallization of the layer to let the waves enter into the central propagation gap, above the ridge. At this point, the waves should continue in the phase-shifter, in the direction of the exit feed. In order to avoid back-propagation, EBG

[1] Additionally, a horizontal feed would require design tricks to ensure the continuity between the metallic bulk of the feed and the metallization of the SIH layer. A trick of that sort is achieved in [155], where a half-wavelength groove is artificially created at the transition to produce a short-circuit between the two guiding parts.

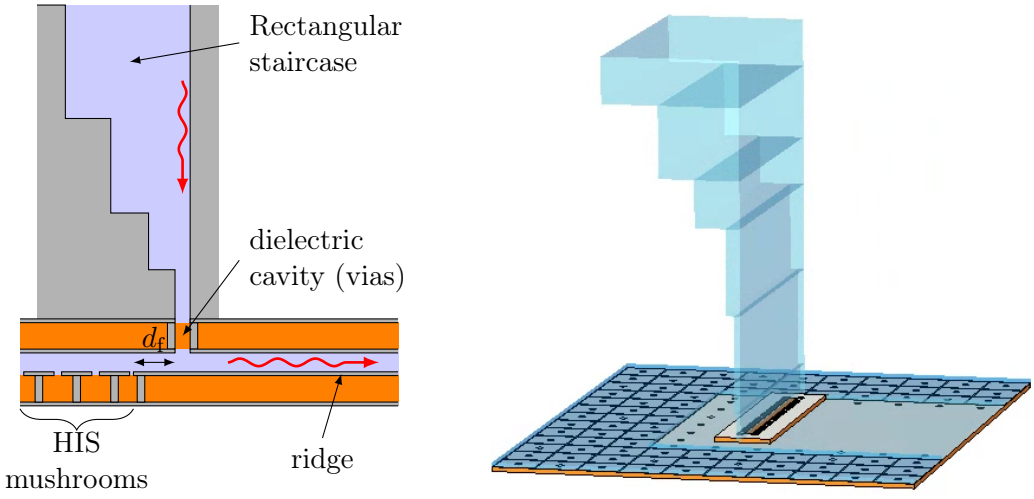


(a) Schematic cross-section. (b) Model simulated in CST.

Figure 6.30: Perpendicular feed of the RGW with a transition from a standard RW.

mushrooms are placed at the end of the waveguide. The same mushrooms as for lateral guiding in paragraph 6.3.1 are used.

On top of minimizing the overall length of the phase-shifter, this vertical feed design offers a number of parameters to control the impedance matching. On top of the staircase dimensions, the dielectric cavity can be tuned, that is its width $w_{\text{cav}}$ and its height $h_{\text{cav}}$, defined by the positions of the metallic vias. Moreover, the slot in the upper metallization needs not be as large as the cavity itself. The width $w_{\text{slot}}$ and height $h_{\text{slot}}$ of the slot can be reduced to create an iris at the transition between the metallic bulk and the SIH layer. Finally, the horizontal position $d_{\text{f}}$ of the feed can also be controlled. It corresponds to the distance between the center of the dielectric cavity and the end of the ridge, as indicated in Fig. 6.30a. Over this distance, the waves do back-propagate, but are reflected by the mushrooms, creating and additional resonating space. In the following, good impedance matching is obtained with a feed at $d_{\text{f}} = 5.04\,\text{mm}$, and a cavity with $w_{\text{cav}} = 11.02\,\text{mm}$ and $h_{\text{cav}} = 0.43\,\text{mm}$. The slot in the upper metallization has the same width as the cavity i.e., $w_{\text{slot}} = 11.02\,\text{mm}$, and the same height as the last staircase step i.e., $h_{\text{slot}} = 0.25\,\text{mm}$.

Fig. 6.31 shows the S-parameters of the resulting RW to RGW transition, simulated in CST with the model in Fig. 6.30b. The ridge and the EBG mushrooms are those designed in paragraph 6.3.1. Good impedance matching is obtained between 13.5 GHz and 16.5 GHz, as well as good transmission performances. Fig. 6.31b illustrates the impact of the losses in this feed. Cases without losses, with only dielectric losses, with only metallic losses, and with all losses are compared. The dielectric losses are added by replacing all substrates by lossy models of Rogers RO3006 substrates, which yield a loss tangent $\tan\delta = 0.002$. All PEC surfaces are replaced by copper, with a conductivity $\sigma = 5.8 \times 10^7\,\text{S}\cdot\text{m}^{-1}$. Most losses are due to the metal dissipation, not to the dielectric. Indeed, not only do the waves mainly propagate in vacuum, but also the Rogers substrate

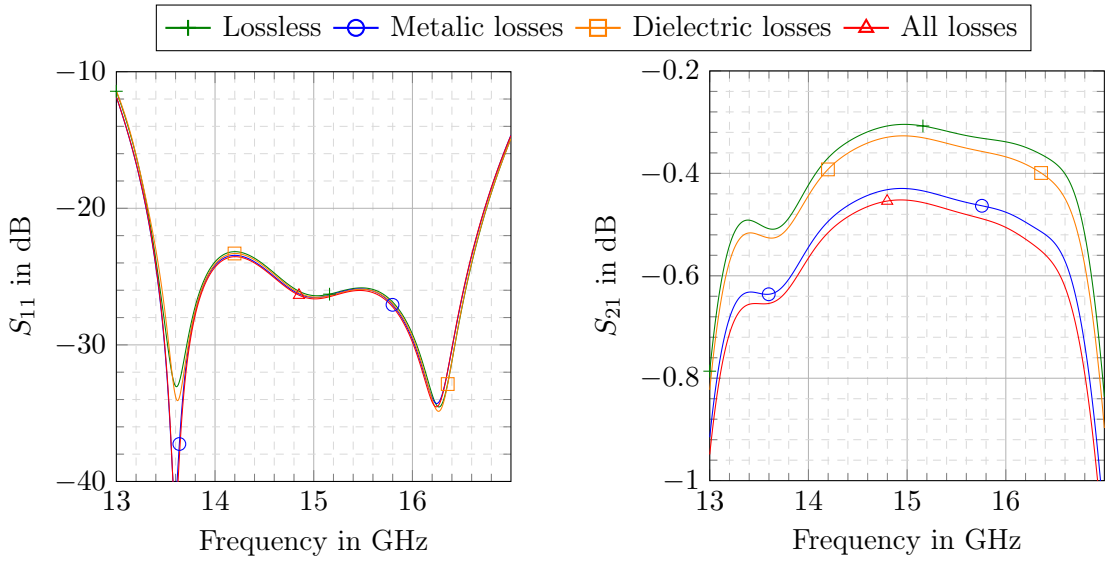


(a) $S_{11}$. (b) $S_{21}$.

Figure 6.31: S-parameters of the RW to RGW transition illustrated in Fig. 6.30, for different lossy cases. The dimensions of the staircase are in Tab. 6.2. The other feed dimensions are $d_f = 5.04\,\text{mm}$, $w_{cav} = w_{slot} = 11.02\,\text{mm}$, $h_{cav} = 0.43\,\text{mm}$ and $h_{slot} = 0.25\,\text{mm}$. Lossy substrates have $\tan\delta = 0.002$, and lossy metals have $\sigma = 5.8 \times 10^7\,\text{S} \cdot \text{m}^{-1}$.

are notably low-loss. Given that a piece of RGW is attached to the feed, with the same length as studied in Fig. 6.27, it can be accounted for approximately 0.1 dB of the losses. Therefore, in the real case (all losses taken into account), each feed transition feed yields a transmission of approximately $-0.4\,\text{dB}$.

### 6.3.4 Prototyping

In the following paragraphs, the overall phase-shifter design is described. It includes all the components studied in this chapter, as well as a system to assemble them together. The CST designs presented here will be used to manufacture the final prototype for in-lab measurements.

#### 6.3.4.1 Sandwich structure

The reconfigurable phase-shifter is formed of several substrate layers, as illustrated in Fig. 6.20b. Not only are some of these layers very thin, and thus quite flexible, but also the gap between these layers must be very precise over the hole propagation plane. That is why we chose to use dielectric separator layers, that are inserted between the SIH layers and the HIS layers. The separators must come as close as possible to the propagation region, in order to ensure the right gap there. In the central gap, the separator of thickness $g = 0.25\,\text{mm}$ is manufactured in a sample of Rogers RO3006. It is cut in a

frame-like shape, such that it completely encompasses the ridge, covering all the EBG mushrooms on the side and at the ends of the ridge. The separators between the SIH and the HIS layers must have a reconfigurable thickness $g_{\mathrm{HIS}}$. Therefore, several thin separators are stacked up, to discretize $g_{\mathrm{HIS}}$ in the range 0-1.5 mm.

Moreover, in order to avoid bending of the layers, the phase-shifter must lay on a plane surface that is not deformable. The different layers and separators must be pressed onto this mounting surface. This can be done with nuts and bolts, going through all the layers of this dielectric sandwich.

Finally, the mounting surface must ensure the alignment of the different elements. This is particularly true for the SIH layers, which must be fixed such that GS is not broken. Similarly, the metallic feed must be placed exactly at the level of the slot in the upper metallization of top SIH layer. These alignments can be guaranteed by alignment pins connected to the mounting structure.

The CST model of the assembled layers is showed in Figs. 6.32 and 6.33. It is to be noted that the nuts and bolts are not pictured. All the dimensions related to the propagation regions are summed up in Tab. 6.3. Dimensions purely related to manufacturing choices, such as the size of the flanges, are not indicated here.

In Fig. 6.33, the subfigures (c) to (k) show the top view of the phase-shifter when adding the different layers from bottom to top, one after the other. In Fig. 6.33d, the first dielectric layer put on the mount is the lower HIS layer. The mushrooms face upwards, and so the metallic patches are visible. It must be kept in mind that the bottom (hidden) face of this layer is fully metallized, grounding the mushrooms. The contrary can be said for the upper SIH layer added in Fig. 6.33j, where the mushrooms face downwards, showing us the fully metallized face of the layer in the top view.

The lower SIH layer in Fig. 6.33f shows how the tapered holes are etched into the metallization of the ridge, surrounded by EBG mushrooms. However, the hidden bottom side of this layer is fully metallic with only etched holes, because the mushrooms must be grounded on the other side. As such, this bottom side looks like the top side of the upper SIH layer, visible in Fig. 6.33h, except that the holes are shifted to create GS. The upper SIH layer in Fig. 6.33h is identical when it comes to bottom and top faces.

As described, the central separator in Fig. 6.33g frames the ridge, which is why only part of the lower SIH layer is visible. The EBG mushrooms are fully covered. The separators between the lower HIS and SIH layers, added in Fig. 6.33e, run along the full phase-shifter length. However, this is not the case for the separators between the upper HIS and SIH layers, added in Fig. 6.33i. Indeed, the metallic feeds must be place directly onto the upper SIH layer, and so the upper separators and the upper HIS layer must be truncated around the feeds. This is clearer in the side view of the phase-shifter in Fig. 6.33b.

Six alignement pins are added to the mount. Two pins per feed ensure the proper alignement of the rectangular staircase with the feeding slots of the upper SIH layer. The two remaining pins, placed diagonally through the structure, align all the dielectric layers. In order to avoid over-constraining the structure, ideally all elements would be held by two pins. This is not possible here, because the upper HIS layer and the feeds are

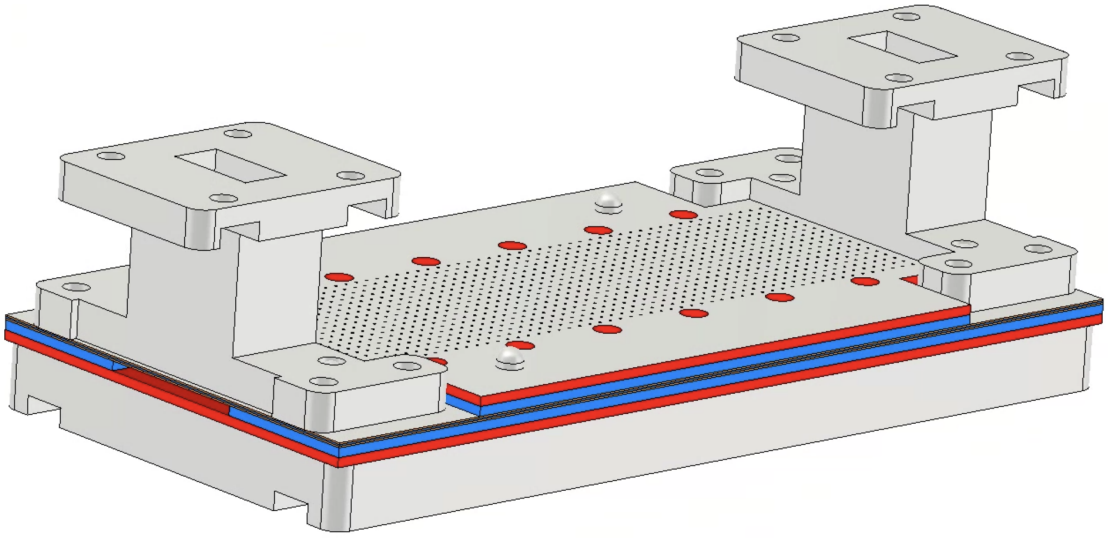

(a)

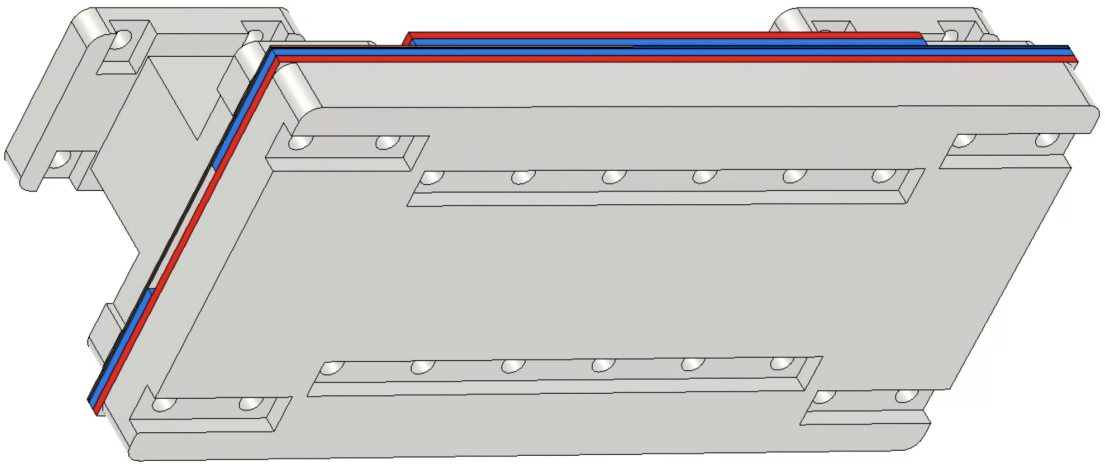

(b)

Figure 6.32: Perspective views of the phase-shifter prototype modeled in CST.

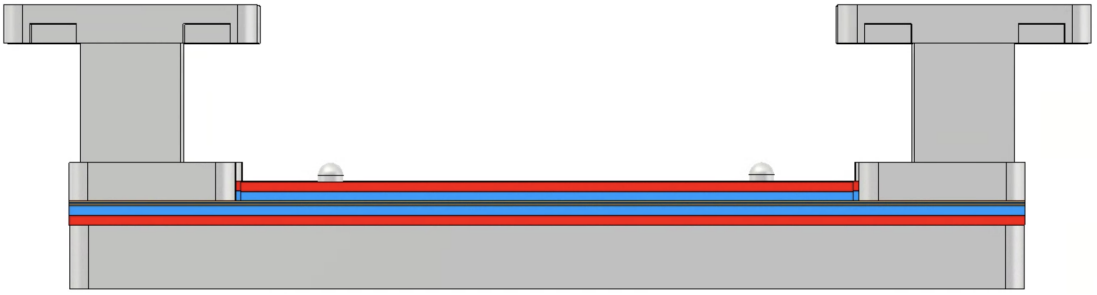

(a) Side view.

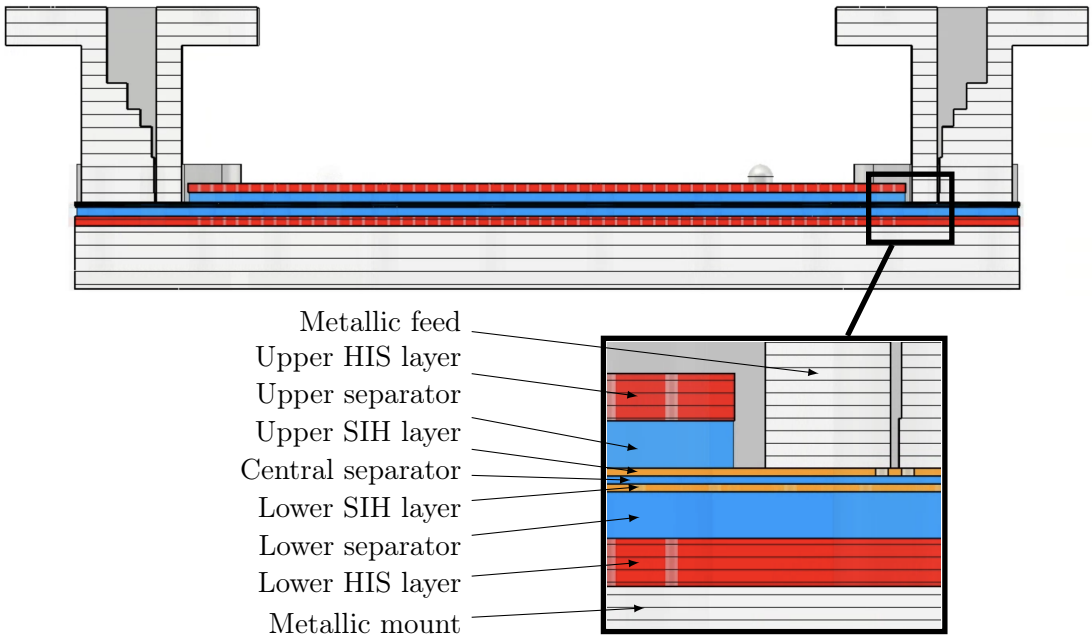


(b) Side cut in the symmetry plane of the structure.

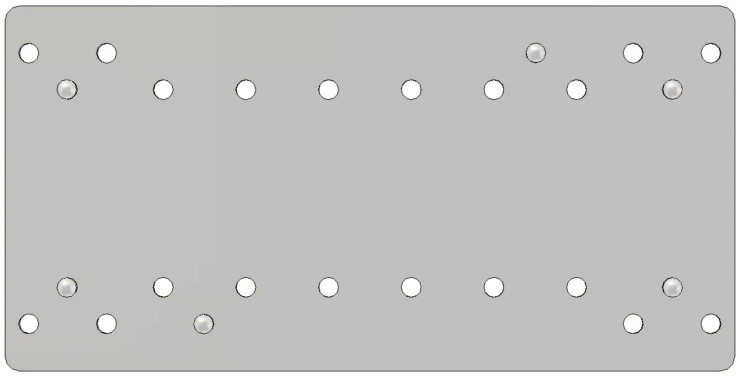

(c) Metallic mount with alignment pins and assembling holes.

Figure 6.33: Description of the different layers of the prototype (Cont. next page).

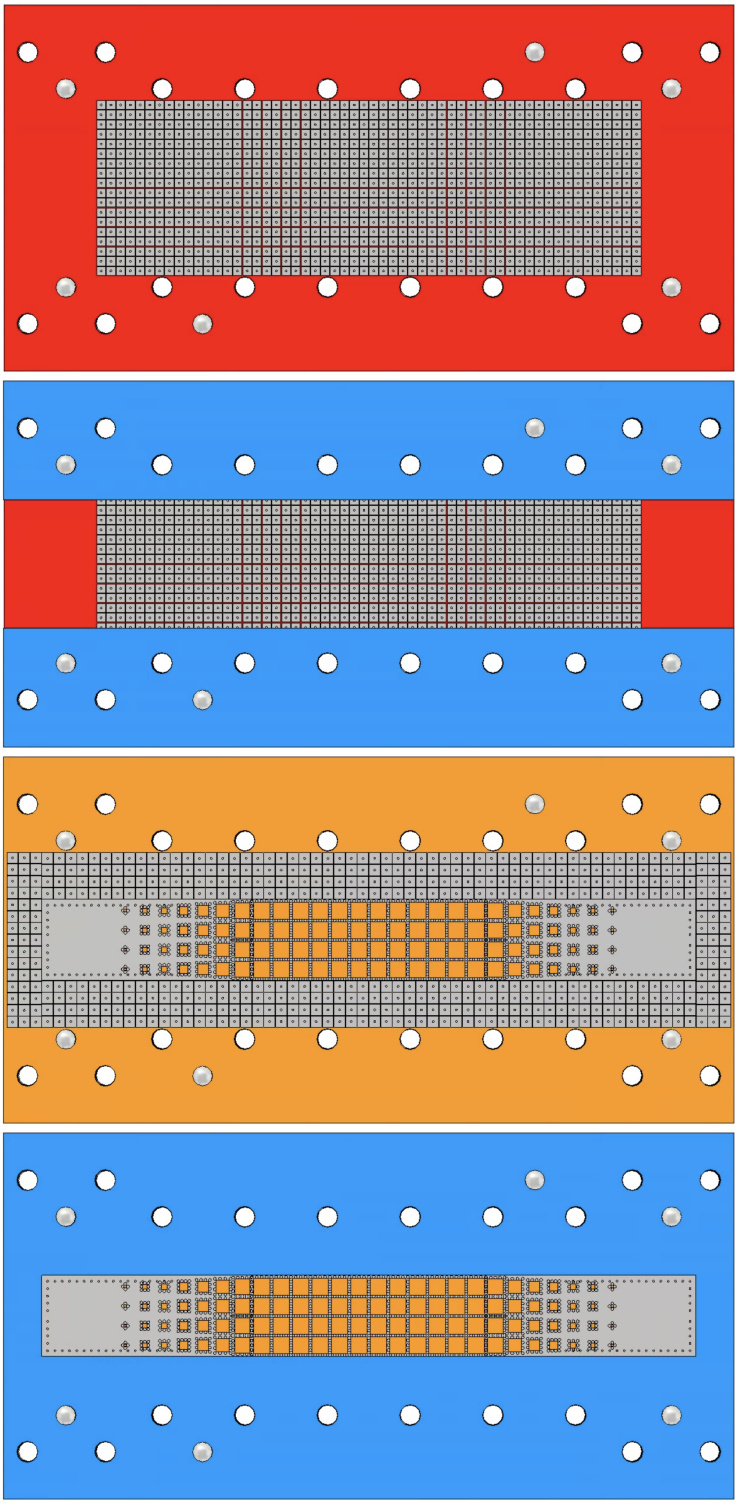

(d) Lower HIS layer (mushroom side).

(e) Lower separators (reconfigurable thickness).

(f) Lower SIH layer with RGW and lateral EBG mushrooms.

(g) Central separator (main propagation layer).

Figure 6.33: (Cont. next page) Different layers of the prototype, from bottom to top.

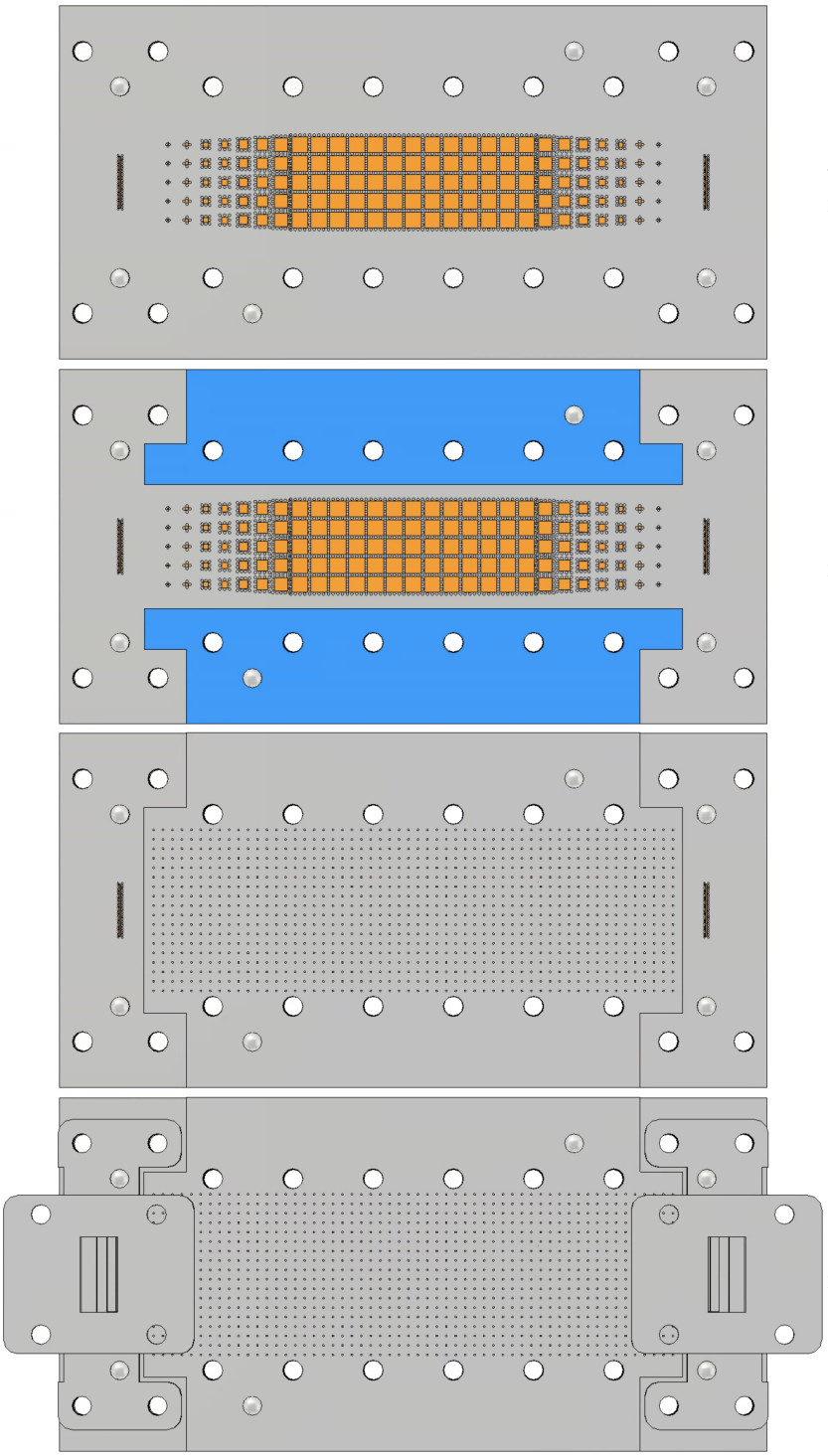

(h) Upper SIH layer with integrated cavities for feeds.

(i) Upper separators (reconfigurable thickness).

(j) Upper HIS layer (ground plane side).

(k) Total structure with metallic feeds.

Figure 6.33: Different layers of the prototype, from bottom to top.

| Name | Description | Value |
|---|---|---|
| $a$ | Maximum square SIH size (for tapering, see Tab. 6.1) | 3.4 mm |
| $a_{\text{lat}}$ | Square mushroom size for the lateral confinement of the RGW | 2.3 mm |
| $a_{\text{HIS}}$ | Square patch size of the HIS mushrooms | 1.85 mm |
| $d_{\text{v}}$ | Distance between two ridge vias | 1.5 mm |
| $d_{\text{e}}$ | Distance between the ridge edge and its vias | 1 mm |
| $d_{\text{f}}$ | Position of the feed (center) with respect to the ridge end | 5.04 mm |
| $g$ | Central gap between the SIH layers | 0.25 mm |
| $g_{\text{HIS}}$ | Gap between the SIH and HIS layers | Reconfigurable |
| $h$ | SIH layer's thickness | 0.25 mm |
| $h_{\text{cav}}$ | Height of the dielectric cavity in the upper SIH layer | 0.43 mm |
| $h_{\text{f}}$ | Height of the RW feed (for staircase dimensions, see Tab. 6.2) | 7.9 mm |
| $h_{\text{HIS}}$ | HIS layer's thickness | 1.52 mm |
| $h_{\text{slot}}$ | Height of the feeding slot in the upper SIH layer | 0.25 mm |
| $p$ | SIH period | 4 mm |
| $p_{\text{lat}}$ | Mushroom period for the lateral confinement of the RGW | 2.4 mm |
| $p_{\text{HIS}}$ | HIS mushroom period | 2 mm |
| $r$ | Radius of the SIH vias | 0.3 mm |
| $r_{\text{lat}}$ | Radius of the mushroom feet for the lateral confinement of the RGW | 0.2 mm |
| $r_{\text{HIS}}$ | Radius of the HIS mushroom feet | 0.2 mm |
| $w_{\text{cav}}$ | Width of the dielectric cavity in upper SIH layer | 11.02 mm |
| $w_{\text{f}}$ | Width of the RW feed | 15.8 mm |
| $w_{\text{slot}}$ | Width of the feeding slot in the upper SIH layer | 11.02 mm |
| $\epsilon_{\text{HIS}}$ | HIS layer's relative permittivity | 3 |
| $\epsilon_{\text{r2}}$ | SIH layer's relative permittivity | 6.5 |
| $\epsilon_{\text{sep}}$ | Relative permittivity of the wedge between both SIH layers | 6.5 |
| $\epsilon_{\text{rs}}$ | Relative permittivity of the reconfigurable wedges between SIH and HIS layers | 3 |

Table 6.3: Parameters of the reconfigurable waveguide design, with the values used in the final prototype.

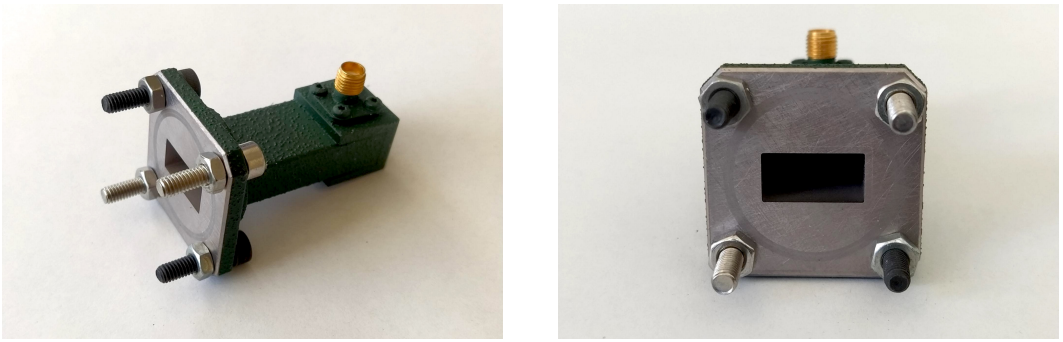

(a) Overall view. (b) Rectangular waveguide input.

Figure 6.34: Pictures of the coaxial-to-rectangular transition used to feed the prototype.

not overlapping, hence the multiple pins. If contraint issues appear during assembly, it is always possible to loosen up some constraints by enlarging the holes of certain layers. All the holes assigned to pressing the layers with nuts and bults are large enough that they do not add alignment constraints. As a precaution, more bolt holes are drilled than may actually be needed in the end.

The metallic RW to RGW transitions are crowned by waveguide flanges. These flanges are sized according to the available WR62 connectors photographed in Fig. 6.34. These connectors are then linked to the network analyzer with coaxial cables. The connectors are fixed to the feed flanges by means of bolts with hexagonal heads. When these bolts are threaded head down through the flanges, the heads embed themselves into the slot below the flanges. These slots are visible in Fig. 6.32b. This way, the heads can not rotate in the slots, thus maintaining the bolt while screwing the nut at the other end. The same slots are machined at the bottom of the metallic mount. Thereby, the bolts that press the different layers together can be operated without need of lifting the phase-shifter off the table. This little design trick facilitates the measurements, because the different layers must be assembled multiple times to change the separators of thickness $g_{\mathrm{HIS}}$ that reconfigure the phase-shift.

Finally, the height of the RW to RGW transitions is quite arbitrary, but practical considerations lead to a balance in height. On the one hand, it must not be too tall, because of the lever it would apply to the substrate layers. This is particularly true given the connectors that are fixed on top of the transitions, and which are quite heavy. It is also for that reason that the RW to RGW transitions have additional flanges at the level of the dielectric layers, with four assembling bolts, in order to prevent any tilt of the total feed column. On the other hand, the RW to RGW must be tall enough that the bolts can be threaded through the flange from below. Here, the total height of the metallic transitions is approximately 3 cm.

#### 6.3.4.2 Materials and manufacturing

**Dielectric substrates** As mentioned before, the substrates chosen for the SIH and the HIS layers are from the Rogers RO3000 laminate series, which offer low dielectric losses. The substrate RO3006 with $\epsilon_{r2} = 6.5$ and thickness 0.25 mm is used for both the SIH layers and the central gap separator. The substrate RO3003 with $\epsilon_{HIS} = 3$ and thickness 1.52 mm is used for the HIS layers. Moreover, given the set of available thicknesses for this substrate (0.13 mm, 0.25 mm, 0.5 mm, 0.75 mm and 1.52 mm), the RO3003 is also used for the reconfigurable separators between the SIH and HIS layers.

The available substrates have a copper plating of thickness $t = 17\,\mu m$. For the behavior of the substrate-integrated waveguide to be as close as the ideal case (PEC plates) as possible, the minimum requirement is for the skin depth of copper to be smaller than $t$. In this way, the fields do not cross through the plates. At a given frequency $f$, the skin depth of a metallic plate of conductivity $\sigma$ if given by [17, p. 19]

$$\delta_s = \sqrt{\frac{1}{\pi f \mu_0 \sigma}}, \tag{6.2}$$

with $\mu_0 = 4\pi \times 10^{-7}$ the vacuum permittivity. For copper, $\sigma = 5.813 \times 10^7\,S \cdot m^{-1}$ [17, p. 719]. Therefore, at the lowest operating frequency, that is $f = 13\,GHz$, the skin depth of the copper plates is $\delta_s = 0.58\,\mu m$. This is much smaller than the plate thickness, and so the available copper plating is suitable for the contemplated frequency range.

**Substrate manufacturing and LPKF machines** All the work on the dielectric layers can be made in-lab, with the two LPKF machines at hand. On the one hand, the LPKF ProtoLaser S4 can cut and drill the dielectric layers, as well as etch the metallization sheet. According to the datasheet, the minimum radius of the laser beam is 20 µm, with a position accuracy of ±10 µm. The minimum width of a metallic track is 75 µm, and must be spaced by at least 25 µm from the next track. On the other hand, the LPKF Contac S4 plates the inner-side of the holes to create the metallic vias. The minimum hole radius is 0.1 mm, with a minimum hole diameter to plate thickness ratio of 1 to 10. In the phase-shifter design, the minimum via radius is 0.2 mm in a layer of thickness 1.52 mm. Therefore, these specifications have the necessary accuracy for the phase-shifter design.

**Metallic feeds and mount** The staircase transition and the mounting plate must be manufactured in low-loss metal blocks. The manufacturing must be particularly accurate. In the case of the mount, the positions and radius of the metallic pins ensure the alignment of the different layers and the feeds. The RW to RGW transitions are even more delicate, because the last steps of the staircase have heights 0.25 mm and 0.35 mm, according to Tab. 6.2. Errors for these dimensions would deteriorate the impedance matching of the feed.

Manufacturing the feed in one metallic bulk is possible, and preferable in terms of accuracy. Nevertheless, the manufacturing cost can be reduced if the feed is built in two

pieces. This possibility is studied in appendix F, notably the question of the field leakage between the different components.

## Chapter landmarks

The homogenization techniques developed in the previous chapters are put to use for the design of a contactless reconfigurable phase-shifter in gap-waveguide technology, leading to the following studies:

- The quasi-static refractive index formula (4.40) is used to accelerate the preliminary studies for the holey metasurfaces. It shows which dielectrics and holes offer the best sensitivity to the hole depth for the reconfiguration. Notably, GS considerably improves the achievable refractive index range as function of the hole depth.
- Although G-S PPWs with SIHs are not accurately characterized by (4.40), the formula is a good qualitative indicator of their behavior. It also appears that the homogenized quasi-static Bloch impedance is surprisingly accurate for SIH metasurface waveguides.
- A fully-integrated prototype is designed to offer a 360° phase-shift. This designs covers the RGW with lateral mushrooms to guide the waves, the tapering of the holes for impedance matching and total phase-shift, and the perpendicular feed to transition from a RW to the ridge.

All designs are validated with CST simulations. The total structure has not been simulated because of the design complexity of the numerous metasurface elements, which overcomes our computer ressources. Manufacturing of the prototype is ongoing, in order to validate the design with experimental results.

# Conclusion

In this thesis, the aim of our studies of glide-symmetric (G-S) parallel-plate waveguides (PPWs) was two-fold. First, finding a modeling technique that would accelerate the practical design of G-S microwave devices. Second, improving the analytical understanding of these structures. In order to meet these goals, the starting point was the dispersion equation obtained by means of mode-matching, which is the only fully-analytic method available to accurately describe G-S waveguides. Some of the resulting new methods have been applied to the design of a reconfigurable phase-shifter, that is particularly cheap to produce due to the use of integrable metasurfaces.

**First goal: fast modeling of glide-symmetric waveguides** The first goal has been met in the quasi-static regime, with the derivation of the closed-form formula for the effective refractive index of holey PPWs. The refractive index of G-S waveguides is stable over a wide frequency range, and so there is no need to obtain the full Brillouin diagram when designing a G-S device. The quasi-static refractive index accurately characterizes the waveguide over a wide band. It can be adapted to arbitrary hole shapes, even shapes with inner conductors such as pins, by following simple steps:

1. Retrieve the modal information for a given hole shape (cut-off frequencies, norm, and fields of the modes).

2. Compute the Fourier transforms of these modes, and evaluate them at periodic points.

3. If analytical forms of the modes are known, dismiss the modes that have no impact on the dispersive behavior of the waveguide.

4. Insert this information into the closed-form formula, which yields the refractive index.

Contrarily to previous methods, no iterative solvers are needed in this process, which makes the implementation of this algorithm straight-forward, without tuning of any execution parameters. This also guarantees unprecedented speed to obtain the refractive index information, with a reduction of the execution time by at least two orders of magnitude compared to previous methods. In the context of parametric studies requiring thousands of simulations, this makes a substantial difference. For canonical hole shapes

such as rectangles or circles, the modal fields are known in closed form, and so the formula is completely analytic. This resulting time gain makes it possible to use the formula in optimization processes, in order to maximize the refractive index or the anisotropy of the waveguide. For arbitrary hole shapes, steps 1 and 2 are covered by an in-house two-dimensional finite element method at the surface of the holes and a fast Fourier transform. These algorithms are still much faster than the three-dimensional discretization needed in a commercial solver such as CST. Consequently, imaginative shapes such as super-ellipses or stars can be explored with no extra effort. This formula is suited for both non-glide-symmetric (nGS) and G-S waveguides, although its validity is larger in the latter case due to the low dispersion of glide symmetry (GS). Still, the denser the structure, the smaller the band of use of the formula, which is perfectly accurate only in the quasi-static regime. Our trials to keep some frequency-dependencies in the closed-form index formula to further improve the frequency validity have lead to interesting improvements.

In order to use holey G-S PPWs for impedance matching of different dielectric media, the quasi-static homogenization has been extended to the notion of Bloch impedance. From the closed-form refractive index formula, the quasi-static fields between the metasurfaces can be computed analytically. For square and circular holes, integrating these transverse fields across the unit cell yields an accurate definition of the impedance of the equivalent transmission line. This impedance is computed quickly without the use of commercial solvers, and completes the fast characterization of holey PPWs.

**Second goal: analytic study of the features of glide-symmetric waveguides**
The quasi-static homogenization is also a powerful tool for the analysis of the features of GS. First, it gives access to the effective behavior of structures which lie at the limit of the physical, and that would be difficult to simulate in commercial solvers. We have observed the convergence of the refractive index for asymptotically small gaps between the metasurfaces. For holey G-S waveguides, a giant refractive index is achieved when the holes are overlapping. Although such small gaps do not make sense in practice, this behavior illustrates how the complexity of the coupling between overlapping holes fundamentally impacts the effective density of the waveguide between G-S and nGS designs. A consequence of this difference is already visible at practical gap sizes, where the G-S index tends to be much larger than the nGS index.

The closed-form quasi-static formula also gives direct insight into the impact of the structure parameters on the refractive index. In order to analyze this impact in more depth, the formula is reduced to two modes in the holes. It is observed that two modes are enough to capture the behavior of G-S and nGS waveguides with canonical holes. In the simplified formula, the difference between these two structures can be clearly isolated. The dielectric materials are shown to have a great influence on this difference. By increasing the density (permittivity and/or permeability) of the hole medium, this difference can be enhanced, yielding structures where the G-S is much larger than the nGS index. But this analysis also highlights that this is not the case in general. Contrarily to what is shown in literature, the nGS index can be made larger than the GS index by increasing the dielectric density in the gap between the metasurfaces. Overall, it appears

that GS drives the effective waveguide density in the direction of the hole density, whereas nGS waveguides behave closer to the gap medium.

With two modes, the Bloch impedance formula can be simplified in a similar way. It is proven analytically that G-S tends to reduce the permittivity of the effective medium compared to its nGS counterpart. If the G-S refractive index is larger, then the Bloch impedance is larger as well, and consequently the effective permeability is much larger. This analytically proves observations that were made in recent publications. Nonetheless, it must be kept in mind that these findings are based on the observation that two modes are enough for the considered canonical waveguides. The limits of this observation remain unexplored. Still, because rectangular and circular holes are the most commonly used hole shapes, these findings explain most of the observations made in literature, and are likely to relate to phenomena that are inherent to GS. Future analyses of the quasi-static fields may give further interpretations to explain these features of GS.

In the end, the validity of the quasi-static homogenization technique is based on the low-dispersive behavior of G-S waveguides. We have tried to better understand this reduced dispersion by analyzing the dispersion equation obtained with mode-matching. For corrugated and holey PPWs, these studies have highlighted the impact of the harmonics depending on their parities. When the waveguide is G-S and when the gap between the metasurfaces decreases, half of the harmonics become negligible in the dispersion equation. The fundamental harmonic is dominant, and its wavenumber shifts linearly with increasing frequency. For corrugated structures with small and medium corrugations, the linearity of the dispersion curve in the first Brillouin zone is proven by simplifying all the frequency dependencies in the dispersion equation. For wider corrugations, such a linearization was not possible, because of the increasing number of modes required to accurately describe the structure. Nevertheless, the dismissal of half the harmonics has made it possible to show that a G-S corrugated waveguide has the same dispersive behavior as a nGS waveguide with half the periodicity. This means that in the first Brillouin zone, the G-S waveguide has a dispersion curve that corresponds to the low-dispersive range of the nGS equivalent structure. It must be noted that this equivalent structure is non-physical for wide corrugations, and that it requires twice as many corrugations to behave like the GS structure under study.

Unfortunately, we have not been able to generalize these results to arbitrary G-S PPWs. Proving the linearity of the dispersion curve in general is an unrealistic task, because depending on the geometry the dispersion may not be negligible, even in the first Brillouin zone, and so the dispersion curve is not linear. We are left with quantitative methods, such as the presented equivalent corrugated structure, or with physical interpretations, such as the mode degeneracy that occurs in the G-S waveguide when the period is half the wavelength, closing the first stopband and reducing the "bending" of the first mode.

**Reconfigurable phase-shifter** Although the homogenization technique developed in this thesis applies to holey PPWs, the design of a reconfigurable integrated phase-shifter illustrated the adaptability of this method. The preliminary studies made with the quasi-

static index formula capture the qualitative behavior of more complex structures such as substrate-integrated holes. This accelerates the design of a complex reconfigurable unit cell, made of several layers of integrated metasurfaces. The manufacturing of this phase-shifter is ongoing, and so unfortunately no experimental results are shown here. Nevertheless, extended simulations show that in theory, a 360° phase-shifter can be built with contactless reconfiguration. It should be kept in mind that the design presented here is a proof of concept. Its length, bulky feed and operating band make it unsuitable for practical applications. Future designs should be upgraded to the Ka band, and focus on the miniaturization of the design. But whatever the operating frequency, as long as the resulting design operates the first Bloch mode of the G-S waveguide, where the dispersion is low, the quasi-static homogenization technique can be used to optimize the holey metasurfaces in preliminary studies.

**Future research perspectives** One of the main strengths of the quasi-static refractive index formula (4.40) is its compactness and generality. Therefore, it could be used to analytically study the impact of the different structure parameters in more depth. For example, what is the upper limit for the refractive index when decreasing the metasurface period, or the gap between the metasurfaces? Can the metasurface holes be designed in such a way that a singularity appears in the denominator of the formula, resulting in giant-index waveguides? Ideally, (4.40) would be reversed to yield the geometry of the waveguide for given propagation features: simplified versions of the formula may be used to this purpose.

In this mindset, several studies about the isotropy of structures have been performed but have not been reported here due to their incompleteness. Indeed, the quasi-static refractive index formula is dependent on the propagation direction in the PPW. Therefore, if the refractive index is isotropic, all the angle dependencies should cancel out in the formula. This has been done for square holes and for circular holes, based on making pairs of transverse electric modes with the same norm and orthogonal field averages. Ideally, an in-depth study of the formula would lead to a set of sufficient, and maybe even necessary, conditions for the isotropy of holey PPWs depending on the shape of the holes. Attempts were made to do so, based on the derivations for square and circular holes. However, these holes have inherent symmetry that guarantees the same propagation features in orthogonal directions. Other examples, such has triangular holes, would give more insight in order to generalize the conditions for isotropy.

Although the use of the finite element method in order to obtain the eigenmodes of arbitrary holes has proven to be quite fast, the process might be further optimized. Maybe other techniques would retrieve the Fourier information of these modes more efficiently. The accelerated study of imaginative shapes such as those in section 4.4 may lead to better understanding of how the fields are disrupted by the metasurfaces. Examining the charge distributions, notably at the edges of the holes, may explain why certain hole shapes lead to denser effective waveguides.

In spite of the promising extensions of the index formula in section 4.5, they do not guarantee a generalized high-frequency validity of the formula. Future research to

keep first-order frequency dependencies may extend this homogenization method further. However, it is difficult to retain more frequency-dependent terms and still obtain a simplified dispersion equation that can be reformulated with the determinant lemma.

Although the impedance-retrieval technique in section 5.2.3 does not rely on commercial solvers, it is motivated by heuristic observations. For square and circular holes, the Bloch impedance works because of the field's transverse electric magnetic (TEM) nature in a particular integration plane between the holes. This has not been proven analytically. In the future, it would be interesting to evaluate the limits of this technique: under which conditions and in which plane is the Bloch mode TEM? How is the accuracy impacted when moving away from this plane? Can this Bloch impedance be computed for arbitrary hole sizes? What about different propagation directions, when the incident wave is not normal to the metasurface interface?

A notable limitation of this thesis is the lack of losses in the analytical formulas. This approach is motivated by the negligible losses in the metallic metasurface waveguides used in practice. However, a generalization of the mode-matching process including the metallic losses (for example by considering a lossy coating around each hole) would clarify the limits of the lossless formula in terms of losses. Moreover, including the losses would also put into perspective more theoretical results, such as the impact of the dielectrics in the holes and in the gap as detailed in section 5.1. Asymptotical studies such as decreasing the gap in section 5.1.3 would also benefit from accounting for the losses, because it is in these cases that losses are most likely to change the fundamental behavior of the waveguide.

While the focus of this thesis has been G-S waveguides, other symmetries might benefit from such mode-matching simplifications in the quasi-static regime. Hexagonal GS has been mentioned in chapter 1. Parity-time symmetries could be implemented by adding alternating losses and gains at the bottom of the holes. Cylindrical geometries making use of twist symmetry may be homogenized as well, and due to their extended use in real-life applications, an equivalent to the formula 4.40 would be most useful.

Finally, the phase-shifter design presented here serves only as a proof-of-concept. Its large electrical size is prohibitive for practical applications. Integration of this concept in antenna arrays would be interesting. Therefore, and depending on the manufacturing technologies available, other reconfigurable unit cells should be developed with wider phase variations. Holes that support TEM modes could be a possible idea to this effect. In order to accelerate the design of such cells, further analytical homogenization models for the reconfigurable unit cells could be developed. For example, the capacitive load created by the high-impedance metasurfaces may be included in the homogenized refractive index formula by using equivalent circuits. Here too, including the losses in the formula would lead to preliminary designs closer to the final prototype.

# List of published and upcoming papers

## Conference papers

B. Fischer and G. Valerio, "Broadband Dispersionless Glide-Symmetric Parallel-Plate Waveguide with Small Corrugations", in *2021 15th European Conference on Antennas and Propagation (EuCAP)*, Düsseldorf, Mar. 2021, pp. 1–4

B. Fischer and G. Valerio, "Ultra-Wideband Homogenization of a Glide-Symmetric Parallel-Plate Waveguide", in *2021 15th European Conference on Antennas and Propagation (EuCAP)*, Düsseldorf, Mar. 2021, pp. 1–4

B. Fischer and G. Valerio, "Wideband Homogenization of a Glide-Symmetric Holey Parallel-Plate Waveguide", in *2021 XXXIVth URSI General Assembly and Scientific Symposium (URSI GASS)*, Rome, Sep. 2021

B. Fischer and G. Valerio, "Wideband Characterization of Holey Glide-Symmetric Parallel-Plate Waveguides", in *2022 16th European Conference on Antennas and Propagation (EuCAP)*, Madrid, Mar. 2022, pp. 1–5

B. Fischer, J. Sarrazin, and G. Valerio, "Reconfigurable Phase-Shifter Based on Glide-Symmetric Substrate-Integrated Holes and High-Impedance Metasurfaces", in *2022 16th European Conference on Antennas and Propagation (EuCAP)*, Madrid, Mar. 2022, pp. 1–5

B. Fischer and G. Valerio, "Homogenization and Dispersion Properties of Glide-Symmetric Corrugated Metasurfaces", in *2022 Microwave Mediterranean Symposium (MMS)*, ISSN: 2157-9830, Pizzo Calabro, May 2022, pp. 1–5

B. Fischer and G. Valerio, "Homogénéisation large bande de métasurfaces creuses avec symétrie glissée pour antennes à lentille plane", in *2022 XXIIèmes Journées Nationales Microondes (JNM) Limoges*, Limoges, Jun. 2022, pp. 1–2

# Journal papers

## Published papers

B. Fischer and G. Valerio, "Quasi-Static Homogenization of Glide-Symmetric Holey Parallel-Plate Waveguides With Ultra-Wideband Validity", *IEEE Transactions on Antennas and Propagation*, vol. 70, no. 11, pp. 10 569–10 582, Nov. 2022, Conference Name: IEEE Transactions on Antennas and Propagation

## Upcoming papers

B. Fischer and G. Valerio, "Dispersion Properties of Glide-Symmetric Corrugated Metasurface Waveguides", *International Journal of Microwave and Wireless Technologies (accepted with minor revisions)*, 2023

B. Fischer and G. Valerio, "Effective Refractive Index Control of Holey Glide-Symmetric Parallel-Plate Waveguides via Quasi-Static Homogenization", *(in the writing process)*, 2023

B. Fischer and G. Valerio, "Quasi-Static Bloch Impedance Analysis of Holey Glide-Symmetric Parallel-Plate Waveguides", *(in the writing process)*, 2023

# Appendix A

# Details to the review of glide-symmetric metasurfaces

## A.1 Spectrum of multiple periodic cells

In order to illustrate the fact that the Floquet condition only gives a lower bound to the periodicity of the wavenumber spectrum, the example of multiple periodic cells is taken, which can be applied to any $p$-periodic structure.

It is worth noticing that if a structure is $p$-periodic, then it is also $qp$-periodic, with $q \in \mathbb{N}$. Therefore, there exist an eigenvalue $s$ such that the Floquet condition is satisfied for the $qp$-translation operator i.e.,

$$\boldsymbol{E}(\boldsymbol{r} + qp\boldsymbol{e}_z) = \boldsymbol{\mathcal{T}}_{qp}\left\{\boldsymbol{E}(\boldsymbol{r})\right\} = s\boldsymbol{E}(\boldsymbol{r})\,. \tag{A.1}$$

After defining a fundamental wavenumber $k_z'$ such that $\mathrm{e}^{-\mathrm{j}k_z' qp} = s$, all higher harmonics can be defined as $k_z^{(n)'} = k_z' + n2\pi/(qp)$, with $n$ an integer. The wavenumber spectrum of the $pq$-periodic model seems to have a higher periodicity than the spectrum of the $p$-periodic model, although both models represent the same structure.

Moreover, a translation of $qp$ is equivalent to $q$ chained translations of $p$ i.e., $\boldsymbol{\mathcal{T}}_{qp} = \boldsymbol{\mathcal{T}}_p^q$. Inserting this result in (1.4) yields

$$\boldsymbol{\mathcal{T}}_p^q\left\{\boldsymbol{E}(\boldsymbol{r})\right\} = t^q\boldsymbol{E}(\boldsymbol{r})\,. \tag{A.2}$$

Comparing (A.2) with (A.1), one gets

$$t^q = s \iff \mathrm{e}^{-\mathrm{j}k_z pq} = \mathrm{e}^{-\mathrm{j}k_z' qp}\,, \tag{A.3}$$

which means that the relationship between the fundamental wavenumber in both models is

$$k_z = k_z' + n\frac{2\pi}{pq} = k_z^{(n)'}\,. \tag{A.4}$$

Would all possible $k_z^{(n)'}$ be in the spectrum of the structure, then equation (A.4) would imply that the wavenumber spectrum of the $p$-periodic model is $2\pi/(pq)$-periodic too. This would be in disagreement with (1.5), which states that the spectrum of the structure has a periodicity bigger or equal to $2\pi/p$. Both statements can only be compatible if some modes $k_z^{(n)'}$ correspond to vanishing fields i.e., the corresponding eigenfield cannot exist within the considered structure. As such, the corresponding $k_z^{(n)'}$ can be removed from the spectrum of the structure, yielding a bigger periodicity, at least $2\pi/p$ according to (1.5).

## A.2 Proof of the generalized Floquet theorem

In this section, the generalized Floquet theorem is proven. For generality, it is applied to twist symmetry. All the following derivations can be easily transposed to glide symmetry (GS).

Let us consider a structure with $N$-fold twist symmetry and period $p$. Each unit cell is made of $N$ subcells of length $p' = p/N$. Adjacent subcells are rotated by an angle $\theta = 2\pi/N$. After $N$ subcells, the orientation of the subcell is back to the one of the first subcell. Let us name the higher symmetries operator $\boldsymbol{\mathcal{L}}_N$, yielding the field in the next subcell with the corresponding rotation, namely

$$\boldsymbol{\mathcal{L}}_N \{\boldsymbol{E}(\boldsymbol{r})\} = \boldsymbol{E}\left(r + p', \theta + \frac{2\pi}{N}, z\right). \tag{A.5}$$

In terms of operators, this means that composing $N$ times the operator $\boldsymbol{\mathcal{L}}_N$ corresponds to the translation operator i.e.,

$$(\boldsymbol{\mathcal{L}}_N)^N = \boldsymbol{\mathcal{T}}_p. \tag{A.6}$$

The generalized Floquet theorem [104] states that, for $\boldsymbol{E}$ a *non-degenerate* non-zero eigenmode of the structure,

$$\exists\, t \in \mathbb{C} \text{ s.t. } [\boldsymbol{\mathcal{T}}_p - t]\, \boldsymbol{E}(\boldsymbol{r}) = 0 \quad \Longleftrightarrow \quad \exists\, \ell \in \mathbb{C} \text{ s.t. } [\boldsymbol{\mathcal{L}}_N - \ell]\, \boldsymbol{E}(\boldsymbol{r}) = 0. \tag{A.7}$$

The theorem can be demonstrated by considering the invariance of Maxwell's equations under translation and rotation. Therefore, Maxwell's equations are invariant under the operator $\boldsymbol{\mathcal{L}}_N$. Moreover, the geometry of the structure (meaning the boundary conditions) are invariant under $\boldsymbol{\mathcal{L}}_N$ too. As a consequence, if $\boldsymbol{E}$ is an eigenmode of the structure under translation $\boldsymbol{\mathcal{T}}_p$ with eigenvalue $t$, then the mode $\boldsymbol{\mathcal{L}}_N \{\boldsymbol{E}(\boldsymbol{r})\}$ is an eigenmode of the structure too, with the same eigenvalue $t$. Therefore, one simultaneously has

$$[\boldsymbol{\mathcal{T}}_p - t]\, \boldsymbol{E}(\boldsymbol{r}) = 0 \tag{A.8}$$

$$\text{and} \quad [\boldsymbol{\mathcal{T}}_p - t]\, \boldsymbol{\mathcal{L}}_N \{\boldsymbol{E}(\boldsymbol{r})\} = 0. \tag{A.9}$$

The important assumption is that $t$ is a non-degenerate eigenvalue, meaning that the eigenspace associated to $t$ is of rank one. As a consequence, (A.9) implies that there exists $\ell \in \mathbb{C}$ such that

$$\boldsymbol{\mathcal{L}}_N \{\boldsymbol{E}(\boldsymbol{r})\} = \ell \boldsymbol{E}(\boldsymbol{r}) \,. \tag{A.10}$$

The converse is straight-forward. If (A.10) is true, then composing the higher-symmetry operator $n$ times implies that $\boldsymbol{E}$ is an eigenvector of $\boldsymbol{\mathcal{T}}_p$ with eigenvalue $\ell^n$ i.e.,

$$\boldsymbol{\mathcal{T}}_p \{\boldsymbol{E}(\boldsymbol{r})\} = \boldsymbol{\mathcal{L}}_N^n \{\boldsymbol{E}(\boldsymbol{r})\} = \ell^n \boldsymbol{E}(\boldsymbol{r}) \,. \tag{A.11}$$

## A.3 Modeling of glide-symmetric metasurface waveguides

### A.3.1 Full-wave solvers

**Commercial solvers** In order to find the dispersion diagram of a periodic structure, one can distinguish between two types of methods: methods that compute the wavenumber as a function of frequency, and methods that find the operating frequency as a function of the phase-shift across the unit cell [169]. The eigensolvers of commercial softwares such as CST and HFSS belong to this second category. Periodic boundary conditions on opposite sides expect to be related by an arbitrary phase-shift. For a given phase-shift, the mode frequencies that fit all boundary conditions are the solutions. Therefore, a parametric change of the phase-shift plots the Brillouin diagram. Such commercial eigensolvers are designed for a wide range of applications and arbitrary geometries. This comes at the cost of computation and memory ressources. A glide-symmetric (G-S) waveguide with interesting features has a small distance between the metasurfaces, compared to the unit cell period, which is in turn electrically small. As a consequence, the meshing rate of the model discretization used in the commercial software is very high, leading to lengthy simulations. For the design of a lens antenna, which requires hundreds or thousands of different geometries, this makes the parametric studies of the unit cell cumbersome.

Moreover, even for lossless materials, the wavenumber $k_{\text{eff}} = \beta_{\text{eff}} - \mathrm{j}\alpha_{\text{eff}}$ of periodic structures may be complex, notably in the stopbands, where the modes are attenuated due to a non-zero $\alpha$. Commercial solvers do not compute the imaginary part of the wavenumber when not related to material losses. This information is important for electromagnetic bandgap (EBG) structures, because it drives the number of EBG rows needed to repress the leakage. Similarly, the leakage rate and the aperture field distribution of leaky-wave antennas (LWAs) is dependent on the imaginary part of $k_{\text{eff}}$ [169].

**Periodic method of moments** By expressing an electromagnetic (EM) problem in integral-equation formulation, it can be solved with the method of moments (MoM). The MoM is well-suited for metasurfaces analysis, because these problem often involve radiation. With the MoM, there is no need to define absorbing boundary conditions,

thanks to the use of Green's functions [185, p. 506]. For periodic structures, a periodic Green's function is defined. It incorporates the radiation of the shifted copies of the considered source, in the form of infinite series [227]. As an example, [228] computes the fields of a one-dimensional (1-D) microstrip line with thin periodic metallizations of arbitrary shape, using periodic Green's functions in a MoM applied to the mixed-potential integral-equation formulation. All the propagating modes are found, whether confined or leaky in space or in the substrate.

The challenges of periodic MoM lie in the singularity extractions of the Green's function [229], [230], and the efficient computation of the infinite series due to periodicity. In [231], several possible acceleration schemes for computing the series are compared. Notably, Ewald's transformation combines the spectral (sum of harmonics) and spatial (periodic sources) representations of the periodic Green's function in order to find a balance between efficiency and accuracy. Extraction and analytic study of the slowly convergent terms is another acceleration procedure [232]. Nonetheless, periodic MoM is confronted to structures where the periodicity is broken due to the feed or the edges of the system. Moreover, metasurfaces that do not lie on planar or cylindrical layers are problematic, which is a growing issue with the conformability of metasurface applications. Then, one is limited by the computational ressources, because these arbitrary systems need full-wave simulation of metasurfaces which are many wavelengths large [52, Chap. 15].

**Periodic time domain boundaries** It is notable that other full-wave techniques have been extended to periodic structures, such as time-domain methods. A finite-difference time-domain method can be applied to metasurfaces when implementing time-domain periodic boundary conditions [233]. This is challenging, because enforcing a phase-shift – which per nature falls under the frequency domain – would require storing the history of the field over many time steps. This can be circumvented by computing two time-responses in parallel with orthogonal phase-shifts, to create complex phasors in time, for which Floquet boundary conditions can be enforced. The advantage of these methods is that they do not require complex root-finding procedures. Nonetheless, iterative manipulation of large matrices is needed, requiring large computation and storage ressources, which may lead to numerical instabilities [169].

### A.3.2 Existing analytic methods

**Metasurface homogenization** Many studies of metasurfaces rely on homogenization techniques. This means that the resonant details of the metasurface are represented by averaged boundary conditions or propagation features, that represent the effective interactions of the incident or surface waves with the surface. As a simple example, [91] homogenizes a metasurface with periodic grooves by considering an incident plane wave on the surface. The reflection coefficient is computed for all reflected modes. Under the subwavelength assumption, all higher-order excited modes are confined, and so only the fundamental mode is necessary for a distant observer. The poles of the reflection

coefficient of this mode yield the effective wavenumber of the surface waves that can propagate along the surface. Similarly, [170] homogenizes a bed of nails metasurface, considering it as a truncated wire medium, in order to obtain closed-form expressions for the reflection coefficient and the surface impedance.

The limits of this procedure are explored in [41], where the unimodal homogenization of a corrugated metasurface is considered within a parallel-plate waveguide (PPW). In this case, the "distant observer" assumption does not hold. If the upper metal plate is too close to the corrugated plate, higher-order Floquet harmonics and more corrugation modes must be considered to capture the vertical interactions between the plates and the horizontal field variations at the surface of the corrugations. Moreover, this method does not capture the singular features of GS. Indeed, if each metasurface is homogenized separately, this model does not take into account the horizontal positions of the metasurfaces with respect to each other – more specifically the half-period shift that characterizes GS.

A multimodal homogenization approach is possible, but it is equivalent to performing the modal analysis presented in section A.3.4. Moreover, it is notable that some accurate models have been found for particular geometries displaying GS, e.g., in [61], where the effective transmission and reflection coefficients of multi-layered metamaterial are found. Each layer is made metallic patches, and so an equivalent surface impedance is found by means of MoM. Then, stacking such metasurfaces can be described as a transmission line model for transverse electric (TE) or transverse magnetic (TM) plane waves. Most importantly, coupling terms are added to account for the effect of the shift between the layers. However, deriving such a model is cumbersome and is valid only for a particular geometry.

**Equivalent circuits** Passive reciprocal two-ports can be represented by an equivalent T-circuit. This representation is suitable for both penetrable and impenetrable metasurfaces, as it connects the average tangential electric and magnetic fields on both sides of the metasurface [51]. When it comes to metasurface waveguides, periodic canonical geometries can also be represented by discrete circuit elements, linked by transmission lines. Equivalent circuits have first been used for simple discontinuities in hollow metallic waveguides [171]. More recently, they have described the transmission and reflection properties for layered arrays of patches and apertures, such as phase resonances or extraordinary optical transmission [52, Chap. 13]. According to the authors, these circuits are limited to metallizations with negligible thickness, and can be used only up to the second resonance of the scatterers – which covers most uses of such metasurfaces.

When it comes to G-S waveguides, the geometry becomes the limiting factor for many circuits. An equivalent circuit model for G-S corrugated PPWs has been evaluated [41]. Each corrugation can be modeled as the equivalent circuit of a classical T-junction, which is well-known [171], and then the waveguide is seen as a cascade of these circuits. A simple dispersion analysis can be executed from the resulting transfer matrix. This works very well for non-glide-symmetric (nGS) waveguides. For G-S structures, this method is limited by the size of the corrugations. Indeed, when the corrugations are wider than half a period, then the upper and lower corrugations overlap, and so the structure cannot

be described as a series of T-junctions.

Overall, while equivalent circuits are very effective simulation tools once they are at hand, they are cumbersome to find, especially for non-canonical geometries and for two-dimensional (2-D) metasurfaces. Notably, it is difficult to include the coupling phenomena between adjacent unit cells, especially in the case of GS, where this coupling is central to the waveguide behavior [52, Chap. 12].

**Single-mode transfer matrix** Transfer matrices are a well-known tool for the analysis of periodic microwave system [17, p. 382]. The system is seen as a cascade of two-ports, each two-port corresponding to one unit cell. The method is based on the assumption that the transfer matrix of the unit cell in the periodic system is equal to that of the isolated two-port [169]. Then, by exciting the unit cell at its two ports, this transfer matrix can be computed from equivalent circuits or from commercial solvers. If the solver yields the S-parameters of the unit cell, the diagonal coefficients of the transfer matrix can be computed as [17, p. 192]

$$A = \frac{(1+S_{11})(1-S_{22})+S_{12}S_{21}}{2S_{21}}\,, \tag{A.12}$$

$$D = \frac{(1+S_{11})(1+S_{22})-S_{12}S_{21}}{2S_{21}}\,. \tag{A.13}$$

Given that the periodic structure is represented by a cascaded two-port transmission line, effective voltages and currents can be defined between the unit cells. The transfer matrix relates the voltage $V_{n+1}$ and current $I_{n+1}$ of the next cell with the voltage $V_n$ and current $I_n$ of the previous cell. This relation can be combined to Floquet's theorem (1.3), which relates these voltages and currents too, yielding

$$\begin{bmatrix} V_{n+1} \\ I_{n+1} \end{bmatrix} = \begin{bmatrix} A & B \\ C & D \end{bmatrix} \begin{bmatrix} V_n \\ I_n \end{bmatrix} = \mathrm{e}^{-\mathrm{j}k_{\mathrm{eff}}p} \begin{bmatrix} V_n \\ I_n \end{bmatrix}\,, \tag{A.14}$$

where $p$ is the period of the unit cell, and $k_{\mathrm{eff}} = \beta_{\mathrm{eff}} - \mathrm{j}\alpha_{\mathrm{eff}}$ is the effective wavenumber of the guided wave. Equation (A.14) shows that $\mathrm{e}^{-\mathrm{j}k_{\mathrm{eff}}p}$ is an eigenvalue of the transfer matrix. Finding these eigenvalues is equivalent to solving the equation

$$\left(A - \mathrm{e}^{-\mathrm{j}k_{\mathrm{eff}}p}\right)\left(D - \mathrm{e}^{-\mathrm{j}k_{\mathrm{eff}}p}\right) - BC = 0\,, \tag{A.15}$$

which, assuming that the network is reciprocal, i.e., $AD - BC = 1$ [17, p. 191], yields

$$1 - A\mathrm{e}^{-\mathrm{j}k_{\mathrm{eff}}p} - D\mathrm{e}^{-\mathrm{j}k_{\mathrm{eff}}p} + \mathrm{e}^{-\mathrm{j}2k_{\mathrm{eff}}p} = 0 \tag{A.16}$$

$$\iff \qquad \cos\left(k_{\mathrm{eff}}p\right) = \frac{A+D}{2}\,. \tag{A.17}$$

In (A.17), the transfer matrix coefficients are frequency-dependent. Therefore (A.17) can be solved as a function of frequency to yield the Brillouin diagram of the periodic waveguide, which is evidently periodic. It should be noted that although (A.17) seems to avoid a root-finding process, this is not exactly true, because a modal analysis is already hidden in the computation of the transfer matrix coefficients $A$ and $D$ [169].

The first disadvantage of the single-mode transfer matrix (SMTM) method is it can only find the discrete spectrum of the uni cell, which is incomplete when considering open structures with a continuous radiating spectrum [169]. Indeed, the modes excited at the ports of a commercial solver have closed boundary conditions, which prevent the excitation of the true unbounded modes to find the transfer matrix of the unit cell. A workaround is to increase the size of the ports by including free-space above the periodic structure, and to change the height of the port to check the invariance of the solutions.

Most importantly, this method does not convey the higher-order modal interactions between adjacent unit cells, which are particularly relevant at a sub-wavelength scale [169]. This is illustrated in [234] with the analysis of a metasurface waveguide made of transverse metal ridges. The metasurface are close enough that the ridges are intertwined. When these ridges are thin compared to the period, then the SMTM is accurate. In this case, G-S and nGS designs have the same first two modes. On the contrary, if the period is small, i.e., the ridges are close to each other, then G-S and nGS behave differently, but the SMTM method does not capture this difference.

When the unit cell displays particular symmetries, it is possible to separate the unit cell in two successive two-ports, whose transfer matrices reflect this symmetry [235]. This has the advantage of reducing by half the computational load in the commercial solver in order to obtain the transfer matrix. However, not only does it not solve the problem of the coupling between adjacent unit cells, but it also loses the coupling information between the two symmetric subcells.

In order to gain coupling information, several unit cells can be regrouped in one big cell, called supercell [169]. This supercell is simulated in the commercial solver in order to obtain the transfer matrix of this group. The effect of higher modes within the structure are captured by this transfer matrix. The number of cells must be large enough to minimize the boundary effects, that is the missing coupling information at the unit cells at the ends of the supercell. As a consequence, this procedure makes the computational load onerous for most applications. Moreover, the solution of the resulting dispersion equation is not unique, because several cells lead to more possible unity roots, making the true wavenumber ambiguous [235]. Finally, for radiating structures such as LWAs, the waves may be attenuated at the end of the supercell, leading to strong numerical inaccuracies in the transfer matrix evaluation.

### A.3.3 Multi-modal transfer matrix method

**Description of the method for periodic structures** Multiports are often associated to the physical presence of different terminals. But it is also possible to associate them to the different modes propagating through the same feed, even if these modes are evanescent in the structure [169]. Therefore, in order to accurately describe the multi-modal coupling between the adjacent cells of a periodic waveguide, a multi-modal transfer matrix (MMTM) method has been developed [43]. For 1-D periodicity, a com-

mercial solver yields the multi-modal scattering matrix of the unit cell, that is

$$\underline{\boldsymbol{S}} = \begin{bmatrix} \underline{\boldsymbol{S}}_{\mathrm{ii}} & \underline{\boldsymbol{S}}_{\mathrm{io}} \\ \underline{\boldsymbol{S}}_{\mathrm{oi}} & \underline{\boldsymbol{S}}_{\mathrm{oo}} \end{bmatrix}, \tag{A.18}$$

where $\underline{\boldsymbol{S}}_{\mathrm{ii}}$ contains the the reflective S-parameters between the input ports, $\underline{\boldsymbol{S}}_{\mathrm{oo}}$ the reflective S-parameters between the output ports, and the remaining matrices express the transmission coefficients. From there, the coefficients of the MMTM are expressed as

$$\underline{\boldsymbol{A}} = \frac{1}{2}\left[\underline{\boldsymbol{I}} + \underline{\boldsymbol{S}}_{\mathrm{ii}}\right]\left[\underline{\boldsymbol{S}}_{\mathrm{oi}}\right]^{-1}\left[\underline{\boldsymbol{I}} - \underline{\boldsymbol{S}}_{\mathrm{oo}}\right] + \frac{1}{2}\underline{\boldsymbol{S}}_{\mathrm{io}}, \tag{A.19}$$

$$\underline{\boldsymbol{B}} = \frac{1}{2}\left[\underline{\boldsymbol{I}} + \underline{\boldsymbol{S}}_{\mathrm{ii}}\right]\left[\underline{\boldsymbol{S}}_{\mathrm{oi}}\right]^{-1}\left[\underline{\boldsymbol{I}} + \underline{\boldsymbol{S}}_{\mathrm{oo}}\right]\underline{\boldsymbol{Z}}_{\mathrm{o}} - \frac{1}{2}\underline{\boldsymbol{S}}_{\mathrm{io}}\underline{\boldsymbol{Z}}_{\mathrm{o}}, \tag{A.20}$$

$$\underline{\boldsymbol{C}} = \frac{1}{2}\left[\underline{\boldsymbol{Z}}_{\mathrm{i}}\right]^{-1}\left[\underline{\boldsymbol{I}} - \underline{\boldsymbol{S}}_{\mathrm{ii}}\right]\left[\underline{\boldsymbol{S}}_{\mathrm{oi}}\right]^{-1}\left[\underline{\boldsymbol{I}} - \underline{\boldsymbol{S}}_{\mathrm{oo}}\right] - \frac{1}{2}\left[\underline{\boldsymbol{Z}}_{\mathrm{i}}\right]^{-1}\underline{\boldsymbol{S}}_{\mathrm{io}}, \tag{A.21}$$

$$\underline{\boldsymbol{D}} = \frac{1}{2}\left[\underline{\boldsymbol{Z}}_{\mathrm{i}}\right]^{-1}\left[\underline{\boldsymbol{I}} - \underline{\boldsymbol{S}}_{\mathrm{ii}}\right]\left[\underline{\boldsymbol{S}}_{\mathrm{oi}}\right]^{-1}\left[\underline{\boldsymbol{I}} + \underline{\boldsymbol{S}}_{\mathrm{oo}}\right]\underline{\boldsymbol{Z}}_{\mathrm{o}} + \frac{1}{2}\left[\underline{\boldsymbol{Z}}_{\mathrm{i}}\right]^{-1}\underline{\boldsymbol{S}}_{\mathrm{io}}\underline{\boldsymbol{Z}}_{\mathrm{o}}, \tag{A.22}$$

where the impedance matrices $\underline{\boldsymbol{Z}}$ are square diagonal, with each diagonal coefficient corresponding to the port impedance of one port. It can be shown that if $\underline{\boldsymbol{Z}}_{\mathrm{i}} = \underline{\boldsymbol{Z}}_{\mathrm{o}}$, then the value of the impedances does not impact the dispersion equation. Note that the four elements of the transfer matrix are square matrices too, relating the vectors of voltages and currents corresponding to the multiple modes. Similarly to the SMTM in (A.14), Floquet's theorem then yields

$$\begin{bmatrix} \underline{\boldsymbol{A}} & \underline{\boldsymbol{B}} \\ \underline{\boldsymbol{C}} & \underline{\boldsymbol{D}} \end{bmatrix} \begin{bmatrix} \boldsymbol{V}_n \\ \boldsymbol{I}_n \end{bmatrix} = \mathrm{e}^{-\mathrm{j}k_{\mathrm{eff}}p} \begin{bmatrix} \boldsymbol{V}_n \\ \boldsymbol{I}_n \end{bmatrix}. \tag{A.23}$$

Consequently, the eigenvalues of the MMTM provide the dispersive features of the periodic waveguide. Contrarily to the single-mode method, the higher-order modes excited at the boundaries between adjacent unit cells are included, and so their impact on propagation is used to find $k_{\mathrm{eff}}$. A priori knowledge such as reciprocity can be integrated in this equation to simplify (A.23) [169]. Finding the eigenvalues of the transfer matrix as a function of frequency is facilitated by the absence of poles or branch points in the dispersion equation obtained with the MMTM, and also by the fast update of the dispersion equation at a given frequency, given that the transfer matrix coefficients are fixed [236]. Moreover, the dispersion equation is a continuous function of frequency, therefore the position of the roots moves continuously in the spectral domain when frequency changes. Previous solutions can be used as initial guesses of iterative processes. It also implies that modes cannot disappear with increasing frequency: they must transition to another type of mode, that is real, complex or evanescent.

This procedure can be generalized to 2-D periodic structures, or even three-dimensional (3-D) metamaterials, by considering additional ports for the orthogonal propagation directions [169]. The method is unchanged. Note that without the multi-modal approach, the transfer matrix method is limited to a $2 \times 2$ matrix per definition, which is not enough to describe the interactions between more ports.

**Extension of the method to glide symmetry** For the SMTM method, it is possible to subdivide symmetric unit cells in several cascaded two-ports in order to reduce the computational load. However, the coupling within these subcells is lost. With the MMTM, this problem is solved. In [43], the MMTM is adapted to G-S metasurface waveguides. For 1-D GS, it is enough to model only half of the unit cell in the commercial solver.

Indeed, GS can be incorporated in this method by considering the parity of the modes with respect to the propagation plane. In the following, the parity of the modes is related to both transverse electric and longitudinal magnetic fields of the modes, because they are responsible for the effective voltages and currents, respectively. Therefore, if the electric field across the gap is (anti)symmetric, then the voltage across the gap is (anti)symmetric as well. Likewise, if the longitudinal magnetic field is (anti)symmetric, the resulting transverse current is (anti)symmetric too. From the generalized Floquet theorem (1.13), the field after half-a-period translation is mirrored with respect to the propagation plane and has a phase-shift of $k_{\text{eff}}p/2$. On the one hand, for modes that are symmetric with respect to the propagation plane, this means that a half-a-period translation leaves the field invariant, except for the phase-shift, because the mirrored field is equal to itself. On the other hand, for antisymmetric modes, a half-a-unit cell translation leads to an inversion of the field. Therefore, considering the MMTM of half-a-unit cell,

$$\begin{bmatrix} \underline{\boldsymbol{A}}_{1/2} & \underline{\boldsymbol{B}}_{1/2} \\ \underline{\boldsymbol{C}}_{1/2} & \underline{\boldsymbol{D}}_{1/2} \end{bmatrix} \begin{bmatrix} \boldsymbol{V}_n \\ \boldsymbol{I}_n \end{bmatrix} = \mathrm{e}^{-\mathrm{j}k_{\text{eff}}\frac{p}{2}} \underline{\boldsymbol{Q}} \begin{bmatrix} \boldsymbol{V}_n \\ \boldsymbol{I}_n \end{bmatrix} \tag{A.24}$$

where $\underline{\boldsymbol{Q}}$ is a diagonal matrix with $+1$ for symmetric modes and $-1$ for antisymmetric modes. Finding $k_{\text{eff}}$ is thus equivalent to solving the generalized eigenvalue problem (A.24).

For metasurfaces that display 2-D GS, a further reduction of the MMTM method is possible. It is sufficient to simulate one quarter of the total unit cell, adding the same sign matrix $\underline{\boldsymbol{Q}}$ in the eigenproblem for the symmetries in the orthogonal direction [43].

**Advantages of the method** On top of capturing the coupling between adjacent cells, or even subcells in the case of GS, one of the main benefits of the MMTM method is the computation of both real and imaginary parts of the refractive index. Consequently, the MMTM method also recovers complex modes, which are not found by the eigensolver of commercial software [169]. This information about the attenuation constant of real and complex modes is central to the design of EBG devices. For example in [172], the attenuation constant is computed for all propagation directions, highlighting the minimum isotropic attenuation that can be achieved in the stopband at a given frequency.

Beyond the information about the attenuation, the MMTM method offers a gain in simulation time, especially for G-S structures, where only a fraction of the unit cell needs to be studied in the commercial solver. Nevertheless, it is difficult to evaluate the time gain, because the compared methods are inherently different: CST's eigensolver performs a sweep of the phase difference across the unit cell, whereas the obtaining the transfer

matrix of a cell require a sweep over frequency. Still, for the same number of points in the Brillouin diagram, experiments have shown a time gain of at least fivefold [43].

Th time gain also depends on the number of modes that are retained in the multimodal process. The number of modes depends on the desired accuracy and on the geometry [169]. Large transverse variations in the unit cells are an indicator of more modes. The number of required modes can also be hinted by the magnitude of the scattering parameters simulated in CST. Typically, modes with S-parameters larger than $-10\,\mathrm{dB}$ are not dismissible [43]. Moreover, the position of the ports influences the convergence as well, with ports better capturing the transverse span of the structure requiring fewer modes. A practical rule is to place the ports in a plane where the ports are the largest, in order to capture the projection of the Floquet modes onto the port modes as much as possible. For example, for nGS holes, it is better to place the port in the middle of a hole instead of in-between holes [236]. It has been observed that mirror-symmetric and broken G-S structures need fewer modes than G-S structures to yield accurate results [149]. From this observation, [43] defines the notion of reducibility of a G-S waveguide, with the example of a PPW loaded with G-S transverse metallic ridges. A reducible structure means that the shifted upper metallic ridges can be mirrored down to the lower metasurface without impacting the propagation features of the waveguide. This is true only if the ridges are thin compared to the periodicity. It is shown that irreducibility is equivalent to needing more than one mode in the MMTM method. This is applicable to 2-D GS too. Bed of nails metasurfaces are considered, where the nails of upper and lower surface may intertwine [43]. More than one mode are required when the pins become large or tall compared to the period. In these cases, the G-S structure is not reducible to a nGS waveguide.

**Applications and flexibility** As an application example, the MMTM method is used in [149] for the analysis of G-S holes or bed of nails inside a rectangular waveguide (RW), in order to study the rejection bands for filters built in this technology. In [173], the method is applied to holey G-S PPWs made of substrate-integrated holes (SIHs), in order to build an anisotropic waveguide for a compressed Luneburg lens. The computation time is of the order of seconds in Matlab, whereas using a full eigenmode study in CST requires several minutes for such complex unit cells (or hours, depending on the required accuracy).

The MMTM method has since been extended to other structures, such as periodic liquid crystal waveguides with anisotropic properties, complex wavenumbers, for unbounded structures, reconfigurable phase-shifters or leaky-wave antennas [174]. It is also notable that this method is applicable to other higher symmetries, such as twist symmetry, where it is sufficient to obtain the transfer matrix of a sub-unitcell of length $p/N$ for an $N$-fold twist [237].

Finally, the MMTM method opens the door to in-depth studies of periodic structures, such as effective constitutive parameter retrieval [175]. By computing the eigenvectors associated to the MMTM, equivalent currents and voltages are defined. Therefore, the impedance associated to the fundamental mode can be computed, and can be considered

as the effective medium impedance if it is computed not too close to the right-end of the first Brillouin zone. From there, the constitutive parameters of the effective propagation medium can be computed.

### A.3.4 Mode-matching method

While the MMTM method is an accurate and flexible simulation technique for periodic metasurfaces, it is still dependent on commercial solvers to get the transfer matrix of the unit cell. In recent year, the only other approach that has captured the multi-modal coupling and has effectively yielded the dispersion equation of G-S waveguides has been the mode-matching method (MMM).

The MMM has been bound to modal wave expansion of fields, and has found particular interest for periodic structures in the context of short wave tubes. The operating wavelength of these devices becomes small with respect to the overall system size. Therefore, classical circuit theory becomes unreliable because it cannot approximate the field effects. Rigorous methods of computation are required to find field solutions that satisfy the boundary conditions. Although closed-form field solutions are ideal, they are not common for arbitrary geometries. As an alternative, infinite series of orthogonal modes that converge rapidly are found to be an effective way to accurately describe all the field effects. In [238], this method is applied to cavity resonators, by dividing the cavities in geometries with sinusoidal field variations. The MMM enforces the field continuity between these regions, effectively identifying the Fourier series of the fields in the different regions. The same method is extended to corrugated PPWs in [88] for thin corrugations (with only one transverse electric magnetic (TEM) mode), and in [239] by enforcing successively a short-circuit and an open-circuit in the symmetry plane of the corrugations.

More recently, the MMM has been extended to PPWs with G-S corrugations in homogeneous media [42], [176]. The extension of the method to corrugations with arbitrary dielectric filling is straight-forward. For optimal results, the ratio between the number of required modes in the corrugations and the number of Floquet harmonics in the gap between the metasurfaces should be approximately equal to the ratio between the corrugation width and the unit cell period [167]. In [177], the MMM is applied to dielectric G-S PPWs, where each metasurface is made of an an alternation between two different dielectric slabs. The gap between the substrates may be a third dielectric. In order to find the dispersion equation of this structure, a secondary mode-matching procedure is implemented between the alternating dielectrics of the metasurfaces.

The overall steps of the MMM are the same for 2-D GS. In [45], the dispersion equation of holey G-S PPWs is found for cylindrical holes of arbitrary cross-section, by using the TM and TE modal decomposition in these holes. The dispersion equation is then solved with a either a root-finding algorithm, or by finding the magnitude minimum of system's matrix determinant. The practical example of circular holes is developed, which is most commonly used due to the facilitated manufacturing process. Nevertheless, drilling holes often implies that the bottom of the holes is conically shaped, due to the tip of the tool. The effective depth of such holes with conical ending can be computed

by means of a preliminary mode-matching step [141]. In [167], the MMM for holey G-S PPWs is further generalized, by filling the holes with an arbitrary dielectric. The power of the method is illustrated by performing various parametric studies, notably by computing the effective waveguide properties for different propagation directions. The anisotropy for rectangular holes is observed in this way. The MMM proves to be much faster than CST, because there is no need to discretize the entire unit cell: there are only unknowns on the surface of one hole, namely the weights of the modes. Due to the enforcement of G-S constraints, the modes of the upper hole are bound to the modes of the lower hole.

The example of equilateral triangular holes is detailed in [34]. The modal functions for such holes are known analytically, and so are their Fourier transforms. For elliptical holes in [168], although the modes have analytical expressions, the projection integrals are evaluated by means of Gauss quadrature. This illustrates one of the challenges of the MMM: it is only applicable to geometries that can be divided in regions where modal decompositions of the fields are known or can be performed numerically. Only canonical geometries yield analytical modal functions, and even then, the related integrals may need to be computed numerically.

Additionally, once the dispersion equation is found, a root-finding procedure is necessary to find the effective wavenumber as a function of frequency. This step is not straight-forward, because the dispersion equation obtained with the MMM has many poles and branch singularities [169]. In the process of plotting the Brillouin diagram, a priori known properties of the modes may accelerate this root-finding procedure, e.g., by searching the next solution between the previous wavenumber and the line of light [168].

In spite of these difficulties, the MMM is the only method that gives the possibility to get analytical information about the dispersive behavior of G-S waveguides, because it does not rely on any numerical preliminary steps.

# Appendix B

# Details to the mode-matching computations

## B.1 Mode-matching for the glide-symmetric corrugated parallel-plate waveguide

This section completes the mode-matching results of section 2.1.3 applied to the structure displayed in Fig. 2.1b.

**Mode-matching: electric field at the lower corrugation** The tangential fields between the different regions of the waveguide must be continuous. It means that the electric field tangential to perfectly electrically conducting (PEC) surfaces must vanish, namely at $y = \pm g/2$ with $a < z < p$. At the frontier between the gap region and the corrugated regions, the $x$-component of the magnetic field and the $z$-component of the electric field must match, namely at $y = -g/2$ with $0 < z < a$, and at $y = +g/2$ with $p/2 < z < p/2 + a$.

Let us first consider the surface of the lower plate i.e., $y = -g/2$ and $0 < z < p$. The $z$-component of the electric field is given by (2.1) in the corrugations, and by (2.2) in the gap region. Between the corrugations i.e., for $a < z < p$, the vanishing tangential electric field yields

$$\sum_{s=-\infty}^{+\infty} \left[ X^{(s)} \sin\left(-k_y^{(s)} \frac{g}{2}\right) + Y^{(s)} \cos\left(k_y^{(s)} \frac{g}{2}\right) \right] \mathrm{e}^{-\mathrm{j}k_z^{(s)} z} = 0\,, \tag{B.1}$$

while at the surface of the corrugations i.e., for $0 < z < a$, the continuity of the tangential electric field yields

$$\sum_{s=-\infty}^{+\infty} \left[ X^{(s)} \sin\left(-k_y^{(s)} \frac{g}{2}\right) + Y^{(s)} \cos\left(k_y^{(s)} \frac{g}{2}\right) \right] \mathrm{e}^{-\mathrm{j}k_z^{(s)} z} = \sum_{m=0}^{+\infty} c_m \cos\left(\tfrac{m\pi}{a} z\right) \sin\left(k_{y,m} h\right). \tag{B.2}$$

In (B.2), the fields must match for any $z$. Both gap and corrugation fields are projected onto the Floquet harmonic basis. In order to extract the coefficient associated to the $s'$-th Floquet harmonic, with $s'$ any integer, the field expressions are multiplied by $\mathrm{e}^{\mathrm{j}k_z^{(s')}z}$ and integrated between 0 and $p$. The left-hand term of (B.2) yields

$$\begin{aligned}\int_0^p E_z^{(\mathrm{gap})}\Big|_{y=-\frac{g}{2}} \mathrm{e}^{\mathrm{j}k_z^{(s')}z}\mathrm{d}z &= \sum_{s=-\infty}^{+\infty}\left[-X^{(s)}\sin\left(k_y^{(s)}\frac{g}{2}\right)+Y^{(s)}\cos\left(k_y^{(s)}\frac{g}{2}\right)\right]\int_0^p \mathrm{e}^{\mathrm{j}\frac{2\pi}{p}(s'-s)z}\mathrm{d}z \\ &= -pX^{(s')}\sin\left(k_y^{(s')}\frac{g}{2}\right)+pY^{(s')}\cos\left(k_y^{(s')}\frac{g}{2}\right), \end{aligned} \tag{B.3}$$

and the right-hand term of (B.2) yields

$$\begin{aligned}\int_0^a E_z^{(\mathrm{cor})}\Big|_{y=-\frac{g}{2}} \mathrm{e}^{\mathrm{j}k_z^{(s')}z}\mathrm{d}z &= \int_0^a \sum_{m=0}^{+\infty} c_m\cos\left(\tfrac{m\pi}{a}z\right)\sin\left(k_{y,m}h\right)\mathrm{e}^{\mathrm{j}k_z^{(s')}z}\mathrm{d}z \\ &= \sum_{m=0}^{+\infty} c_m\sin\left(k_{y,m}h\right)\int_0^a \cos\left(\tfrac{m\pi}{a}z\right)\mathrm{e}^{\mathrm{j}k_z^{(s')}z}\mathrm{d}z\,. \end{aligned} \tag{B.4}$$

The integral in this last expression can be computed as

$$\int_0^a \cos\left(\tfrac{m\pi}{a}z\right)\mathrm{e}^{\mathrm{j}k_z^{(s')}z}\mathrm{d}z = \mathrm{j}k_z^{(s')}\frac{1-(-1)^m\mathrm{e}^{\mathrm{j}k_z^{(s')}a}}{{k_z^{(s')}}^2-\left(\frac{m\pi}{a}\right)^2}, \tag{B.5}$$

therefore

$$\int_0^a E_z^{(\mathrm{cor})}\Big|_{y=-\frac{g}{2}} \mathrm{e}^{\mathrm{j}k_z^{(s')}z}\mathrm{d}z = \sum_{m=0}^{+\infty} c_m\sin\left(k_{y,m}h\right)\mathrm{j}k_z^{(s')}\frac{1-(-1)^m\mathrm{e}^{\mathrm{j}k_z^{(s')}a}}{{k_z^{(s')}}^2-\left(\frac{m\pi}{a}\right)^2}. \tag{B.6}$$

After projecting the fields onto the same harmonic basis, the harmonic coefficients in the gap region and in the corrugations must be equal. Therefore, for any harmonic of order $s$, equating (B.3) and (B.6) yields

$$-pX^{(s)}\sin\left(k_y^{(s)}\frac{g}{2}\right)+pY^{(s)}\cos\left(k_y^{(s)}\frac{g}{2}\right) = \sum_{m=0}^{+\infty} c_m\sin\left(k_{y,m}h\right)\mathrm{j}k_z^{(s)}\frac{1-(-1)^m\mathrm{e}^{\mathrm{j}k_z^{(s)}a}}{{k_z^{(s)}}^2-\left(\frac{m\pi}{a}\right)^2}. \tag{B.7}$$

**Mode-matching: electric field at the upper corrugation** The same procedure can be applied on the upper corrugated plate. According to the generalized Floquet theorem, the field at the surface of the upper corrugation is equal to the field in the lower corrugation with a phase-shift of $k_z\frac{p}{2}$ or $k_z\frac{p}{2}+\pi$. Combining this phase-shift with mode-matching at the surface of the upper corrugation i.e., for $y=g/2$ and $p/2<z<p/2+a$, yields

$$E_z^{(\mathrm{gap})}(z+\tfrac{p}{2})\Big|_{y=\frac{g}{2}} = E_z^{(\mathrm{cor})}(z+\tfrac{p}{2})\Big|_{y=\frac{g}{2}} = \pm\mathrm{e}^{-\mathrm{j}k_z\frac{p}{2}}\,E_z^{(\mathrm{cor})}(z)\Big|_{y=-\frac{g}{2}} \tag{B.8}$$

Given (2.1), the tangential electric field in the upper corrugation is

$$E_z^{(\mathrm{cor})}(z+\tfrac{p}{2})\Big|_{y=\frac{g}{2}} = \pm \mathrm{e}^{-\mathrm{j}k_z\frac{p}{2}}\, E_z^{(\mathrm{cor})}(z)\Big|_{y-=\frac{g}{2}} = \pm \mathrm{e}^{-\mathrm{j}k_z\frac{p}{2}} \left( \sum_{m=0}^{+\infty} c_m \cos\left(\tfrac{m\pi}{a} z\right) \sin\left(k_{y,m} h\right) \right). \tag{B.9}$$

Projecting this field onto the basis of Floquet harmonics yields the coefficient associated to the $s'$-th Floquet harmonic

$$\begin{aligned}
&\int_{\frac{p}{2}}^{\frac{p}{2}+a} \pm \mathrm{e}^{-\mathrm{j}k_z\frac{p}{2}} \sum_{m=0}^{+\infty} c_m \cos\left(\tfrac{m\pi}{a} z\right) \sin\left(k_{y,m} h\right) \mathrm{e}^{\mathrm{j}k_z^{(s')} z} \mathrm{d}z \\
&= \pm \mathrm{e}^{-\mathrm{j}k_z\frac{p}{2}} \sum_{m=0}^{+\infty} c_m \sin\left(k_{y,m} h\right) \mathrm{e}^{\mathrm{j}k_z^{(s')}\frac{p}{2}} \int_0^a \cos\left(\tfrac{m\pi}{a}\left[z+\tfrac{p}{2}\right]\right) \mathrm{e}^{\mathrm{j}k_z^{(s')} z} \mathrm{d}z \\
&= \pm \mathrm{e}^{-\mathrm{j}k_z\frac{p}{2}} \sum_{m=0}^{+\infty} c_m \sin\left(k_{y,m} h\right) \mathrm{j}k_z^{(s')} \frac{1-(-1)^m \mathrm{e}^{\mathrm{j}k_z^{(s')} a}}{{k_z^{(s')}}^2 - \left(\frac{m\pi}{a}\right)^2}.
\end{aligned} \tag{B.10}$$

Similarly, the coefficient associated to the $s'$-th Floquet harmonic (2.2) is

$$\begin{aligned}
&\int_{\frac{p}{2}}^{\frac{3p}{2}} \sum_{s=-\infty}^{+\infty} \left[ X^{(s)} \sin\left(k_y^{(s)}\frac{g}{2}\right) + Y^{(s)} \cos\left(k_y^{(s)}\frac{g}{2}\right) \right] \mathrm{e}^{-\mathrm{j}k_z^{(s)}\left[z+\frac{p}{2}\right]} \mathrm{e}^{\mathrm{j}k_z^{(s')} z} \mathrm{d}z \\
&= p\, \mathrm{e}^{-\mathrm{j}k_z^{(s')}\frac{p}{2}} \left[ X^{(s')} \sin\left(k_y^{(s')}\frac{g}{2}\right) + Y^{(s')} \cos\left(k_y^{(s')}\frac{g}{2}\right) \right] \\
&= p(-1)^{s'} \mathrm{e}^{-\mathrm{j}k_z\frac{p}{2}} \left[ X^{(s')} \sin\left(k_y^{(s')}\frac{g}{2}\right) + Y^{(s')} \cos\left(k_y^{(s')}\frac{g}{2}\right) \right],
\end{aligned} \tag{B.11}$$

where the last line uses the fact that $\mathrm{e}^{-\mathrm{j}k_z^{(s')}\frac{p}{2}} = (-1)^{s'} \mathrm{e}^{-\mathrm{j}k_z\frac{p}{2}}$. Matching the coefficients (B.10) and (B.11) yields

$$X^{(s)} \sin\left(k_y^{(s)}\frac{g}{2}\right) + Y^{(s)} \cos\left(k_y^{(s)}\frac{g}{2}\right) = \pm \sum_{m=0}^{+\infty} \mathrm{j}(-1)^s \tfrac{k_z^{(s)}}{p} c_m \sin\left(k_{y,m} h\right) \frac{1-(-1)^m \mathrm{e}^{\mathrm{j}k_z^{(s)} a}}{{k_z^{(s)}}^2 - \left(\frac{m\pi}{a}\right)^2}. \tag{B.12}$$

**Expression of the Floquet harmonic coefficients** Equations (B.7) and (B.12) form the system

$$\begin{cases} -X^{(s)}\sin\left(k_y^{(s)}\frac{g}{2}\right)+Y^{(s)}\cos\left(k_y^{(s)}\frac{g}{2}\right)=\mathrm{j}\frac{k_z^{(s)}}{p}\sum\limits_{m=0}^{+\infty}c_m\sin\left(k_{y,m}h\right)\dfrac{1-(-1)^m\mathrm{e}^{\mathrm{j}k_z^{(s)}a}}{{k_z^{(s)}}^2-\left(\frac{m\pi}{a}\right)^2} \\ X^{(s)}\sin\left(k_y^{(s)}\frac{g}{2}\right)+Y^{(s)}\cos\left(k_y^{(s)}\frac{g}{2}\right)=\pm(-1)^s\mathrm{j}\frac{k_z^{(s)}}{p}\sum\limits_{m=0}^{+\infty}c_m\sin\left(k_{y,m}h\right)\dfrac{1-(-1)^m\mathrm{e}^{\mathrm{j}k_z^{(s)}a}}{{k_z^{(s)}}^2-\left(\frac{m\pi}{a}\right)^2} \end{cases}. \tag{B.13}$$

From (B.13), the coefficients $X^{(s)}$ and $Y^{(s)}$ of the $s$-th Floquet harmonic in the gap are

$$\begin{cases} X^{(s)}=-\dfrac{1\mp(-1)^s}{2\sin\left(k_y^{(s)}\frac{g}{2}\right)}\mathrm{j}\frac{k_z^{(s)}}{p}\sum\limits_{m=0}^{+\infty}c_m\sin\left(k_{y,m}h\right)\dfrac{1-(-1)^m\mathrm{e}^{\mathrm{j}k_z^{(s)}a}}{{k_z^{(s)}}^2-\left(\frac{m\pi}{a}\right)^2} \\ Y^{(s)}=\dfrac{1\pm(-1)^s}{2\cos\left(k_y^{(s)}\frac{g}{2}\right)}\mathrm{j}\frac{k_z^{(s)}}{p}\sum\limits_{m=0}^{+\infty}c_m\sin\left(k_{y,m}h\right)\dfrac{1-(-1)^m\mathrm{e}^{\mathrm{j}k_z^{(s)}a}}{{k_z^{(s)}}^2-\left(\frac{m\pi}{a}\right)^2} \end{cases}. \tag{B.14}$$

Depending on the sign used in the generalized Floquet theorem, (B.14) shows that the electric $z$-component of each Floquet harmonics is either symmetric (cosine dependency on $y$) or antisymmetric (sine dependency on $y$). Indeed, when $X^{(s)}$ is different from zero, then $Y^{(s)}$ is zero, and vice versa. All harmonics with even order $s$ have the same symmetry, and so do all harmonics with odd order $s$.

**Mode-matching: magnetic field at the lower corrugation** Similarly to the electric field, the tangential magnetic field continuity must be ensured at $y=-g/2$ and $0<z<a$. From the magnetic field equations in (2.1) and (2.2), this results in the equality

$$\sum_{s=-\infty}^{+\infty}\frac{\mathrm{e}^{-\mathrm{j}k_z^{(s)}z}}{k_y^{(s)}}\left[X^{(s)}\cos\left(k_y^{(s)}\frac{g}{2}\right)+Y^{(s)}\sin\left(k_y^{(s)}\frac{g}{2}\right)\right]=\sum_{m=0}^{+\infty}\frac{c_m}{k_{y,m}}\cos\left(\tfrac{m\pi}{a}z\right)\cos\left(k_{y,m}h\right). \tag{B.15}$$

Instead of using the basis of Floquet harmonics, the magnetic field components are projected onto the basis of corrugation modes. Consequently, the coefficient associated to the $m'$-th mode in the gap region is

$$\begin{aligned} &\int_0^a\sum_{s=-\infty}^{+\infty}\frac{1}{k_y^{(s)}}\left[X^{(s)}\cos\left(k_y^{(s)}\frac{g}{2}\right)+Y^{(s)}\sin\left(k_y^{(s)}\frac{g}{2}\right)\right]\mathrm{e}^{-\mathrm{j}k_z^{(s)}z}\cos\left(\tfrac{m'\pi}{a}z\right)\mathrm{d}z \\ &=-\sum_{s=-\infty}^{+\infty}\frac{1}{k_y^{(s)}}\left[X^{(s)}\cos\left(k_y^{(s)}\frac{g}{2}\right)+Y^{(s)}\sin\left(k_y^{(s)}\frac{g}{2}\right)\right]\mathrm{j}k_z^{(s)}\frac{1-(-1)^{m'}\mathrm{e}^{-\mathrm{j}k_z^{(s)}a}}{{k_z^{(s)}}^2-\left(\frac{m'\pi}{a}\right)^2}. \end{aligned} \tag{B.16}$$

Similarly, the coefficient associated to the $m'$-th mode in the corrugated region is

$$\int_0^a \sum_{m=0}^{+\infty} c_m \frac{1}{k_{y,m}} \cos\left(\tfrac{m\pi}{a}z\right) \cos\left(k_{y,m}h\right) \cos\left(\tfrac{m'\pi}{a}z\right) \mathrm{d}z$$
$$= \frac{a}{2^{\min\{1,m'\}}} c_{m'} \frac{1}{k_{y,m'}} \cos\left(k_{y,m'}h\right). \tag{B.17}$$

Therefore, matching the mode coefficients from (B.16) and (B.17) yields

$$-\sum_{s=-\infty}^{+\infty} \frac{1}{k_y^{(s)}} \left[X^{(s)} \cos\left(k_y^{(s)}\frac{g}{2}\right) + Y^{(s)} \sin\left(k_y^{(s)}\frac{g}{2}\right)\right] \mathrm{j}k_z^{(s)} \frac{1-(-1)^{m'}\mathrm{e}^{-\mathrm{j}k_z^{(s)}a}}{{k_z^{(s)}}^2 - \left(\frac{m'\pi}{a}\right)^2}$$
$$= \frac{a}{2^{\min\{1,m'\}}} c_{m'} \frac{1}{k_{y,m'}} \cos\left(k_{y,m'}h\right). \tag{B.18}$$

**Matrix equation for corrugation coefficients** The gap coefficients $X^{(s)}$ and $Y^{(s)}$ can be totally removed from (B.18) by replacing them with their expressions in (B.14). This yields

$$\sum_{s=-\infty}^{+\infty} \begin{bmatrix} \tan\left(k_y^{(s)}\frac{g}{2}\right)\frac{1\pm(-1)^s}{2} \\ -\cot\left(k_y^{(s)}\frac{g}{2}\right)\frac{1\mp(-1)^s}{2} \end{bmatrix} \sum_{m=0}^{+\infty} c_m \frac{{k_z^{(s)}}^2}{k_y^{(s)}} \frac{\sin\left(k_{y,m}h\right) f_{m'm}^{(s)}}{\left[{k_z^{(s)}}^2 - \left(\frac{m\pi}{a}\right)^2\right]\left[{k_z^{(s)}}^2 - \left(\frac{m'\pi}{a}\right)^2\right]}$$
$$= \frac{pa}{2^{\min\{1,m'\}}} c_{m'} \frac{1}{k_{y,m'}} \cos\left(k_{y,m'}h\right), \tag{B.19}$$

with

$$f_{m'm}^{(s)} = \left[1-(-1)^m \mathrm{e}^{\mathrm{j}k_z^{(s)}a}\right]\left[1-(-1)^{m'}\mathrm{e}^{-\mathrm{j}k_z^{(s)}a}\right]$$
$$= \begin{cases} 4\sin^2\left(k_z^{(s)}\frac{a}{2}\right), & \text{if } m' \text{ and } m \text{ are both even,} \\ 4\cos^2\left(k_z^{(s)}\frac{a}{2}\right), & \text{if } m' \text{ and } m \text{ are both odd,} \\ \mathrm{j}(-1)^{m'} 4\sin\left(k_z^{(s)}\frac{a}{2}\right)\cos\left(k_z^{(s)}\frac{a}{2}\right), & \text{if } m'+m \text{ is odd.} \end{cases} \tag{B.20}$$

Equation (B.19) can be rearranged as

$$\sum_{m=0}^{+\infty} \left(\alpha_{m'm} + \delta_{m'm}\gamma_m\right) \sin\left(k_{y,m}h\right) c_m = 0, \tag{B.21}$$

where $\delta_{m'm}$ is the Kroenecker symbol, and where

$$\alpha_{m'm} = \sum_{s=-\infty}^{+\infty} \begin{bmatrix} \cot\left(k_y^{(s)}\frac{g}{2}\right)\frac{1\mp(-1)^s}{2} \\ -\tan\left(k_y^{(s)}\frac{g}{2}\right)\frac{1\pm(-1)^s}{2} \end{bmatrix} \frac{{k_z^{(s)}}^2}{k_y^{(s)}} \frac{f_{m'm}^{(s)}}{\left[{k_z^{(s)}}^2 - \left(\frac{m\pi}{a}\right)^2\right]\left[{k_z^{(s)}}^2 - \left(\frac{m'\pi}{a}\right)^2\right]}, \tag{B.22}$$

and

$$\gamma_m = \frac{pa}{2^{\min\{1,m\}}} \frac{1}{k_{y,m}} \cot(k_{y,m}h)\,. \tag{B.23}$$

Equation (B.21) must be verified for any positive mode order $m'$. The resulting set of equations can be formalized as the matrix equation (2.7).

## B.2 Gradient theorem for the simplification of the holey parallel-plate waveguide dispersion equation

**Green's theorem** Let $S$ be a region in the $zx$-plane bounded by a simple closed and piece-wise smooth contour $\partial S$. Let $L(z,x)$ and $M(z,x)$ be two functions of class $\mathcal{C}^1$ on $S$. Green's theorem states that [180, p. 431]

$$\iint_S \left( \frac{\partial M(z,x)}{\partial z} - \frac{\partial L(z,x)}{\partial x} \right) \mathrm{d}z\mathrm{d}x = \int_{\partial S} \left( L(z,x)\mathrm{d}z + M(z,x)\mathrm{d}x \right)\,. \tag{B.24}$$

**Two-dimensional divergence theorem** At each point of the oriented curve $\partial S$, the infinitesimal path element is called $\mathbf{d}\boldsymbol{\ell}$, with norm $\mathrm{d}\ell = \sqrt{\mathrm{d}z^2 + \mathrm{d}x^2}$. It is orthogonal to the exterior normal $\boldsymbol{n}$. Therefore,

$$\mathbf{d}\boldsymbol{\ell} = \begin{bmatrix} \mathrm{d}z \\ \mathrm{d}x \end{bmatrix} \quad \text{and} \quad \boldsymbol{n}\mathrm{d}\ell = \begin{bmatrix} \mathrm{d}x \\ -\mathrm{d}z \end{bmatrix}\,. \tag{B.25}$$

A vector field $\boldsymbol{F}(z,x)$ is considered on $S$, such that its cartesian components $F_z(z,x)$ and $F_x(z,x)$ are of class $\mathcal{C}^1$. Assigning $L = -F_x$ and $M = F_z$ in Green's theorem (B.24), on the one hand

$$\iint_S \left( \frac{\partial F_z(z,x)}{\partial z} + \frac{\partial F_x(z,x)}{\partial x} \right) \mathrm{d}z\mathrm{d}x = \iint_S \nabla \cdot \boldsymbol{F}(z,x)\mathrm{d}z\mathrm{d}x\,, \tag{B.26}$$

and on the other hand

$$\int_{\partial S} \left( -F_x(z,x)\mathrm{d}z + F_z(z,x)\mathrm{d}x \right) = \int_{\partial S} \boldsymbol{F}(z,x) \cdot \boldsymbol{n}\mathrm{d}\ell\,. \tag{B.27}$$

Therefore, a 2D extension of the Gauss' divergence theorem [180, p. 463] is obtained,

$$\iint_S \nabla \cdot \boldsymbol{F}\mathrm{d}z\mathrm{d}x = \int_{\partial S} \boldsymbol{F} \cdot \boldsymbol{n}\mathrm{d}\ell\,. \tag{B.28}$$

**Gradient theorem** The 2D divergence theorem (B.28) is applied to a vector field $\boldsymbol{F}(z,x)$. It can easily be extended to the gradient of a scalar field $f(z,x)$. Introducing a constant vector field $\boldsymbol{a}$, (B.28) yields

$$\begin{aligned}\boldsymbol{a}\cdot\iint_S \nabla f(z,x)\mathrm{d}z\mathrm{d}x &= \iint_S \nabla\cdot\{f(z,x)\boldsymbol{a}\}\,\mathrm{d}z\mathrm{d}x\\ &= \int_{\partial S} f(z,x)\boldsymbol{a}\cdot\boldsymbol{n}\mathrm{d}\ell = \boldsymbol{a}\cdot\int_{\partial S} f(z,x)\boldsymbol{n}\mathrm{d}\ell\,.\end{aligned} \tag{B.29}$$

Multiplying (B.29) by $\boldsymbol{a}/||\boldsymbol{a}||^2$ from the left, one obtains the gradient theorem

$$\iint_S \nabla f\mathrm{d}z\mathrm{d}x = \int_{\partial S} f\boldsymbol{n}\mathrm{d}\ell\,. \tag{B.30}$$

## B.3 Projected modal functions for canonical holes

### B.3.1 Mode-matching for rectangular holes

Rectangular holes have the modal functions (2.51) for transverse magnetic (TM) modes and (2.52) for transverse electric (TE) modes. These expressions are combinations of trigonometric functions, and so the computation of their Fourier transforms is straightforward. For holes of size $a_z \times a_x$, each modal function is defined by two integer orders $q$ and $m$, with corresponding cut-off wavenumbers [17, p. 117]

$$k_{qm} = \sqrt{\left(\tfrac{m\pi}{a_z}\right)^2 + \left(\tfrac{q\pi}{a_x}\right)^2}, \tag{B.31}$$

which is valid for both TM and TE modes.

**TM modes** For the TM modes (2.51), $m > 0$ and $q > 0$. According to (2.50), the square norm of the transverse field is

$$I^{\mathrm{e}}_{qm} = \frac{1}{{k^{\mathrm{e}}_{qm}}^2}\frac{\pi^2}{4}\left[m^2\frac{a_x}{a_z} + q^2\frac{a_z}{a_x}\right]. \tag{B.32}$$

According to (2.49), the longitudinal projected modal function (PMF) is

$$\tilde{e}^{(s\ell)}_{y,qm} = \frac{qm\pi^2}{a_z a_x}\zeta^z_m\left(k^{(s)}_z\right)\zeta^x_q\left(k^{(\ell)}_x\right), \tag{B.33}$$

where

$$\zeta^z_m(k) = \frac{1-(-1)^m\mathrm{e}^{-\mathrm{j}ka_z}}{\left(\tfrac{m\pi}{a_z}\right)^2 - k^2}\,. \tag{B.34}$$

**TE modes** For the TE modes (2.52), $(q,m) \neq (0,0)$. According to (2.32), the square norm of the transverse field is

$$I^{\mathrm{h}}_{qm} = \frac{1}{k^2_{qm}} \frac{\pi^2}{2^{1+\min(1,q,m)}} \left( \frac{a_x}{a_z} m^2 + \frac{a_z}{a_x} q^2 \right) . \tag{B.35}$$

The PMF can be then computed as

$$\tilde{e}^{\mathrm{h}(s\ell)}_{z,qm} = \mathrm{j} \frac{k_z^{(s)}}{k_{qm}} \frac{q^2\pi^2}{a_x^2} \zeta^z_m \left( k_z^{(s)} \right) \zeta^x_q \left( k_x^{(\ell)} \right) , \tag{B.36}$$

and

$$\tilde{e}^{\mathrm{h}(s\ell)}_{x,qm} = -\mathrm{j} \frac{k_x^{(\ell)}}{k_{qm}} \frac{m^2\pi^2}{a_z^2} \zeta^z_m \left( k_z^{(s)} \right) \zeta^x_q \left( k_x^{(\ell)} \right) . \tag{B.37}$$

### B.3.2 Mode-matching for circular holes

The holes are cylinders of depth $h$ and circular cross-section of radius $a$. There are only TM and TE modes that propagate in such a cylindrical waveguide, which are characterized by two orders : the order $q$ of the first-kind Bessel function that shapes the radial profile of the fields, and the $m$-th non-trivial root of this function, which corresponds to the radius where the Bessel function reaches the contour of the guide. For each order pair $(q,m)$, there are two orthogonal TM modal functions, as well as two orthogonal TE modal functions. Therefore, a third order $t = 1, 2$ is introduced to distinguish between to modal functions with the same orders $(q,m)$.

In the following, polar coordinates $(\rho, \phi)$ are considered, such that $z = \rho\cos\phi$ and $x = \rho\sin\phi$. First, useful identities are listed, notably regarding Bessel functions. Then, the PMFs of the TM modes are considered, and finally the same is done for the TE modes.

#### B.3.2.1 Fourier transforms and useful identities

**Bessel function identities** A Bessel function of the first kind and order $q$ has the integral form

$$J_q(x) = \frac{1}{2\pi} \int_{-\pi}^{\pi} \mathrm{e}^{\mathrm{j}(q\phi - x\sin\phi)} \mathrm{d}\phi \, . \tag{B.38}$$

It is related to its $J'_q$ its derivative with [240]

$$J'_q(x) = \frac{1}{2} \left[ J_{q-1}(x) - J_{q+1}(x) \right] , \tag{B.39}$$

$$\text{and} \quad \frac{q}{x} J_q(x) = \frac{1}{2} \left[ J_{q-1}(x) + J_{q+1}(x) \right] . \tag{B.40}$$

From this, it can derived that

$$J'_q(x) = \frac{q}{x} J_q(x) - J_{q+1}(x) \ , \tag{B.41}$$

and

$$\left[J'_q(x)\right]^2 + \left[\frac{q}{x} J_q(x)\right]^2 = \frac{1}{2}\left[J_{q-1}(x)\right]^2 + \frac{1}{2}\left[J_{q+1}(x)\right]^2 \ . \tag{B.42}$$

A useful integral involving squared Bessel functions is

$$\int_0^a \rho J_{q-1}^2(k_{qm}\rho)\,\mathrm{d}\rho = \frac{a^2}{2} J_{q-1}^2(k_{qm}a) \ . \tag{B.43}$$

Moreover, in [241, p. 629], it is shown that

$$\int x J_n(\alpha x) J_n(\beta x)\,\mathrm{d}x = \frac{x}{\alpha^2-\beta^2}\left[\alpha J_{n+1}(\alpha x) J_n(\beta x) - \beta J_n(\alpha x) J_{n+1}(\beta x)\right] \tag{B.44}$$

$$= \frac{x}{\alpha^2-\beta^2}\left[\beta J_n(\alpha x) J_{n-1}(\beta x) - \alpha J_{n-1}(\alpha x) J_n(\beta x)\right] \ , \tag{B.45}$$

which yields the particular case

$$\int_0^a \rho J_q(k_{qm}\rho) J_q(k_\theta \rho)\,\mathrm{d}\rho = \frac{a}{k_\theta^2 - k_{qm}^2} k_{qm} J'_q(p_{qm}) J_q(k_\theta a) \ . \tag{B.46}$$

**Fourier transform** The spectral cartesian coordinates $(k_z, k_x)$ can be converted in spectral polar coordinates $(k_\theta, \theta)$ such that $k_x = k_\theta \sin\theta$ and $k_z = k_\theta \cos\theta$. For a field component $e$, in spatial polar coordinates $(\rho, \phi)$, the Fourier transform expressed in spectral polar coordinates can be computed as

$$\begin{aligned}
\tilde{e}(k_\theta, \theta) &= \int_{-\infty}^{\infty}\int_{-\infty}^{\infty} e(z,x) \mathrm{e}^{-\mathrm{j}k_x x - \mathrm{j}k_z z}\mathrm{d}x\mathrm{d}z \\
&= \int_0^{\infty}\int_{2\pi} e(\rho,\phi) \mathrm{e}^{-\mathrm{j}k_\theta \sin\theta \rho \sin\phi - \mathrm{j}k_\theta \cos\theta \rho\cos\phi} \rho \mathrm{d}\phi\mathrm{d}\rho \\
&= \int_0^{\infty}\int_{2\pi} e(\rho,\phi) \mathrm{e}^{-\mathrm{j}k_\theta \rho \cos(\theta-\phi)} \rho \mathrm{d}\phi\mathrm{d}\rho \, .
\end{aligned} \tag{B.47}$$

**Other useful integrals** With $n$ and integer, $k_\theta$ a wavenumber, and $\rho$ and $\theta$ real constants, one has

$$\begin{aligned}\int_{2\pi} \mathrm{e}^{\mathrm{j}n\phi}\mathrm{e}^{-\mathrm{j}\rho k_\theta\cos(\theta-\phi)}\mathrm{d}\phi &= \int_{2\pi} \mathrm{e}^{\mathrm{j}n\phi-\mathrm{j}(\rho k_\theta)\sin\left(\frac{\pi}{2}-\theta+\phi\right)}\mathrm{d}\phi \\ &= \int_{2\pi} \mathrm{e}^{\mathrm{j}n\left(\phi'-\frac{\pi}{2}+\theta\right)-\mathrm{j}(\rho k_\theta)\sin(\phi')}\mathrm{d}\phi' \\ &= \mathrm{e}^{\mathrm{j}n\left(\theta-\frac{\pi}{2}\right)}\int_{2\pi} \mathrm{e}^{\mathrm{j}n\phi'-\mathrm{j}(\rho k_\theta)\sin(\phi')}\mathrm{d}\phi' \\ &= \mathrm{e}^{\mathrm{j}n\theta}\,(-\mathrm{j})^n\,2\pi J_n\left(\rho k_\theta\right)\,, \end{aligned} \tag{B.48}$$

where the variable change $\phi' = \phi + \frac{\pi}{2} - \theta$ is applied, and where the integral definition of the Bessel function (B.38) is used. As such, it is noticeable that

$$\begin{aligned}\int_{2\pi} \cos\left(n\phi\right)\mathrm{e}^{-\mathrm{j}\rho k_\theta\cos(\theta-\phi)}\mathrm{d}\phi &= \frac{1}{2}\int_{2\pi} \mathrm{e}^{\mathrm{j}n\phi}\mathrm{e}^{-\mathrm{j}\rho k_\theta\cos(\theta-\phi)}\mathrm{d}\phi + \frac{1}{2}\int_{2\pi} \mathrm{e}^{-\mathrm{j}n\phi}\mathrm{e}^{-\mathrm{j}\rho k_\theta\cos(\theta-\phi)}\mathrm{d}\phi \\ &= \frac{1}{2}\mathrm{e}^{\mathrm{j}n\theta}\,(-\mathrm{j})^n\,2\pi J_n\left(\rho k_\theta\right) + \frac{1}{2}\mathrm{e}^{-\mathrm{j}n\theta}\,(-\mathrm{j})^{-n}\,2\pi J_{-n}\left(\rho k_\theta\right) \\ &= 2\pi\,(-\mathrm{j})^n\cos\left(n\theta\right)J_n\left(\rho k_\theta\right)\,, \end{aligned} \tag{B.49}$$

and similarly,

$$\int_{2\pi} \sin\left(n\phi\right)\mathrm{e}^{-\mathrm{j}\rho k_\theta\cos(\theta-\phi)}\mathrm{d}\phi = 2\pi\,(-\mathrm{j})^n\sin\left(n\theta\right)J_n\left(\rho k_\theta\right)\,. \tag{B.50}$$

**Undefined forms** Using L'Hôpital's rule, it can be shown that

$$\lim_{x\to k_{qm}}\frac{J_q\left(xa\right)}{x^2-k_{qm}^2} = \frac{a^2J_q'\left(p_{qm}\right)}{2p_{qm}}\,, \quad \text{and} \quad \lim_{x\to -k_{qm}}\frac{J_q\left(xa\right)}{x^2-k_{qm}^2} = \begin{cases}\frac{a^2J_q'(p_{qm})}{2p_{qm}} & \text{if } q \text{ is even,}\\ -\frac{a^2J_q'(p_{qm})}{2p_{qm}} & \text{if } q \text{ is odd.}\end{cases} \tag{B.51}$$

### B.3.2.2 Transverse magnetic modes

For holes of radius $a$, the longitudinal electric field for $t = 1$ has the form [17, p. 128]

$$e_{y,qm1}(\rho,\phi) = \sin\left(q\phi\right)J_q\left(k_{qm}\rho\right)\,, \tag{B.52}$$

with polar coordinates $(\rho,\phi)$ and the cut-off frequency $k_{qm} = p_{qm}/a$, $p_{qm}$ being the $m$-th zero of the Bessel function. This definition is valid within the hole surface $S$, with $e_{y,qm1} = 0$ outside the hole.

**PMF** The longitudinal PMF (2.49) can be seen as the Fourier transform of the modal function. Given (B.50) and (B.46), the Fourier transform (B.47) of (B.52) is

$$\int_0^a \int_{2\pi} e_{y,qm1}(\rho,\phi)\mathrm{e}^{-\mathrm{j}k_\theta\rho\cos(\theta-\phi)}\rho\mathrm{d}\phi\mathrm{d}\rho = \int_0^a J_q\left(k_{qm}\rho\right)\rho\int_{2\pi}\sin\left(q\phi\right)\mathrm{e}^{-\mathrm{j}k_\theta\rho\cos(\theta-\phi)}\mathrm{d}\phi\mathrm{d}\rho$$
$$= k_{qm}\frac{2\pi a}{\mathrm{j}^q}\frac{J_q'\left(p_{qm}\right)J_q\left(k_\theta a\right)}{k_\theta^2-k_{qm}^2}\sin\left(q\theta\right) \quad . \text{(B.53)}$$

The corresponding PMF is this Fourier transform evaluated at the Floquet wavenumber $k_z^{(s)}$ and $k_x^{(\ell)}$. For $t=2$, the derivation follows the same steps, yielding a cosine function in (B.53).

**Square norm** Using the gradient in polar coordinates,

$$\nabla_{\mathrm{t}}e_{y,qm1}(\rho,\phi) = \begin{bmatrix}\frac{\partial}{\partial\rho}e_{y,qm1}(\rho,\phi)\\ \frac{1}{\rho}\frac{\partial}{\partial\phi}e_{y,qm1}(\rho,\phi)\end{bmatrix} = \begin{bmatrix}k_{qm}\sin\left(q\phi\right)J_q'\left(k_{qm}\rho\right)\\ \frac{q}{\rho}\cos\left(q\phi\right)J_q\left(k_{qm}\rho\right)\end{bmatrix}, \quad \text{(B.54)}$$

the squared norm of the transverse fields is

$$\begin{aligned}
I_{qm1}^{\mathrm{e}} &= \frac{1}{k_{qm}^2}\int_0^a\int_0^{2\pi}\left(k_{qm}\sin\left(q\phi\right)J_q'\left(k_{qm}\rho\right)\right)^2+\left(\frac{q}{\rho}\cos\left(q\phi\right)J_q\left(k_{qm}\rho\right)\right)^2\mathrm{d}\phi\rho\mathrm{d}\rho\\
&= \int_0^a \rho J_q'^2\left(k_{qm}\rho\right)\mathrm{d}\rho\int_0^{2\pi}\sin^2\left(q\phi\right)\mathrm{d}\phi+\frac{1}{k_{qm}^2}\int_0^a\frac{q^2}{\rho}J_q^2\left(k_{qm}\rho\right)\mathrm{d}\rho\int_0^{2\pi}\cos^2\left(q\phi\right)\mathrm{d}\phi\\
&= \pi\int_0^a\rho\left[J_q'^2\left(k_{qm}\rho\right)+\frac{q^2}{k_{qm}^2\rho^2}J_q^2\left(k_{qm}\rho\right)\right]\mathrm{d}\rho\\
&= \frac{\pi}{2}\left(\int_0^a\rho J_{q-1}^2\left(k_{qm}\rho\right)\mathrm{d}\rho+\int_0^a\rho J_{q+1}^2\left(k_{qm}\rho\right)\mathrm{d}\rho\right)\\
&= \frac{\pi a^2}{4}\left(J_{q-1}^2\left(k_{qm}a\right)+J_{q+1}^2\left(k_{qm}a\right)\right)\\
&= \frac{\pi a^2}{2}J_q'^2\left(p_{qm}\right), \quad \text{(B.55)}
\end{aligned}$$

where $q>0$, given the definition of TM modes for circular holes with $t=1$, and where the identities (B.42) and (B.43) are used in the derivation. The same result is obtained for $t=2$.

#### B.3.2.3 Transverse electric modes

The TE modes that are eigenmodes of the circular waveguide have a longitudinal magnetic component. The latter has an azimuthal dependency that is either a sine or a cosine, resulting in two generate modes for each pair of orders $(q,m)$.

For TE modes with an azimuthal sine dependency ($t = 1$), the transverse electric modal functions in polar coordinates are

$$e^{\mathrm{h}}_{\rho,qm1} = -\cos(q\phi)\,\frac{q}{k'_{qm}\rho}J_q\left(k'_{qm}\rho\right)\,, \tag{B.56}$$

$$\text{and}\quad e^{\mathrm{h}}_{\phi,qm1} = \sin(q\phi)\,J'_q\left(k'_{qm}\rho\right)\,, \tag{B.57}$$

with the cut-off wavenumver $k'_{qm} = p'_{qm}/a$, $p'_{qm}$ being the $m$-th zero of the derivative of the first-kind Bessel function of order $q$. Then the vector components in cartesian coordinates are

$$e^{\mathrm{h}}_{z,qm1} = -\cos\phi\cos(q\phi)\,\frac{q}{k'_{qm}\rho}J_q\left(k'_{qm}\rho\right) - \sin\phi\sin(q\phi)\,J'_q\left(k'_{qm}\rho\right)\,, \tag{B.58}$$

$$\text{and}\quad e^{\mathrm{h}}_{x,qm1} = -\sin\phi\cos(q\phi)\,\frac{q}{k'_{qm}\rho}J_q\left(k'_{qm}\rho\right) + \cos\phi\sin(q\phi)\,J'_q\left(k'_{qm}\rho\right)\,. \tag{B.59}$$

**PMF** Using Bessel identities (B.39) and (B.40), it comes that

$$e^{\mathrm{h}}_{z,qm1} = -\cos\phi\cos(q\phi)\,\frac{1}{2}\begin{bmatrix} J_{q-1}\left(k'_{qm}\rho\right) \\ +J_{q+1}\left(k'_{qm}\rho\right)\end{bmatrix} - \sin\phi\sin(q\phi)\,\frac{1}{2}\begin{bmatrix} J_{q-1}\left(k'_{qm}\rho\right) \\ -J_{q+1}\left(k'_{qm}\rho\right)\end{bmatrix}\,, \tag{B.60}$$

$$e^{\mathrm{h}}_{x,qm1} = -\sin\phi\cos(q\phi)\,\frac{1}{2}\begin{bmatrix} J_{q-1}\left(k'_{qm}\rho\right) \\ +J_{q+1}\left(k'_{qm}\rho\right)\end{bmatrix} + \cos\phi\sin(q\phi)\,\frac{1}{2}\begin{bmatrix} J_{q-1}\left(k'_{qm}\rho\right) \\ -J_{q+1}\left(k'_{qm}\rho\right)\end{bmatrix}\,, \tag{B.61}$$

and so

$$e^{\mathrm{h}}_{z,qm1} = -\frac{1}{2}\cos([q-1]\phi)\,J_{q-1}\left(k'_{qm}\rho\right) - \frac{1}{2}\cos([q+1]\phi)\,J_{q+1}\left(k'_{qm}\rho\right)\,, \tag{B.62}$$

$$\text{and}\quad e^{\mathrm{h}}_{x,qm1} = \frac{1}{2}\sin([q-1]\phi)\,J_{q-1}\left(k'_{qm}\rho\right) - \frac{1}{2}\sin([q+1]\phi))J_{q+1}\left(k'_{qm}\rho\right)\,. \tag{B.63}$$

With integrals (B.49) and (B.50), the Fourier transform (B.47) of the $z$-component is

$$\begin{aligned}\tilde{e}^{\mathrm{h}}_{z,qm1} = &-\int_0^a\int_{2\pi}\frac{1}{2}\cos([q-1]\phi)\,J_{q-1}\left(k'_{qm}\rho\right)\mathrm{e}^{-\mathrm{j}k_\theta\rho\cos(\theta-\phi)}\rho\mathrm{d}\phi\mathrm{d}\rho \\ &-\int_0^a\int_{2\pi}\frac{1}{2}\cos([q+1]\phi)\,J_{q+1}\left(k'_{qm}\rho\right)\mathrm{e}^{-\mathrm{j}k_\theta\rho\cos(\theta-\phi)}\rho\mathrm{d}\phi\mathrm{d}\rho\end{aligned} \tag{B.64}$$

$$= -\pi\,(-\mathrm{j})^{q-1}\cos([q-1]\theta)\int_0^a\rho J_{q-1}\left(k'_{qm}\rho\right)J_{q-1}\left(k_\theta\rho\right)\mathrm{d}\rho \tag{B.65}$$

$$-\pi\,(-\mathrm{j})^{q+1}\cos([q+1]\theta)\int_0^a\rho J_{q+1}\left(k'_{qm}\rho\right)J_{q+1}\left(k_\theta\rho\right)\mathrm{d}\rho\,. \tag{B.66}$$

Similarly, the Fourier transform of the $x$-component is

$$\begin{aligned}\tilde{e}^{\mathrm{h}}_{x,qm1} = \pi\,(-\mathrm{j})^{q-1}\sin\left([q-1]\theta\right)\int_0^a \rho J_{q-1}\left(k'_{qm}\rho\right)J_{q-1}\left(k_\theta\rho\right)\mathrm{d}\rho \\ -\pi\,(-\mathrm{j})^{q+1}\sin\left([q+1]\theta\right)\int_0^a \rho J_{q+1}\left(k'_{qm}\rho\right)J_{q+1}\left(k_\theta\rho\right)\mathrm{d}\rho\,. \end{aligned} \tag{B.67}$$

The integrals are solved with (B.45). Using (B.41), evaluating the Fourier transforms at the polar coordinates $k_\theta^{(s\ell)}$ and $\theta^{(s\ell)}$ yields the PMFs

$$\tilde{e}^{\mathrm{h}(s\ell)}_{z,qm1} = \frac{\pi\,(-\mathrm{j})^{q-1}\,a}{k'^2_{qm} - {k_\theta^{(s\ell)}}^2}\begin{bmatrix} -\cos\left([q-1]\theta^{(s\ell)}\right)\begin{bmatrix} k'_{qm}J_q\left(p'_{qm}\right)J_{q-1}\left(k_\theta^{(s\ell)}a\right) \\ -k_\theta^{(s\ell)}J_{q-1}\left(p'_{qm}\right)J_q\left(k_\theta^{(s\ell)}a\right)\end{bmatrix} \\ +\cos\left([q+1]\theta^{(s\ell)}\right)\begin{bmatrix} k_\theta^{(s\ell)}J_{q+1}\left(p'_{qm}\right)J_q\left(k_\theta^{(s\ell)}a\right) \\ -k'_{qm}J_q\left(p'_{qm}\right)J_{q+1}\left(k_\theta^{(s\ell)}a\right)\end{bmatrix}\end{bmatrix}, \tag{B.68}$$

and

$$\tilde{e}^{\mathrm{h}(s\ell)}_{x,qm1} = \frac{\pi\,(-\mathrm{j})^{q-1}\,a}{k'^2_{qm} - {k_\theta^{(s\ell)}}^2}\begin{bmatrix} \sin\left([q-1]\theta^{(s\ell)}\right)\begin{bmatrix} k'_{qm}J_q\left(p'_{qm}\right)J_{q-1}\left(k_\theta^{(s\ell)}a\right) \\ -k_\theta^{(s\ell)}J_{q-1}\left(p'_{qm}\right)J_q\left(k_\theta^{(s\ell)}a\right)\end{bmatrix} \\ +\sin\left([q+1]\theta^{(s\ell)}\right)\begin{bmatrix} k_\theta^{(s\ell)}J_{q+1}\left(p'_{qm}\right)J_q\left(k_\theta^{(s\ell)}a\right) \\ -k'_{qm}J_q\left(p'_{qm}\right)J_{q+1}\left(k_\theta^{(s\ell)}a\right)\end{bmatrix}\end{bmatrix}, \tag{B.69}$$

It is notable that when $k_\theta^{(s\ell)} = \pm k'_{qm}$, (B.68) and (B.69) become undefined. This singularity can be solved by using the relations (B.51) derived with L'Hôpital's rule, and reformulating the PMFs with (B.40) and (B.39).

The same derivation steps can be used to find the PMFs for $t = 2$, where only signs and trigonometric functions differ.

**Square norm** According to (2.32), and with $q > 0$, the square norm of the TE mode is

$$\begin{aligned}
I^{\mathrm{h}}_{qm1} &= \int_0^{2\pi} \sin^2(q\phi)\,\mathrm{d}\phi \int_0^a {J'_q}^2\left(k'_{qm}\rho\right)\rho\mathrm{d}\rho + \int_0^{2\pi} \cos^2(q\phi)\,\mathrm{d}\phi \int_0^a \left(\frac{q}{k'_{qm}\rho}J_q\left(k'_{qm}\rho\right)\right)^2 \rho\mathrm{d}\rho \\
&= \pi \int_0^a \left[{J'_q}^2\left(k'_{qm}\rho\right) + \left(\frac{q}{k'_{qm}\rho}J_q\left(k'_{qm}\rho\right)\right)^2\right]\rho\mathrm{d}\rho \\
&= \frac{\pi}{2}\int_0^a \rho\left[J_{q-1}(k'_{qm}\rho)\right]^2\mathrm{d}\rho + \frac{\pi}{2}\int_0^a \rho\left[J_{q+1}(k'_{qm}\rho)\right]^2\mathrm{d}\rho \\
&= \frac{\pi a^2}{4}\left[J^2_{q-1}(p'_{qm}) + J^2_{q+1}(p'_{qm}) - J_q(p'_{qm})\left(J_{q-2}(p'_{qm}) + J_{q+2}(p'_{qm})\right)\right] \\
&= \frac{\pi a^2}{4}\left[2\frac{q^2}{{p'_{qm}}^2}J^2_q(p'_{qm}) - J_q(p'_{qm})\left(2\frac{q^2}{{p'_{qm}}^2}J_q(p'_{qm}) + 2J''_q(p'_{qm})\right)\right] \\
&= -\frac{\pi a^2}{2}J_q(p'_{qm})J''_q(p'_{qm})\,,
\end{aligned} \tag{B.70}$$

where identities (B.42), (B.43) and (B.41) are used. The same result is found for $t = 2$, even if $q = 0$.

# Appendix C

# Details to the dispersion study computations

## C.1 Linearization of the glide-symmetric dispersion equation for one or two modes

### C.1.1 Simplification of the dispersion matrix for small gap and small corrugations

The dispersion of the glide-symmetric (G-S) corrugated parallel-plate waveguide (PPW) is of the form $|\underline{\boldsymbol{M}}| = 0$, where the coefficients of the dispersion matrix $\underline{\boldsymbol{M}}$ are given by

$$\begin{aligned} M_{m'm} = \delta_{m'm} \frac{pa}{2^{\min\{1,m\}}} \frac{\cot(k_{y,m}h)}{k_{y,m}} \\ + \sum_{\substack{s=-\infty \\ s \text{ even}}}^{+\infty} \cot\left(k_y^{(s)} \frac{g}{2}\right) \frac{{k_z^{(s)}}^2}{k_y^{(s)}} \frac{f_{m'm}^{(s)}}{\left[{k_z^{(s)}}^2 - \left(\frac{m\pi}{a}\right)^2\right]\left[{k_z^{(s)}}^2 - \left(\frac{m'\pi}{a}\right)^2\right]} \\ - \sum_{\substack{s=-\infty \\ s \text{ odd}}}^{+\infty} \tan\left(k_y^{(s)} \frac{g}{2}\right) \frac{{k_z^{(s)}}^2}{k_y^{(s)}} \frac{f_{m'm}^{(s)}}{\left[{k_z^{(s)}}^2 - \left(\frac{m\pi}{a}\right)^2\right]\left[{k_z^{(s)}}^2 - \left(\frac{m'\pi}{a}\right)^2\right]}, \end{aligned} \tag{C.1}$$

with $k_{y,m} = \sqrt{k_0^2 - \left(\frac{m\pi}{a}\right)^2}$, $k_y^{(s)} = \sqrt{k_0^2 - {k_z^{(s)}}^2}$, $k_z^{(s)} = k_z + s\frac{2\pi}{p}$, and

$$f_{m'm}^{(s)} = \begin{cases} 4\sin^2\left(k_z^{(s)}\frac{a}{2}\right), & \text{if } m' \text{ and } m \text{ are both even,} \\ 4\cos^2\left(k_z^{(s)}\frac{a}{2}\right), & \text{if } m' \text{ and } m \text{ are both odd,} \\ \mathrm{j}(-1)^{m'} 4\sin\left(k_z^{(s)}\frac{a}{2}\right)\cos\left(k_z^{(s)}\frac{a}{2}\right), & \text{if } m' \text{ and } m \text{ have different parities.} \end{cases} \tag{C.2}$$

These coefficients are simplified under the following assumptions:

1. Subwavelength assumption: $p \leq \lambda_0/2$.
2. Observation restricted to the first Brillouin zone: $0 \leq k_0 \leq k_z \leq \frac{\pi}{p}$.
3. Shallow corrugations: $h \leq \frac{p}{8}$.
4. Small gap: $g \leq \frac{p}{4}$.
5. Thin corrugations: $a < p$.

From assumption 4, it comes that

$$\frac{g}{2}\sqrt{k_z^2 - k_0^2} \leq \frac{g}{2}k_z \leq \frac{g}{2}\frac{\pi}{p} \leq \frac{\pi}{8}\,, \quad \text{hence} \quad \coth\left[\tfrac{g}{2}\sqrt{k_z^2 - k_0^2}\right] \simeq \frac{2}{g\sqrt{k_z^2 - k_0^2}}\,. \tag{C.3}$$

However, assumption 1 is quite lax compared to the assumption (3.4), which is already enforced for all symmetric harmonics to be negligible.

From assumptions 2 and 3, it comes that

$$hk_0 \leq h\frac{\pi}{p} \leq \frac{\pi}{8}\,, \quad \text{hence} \quad \cot(hk_0) \simeq \frac{1}{hk_0}\,. \tag{C.4}$$

From assumptions 2 and 5, it comes that

$$\sin\left(k_z\tfrac{a}{2}\right) \simeq k_z\tfrac{a}{2}\,, \quad \text{and} \quad \cos\left(k_z\tfrac{a}{2}\right) \simeq 1\,. \tag{C.5}$$

Additionally, for $|s| \geq 2$

$$\sin\left(k_z^{(s)}\tfrac{a}{2}\right) = \sin\left(k_z\tfrac{a}{2} + s\pi\tfrac{a}{p}\right) \simeq \sin\left(s\pi\tfrac{a}{p}\right). \tag{C.6}$$

The reason why this is true is not because $s\pi a/p$ might be much larger than $k_z a/2$ for large $|s|$, but because the variations of $k_z a/2$ are small compared to $\pi$, such that the sine function is approximated locally by a constant. Similarly,

$$\cos\left(k_z^{(s)}\tfrac{a}{2}\right) \simeq \cos\left(s\pi\tfrac{a}{p}\right). \tag{C.7}$$

Moreover, for $m \geq 1$,

$$k_0^2 - \left(m\frac{\pi}{a}\right)^2 \simeq -\left(m\frac{\pi}{a}\right)^2\,, \quad \text{and} \quad k_z^2 - \left(m\frac{\pi}{a}\right)^2 \simeq -\left(m\frac{\pi}{a}\right)^2\,. \tag{C.8}$$

More generally, for $s \geq 2$

$$\left(k_z^{(s)}\right)^2 - \left(m\frac{\pi}{a}\right)^2 \simeq \left(s\frac{2\pi}{p}\right)^2 - \left(m\frac{\pi}{a}\right)^2\,, \tag{C.9}$$

where one implicitly assumes that $4s + 1 \ll (2s)^2$. This is acceptable only for $|s| \geq 2$. The subsequent simplifications could not be made for all higher harmonics if the odd harmonics were not neglected, particularly the harmonics of order $s = \pm 1$. Given that for the non-glide-symmetric (nGS) case, these two harmonics are not negligible, the following low-dispersive behavior cannot be applied without glide symmetry (GS).

### C.1.2 One mode: dismissal of all higher-harmonic terms

For $m' = m = 0$,

$$\begin{aligned} M_{00}(k_z,k) &\simeq \frac{pa}{hk_0^2} - \sum_{\substack{s=-\infty \\ s \text{ even}}}^{+\infty} \frac{4\sin^2\left(k_z^{(s)}\frac{a}{2}\right)\coth\left[\frac{g}{2}\sqrt{\left(k_z^{(s)}\right)^2 - k_0^2}\right]}{\left(k_z^{(s)}\right)^2\sqrt{\left(k_z^{(s)}\right)^2 - k_0^2}} \\ &\simeq \frac{pa}{hk_0^2} - \frac{2a^2}{gk_0^2\left[n^2-1\right]} - \sum_{\substack{s=-\infty \\ s \text{ even} \\ s\neq 0}}^{+\infty} \frac{4\sin^2\left(s\pi\frac{a}{p}\right)\coth\left|s\pi\frac{g}{p}\right|}{\left|s\frac{2\pi}{p}\right|^3} \\ &\simeq \frac{pa}{hk_0^2} - \frac{2a^2}{gk_0^2\left[n^2-1\right]} - \sum_{\substack{s=2 \\ s \text{ even}}}^{+\infty} \frac{8\sin^2\left(s\pi\frac{a}{p}\right)\coth\left(s\pi\frac{g}{p}\right)}{\left(s\frac{2\pi}{p}\right)^3}. \end{aligned} \tag{C.10}$$

It can be shown that the sum of higher-harmonic terms is negligible with respect to the harmonic term of order $s = 0$. Indeed, one the one hand

$$\frac{2a^2}{gk_0^2\left[n^2-1\right]} = \frac{2a^2}{g\left[k_z^2 - k_0^2\right]} \geq \frac{2a^2}{gk_z} \geq \frac{2a^2p^2}{g\pi^2}, \tag{C.11}$$

while on the other hand

$$\frac{8\sin^2\left(s\pi\frac{a}{p}\right)\coth\left(s\pi\frac{g}{p}\right)}{\left(s\frac{2\pi}{p}\right)^3} = \frac{a^2p\,\mathrm{sinc}^2\left(s\pi\frac{a}{p}\right)\coth\left(s\pi\frac{g}{p}\right)}{s\pi} \leq \frac{a^2p\coth\left(s\pi\frac{g}{p}\right)}{s\pi} \simeq \frac{a^2p^2}{gs^2\pi^2} \tag{C.12}$$

where the rough approximate $\coth(s\pi g/p) \simeq p/(s\pi g)$ is used given that $g \ll p$. In the worst case ($g = p/4$), the error is about a factor of $2/3$. Consequently, the ratio between the fundamental-harmonic term and the harmonic term for any $|s| \geq 2$ is

$$\left(\frac{2a^2}{gk_0^2\left[n^2-1\right]}\right)\left(\frac{\left(s\frac{2\pi}{p}\right)^3}{8\sin^2\left(s\pi\frac{a}{p}\right)\coth\left(s\pi\frac{g}{p}\right)}\right) \geq 2s^2\,. \tag{C.13}$$

Given that the latter ratio is much larger than one for any $|s| \geq 2$, the fundamental harmonic is dominant, and all higher-harmonic terms can be discarded. Therefore,

$$M_{00}(k_z,k) \simeq \frac{pa}{hk_0^2} - \frac{2a^2}{gk_0^2\left[n^2-1\right]}. \tag{C.14}$$

### C.1.3 Two modes: simplification of the dispersion matrix coefficients

All following simplifications are made under the assumptions of section C.1.1.

The coefficient $M_{00}$ is simplified in the previous appendix section.

For $m' = 0$ and $m = 1$,

$$\begin{aligned} M_{01}(k_z, k_0) &= -\sum_{\substack{s=-\infty \\ s \text{ even}}}^{+\infty} \frac{\mathrm{j}4 \sin\left(k_z^{(s)} \frac{a}{2}\right) \cos\left(k_z^{(s)} \frac{a}{2}\right) \coth\left[\frac{g}{2}\sqrt{\left(k_z^{(s)}\right)^2 - k_0^2}\right]}{\left[\left(k_z^{(s)}\right)^2 - \left(\frac{\pi}{a}\right)^2\right]\sqrt{\left(k_z^{(s)}\right)^2 - k_0^2}} \\ &\simeq -\frac{\mathrm{j}4na}{gk_0\left[k_z^2 - \left(\frac{\pi}{a}\right)^2\right][n^2-1]} - \sum_{\substack{s=-\infty \\ s \text{ even} \\ s\neq 0}}^{+\infty} \frac{\mathrm{j}4 \sin\left(s\pi\frac{a}{p}\right) \cos\left(s\pi\frac{a}{p}\right) \coth\left[s\pi\frac{g}{p}\right]}{\left[\left(s\frac{2\pi}{p}\right)^2 - \left(\frac{\pi}{a}\right)^2\right] s\frac{2\pi}{p}} \\ &\simeq \frac{\mathrm{j}4na^3}{gk_0\pi^2\left[n^2-1\right]} \\ &= \frac{1}{k_0}\tilde{M}_{01}(n) \simeq -M_{10}(k_z, k_0)\,, \end{aligned} \tag{C.15}$$

where $\tilde{M}_{01}$ is a function of $n$. The higher-harmonic terms are not discarded from an approximation: they cancel out with the harmonic term of opposite order.

For $m' = m = 1$,

$$\begin{aligned} M_{11}(k_z, k) &\simeq -\frac{pa^2 \coth\left(\pi\frac{h}{a}\right)}{2\pi} - \sum_{\substack{s=-\infty \\ s \text{ even}}}^{+\infty} \frac{4\cos^2\left(k_z^{(s)}\frac{a}{2}\right)\left(k_z^{(s)}\right)^2 \coth\left[\frac{g}{2}\sqrt{\left(k_z^{(s)}\right)^2 - k_0^2}\right]}{\left[\left(k_z^{(s)}\right)^2 - \left(\frac{\pi}{a}\right)^2\right]^2\sqrt{\left(k_z^{(s)}\right)^2 - k_0^2}} \\ &\simeq -\frac{pa^2 \coth\left(\pi\frac{h}{a}\right)}{2\pi} - \frac{8n^2}{g\left[k_z^2 - \left(\frac{\pi}{a}\right)^2\right]^2[n^2-1]} - \sum_{\substack{s=-\infty \\ s \text{ even} \\ s\neq 0}}^{+\infty} \frac{4\cos^2\left(s\pi\frac{a}{p}\right)\left(s\frac{2\pi}{p}\right)\coth\left[s\pi\frac{g}{p}\right]}{\left[\left(s\frac{2\pi}{p}\right)^2 - \left(\frac{\pi}{a}\right)^2\right]^2} \\ &\simeq -\frac{pa^2 \coth\left(\pi\frac{h}{a}\right)}{2\pi} - \frac{8a^4n^2}{g\pi^4[n^2-1]} - \sum_{\substack{s=2 \\ s \text{ even}}}^{+\infty} \frac{8\cos^2\left(s\pi\frac{a}{p}\right)\left(s\frac{2\pi}{p}\right)\coth\left[s\pi\frac{g}{p}\right]}{\left[\left(s\frac{2\pi}{p}\right)^2 - \left(\frac{\pi}{a}\right)^2\right]^2} \\ &= \tilde{M}_{11}\,, \end{aligned} \tag{C.16}$$

where $\tilde{M}_{11}$ is a constant which depends neither on $k_z$ nor on $k_0$.

**Treatment of the singularity in the simplified 2-mode dispersion equation** When solving the simplified dispersion equation (3.16) numerically, particular attention must be paid to the special case where $a = p/(2|s|)$, with $s$ an even integer e.g., $a = p/4$. In this case, the higher-harmonic term of order $s$ is undetermined, given that both

$\cos^2(s\pi\frac{a}{p}) = 0$ and $\left[(s\frac{2\pi}{p})^2 - (\frac{\pi}{a})^2\right]^2 = 0$. Considering the function

$$f(x) = \left[\frac{\cos^2\left(x\pi\frac{a}{p}\right)}{\left(x\frac{2\pi}{p}\right)^2 - \left(\frac{\pi}{a}\right)^2}\right]^2 , \tag{C.17}$$

it can be shown that

$$\lim_{x\to\pm\frac{p}{2a}} f(x) = \frac{a^4}{16\pi^2} . \tag{C.18}$$

This result must be included in the numerical solver, so that there is no undetermined form when $a = p/(2|s|)$.

## C.2 Equivalence of glide-symmetric and non-glide corrugated parallel-plate waveguide for small gap

If the gap $g$ satisfies the assumption (3.4), the G-S corrugated PPW is equivalent to a scaled nGS structure in the first Brillouin zone, with double gap $\hat{g} = 2g$ and half cell-length $\hat{p} = p/2$.

In the following all values with a hat notation belong to the equivalent nGS structure, while all values without a hat belong the G-S structure. This also applies to harmonic wavenumbers e.g.,

$$k_z^{(s)} = k_z + s\tfrac{2\pi}{p} , \quad \text{whereas} \quad \hat{k}_z^{(s)} = k_z + s\tfrac{2\pi}{\hat{p}} = k_z + (2s)\tfrac{2\pi}{p} . \tag{C.19}$$

In the first Brillouin zone i.e., for $k_0 \le k_z \le \frac{\pi}{p}$, it can be shown that the assumption (3.4) entails

$$\cot\left(\frac{\hat{g}}{2}\sqrt{k_0^2 - {k_z^{(s)}}^2}\right) = -\mathrm{j}\coth\left(\frac{\hat{g}}{2}\sqrt{{k_z^{(s)}}^2 - k_0^2}\right) \simeq -\mathrm{j}\frac{2}{\hat{g}\sqrt{{k_z^{(s)}}^2 - k_0^2}} . \tag{C.20}$$

Indeed, for $s \ge 2$,

$$\sqrt{{k_z^{(s)}}^2 - k_0^2} \simeq \sqrt{\left(s\tfrac{2\pi}{p}\right)^2 - k_0^2} \simeq \left|s\frac{2\pi}{p}\right| . \tag{C.21}$$

The hyperbolic cotangent function is equal to the inverse function up to a few percents as long as its argument is smaller than 1/2. Approximation (C.20) is thus valid if the argument of the cotangent function is smaller than 1/2 for its largest harmonic order $S$. Given (C.21), this yields the condition

$$S\frac{2\pi}{p}\frac{\hat{g}}{2} = S\pi\frac{2g}{p} < \frac{1}{2} \quad \Longleftrightarrow \quad g < \frac{p}{4S\pi} . \tag{C.22}$$

For any $Q > 1$, (3.4) is more restrictive than (C.22). Therefore, if the gap $g$ fulfills (3.4) i.e., if the symmetric harmonics can be discarded, then (C.20) is valid.

Under these assumptions, the G-S dispersion matrix coefficients (2.8) can be approximated by

$$\begin{aligned} M_{m'm} &\simeq \delta_{m'm}\frac{pa}{2^{\min\{1,m\}}}\frac{\cot(k_{y,m}h)}{k_{y,m}} - \sum_{\substack{s=-\infty \\ s \text{ even}}}^{+\infty} \frac{2\left(k_z^{(s)}\right)^2}{g\left[{k_z^{(s)}}^2-k_0^2\right]} \frac{f_{m'm}^{(s)}}{\left[{k_z^{(s)}}^2-\left(\frac{m\pi}{a}\right)^2\right]\left[{k_z^{(s)}}^2-\left(\frac{m'\pi}{a}\right)^2\right]} \\ &= \delta_{m'm}\frac{pa}{2^{\min\{1,m\}}}\frac{\cot(k_{y,m}h)}{k_{y,m}} - \sum_{s=-\infty}^{+\infty} \frac{2\left(k_z^{(2s)}\right)^2}{g\left[{k_z^{(2s)}}^2-k_0^2\right]} \frac{f_{m'm}^{(2s)}}{\left[{k_z^{(2s)}}^2-\left(\frac{m\pi}{a}\right)^2\right]\left[{k_z^{(2s)}}^2-\left(\frac{m'\pi}{a}\right)^2\right]}\,, \end{aligned} \tag{C.23}$$

while the nGS dispersion matrix coefficients (2.10) can be approximated by

$$\begin{aligned} \hat{M}_{m'm} &\simeq \delta_{m'm}\frac{\hat{p}a}{2^{\min\{1,m\}}}\frac{\cot(k_{y,m}h)}{k_{y,m}} + \sum_{s=-\infty}^{+\infty} \frac{2\left(\hat{k}_z^{(s)}\right)^2}{\hat{g}\left[\left(\hat{k}_z^{(s)}\right)^2-k_0^2\right]} \frac{f_{m'm}^{(s)}}{\left[\left(\hat{k}_z^{(s)}\right)^2-\left(\frac{m\pi}{a}\right)^2\right]\left[\left(\hat{k}_z^{(s)}\right)^2-\left(\frac{m'\pi}{a}\right)^2\right]} \\ &= \frac{1}{2}\left\{ \begin{array}{l} \delta_{m'm}\dfrac{pa}{2^{\min\{1,m\}}}\dfrac{\cot(k_{y,m}h)}{k_{y,m}} \\ + \displaystyle\sum_{s=-\infty}^{+\infty} \frac{2\left(\hat{k}_z^{(s)}\right)^2}{g\left[\left(\hat{k}_z^{(s)}\right)^2-k_0^2\right]} \frac{f_{m'm}^{(s)}}{\left[\left(\hat{k}_z^{(s)}\right)^2-\left(\frac{m\pi}{a}\right)^2\right]\left[\left(\hat{k}_z^{(s)}\right)^2-\left(\frac{m'\pi}{a}\right)^2\right]} \end{array} \right\}. \end{aligned} \tag{C.24}$$

Considering that

$$k_z^{(2s)} = k_z + 2s\frac{2\pi}{p} = k_z + s\frac{2\pi}{p/2} = k_z + s\frac{2\pi}{\hat{p}} = \hat{k}_z^{(s)}\,, \tag{C.25}$$

it comes out that for any $m'$ and $m$,

$$\hat{M}_{m'm} = \frac{1}{2}M_{m'm}\,. \tag{C.26}$$

Given that the dispersion equation is solved when the determinant of $\underline{\boldsymbol{M}}$ is zero, the 1/2 factor does not change the solution space. As a consequence, at low-frequencies and under the assumption (3.4), the G-S structure with cell-length $p$ and gap $g$ is equivalent to the nGS structure with cell-length $p/2$ and gap $2g$.

# Appendix D

# Details to the quasi-static homogenization computations

## D.1 Quasi-static dispersion equation for the corrugated parallel-plate waveguide

In this section, the coefficients (2.8) of the dispersion matrix $\underline{\boldsymbol{M}}$ for the glide-symmetric (G-S) corrugated parallel-plate waveguide (PPW) are simplified in the quasi-static regime.

In (4.4), the dispersion matrix is subdivided according to the nature of the modes, that is transverse electric magnetic (TEM) or transverse magnetic (TM). The first row and the first column of the matrix are then multiplied by $k_0$, which does not change the dispersion equation. Finally, the matrix coefficients are subdivided in terms with different physical meaning. In the following, these terms are simplified when $k_0 \to 0$. This implies that $k_z \to 0$, and so the higher-harmonic wavenumbers are simplified according to (4.1).

**Diagonal terms** The diagonal terms $\gamma_m$ are defined as

$$\gamma_m = \begin{cases} \frac{pa\cot(k_0 h)}{k_0} & \text{if } m = 0, \\ \frac{pa}{2}\frac{\cot(k_{y,m} h)}{k_{y,m}} & \text{else.} \end{cases} \tag{D.1}$$

In the quasi-static regime, this yields

$$\gamma_m \underset{k_0 \to 0}{=} \bar{\gamma}_m = \begin{cases} \frac{pa}{k_0^2 h} & \text{if } m = 0, \\ -\frac{pa^2}{2}\frac{\coth\left(\frac{m\pi}{a} h\right)}{m\pi} & \text{else.} \end{cases} \tag{D.2}$$

**Higher-harmonic projections** The projection of a corrugation mode $m$ onto the Floquet harmonic $s$ at the corrugation surface yields the term $e_m^{(s)}$. For higher harmonics,

that is $s \neq 0$, this projection is defined as

$$e_m^{(s)} = \begin{cases} \frac{\mathrm{j}2\sin\left(k_z^{(s)}\frac{a}{2}\right)}{{k_z^{(s)}}^2-\left(\frac{m\pi}{a}\right)^2} & \text{if } m \text{ even}, \\ \frac{2\cos\left(k_z^{(s)}\frac{a}{2}\right)}{{k_z^{(s)}}^2-\left(\frac{m\pi}{a}\right)^2} & \text{if } m \text{ odd}. \end{cases} \tag{D.3}$$

In the quasi-static regime, all wavenumbers become frequency-independent constants, and thus so does $e_m^{(s)}$, which becomes

$$e_m^{(s)} \underset{k_0\to 0}{=} \bar{e}_m^{(s)} = \begin{cases} \frac{\mathrm{j}2\sin\left(s\pi\frac{a}{p}\right)}{\left(s\frac{2\pi}{p}\right)^2-\left(\frac{m\pi}{a}\right)^2} & \text{if } m \text{ even}, \\ \frac{2\cos\left(s\pi\frac{a}{p}\right)}{\left(s\frac{2\pi}{p}\right)^2-\left(\frac{m\pi}{a}\right)^2} & \text{if } m \text{ odd}. \end{cases} \tag{D.4}$$

**Fundamental-harmonic projection** The fundamental-harmonic term is isolated. Similarly to higher harmonics, the projection of a mode $m$ onto the fundamental harmonic yields

$$e_m^{(0)} = \begin{cases} \frac{\mathrm{j}2\sin\left(k_z\frac{a}{2}\right)}{k_z^2-\left(\frac{m\pi}{a}\right)^2} & \text{if } m \text{ even}, \\ \frac{2\cos\left(k_z\frac{a}{2}\right)}{k_z^2-\left(\frac{m\pi}{a}\right)^2} & \text{if } m \text{ odd}. \end{cases} \tag{D.5}$$

In the quasi-static regime, one must distinguish TEM and TM modes, that is $m = 0$ and $m > 0$, respectively. For $m = 0$,

$$e_0^{(0)} \underset{k_0\to 0}{=} \bar{e}_0^{(0)} = \frac{\mathrm{j}a}{k_z}, \tag{D.6}$$

whereas for $m > 0$,

$$e_m^{(0)} \underset{k_0\to 0}{=} \bar{e}_m^{(0)} = \begin{cases} -\frac{\mathrm{j}k_z a^3}{(m\pi)^2} \underset{k_0\to 0}{=} 0 & \text{if } m \text{ even}, \\ -\frac{2a^2}{(m\pi)^2} & \text{if } m \text{ odd}. \end{cases} \tag{D.7}$$

Therefore, for $m > 0$, $\bar{e}_m^{(0)}$ can be considered to be frequency-independent.

## D.2 Analytic approximations of the refractive index for the corrugated parallel-plate waveguide

The closed-form formula (4.16) for the quasi-static refractive index of a corrugated PPW is a function of the inverse of the matrix $\underline{\mathbf{\Sigma}}$, which must be computed numerically.

First of all, it is notable that $\underline{\mathbf{\Sigma}}$ is a symmetric checkerboard matrix, meaning that $\Sigma_{m'm} = 0$ if $m' + m$ is odd. Indeed, according to (4.12), the coefficients $\Sigma_{m'm}$ with

$m'+m$ odd contain only the higher-harmonic projections. Given (D.4), these projections are antisymmetric with respect to the harmonic order $s$. Therefore, when summing these projections from $s=-\infty$ to $+\infty$ (not $s=0$), all the terms cancel out.

The inversion of a checkerboard matrix is a checkerboard matrix too, and there is not a simple closed-form expression for this inverse. In the following paragraphs, several simplifications of this matrix are explored to obtained a more explicit expression of $n$, where the inverse has a closed-form expression too.

### D.2.1 Reduction to a diagonal matrix

The matrix $\underline{\mathbf{\Sigma}}$ is defined in (4.12). A first approach is to keep only the diagonal terms of $\underline{\mathbf{\Sigma}}$. All non-diagonal coefficients are set to zero. The resulting matrix is invertible, and its inverse is diagonal as well, yielding

$$\left[\bar{\boldsymbol{e}}^{(0)}\right]^{\mathrm{T}} \underline{\mathbf{\Sigma}}^{-1} \bar{\boldsymbol{e}}^{(0)} = \sum_{\substack{m=1 \\ m \text{ odd}}}^{M} \frac{4a^4}{m^4\pi^4} \left[ \bar{\gamma}_m + \sum_{\substack{s=-\infty \\ s\neq 0}}^{+\infty} \bar{f}^{(s)} \bar{e}_{m'}^{(s)} \bar{e}_{m}^{(s)*} \right]^{-1} , \tag{D.8}$$

where the values of $\bar{\gamma}_m$, $\bar{f}^{(s)}$, and $\bar{e}_m^{(s)}$ are given in (D.2), (4.3), and (D.4), respectively. Note that only the odd mode orders $m$ are summed, because for even orders, the quasi-static modal projections (D.7) are null.

This expression can be inserted in (4.16) to avoid the use of numerical matrix inversion algorithms.

### D.2.2 Reduction to an arrowhead matrix

Simulations show that for most corrugation widths $a$, it is enough to reduce the matrix $\underline{\mathbf{\Sigma}}$ to an arrowhead matrix, keeping only the coefficients on the diagonal, the first row, and the first column. The remaining coefficients draw an arrow, hence the name *arrowhead*.

The inverse of an arrowhead matrix is a checkerboard matrix [242]: $(\underline{\mathbf{\Sigma}})^{-1}_{m'm} = 0$ when $m'+m$ is odd. All remaining matrix coefficients are derived in the following paragraph D.2.2.1, where the analytic expressions for the inverse coefficients are given by (D.13), (D.14), (D.15) and (D.16). If the arrowhead matrix is also a checkerboard matrix, then additionnally, $(\underline{\mathbf{\Sigma}})^{-1}_{m'm} = 0$ when $m' \neq m$ are both even.

After inserting these inverse coefficients of $\underline{\mathbf{\Sigma}}$ in (4.16), the overall formula has a complicated form. Nevertheless, it allows for an explicit expression of the equivalent refractive index in (4.16). It is noticeable that, when the non-diagonal terms of $\underline{\mathbf{\Sigma}}$ are neglected, the same inverse coefficients as in section D.2.1 are obtained.

#### D.2.2.1 Inverse of a symmetric arrowhead matrix

In D.2.2, the matrix $\underline{\mathbf{\Sigma}}$ must be inverted to compute the low-frequency equivalent refractive index. It has a size $M \times M$, it is sparse and symmetric. Moreover, it is reduced to

an arrowhead matrix. An arrowhead matrix $\underline{\boldsymbol{B}}$ has the general form

$$\underline{\boldsymbol{B}} = \begin{bmatrix} B_{11} & B_{12} & B_{13} & B_{14} & B_{15} & B_{16} & B_{17} & \dots & B_{1M} \\ B_{12} & B_{22} & 0 & 0 & 0 & 0 & 0 & \dots & 0 \\ B_{13} & 0 & B_{33} & 0 & 0 & 0 & 0 & \dots & 0 \\ B_{14} & 0 & 0 & B_{44} & 0 & 0 & 0 & \dots & 0 \\ B_{15} & 0 & 0 & 0 & B_{55} & 0 & 0 & \dots & 0 \\ B_{16} & 0 & 0 & 0 & 0 & B_{66} & 0 & \dots & 0 \\ B_{17} & 0 & 0 & 0 & 0 & 0 & B_{77} & \dots & 0 \\ \vdots & \vdots & \vdots & \vdots & \vdots & \vdots & \vdots & \ddots & \vdots \\ B_{1M} & 0 & 0 & 0 & 0 & 0 & 0 & \dots & B_{MM} \end{bmatrix} . \tag{D.9}$$

This matrix can be divided in several blocks,

$$\underline{\boldsymbol{B}} = \begin{bmatrix} B_{11} & \boldsymbol{b}^{\mathrm{T}} \\ \boldsymbol{b} & \underline{\boldsymbol{D}} \end{bmatrix} , \tag{D.10}$$

where $B_{11}$ is the $1\times1$ block made of the eponym matrix coefficient, $\underline{\boldsymbol{D}}$ is a $(M-1)\times(M-1)$ block covering all remaining diagonal coefficients $B_{mm}$, with $m > 1$, and $\boldsymbol{b}^{\mathrm{T}}$ is a column vector of size $(M-1)$. According to the matrix block inversion formula [189, p. 123], the arrowhead matrix can be inverted as

$$\underline{\boldsymbol{B}}^{-1} = \begin{bmatrix} \frac{1}{\rho} & -\frac{1}{\rho}\boldsymbol{b}^{\mathrm{T}}\underline{\boldsymbol{D}}^{-1} \\ -\frac{1}{\rho}\underline{\boldsymbol{D}}^{-1}\boldsymbol{b} & \underline{\boldsymbol{D}}^{-1} + \frac{1}{\rho}\underline{\boldsymbol{D}}^{-1}\left(\boldsymbol{b}\boldsymbol{b}^{\mathrm{T}}\right)\underline{\boldsymbol{D}}^{-1} \end{bmatrix} , \tag{D.11}$$

where

$$\rho = B_{11} - \boldsymbol{b}^{\mathrm{T}}\underline{\boldsymbol{D}}^{-1}\boldsymbol{b} . \tag{D.12}$$

Equation (D.11) illustrates that an arrowhead matrix is invertible if and only if $\rho \neq 0$. This is equivalent to what is done in [243], where equation (3) is equivalent to (D.11) when applying a suitable symmetrical permutation.

The inverse arrowhead matrix coefficients can be found by expanding (D.11). For any $m > 1$, the diagonal coefficients of the inverted matrix $\underline{\boldsymbol{B}}^{-1}$ are equal to

$$\left(\underline{\boldsymbol{B}}^{-1}\right)_{mm} = \frac{1}{B_{mm}} + \frac{B_{1m}^2}{B_{11}B_{mm}^2 - B_{mm}^2 \sum\limits_{s=2}^{M} \frac{B_{1s}^2}{B_{ss}}} . \tag{D.13}$$

For $m = 1$, the diagonal coefficient is equal to

$$\left(\underline{\boldsymbol{B}}^{-1}\right)_{11} = \frac{1}{B_{11} - \sum\limits_{s=2}^{M} \frac{B_{1s}^2}{B_{ss}}} . \tag{D.14}$$

For any non-diagonal coefficient $(\underline{\boldsymbol{B}}^{-1})_{1m}$, with $m \geq 2$,

$$\left(\underline{\boldsymbol{B}}^{-1}\right)_{1m} = -\frac{B_{1m}}{B_{11}B_{mm} - B_{mm}\sum\limits_{s=2}^{M}\dfrac{B_{1s}^2}{B_{ss}}}\,. \tag{D.15}$$

Finally, all non-diagonal coefficients $(\underline{\boldsymbol{B}}^{-1})_{qm}$, with $q \geq 3$ and $m \geq 3$, $m \neq q$, are equal to

$$\left(\underline{\boldsymbol{B}}^{-1}\right)_{qm} = \frac{B_{1q}B_{1m}}{\left[B_{11}B_{mm}B_{qq} - B_{mm}B_{qq}\sum\limits_{s=2}^{M}\dfrac{B_{1s}^2}{B_{ss}}\right]}\,. \tag{D.16}$$

It appears that in general, the inverse of an arrowhead matrix is a full matrix..

### D.2.3 Numerical comparison of the derived low-frequency index formulas

In this subsection, the low-frequency effective refractive index (4.16) is compared to the simplifications made in paragraphs D.2.1 and D.2.2, namely the diagonal and arrowhead reductions of the matrix $\underline{\boldsymbol{\Sigma}}$, respectively. Although these simplifications make it less cumbersome to compute the refractive index, a decrease of the precision is to be expected for these solutions, given that several coefficients of $\underline{\boldsymbol{\Sigma}}$ are being discarded.

Fig. D.1 displays the computed low-frequency refractive index as a function of the corrugation width $a$. In all cases, 10 modes and 50 harmonics are taken into account, while the remaining structure parameters are $p = 4\,\mathrm{mm}$, $h = 0.5\,\mathrm{mm}$ and $g = 0.1\,\mathrm{mm}$.

Fig. D.1 illustrates how the diagonal simplification yields a good approximation of the index only for a corrugation width smaller than a quarter-cell. Nevertheless, only few additional coefficients are necessary to fall back on the right curve, since the arrowhead approximation yields a quite accurate index for all corrugation widths.

## D.3 Reducing the number of modes for canonical holes

In the following derivation, $\mathrm{i} = \mathrm{e}, \mathrm{h}$ is used to designate TM and transverse electric (TE) modes without distinction.

According to the closed-form index formula (4.40), a mode of type i and order $m$ has no impact if and only if none of its projected modal functions (PMFs) yield a non-zero contribution in the product $\boldsymbol{u}^{\mathrm{i}\mathrm{H}}\underline{\boldsymbol{\Sigma}}^{\mathrm{i}-1}\boldsymbol{u}^{\mathrm{i}}$. For a given mode $m$, if

$$u_m^{\mathrm{i}} = 0\,, \tag{D.17}$$

then for any order $m'$, the inverse matrix coefficient $(\underline{\boldsymbol{\Sigma}}^{\mathrm{i}})^{-1}_{m'm}$ disappears from (4.40). However, this is not enough to completely dismiss the corresponding $m^{\mathrm{th}}$ mode. Indeed, other coefficients of $\left(\underline{\boldsymbol{\Sigma}}^{\mathrm{i}}\right)^{-1}$ may be dependent on the $m^{\mathrm{th}}$ mode, due to the inverse

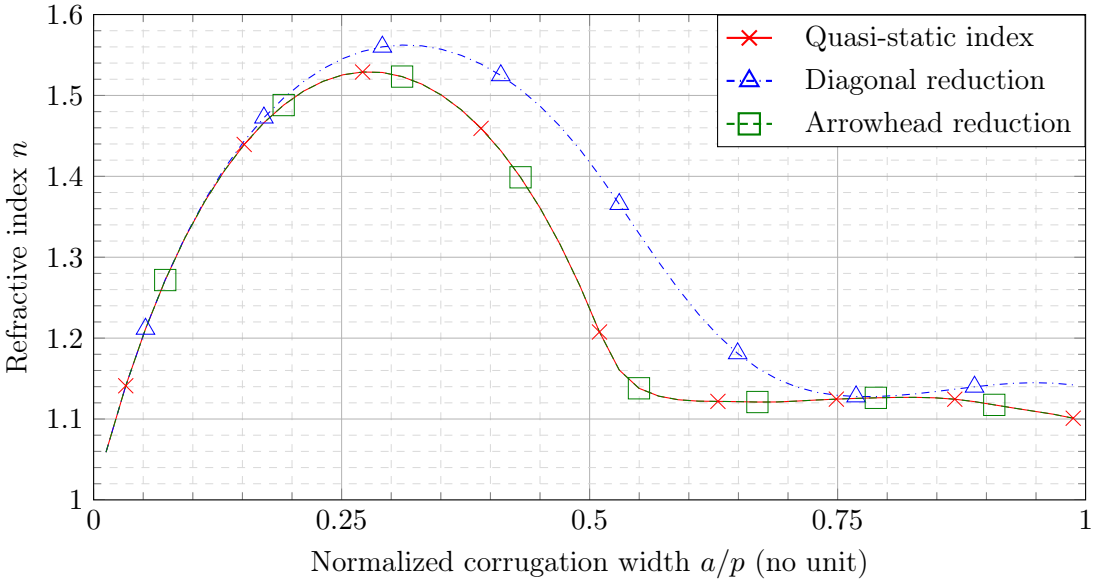


Figure D.1: Low-frequency effective refractive index $n$ as a function of the corrugation width $a$. 10 modes and 50 harmonics are considered. Other structure parameters are $p = 4\,\text{mm}$, $h = 0.5\,\text{mm}$ and $g = 0.1\,\text{mm}$. The true low-frequency refractive index is compared to the simplified analytical models derived in the previous sections: the simplified version with only diagonal coefficients from section D.2.1, and the arrowhead simplification from section D.2.2.

operation. Nevertheless, (D.17) can be completed by another condition to be made sufficient for the dismissal of the mode.

Let $m_0$ be a mode that satisfies (D.17), making it a candidate for dismissal. Let $\mathcal{M}_1$ be the set of orders $m_1$ for all the modes that have not been dismissed. In order for $m_0$ to have no impact in the inverse matrix $\left(\underline{\mathbf{\Sigma}}^{\text{i}}\right)^{-1}$, all the coefficients of the matrix $\underline{\mathbf{\Sigma}}^{\text{i}}$ must be zero on the $m_0^{\text{th}}$ row and columns if they correspond to modes that are kept i.e., to modes that belong to $\mathcal{M}_1$. This can be expressed mathematically by the condition

$$\forall\, m_1 \in \mathcal{M}_1,\ \ \Sigma^{\text{i}}_{m_0 m_1} = \Sigma^{\text{i}}_{m_1 m_0} = 0\,. \tag{D.18}$$

If a mode $m_0$ satisfies both conditions (D.17) and (D.18), then it is dispensable. This is proven more rigorously in the following.

In opposition to $\mathcal{M}_1$, let $\mathcal{M}_0$ be the set of orders $m_0$ for all the modes that have been dismissed. Given that (2.42) requires the determinant of the dispersion matrix to be null, the modes can be put in an arbitrary order, meaning that the lines and columns of $\underline{\mathbf{\Sigma}}^{\text{i}}$ can be permuted at will. As such, $\underline{\mathbf{\Sigma}}^{\text{i}}$ can be rearranged such that its first rows and columns correspond to orders in $\mathcal{M}_0$, whereas the remaining rows and columns correspond to orders in $\mathcal{M}_1$. Given the second condition (D.18), the rearranged matrix is a block diagonal matrix. Therefore, its inverse is made of the inverse of its blocks [189,

p. 123], namely

$$\left(\underline{\boldsymbol{\Sigma}}^{\mathrm{i}}\right)^{-1} = \begin{bmatrix} \underline{\boldsymbol{\Sigma}}_0^{\mathrm{i}} & \mathbf{0} \\ \mathbf{0} & \underline{\boldsymbol{\Sigma}}_1^{\mathrm{i}} \end{bmatrix}^{-1} = \begin{bmatrix} \left(\underline{\boldsymbol{\Sigma}}_0^{\mathrm{i}}\right)^{-1} & \mathbf{0} \\ \mathbf{0} & \left(\underline{\boldsymbol{\Sigma}}_1^{\mathrm{i}}\right)^{-1} \end{bmatrix}, \tag{D.19}$$

where $\underline{\boldsymbol{\Sigma}}_0^{\mathrm{i}}$ and $\underline{\boldsymbol{\Sigma}}_1^{\mathrm{i}}$ are the blocks of $\underline{\boldsymbol{\Sigma}}^{\mathrm{i}}$ that relate only to mode orders in $\mathcal{M}_0$ and $\mathcal{M}_1$, respectively. Similarly, $\boldsymbol{u}^{\mathrm{i}}$ is divided in two subvectors $\boldsymbol{u}_0^{\mathrm{i}}$ and $\boldsymbol{u}_1^{\mathrm{i}}$. Given the first condition (D.17), $\boldsymbol{u}_0^{\mathrm{i}}$ is the null vector. Therefore, the product of $\boldsymbol{u}^{\mathrm{i}}$ with $\underline{\boldsymbol{\Sigma}}^{\mathrm{i}}$ yields

$$\left[\boldsymbol{u}^{\mathrm{i}}\right]^{\mathrm{H}} \left[\underline{\boldsymbol{\Sigma}}^{\mathrm{i}}\right]^{-1} \boldsymbol{u}^{\mathrm{i}} = \begin{bmatrix} \mathbf{0} \\ \boldsymbol{u}_1^{\mathrm{i}} \end{bmatrix}^{\mathrm{H}} \begin{bmatrix} \left(\underline{\boldsymbol{\Sigma}}_0^{\mathrm{i}}\right)^{-1} & \mathbf{0} \\ \mathbf{0} & \left(\underline{\boldsymbol{\Sigma}}_1^{\mathrm{i}}\right)^{-1} \end{bmatrix} \begin{bmatrix} \mathbf{0} \\ \boldsymbol{u}_1^{\mathrm{i}} \end{bmatrix} = \left[\boldsymbol{u}_1^{\mathrm{i}}\right]^{\mathrm{H}} \left[\underline{\boldsymbol{\Sigma}}_1^{\mathrm{i}}\right]^{-1} \boldsymbol{u}_1^{\mathrm{i}} . \tag{D.20}$$

As such, the refractive index does not depend on the modes with orders in $\mathcal{M}_0$.

In order to distinguish $\mathcal{M}_0$ from $\mathcal{M}_1$, a good starting point is to check the condition (D.17). Indeed, according to (4.35) for TM modes and (4.36) for TE modes, $u_m^{\mathrm{i}} = 0$ for all propagation directions if and only if the corresponding PMFs are zero. That is,

$$\text{(D.17) is true for a mode } m \iff \begin{cases} \bar{e}_{y,m}^{(00)} = 0 & \text{for a TM mode,} \\ \bar{e}_{z,m}^{\mathrm{h}(00)} = \bar{e}_{x,m}^{\mathrm{h}(00)} = 0 & \text{for a TE mode.} \end{cases} \tag{D.21}$$

This gives a good initial point to sort modes between $\mathcal{M}_0$ and $\mathcal{M}_1$. Then, condition (D.18) can be checked. However, if it appears that (D.18) is not satisfied for a mode previously sorted in $\mathcal{M}_0$, then it is not enough to transfer it into $\mathcal{M}_1$ and continue checking condition (D.18) for the remaining orders $m_0$. As soon as $\mathcal{M}_1$ is changed by adding a new mode, all the modes of $\mathcal{M}_0$ must be reexamined.

## D.4 Homogenization for rectangular and circular holes

### D.4.1 Homogenization for rectangular holes

#### D.4.1.1 Modal functions and quasi-static projections

**TM modes** For TM modes of orders $m > 0$ and $q > 0$, the longitudinal electrical TM components are defined in (2.51). The corresponding Fourier transforms (B.33) yield the quasi-static PMFs, for any $(s, \ell)$,

$$\bar{e}_{y,qm}^{(s\ell)} = \frac{qm\pi^2}{a_z a_x} \zeta_z\left(m, s\right) \zeta_x\left(q, \ell\right) , \tag{D.22}$$

where

$$\zeta_z(m,s) = \begin{cases} \mp \mathrm{j} \frac{a_z^2}{2\pi m} & \text{if } \frac{m}{a_z} = \pm \frac{s2}{p_z}, \\ \frac{1-(-1)^m \mathrm{e}^{-\mathrm{j}s2\pi\frac{a_z}{p_z}}}{\left(\frac{m\pi}{a_z}\right)^2 - \left(s\frac{2\pi}{p_z}\right)^2} & \text{else.} \end{cases} \tag{D.23}$$

When implementing these PMFs numerically, indexing the different cases of (D.23) is important in order to avoid undetermined cases, which are likely to happen when many harmonic and mode orders are considered. The cut-off frequencies $k_{qm}$ are defined in (B.31), and the squared norms of the modes in (B.32)

**TE modes** For TE modes with orders $(q,m) \neq (0,0)$, the transverse field components (2.52) have squared norms (B.35) and PMFs (B.36) and (B.37). Therefore, in the quasi-static regime, the coefficients for the refractive index formula are

$$\bar{e}^{\mathrm{h}(s\ell)}_{z,qm} = \begin{cases} \frac{\pi q a_z}{a_x} \zeta_x\left(q,\ell\right) & \text{if } m = s = 0, \\ \mathrm{j}\frac{sq^2 2\pi^3}{p_z a_x^2 k_{qm}} \zeta_z\left(m,s\right)\zeta_x\left(q,\ell\right) & \text{else,} \end{cases} \tag{D.24}$$

and

$$\bar{e}^{\mathrm{h}(s\ell)}_{x,qm} = \begin{cases} -\frac{\pi m a_x}{a_z} \zeta_z\left(m,s\right) & \text{if } q = \ell = 0, \\ -\mathrm{j}\frac{\ell m^2 2\pi^3}{p_x a_z^2 k_{qm}} \zeta_z\left(m,s\right)\zeta_x\left(q,\ell\right) & \text{else,} \end{cases} \tag{D.25}$$

where the functions $\zeta$ are the same as in (D.23).

### D.4.1.2 Dismissible modes

Appendix D.3 explains how some modes of canonical hole shapes can be dismissed because they do not impact the dispersive behavior of the waveguide.

**TM modes** Equation (D.22) indicates that $u^{\mathrm{e}}_{qm} = 0$ for all TM modes where either $q$ or $m$ is even. Indeed, for $s = 0$ and $m$ even, according to (D.23), $\zeta_z(m,0) = 0$. The same is true for $q$. Therefore,

$$\bar{e}^{(00)}_{y,qm} = 0 \quad \text{for all } q \text{ even or } m \text{ even}\,. \tag{D.26}$$

To prove condition (D.18), let $m_0$ be an even order, and $m_1$ be an odd order. Then, according to the definition of the rectangular PMFs (D.22), the term $\bar{e}^{(s\ell)}_{y,m_0}\bar{e}^{(s\ell)*}_{y,m_1}$ in the matrix coefficients (4.32) contains the product

$$\begin{aligned} \zeta_z\left(m_0,s\right)\zeta_z\left(m_1,s\right)^* &= \left(1-(-1)^{m_0}\mathrm{e}^{-\mathrm{j}s2\pi\frac{a_z}{p_z}}\right)\left(1-(-1)^{m_1}\mathrm{e}^{-\mathrm{j}s2\pi\frac{a_z}{p_z}}\right)^* \\ &= 2\mathrm{j}\sin\left(s2\pi\frac{a_z}{p_z}\right)\,. \end{aligned} \tag{D.27}$$

This term is antisymmetric with respect to $s$. The matrix coefficient (4.32) is made of a sum over all harmonic orders $s \neq 0$. Therefore, for opposite orders $s$, the terms in the sum cancel out, such that $\Sigma^{\mathrm{e}}_{m_0 m_1} = 0$. The same can be shown $\Sigma^{\mathrm{e}}_{m_1 m_0}$, as well as for the orders $q$.

Consequently, all TM modes with $q$ or $m$ even belong to $\mathcal{M}_0$, as they satisfy both conditions (D.17) and (D.18). They can be dismissed when computing the low-frequency refractive index.

**TE modes** For TE modes, considering (D.24) and (D.25), one must be more careful, because some of the modes where $u^{\mathrm{h}}_{qm} = 0$ still have an impact on the inverse matrix $\left[\underline{\mathbf{\Sigma}}^{\mathrm{h}}\right]^{-1}$ i.e., they do not satisfy the second condition (D.18). Similarly to TM modes, when $q$ is even or $m$ is even, then $\zeta_z(m,0) = 0$ or $\zeta_z(q,0) = 0$. Moreover, in most cases, $\bar{e}^{\mathrm{h}(00)}_{z,m}$ and $\bar{e}^{\mathrm{h}(00)}_{z,m}$ are proportional to $s$ and $\ell$, respectively, and so they are null when $s = 0$ or $\ell = 0$. In the end, (D.24) and (D.25) show that

$$\begin{aligned} \bar{e}^{\mathrm{h}(00)}_{z,m} = \bar{e}^{\mathrm{h}(00)}_{x,m} = 0 \quad & \text{for all } (q,m), \\ & \text{except when one order is null and the other is odd.} \end{aligned} \tag{D.28}$$

However, restricting $\mathcal{M}_1$ to the pairs $(q,m)$ where one index is null and the other odd is not correct, because not all corresponding coefficients of the matrix $\underline{\mathbf{\Sigma}}^{\mathrm{e}}$ in (4.34) satisfy the second condition (D.18). In (4.34), the problem does not come from the term that involves the fundamental PMFs, which is null if the first condition (D.17) is satisfied. It is the sum over the higher-harmonic PMFs that yields

$$\begin{aligned} &\left(\tfrac{s2\pi}{p_z}\bar{e}^{\mathrm{h}(s\ell)}_{x,m'} - \tfrac{\ell 2\pi}{p_x}\bar{e}^{\mathrm{h}(s\ell)}_{z,m'}\right)\left(\tfrac{s2\pi}{p_z}\bar{e}^{\mathrm{h}(s\ell)}_{x,m} - \tfrac{\ell 2\pi}{p_x}\bar{e}^{\mathrm{h}(s\ell)}_{z,m}\right)^* \\ &= \left(\tfrac{s2\pi}{p_z}\right)^2 \bar{e}^{\mathrm{h}(s\ell)}_{x,m'}\bar{e}^{\mathrm{h}(s\ell)*}_{x,m} + \left(\tfrac{\ell 2\pi}{p_x}\right)^2 \bar{e}^{\mathrm{h}(s\ell)}_{z,m'}\bar{e}^{\mathrm{h}(s\ell)*}_{z,m} - \tfrac{s2\pi}{p_z}\tfrac{\ell 2\pi}{p_x}\left(\bar{e}^{\mathrm{h}(s\ell)}_{x,m'}\bar{e}^{\mathrm{h}(s\ell)*}_{z,m} + \bar{e}^{\mathrm{h}(s\ell)}_{z,m'}\bar{e}^{\mathrm{h}(s\ell)*}_{x,m}\right) \end{aligned} \tag{D.29}$$

In order for these terms to cancel out when summing over all higher harmonics, each term must be antisymmetric with respect to $s$ and/or $\ell$. This is true when $m'$ and $m$ have different parities, or when $q'$ and $q$ have different parities. Therefore, the only way to ensure the second condition (D.18) is to dismiss only the TE modes where $q+m$ is even i.e., when $q$ and $m$ are both even or both odd. Then, $(q_1,m_1) \in \mathcal{M}_1$ implies that $q_1$ and $m_1$ have different parities, and $(q_0,m_0) \in \mathcal{M}_0$ implies that $q$ and $m$ have the same parity , thus ensuring that $\Sigma^{\mathrm{h}}_{q_1m_1,q_0m_0} = 0$, because either $(q_1,q_0)$ or $(m_1,m_0)$ form a pair of orders with different parities, and so (D.29) is antisymmetric with either $s$ or $\ell$. All the modes in the resulting $\mathcal{M}_0$ satisfy the first condition (D.17). They represent approximately one quarter of the TE modes.

## D.4.2 Homogenization for circular holes

### D.4.2.1 Modal functions and quasi-static projections

**TM modes** For TM modes, the quasi-static simplifications of the PMFs defined in (B.53) are, for $q > 0$ and $m > 0$,

$$\bar{e}^{(s\ell)}_{y,qm1} = \frac{2\pi p_{qm}}{\mathrm{j}^q} \frac{J'_q\left(p_{qm}\right) J_q\left(\Gamma^{(s\ell)}a\right)}{{\Gamma^{(s\ell)}}^2 - \left(\frac{p_{qm}}{a}\right)^2} \sin\left(q\bar{\theta}^{(s\ell)}\right) , \tag{D.30}$$

and, for $m > 0$,

$$\bar{e}^{(s\ell)}_{y,qm2} = \frac{2\pi p_{qm}}{\mathrm{j}^q} \frac{J'_q\left(p_{qm}\right) J_q\left(\Gamma^{(s\ell)}a\right)}{{\Gamma^{(s\ell)}}^2 - \left(\frac{p_{qm}}{a}\right)^2} \cos\left(q\bar{\theta}^{(s\ell)}\right) . \tag{D.31}$$

with $\bar{\theta}^{(s\ell)} = \operatorname{atan}\left[\frac{\ell p_z}{s p_x}\right]$. Note that this term is never undetermined, even for $s = 0$. For $s = \ell = 0$, $\bar{\theta}^{(00)} = 0$. It is reminded that $p_{qm}$ is the $m$-th root of the Bessel function of first kind and order $q$, and $\Gamma^{(s\ell)} = \sqrt{(s2\pi/p_z)^2 + (\ell 2\pi/p_x)^2}$. The corresponding squared modal norms are given in (B.55).

**TE modes** For TE modes with cosine radial component in (2.55) i.e., for $t = 1$ and $m > 0$ and $q > 0$, the quasi-static projected modal functions are derived from (B.68) as

$$\bar{e}^{\mathrm{h}(s\ell)}_{z,qm1} = \frac{\pi\,(-\mathrm{j})^{q-1}\,a}{\left(\frac{p'_{qm}}{a}\right)^2 - \Gamma^{(s\ell)2}} \left[\begin{array}{l} -\cos\left([q-1]\bar{\theta}^{(s\ell)}\right)\left[\begin{array}{l}\frac{p'_{qm}}{a} J_q\left(p'_{qm}\right) J_{q-1}\left(\Gamma^{(s\ell)}a\right) \\ -\Gamma^{(s\ell)} J_{q-1}\left(p'_{qm}\right) J_q\left(\Gamma^{(s\ell)}a\right)\end{array}\right] \\ +\cos\left([q+1]\bar{\theta}^{(s\ell)}\right)\left[\begin{array}{l}\Gamma^{(s\ell)} J_{q+1}\left(p'_{qm}\right) J_q\left(\Gamma^{(s\ell)}a\right) \\ -\frac{p'_{qm}}{a} J_q\left(p'_{qm}\right) J_{q+1}\left(\Gamma^{(s\ell)}a\right)\end{array}\right]\end{array}\right], \quad \text{(D.32)}$$

and from (B.69) as

$$\bar{e}^{\mathrm{h}(s\ell)}_{x,qm1} = \frac{\pi\,(-\mathrm{j})^{q-1}\,a}{\left(\frac{p'_{qm}}{a}\right)^2 - \Gamma^{(s\ell)2}} \left[\begin{array}{l} \sin\left([q-1]\bar{\theta}^{(s\ell)}\right)\left[\begin{array}{l}\frac{p'_{qm}}{a} J_q\left(p'_{qm}\right) J_{q-1}\left(\Gamma^{(s\ell)}a\right) \\ -\Gamma^{(s\ell)} J_{q-1}\left(p'_{qm}\right) J_q\left(\Gamma^{(s\ell)}a\right)\end{array}\right] \\ +\sin\left([q+1]\bar{\theta}^{(s\ell)}\right)\left[\begin{array}{l}\Gamma^{(s\ell)} J_{q+1}\left(p'_{qm}\right) J_q\left(\Gamma^{(s\ell)}a\right) \\ -\frac{p'_{qm}}{a} J_q\left(p'_{qm}\right) J_{q+1}\left(\Gamma^{(s\ell)}a\right)\end{array}\right]\end{array}\right]. \quad \text{(D.33)}$$

Similarly, for the TE modes with sine radial component defined in (2.56) i.e., for $t = 2$ and $m > 0$, the quasi-static projected modal functions are

$$\bar{e}^{\mathrm{h}(s\ell)}_{z,qm2} = \frac{\pi\,(-\mathrm{j})^{q-1}\,a}{\left(\frac{p'_{qm}}{a}\right)^2 - \Gamma^{(s\ell)2}} \left[\begin{array}{l} \sin\left([q-1]\bar{\theta}^{(s\ell)}\right)\left[\begin{array}{l}\frac{p'_{qm}}{a} J_q\left(p'_{qm}\right) J_{q-1}\left(\Gamma^{(s\ell)}a\right) \\ -\Gamma^{(s\ell)} J_{q-1}\left(p'_{qm}\right) J_q\left(\Gamma^{(s\ell)}a\right)\end{array}\right] \\ -\sin\left([q+1]\bar{\theta}^{(s\ell)}\right)\left[\begin{array}{l}\Gamma^{(s\ell)} J_{q+1}\left(p'_{qm}\right) J_q\left(\Gamma^{(s\ell)}a\right) \\ -\frac{p'_{qm}}{a} J_q\left(p'_{qm}\right) J_{q+1}\left(\Gamma^{(s\ell)}a\right)\end{array}\right]\end{array}\right], \quad \text{(D.34)}$$

and

$$\bar{e}^{\mathrm{h}(s\ell)}_{x,qm2} = \frac{\pi\,(-\mathrm{j})^{q-1}\,a}{\left(\frac{p'_{qm}}{a}\right)^2 - \Gamma^{(s\ell)2}} \left[\begin{array}{l} \cos\left([q-1]\bar{\theta}^{(s\ell)}\right)\left[\begin{array}{l}\frac{p'_{qm}}{a} J_q\left(p'_{qm}\right) J_{q-1}\left(\Gamma^{(s\ell)}a\right) \\ -\Gamma^{(s\ell)} J_{q-1}\left(p'_{qm}\right) J_q\left(\Gamma^{(s\ell)}a\right)\end{array}\right] \\ +\cos\left([q+1]\bar{\theta}^{(s\ell)}\right)\left[\begin{array}{l}\Gamma^{(s\ell)} J_{q+1}\left(p'_{qm}\right) J_q\left(\Gamma^{(s\ell)}a\right) \\ -\frac{p'_{qm}}{a} J_q\left(p'_{qm}\right) J_{q+1}\left(\Gamma^{(s\ell)}a\right)\end{array}\right]\end{array}\right], \quad \text{(D.35)}$$

where $p'_{qm}$ is the $m$-th root of the derivative of the $q$-th Bessel function of first kind. The corresponding squared modal norms are given in (B.70).

#### D.4.2.2 Dismissible modes

The same procedure for dispensable modes can be followed as for rectangular holes. According to (D.30) and (D.31), $u^{\mathrm{e}}_{qmt} \neq 0$ only for $q = 0$ and $t = 2$. However, not all the TM modes where $t = 1$ or $q > 0$ satisfy the second condition (D.18). After considering the complete matrix $\underline{\mathbf{\Sigma}}^{\mathrm{e}}$ in (4.32), all TM modes with $t = 1$ are dispensable, as well as the TM modes with $q$ odd. Therefore, only TM modes with $t = 2$ and $q$ even are kept in the index formula, which represent a quarter of all the initial TM modes.

Similarly, according (D.32) to (D.35), $u^{\mathrm{h}}_{qmt} = 0$ when $q \neq 1$. But not all these modes belong to $\mathcal{M}_0$: condition (D.18) is only fully satisfied for TE modes where $q$ is even. Therefore, all TE modes with $q$ odd are kept, which represent half of the initial TE modes.

## D.5 Finite element method for cylindrical waveguide

**Helmholtz's equation** A cylindrical waveguide of longitudinal axis $y$ has an arbitrary invariant cross-section $S$ in the $zx$-plane. Such a cylindrical structure can guide both TM and TE modes. TEM modes may also propagate if one or more inner conductors are present, and they will be treated separately below. TM modes have an electric longitudinal field component $E_y(z, x, y) = e_y(z, x)\mathrm{e}^{-\mathrm{j}\beta y}$, with $\beta$ the propagation constant of the mode. TE modes have a magnetic longitudinal field component $H_y(z, x, y) = h_y(z, x)\mathrm{e}^{-\mathrm{j}k_y y}$. In both cases, we solve Helmholtz's equation for the longitudinal field component $f_y$, which represents the modal functions $e_y$ or $h_y$ for TM and TE modes, respectively. Helmholtz's equation yields [17, p. 16]

$$\nabla_{\mathrm{t}} \cdot \nabla_{\mathrm{t}} f_y + k_{\mathrm{c}}^2 f_y = 0\,, \tag{D.36}$$

where $\nabla_{\mathrm{t}}$ is the transverse nabla operator $[\partial/\partial z, \partial/\partial x]$, and $k_{\mathrm{c}}$ is the cut-off wavenumber of the mode. The propagation constant is related to $k_{\mathrm{c}}$ with $k_y = \sqrt{k^2 - k_{\mathrm{c}}^2}$, where $k$ is the free-space wavenumber for the medium that fills the waveguide.

Each function $f_y$ that satisfies (D.36), as well as the boundary conditions, represents a mode within the waveguide. On the one hand, the eigenvalues of TE modes are the eigensolutions of a Neumann differential problem. On the one hand, the eigenvalues of TM modes are the eigensolutions of a Dirichlet problem. In order to find these solutions numerically, (D.36) is discretized in a two-dimensional finite element method (FEM) process.

**Basis functions** In order to handle a problem of finite dimension, the number of degrees of freedom given to the solution is reduced. First, the cross-section $S$ is discretized with a mesh of triangles, resulting in $N$ distinct triangle vertices. The resulting mesh must capture the details of the cross-section geometry. We do this directly in Matlab,

with the partial derivative equation toolbox function `generateMesh`, which creates a triangular mesh with possible mesh refinement at the contour details. In the following, each triangle is called a mesh *element*, and is characterized by a unique number $e \in [\![1, E]\!]$, with $E$ the total number of triangles in the mesh. Its area is called $\mathcal{A}^{(e)}$

Then, $f_y$ is approximated by a function $\tilde{f}_y$, which is decomposed as a sum of $N$ basis functions $\Lambda_i(z, x)$, namely

$$f_y \simeq \tilde{f}_y = \sum_{i=1}^{N} \alpha_i \Lambda_i \,, \tag{D.37}$$

where $\alpha_i$ is the unknown weight of each basis function. For each vertex nb.$i$, there is an associated basis function $\Lambda_i$, defined as a pyramidal function which is only non-zero on the triangles that touch the considered vertex. For each triangle $e$, the portion of the basis function $\Lambda_i$ confined to $e$ is defined as

$$\Lambda_i^{(e)}(x, y) = \begin{cases} \zeta_i^{(e)}(x, y) = \frac{\mathcal{A}_i^{(e)}(x,y)}{\mathcal{A}^{(e)}} & \text{if the point } (x, y) \text{ lies in the element } e, \\ 0 & \text{else.} \end{cases} \tag{D.38}$$

The area $\mathcal{A}_i^{(e)}(x, y)$ corresponds to the triangle formed by the point $(x, y)$ and the side of $e$ that is opposite to the vertex $i$.

**Testing procedure** Helmholtz's equation is tested $N$ times in the cross-section using Galerkin's method. As such, the test functions are the same as the basis functions. Testing (D.36) with a test function $\Lambda_j$ yields

$$\iint_S \Lambda_j \nabla_\mathrm{t} \cdot \nabla_\mathrm{t} f_y \mathrm{d}s + k_\mathrm{c}^2 \iint_S \Lambda_j f_y \mathrm{d}s = 0 \,, \tag{D.39}$$

According to the product rule and Gauss's theorem (B.28),

$$\begin{aligned} \iint_S \Lambda_j \nabla_\mathrm{t} \cdot \nabla_\mathrm{t} f_y \mathrm{d}s &= \iint_S \nabla_\mathrm{t} \cdot (\Lambda_j \nabla_\mathrm{t} f_y) \, \mathrm{d}s - \iint_S \nabla_\mathrm{t} \Lambda_j \cdot \nabla_\mathrm{t} f_y \mathrm{d}s \\ &= \int_{\delta S} \Lambda_j \nabla_\mathrm{t} f_y \cdot \boldsymbol{n} \mathrm{d}\ell - \iint_S \nabla_\mathrm{t} \Lambda_j \cdot \nabla_\mathrm{t} f_y \mathrm{d}s \,, \end{aligned} \tag{D.40}$$

where $\delta S$ is the contour of the cross-section $S$, and $\boldsymbol{n}$ is the exterior normal at each point of the contour. Combining (D.39) and (D.40), this yields

$$\iint_S \nabla_\mathrm{t} \Lambda_j \cdot \nabla_\mathrm{t} f_y \mathrm{d}s - \int_{\delta S} \Lambda_j \nabla_\mathrm{t} f_y \cdot \boldsymbol{n} \mathrm{d}\ell = k_\mathrm{c}^2 \iint_S \Lambda_j f_y \mathrm{d}s \,, \tag{D.41}$$

which, inserting the basis function decomposition (D.37), can be approximated by

$$\sum_{i=1}^{N} \alpha_i \left[ \iint_S \nabla_\mathrm{t} \Lambda_j \cdot \nabla_\mathrm{t} \Lambda_i \mathrm{d}s - \int_{\delta S} \Lambda_j \nabla_\mathrm{t} \Lambda_i \cdot \boldsymbol{n} \mathrm{d}\ell \right] = k_\mathrm{c}^2 \sum_{i=1}^{N} \alpha_i \iint_S \Lambda_j \Lambda_i \mathrm{d}s \,. \tag{D.42}$$

Given that (D.42) is true for all $j \in [\![1, N]\!]$, it can be rewritten as the matrix equation

$$\underline{\boldsymbol{R}}\boldsymbol{\alpha} = k_c^2 \underline{\boldsymbol{S}}\boldsymbol{\alpha}\,,\,. \tag{D.43}$$

with $\boldsymbol{\alpha}$ the vector of unknown vertex coefficients $\alpha_m$, and the two $N \times N$ square matrices $\underline{\boldsymbol{R}}$ and $\underline{\boldsymbol{S}}$, whose coefficients are identified as

$$R_{ji} = \iint_S \nabla_t \Lambda_j \cdot \nabla_t \Lambda_i \mathrm{d}s - \int_{\delta S} \Lambda_j \nabla_t \Lambda_i \cdot \boldsymbol{n} \mathrm{d}\ell\,, \tag{D.44}$$

and

$$S_{ji} = \iint_S \Lambda_j \Lambda_i \mathrm{d}s\,. \tag{D.45}$$

**Computation of the matrix coefficients** The different elements in the matrices (D.44) and (D.45) can be expressed analytically for the pyramidal test and basis functions $\Lambda_i$. All integrals in the matrix coefficients $R_{ji}$ and $S_{ji}$ can be decomposed as

$$\iint_S g(\Lambda_j, \Lambda_i)\mathrm{d}s = \sum_{e=1}^{E} \iint_{\mathcal{A}^{(e)}} g(\Lambda_j^{(e)}, \Lambda_i^{(e)})\mathrm{d}s \tag{D.46}$$

with $g$ representing either the product, the dot product of the gradients, or the product of $\Lambda_i$ with the gradient of $\Lambda_j$. It is noticeable that $\iint_S g(\Lambda_i \Lambda_j)\mathrm{d}s \neq 0$ only if $i$ and $j$ belong to a same triangle. Therefore, the easiest way to fill these matrices is to proceed with a loop on the mesh triangle $e$. For each element, three different pyramidal functions $\Lambda_i$ interact, one per triangle vertex. As such, in the element $e$, there are 9 different integral contributions from the functions $\Lambda_i^{(\mathrm{e})}$ and $\Lambda_j^{(\mathrm{e})}$, which must then be assigned to the corresponding matrix coefficients, according to the vertex pair $(i, j)$.

It can be shown that for the matrix $\underline{\boldsymbol{S}}$, the contributions of a triangle $e$ are expressed as

$$\iint_{\mathcal{A}^{(e)}} \Lambda_j^{(\mathrm{e})} \Lambda_i^{(\mathrm{e})} \mathrm{d}s = 2A^{(\mathrm{e})} \int_0^1 \int_0^{1-\zeta_j} \zeta_i \zeta_j \mathrm{d}\zeta_i \mathrm{d}\zeta_j = \begin{cases} A^{(\mathrm{e})}/6 & \text{if } i = j, \\ A^{(\mathrm{e})}/12 & \text{if } i \neq j. \end{cases} \tag{D.47}$$

Similarly, for the matrix $\underline{\boldsymbol{R}}$, the contributions of a triangle $e$ for the gradient product is

$$\iint_{\mathcal{A}^{(e)}} \nabla_t \Lambda_j^{(e)} \cdot \nabla_t \Lambda_i^{(e)} \mathrm{d}s = 2A^{(\mathrm{e})} \int_0^1 \int_0^{1-\zeta_j} \frac{\hat{\boldsymbol{y}} \times \boldsymbol{\ell}_i}{2A^{(\mathrm{e})}} \frac{\hat{\boldsymbol{y}} \times \boldsymbol{\ell}_j}{2A^{(\mathrm{e})}} \zeta_i \mathrm{d}\zeta_j = \frac{\boldsymbol{\ell}_i \cdot \boldsymbol{\ell}_j}{4A^{(\mathrm{e})}}\,, \tag{D.48}$$

with $\hat{\boldsymbol{y}}$ the direction normal to the hole surface, and $\boldsymbol{\ell}_i$ the vector that corresponds to the side of the triangle $e$ opposite to its vertex $i$, with the direction associated to each side consistant within the triangle.

The contour integral in (D.44) is not computed, because it vanishes for both TM and TE modes, as explained in the following paragraphs.

**TM modes** For TM modes [185, p. 446], $f_y$ is the electric longitudinal component $e_y$. This function is zero on the contours of the holes, where the perfectly electrically conducting (PEC) walls make the tangential electric field go to zero. Therefore, the differential Helmholtz equation (D.36) is associated to Dirichlet boundary conditions. As a consequence, the approximated discretized function (D.37) has $\alpha_i = 0$ when $i$ is a vertex located on the hole contour. Therefore, in (D.44), the contour integral vanishes. The generalized eigenvalue problem (D.43) can therefore be solved for matrix coefficients $S_{ji}$ and $R_{ji}$ containing only the integrals (D.47) and (D.48), respectively. Moreover, there is no need to find the field values on the hole contour. Therefore, the matrix $\underline{\boldsymbol{R}}$ and $\underline{\boldsymbol{S}}$ can be truncated to the test and basis function of orders $i$ and $j$ which correspond to triangle vertices that lie strictly within the triangle. To put it differently, the number of degrees of freedom in this TM FEM problem is equal to the number of inner triangle vertices,where $\alpha_i \neq 0$.

**TE modes** For TE modes [185, p. 447], the coefficients of the matrices $\underline{\boldsymbol{R}}$ and $\underline{\boldsymbol{S}}$ in the generalized eigenvalue problem (D.43) are the same as for TM modes. Indeed, the contour integral in (D.44) vanishes as well, but not for the same reason. For TE modes, we are solving for the magnetic longitudinal field component, which is not necessarily zero on the hole contour. The boundary conditions are of the Neumann type, that is

$$\nabla_{\mathrm{t}} h_y \cdot \boldsymbol{n} = 0 \tag{D.49}$$

on the hole contour, with $\boldsymbol{n}$ the normal vector to each point of the contour. When $h_y$ is approximated with the basis functions $\Lambda_i$, this term appears in (D.44), making the integral disappear. However, the overall problem is not the same as for TM modes, because the number of degrees of freedom is larger i.e., the number of unknown weights $\alpha_i$. The size of the matrices $\underline{\boldsymbol{R}}$ and $\underline{\boldsymbol{S}}$ is $N \times N$, because all the triangle vertices are considered, including the vertices lying on the hole contour.

**TEM modes** The quasi-static homogenization technique in section 4.2 accepts TEM modes. A TEM field is possible in the holes when inner conductors are present, that is closed contours that do not cross the outer hole envelope. For $Q$ inner conductors, this TEM field can be decomposed as a sum of $Q$ orthogonal TEM modes, one for each inner conductor. These modes have neither electric nor magnetic longitudinal field components. Nevertheless, the transverse electric field of each mode of order $q \in [\![1, Q]\!]$ can be expressed as the gradient of a scalar potentiel $\Phi_q$ [17, pp. 98-99], that is

$$\boldsymbol{e}_q(z, x) = -\nabla_{\mathrm{t}} \Phi_q(z, x)\,, \tag{D.50}$$

which satisfies the Laplace equation

$$\nabla_{\mathrm{t}} \cdot \nabla_{\mathrm{t}} \Phi_q = 0\,. \tag{D.51}$$

Comparing (D.51) to the Helmholtz equation (D.36) confirms that these TEM modes have no cut-off frequency i.e., $k_c = 0$.

For each mode $q$ corresponding to the $q$-th conductor, the scalar potential is approximated by pyramidal basis functions

$$\Phi_q \simeq \tilde{\Phi}_q = \sum_i \alpha_i \Lambda_i + \sum_n \Lambda_n \,, \tag{D.52}$$

where the orders $i$ represent all the vertices that do not lie on any contour, whereas $n$ represents all the vertices that lie on the contour of the $q$-th conductor. Indeed, the scalar potential $\Phi_q$ is zero on all contours, except on the $q$-th conductor, where the potential can be taken as one without loss of generality.

The Laplace equation (D.51) can be tested similarly to (D.39), except that only test functions associated to inner nodes are considered. Gauss's theorem (D.40) is applied as well, and the contour integral vanishes on the contour, because the test functions of the inner nodes are all null on the contours. After inserting the basis decomposition (D.52), each test function $j$ yields

$$\sum_i \alpha_i \iint_S \nabla_\mathrm{t}\Lambda_j \cdot \nabla_\mathrm{t}\Lambda_i \mathrm{d}s = -\sum_n \iint_S \nabla_\mathrm{t}\Lambda_j \cdot \nabla_\mathrm{t}\Lambda_n \mathrm{d}s \,. \tag{D.53}$$

where both $i$ and $j$ represent inner vertices, whereas the orders $n$ represent vertices of the $q$-th contour. This corresponds to matrix equation

$$\underline{\boldsymbol{R}}\boldsymbol{\alpha} = \boldsymbol{b} \,. \tag{D.54}$$

The matrix $\underline{\boldsymbol{R}}$ is like in (D.43), with vertices that are on none of the contours. Each coefficient of the vector $\boldsymbol{b}$ correspond to one of these inner vertices, but it contains a sum over the vertices of the $q$-th conductor contour. Equation (D.54) can be solved for the field coefficients $\boldsymbol{\alpha}$ by a simple matrix inversion.

# Appendix E

# Details to the analysis of the quasi-static properties of glide-symmetric waveguides

## E.1 Constitutive parameter retrieval from the S-parameters

In this appendix, the goal is to validate the constitutive parameter retrieval from the S-parameters of a waveguide, as described in [191]. In order to do so, we consider the simple case of a dielectric parallel-plate waveguide (PPW) of length $L$, height $h$ and width $w$. The effective relative permeability $\mu_\mathrm{r}$ and permittivity $\epsilon_\mathrm{r}$ are known in the reference simulation, but the S-parameter study does not make use of this information and should retrieve the same values.

The waveguide is modeled in the frequency solver of CST Microwave Studio. Two waveguide ports are placed at each end of the waveguide, fitting the waveguide dimensions ($h$,$w$). After running the simulation, at each frequency $f$, three values are obtained : the port impedance $Z_\mathrm{p}$, and the S-parameters $S_{21}$ and $S_{11}$. According to [191], this is enough to retrieve the effective relative permeability $\mu_\mathrm{r}$ and permittivity $\epsilon_\mathrm{r}$.

**Retrieval of impedance and effective refractive index** From [191, eq. 2a], the normalized impedance is computed as

$$z = \pm\sqrt{\frac{(1+S_{11})^2 - S_{21}^2}{(1-S_{11})^2 - S_{21}^2}}\,, \tag{E.1}$$

where the sign is conditioned by $\mathrm{Re}\{z\} \geq 0$.

Once $z$ is found, the effective phaseshift between the two ports is [191, eq. 6]

$$\mathrm{e}^{-\mathrm{j}nk_0L} = \frac{S_{21}}{1 - S_{11}\frac{z-1}{z+1}}\,, \tag{E.2}$$

Table E.1: Values of $\mathrm{Re}\{n\}$ obtained by applying (E.3) to different values of $m$.

| m | -3 | -2 | -1 | 0 | 1 | 2 | 3 |
|---|---|---|---|---|---|---|---|
| $L = 5\,\mathrm{mm}$ | -14.69 | -9.70 | -4.70 | 0.30 | **5.29** | 10.29 | 15.29 |
| $L = 3\,\mathrm{mm}$ | -28.02 | -19.69 | -11.36 | -3.03 | **5.29** | 13.62 | 21.94 |

where $k_0 = 2\pi f\sqrt{\epsilon_0\mu_0}$ is the free-space wavenumber, with vacuum permittivity $\epsilon_0$ and permeability $\mu_0$. Note that for a matched waveguide, $S_{11} = 0$, therefore $z = 1$, and $\mathrm{e}^{-\mathrm{j}nk_0L} = S_{21}$. [1]

As an example, a dielectric slab of length $L = 5\,\mathrm{mm}$ is simulated in CST with $\mu_\mathrm{r} = 7$ and $\epsilon_\mathrm{r} = 4$, hence $n = 5.29$. At $f = 12\,\mathrm{GHz}$, we measure $S_{11} = 0$ and $S_{21} = 0.931 - \mathrm{j}0.364$. Computing the phaseshift shows that $\mathrm{e}^{-\mathrm{j}nk_0L} = S_{21}$, with a minus sign. Here, there is no need to consider $S_{11}$ and $S_{21}$ as functions of frequency, because of the non-dispersive nature of the ideal dielectric PPW.

The effective refractive index is computed as

$$n = \frac{1}{k_0 L}\left(-\mathrm{Im}\left\{\mathrm{e}^{-\mathrm{j}nk_0L}\right\} + 2\pi m + \mathrm{jRe}\left\{\mathrm{e}^{-\mathrm{j}nk_0L}\right\}\right), \tag{E.3}$$

where $m \in \mathbb{Z}$ defines the branch point for the real part of $n$. In order for the correct $m$ to be chosen, the simulations must be run for two different lengths $L$ [244]. The correct value of $m$ yields the same refractive index $n$ that is a candidate for both lengths. Using the same example as before, the different values of $\mathrm{Re}\{n\}$ depending on $m$ are listed in Table E.1, for lengths $L = 5\,\mathrm{mm}$, and for $L = 3\,\mathrm{mm}$. It appears that the common refractive index $\mathrm{Re}\{n\} = 5.29$ is obtained for $m = 1$.

When using (E.2) in (E.3), the refractive index $n$ is obtained from the previously computed impedance $z$. According to [191], correctly choosing the sign of $z$ enforces $\mathrm{Im}\{n\} \leq 0$, as required by passive structures.

**Retrieval of permittivity and permeability** For a homogeneous slab of height $h$ and width $w$, the constitutive parameters are related to the impedance and the effective refractive index as

$$\mu_\mathrm{r} = n\left(z\frac{Z_\mathrm{p}w}{\eta_0 h}\right) \quad \text{and} \quad \epsilon_\mathrm{r} = n\Big/\left(z\frac{Z_\mathrm{p}w}{\eta_0 h}\right), \tag{E.4}$$

with the waveguide port impedance $Z_\mathrm{p}$, and where $\eta_0 = \sqrt{\mu_0/\epsilon_0}$ is the vacuum impedance. After a CST simulation, all parameters needed in (E.4) are available. The port impedance $Z_\mathrm{p}$ is given as a function of frequency. Effective index $n$ and impedance $z$ are computed from the S-parameters as described in the previous paragraph. For a homogeneous dielectric slab, $w$ and $h$ are well-defined, and the waveguide port has the same dimensions.

[1] Contrarily to [191], the phaseshift due to propagation is defined with a minus sign in (E.2). The S-parameters yielded by CST follow the same convention, and so this minus sign must be kept if CST data is to be used as input.

## E.2 Study of the Bloch impedance for square holes

Chapter 5 derives an analytical method to compute the Bloch impedance of a holey metasurface waveguide. In this appendix, some of the underlying conditions for the validity of this Bloch impedance are derived in the case of square holes.

### E.2.1 TEM fields in the integration plane for square holes

For square holes, the Bloch impedance (5.36) is computed in the plane between two adjacent holes, that is $z_0 = a/2 - p/2$. Indeed, the fields are observed to be transverse electric magnetic (TEM) there. In this appendix, this is proven analytically for square holes, that is $a_z = a_x$ and $p_z = p_x$.

**Electric field** According to the quasi-static field expressions (5.31), and for square unit cells, the quasi-static longitudinal electric field for $s + \ell$ even is

$$E_z^{(s\ell)} = -\frac{\mathrm{j}\bar{F}^{(s\ell)} \sin\left(\mathrm{j}\Gamma^{(s\ell)} y\right)}{p^2 \sin\left(\mathrm{j}\Gamma^{(s\ell)} \frac{g}{2}\right)} \left(\frac{s2\pi}{p}\right) \bar{d}^{\mathrm{e}(s\ell)} \,. \tag{E.5}$$

In appendix D.4.1.2, the quasi-static study of waveguides with square holes shows that only a limited number of transverse magnetic (TM) modes are excited in the holes (both mode orders must be odd). For these modes, the quasi-static Fourier transforms (FTs) satisfy

$$\bar{e}_{y,m}^{\mathrm{e}(-s,\ell)} = \mathrm{e}^{\mathrm{j}\frac{s2\pi a}{p}} \bar{e}_{y,m}^{\mathrm{e}(s,\ell)} \,. \tag{E.6}$$

Therefore, according to (5.24)

$$\bar{d}^{\mathrm{e}(-s,\ell)} = \mathrm{e}^{-\mathrm{j}\frac{s2\pi a}{p}} \bar{d}^{\mathrm{e}(s,\ell)} \,. \tag{E.7}$$

When inserting (E.7) in (E.5) and evaluating $\bar{F}^{(s\ell)}$ in the plane $z_0 = a/2 - p/2$, it comes that for any position $(x, y)$,

$$E_z^{(-s,\ell)} = -E_z^{(s,\ell)} \,. \tag{E.8}$$

Therefore, when summing all harmonics, electric field components with opposite $s$ cancel out in the considered integration plane. The same applies to harmonics with $s + \ell$ odd defined in (5.34). For $s = 0$, (E.5) is obviously zero. For the fundamental harmonic, the longitudinal electric field component in (5.27) vanishes in the quasi-static regime.

**Magnetic field** The proof is similar to that of the electric field. From appendix D.4.1.2, it can be shown that the only excited transverse electric (TE) modes (with mode orders $m$ even and $q$ odd) have quasi-static FTs that satisfy

$$\bar{e}_{x,m}^{\mathrm{h}(-s,\ell)} = -\mathrm{e}^{\mathrm{j}\frac{s2\pi a}{p}} \bar{e}_{x,m}^{\mathrm{h}(s,\ell)} \;\text{ and }\; \bar{e}_{z,m}^{\mathrm{h}(-s,\ell)} = \mathrm{e}^{\mathrm{j}\frac{s2\pi a}{p}} \bar{e}_{z,m}^{\mathrm{h}(s,\ell)} \,. \tag{E.9}$$

From (5.24), this leads to

$$\vec{d}_x^{\,\mathrm{h}(s,\ell)} = -\mathrm{e}^{\mathrm{j}\frac{s2\pi a}{p}}\vec{d}_x^{\,\mathrm{h}(-s,\ell)} \text{ and } \vec{d}_z^{\,\mathrm{h}(s,\ell)} = \mathrm{e}^{\mathrm{j}\frac{s2\pi a}{p}}\vec{d}_z^{\,\mathrm{h}(-s,\ell)}\,. \tag{E.10}$$

And so, in the plane $z = a/2 - p/2$, the magnetic field components $H_z^{(s\ell)}$ in (5.31) and (5.34) cancel out for opposite orders $s$. When $s = 0$, the harmonic is null. And for the fundamental harmonic, developing the $z$-component of (5.27) shows that $H_z^{(00)}$ is proportional to $\vec{d}_x^{\,\mathrm{h}(00)}$. This term is null, because for all the excited modes (that is $q$ odd as derived in appendix D.4.1.2), $\bar{e}_{x,m}^{\mathrm{h}(00)} = 0$.

### E.2.2 Bloch voltage impact of odd-order harmonics

In chapter 5, the Bloch impedance (5.36) is simplified with two dominant hole modes in section 5.2.4. This yields the closed-form analytic expressions for the impedance (5.66) and (5.67), which can be studied to prove the effective material properties of glide-symmetric (G-S) waveguides. Nevertheless, these proofs are based on the dismissal of the odd-order harmonics in (5.67) for the non-glide-symmetric (nGS) structure, which could not be shown in the general case. But given that the notion of impedance is only defined for canonical hole shapes, this feature needs only be demonstrated in these cases. In this section, the example of square holes is considered, where numerical simulation have shown that the odd-order harmonics have no contribution to the nGS Bloch impedance.

For square holes, the term $\bar{d}_y^{\mathrm{e}(s\ell)}$ is defined in (5.24) as

$$\bar{d}^{\mathrm{e}(s\ell)} = -\mathrm{j}\sum_{q>0}\sum_{m>0}\frac{c_{qm}^{\mathrm{e}}}{k_{qm}^{\mathrm{e}}}\bar{e}_{y,qm}^{\mathrm{e}(s\ell)*}\,, \tag{E.11}$$

where each TM mode propagating in a square hole is defined by a pair of positive integers $(q, m)$. The corresponding modal FTs can be found in appendix B.3.1. It can be shown that

$$\bar{e}_{y,qm}^{\mathrm{e}(s\ell)} = \bar{e}_{y,mq}^{\mathrm{e}(\ell s)}\,. \tag{E.12}$$

Because of that, the kernel of the dispersion matrix in (5.23) is invariant when swaping the TM modes of orders $(q, m)$ and $(m, q)$. This means that $c_{qm}^{\mathrm{e}} = c_{mq}^{\mathrm{e}}$, which is not surprising when looking at the symmetry of the electric field in Fig. 5.15b. Therefore, given (E.11) and (E.12),

$$\bar{d}^{\mathrm{e}(\ell s)} = \bar{d}^{\mathrm{e}(s\ell)}\,. \tag{E.13}$$

The Bloch voltage contribution $V_{\mathrm{B}}^{(s\ell)}$ of higher-order harmonics is defined in (5.62). The term $\bar{F}^{(s\ell)}$ is evaluated at the point $(z_0, x_0) = (a/2 - p/2, a/2)$, because that is the path where the electric component $E_y$ is integrated. Hence

$$V_{\mathrm{B}}^{(s\ell)} = (-1)^s\,\frac{2}{p^2}\mathrm{e}^{-\mathrm{j}\pi\frac{a}{p}(s+\ell)}\bar{d}^{\mathrm{e}(s\ell)}\,. \tag{E.14}$$

When exchanging $s$ and $\ell$, and given (E.13), it comes that

$$V_{\mathrm{B}}^{(\ell s)} = (-1)^{\ell} \frac{2}{p^2} \mathrm{e}^{-\mathrm{j}\pi\frac{a}{p}(s+\ell)} \bar{d}^{\mathrm{e}(s\ell)} . \tag{E.15}$$

For even-order harmonics, it means that $V_{\mathrm{B}}^{(\ell s)} = V_{\mathrm{B}}^{(s\ell)}$, because $s$ and $\ell$ have the same parity. However, in the nGS case for odd-order harmonics, $s$ and $\ell$ have different parities, leading to different signs in (E.14) and (E.15). This proves that odd-order harmonic contributions cancel out in the nGS Bloch voltage, that is

$$V_{\mathrm{B}}^{(\ell s)} = -V_{\mathrm{B}}^{(s\ell)} . \tag{E.16}$$

# Appendix F

# Design considerations for the feed of the phase-shifter

Section 6.3.3 describes a rectangular waveguide (RW) to ridge gap waveguide (RGW) transition based on a staircase. Manufacturing this transition in one metallic piece is difficult, because of the very thin steps of the staircase. In spite of this, being able to get the transition in one bulk is important for the prototype performance:

- There is no leakage between the different pieces that recreate the total transition.
- There is no risk of misalignment between these pieces, which would create additional leakage at the waveguide flanges.
- The last step of the staircase has a height of 0.25 mm. The variable space between the pieces would increase the height of this step, leading to further impedance mismatch of the feed.

While the fabrication of the feed in one single metallic piece is possible, in the following the scenario of a two-piece feed is considered as a alternative solution. More specifically, some leads are given on how the leakage could be reduced between the pieces giving shape to the overall feed.

The simplest way of manufacturing the feed in two pieces would be to hollow out the staircase in one metal plate, and to close it with another plate. Nevertheless, there might be a small gap between these plates, resulting in leakage at the border of the waveguide. In order to suppress this leakage, glide-symmetric (G-S) holes are placed on both plates to create an electromagnetic bandgap (EBG) waveguide [140]. The gap between the pieces is assumed to be at most 50 µm thick. In Fig. F.1 a holey G-S unit cell is designed to yield a stopband in the Ku band with such a gap between the metallic plates. The circular holes have a period 12 mm, a radius 5.5 mm and a depth 7 mm. This structure can be used to prevent leakage between 10 and 19 GHz in all propagation directions.

Naturally, the unit cell simulated in Fig. F.1 assumes periodic boundary conditions, and so it is not sure if one row of holes will prevent leakage efficiently. In Fig. F.2, a

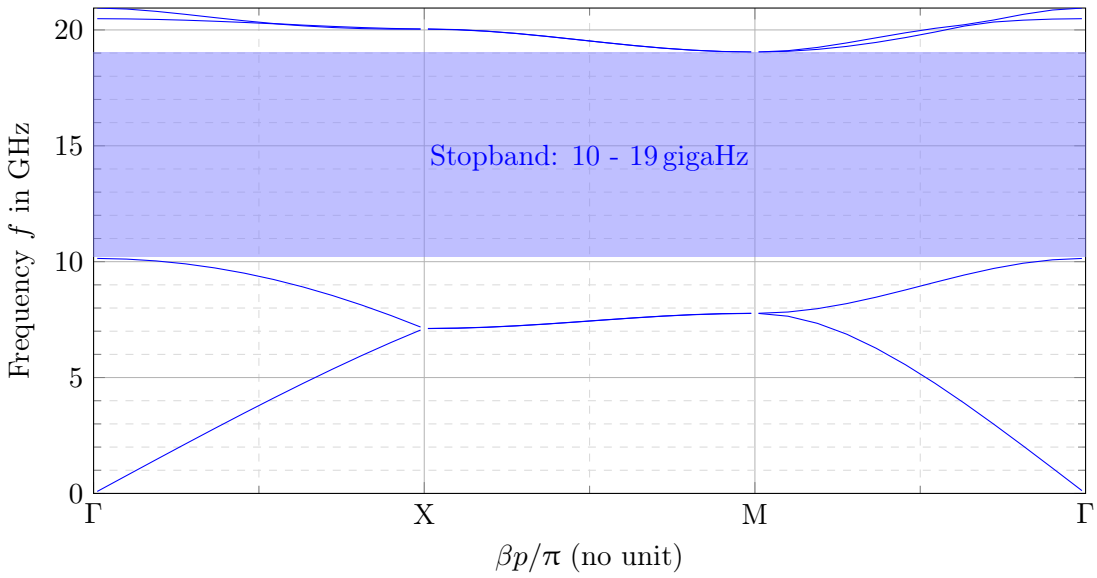


Figure F.1: Brillouin diagram of the EBG unit cell with G-S holes in metallic plates. The gap between the plates is 50 µm. The holes have a period 12 mm, a radius 5.5 mm and a depth 7 mm.

WR62 RW of length 60 mm is simulated in CST. It is built in two pieces, separated by a leakage gap of 50 µm. Fig. F.2b shows how the fields leak when no additional measures are taken, resulting in poor transmission performances in Fig. F.2f. In Fig. F.3c, one row of the G-S holes (as described in Fig. F.1) are added on either side of the waveguide. It appears that one row of holes is enough to prevent lateral leakage. Nevertheless, the corresponding S-parameters are not satisfactory, because the space between the holes and the waveguide create additional resonances which deteriorate the impedance matching of the waveguide, as seen in Fig. F.2e. This phenomenon is first described in [146], where a multi-layer transmission line is designed with G-S EBG holes between the layers. In order to avoid these resonances, it is suggested to add thin corrugations between the waveguide and the holes, to prevent the propagation of waves there. A similar design is developed in [149], for a filter and a phase-shifter in gap-waveguide technology with G-S holes, or in [215] for a reconfigurable phase-shifter. Indeed, in Fig. F.2 it appears that holes with corrugations not only prevent lateral leakage, but they also restore the impedance matching of the waveguide.

The same concept is applied to the phase-shifter feed in Fig. F.3. One side of the metallic bulk contains the staircase, the corrugations, and one row of holes on each waveguide side. This side is closed by the second metallic plate, in which only the G-S holes are drilled. In order to maximize the performance, the corrugation sized are optimized, yielding a width 1.22 mm, a depth 1.38 mm and a length 4.05 mm. It appears that holes with corrugations considerably improve the performance of the feed compared

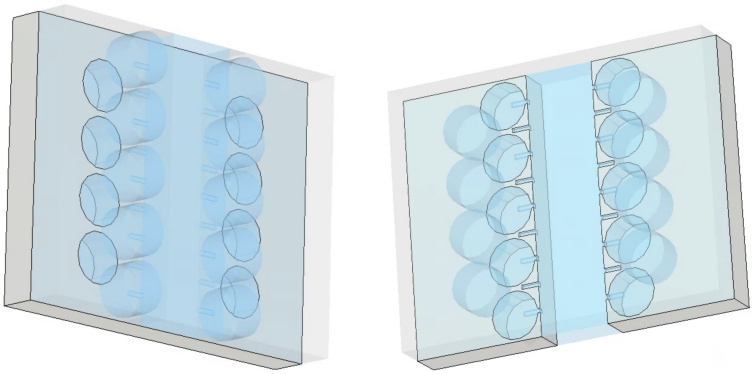

(a) Both pieces of the waveguide, with holes and corrugations.

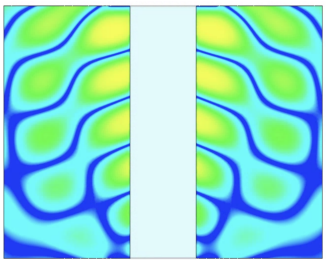

(b) Magnitude of the electric field in the leakage plane, without holes.

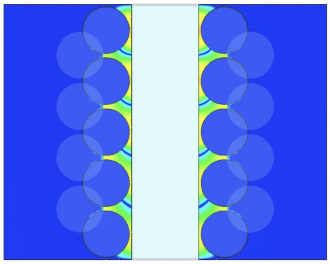

(c) Magnitude of the electric field in the leakage plane, with holes.

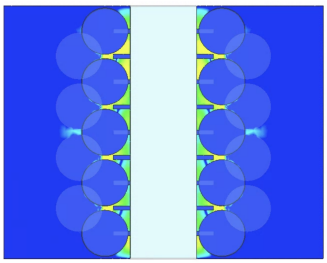

(d) Magnitude of the electric field in the leakage plane, with holes and corrugations.

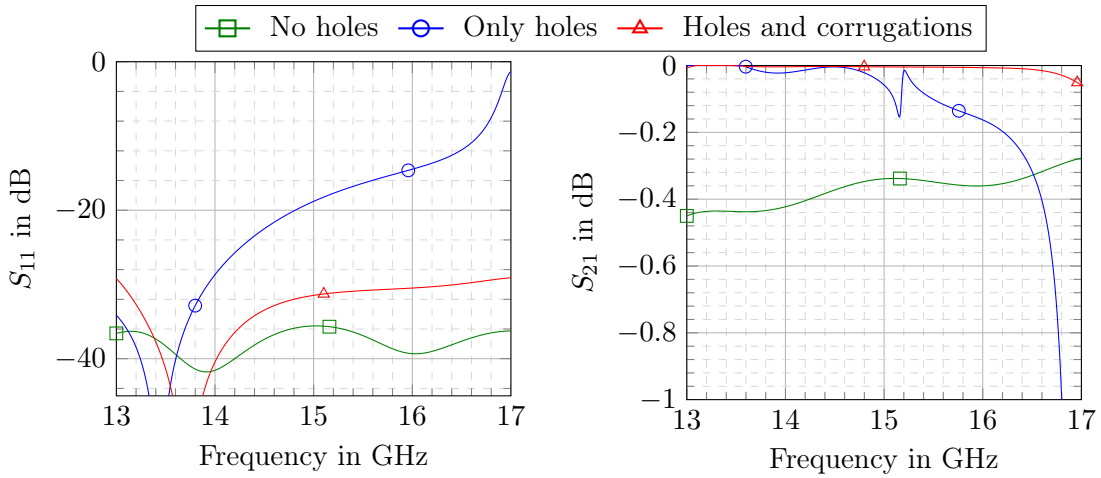


(e) Resulting $S_{11}$.

(f) Resulting $S_{21}$.

Figure F.2: Study of the leakage in a RW made of two pieces with cross-section of $7.9 \times 15.8\,\text{mm}$ and length of 60 mm. The leakage gap is of 50 µm. The G-S holes have a period 12 mm, a radius 5.5 mm and a depth 7 mm. The corrugations are $1 \times 1 \times 4\,\text{mm}$ big.

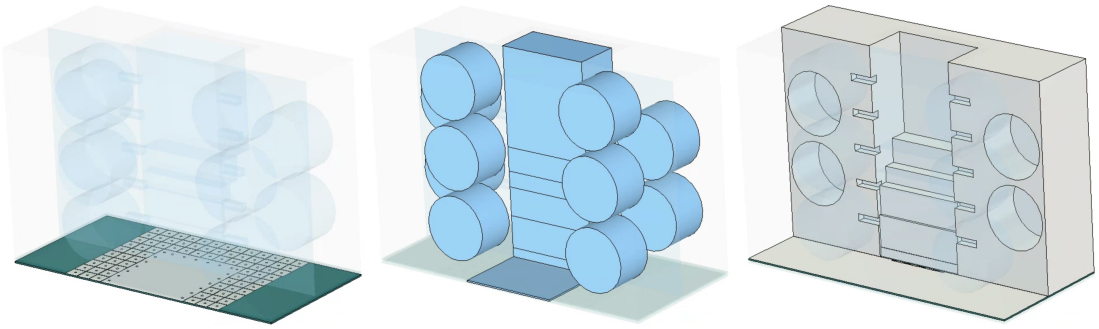

(a) Feed model in CST, with holes and corrugations.

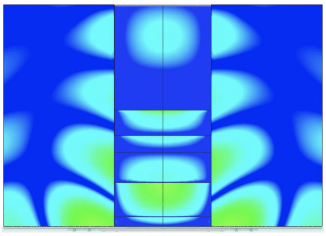

(b) Magnitude of the electric field in the leakage plane, without holes.

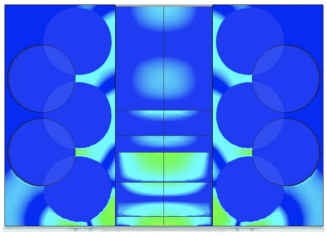

(c) Magnitude of the electric field in the leakage plane, with holes.

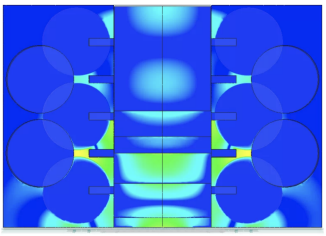

(d) Magnitude of the electric field in the leakage plane, with holes and corrugations.

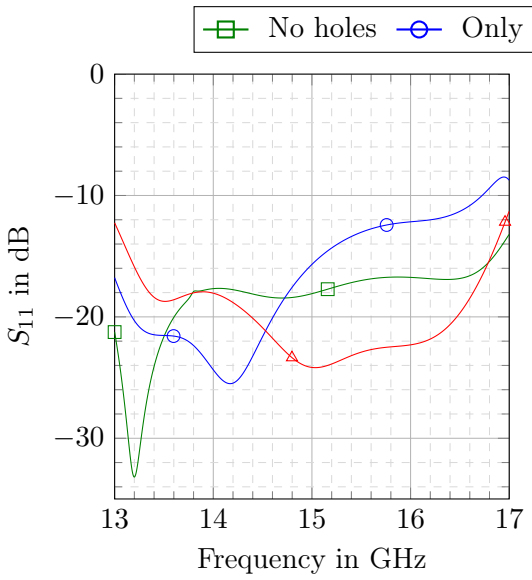


(e) Resulting $S_{11}$.

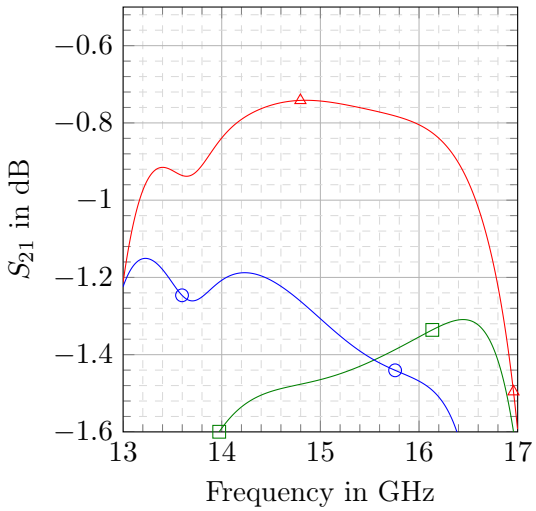


(f) Resulting $S_{21}$.

Figure F.3: Study of the lateral leakage for the same feed as in Fig. 6.3.3, except for a 50 µm gap between the two pieces of the staircase. Rows of G-S holes are added with period 12 mm, radius 5.5 mm and depth 7 mm. The corrugations have a width 1.22 mm, a depth 1.38 mm and a length 4.05 mm.

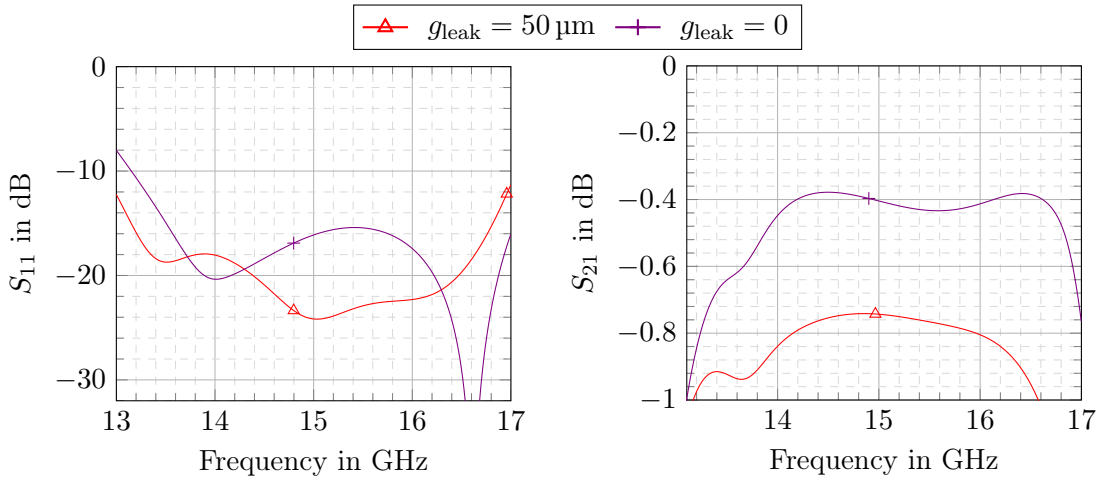


(a) (b)

Figure F.4: S-parameters of the same feed as in Fig. F.3, with holes and corrugations to prevent leakage. Two scenarios are compared: the gap between the feed pieces is 50 µm, or there is no gap at all.

to the other cases (no holes or no corrugations), in terms of both impedance matching and transmission coefficient.

Nevertheless, the transmission is not as good as without leakage in Fig. 6.31, where $S_{21} = -0.3\,\text{dB}$. The reason is visible in Fig. F.3d: it appears that in spite of the EBG holes, the presence of the metallized substrate-integrated hole (SIH) layer creates a tunnel at the lower end of the feed, through which the waves escape. Moreover, another issue comes from the unpredictability of the leakage gap. Fig. F.4 compares the S-parameter of the structure with and without leakage gap, when the holes and corrugations are present. It shows that the corrugations and the holes deteriorate the initial performance of the feed in terms of impedance matching, even when there is no gap and no leakage. Therefore, although this design is still our best option at hand against leakage at the staircase transition, it would definitely be best to manufacture this feed in one piece.

Nonetheless, even if the feed is manufactured in one piece, there might still be leakage at the waveguide flanges. For example, EBG mushrooms could be embedded in the upper SIH layer, facing towards the feed on both sides of the feeding slot. Unfortunately, simulations to suppress this leakage were unsatisfactory, because of the strong dependency on the leakage gap for the impedance matching of the feed. Therefore, no further alterations are made to the design for now, with the hope that assembling the feeds firmly together will reduce this leakage enough during measurements.

# Notations, conventions and acronyms

## Mathematical notations

In this report, following mathematical symbols and conventions are found:

- j is the imaginary number such that $\sqrt{-1} = \mathrm{j}$. The complex conjugate of a number $z$ is written $z^*$. Its absolute value is defined as $|z| = zz^*$.
- The Kronecker symbol is defined as $\delta_{ij}$, and is equal to 1 for $i = j$ and zero otherwise.
- Bessel functions of the first kind and order $q$ are written $J_q$, with first-order derivative $J'_q$ and second-order derivative $J''_q$.
- For simplicity, the notation of infinite sums is reduced to $\sum_{s,\ell}$, which is equivalent to the double sum $\sum_{s=-\infty}^{\infty} \sum_{\ell=-\infty}^{\infty}$.
- Vectors are represented by bold letters. Unless specified, column vectors are meant. The $m$-th coefficient of a vector $\boldsymbol{a}$ is written $a_m$.
- Matrices are also bold, but are always uppercase and underlined, e.g., $\underline{\boldsymbol{M}}$. The determinant of the matrix is $|\underline{\boldsymbol{M}}|$. The transpose matrix is written $\underline{\boldsymbol{M}}^{\mathrm{T}}$, while its hermitian is written $\underline{\boldsymbol{M}}^{\mathrm{H}}$. The coefficients of the matrix are written $M_{qm}$, with two integer subscripts $q$ and $m$, meaning that this coefficient lies at the intersection of the $q$-th row and the $m$-th column of the matrix.
- Matrix and dot products are represented by the center point $\cdot$. The vector cross-product is written $\times$.
- The nabla operator $\nabla$ can be found in its two-dimensional form. It is then written $\nabla_{\mathrm{t}}$, with t standing for *transverse*, given that it is applied to the transverse components of the considered field.

## Physical notations

Writing choices for physical values are clarified as they are introduced. However, a few underlying and recurring notations are notable:

- The subscript zero is used to designate vacuum-related values, e.g., the vacuum permittivity $\epsilon_0$ or speed of light in vacuum $c_0$.
- In waveguides, a non-italic superscript is used to distinguish different mode types: e for transverse magnetic (TM) modes, h for transverse electric (TE) modes, and t for transverse electric magnetic (TEM) modes. Moreover, the subscript indicates the field component, e.g., $x$, $y$, or $z$ in a cartesian coordinate system, or t for the transverse field component.
- The letter $k$ is used for wavenumbers. In particular, in holey parallel-plate waveguides (PPWs), the wavenumbers of the modes in the holes are written differently from the wavenumbers of the Floquet harmonics in the gap between the metasurfaces. In the holes, the modes have orders which are described by the integer variables $m$ (and/or $q$, depending on the number of orders necessary), and are indicated as a subscript. For example, $k_m^{\mathrm{e}}$ is the wavenumber of the $m$-th TM mode in the holes. On the other hand, for Floquet harmonics, integer orders $s$ (and/or $\ell$ in the two-dimensional case) are written in parenthesis as a superscript, e.g., $k_z^{(s\ell)}$ designates the wavenumber of the Floquet harmonic of orders $s$ and $\ell$ along the $z$-axis. When primed variables are used, such as $s'$ or $m'$, it is only to extend the available range of integer variables.
- In the mode-matching method used in chapters 2 to 5, the projections of the hole modes onto the Floquet harmonics is used, called projected modal functions (PMFs). A modal function of order $m$ is written $e_{z,m}^{\mathrm{i}}$, where i is the mode type, and the field direction is indicated by the first subscript (here $z$ as an example). Then, its PMF onto the Floquet harmonic of orders $(s, \ell)$ is written $\tilde{e}_{z,m}^{\mathrm{i}(s\ell)}$, where the tilde indicates the spectral domain. In chapter 4, the homogenization process involves quasi-static PMFs, which are then written with a bar instead of a tilde, e.g., $\bar{e}_{z,m}^{\mathrm{i}(s\ell)}$.
- The underlying time-convention used for time-harmonic fields of angular frequency $\omega$ is $\mathrm{e}^{\mathrm{j}\omega t}$.

## Acronyms

**1-D** one-dimensional

**2-D** two-dimensional

**3-D** three-dimensional

**EBG** electromagnetic bandgap

**EM** electromagnetic

**FEM** finite element method

**FFT** fast Fourier transform

**FSS** frequency-selective surface

**FT** Fourier transform

**G-S** glide-symmetric

**GS** glide symmetry

**HIS** high-impedance surface

**IoT** internet of things

**LWA** leaky-wave antenna

**MMM** mode-matching method

**MMTM** multi-modal transfer matrix

**MoM** method of moments

**nGS** non-glide-symmetric

**PEC** perfectly electrically conducting

**PMC** perfectly magnetically conducting

**PMF** projected modal function

**PPW** parallel-plate waveguide

**RGW** ridge gap waveguide

**RW** rectangular waveguide

**SG** symétrie glissée

**SIH** substrate-integrated hole

**SIW** substrate-integrated waveguide

**SMTM** single-mode transfer matrix

**SPP** surface plasmon polariton

**TE** transverse electric

**TEM** transverse electric magnetic

**TM** transverse magnetic

# References


[1] T. Yilmaz and O. B. Akan, "On the use of the millimeter wave and low terahertz bands for Internet of Things", in *2015 IEEE 2nd World Forum on Internet of Things (WF-IoT)*, Dec. 2015, pp. 177–180.

[2] Y. Wang, Z. Zhang, P. Zhang, Z. Ma, and G. Liu, "A new cloud-based network framework for 5G massive Internet of Things connections", in *2017 IEEE 17th International Conference on Communication Technology (ICCT)*, ISSN: 2576-7828, Oct. 2017, pp. 412–416.

[3] L. Kong, M. K. Khan, F. Wu, G. Chen, and P. Zeng, "Millimeter-Wave Wireless Communications for IoT-Cloud Supported Autonomous Vehicles: Overview, Design, and Challenges", *IEEE Communications Magazine*, vol. 55, no. 1, pp. 62–68, Jan. 2017, Conference Name: IEEE Communications Magazine.

[4] H. Wymeersch, J. He, B. Denis, A. Clemente, and M. Juntti, "Radio Localization and Mapping With Reconfigurable Intelligent Surfaces: Challenges, Opportunities, and Research Directions", *IEEE Vehicular Technology Magazine*, vol. 15, no. 4, pp. 52–61, Dec. 2020, Conference Name: IEEE Vehicular Technology Magazine.

[5] K. Sakaguchi, T. Haustein, S. Barbarossa, E. C. Strinati, A. Clemente, G. Destino, A. Pärssinen, I. Kim, H. Chung, J. Kim, W. Keusgen, R. J. Weiler, K. Takinami, E. Ceci, A. Sadri, L. Xian, A. Maltsev, G. K. Tran, H. Ogawa, K. Mahler, and R. W. H. Jr, "Where, When, and How mmWave is Used in 5G and Beyond", *IEICE TRANSACTIONS on Electronics*, vol. E100-C, no. 10, pp. 790–808, Oct. 2017, Publisher: The Institute of Electronics, Information and Communication Engineers.

[6] H. Magsi, A. H. Sodhro, F. A. Chachar, S. A. K. Abro, G. H. Sodhro, and S. Pirbhulal, "Evolution of 5G in Internet of medical things", in *2018 International Conference on Computing, Mathematics and Engineering Technologies (iCoMET)*, Mar. 2018, pp. 1–7.

[7] S. K. Rao and R. Prasad, "Impact of 5G Technologies on Smart City Implementation", *Wireless Personal Communications*, vol. 100, no. 1, pp. 161–176, May 2018.

[8] H. Dai, Z. Zheng, and Y. Zhang, "Blockchain for Internet of Things: A Survey", *IEEE Internet of Things Journal*, vol. 6, no. 5, pp. 8076–8094, Oct. 2019, Conference Name: IEEE Internet of Things Journal.

[9] S. W. Asmar, *Radio science techniques for deep space exploration*, ser. JPL deep-space communications and navigation series. Hoboken, NJ, USA: John Wiley & Sons, 2022.

[10] X. Li, J. Wang, G. Goussetis, and L. Wang, "Circularly Polarized High Gain Leaky-Wave Antenna for CubeSat Communication", *IEEE Transactions on Antennas and Propagation*, pp. 1–1, 2022, Conference Name: IEEE Transactions on Antennas and Propagation.

[11] Y. Wang, J. Li, L. Huang, Y. Jing, A. Georgakopoulos, and P. Demestichas, "5G Mobile: Spectrum Broadening to Higher-Frequency Bands to Support High Data Rates", *IEEE Vehicular Technology Magazine*, vol. 9, no. 3, pp. 39–46, Sep. 2014, Conference Name: IEEE Vehicular Technology Magazine.

[12] T. S. Rappaport, S. Sun, R. Mayzus, H. Zhao, Y. Azar, K. Wang, G. N. Wong, J. K. Schulz, M. Samimi, and F. Gutierrez, "Millimeter Wave Mobile Communications for 5G Cellular: It Will Work!", *IEEE Access*, vol. 1, pp. 335–349, 2013, Conference Name: IEEE Access.

[13] P. Yang, Y. Xiao, M. Xiao, and S. Li, "6G Wireless Communications: Vision and Potential Techniques", *IEEE Network*, vol. 33, no. 4, pp. 70–75, Jul. 2019, Conference Name: IEEE Network.

[14] M. Giordani, M. Polese, M. Mezzavilla, S. Rangan, and M. Zorzi, "Toward 6G Networks: Use Cases and Technologies", *IEEE Communications Magazine*, vol. 58, no. 3, pp. 55–61, Mar. 2020, Conference Name: IEEE Communications Magazine.

[15] E. C. Strinati, G. C. Alexandropoulos, H. Wymeersch, B. Denis, V. Sciancalepore, R. D'Errico, A. Clemente, D.-T. Phan-Huy, E. De Carvalho, and P. Popovski, "Reconfigurable, Intelligent, and Sustainable Wireless Environments for 6G Smart Connectivity", *IEEE Communications Magazine*, vol. 59, no. 10, pp. 99–105, Oct. 2021, Conference Name: IEEE Communications Magazine.

[16] H. Cui, J. Zhang, Y. Geng, Z. Xiao, T. Sun, N. Zhang, J. Liu, Q. Wu, and X. Cao, "Space-air-ground integrated network (SAGIN) for 6G: Requirements, architecture and challenges", *China Communications*, vol. 19, no. 2, pp. 90–108, Feb. 2022, Conference Name: China Communications.

[17] D. M. Pozar, *Microwave Engineering*, 4th ed. Hoboken, NJ: John Wiley & Sons, Dec. 2011, tex.ids: pozarMicrowaveEngineering2011a, pozarMicrowaveEngineering2011b, pozarMicrowaveEngineering2012.

[18] A. De Domenico, R. Gerzaguet, N. Cassiau, A. Clemente, R. D'Errico, C. Dehos, J. L. Gonzalez, D. Ktenas, L. Manat, V. Savin, and A. Siligaris, "Making 5G Millimeter-Wave Communications a Reality [Industry Perspectives]", *IEEE Wireless Communications*, vol. 24, no. 4, pp. 4–9, Aug. 2017, Conference Name: IEEE Wireless Communications.

[19] W. Chen, Y. Hsieh, C. Tsai, Y. Chen, C. Chang, and S. Chang, "A compact two-dimensional phased array using grounded coplanar-waveguides butler matrices", in *2012 42nd European Microwave Conference*, tex.ids: chenCompactTwodimensionalPhased2012, Oct. 2012, pp. 747–750.

[20] O. Quevedo-Teruel, M. Ebrahimpouri, and F. Ghasemifard, "Lens Antennas for 5G Communications Systems", *IEEE Communications Magazine*, vol. 56, no. 7, pp. 36–41, Jul. 2018, tex.ids= quevedo-teruelLensAntennas5G2018a, quevedo-teruelLensAntennas5G2018b conferenceName: IEEE Communications Magazine.

[21] B. Fuchs, O. Lafond, S. Rondineau, M. Himdi, and L. L. Coq, "Off-Axis Performances of Half Maxwell Fish-Eye Lens Antennas at 77 GHz", *IEEE Transactions on Antennas and Propagation*, vol. 55, no. 2, pp. 479–482, Feb. 2007, Conference Name: IEEE Transactions on Antennas and Propagation.

[22] A. Demetriadou and Y. Hao, "A Grounded Slim Luneburg Lens Antenna Based on Transformation Electromagnetics", *IEEE Antennas and Wireless Propagation Letters*, vol. 10, pp. 1590–1593, 2011, Conference Name: IEEE Antennas and Wireless Propagation Letters.

[23] J. Thornton, D. Smith, S. J. Foti, and Y. Y. Jiang, "Reduced height Luneburg lens antennas for satellite communications-on-the-move", in *2015 Conference on Microwave Techniques (COMITE)*, Apr. 2015, pp. 1–4.

[24] K. Sato and H. Ujiie, "A plate Luneberg lens with the permittivity distribution controlled by hole density", *Electronics and Communications in Japan (Part I: Communications)*, vol. 85, no. 9, pp. 1–12, 2002, _eprint: https://onlinelibrary.wiley.com/doi/pdf/10.1002/ecja.1120.

[25] J.-M. Poyanco, F. Pizarro, and E. Rajo-Iglesias, "Cost-effective wideband dielectric planar lens antenna for millimeter wave applications", en, *Scientific Reports*, vol. 12, no. 1, p. 4204, Mar. 2022, Number: 1 Publisher: Nature Publishing Group.

[26] C. L. Holloway, E. F. Kuester, J. A. Gordon, J. O'Hara, J. Booth, and D. R. Smith, "An Overview of the Theory and Applications of Metasurfaces: The Two-Dimensional Equivalents of Metamaterials", *IEEE Antennas and Propagation Magazine*, vol. 54, no. 2, pp. 10–35, Apr. 2012, Conference Name: IEEE Antennas and Propagation Magazine.

[27] A. Alex-Amor, Á. Palomares-Caballero, and C. Molero, "3-D Metamaterials: Trends on Applied Designs, Computational Methods and Fabrication Techniques", en, *Electronics*, vol. 11, no. 3, p. 410, Jan. 2022, Number: 3 Publisher: Multidisciplinary Digital Publishing Institute.

[28] L. Xue and V. F. Fusco, "Printed holey plate Luneburg lens", *Microwave and Optical Technology Letters*, vol. 50, no. 2, pp. 378–380, 2008, _eprint: https://onlinelibrary.wiley.com/doi/pdf/10.1002/mop.23087.

[29] M. Bosiljevac, M. Casaletti, F. Caminita, Z. Sipus, and S. Maci, "Non-Uniform Metasurface Luneburg Lens Antenna Design", *IEEE Transactions on Antennas and Propagation*, vol. 60, no. 9, pp. 4065–4073, Sep. 2012, Conference Name: IEEE Transactions on Antennas and Propagation.

[30] J. A. Dockrey, M. J. Lockyear, S. J. Berry, S. A. R. Horsley, J. R. Sambles, and A. P. Hibbins, "Thin metamaterial Luneburg lens for surface waves", *Physical Review B*, vol. 87, no. 12, p. 125 137, Mar. 2013, Publisher: American Physical Society.

[31] M. Huang, S. Yang, F. Gao, R. Quarfoth, and D. Sievenpiper, "A 2-D Multibeam Half Maxwell Fish-Eye Lens Antenna Using High Impedance Surfaces", *IEEE Antennas and Wireless Propagation Letters*, vol. 13, pp. 365–368, 2014, Conference Name: IEEE Antennas and Wireless Propagation Letters.

[32] O. Dahlberg, R. C. Mitchell-Thomas, and O. Quevedo-Teruel, "Reducing the Dispersion of Periodic Structures with Twist and Polar Glide Symmetries", *Scientific Reports*, vol. 7, no. 1, pp. 1–6, Aug. 2017, tex.ids= dahlbergReducingDispersionPeriodic2017a, dahlbergReducingDispersionPeriodic2017b number: 1 publisher: Nature Publishing Group.

[33] O. Quevedo-Teruel, M. Ebrahimpouri, and M. N. M. Kehn, "Ultrawideband Metasurface Lenses Based on Off-Shifted Opposite Layers", *IEEE Antennas and Wireless Propagation Letters*, vol. 15, pp. 484–487, Dec. 2016, tex.ids: quevedo-teruelUltrawidebandMetasurfaceLenses2016a, quevedo-teruelUltrawidebandMetasurfaceLenses2016b.

[34] A. Alex-Amor, G. Valerio, F. Ghasemifard, F. Mesa, P. Padilla, J. M. Fernández-González, and O. Quevedo-Teruel, "Wave Propagation in Periodic Metallic Structures with Equilateral Triangular Holes", *Applied Sciences*, vol. 10, no. 5, p. 1600, Jan. 2020, tex.ids= alex-amorWavePropagationPeriodic2020a number: 5 publisher: Multidisciplinary Digital Publishing Institute.

[35] M. Ebrahimpouri and O. Quevedo-Teruel, "Ultrawideband Anisotropic Glide-Symmetric Metasurfaces", *IEEE Antennas and Wireless Propagation Letters*, vol. 18, no. 8, pp. 1547–1551, Aug. 2019, tex.ids= ebrahimpouriUltrawidebandAnisotropicGlideSymmetric2019a conferenceName: IEEE Antennas and Wireless Propagation Letters.

[36] A. Palomares-Caballero, A. Alex-Amor, P. Padilla, F. Luna, and J. Valenzuela-Valdes, "Compact and Low-Loss V-Band Waveguide Phase Shifter Based on Glide-Symmetric Pin Configuration", *IEEE Access*, vol. 7, pp. 31 297–31 304, 2019, tex.ids= palomares-caballeroCompactLowLossVBand2019a conferenceName: IEEE Access.

[37] M. Ebrahimpouri, E. Rajo-Iglesias, Z. Sipus, and O. Quevedo-Teruel, "Cost-Effective Gap Waveguide Technology Based on Glide-Symmetric Holey EBG Structures", *IEEE Transactions on Microwave Theory and Techniques*, vol. 66, no. 2, pp. 927–934, Feb. 2018, tex.ids= ebrahimpouriCostEffectiveGapWaveguide2018a, ebrahimpouriCostEffectiveGapWaveguide2018b conferenceName: IEEE Transactions on Microwave Theory and Techniques.

[38] P. J. Crepeau and P. R. McIsaac, "Consequences of symmetry in periodic structures", *Proceedings of the IEEE*, vol. 52, no. 1, pp. 33–43, Jan. 1964, tex.ids: crepeauConsequencesSymmetryPeriodic1964a, crepeauConsequencesSymmetryPeriodic1964b.

[39] R. Mittra and S. Laxpati, "Propagation in a Wave Guide with Glide Reflection Symmetry", *Canadian Journal of Physics*, vol. 43, no. 2, pp. 353–372, Feb. 1965, tex.ids: mittraPropagationWaveGuide1965a, mittraPropagationWaveGuide1965b.

[40] A. Hessel and A. Oliner, "Basic properties of periodic waveguides with glide reflection symmetry", in *Electromagnetic wave theory, proceedings of a symposium held at Delft, the Netherlands, September 1965 Part 1*, J. Brown, Ed., OCLC: 893431115 tex.ids: hesselBasicPropertiesPeriodic1967, hesselBasicPropertiesPeriodic1967b, New York, Pergamon, 1967, pp. 251–260.

[41] G. Valerio, Z. Sipus, A. Grbic, and O. Quevedo-Teruel, "Accurate Equivalent-Circuit Descriptions of Thin Glide-Symmetric Corrugated Metasurfaces", *IEEE Transactions on Antennas and Propagation*, vol. 65, no. 5, pp. 2695–2700, May 2017, tex.ids= valerioAccurateEquivalentCircuitDescriptions2017a, valerioAccurateEquivalentCircuitDescriptions2017b conferenceName: IEEE Transactions on Antennas and Propagation.

[42] F. Ghasemifard, M. Norgren, and O. Quevedo-Teruel, "Dispersion Analysis of 2-D Glide-Symmetric Corrugated Metasurfaces Using Mode-Matching Technique", *IEEE Microwave and Wireless Components Letters*, vol. 28, no. 1, pp. 1–3, Jan. 2018, tex.ids= ghasemifardDispersionAnalysis2D2018a, ghasemifardDispersionAnalysis2D2018b conferenceName: IEEE Microwave and Wireless Components Letters.

[43] M. Bagheriasl, O. Quevedo-Teruel, and G. Valerio, "Bloch Analysis of Artificial Lines and Surfaces Exhibiting Glide Symmetry", *IEEE Transactions on Microwave Theory and Techniques*, vol. 67, no. 7, pp. 2618–2628, Jul. 2019, tex.ids= bagheriaslBlochAnalysisArtificial2019a, bagheriaslBlochAnalysisArtificial2019b conferenceName: IEEE Transactions on Microwave Theory and Techniques.

[44] M. Ebrahimpouri, L. F. Herran, and O. Quevedo-Teruel, "Wide-Angle Impedance Matching Using Glide-Symmetric Metasurfaces", *IEEE Microwave and Wireless Components Letters*, vol. 30, no. 1, pp. 8–11, Jan. 2020, tex.ids= ebrahimpouriWideAngleImpedanceMatching2020a conferenceName: IEEE Microwave and Wireless Components Letters.

[45] F. Ghasemifard, M. Norgren, O. Quevedo-Teruel, and G. Valerio, "Analyzing Glide-Symmetric Holey Metasurfaces Using a Generalized Floquet Theorem", *IEEE Access*, vol. 6, pp. 71 743–71 750, Nov. 2018, tex.ids: ghasemifardAnalyzingGlideSymmetricHoley2018a, ghasemifardAnalyzingGlideSymmetricHoley2018b, ghasemifardAnalyzingGlideSymmetricHoley2018c.

[46] J. A. Dockrey, S. a. R. Horsley, I. R. Hooper, J. R. Sambles, and A. P. Hibbins, "Direct observation of negative-index microwave surface waves", en, *Scientific Reports*, vol. 6, no. 1, p. 22 018, Feb. 2016, Number: 1 Publisher: Nature Publishing Group.

[47] M. Casaletti, G. Valerio, O. Quevedo-Teruel, and P. Burghignoli, "An overview of metasurfaces for thin antenna applications", *Comptes Rendus. Physique*, vol. 21, no. 7-8, pp. 659–676, 2020, tex.ids= casalettiOverviewMetasurfacesThin2020.

[48] J. Pendry, A. Holden, D. Robbins, and W. Stewart, "Magnetism from conductors and enhanced nonlinear phenomena", *IEEE Transactions on Microwave Theory and Techniques*, vol. 47, no. 11, pp. 2075–2084, Nov. 1999, Conference Name: IEEE Transactions on Microwave Theory and Techniques.

[49] T. Kodera, D. L. Sounas, and C. Caloz, "Artificial Faraday rotation using a ring metamaterial structure without static magnetic field", *Applied Physics Letters*, vol. 99, no. 3, p. 031 114, Jul. 2011, Publisher: American Institute of Physics.

[50] T. Chang, J. U. Kim, S. K. Kang, H. Kim, D. K. Kim, Y.-H. Lee, and J. Shin, "Broadband giant-refractive-index material based on mesoscopic space-filling curves", *Nature Communications*, vol. 7, no. 12661, Aug. 2016, tex.ids: changBroadbandGiantrefractiveindexMaterial2016a, changBroadbandGiantrefractiveindexMaterial2016b.

[51] S. B. Glybovski, S. A. Tretyakov, P. A. Belov, Y. S. Kivshar, and C. R. Simovski, "Metasurfaces: From microwaves to visible", en, *Physics Reports*, Metasurfaces: From microwaves to visible, vol. 634, pp. 1–72, May 2016.

[52] O. Quevedo-Teruel, H. Chen, A. Díaz-Rubio, G. Gok, A. Grbic, G. Minatti, E. Martini, S. Maci, G. V. Eleftheriades, M. Chen, N. I. Zheludev, N. Papasimakis, S. Choudhury, Z. A. Kudyshev, S. Saha, H. Reddy, A. Boltasseva, V. M. Shalaev, A. V. Kildishev, D. Sievenpiper, C. Caloz, A. Alù, Q. He, L. Zhou, G. Valerio, E. Rajo-Iglesias, Z. Sipus, F. Mesa, R. Rodríguez-Berral, F. Medina, V. Asadchy, S. Tretyakov, and C. Craeye, "Roadmap on metasurfaces", *Journal of Optics*, vol. 21, no. 7, p. 073 002, Jul. 2019, Publisher: IOP Publishing.

[53] R. S. Anwar, L. Mao, and H. Ning, "Frequency Selective Surfaces: A Review", en, *Applied Sciences*, vol. 8, no. 9, p. 1689, Sep. 2018, Number: 9 Publisher: Multidisciplinary Digital Publishing Institute.

[54] Y. Li, L. Li, Y. Zhang, and C. Zhao, "Design and Synthesis of Multilayer Frequency Selective Surface Based on Antenna-Filter-Antenna Using Minkowski Fractal Structures", *IEEE Transactions on Antennas and Propagation*, vol. 63, no. 1, pp. 133–141, Jan. 2015, Conference Name: IEEE Transactions on Antennas and Propagation.

[55] M. Chen, E. Abdo-Sánchez, A. Epstein, and G. V. Eleftheriades, "Theory, design, and experimental verification of a reflectionless bianisotropic Huygens' metasurface for wide-angle refraction", *Physical Review B*, vol. 97, no. 12, p. 125 433, Mar. 2018, Publisher: American Physical Society.

[56] L. Di Palma, A. Clemente, L. Dussopt, R. Sauleau, P. Potier, and P. Pouliguen, "Circularly Polarized Transmitarray With Sequential Rotation in Ka-Band", *IEEE Transactions on Antennas and Propagation*, vol. 63, no. 11, pp. 5118–5124, Nov. 2015, Conference Name: IEEE Transactions on Antennas and Propagation.

[57] D. Wang, R. Gillard, and R. Loison, "A 60GHz passive repeater array with endfire radiation based on metal groove unit-cells", in *2015 9th European Conference on Antennas and Propagation (EuCAP)*, ISSN: 2164-3342, Apr. 2015, pp. 1–4.

[58] R. Mittra, C. Chan, and T. Cwik, "Techniques for analyzing frequency selective surfaces-a review", *Proceedings of the IEEE*, vol. 76, no. 12, pp. 1593–1615, Dec. 1988, Conference Name: Proceedings of the IEEE.

[59] R. Pous and D. Pozar, "A frequency-selective surface using aperture-coupled microstrip patches", *IEEE Transactions on Antennas and Propagation*, vol. 39, no. 12, pp. 1763–1769, Dec. 1991, Conference Name: IEEE Transactions on Antennas and Propagation.

[60] C. Pfeiffer and A. Grbic, "Metamaterial Huygens' Surfaces: Tailoring Wave Fronts with Reflectionless Sheets", *Physical Review Letters*, vol. 110, no. 19, p. 197 401, May 2013, Publisher: American Physical Society.

[61] D. Cavallo, "Dissipation Losses in Artificial Dielectric Layers", *IEEE Transactions on Antennas and Propagation*, vol. 66, no. 12, pp. 7460–7465, Dec. 2018, tex.ids= cavalloDissipationLossesArtificial2018a conferenceName: IEEE Transactions on Antennas and Propagation.

[62] C. Jouanlanne, A. Clemente, M. Huchard, J. Keignart, C. Barbier, T. Le Nadan, and L. Petit, "Wideband Linearly Polarized Transmitarray Antenna for 60 GHz Backhauling", *IEEE Transactions on Antennas and Propagation*, vol. 65, no. 3, pp. 1440–1445, Mar. 2017, Conference Name: IEEE Transactions on Antennas and Propagation.

[63] K. Pham, N. T. Nguyen, A. Clemente, L. Di Palma, L. Le Coq, L. Dussopt, and R. Sauleau, "Design of Wideband Dual Linearly Polarized Transmitarray Antennas", *IEEE Transactions on Antennas and Propagation*, vol. 64, no. 5, pp. 2022–2026, May 2016, Conference Name: IEEE Transactions on Antennas and Propagation.

[64] F. Diaby, A. Clemente, K. T. Pham, R. Sauleau, and L. Dussopt, "Circularly Polarized Transmitarray Antennas at Ka-Band", *IEEE Antennas and Wireless Propagation Letters*, vol. 17, no. 7, pp. 1204–1208, Jul. 2018, Conference Name: IEEE Antennas and Wireless Propagation Letters.

[65] A. Guerra, F. Guidi, A. Clemente, R. D'Errico, L. Dussopt, and D. Dardari, "Application of transmitarray antennas for indoor mapping at millimeter-waves", in *2015 European Conference on Networks and Communications (EuCNC)*, Jun. 2015, pp. 77–81.

[66] K. T. Pham, A. Clemente, E. Fourn, F. Diaby, L. Dussopt, and R. Sauleau, "Low-Cost Metal-Only Transmitarray Antennas at Ka-Band", *IEEE Antennas and Wireless Propagation Letters*, vol. 18, no. 6, pp. 1243–1247, Jun. 2019, Conference Name: IEEE Antennas and Wireless Propagation Letters.

[67] D. Cadoret, L. Marnat, R. Loison, R. Gillard, H. Legay, and B. Salome, "A Dual Linear Polarized Printed Reflectarray using Slot Loaded Patch Elements", in *The Second European Conference on Antennas and Propagation, EuCAP 2007*, ISSN: 0537-9989, Nov. 2007, pp. 1–5.

[68] S. Gharbieh, M. García-Vigueras, R. Loison, A. Harmouch, and A. Jrad, "Design of Polarizing Cells for Broadband Reflectors", in *2019 IEEE International Symposium on Antennas and Propagation and USNC-URSI Radio Science Meeting*, ISSN: 1947-1491, Jul. 2019, pp. 467–468.

[69] H. Salti, R. Gillard, R. Loison, and L. Le Coq, "A Reflectarray Antenna Based on Multiscale Phase-Shifting Cell Concept", *IEEE Antennas and Wireless Propagation Letters*, vol. 8, pp. 363–366, 2009, Conference Name: IEEE Antennas and Wireless Propagation Letters.

[70] L. Marnat, R. Loison, R. Gillard, D. Bresciani, and H. Legay, "Accurate synthesis of a dual linearly polarized reflectarray", in *2009 3rd European Conference on Antennas and Propagation*, ISSN: 2164-3342, Mar. 2009, pp. 2523–2526.

[71] L. Moustafa, R. Gillard, F. Peris, R. Loison, H. Legay, and E. Girard, "The Phoenix Cell: A New Reflectarray Cell With Large Bandwidth and Rebirth Capabilities", *IEEE Antennas and Wireless Propagation Letters*, vol. 10, pp. 71–74, 2011, Conference Name: IEEE Antennas and Wireless Propagation Letters.

[72] L. Marnat, R. Loison, R. Gillard, D. Bresciani, and H. Legay, "Comparison of Synthesis Strategies for a Dual-Polarized Reflectarray", en, *International Journal of Antennas and Propagation*, vol. 2012, e708429, Jul. 2012, Publisher: Hindawi.

[73] C. Yann, R. Loison, R. Gillard, M. Labeyrie, and J.-P. Martinaud, "A New Approach Combining Surrounded-Element and Compression Methods for Analyzing Reconfigurable Reflectarray Antennas", *IEEE Transactions on Antennas and Propagation*, vol. 60, no. 7, pp. 3215–3221, Jul. 2012, Conference Name: IEEE Transactions on Antennas and Propagation.

[74] A. Guarriello, G. Courtin, R. Loison, and R. Gillard, "A General Equivalent Circuit Model for Phoenix Cells", *IEEE Transactions on Antennas and Propagation*, vol. 69, no. 11, pp. 7982–7986, Nov. 2021, Conference Name: IEEE Transactions on Antennas and Propagation.

[75] V. Richard, R. Loison, R. Gillard, H. Legay, and M. Romier, "Optimized Artificial Neural Network for reflectarray cell modelling", in *2016 IEEE International Symposium on Antennas and Propagation (APSURSI)*, ISSN: 1947-1491, Jun. 2016, pp. 1211–1212.

[76] V. Richard, R. Loison, R. Gillard, H. Legay, and M. Romier, "Loss analysis of a reflectarray cell using ANNs with accurate magnitude prediction", in *2017 11th European Conference on Antennas and Propagation (EUCAP)*, Mar. 2017, pp. 2396–2399.

[77] P.-Y. Chen, C. Argyropoulos, and A. Alù, "Broadening the Cloaking Bandwidth with Non-Foster Metasurfaces", *Physical Review Letters*, vol. 111, no. 23, p. 233 001, Dec. 2013, Publisher: American Physical Society.

[78] F. Bichelot, R. Loison, and L. Le Coq, "FSS-EBG antenna with improved directivity bandwidth : Theory, design and measurements", in *2007 IEEE Antennas and Propagation Society International Symposium*, ISSN: 1947-1491, Jun. 2007, pp. 5423–5426.

[79] G. Minatti, M. Faenzi, M. Sabbadini, and S. Maci, "Bandwidth of Gain in Metasurface Antennas", *IEEE Transactions on Antennas and Propagation*, vol. 65, no. 6, pp. 2836–2842, Jun. 2017, Conference Name: IEEE Transactions on Antennas and Propagation.

[80] T. M. McManus, J. A. Valiente-Kroon, S. a. R. Horsley, and Y. Hao, "Illusions and Cloaks for Surface Waves", en, *Scientific Reports*, vol. 4, no. 1, p. 5977, Aug. 2014, Number: 1 Publisher: Nature Publishing Group.

[81] C. G. King, S. A. R. Horsley, and T. G. Philbin, "Zero reflection and transmission in graded index media", en, *Journal of Optics*, vol. 19, no. 8, p. 085 603, Jul. 2017, Publisher: IOP Publishing.

[82] S. A. R. Horsley and I. R. Hooper, "One dimensional electromagnetic waves on flat surfaces", en, *Journal of Physics D: Applied Physics*, vol. 47, no. 43, p. 435 103, Oct. 2014, Publisher: IOP Publishing.

[83] O. Quevedo-Teruel, R. C. Mitchell-Thomas, T. M. McManus, S. A. R. Horsley, and Y. Hao, "Conformal surface lenses from a bed of nails", in *The 8th European Conference on Antennas and Propagation (EuCAP 2014)*, ISSN: 2164-3342, Apr. 2014, pp. 269–270.

[84] S. a. R. Horsley, I. R. Hooper, R. C. Mitchell–Thomas, and O. Quevedo–Teruel, "Removing singular refractive indices with sculpted surfaces", en, *Scientific Reports*, vol. 4, no. 1, p. 4876, May 2014, Number: 1 Publisher: Nature Publishing Group.

[85] R. C. Mitchell-Thomas, O. Quevedo-Teruel, T. M. McManus, S. A. R. Horsley, and Y. Hao, "Lenses on curved surfaces", en, *Optics Letters*, vol. 39, no. 12, p. 3551, Jun. 2014.

[86] R. C. Mitchell-Thomas, T. M. McManus, O. Quevedo-Teruel, S. A. R. Horsley, and Y. Hao, "Perfect Surface Wave Cloaks", *Physical Review Letters*, vol. 111, no. 21, p. 213 901, Nov. 2013, Publisher: American Physical Society.

[87] H. M. Barlow and A. L. Cullen, "Surface waves", *Proceedings of the IEE - Part III: Radio and Communication Engineering*, vol. 100, no. 68, pp. 329–341, Nov. 1953, Publisher: IET Digital Library.

[88] L. Brillouin, "Wave Guides for Slow Waves", *Journal of Applied Physics*, vol. 19, no. 11, pp. 1023–1041, Nov. 1948, Publisher: American Institute of Physics.

[89] W. L. Barnes, A. Dereux, and T. W. Ebbesen, "Surface plasmon subwavelength optics", en, *Nature*, vol. 424, no. 6950, pp. 824–830, Aug. 2003, Number: 6950 Publisher: Nature Publishing Group.

[90] J. Zhang, L. Zhang, and W. Xu, "Surface plasmon polaritons: Physics and applications", en, *Journal of Physics D: Applied Physics*, vol. 45, no. 11, p. 113 001, Feb. 2012, Publisher: IOP Publishing.

[91] F. J. Garcia-Vidal, L. Martín-Moreno, and J. B. Pendry, "Surfaces with holes in them: New plasmonic metamaterials", *Journal of Optics A: Pure and Applied Optics*, vol. 7, no. 2, S97–S101, Jan. 2005, tex.ids: garcia-vidalSurfacesHolesThem2005a, garcia-vidalSurfacesHolesThem2005b.

[92] P.-S. Kildal, "Artificially soft and hard surfaces in electromagnetics", *IEEE Transactions on Antennas and Propagation*, vol. 38, no. 10, pp. 1537–1544, Oct. 1990, tex.ids: kildalArtificiallySoftHard1990a, kildalArtificiallySoftHard1990b.

[93] C. D. Diallo, E. Girard, H. Legay, and R. Sauleau, "All-metal Ku-band Luneburg lens antenna based on variable parallel plate spacing Fakir bed of nails", in *2017 11th European Conference on Antennas and Propagation (EUCAP)*, Mar. 2017, pp. 1401–1404.

[94] P.-H. Tichit, S. N. Burokur, D. Germain, and A. de Lustrac, "Design and experimental demonstration of a high-directive emission with transformation optics", *Physical Review B*, vol. 83, no. 15, p. 155 108, Apr. 2011, Publisher: American Physical Society.

[95] A. Li, S. Kim, Y. Luo, Y. Li, J. Long, and D. F. Sievenpiper, "High-Power Transistor-Based Tunable and Switchable Metasurface Absorber", *IEEE Transactions on Microwave Theory and Techniques*, vol. 65, no. 8, pp. 2810–2818, Aug. 2017, Conference Name: IEEE Transactions on Microwave Theory and Techniques.

[96] X. Zhao, J. Schalch, J. Zhang, H. R. Seren, G. Duan, R. D. Averitt, and X. Zhang, "Electromechanically tunable metasurface transmission waveplate at terahertz frequencies", EN, *Optica*, vol. 5, no. 3, pp. 303–310, Mar. 2018, Publisher: Optica Publishing Group.

[97] M. Kharbech, R. Gillard, R. Loison, H. Legay, and E. Girard, "Compact frequency agile slot ring resonators for reflectarray phase shifting cells", in *Proceedings of the 5th European Conference on Antennas and Propagation (EUCAP)*, ISSN: 2164-3342, Apr. 2011, pp. 2113–2116.

[98] S. V. Hum and J. Perruisseau-Carrier, "Reconfigurable Reflectarrays and Array Lenses for Dynamic Antenna Beam Control: A Review", *IEEE Transactions on Antennas and Propagation*, vol. 62, no. 1, pp. 183–198, Jan. 2014, Conference Name: IEEE Transactions on Antennas and Propagation.

[99] M. Mavridou and A. P. Feresidis, "Dynamically Reconfigurable High Impedance and Frequency Selective Metasurfaces Using Piezoelectric Actuators", *IEEE Transactions on Antennas and Propagation*, vol. 64, no. 12, pp. 5190–5197, Dec. 2016, Conference Name: IEEE Transactions on Antennas and Propagation.

[100] S. A. Long and G. H. Huff, "A Fluidic Loading Mechanism for Phase Reconfigurable Reflectarray Elements", *IEEE Antennas and Wireless Propagation Letters*, vol. 10, pp. 876–879, 2011, Conference Name: IEEE Antennas and Wireless Propagation Letters.

[101] A. Clemente, L. Dussopt, R. Sauleau, P. Potier, and P. Pouliguen, "1-Bit Reconfigurable Unit Cell Based on PIN Diodes for Transmit-Array Applications in $X$ -Band", *IEEE Transactions on Antennas and Propagation*, vol. 60, no. 5, pp. 2260–2269, May 2012, Conference Name: IEEE Transactions on Antennas and Propagation.

[102] L. Di Palma, A. Clemente, L. Dussopt, R. Sauleau, P. Potier, and P. Pouliguen, "Radiation Pattern Synthesis for Monopulse Radar Applications With a Reconfigurable Transmitarray Antenna", *IEEE Transactions on Antennas and Propagation*, vol. 64, no. 9, pp. 4148–4154, Sep. 2016, Conference Name: IEEE Transactions on Antennas and Propagation.

[103] L. Di Palma, A. Clemente, L. Dussopt, R. Sauleau, P. Potier, and P. Pouliguen, "Circularly-Polarized Reconfigurable Transmitarray in Ka-Band With Beam Scanning and Polarization Switching Capabilities", *IEEE Transactions on Antennas and Propagation*, vol. 65, no. 2, pp. 529–540, Feb. 2017, Conference Name: IEEE Transactions on Antennas and Propagation.

[104] A. Hessel, M. H. Chen, R. C. M. Li, and A. A. Oliner, "Propagation in periodically loaded waveguides with higher symmetries", *Proceedings of the IEEE*, vol. 61, no. 2, pp. 183–195, Feb. 1973, tex.ids: hesselPropagationPeriodicallyLoaded1973a, hesselPropagationPeriodicallyLoaded1973b.

[105] J. D. de Pineda, A. P. Hibbins, and J. R. Sambles, "Microwave edge modes on a metasurface with glide symmetry", *Physical Review B*, vol. 98, no. 20, p. 205 426, Nov. 2018, Publisher: American Physical Society.

[106] M. G. Silveirinha, "$\mathcal{P}\cdot\mathcal{T}\cdot\mathcal{D}$ symmetry-protected scattering anomaly in optics", *Physical Review B*, vol. 95, no. 3, p. 035 153, Jan. 2017, Publisher: American Physical Society.

[107] E. Martini, M. G. Silveirinha, and S. Maci, "Exact Solution for the Protected TEM Edge Mode in a PTD-Symmetric Parallel-Plate Waveguide", *IEEE Transactions on Antennas and Propagation*, vol. 67, no. 2, pp. 1035–1044, Feb. 2019, Conference Name: IEEE Transactions on Antennas and Propagation.

[108] K. A. Hecht and M. J. Mencagli, "PTD Symmetric Wideband Absorbers", in *2022 16th European Conference on Antennas and Propagation (EuCAP)*, Mar. 2022, pp. 1–2.

[109] I. Nadeem, E. Martini, A. Toccafondi, and S. Maci, "Implementation of an Open Ended PTD-Symmetric Edge Waveguide", in *2022 16th European Conference on Antennas and Propagation (EuCAP)*, Mar. 2022, pp. 1–4.

[110] O. Quevedo-Teruel, Q. Chen, F. Mesa, N. J. G. Fonseca, and G. Valerio, "On the Benefits of Glide Symmetries for Microwave Devices", *IEEE Journal of Microwaves*, vol. 1, no. 1, pp. 457–469, Oct. 2020, tex.ids= quevedo-teruelBenefitsGlideSymmetries2021 conferenceName: IEEE Journal of Microwaves.

[111] A. Monje-Real, N. J. G. Fonseca, O. Zetterstrom, E. Pucci, and O. Quevedo-Teruel, "Holey Glide-Symmetric Filters for 5G at Millimeter-Wave Frequencies", *IEEE Microwave and Wireless Components Letters*, vol. 30, no. 1, pp. 31–34, Jan. 2020, tex.ids= monje-realHoleyGlideSymmetricFilters2020a conferenceName: IEEE Microwave and Wireless Components Letters.

[112] M. Camacho, R. C. Mitchell-Thomas, A. P. Hibbins, J. R. Sambles, and O. Quevedo-Teruel, "Designer surface plasmon dispersion on a one-dimensional periodic slot metasurface with glide symmetry", *Optics Letters*, vol. 42, no. 17, pp. 3375–3378, Sep. 2017, tex.ids= camachoDesignerSurfacePlasmon2017a, camachoDesignerSurfacePlasmon2017b publisher: Optica Publishing Group.

[113] H.-R. Zu, B. Wu, and T. Su, "Beam Manipulation of Antenna With Large Frequency-Scanning Angle Based on Field Confinement of Spoof Surface Plasmon Polaritons", *IEEE Transactions on Antennas and Propagation*, vol. 70, no. 4, pp. 3022–3027, Apr. 2022, Conference Name: IEEE Transactions on Antennas and Propagation.

[114] A. Tamayo-Dominguez, J.-M. Fernandez-Gonzalez, and O. Quevedo-Teruel, "One-Plane Glide-Symmetric Holey Structures for Stop-Band and Refraction Index Reconfiguration", *Symmetry*, vol. 11, no. 4, p. 495, Apr. 2019, Number: 4 Publisher: Multidisciplinary Digital Publishing Institute.

[115] B. A. Mouris, A. Fernández-Prieto, R. Thobaben, J. Martel, F. Mesa, and O. Quevedo-Teruel, "On the Increment of the Bandwidth of Mushroom-Type EBG Structures With Glide Symmetry", *IEEE Transactions on Microwave Theory and Techniques*, vol. 68, no. 4, pp. 1365–1375, Apr. 2020, tex.ids= mourisIncrementBandwidthMushroomType2020a conferenceName: IEEE Transactions on Microwave Theory and Techniques.

[116] B. A. Mouris, A. Fernández-Prieto, R. Thobaben, J. Martel, F. Mesa, and O. Quevedo-Teruel, "Glide Symmetry to Improve the Bandgap Operation of Periodic Microstrip Defected Ground Structures", in *2020 50th European Microwave Conference (EuMC)*, tex.ids= mourisGlideSymmetryImprove2021, Jan. 2021, pp. 483–486.

[117] Q. Chen, F. Ghasemifard, G. Valerio, and O. Quevedo-Teruel, "Modeling and Dispersion Analysis of Coaxial Lines With Higher Symmetries", *IEEE Transactions on Microwave Theory and Techniques*, vol. 66, no. 10, pp. 4338–4345, Oct. 2018, tex.ids= chenModelingDispersionAnalysis2018a, chenModelingDispersionAnalysis2018b conferenceName: IEEE Transactions on Microwave Theory and Techniques.

[118] F. Ghasemifard, M. Norgren, and O. Quevedo-Teruel, "Twist and Polar Glide Symmetries: An Additional Degree of Freedom to Control the Propagation Characteristics of Periodic Structures", *Scientific Reports*, vol. 8, no. 1, pp. 1–7, Jul. 2018, tex.ids= ghasemifardTwistPolarGlide2018a, ghasemifardTwistPolarGlide2018b number: 1 publisher: Nature Publishing Group.

[119] P. Padilla, L. F. Herrán, A. Tamayo-Domínguez, J. F. Valenzuela-Valdés, and O. Quevedo-Teruel, "Glide Symmetry to Prevent the Lowest Stopband of Printed Corrugated Transmission Lines", *IEEE Microwave and Wireless Components Letters*, vol. 28, no. 9, pp. 750–752, Sep. 2018, tex.ids= padillaGlideSymmetryPrevent2018a, padillaGlideSymmetryPrevent2018b conferenceName: IEEE Microwave and Wireless Components Letters.

[120] J. Chen, Q. Cheng, W. Yuan, L. Wang, W. X. Tang, L. Wang, and T. J. Cui, "Generation of High-Order Waveguide Modes with Reduced Symmetric Protection", *Physical Review Applied*, vol. 14, no. 2, p. 024 040, Aug. 2020, tex.ids= chenGenerationHighOrderWaveguide2020a publisher: American Physical Society.

[121] M. M. Shanei, D. Fathi, F. Ghasemifard, and O. Quevedo-Teruel, "All-silicon reconfigurable metasurfaces for multifunction and tunable performance at optical frequencies based on glide symmetry", *Scientific Reports*, vol. 9, no. 1, p. 13 641, Sep. 2019, tex.ids= shaneiAllsiliconReconfigurableMetasurfaces2019a number: 1 publisher: Nature Publishing Group.

[122] P. Padilla, Á. Palomares-Caballero, A. Alex-Amor, J. Valenzuela-Valdés, J. M. Fernández-González, and O. Quevedo-Teruel, "Broken Glide-Symmetric Holey Structures for Bandgap Selection in Gap-Waveguide Technology", *IEEE Microwave and Wireless Components Letters*, vol. 29, no. 5, pp. 327–329, May 2019, tex.ids= padillaBrokenGlideSymmetricHoley2019a conferenceName: IEEE Microwave and Wireless Components Letters.

[123] M. Camacho, R. C. Mitchell-Thomas, A. P. Hibbins, J. R. Sambles, and O. Quevedo-Teruel, "Mimicking glide symmetry dispersion with coupled slot metasurfaces", *Applied Physics Letters*, vol. 111, no. 12, p. 121 603, Sep. 2017, tex.ids= camachoMimickingGlideSymmetry2017a, camachoMimickingGlideSymmetry2017b publisher: American Institute of Physics.

[124] D. B. Moore, G. P. Ward, J. D. Smith, A. P. Hibbins, J. R. Sambles, and T. A. Starkey, "Confined acoustic line modes within a glide-symmetric waveguide", en, *Scientific Reports*, vol. 12, no. 1, p. 10 954, Jun. 2022, Number: 1 Publisher: Nature Publishing Group.

[125] Z. Yue, Z. Zhang, H.-X. Wang, W. Xiong, Y. Cheng, and X. Liu, "Glided acoustic higher-order topological insulators based on spoof surface acoustic waves", en, *New Journal of Physics*, Apr. 2022.

[126] J. A. I. Martínez, N. Laforge, M. Kadic, and V. Laude, "Glide-Reflection Symmetric Topological Phononic Crystal Waveguide", *arXiv:2203.02692 [physics]*, Mar. 2022, arXiv: 2203.02692.

[127] F. Yazdi, T. Mealy, A. Nikzamir, R. Marosi, and F. Capolino, "Third Order Modal Exceptional Degeneracy in Waveguides with Glide-Time Symmetry", *arXiv:2110.14095 [physics]*, Mar. 2022, arXiv: 2110.14095.

[128] Q. Chen, F. Ghasemifard, and O. Quevedo-Teruel, "Dispersion analysis of coaxial line loaded with twist-symmetric half-rings", in *2018 International Workshop on Antenna Technology (iWAT)*, tex.ids= chenDispersionAnalysisCoaxial2018a, chenDispersionAnalysisCoaxial2018b ISSN: null, Mar. 2018, pp. 1–3.

[129] O. Quevedo-Teruel, O. Dahlberg, and G. Valerio, "Propagation in Waveguides With Transversal Twist-Symmetric Holey Metallic Plates", *IEEE Microwave and Wireless Components Letters*, vol. 28, no. 10, pp. 858–860, Oct. 2018, tex.ids= quevedo-teruelPropagationWaveguidesTransversal2018a, quevedo-teruelPropagationWaveguidesTransversal2018b conferenceName: IEEE Microwave and Wireless Components Letters.

[130] O. Dahlberg, G. Valerio, and O. Quevedo-Teruel, "Fully Metallic Flat Lens Based on Locally Twist-Symmetric Array of Complementary Split-Ring Resonators", *Symmetry*, vol. 11, no. 4, p. 581, Apr. 2019, tex.ids= dahlbergFullyMetallicFlat2019a number: 4 publisher: Multidisciplinary Digital Publishing Institute.

[131] O. Dahlberg, F. Ghasemifard, G. Valerio, and O. Quevedo-Teruel, "Propagation characteristics of periodic structures possessing twist and polar glide symmetries", *EPJ Applied Metamaterials*, vol. 6, p. 14, 2019, Publisher: EDP Sciences.

[132] A. N. Askarpour, Y. Zhao, and A. Alù, "Wave propagation in twisted metamaterials", *Physical Review B*, vol. 90, no. 5, p. 054 305, Aug. 2014, Publisher: American Physical Society.

[133] O. Quevedo-Teruel, "Glide symmetries and their application for electromagnetic periodic structures", in *2019 International Symposium on Antennas and Propagation (ISAP)*, tex.ids= quevedo-teruelGlideSymmetriesTheir2019a, Oct. 2019, pp. 1–3.

[134] O. Quevedo-Teruel, "Periodic Structures with Glide Symmetry and their Application to Antenna Design", in *2020 International Workshop on Antenna Technology (iWAT)*, tex.ids= quevedo-teruelPeriodicStructuresGlide2020a, Feb. 2020, pp. 1–4.

[135] R. Quesada, D. Martín-Cano, F. J. García-Vidal, and J. Bravo-Abad, "Deep-subwavelength negative-index waveguiding enabled by coupled conformal surface plasmons", *Optics Letters*, vol. 39, no. 10, pp. 2990–2993, May 2014, tex.ids: quesadaDeepsubwavelengthNegativeindexWaveguiding2014a, quesadaDeepsubwavelengthNegativeindexWaveguiding2014b.

[136] G. Zhang, Q. Zhang, Y. Chen, and R. D. Murch, "High-Scanning-Rate and Wide-Angle Leaky-Wave Antennas Based on Glide-Symmetry Goubau Line", *IEEE Transactions on Antennas and Propagation*, vol. 68, no. 4, pp. 2531–2540, Apr. 2020, tex.ids= zhangHighScanningRateWideAngleLeakyWave2020a conferenceName: IEEE Transactions on Antennas and Propagation.

[137] J. J. Wu, C. Wu, D. J. Hou, K. Liu, and T. Yang, "Propagation of Low-Frequency Spoof Surface Plasmon Polaritons in a Bilateral Cross-Metal Diaphragm Channel Waveguide in the Absence of Bandgap", *IEEE Photonics Journal*, vol. 7, no. 1, pp. 1–8, Feb. 2015, tex.ids: wuPropagationLowFrequencySpoof2015a, wuPropagationLowFrequencySpoof2015b.

[138] J. Martínez, A. Coves, F. Mesa, and O. Quevedo-Teruel, "Passband broadening of sub-wavelength resonator-based glide-symmetric SIW filters", *AEU - International Journal of Electronics and Communications*, vol. 125, p. 153 362, Oct. 2020, tex.ids= martinezPassbandBroadeningSubwavelength2020a, martinezPassbandBroadeningSubwavelength2020b.

[139] A. Tamayo-Dominguez, J.-M. Fernández-González, and O. Quevedo-Teruel, "Mechanically Reconfigurable Waveguide Filter Based on Glide Symmetry at Millimetre-Wave Bands", en, *Sensors*, vol. 22, no. 3, p. 1001, Jan. 2022, Number: 3 Publisher: Multidisciplinary Digital Publishing Institute.

[140] M. Ebrahimpouri, O. Quevedo-Teruel, and E. Rajo-Iglesias, "Design Guidelines for Gap Waveguide Technology Based on Glide-Symmetric Holey Structures", *IEEE Microwave and Wireless Components Letters*, vol. 27, no. 6, pp. 542–544, Jun. 2017, tex.ids= ebrahimpouriDesignGuidelinesGap2017a, ebrahimpouriDesignGuidelinesGap2017b conferenceName: IEEE Microwave and Wireless Components Letters.

[141] Z. Sipus, K. Cavar, and M. Bosiljevac, "Waveguide Technology Based on Glide-Symmetric Holey Structures: Design Considerations", in *2020 International Workshop on Antenna Technology (iWAT)*, tex.ids= sipusWaveguideTechnologyBased2020a, Feb. 2020, pp. 1–4.

[142] Q. Liao, E. Rajo-Iglesias, and O. Quevedo-Teruel, "$Ka$ -Band Fully Metallic TE40 Slot Array Antenna With Glide-Symmetric Gap Waveguide Technology", *IEEE Transactions on Antennas and Propagation*, vol. 67, no. 10, pp. 6410–6418, Oct. 2019, tex.ids= liaoKaBandFully2019a conferenceName: IEEE Transactions on Antennas and Propagation.

[143] M. Ebrahimpouri, A. Algaba Brazalez, L. Manholm, and O. Quevedo-Teruel, "Using Glide-Symmetric Holes to Reduce Leakage Between Waveguide Flanges", *IEEE Microwave and Wireless Components Letters*, vol. 28, no. 6, pp. 473–475, Jun. 2018, tex.ids= ebrahimpouriUsingGlideSymmetricHoles2018a, ebrahimpouriUsingGlideSymmetricHoles2018b conferenceName: IEEE Microwave and Wireless Components Letters.

[144] M. Ebrahimpouri, E. Rajo-Iglesias, Z. Sipus, and O. Quevedo-Teruel, "Low-cost metasurface using glide symmetry for integrated waveguides", in *2016 10th European Conference on Antennas and Propagation (EuCAP)*, tex.ids: ebrahimpouriLowcostMetasurfaceUsing2016, ebrahimpouriLowcostMetasurfaceUsing2016b ISSN: null, Apr. 2016, pp. 1–2.

[145] M. Ebrahimpouri, O. Quevedo-Teruel, and E. Rajo-Iglesias, "Design of microwave components in groove gap waveguide technology implemented by holey EBG", in *2017 11th European Conference on Antennas and Propagation (EUCAP)*, tex.ids= ebrahimpouriDesignMicrowaveComponents2017a, ebrahimpouriDesignMicrowaveComponents2017b ISSN: null, Mar. 2017, pp. 746–748.

[146] A. Vosoogh, H. Zirath, and Z. S. He, "Novel Air-Filled Waveguide Transmission Line Based on Multilayer Thin Metal Plates", *IEEE Transactions on Terahertz Science and Technology*, vol. 9, no. 3, pp. 282–290, May 2019, tex.ids= vosooghNovelAirFilledWaveguide2019a conferenceName: IEEE Transactions on Terahertz Science and Technology.

[147] Á. Palomares-Caballero, A. Alex-Amor, J. Valenzuela-Valdés, and P. Padilla, "Millimeter-Wave 3-D-Printed Antenna Array Based on Gap-Waveguide Technology and Split E-Plane Waveguide", *IEEE Transactions on Antennas and Propagation*, vol. 69, no. 1, pp. 164–172, Jan. 2021, tex.ids= palomares-caballeroMillimeterWave3DPrintedAntenna2020 conferenceName: IEEE Transactions on Antennas and Propagation.

[148] E. Rajo-Iglesias, M. Ebrahimpouri, and O. Quevedo-Teruel, "Wideband Phase Shifter in Groove Gap Waveguide Technology Implemented With Glide-Symmetric Holey EBG", *IEEE Microwave and Wireless Components Letters*, vol. 28, no. 6, pp. 476–478, Jun. 2018, tex.ids= rajo-iglesiasWidebandPhaseShifte rajo-iglesiasWidebandPhaseShifter2018b conferenceName: IEEE Microwave and Wireless Components Letters.

[149] Á. Palomares-Caballero, A. Alex-Amor, P. Padilla, and J. F. Valenzuela-Valdés, "Dispersion and Filtering Properties of Rectangular Waveguides Loaded With Holey Structures", *IEEE Transactions on Microwave Theory and Techniques*, vol. 68, no. 12, pp. 5132–5144, Dec. 2020, tex.ids= palomares-caballeroDispersionFilteringProperties2020 conferenceName: IEEE Transactions on Microwave Theory and Techniques.

[150] B. A. Mouris, A. Fernández-Prieto, J. L. M. d. Río, R. Thobaben, J. Martel, F. Mesa, F. Medina, and O. Quevedo-Teruel, "Glide Symmetry Applied to Printed Common-Mode Rejection Filters", *IEEE Transactions on Microwave Theory and Techniques*, vol. 70, no. 2, pp. 1198–1210, Feb. 2022, Conference Name: IEEE Transactions on Microwave Theory and Techniques.

[151] A. Algaba Brazalez, L. Manholm, O. Quevedo-teruel, and M. Ebrahimpouri Hamlkar, "Waveguide Interconnection with Glide Symmetrically Positioned Holes for Avoiding Leakage", United States Patent 20200220245, Library Catalog: FreePatentsOnline, Jul. 2020.

[152] D. Sun, X. Chen, and L. Guo, "Compact Corrugated Plate for Double-Sided Contactless Waveguide Flange", *IEEE Microwave and Wireless Components Letters*, vol. 31, no. 2, pp. 129–132, Feb. 2021, tex.ids= sunCompactCorrugatedPlate2020 conferenceName: IEEE Microwave and Wireless Components Letters.

[153] O. Zetterstrom, E. Pucci, P. Padilla, L. Wang, and O. Quevedo-Teruel, "Low-Dispersive Leaky-Wave Antennas for mmWave Point-to-Point High-Throughput Communications", *IEEE Transactions on Antennas and Propagation*, vol. 68, no. 3, pp. 1322–1331, Mar. 2020, Conference Name: IEEE Transactions on Antennas and Propagation.

[154] Q. Chen, O. Zetterstrom, E. Pucci, A. Palomares-Caballero, P. Padilla, and O. Quevedo-Teruel, "Glide-Symmetric Holey Leaky-Wave Antenna With Low Dispersion for 60 GHz Point-to-Point Communications", *IEEE Transactions on Antennas and Propagation*, vol. 68, no. 3, pp. 1925–1936, Mar. 2020, tex.ids= chenGlideSymmetricHoleyLeakyWave2020a conferenceName: IEEE Transactions on Antennas and Propagation.

[155] Q. Chen, F. Mesa, P. Padilla, X. Yin, and O. Quevedo-Teruel, "Efficient Leaky-Lens Antenna at 60 GHz Based on a Substrate-Integrated-Holey Metasurface", *IEEE Transactions on Antennas and Propagation*, vol. 68, no. 12, pp. 7777–7784, Dec. 2020, tex.ids= chenEfficientLeakyLensAntenna2020 conferenceName: IEEE Transactions on Antennas and Propagation.

[156] X. Zhang, S. Liu, L. Liao, and J. Lou, "Surface plasmonic waveguide and ultra-wideband bandpass filter using double-layered glide symmetric corrugated lines", en, *Journal of Physics D: Applied Physics*, 2022.

[157] O. Quevedo-Teruel, J. Miao, M. Mattsson, A. Algaba-Brazalez, M. Johansson, and L. Manholm, "Glide-Symmetric Fully Metallic Luneburg Lens for 5G Communications at Ka-Band", *IEEE Antennas and Wireless Propagation Letters*, vol. 17, no. 9, pp. 1588–1592, Sep. 2018, tex.ids= quevedo-teruelGlideSymmetricFullyMetallic2018a, quevedo-teruelGlideSymmetricFullyMetallic2018b conferenceName: IEEE Antennas and Wireless Propagation Letters.

[158] K. Liu, F. Ghasemifard, and O. Quevedo-Teruel, "Broadband metasurface Luneburg lens antenna based on glide-symmetric bed of nails", in *2017 11th European Conference on Antennas and Propagation (EUCAP)*, tex.ids= liuBroadbandMetasurfaceLuneburg2017a, liuBroadbandMetasurfaceLuneburg2017b ISSN: null, Mar. 2017, pp. 358–360.

[159] R. C. Mitchell-Thomas, J. R. Sambles, and A. P. Hibbins, "High index metasurfaces for graded lenses using glide symmetry", in *2017 11th European Conference on Antennas and Propagation (EUCAP)*, Mar. 2017, pp. 1396–1397.

[160] B. Majumder, S. S. Vinnakota, S. Upadhyay, and K. Kandasamy, "Dielectric Metasurface Inspired Directional Multi-port Luneburg Lens as a Medium for 5G Wireless Power Transfer - A Design Methodology", *IEEE Photonics Journal*, pp. 1–1, 2022, Conference Name: IEEE Photonics Journal.

[161] B. Majumder, V. S. Sankar, and H. Meena, "Design of an Artificially Engineered all Metallic Lens Antenna", in *2020 IEEE Asia-Pacific Microwave Conference (APMC)*, tex.ids= majumderDesignArtificiallyEngineered2020a, Dec. 2020, pp. 1072–1074.

[162] O. Zetterstrom, R. Hamarneh, and O. Quevedo-Teruel, "Experimental Validation of a Metasurface Luneburg Lens Antenna Implemented with Glide-Symmetric Substrate-Integrated-Holes", *IEEE Antennas and Wireless Propagation Letters*, pp. 1–1, 2021, Conference Name: IEEE Antennas and Wireless Propagation Letters.

[163] P. Arnberg, O. Barreira Petersson, O. Zetterstrom, F. Ghasemifard, and O. Quevedo-Teruel, "High Refractive Index Electromagnetic Devices in Printed Technology Based on Glide-Symmetric Periodic Structures", *Applied Sciences*, vol. 10, no. 9, p. 3216, Jan. 2020, tex.ids= arnbergHighRefractiveIndex2020a number: 9 publisher: Multidisciplinary Digital Publishing Institute.

[164] P. Bantavis, P. Bantavis, C. G. Gonzalez, R. Sauleau, G. Goussetis, S. Tubau, and H. Legay, "Broadband graded index Gutman lens with a wide field of view utilizing artificial dielectrics: A design methodology", *Optics Express*, vol. 28, no. 10, pp. 14 648–14 661, May 2020, tex.ids= bantavisBroadbandGradedIndex2020a publisher: Optical Society of America.

[165] W. Yuan, J. F. Chen, C. Zhang, W. X. Tang, L. Wang, Q. Cheng, and T. J. Cui, "Glide-Symmetric Lens Antenna in Gap Waveguide Technology", *IEEE Transactions on Antennas and Propagation*, vol. 68, no. 4, pp. 2612–2620, Apr. 2020, tex.ids= yuanGlideSymmetricLensAntenna2020a conferenceName: IEEE Transactions on Antennas and Propagation.

[166] X. Zeng, Q. Chen, O. Zetterstrom, and O. Quevedo-Teruel, "Fully Metallic Glide-Symmetric Leaky-Wave Antenna at Ka-band with Lens-Augmented Scanning", *IEEE Transactions on Antennas and Propagation*, pp. 1–1, 2022, Conference Name: IEEE Transactions on Antennas and Propagation.

[167] G. Valerio, F. Ghasemifard, Z. Sipus, and O. Quevedo-Teruel, "Glide-Symmetric All-Metal Holey Metasurfaces for Low-Dispersive Artificial Materials: Modeling and Properties", *IEEE Transactions on Microwave Theory and Techniques*, vol. 66, no. 7, pp. 3210–3223, Jul. 2018, tex.ids= valerioGlideSymmetricAllMetalHoley2018a, valerioGlideSymmetricAllMetalHoley2018b conferenceName: IEEE Transactions on Microwave Theory and Techniques.

[168] A. Alex-Amor, F. Ghasemifard, G. Valerio, M. Ebrahimpouri, P. Padilla, J. M. F. González, and O. Quevedo-Teruel, "Glide-Symmetric Metallic Structures With Elliptical Holes for Lens Compression", *IEEE Transactions on Microwave Theory and Techniques*, vol. 68, no. 10, pp. 4236–4248, Oct. 2020, tex.ids= alex-amorGlideSymmetricMetallicStructures2020a conferenceName: IEEE Transactions on Microwave Theory and Techniques.

[169] F. Mesa, G. Valerio, R. Rodríguez-Berral, and O. Quevedo-Teruel, "Simulation-Assisted Efficient Computation of the Dispersion Diagram of Periodic Structures: A comprehensive overview with applications to filters, leaky-wave antennas and metasurfaces", *IEEE Antennas and Propagation Magazine*, vol. 63, no. 5, pp. 33–45, Oct. 2021, tex.ids= mesaSimulationAssistedEfficientComputation2020 conferenceName: IEEE Antennas and Propagation Magazine.

[170] M. G. Silveirinha, C. A. Fernandes, and J. R. Costa, "Electromagnetic Characterization of Textured Surfaces Formed by Metallic Pins", *IEEE Transactions on Antennas and Propagation*, vol. 56, no. 2, pp. 405–415, Feb. 2008, Conference Name: IEEE Transactions on Antennas and Propagation.

[171] N. Marcuvitz, *Waveguide handbook*, ser. IEE electromagnetic waves series 21. London, UK: P. Peregrinus on behalf of the Institution of Electrical Engineers, 1986, tex.ids: marcuvitzWaveguideHandbook1986a, marcuvitzWaveguideHandbook1986b, marcuvitzWaveguideHandbook1986c.

[172] Q. Chen, F. Mesa, and O. Quevedo-Teruel, "Dispersion Analysis of Glide-Symmetric Holey Metasurface Based on Multimodal Transfer-Matrix Approach", in *2021 15th European Conference on Antennas and Propagation (EuCAP)*, tex.ids= chenDispersionAnalysisGlideSymmetric2021, Mar. 2021, pp. 1–4.

[173] Q. Chen, F. Giusti, G. Valerio, F. Mesa, and O. Quevedo-Teruel, "Anisotropic glide-symmetric substrate-integrated-holey metasurface for a compressed ultrawideband Luneburg lens", *Applied Physics Letters*, vol. 118, no. 8, p. 084 102, Feb. 2021, tex.ids= chenAnisotropicGlidesymmetricSubstrateintegratedholey2021 publisher: American Institute of Physics.

[174] A. Alex-Amor, A. Palomares-Caballero, F. Mesa, O. Quevedo-Teruel, and P. Padilla, "Dispersion Analysis of Periodic Structures in Anisotropic Media: Application to Liquid Crystals", *arXiv:2007.07648 [physics]*, Jul. 2020, arXiv: 2007.07648.

[175] A. C. Escobar, J. P. D. Risco, O. Quevedo-Teruel, F. Mesa, and J. D. Baena, "Retrieval of the Constitutive Parameters and Dispersion Relation of Glide-Symmetric Metamaterials via the Multimodal Transfer Matrix Method", in *2020 Fourteenth International Congress on Artificial Materials for Novel Wave Phenomena (Metamaterials)*, tex.ids= escobarRetrievalConstitutiveParameters2020a, Sep. 2020, pp. 312–314.

[176] F. Ghasemifard, M. Ebrahimpouri, M. Norgren, and O. Quevedo-Teruel, "Mode matching analysis of two dimensional glide-symmetric corrugated metasurfaces", in *2017 11th European Conference on Antennas and Propagation (EUCAP)*, tex.ids= ghasemifardModeMatchingAnalysis2017a, ghasemifardModeMatchingAnalysis2017b ISSN: null, Mar. 2017, pp. 749–751.

[177] Z. Sipus and M. Bosiljevac, "Modeling of Glide-Symmetric Dielectric Structures", *Symmetry*, vol. 11, no. 6, p. 805, Jun. 2019, tex.ids= sipusModelingGlideSymmetricDielectric2019a number: 6 publisher: Multidisciplinary Digital Publishing Institute.

[178] V. Galdi and I. M. Pinto, "A simple algorithm for accurate location of leaky-wave poles for grounded inhomogeneous dielectric slabs", *Microwave and Optical Technology Letters*, vol. 24, no. 2, pp. 135–140, 2000, tex.ids: galdiSimpleAlgorithmAccurate2000a, galdiSimpleAlgorithmAccurate2000b.

[179] V. I. Kukulin, V. M. Krasnopol'sky, and J. Horáček, *Theory of Resonances: Principles and Applications*, eng. Dordrecht: Springer Netherlands, 2010, OCLC: 958542068.

[180] J. E. Marsden and A. Tromba, *Vector calculus*, 6th ed. New York: W.H. Freeman and Company, 2012.

[181] O. R. Asfar and A. H. Nayfeh, "The Application of the Method of Multiple Scales to Wave Propagation in Periodic Structures", *SIAM Review*, vol. 25, no. 4, pp. 455–480, Oct. 1983, Publisher: Society for Industrial and Applied Mathematics.

[182] D. A. Harville, *Matrix algebra from a statistician's perspective*. New York: Springer, 1997.

[183] B. Fischer and G. Valerio, "Quasi-Static Homogenization of Glide-Symmetric Holey Parallel-Plate Waveguides With Ultra-Wideband Validity", *IEEE Transactions on Antennas and Propagation*, vol. 70, no. 11, pp. 10 569–10 582, Nov. 2022, Conference Name: IEEE Transactions on Antennas and Propagation.

[184] J. Kiefer, "Sequential Minimax Search for a Maximum", *Proceedings of the American Mathematical Society*, vol. 4, no. 3, pp. 502–506, 1953, Publisher: American Mathematical Society.

[185] J.-M. Jin, *Theory and Computation of Electromagnetic Fields: Jin/Electromagnetic Fields*. Hoboken, NJ, USA: John Wiley & Sons, Inc., May 2010.

[186] J. Stoer and R. Bulirsch, *Introduction to Numerical Analysis*, 3rd ed, ser. Texts in applied mathematics 12. New York, New York, USA: Springer, 2002.

[187] A. A. Brazález, L. Manholm, M. Johansson, O. Quevedo-Teruel, and J. Miao, "Investigation of a Ka-band Luneburg lens made of a glide-symmetric holey structure", in *2017 International Symposium on Antennas and Propagation (ISAP)*, tex.ids= brazalezInvestigationKabandLuneburg2017a, brazalezInvestigationKabandLuneburg2017b ISSN: null, Oct. 2017, pp. 1–2.

[188] A. Torki, M. Ebrahimpouri, and O. Quevedo-Teruel, "A planar steerable 60 GHz leaky wave antenna with Luneburg lens feed", in *2016 IEEE International Symposium on Antennas and Propagation (APSURSI)*, ISSN: 1947-1491, Jun. 2016, pp. 1405–1406.

[189] C. D. Meyer, *Matrix Analysis and Applied Linear Algebra*. Philadelphia, Pennsylvania, USA: Society for Industrial and Applied Mathematics, 2000.

[190] D. Cavallo and C. Felita, "Analytical Formulas for Artificial Dielectrics With Nonaligned Layers", *IEEE Transactions on Antennas and Propagation*, vol. 65, no. 10, pp. 5303–5311, Oct. 2017, tex.ids: cavalloAnalyticalFormulasArtificial2017a, cavalloAnalyticalFormulasArtificial2017b.

[191] X. Chen, T. M. Grzegorczyk, B.-I. Wu, J. Pacheco, and J. A. Kong, "Robust method to retrieve the constitutive effective parameters of metamaterials", *Physical Review E*, vol. 70, no. 1, p. 016 608, Jul. 2004, Publisher: American Physical Society.

[192] M. Bagheriasl, J. Sarrazin, and G. Valerio, "Reconfigurable Waveguides Using Glide-Symmetric Bed of Nails: Design of an All-Metal Switch at Millimetre-Wave Band", *arXiv:2007.08021 [eess]*, Jul. 2020, arXiv: 2007.08021.

[193] J.-W. Lian, Y.-L. Ban, Q.-L. Yang, B. Fu, Z.-F. Yu, and L.-K. Sun, "Planar Millimeter-Wave 2-D Beam-Scanning Multibeam Array Antenna Fed by Compact SIW Beam-Forming Network", *IEEE Transactions on Antennas and Propagation*, vol. 66, no. 3, pp. 1299–1310, Mar. 2018, Conference Name: IEEE Transactions on Antennas and Propagation.

[194] Q.-L. Yang, Y.-L. Ban, J.-W. Lian, Z.-F. Yu, and B. Wu, "SIW Butler Matrix with Modified Hybrid Coupler for Slot Antenna Array", *IEEE Access*, vol. 4, pp. 9561–9569, 2016, Conference Name: IEEE Access.

[195] R. H. Reed, "Modified magic tee phase-shifter", *Transactions of the IRE Professional Group on Antennas and Propagation*, vol. 1, no. 1, pp. 126–134, Feb. 1952, Conference Name: Transactions of the IRE Professional Group on Antennas and Propagation.

[196] Y. Cheng, W. Hong, and K. Wu, "Novel Substrate Integrated Waveguide fixed phase shifter for 180-degree Directional Coupler", in *2007 IEEE/MTT-S International Microwave Symposium*, ISSN: 0149-645X, Jun. 2007, pp. 189–192.

[197] K. Sellal, L. Talbi, and T. Denidni, "Design of a Substrate Integrated Waveguide Phase Shifter", in *2006 2nd International Conference on Information Communication Technologies*, vol. 2, Apr. 2006, pp. 2155–2160.

[198] W. Che, E. K.-N. Yung, and K. Wu, "Millimeter-wave substrate integrated waveguide ferrite phase shifter for wireless communication application", in *2003 IEEE Topical Conference on Wireless Communication Technology*, Oct. 2003, pp. 320–324.

[199] I. Boudreau, K. Wu, and D. Deslandes, "Broadband phase shifter using air holes in Substrate Integrated Waveguide", in *2011 IEEE MTT-S International Microwave Symposium*, ISSN: 0149-645X, Jun. 2011, pp. 1–4.

[200] M. Ebrahimpouri, S. Nikmehr, and A. Pourziad, "Broadband Compact SIW Phase Shifter Using Omega Particles", *IEEE Microwave and Wireless Components Letters*, vol. 24, no. 11, pp. 748–750, Nov. 2014, Conference Name: IEEE Microwave and Wireless Components Letters.

[201] F. Parment, A. Ghiotto, T.-P. Vuong, J.-M. Duchamp, and K. Wu, "Double Dielectric Slab-Loaded Air-Filled SIW Phase Shifters for High-Performance Millimeter-Wave Integration", *IEEE Transactions on Microwave Theory and Techniques*, vol. 64, no. 9, pp. 2833–2842, Sep. 2016, Conference Name: IEEE Transactions on Microwave Theory and Techniques.

[202] A. Tribak, Á. Mediavilla Sánchez, J. Zbitou, and J. L. Cano de Diego, "Novel ridged waveguide differential phase shifter for satellite application", eng, *International Journal of Microwave and Optical Technology, 2014, 9(6), 409-414*, Nov. 2014, Accepted: 2016-10-24T14:29:58Z Publisher: Electrical Engineering Department,University of Nevada.

[203] P.-S. Kildal, E. Alfonso, A. Valero-Nogueira, and E. Rajo-Iglesias, "Local Metamaterial-Based Waveguides in Gaps Between Parallel Metal Plates", *IEEE Antennas and Wireless Propagation Letters*, vol. 8, pp. 84–87, 2009, Conference Name: IEEE Antennas and Wireless Propagation Letters.

[204] E. Rajo-Iglesias, M. Ferrando-Rocher, and A. U. Zaman, "Gap Waveguide Technology for Millimeter-Wave Antenna Systems", *IEEE Communications Magazine*, vol. 56, no. 7, pp. 14–20, Jul. 2018, Conference Name: IEEE Communications Magazine.

[205] M. A. Abdelaal, S. I. Shams, and A. A. Kishk, "Compact RGW Differential Phase Shifter for Millimeter-Wave Applications", in *2018 18th International Symposium on Antenna Technology and Applied Electromagnetics (ANTEM)*, ISSN: 2473-3555, Aug. 2018, pp. 1–2.

[206] N. Memeletzoglou and E. Rajo-Iglesias, "Array of stacked leaky-wave antennas in groove gap waveguide technology", en, *Scientific Reports*, vol. 11, no. 1, p. 2260, Jan. 2021, tex.ids= memeletzoglouArrayStackedLeakywave2021 number: 1 publisher: Nature Publishing Group.

[207] M.-H. Chung, D.-H. Je, S.-T. Han, and S.-R. Kim, "Development of a 85-115 GHz 90-deg phase shifter using corrugated square waveguide", in *2014 44th European Microwave Conference*, Oct. 2014, pp. 1146–1149.

[208] Z. Qamar, S. Y. Zheng, W. S. Chan, and D. Ho, "An Equal-Length Multiway Differential Metamaterial Phase Shifter", *IEEE Transactions on Microwave Theory and Techniques*, vol. 65, no. 1, pp. 136–146, Jan. 2017, Conference Name: IEEE Transactions on Microwave Theory and Techniques.

[209] S. A. Razavi and A. U. Zaman, "A compact phase shifter in groove gap waveguide for millimeter-wave applications", in *12th European Conference on Antennas and Propagation (EuCAP 2018)*, Apr. 2018, pp. 1–3.

[210] S. Adhikari, A. Ghiotto, S. Hemour, and K. Wu, "Tunable non-reciprocal ferrite loaded SIW phase shifter", in *2013 IEEE MTT-S International Microwave Symposium Digest (MTT)*, ISSN: 0149-645X, Jun. 2013, pp. 1–3.

[211] P. Padilla, A. Muñoz-Acevedo, and M. Sierra-Castañer, "Low loss 360° Ku band electronically reconfigurable phase shifter", en, *AEU - International Journal of Electronics and Communications*, vol. 64, no. 11, pp. 1100–1104, Nov. 2010.

[212] E. Villa, B. Aja, J. Cagigas, E. Artal, and L. de la Fuente, "Four-State Full Q-Band Phase Shifter Using Smooth-Ridged Waveguides", *IEEE Microwave and Wireless Components Letters*, vol. 27, no. 11, pp. 995–997, Nov. 2017, Conference Name: IEEE Microwave and Wireless Components Letters.

[213] K. T. Trinh, J. Feng, S. H. Shehab, and N. C. Karmakar, "1.4 GHz Low-Cost PIN Diode Phase Shifter for $L$ -Band Radiometer Antenna", *IEEE Access*, vol. 7, pp. 95 274–95 284, 2019, Conference Name: IEEE Access.

[214] M. Nickel, A. Jiménez-Sáez, P. Agrawal, A. Gadallah, A. Malignaggi, C. Schuster, R. Reese, H. Tesmer, E. Polat, D. Wang, P. Schumacher, R. Jakoby, D. Kissinger, and H. Maune, "Ridge Gap Waveguide Based Liquid Crystal Phase Shifter", *IEEE Access*, vol. 8, pp. 77 833–77 842, 2020, Conference Name: IEEE Access.

[215] Á. Palomares-Caballero, A. Alex-Amor, P. Escobedo, J. Valenzuela-Valdés, and P. Padilla, "Low-Loss Reconfigurable Phase Shifter in Gap-Waveguide Technology for mm-Wave Applications", *IEEE Transactions on Circuits and Systems II: Express Briefs*, vol. 67, no. 12, pp. 3058–3062, Dec. 2020, tex.ids= palomares-caballeroLowLossReconfigurablePhase2020a conferenceName: IEEE Transactions on Circuits and Systems II: Express Briefs.

[216] Z. Rahimian Omam, W. M. Abdel-Wahab, A. Pourziad, S. Nikmehr, A. Palizban, S. Gigoyan, and S. Safavi-Naeini, "Tunable Substrate Integrated Waveguide Phase Shifter Using High Dielectric Constant Slab", *IEEE Microwave and Wireless Components Letters*, vol. 30, no. 5, pp. 485–488, May 2020, Conference Name: IEEE Microwave and Wireless Components Letters.

[217] Á. Palomares-Caballero, A. Alex-Amor, P. Padilla, and J. F. Valenzuela-Valdés, "Reconfigurable Phase Shifter in Waveguide Technology Based on Glide-Symmetric Holey Structures", in *2021 15th European Conference on Antennas and Propagation (EuCAP)*, tex.ids= palomares-caballeroReconfigurablePhaseShifter2021, Mar. 2021, pp. 1–4.

[218] Y.-M. Yang, C.-W. Yuan, G.-X. Cheng, and B.-L. Qian, "Ku-Band Rectangular Waveguide Wide Side Dimension Adjustable Phase Shifter", *IEEE Transactions on Plasma Science*, vol. 43, no. 5, pp. 1666–1669, May 2015, Conference Name: IEEE Transactions on Plasma Science.

[219] D. Sánchez-Escuderos, J. I. Herranz-Herruzo, M. Ferrando-Rocher, and A. Valero-Nogueira, "Mechanical phase shifter in gap-waveguide technology", in *2020 14th European Conference on Antennas and Propagation (EuCAP)*, Mar. 2020, pp. 1–5.

[220] H. Abdollahy, A. Farahbakhsh, and M. H. Ostovarzadeh, "Mechanical reconfigurable phase shifter based on gap waveguide technology", en, *AEU - International Journal of Electronics and Communications*, vol. 132, p. 153 655, Apr. 2021, tex.ids= abdollahyMechanicalReconfigurablePhase2021, abdollahyMechanicalReconfigurablePhase2021a.

[221] F. Ghasemifard, F. Mesa, G. Valerio, and O. Quevedo-Teruel, "Propagation Characteristics in Substrate Integrated Holey Metasurfaces", in *2020 14th European Conference on Antennas and Propagation (EuCAP)*, tex.ids= ghasemifardPropagationCharacteristicsSubstrate2020a, Mar. 2020, pp. 1–4.

[222] R. Hamarneh, O. Zetterstrom, and O. Quevedo-Teruel, "Glide-Symmetric Luneburg Lens Using Substrate-Integrated-Holes for 5G Communications at Ka-Band", in *2020 14th European Conference on Antennas and Propagation (EuCAP)*, tex.ids= hamarnehGlideSymmetricLuneburgLens2020a, Mar. 2020, pp. 1–5.

[223] O. Zetterstrom and O. Quevedo-Teruel, "Metasurface Luneburg Lens Antenna Implemented with Substrate-Integrated-Holes at Ka-Band", in *2021 15th European Conference on Antennas and Propagation (EuCAP)*, tex.ids= zetterstromMetasurfaceLuneburgLens2021, Mar. 2021, pp. 1–3.

[224] F. Xu and K. Wu, "Guided-wave and leakage characteristics of substrate integrated waveguide", *IEEE Transactions on Microwave Theory and Techniques*, vol. 53, no. 1, pp. 66–73, Jan. 2005, Conference Name: IEEE Transactions on Microwave Theory and Techniques.

[225] D. Sievenpiper, L. Zhang, R. Broas, N. Alexopolous, and E. Yablonovitch, "High-impedance electromagnetic surfaces with a forbidden frequency band", *IEEE Transactions on Microwave Theory and Techniques*, vol. 47, no. 11, pp. 2059–2074, Nov. 1999, Conference Name: IEEE Transactions on Microwave Theory and Techniques.

[226] P.-S. Kildal, A. Zaman, E. Rajo-Iglesias, E. Alfonso, and A. Valero-Nogueira, "Design and experimental verification of ridge gap waveguide in bed of nails for parallel-plate mode suppression", *Antennas Propagation IET Microwaves*, vol. 5, no. 3, pp. 262–270, Feb. 2011, Conference Name: Antennas Propagation IET Microwaves.

[227] F. Capolino, D. R. Jackson, D. R. Wilton, and L. B. Felsen, "Comparison of Methods for Calculating the Field Excited by a Dipole Near a 2-D Periodic Material", *IEEE Transactions on Antennas and Propagation*, vol. 55, no. 6, pp. 1644–1655, Jun. 2007, Conference Name: IEEE Transactions on Antennas and Propagation.

[228] P. Baccarelli, C. Di Nallo, S. Paulotto, and D. Jackson, "A full-wave numerical approach for modal analysis of 1-D periodic microstrip structures", *IEEE Transactions on Microwave Theory and Techniques*, vol. 54, no. 4, pp. 1350–1362, Jun. 2006, Conference Name: IEEE Transactions on Microwave Theory and Techniques.

[229] M. Khayat and D. Wilton, "Numerical evaluation of singular and near-singular potential Integrals", *IEEE Transactions on Antennas and Propagation*, vol. 53, no. 10, pp. 3180–3190, Oct. 2005, Conference Name: IEEE Transactions on Antennas and Propagation.

[230] M. A. Khayat, D. R. Wilton, and P. W. Fink, "An Improved Transformation and Optimized Sampling Scheme for the Numerical Evaluation of Singular and Near-Singular Potentials", *IEEE Antennas and Wireless Propagation Letters*, vol. 7, pp. 377–380, 2008, Conference Name: IEEE Antennas and Wireless Propagation Letters.

[231] G. Valerio, P. Baccarelli, P. Burghignoli, and A. Galli, "Comparative Analysis of Acceleration Techniques for 2-D and 3-D Green's Functions in Periodic Structures Along One and Two Directions", *IEEE Transactions on Antennas and Propagation*, vol. 55, no. 6, pp. 1630–1643, Jun. 2007, tex.ids= valerioComparativeAnalysisAcceleration2007 conferenceName: IEEE Transactions on Antennas and Propagation.

[232] G. Valerio, A. Galli, D. R. Wilton, and D. R. Jackson, "An enhanced integral-equation formulation for accurate analysis of frequency-selective structures", *International Journal of Microwave and Wireless Technologies*, vol. 4, no. 3, pp. 365–372, Jun. 2012, Publisher: Cambridge University Press.

[233] W. Ko and R. Mittra, "Implementation of Floquet boundary condition in FDTD for FSS analysis", in *Proceedings of IEEE Antennas and Propagation Society International Symposium*, Jun. 1993, 14–17 vol.1.

[234] F. Mesa, R. Rodríguez-Berral, and F. Medina, "Considerations on the Usage of Transmission Matrices to Study the Dispersion Behavior of Glide-Symmetry Structures", in *2019 13th European Conference on Antennas and Propagation (EuCAP)*, tex.ids= mesaConsiderationsUsageTransmission2019a, Mar. 2019, pp. 1–4.

[235] F. Mesa, R. Rodríguez-Berral, and F. Medina, "On the Computation of the Dispersion Diagram of Symmetric One-Dimensionally Periodic Structures", *Symmetry*, vol. 10, no. 8, p. 307, Aug. 2018, tex.ids= mesaComputationDispersionDiagram2018a, mesaComputationDispersionDiagram2018b number: 8 publisher: Multidisciplinary Digital Publishing Institute.

[236] Q. Chen, F. Mesa, X. Yin, and O. Quevedo-Teruel, "Accurate Characterization and Design Guidelines of Glide-Symmetric Holey EBG", *IEEE Transactions on Microwave Theory and Techniques*, vol. 68, no. 12, pp. 4984–4994, Dec. 2020, tex.ids= chenAccurateCharacterizationDesign2020 conferenceName: IEEE Transactions on Microwave Theory and Techniques.

[237] M. Bagheriasl and G. Valerio, "Bloch Analysis of Electromagnetic Waves in Twist-Symmetric Lines", *Symmetry*, vol. 11, no. 5, p. 620, May 2019, tex.ids= bagheriaslBlochAnalysisElectromagnetic2019a number: 5 publisher: Multidisciplinary Digital Publishing Institute.

[238] W. C. Hahn, "A New Method for the Calculation of Cavity Resonators", en, *Journal of Applied Physics*, vol. 12, no. 1, pp. 62–68, Jan. 1941.

[239] S. Cohn, "Analysis of a Wide-Band Waveguide Filter", *Proceedings of the IRE*, vol. 37, no. 6, pp. 651–656, Jun. 1949, Conference Name: Proceedings of the IRE.

[240] F. W. J. Olver, D. W. Lozier, R. F. Boisvert, and C. W. Clark, *NIST Handbook of Mathematical Functions Paperback and CD-ROM*, Anglais. Cambridge ; New York: Cambridge University Press, May 2010.

[241] D. Zwillinger, *Table of Integrals, Series, and Products*, 7th ed. Burlington: Elsevier, 2007, OCLC: 703855094.

[242] P. Christiano, "Inverse Property of a Zero-Checkerboard Matrix", *Journal of Applied Mechanics*, vol. 37, no. 1, pp. 192–192, Mar. 1970, Publisher: American Society of Mechanical Engineers Digital Collection.

[243] D. K. Salkuyeh and F. P. A. Beik, "An Explicit Formula for the Inverse of Arrowhead and Doubly Arrow Matrices", *International Journal of Applied and Computational Mathematics*, vol. 4, no. 3, p. 96, May 2018.

[244] D. R. Smith, S. Schultz, P. Markoš, and C. M. Soukoulis, "Determination of effective permittivity and permeability of metamaterials from reflection and transmission coefficients", *Physical Review B*, vol. 65, no. 19, p. 195 104, Apr. 2002, Publisher: American Physical Society.